HARVARD
Kenneth C. Griffin

GRADUATE SCHOOL
OF ARTS AND SCIENCES

THESIS ACCEPTANCE CERTIFICATE

The undersigned, appointed by the

Department of Physics

have examined a dissertation entitled

Laser Cooling, Optical Trapping, and Quantum Control of Polyatomic Molecules

presented by Nathaniel Vilas

candidate for the degree of Doctor of Philosophy and hereby certify that it is worthy of acceptance.

Signature _____

Typed name: Prof. John Doyle

Signature _____

Typed name: Prof. Kang-Kuen Ni

Signature _____

Typed name: Prof. Susanne Yelin

Date: April 17, 2025

Laser Cooling, Optical Trapping, and Quantum Control of Polyatomic Molecules

A DISSERTATION PRESENTED
BY
NATHANIEL VILAS
TO
THE DEPARTMENT OF PHYSICS

IN PARTIAL FULFILLMENT OF THE REQUIREMENTS
FOR THE DEGREE OF
DOCTOR OF PHILOSOPHY
IN THE SUBJECT OF
PHYSICS

HARVARD UNIVERSITY
CAMBRIDGE, MASSACHUSETTS
APRIL 2025

©2025 – Nathaniel Vilas
all rights reserved.

Thesis advisor: Professor John M. Doyle Nathaniel Vilas

Laser Cooling, Optical Trapping, and Quantum Control of Polyatomic Molecules

Abstract

Polyatomic molecules contain diverse structures – including rotational and vibrational degrees of freedom, nuclear and electronic spins, and electric dipole moments – that make them promising for a range of quantum science applications. These include quantum information science, quantum simulation, studies of ultracold collisions and ultracold chemistry, and precision searches for physics beyond the Standard Model. However, maximizing the potential of polyatomic molecules for these applications requires them to be cooled to ultracold temperatures (<1 mK), trapped in three dimensions, and controlled at the single quantum state level. Significant progress has been made with diatomic molecules over the last fifteen years, but the increased complexity of polyatomic species (defined as molecules containing more than two atoms) makes them more challenging to control at the same level.

In this thesis, we describe our work bringing a linear triatomic molecule, calcium monohydroxide (CaOH), into the quantum regime. We demonstrate laser cooling of CaOH molecules to microkelvin temperatures, confinement in a magneto-optical trap (MOT), and loading of conservative optical dipole traps and optical tweezer arrays. We characterize the lifetime of low-lying vibrational states of CaOH in optical traps, including the vibrational bending mode, whose parity-doublet states are a key resource for many applications. Next, we develop techniques for preparing CaOH molecules in a single internal quantum state and for coherently manipulating

the internal state with microwave and radio-frequency fields. We also show that we can nondestructively and state-selectively detect trapped CaOH molecules, including single molecules in optical tweezers.

We demonstrate the applicability of these tools to applications including precision measurements, quantum information science, and ultracold collisions. We establish a method for future CP-violating physics searches with optically trapped polyatomic molecules, by identifying states that are sensitive to the electron electric dipole moment (eEDM) and showing that these states have long coherence times in CaOH. We identify potential qubit states in the CaOH bending mode and show that they can be coherently controlled at the single-molecule level in an optical tweezer array. Finally, we observe and characterize single quantum-state-controlled collisions between ultracold CaOH molecules, and identify states in the bending mode that could potentially be used for evaporative cooling to quantum degeneracy.

Compared to linear triatomic molecules, nonlinear molecules contain even more structures that can be harnessed for quantum science applications, at the cost of making them even more challenging to cool and control. Towards this goal, in this thesis we describe work demonstrating 1D laser cooling of a beam of $CaOCH_3$, a symmetric top molecule. This contributes to a growing body of evidence that complex polyatomic molecules could soon be cooled, trapped, and controlled at ultracold temperatures.

Contents

Title **i**

Copyright **ii**

Abstract **iii**

Contents **v**

Dedication **ix**

Citations to Previous Work **x**

Acknowledgments **xii**

1 Introduction **1**
- 1.1 Towards quantum control of complex quantum objects . . . 3
- 1.2 Applications of ultracold polyatomic molecules . . . 5
- 1.3 Methods for creating cold and ultracold molecules . . . 17
- 1.4 Laser cooling of molecules . . . 22
- 1.5 Overview of this thesis . . . 26

2 CaOH Molecular Structure **28**
- 2.1 Overview . . . 29
- 2.2 Electronic structure . . . 30
- 2.3 Vibrational structure . . . 33
- 2.4 Rotation and spin . . . 41
- 2.5 Structure of states relevant to this work . . . 45
- 2.6 The $\widetilde{X}^2\Sigma^+$ ground state of CaOH . . . 52
- 2.7 The $\widetilde{A}^2\Pi$ excited state . . . 68
- 2.8 Electric dipole transitions . . . 84

3 A Cryogenic Buffer Gas Beam of CaOH **90**
- 3.1 Overview of the CaOH beam box . . . 91
- 3.2 Buffer gas cell and molecule production . . . 94
- 3.3 Chemically enhanced CaOH molecule production . . . 98

3.4 Modifications to the cell for radiative laser slowing . . . 103
3.5 Cell geometry optimization . . . 111
3.6 In search of the optimal MOT: techniques and observations . . . 118

4 A Closed Optical Cycle for CaOH Laser Cooling **122**
4.1 Optical cycling of molecules: overview . . . 124
4.2 Rovibronic branching . . . 127
4.3 Measurement of CaOH vibrational branching ratios . . . 141
4.4 Repumping scheme . . . 170

5 Radiative Slowing, Magneto-Optical Trapping, and Sub-Doppler Cooling of CaOH **174**
5.1 Vacuum apparatus . . . 175
5.2 Laser systems . . . 178
5.3 Radiative slowing . . . 187
5.4 Magneto-optical trapping . . . 212
5.5 Sub-Doppler cooling . . . 237
5.6 Blue-detuned conveyor-belt MOT . . . 246

6 Optical Trapping and Vibrational Lifetimes of CaOH **256**
6.1 Theory: optical dipole trapping of molecules . . . 257
6.2 Optical trapping of CaOH . . . 273
6.3 Transfer into the bending mode . . . 283
6.4 Vibrational state lifetimes . . . 286

7 Coherent Control of CaOH and the "eEDM Pathfinder" Experiment **301**
7.1 Overview: microwave manipulation of CaOH in the bending mode . . . 302
7.2 Experimental setup . . . 303
7.3 Microwave spectroscopy . . . 308
7.4 Optical pumping into a single hyperfine state . . . 311
7.5 Coherent state transfer . . . 318
7.6 The "EDM pathfinder" experiment . . . 320

8 An Optical Tweezer Array of CaOH **336**
8.1 Initial setup and challenges . . . 338
8.2 Wavelength dependence and excited state coupling . . . 348
8.3 Overview of the optimized experimental sequence . . . 356
8.4 Tweezer imaging . . . 358
8.5 Single quantum state control in optical tweezers . . . 365
8.6 Summary and outlook . . . 371

9 Controlled Collisions of Optically Trapped CaOH Molecules **372**
9.1 Overview of prior work . . . 374
9.2 Overview of the experiment . . . 376
9.3 Experimental setup . . . 378
9.4 Observation of collisions between CaOH molecules . . . 386
9.5 Single-state collisions in the vibrational bending mode . . . 395
9.6 Conclusion . . . 425

10 Direct Laser Cooling of Symmetric Top Molecules **427**
10.1 Overview of $CaOCH_3$ molecular structure . . . 429
10.2 Closed cycling transitions for symmetric tops . . . 436
10.3 Optical cycling in $CaOCH_3$ . . . 440
10.4 Sisyphus laser cooling of $CaOCH_3$ . . . 447
10.5 Conclusion and outlook . . . 459

11 Outlook **461**
11.1 Quantum science with CaOH . . . 462
11.2 Ultracold collisions with CaOH . . . 470
11.3 Improved cooling and state purity . . . 470
11.4 Towards laser cooling of more complex molecules . . . 472

Appendix A Matrix Elements **480**
A.1 Computational procedure . . . 481
A.2 Useful spherical tensor algebra results . . . 482
A.3 The $\widetilde{X}^2\Sigma^+$ state of CaOH . . . 489
A.4 The $\widetilde{A}^2\Pi$ state of CaOH . . . 503
A.5 Electric dipole transitions . . . 512
A.6 AC Stark shifts . . . 514

Appendix B Branching Ratio Calculations **537**
B.1 FCF calculations in the harmonic approximation . . . 540
B.2 Renner-Teller perturbation . . . 543
B.3 Fermi resonance . . . 551
B.4 Calculation results . . . 553

Appendix C Experimental Details **556**
C.1 Preparation of MOT and cooling light . . . 557
C.2 Experimental control . . . 564
C.3 Stability of the 1K system . . . 566

Appendix D Rate Equation Modeling of CaOH Internal State Dynamics **568**

D.1 Rate equation model of the vibrational lifetime measurement sequence 569
D.2 Vibrational lifetime fitting and results 575
D.3 Rate equations including collisions 579

Appendix E Optical Transitions in CaOH and $CaOCH_3$ **584**
E.1 Wavemeter offset 585
E.2 Observed optical transitions in CaOH 585
E.3 Spectroscopy of CaOH repumping transitions 585
E.4 Laser cooling transitions in $CaOCH_3$ 591

References **593**

To my parents, for all the opportunities you have provided me.

Citations to Previous Work

Portions of this thesis or results described herein have previously been published in the references below. Where appropriate, citations and acknowledgments are also provided in the body of the thesis for derivative or collaborative work.

1. D. Mitra, N. B. Vilas, C. Hallas, L. Anderegg, B. L. Augenbraun, L. Baum, C. Miller, S. Raval, and J. M. Doyle, "Direct Laser Cooling of a Symmetric Top Molecule," Science **369**, 1366 (2020).

2. L. Baum, N. B. Vilas, C. Hallas, B. L. Augenbraun, S. Raval, D. Mitra, and J. M. Doyle, "Establishing a nearly closed cycling transition in a polyatomic molecule," Phys. Rev. A **103**, 043313 (2021).

3. C. Zhang, B. L. Augenbraun, Z. D. Lasner, N. B. Vilas, J. M. Doyle, and L. Cheng, "Accurate prediction and measurement of vibronic branching ratios for laser cooling linear polyatomic molecules," J. Chem. Phys. **155**, 091101 (2021).

4. N. B. Vilas, C. Hallas, L. Anderegg, P. Robichaud, A. Winnicki, D. Mitra, and J. M. Doyle, "Magneto-optical trapping and sub-Doppler cooling of a polyatomic molecule," Nature **606**, 70-74 (2022).

5. C. Hallas, N. B. Vilas, L. Anderegg, P. Robichaud, A. Winnicki, C. Zhang, L. Cheng, and J. M. Doyle, "Optical trapping of a polyatomic molecule in an ℓ-type parity doublet state," Phys. Rev. Lett. **130**, 153202 (2023).

6. N. B. Vilas, C. Hallas, L. Anderegg, P. Robichaud, C. Zhang, S. Dawley, L. Cheng, and J. M. Doyle, "Blackbody thermalization and vibrational lifetimes of trapped polyatomic molecules," Phys. Rev. A **107**, 062802 (2023).

7. L. Anderegg, N. B. Vilas, C. Hallas, P. Robichaud, A. Jadbabaie, J. M. Doyle, and N. R. Hutzler, "Quantum control of trapped polyatomic molecules for eEDM searches," Science **382**, 665 (2023).

8. Benjamin L. Augenbraun, Loïc Anderegg, Christian Hallas, Zack D. Lasner, Nathaniel B. Vilas, and John M. Doyle, "Direct Laser Cooling of Polyatomic Molecules," in *Advances in Atomic, Molecular, and Optical Physics*, Vol. 72, pp. 89-182 (2023).

9. Nathaniel B. Vilas, Paige Robichaud, Christian Hallas, Grace K. Li, Loïc Anderegg, and John M. Doyle, "An optical tweezer array of ultracold polyatomic molecules," Nature **628**, 282-286 (2024).

10. Christian Hallas, Grace K. Li, Nathaniel B. Vilas, Paige Robichaud, Loïc Anderegg, and John M. Doyle, "High Compression Blue-Detuned Magneto-Optical Trap of Polyatomic Molecules," arXiv:2404.03636 (2024).

11. Nathaniel B. Vilas, Paige Robichaud, Christian Hallas, Junheng Tao, Loïc Anderegg, Grace K. Li, Hana Lampson, Lucie D. Augustovičová, John L. Bohn, and John M. Doyle, "Quantum-state-controlled collisions of ultracold polyatomic molecules." arXiv:2505.09592 (2025).

Acknowledgments

I AM INDEBTED to a huge number of people who helped me on this journey over the past seven years. First and foremost, I thank my advisor, John, for giving me so many opportunities over the years. You welcomed me into your lab even when I wasn't sure what research I wanted to pursue, and in hindsight I couldn't have imagined a better fit. I have learned so much from you, and about much more than just molecules and experimental physics.

I also thank Profs. Kang-Kuen Ni and Susanne Yelin for serving on my committee. Kang-Kuen: progress with ultracold molecules in your lab was a frequent source of inspiration during my PhD, and I have appreciated our conversations about molecules, your advice, and your support. Thank you, Susanne, for the valuable conversations – especially in recent years when you provided candid advice on my path after the PhD – and for somehow ending up in the same ski group as me nearly every year at the CUA retreat.

The CaOH experiment only functions because of the hard work and countless contributions of many students and postdocs, and none of the results in this thesis would have been possible without the whole team. Louis: thank you for laying the groundwork for the experiment, teaching me so much in my first two years of grad school, answering my incessant questions, and dragging us through our first efforts to laser cool CaOH. Christian: thank you for putting up with me since day one. Your contributions have been invaluable, including your expertise on key parts of the apparatus, your intense focus on critical projects, and your constant ideas and discussions. Debayan: thanks for your contributions to the CaOH experiment over the first few years, including

designing and building many of our most important lasers, electronics, and vacuum systems. Thanks, too, for helping inspire us to push further into the large-molecule frontier, and for acting as a social catalyst in the group. Loïc: thank you for bringing all your expertise over from the CaF side of the lab and driving our experiment forward much more rapidly than I thought possible. I learned so much from you about how to effectively and efficiently run complicated experiments, and I doubt that half as much would have been accomplished without you there. Paige: thanks for all your key work over the last few years, including designing and building the tweezer system, pushing forward our understanding of beam boxes, and being the only one in at a reasonable time to start taking data every morning. I know the experiment will be in good hands with you as senior grad student in the coming years. I also thank Shivam, Andrew, Grace, Junheng, Hana, and Giseok for all your contributions to both the science and the culture of the experiment.

The work presented in this thesis was boosted tremendously by the work of our collaborators. Lan Cheng and Chaoqun Zhang showed that *ab initio* calculations can capture CaOH properties with, frankly, an incredible level of accuracy. Nick Hutzler and Arian Jadbabaie helped us discover how to use optically trapped polyatomic molecules for precision measurements, and Arian in particular brought a huge amount of enthusiasm to the project during his extended Harvard visit. John Bohn and Lucie Augustovičová exercised incredible patience in dealing with my barrage of collision-related questions and emails over the past year, and their calculations significantly aided our understanding of polyatomic molecular collisions.

I thank many others at Harvard without whom the experiments would not be possible, including Jim MacArthur in the electronics shop and Stan Cotreau, Steve Sansone, Andy DiMambro, and Alejandro Lopez in the machine shop. Thanks to Erica Mantone for your heroic (and often thankless) work keeping the group afloat daily, and to Adam Ackerman, Silke Exner, Lisa Cacciabaudo, and many others working behind the scenes so that we have less

to worry about.

Being a member of the Doyle group has been a distinct pleasure, and I have appreciated all the support – scientific and otherwise – from group members on every experiment. I especially thank Ben and Zack for being there to discuss molecular structure, and Yicheng for his endless patience with my questions and for sharing his incredible technical knowledge with me and the group. I have also enjoyed the social environment in the Doyle group over the past few years, with summer Friday afternoon "group meetings," daily lunch conversations, the fantasy football league, birthday donuts, and Abdullah's milk-laden emails being just a few highlights.

Outside of the Doyle group, I am grateful to have been part of a grad student cohort composed of many wonderful human beings. I will fondly remember our collective effort to put together what likely ended up being the last Harvard physics puppet show ever, with the additional hurdles thrown our way by the COVID shutdown making it all the more momentous. It has been bittersweet to see everyone move on to the next adventure.

I am grateful for the friends I made during my time at Harvard. Lewis, Jonathan (Z), and Nick: thanks for overriding my vote and letting me move in with you at the inaugural BBB. My time living with you was a highlight of the early years of grad school, and I am especially thankful to you for putting up with me during the COVID shutdown and helping to inject plenty of fun into the situation. Jonathan D: thanks for being another great roommate, cooking (and smoking!) fantastic meals for us, and for sharing an enjoyment of BSO concerts with me. I certainly hope to remain lifelong friends with the four of you and the rest of the "extended universe": DaLi, Mar, Eve, Cindy, and Alba. Thank you also to Matthew, who has been a near-constant presence in my life since our time together at Williams. Your regular prodding – e.g. to get me outside for a bike ride or a skate – has helped me maintain some sanity through grad school.

Thanks to Tiku Majumder for mentoring me at Williams and helping me on the path towards physics grad-

uate school. Your periodic email updates – about Williams physics or the latest Berkshire symphony program – are always a pleasure, along with the Williams reunions you've helped organize at AMO conferences. Thanks also to Steve Naculich, who proved to be a role model for me at a very young age, showing me (unintentionally) that because I played piano, perhaps I should also study physics...

I am endlessly grateful for my family. Mom and dad: thank you for the love and support you provided, and the sacrifices you made, over the last thirty years. I don't take the opportunities I have had for granted, and this PhD was only possible because of them. It has been a special privilege to have the three-hour train ride to Maine available as an outlet on any given weekend. Hannah: thanks for your love and support, and for showing me that it's actually possible to get two degrees, do a Fulbright, and work at least three jobs over the time it took me to complete one PhD.

Finally, I thank Hanna for all the joy you have brought me over the last four and a half years. Meeting you was unquestionably the highlight of my time as a graduate student, and you have improved my life immeasurably. Thanks for putting up with all the late dinners, and being there to make me smile and laugh after even the toughest days at work. I can't wait for our next chapter together in Berkeley.

1

Introduction

Since the advent of laser cooling [1, 2], cold atoms have become a highly successful platform for a wide range of scientific goals. These include quantum computation [3, 4], quantum simulation [5, 6], quantum gas studies [7, 8], optical atomic clocks [9], quantum-enhanced sensing [10], and precision searches for physics beyond the Standard Model [11]. The key ingredients that have made cold and ultracold atoms so successful at these

goals are (1) the ability to cool and trap them at microkelvin temperatures (or lower), so that they can be held in place and interrogated for long periods of time, and (2) the ability to isolate them from the environment and coherently control their internal states with very high fidelity. Over the past few decades, there has been a push towards higher levels of control, to the point that individual atoms can now be prepared and manipulated in single internal and motional quantum states. Using such exquisitely controlled single atoms, complex quantum systems can be built from the ground up and harnessed for diverse science goals.

While useful complex systems can be built up from many atoms, an alternate direction is to add more complexity to the internal degrees of freedom of each constituent particle. This both increases the diversity of applications available from the single-particle physics, and also exponentially increases the size of the Hilbert space once interactions are introduced and systems are scaled up. Molecules offer this opportunity due to their abundant vibrational, rotational, and spin degrees of freedom. However, these same degrees of freedom make cooling and controlling them dramatically more challenging. Over the last 20 years, significant progress has been made in overcoming these challenges with diatomic molecules, both by direct laser cooling [12–14] and by coherent association of laser-cooled atoms [15–17]. Polyatomic molecules (defined in this thesis as molecules containing more than two atoms) are the next frontier, with the wide variety of structures in these molecules offering a tantalizing opportunity for future scientific progress.

In this thesis, we present our contributions to the new field of ultracold, quantum-controlled polyatomic molecules. We describe our work laser cooling and trapping polyatomic molecules at ultracold temperatures (<1 mK), focusing on the linear triatomic molecule CaOH. Using an optical cycling scheme capable of scattering an average of more than 10,000 optical photons from CaOH molecules, we demonstrate the first magneto-optical trap (MOT) of a polyatomic molecule, cool trapped CaOH molecules to below 100 μK, and load them

into conservative optical traps. We also demonstrate the ability to load and control single CaOH molecules in optical tweezers. We develop a set of tools for controlling the internal quantum states of optically trapped CaOH molecules. These tools are used to demonstrate applications of ultracold polyatomic molecules in quantum information science, precision measurement, and ultracold collisions. Finally, we demonstrate 1D laser cooling of $CaOCH_3$ molecules, suggesting that even larger polyatomic molecules could be cooled, trapped, and harnessed for quantum science applications in the future.

1.1 Towards quantum control of complex quantum objects

Over the past several decades, it has proven advantageous to develop control techniques for increasingly complex atomic and molecular systems. Extending the laser cooling toolbox from alkali atoms to alkaline earth [18, 19], lanthanide [18, 20, 21], and transition metal species [22, 23] has broadened the scope of applications available, including optical atomic clocks [9], high-fidelity atomic quantum information storage and processing [24–26], and quantum simulation with strong magnetic dipole interactions [27, 28]. Extending the AMO toolbox to diatomic molecules has likewise opened up an array of science possibilities (described more below). There are, of course, difficulties associated with controlling more complex systems, but these generally have led to novel – and sometimes unexpected – opportunities. A main challenge in controlling molecules is taming their rotational and vibrational degrees of freedom. However, these same degrees of freedom are key to the diverse applications for which molecules could be used once cooled and trapped at ultracold temperatures.

As we extend cooling and quantum control techniques from atoms to diatomic molecules and then to polyatomic molecules, it is natural to question the limits of quantum control. As molecules become larger they begin

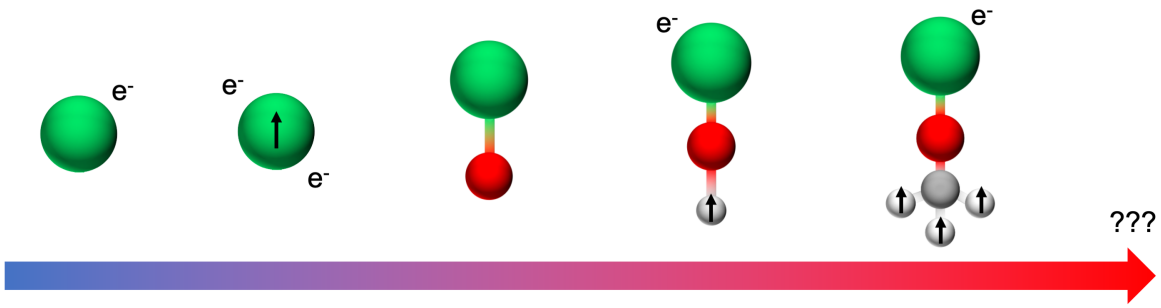

Figure 1.1: Towards quantum control of objects with increasing complexity. Increasing the number of degrees of freedom – electrons, nuclear spins, rotations, vibrations, etc. – makes control more challenging but also enables a broad range of applications. In this thesis, we focus on CaOH (second from right), while presenting first steps towards full control of $CaOCH_3$ (right).

to look more like macroscopic objects, and it will become harder to control all quantum degrees of freedom while fighting off decoherence, thermalization, and the onset of classical physics. While it is now known that atoms and certain diatomic molecules [17, 29–32] are amenable to full quantum control, we are only at the early stages of understanding the limits of this controllability. A number of proposals have suggested the possibility of laser cooling and controlling polyatomic molecules, ranging from linear triatomic molecules up to large organic molecules and even molecules bound to surfaces [33–41]. As we push further into this limit, the density of states dramatically increases, making it more difficult to resolve quantum states and quantum behavior, while potentially giving the environment more opportunities to cause decoherence.[1]

In this work, we show that laser cooling and quantum control are both possible for a triatomic molecule, CaOH, demonstrating the ability to scatter >10000 optical photons from CaOH and control single internal quantum states over timescales of hundreds of milliseconds [42–46]. However, even at this molecular size we have observed limitations due to coupling to the room temperature environment [44], which motivates cool-

[1] On the flip slide, the huge number of states in molecules also provides an opportunity to find states that are especially immune to decoherence.

ing to cryogenic temperatures in future work. Additionally, we have demonstrated that a six-atom molecule, $CaOCH_3$, can be optically manipulated to the point where 100 photons can be rapidly scattered, enabling one-dimensional laser cooling [47]. This is a promising first step towards quantum control of molecules with significant complexity. It will be interesting to pursue control of even larger molecules, in search of insight into the ways in which quantum control is challenged as objects become more macroscopic. Early experimental work in this direction has shown both promise [48–50] and challenges [51, 52] for control of complex polyatomic molecules.

1.2 Applications of ultracold polyatomic molecules

Molecules are appealing candidates for applications including quantum information science [53], quantum simulation [54, 55], studies of cold and ultracold collisions and chemistry [56–58], and precision searches for new physics beyond the Standard Model [11], among others [59]. Key to the appeal of molecular systems for many of these applications are their electric dipole moments, which enable strong, long-range, and potentially highly coherent dipolar interactions between molecules in their electronic ground state. More generally speaking, the large number of degrees of freedom present in molecules – most notably their rotational structure – can be used as a tool for a variety of scientific goals. Conversely, much of the complexity (both desired and undesired) that arises in molecular systems occurs precisely because of the high density of states inherent to molecules.

There is a large body of experimental work demonstrating the variety of scientific questions and technological applications that can can be studied and advanced with *diatomic* molecules. These have included quantum simulation [60–62], quantum information science [31, 32, 63, 64], ultracold collisional studies [65–74], collisional

engineering and evaporative cooling [29, 75–79], ultracold chemistry [80–82], and precision searches for physics beyond the Standard Model [83–87].

Polyatomic molecules, compared to diatomic molecules, possess even more degrees of freedom, many of which have no analogue in atoms or diatomic molecules. For example, polyatomic molecules generically have three nonzero moments of inertia, increasing the richness of their rotational structure (and, as we will see, the ease with which their electric dipole moments can be aligned). The density of vibrational states also increases rapidly with molecule size, which can be considered a hindrance for cooling and quantum control, but can also potentially be harnessed for science applications [88–90]. The increasing number of atoms in polyatomic molecules admits the possibility of large internal nuclear spin Hilbert spaces, where one can imagine using techniques similar to those of early NMR quantum computing [91], but in ultracold molecules with external control. More broadly, the wide variety of structures and symmetries available when considering polyatomic molecules admits the possibility of being to be able to choose a molecular geometry that is best suited to the desired application.

1.2.1 Parity doublet structure in polyatomic molecules

One especially appealing feature of polyatomic molecules is the existence of "parity-doublet" states in the ground electronic manifold. These are nearly-degenerate pairs of quantum states with opposite parity that can be mixed by a small DC electric field (often $\lesssim$ 100 V/cm depending on the molecule), enabling the molecule to be easily polarized in the laboratory frame. Because this method of polarizing the molecule does not mix end-over-end rotational levels (which requires much larger electric fields, typically >1 kV/cm), the polarized molecules contain states with positive, negative, and near-zero lab-frame dipole moment (see Fig. 1.2(a)).

This structure is a general feature of molecules that have a nonzero projection of the total angular momentum

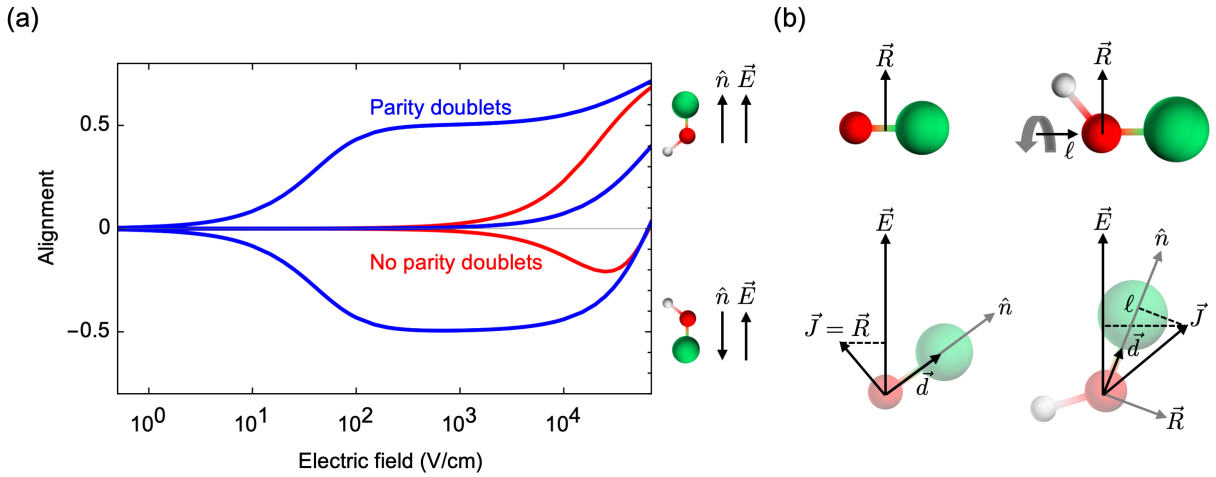

Figure 1.2: Parity doublet structure and molecular polarization. (a) Molecular polarization as a function of applied laboratory electric field. Molecules with parity doublet states are aligned at low electric fields and have states with positive, negative, and zero dipole moment. By comparison, molecules without parity doublet structure are not aligned until end-over-end rotational states are mixed, which occurs at much higher fields. The molecular parameters in this plot are those of CaOH. (b) Alignment of molecules with angular momentum parallel to the dipole moment. In diatomic molecules without parity doublets, the rotational angular momentum $\vec{R}$ is perpendicular to the dipole moment $\vec{d}$. As the molecule (with total angular momentum $\vec{J} = \vec{R}$) precesses about the electric field $\vec{E}$, the dipole moment averages to zero in the laboratory frame. In molecules with angular momentum along the internuclear axis (e.g. vibrational angular momentum ℓ in linear triatomics), there is a nonzero projection of $\vec{J}$ onto the molecular axis. Therefore, the dipole moment averages to a nonzero value as the molecule precesses about the electric field.

along the molecule-frame dipole moment. The angular momentum quantum numbers of such a molecule are J, the total angular momentum, K, the projection of J onto the molecular symmetry axis, and M, the projection of J onto the laboratory Z axis. As long as $\langle K \rangle \neq 0$, there will be a nonzero dipole moment in the laboratory frame, as shown in Fig. 1.2(b). States with $K \neq 0$ are universally present in polyatomic molecules: linear polyatomic molecules have angular momentum $K = \ell$ about the internuclear axis in vibrational bending modes, while nonlinear polyatomic molecules have nonzero moments of inertia about the symmetry axis even in the electronic and vibrational ground state.

At zero electric field, there are two non-degenerate, opposite-parity eigenstates $2^{1/2}|\pm\rangle = |J, K, M\rangle \pm (-1)^{J-K}|J, -K, M\rangle$, both of which have $\langle K \rangle = 0$ and are not polarized. However, small electric fields will mix these parity doublet states and begin to align the molecule, as described below. The degeneracy of the parity doublet states is lifted by a range of mechanisms, including Coriolis interactions, nuclear spin-rotation interactions, hyperfine interactions, or molecular asymmetry [92]. Among the molecule classes that have been considered for direct laser cooling [33, 34, 37], linear polyatomic molecules typically have parity doublet splittings of tens of MHz [93, 94], symmetric top molecules have parity doublet splittings smaller than 1 MHz [95], and near-prolate asymmetric top molecules typically have splitting on the order of 100 MHz.

For the parity doublet states $|\pm\rangle$ described above, the Hamiltonian under the influence of an external DC electric field $\mathcal{E}$ is [96]

$$H = \begin{pmatrix} -\hbar\Delta/2 & -d\mathcal{E} \\ -d\mathcal{E} & \hbar\Delta/2 \end{pmatrix} \tag{1.1}$$

where Δ is the parity doublet splitting and

$$d\mathcal{E} \equiv \langle +|\vec{d}\cdot\vec{\mathcal{E}}|-\rangle = d_0\mathcal{E}\frac{KM}{J(J+1)} \tag{1.2}$$

where d_0 is the permanent dipole moment of the molecule. The energy eigenvalues are therefore

$$E_\pm = \pm\frac{1}{2}\hbar\Delta\left[1+4\left(\frac{d\mathcal{E}}{\hbar\Delta}\right)^2\right]^{1/2} \tag{1.3}$$

At low electric fields $d\mathcal{E}/\hbar\Delta \ll 1$ the states split apart quadratically, while at high electric fields $d\mathcal{E}/\hbar\Delta \gg 1$ the molecule becomes aligned in the laboratory frame and follows linear Stark shifts:

$$E \approx -d_0\mathcal{E}\frac{KM}{J(J+1)}, \tag{1.4}$$

where K and M are signed quantities. The structure of the molecule in this "polarized" regime is applicable to a number of applications.

1.2.2 Polyatomic molecules for quantum science

Ultracold molecules are a promising platform for quantum simulation and quantum information processing due to their large electric dipole moments and the intrinsically long coherence times achievable in low-lying rotational states. Heteronuclear molecules have molecule-frame electric dipole moments, typically on the order of several debye (D), that can be accessed in the electronic ground state, eliminating the need for the short-lived excited electronic levels often employed in atomic systems. The molecules may interact via the electric dipole-dipole in-

teraction, whose long-range and anisotropic behavior enables access to a diverse variety of Hamiltonians for quantum simulation, as well as enabling entangling gates for quantum information applications. While not always required to achieve interactions, it can be advantageous to realize a molecular dipole moment in the laboratory frame by aligning the atoms or molecules with an external electric field (either DC or microwave). See Ref. [55] for a recent review on quantum simulation and quantum information applications for ultracold polar molecules.

Quantum information science

Since the seminal proposal by DeMille [53], ultracold polar molecules have generated significant interest as a platform for quantum information applications [97–99]. The key element of these proposals is the fact that polar molecules have many long-lived rotational and vibrational degrees of freedom which enable storage of quantum information, while dipole-dipole interactions enable transfer of information and entanglement between individual molecules. Recent progress toward this goal has been realized with diatomic molecules, with dipolar coupling and entanglement demonstrated between diatomic molecules trapped in optical tweezer arrays [31, 32, 63, 64].

The linear Stark shifts discussed above for polyatomic molecules make them especially appealing for certain quantum computing and entanglement schemes [100–102]. There have been several proposals to use the structure of polyatomic molecules in the linear Stark shift regime to encode qubit states and implement entangling gates using long-range dipolar interactions [100, 101]. For example, Ref. [100] identified two sets of polarized states that could be used as qubits in a quantum computer, and proposed a method for realizing a CNOT entangling gate between two molecules. It was also pointed out that polyatomic molecules in this linear Stark shift regime share certain similarities with the NMR quantum computing platform [103], offering the possibility of mapping techniques over that community. However, molecules in optical tweezer arrays offer the possibility of

isolating individual qubits and controlling entanglement on demand more cleanly and more scalably than has been done with liquid-phase NMR.

In Ref. [101], a slightly different quantum computing scheme was proposed that also harnesses the parity-doublet structure of polyatomic molecules. Here, the qubit states are contained within the $M = 0$ manifold, which eliminates first-order electric field sensitivity, thereby improving robustness to external perturbations. Interactions are switched on using a third state in either the $M = +1$ or $M = -1$ manifold, and entanglement is generated using an interaction blockade mechanism. Using the linear Stark shift structure to switch dipole-dipole interactions on and off in this manner is a key advantage of polyatomic molecules. While the dipolar blockade interaction will be quite weak, it would also be possible to use resonant dipolar interactions between polarized states to implement CZ gates.

A third option is to use parity-doublet states at zero electric field to encode qubits. These states can interact using dipolar spin-exchange interactions like those observed in diatomic molecules [31, 32, 63]. However, these states differ only in their parity, with all other quantum numbers being identical, so there is the possibility for improved coherence in these states compared to the rotational qubit states available in diatomic molecules.

The large number of rotational and vibrational degrees of freedom in polyatomic molecules enhances the potential of polyatomic molecules for quantum information applications. For instance, error-correcting logical qubits could be constructed from coherent superpositions of rotational states, as proposed in Ref. [104]. This could represent a more hardware-efficient approach to logical quantum computation compared to current protocols that encode logical information using large numbers of physical qubits [105]. The large number of internal states in polyatomic molecules could also make them uniquely amenable to "qudit" schemes where multiple bits of information are stored in the same molecule, as described by [88, 99]. Such schemes could significantly

increase the speed and fidelity of molecular quantum computers by performing the majority of gates using single-molecule operations, and only coupling molecules via dipole-dipole interactions when necessary.

One challenge of working with polar molecules (including polyatomics) is that gate times are relatively slow due to the ∼kHz-level interactions between molecules in optical tweezers. One possibility for overcoming this challenge is to use Rydberg atoms to mediate gates between polar molecules, which would significantly speed up entangling gate speeds [106, 107]. Performing quantum information storage and processing with arrays of polyatomic molecules, where each molecule is an error-corrected logical qubit and fast entangling gates are mediated via Rydberg atoms, could be an appealing goal for polyatomic molecule-based quantum computation. However, there are significant challenges for realizing this vision; for example, more work is required to determine how to perform entangling gates between single-molecule logical qubits or qudits.

Quantum simulation

The long range and anisotropic dipolar interactions between polar molecules lend themselves to quantum simulation applications, in particular to simulation of quantum magnetism models where molecules pinned in a lattice act as effective spins [57, 59]. See Ref. [108] for a review of this topic. To date, much of this work has been focused on diatomic molecules, which are naturally suited to simulation of Heisenberg XY models, as first demonstrated experimentally using KRb molecules [60]. In theoretical work, it was shown that microwave-dressed diatomic molecules with unpaired electron spins can be used to simulate even more general spin models [54], though the technical requirements of this proposal have not yet been realized in present day experiments.

Compared to diatomic molecules, polyatomic molecules are naturally suited to simulation of a greater diversity of quantum magnetism models [108–110]. For instance, the unique rotational structure of molecules with

parity doublet states enables simulation of XYZ spin models via microwave dressing [108]. Critically, the technical requirements of this proposal are significantly reduced compared to methods available for simulating an XYZ Hamiltonian with diatomic molecules, which requires more microwave frequencies, significantly smaller lattice spacings, and/or complex microwave pulse sequences [54, 61, 111]. Another benefit of large polyatomic molecules may be their small fine and hyperfine splittings, which can be made comparable to the dipole-dipole interaction energy at larger molecular spacings. For instance, operating in the regime where the dipolar interaction energy is comparable to the spin-rotation interaction energy in molecules with an unpaired spin would enable simulation of a diverse array of lattice spin models, as described in [54]. These small energy-level splittings could, however, present a challenge for achieving full control of individual quantum states in the molecule, e.g., due to off-resonant excitations during control pulses.

Perhaps the most natural application of the linear Stark shifts in polyatomic molecules is to simulate lattice spin models involving polarized, integer-spin dipoles [109]. The electric dipole moments in polar molecules enable interaction strengths that can be several orders of magnitude larger than in magnetic dipoles, which are currently used for similar studies [27, 28]. Importantly, this analogy can be extended to molecular states with arbitrarily large J, enabling quantum simulation of magnetic dipoles with integer spin $S = J$. These features could have interesting applications in simulation of lattice spin models as well as in the study of bulk dipolar gases (see [112] for a review on the subject), which have previously been studied using magnetic atoms with much smaller interaction energies.

1.2.3 Ultracold collisions and chemistry

While the collisional physics of ultracold atoms is relatively well understood [113], collisions between molecules are significantly more complex due to their strong electric dipole interactions and the large density of states involved.[2] Even for collisions between diatomic molecules, accurate modeling of short range potentials is challenging, with many models resorting to qualitative and/or statistical arguments about short range processes while accurately modeling the electric dipole interactions that occur at long range. It has widely been observed in experiments with ultracold diatomic molecules that collisions are reasonably well described by the universal loss picture [67–69, 74, 80]. In this model, molecules collide via dipolar interactions at long range, but any molecules that are transmitted through the long range potential are lost with a probability near unity at short range [114, 115]. The short range losses could arise from a number of mechanisms, including chemical reactions or the creation of long-lived complexes, which can collide again or be optically excited by trapping light [71, 72, 116–118]. A number of other phenomena have been observed in collisions of ultracold diatomic molecules, including scattering resonances (shape resonances and Feshbach resonances) [73], and tuning of collision rates by aligning the molecular dipole moment [65, 66, 70]. Finally, there is a large body of work engineering long-range dipolar interactions to suppress collisional loss by "shielding" the molecules from interacting at short range. These include electrostatic [75, 76, 78, 119] and microwave shielding [29, 77, 79, 120] methods. These have recently been used to achieve quantum degenerate gases of polar diatomic molecules [29, 75, 79]. See Refs. [56, 58, 59, 118, 121] for a number of reviews on cold and ultracold molecular collisions.

[2] Rigorously speaking, "ultracold" collisions occur when only a single partial wave contributes, which often does not happen until temperatures approach 1 μK. Nonetheless, the ultracold regime is often more loosely defined to occur at temperatures $\lesssim$1 mK. "Cold" collisions are anything hotter than ultracold and $\lesssim$1 K [56, 59].

Much less is known about collisions of polyatomic molecules. Collisions between polyatomic molecules have not previously been observed at temperatures below 1 mK, and only a few studies exist in the cold temperature regime [122–124]. Compared to diatomic molecules, the short-range potentials are even more dense and complicated, suggesting that a universal loss picture will likely be applicable (see chapter 9 of this thesis). The long-range interactions, meanwhile, differ from diatomic molecules primarily due to the influence of parity-doublet structure. The collisional properties of parity doublet molecules have been extensively studied theoretically [125–131]. Along with having unique state dependence and electric field tuning properties, polar parity-doublet molecules are expected to exhibit field-linked resonances arising from weakly bound dimers supported by the long-range potential [126, 131–133], and to also potentially have states with favorable properties for evaporative cooling [130, 131]. In addition to evaporative cooling via direct molecule-molecule collisions (using a shielded interaction potential), the possibility exists to sympathetically cool polyatomic molecules via collisions with ultracold atoms [134–136] (as is already commonly done in the cold regime via buffer gas cooling [137, 138]).

At short range, studying ultracold collisions shifts from one of understanding dipolar interaction potentials to one of understanding ultracold chemistry. Classically, chemical reaction rates roughly follow the Arrhenius scaling $\sim e^{-E_a/k_B T}$, where E_a is the activation energy and T is the temperature. This would predict that reaction rates tend to zero as $T \to 0$ whenever there is a nonzero reaction barrier E_a. However, in the quantum regime this model breaks down due to the large de Broglie wavelength of the interacting particles. In this regime, quantum tunneling, reflection, and resonances can play a substantial role. Detailed studies of reactions between diatomic, bialkali molecules have recently been performed at ultracold temperatures by directly detecting reaction products. These have enabled detailed characterization of the state-dependence and coherence properties of ultracold chemical reactions [81, 82, 139]. Extending these studies to polyatomic molecules would begin to shed

light on more complex chemical reaction processes, where multiple reaction pathways and product channels are available [58]. See Refs. [58, 121] for more on cold and ultracold chemistry studies.

1.2.4 Precision measurements

Ultracold polyatomic molecules have a number of appealing applications in precision measurement, specifically in probes of Standard Model and beyond-Standard Model physics [11, 96]. One fruitful avenue for these tests has been searches for time-reversal violating[3] moments of fundamental particles, for instance the electron electric dipole moment (eEDM), nuclear Schiff moments, and nuclear magnetic quadrupole moments (MQM). Molecules have inherently enhanced sensitivity to these moments due to their large internal electric fields. A number of new bounds on the eEDM have been set with diatomic molecules (using molecular beams or trapped molecular ions) over the past 15 years [83–87]. Polyatomic molecules are appealing candidates for the next generation of searches for CP-violating moments [140–145] because they can be laser cooled without sacrificing parity-doublet structure, which played an important role in systematic error rejection in earlier measurements. Laser cooling, of course, would be beneficial because it can lead to long coherence times, large numbers, and small trapping volumes, all of which will be beneficial for statistics as well as for rejection of certain systematic errors. The closely-spaced parity doublet states in polyatomic molecules have also been proposed as a resource for measuring nuclear-spin-dependent parity-violation effects within the Standard Model [146].

Another appealing application of ultracold polyatomic molecules is in searches for time variation of fundamental constants, drifts or oscillations of which could be a signature of beyond-Standard-Model physics, including ultralight dark matter [11]. Due to the rich rotational and vibrational structure of polyatomic molecules, one

[3] Or, equivalently, CP-violating (because of CPT symmetry).

can often find near-degenerate states with differential sensitivity to constants like the proton-to-electron mass ratio, $\mu = m_p/m_e$. Such near-degeneracies enhance the fractional sensitivity of transition frequencies to these constants, making them appealing for precision measurements. It has been proposed that a measurement of time variation in μ could be carried out in SrOH using a near-degeneracy between a bending and stretching vibrational mode of the molecule, and this could also be extended to a similar set of states in CaOH [89].

Another interesting direction is to study chiral molecules, which are necessarily polyatomic. For example, the chiral analogue of $CaOCH_3$ (laser cooling of which is described in chapter 10 of this thesis) is CaOCHDT, which could potentially be laser cooled [37]. Along with potentially shedding light on biological homochirality [147, 148], precision measurements of chiral molecules could serve as probes of parity-violating interactions [149]. Additionally, chiral molecules could serve as sensors for parity-violating cosmic fields [150].

1.3 Methods for creating cold and ultracold molecules

Most of the applications of polyatomic molecules discussed above require, or at least significantly benefit from, cooling and trapping at ultracold temperatures $\lesssim 1$ mK. Trapping molecules in one location increases interrogation times, while cooling their external motion and internal structure increases coherence and allows preparation and manipulation of single quantum states.

In this thesis, we employ the technique of direct laser cooling to achieve these goals, motivated by its success as the key enabler of ultracold atom physics [1, 2, 151]. Not only is laser cooling an efficient method of generating trapped atomic and molecular gases at ultracold temperatures, but it also naturally facilitates other goals of quantum control, including single quantum state preparation and high-fidelity, nondestructive state detection.

Moreover, as we will discuss later, laser cooling is potentially applicable to polyatomic molecules with a variety of structures. The challenge for laser cooling is that electronic excitation of a molecule typically causes it to either dissociate or to redistribute its population into many vibrational and rotational states. Therefore, we will need to limit ourselves to specific molecules with certain favorable properties (nonetheless, a broad class of molecules with diverse structures are suspected to have these properties).

A number of other techniques have been demonstrated for cooling and trapping molecules at cold and ultracold temperatures. These approaches are complementary to laser cooling, and have their own advantages depending on the specific application. For studies of molecules at cold temperatures, buffer gas cooling or supersonic expansion combined with magnetic or electrostatic trapping is an established approach, and has the advantage of being applicable to any molecule with a magnetic or electric dipole moment, respectively [152]. Moreover, it is possible to cool these trapped molecules using Sisyphus techniques [153], which have allowed polyatomic molecules to be directly cooled below 1 mK in an electrostatic trap without electronic excitation [154]. Another approach is association of ultracold atoms into molecules, via photoassociation or coherent state transfer. This approach is advantageous because the molecules can inherit the very high phase space density of the parent atomic ensembles, leading to record low temperatures and to the first quantum degenerate gases of polar molecules [29, 75, 79, 155]. The disadvantage of this approach is that it is limited to molecules containing atoms that are laser coolable. Also, unlike laser-cooled molecules, these molecules cannot be nondestructively detected (at least not optically), and many of the optical manipulation techniques from the cold atom community are no longer applicable. There has also been significant progress trapping and controlling molecular ions [85, 156, 157], though here we focus on efforts to cool and trap neutral molecules.

In this section, we present a brief overview of the various methods used to cool and trap neutral molecules at

cold to ultracold temperatures.

1.3.1 Buffer gas cooling

In buffer gas cooling, molecules (or atoms) are cooled via elastic collisions with a gas of inert atoms. This is often done at cryogenic temperatures, using He or Ne as the buffer gas. In a typical apparatus, hot molecules are introduced (by injection from a room temperature bottle, by laser ablation of a target, or a combination of both) into a copper buffer gas cell that is cooled to around ∼1-10 K. The molecules collide and thermalize with the buffer gas atoms, which are in turn cooled by collisions with the walls of the cell. This technique is useful not only because it cools the motion of the molecules, but also because it efficiently cools their rotational degrees of freedom, significantly increasing available population in the lowest few rotational states (vibrational degrees of freedom are less effectively thermalized). See Ref. [137] for a review of this technique.

Buffer gas cooled molecules can be magnetically trapped directly in the cell [158, 159], or extracted into a beam through an aperture. The latter case produces a cryogenic buffer gas beam (CBGB), as reviewed in Ref. [138]. CBGBs can have high molecular flux and low forward velocity, combined with cold internal state distributions, making them an ideal starting point for laser cooling and trapping experiments. Another technique for trapping buffer-gas cooled molecules is optical loading, where a small number of photons are scattered to flip the spin of the molecule and load a superconducting magnetic trap from a CBGB [160]. It has also been proposed to load deep optical traps using buffer-gas cooled molecules [161].

We use a CBGB as the starting point for the laser cooling experiments described in this thesis.

1.3.2 Stark, Zeeman, and mechanical deceleration techniques

Molecules with electric or magnetic dipole moments can be decelerated and trapped using electric or magnetic fields, which use the interaction of polarized dipoles with spatially varying fields to apply forces. Stark deceleration [162] and Zeeman deceleration [163] are two techniques that have been successfully applied for slowing of molecular beams. They rely on time-dependent potentials and are generally best suited to pulsed supersonic beam sources, due to the small velocity spread and short pulse length produced by these sources. Slowing of molecular beams can also be done using deep optical potentials [164]. See Ref. [152] for a review of these techniques. For continuous beams or those with longer pulse durations (e.g. cryogenic buffer gas beams), an alternative technique is Zeeman-Sisyphus deceleration, which uses a time-independent magnetic field profile, combined with optical pumping near field maxima and minima, to slow molecules using only a few scattered photons [165, 166]. Centrifugal deceleratation has also been demonstrated for such beams, and relies on the centrifugal acceleration experienced by molecules moving through a rotating, spiral-shaped electrostatic guide [123, 167]. These techniques have been used to load electrostatic and magnetic traps [168–173], including for the polyatomic molecules CH_3 and CH_3F [124, 174].

1.3.3 Optoelectrical Sisyphus cooling

Cooling of electrostatically trapped polyatomic molecules has been demonstrated using a technique called optoelectrical Sisyphus cooling [175, 176]. In this technique, polar molecules with linear Stark shifts are trapped in a homogeneous electrostatic trap with steep walls, and optically pumped into a low-field seeking state.[4] When a

[4] This optical pumping has so far been done with vibrational transitions, since optical transitions are not accessible in the closed-shell molecules that have been used to date.

molecule climbs one of the walls, it is transferred from a strongly trapped state to a more weakly trapped state, such that it loses kinetic energy after returning to the center of the trap. In this way, a large amount of energy can be removed for every scattered photon. This technique has been used to cool CH_3F to below 100 mK and H_2CO to below 1 mK [154, 176]. These cooled, trapped molecules have been used for high-resolution spectroscopy and to study coherence properties of rotational states in polyatomic molecules [177, 178]. They could also be used to study collisions of polyatomic molecules at submillikelvin temperatures [124].

1.3.4 Coherent association of laser-cooled atoms

One highly successful approach for producing ultracold molecules is to start with ultracold atoms (ideally at or near quantum degeneracy), and then to coherently associate them into ground state molecules. This is typically used to create diatomic molecules consisting of two alkali atoms. This approach was pioneered in Ref. [179] for KRb, where ultracold potassium and rubidium atoms were first transferred into a weakly bound molecular excited state using a Feshbach resonance, and then transferred to the rovibrational ground state using stimulated Raman adiabatic passage (STIRAP). These techniques have since been extended to a large number of bialkali molecules. A highly incomplete list of notable advancements includes loading NaCs and RbCs into optical tweezer arrays [180, 181], the development of a quantum gas microscope of NaRb [61], and the formation of quantum degenerate gases of KRb, NaK, and NaCs [29, 75, 79, 155].

While the extent to which these techniques can be scaled to polyatomic molecules is not yet clear, there have been several experimental efforts in this direction. Weakly bound triatomic NaK_2 molecules have been formed by magneto-association using a Feshbach resonance between NaK molecules and K atoms [182–185]. In another approach, microwave field-linked resonances have been used for electroassociation of weakly bound tetratomic

$(NaK)_2$ molecules [132, 133]. In both cases, the phase space densities of these molecular samples are orders of magnitude larger than what has been achieved for polyatomic molecules with other techniques (including those described in this thesis). However, finding a pathway to transfer these weakly-bound molecules into the rovibrational ground state will be a significant challenge.

1.4 Laser cooling of molecules

Laser cooling requires an atom or molecule to repeatedly absorb and emit optical photons from a coherent light source (laser). At a fundamental level, the coherent, "low temperature" spectrum of the laser, combined with the low temperature of the vacuum into which the molecule emits photons, may be used to cool the molecule's internal and external degrees of freedom.[5] In practice, this is done by tuning the laser wavelength very close to resonance with a specific electronic transition, so that molecules can be selectively excited based on their velocity and/or position.[6] Each time the atom or molecule absorbs a photon from the laser, it will receive a momentum kick, then spontaneously emit a photon as it decays back to the initial ground state, where it can reabsorb a new photon. This is what is called an "optical cycle." Applying many such momentum kicks as the molecule cycles photons allows strong forces to be applied.[7] While this works well for atoms because of their relatively sparse spectra, the complex rotational and vibrational structure of molecules increases the challenge.

Laser cooling of molecules as used today was first suggested by Di Rosa [189], who proposed that a number

[5] Note that alternative approaches to laser cooling have been proposed and/or demonstrated. For instance, it has been suggested that thermal light can be used for cooling in certain instances [186, 187]. It has also been proposed that molecules can be rotationally cooled even if their rotational structure is optically unresolvable [188].

[6] For example, if the laser is slightly red detuned and incident from multiple directions, it will remove motional energy via Doppler cooling.

[7] Note that the momentum kicks from spontaneous decay photons average to zero, since spontaneous decay is isotropic.

of diatomic molecules with favorable electronic and vibrational branching properties could be laser cooled. The key was that, with a suitable choice of structure, the spontaneous decay after electronic excitation would be very unlikely to populate undesired vibrational states. Therefore, lasers addressing just a few vibrational levels in the electronic ground state could be used for optical cycling and laser cooling. A few years later, optically closed rotational transitions were also identified [190], with the key being that driving an $N'' = 1 \rightarrow N' = 0$ transition (where N'' is the rotational angular momentum quantum number in the ground electronic state and N' refers to the excited state) would prevent multiple rotational states from being populated.[8]

Following these proposals, a number of pioneering experiments were carried out with SrF molecules in the DeMille group, who first demonstrated transverse laser cooling of a molecular beam [191], then loaded a magneto-optical trap (MOT) of SrF [192]. Since then, several other diatomic molecules have been loaded into MOTs, including CaF [193, 194], YO [195], and BaF [196]. This has led to a number of advances with laser cooled diatomic molecules, including magnetic trapping [197, 198], optical trapping [199–201], and loading of optical tweezer arrays [202, 203]. This has enabled studies of ultracold molecular collisions [69, 74, 77, 204] and advances in quantum information science [30–32, 205, 206], among other research directions. There are ongoing efforts to laser cool a number of other diatomic molecules [207, 208], including species with distinct electronic structure, such as AlF, AlCl, and CH [209–211]. See Refs. [12–14] for reviews of molecular laser cooling research, with a focus on diatomic molecules.

[8] In contrast, driving the "natural" choice, from $N'' = 0$ to $N' = 1$, allows decay back to $N'' = 2$, which would need to be repumped.

1.4.1 Laser cooling of polyatomic molecules

As laser cooling of diatomic molecules was becoming established, it was recognized that certain classes of polyatomic molecules could also be laser cooled [33–41]. Many of these molecules are based on the paradigm of "optical cycling centers" (OCCs). One way to understand the electronic structure of CaF and other laser coolable diatomic molecules is as follows: the molecule is formed by ionic bonding, wherein the Ca atom donates one of its two valence electrons to close the F atom's valence shell. The remaining valence electron remains localized near the Ca atom, whose electronic structure now looks similar to that of a Ca^+ ion [212]. All of the electronic excitation is therefore hosted by the Ca^+ ion, which is the OCC. CaF is an example of the ML molecular paradigm, consisting of an alkaline-earth-like metal (M=Ca, Sr, Ba, Yb, ...) bonded to an electronegative ligand. In the diatomic case, L is a halogen like fluorine. To extend this paradigm to polyatomic molecules, we replace the fluorine with a group that chemically behaves the same way, by attracting a single valence electron. Such ligands include OH, OCH_3, NH_2, and even larger chemical groups [34, 37–39]. See Fig. 1.3 for examples of molecules that have been proposed for laser cooling. Because the OCC is delocalized from the ligand, electronic excitation is expected to minimally perturb the vibrational degrees of freedom of these molecules, preserving favorable optical cycling properties.

These ideas were first tested in pioneering experiments in the Doyle group with SrOH, where radiation pressure forces [216], transverse laser cooling [217], and bichromatic force deflection [218] of a molecular beam were demonstrated. Soon thereafter, transverse laser cooling was also demonstrated for YbOH [219] and CaOH [220]. This set the stage for full 3D laser cooling and trapping of a linear polyatomic molecule, CaOH, which is the main topic of this thesis work. During the work described in this thesis, we also demonstrated transverse laser cooling

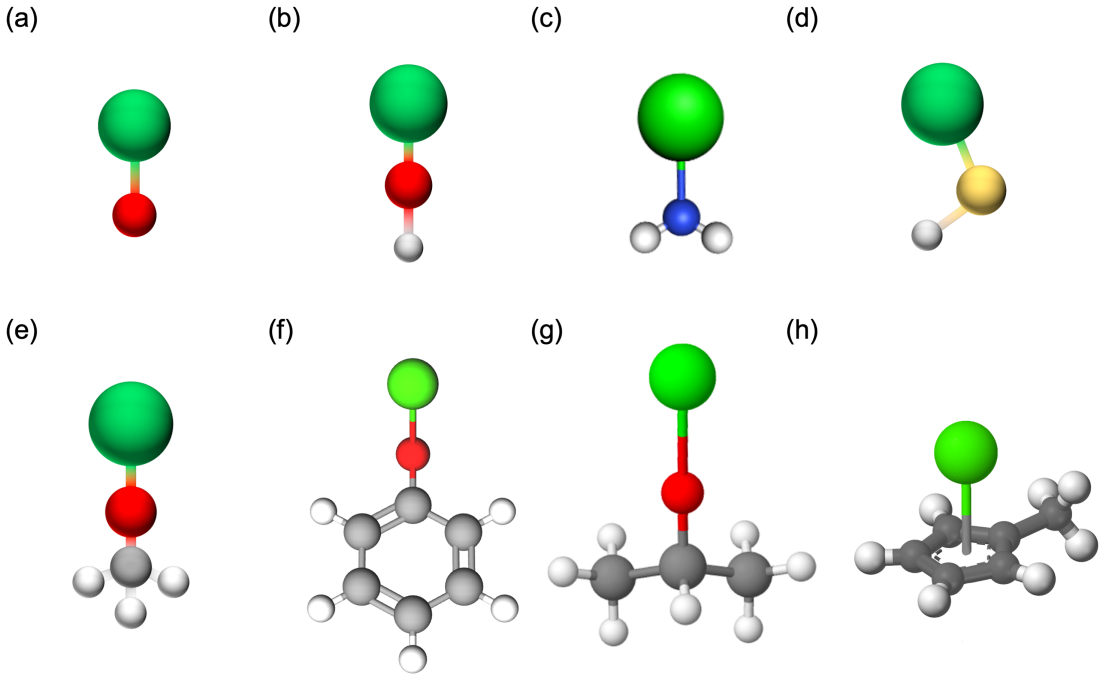

Figure 1.3: Examples of molecules that have been laser cooled or proposed for laser cooling. The green atom is the optical cycling center, which is Ca in the specific molecules listed here, but could also be Sr or other alkaline earth-like atoms. (a) CaF [193, 194] (b) CaOH [33, 42, 213] (this work) (c) $CaNH_2$ [37, 214, 215] (d) CaSH [37, 214, 215] (e) $CaOCH_3$ [47, 213] (this work) (f) $CaOC_6H_5$ (i.e. CaOPh) [38, 50] (g) $CaOCH(CH_3)_2$ [37] (h) $CaC_5H_4CH_3$ [37].

of a beam of $CaOCH_3$ molecules [47]. Following our work with CaOH, SrOH molecules were recently loaded into a MOT [221]. Preliminary attempts have also been made to laser cool asymmetric top molecules, primarily $CaNH_2$ [51].

1.4.2 Anatomy of a molecular laser cooling experiment

Today's molecular laser cooling experiments follow a standard experimental roadmap, shown in Fig. 1.4. Molecules are produced in a cryogenic buffer gas cell, then extracted into a cryogenic buffer gas beam (CBGB) [138], with cold internal state distributions and forward velocities on the order of 100 m/s. Next, the molecular beam is radiatively slowed [222–224], and the molecules are loaded into a magneto optical trap (MOT) [42, 192–196, 221]. While molecular MOTs are typically red-detuned, there has been recent progress transferring into blue-detuned MOTs and "conveyor-belt" MOTs, which can provide significantly higher density [204, 225–230]. From the MOT (red or blue detuned), molecules can be loaded into magnetic [197, 198] or optical [199] traps. In this work, we will pursue optical trapping, which requires sub-Doppler cooling [42, 43, 193, 199, 231–233], followed by cooling into an optical dipole trap (ODT) [43, 199–201]. Once optically trapped, the molecules can be held for several seconds and be coherently manipulated with microwave or radio-frequency radiation. This can be done either in the ODT or after transferring into an optical tweezer array [46, 202].

1.5 Overview of this thesis

In this thesis, we describe our work laser cooling, trapping, and coherently controlling the internal states of CaOH. The outline is as follows. In chapter 2, we present an overview of molecular structure, with an emphasis on CaOH. In chapter 3, we describe the cryogenic buffer gas beam source used to produce cold CaOH molecules.

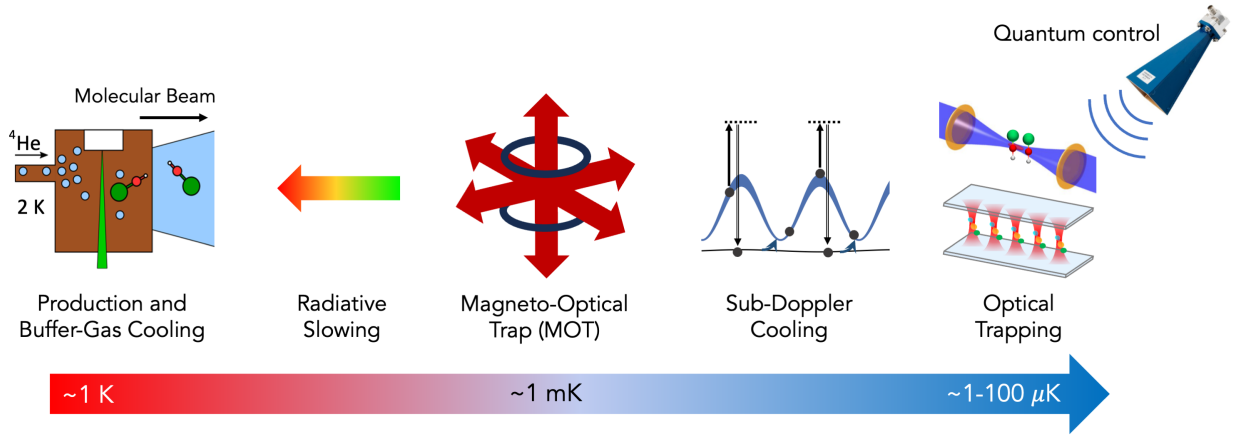

Figure 1.4: Typical sequence for molecular laser cooling experiments pursued in this work.

In chapter 4, we describe the implementation of an optical cycling transition capable of scattering >10,000 photons from CaOH for laser cooling. In chapter 5, we describe our work on radiative slowing, magneto-optical trapping, and sub-Doppler cooling of CaOH. In chapter 6, we describe our work optically trapping CaOH and measuring the trap lifetime of low-lying vibrational states. In chapter 7, we describe our work coherently controlling CaOH in the ODT in the parity-doubled vibrational bending mode. These coherent control capabilities are then used for a proof-of-principle demonstration of techniques needed for a future electron electric dipole moment (eEDM) search with polyatomic molecules. In chapter 8, we describe our work loading single CaOH molecules into a small optical tweezer array and coherently controlling their internal states. This lays the groundwork for future quantum information and quantum simulation experiments with polyatomic molecules. In chapter 9, we describe the observation and characterization of collisions between ultracold CaOH molecules. In chapter 10, we change gears and describe an experiment demonstrating early progress towards laser cooling *nonlinear* polyatomic molecules. Specifically, here we demonstrate transverse laser cooling of a molecular beam of $CaOCH_3$. Finally, in chapter 11, we conclude the thesis and discuss prospects for future work.

2

CaOH Molecular Structure

Molecules are complex objects with internal structure spanning a wide range of energy scales. These include electronic structure, the typical energy scale of which is around $\sim k_B \times 10^4 - 10^5$ K, as well as vibrational ($\sim 10^2 - 10^3$ K) and rotational ($\sim$1 K) structure. Fine and hyperfine structures arising from electronic and nuclear spins appear at even lower energies ($\ll$ 1 K). A goal of the work described in this thesis is to control

CaOH molecules at the level of a single quantum mechanical state, requiring that each of these structures be well understood. Moreover, a thorough understanding of molecular structure is essential for designing and applying laser cooling techniques to molecules. In this chapter, we provide an overview of molecular structure and describe the molecular states relevant to our work with CaOH.

2.1 Overview

A pillar of quantum mechanical descriptions of molecular structure is the Born-Oppenheimer (BO) approximation. In principle, one can write down the exact molecular Hamiltonian $\hat{H}$, and solve for the wavefunctions $\psi(\boldsymbol{r}, \boldsymbol{R})$ as a function of the spatial coordinates of the electrons, $\boldsymbol{r}$, and the nuclei, $\boldsymbol{R}$. However, this cannot be done exactly for any molecule [234]. Instead, we typically make the BO approximation in order to proceed further. Not only is this approximation physically well motivated, it also enables significant physical intuition by dividing the Hamiltonian and wavefunctions according to the structural energy scales described above. Significantly more details on the mathematics underpinning the BO approximation (and related approximations) can be found in Ref. [234].

The key idea is that the timescale for electronic motion is orders of magnitude faster than the timescale for nuclear motion due to the electrons' much lighter mass. Loosely speaking, for any change in the nuclear configuration $\boldsymbol{R}$, the electronic configuration will almost *instantaneously* adapt, resulting in an electronic wavefunction $\psi_e(\boldsymbol{r}; \boldsymbol{R})$ that depends parametrically on the nuclear coordinates $\boldsymbol{R}$. Accordingly, the wavefunction can be written as the product of the electronic and nuclear wavefunctions,

$$\psi(\boldsymbol{r}, \boldsymbol{R}) \approx \psi_e(\boldsymbol{r}; \boldsymbol{R})\psi_n(\boldsymbol{R}) \tag{2.1}$$

each of which obeys its own Schrödinger equation

$$\hat{H}_e \psi_e(\boldsymbol{r}; \boldsymbol{R}) = E_e(\boldsymbol{R}) \psi_e(\boldsymbol{r}; \boldsymbol{R}) \tag{2.2}$$

$$[\hat{H}_n + E_e(\boldsymbol{R})] \psi_n(\boldsymbol{R}) = E_n \psi_n(\boldsymbol{R}) \tag{2.3}$$

where we have divided the Hamiltonian into electronic and nuclear contributions $\hat{H} = \hat{H}_e + \hat{H}_n$. In particular, note that the electronic energy $E_e(\boldsymbol{R})$ appears in the nuclear Schrödinger equation as a potential energy term, reflecting the fact that the electrons are responsible for the molecular potential seen by the nuclei.

We can proceed one step further by dividing the nuclear wavefunction into vibrational and rotational components, $\psi_n = \psi_v \psi_r$, so long as we make an appropriate choice of reference frame [234]. Having separated the molecular wavefunction into electronic, vibrational, and rotational constituents, we now proceed to describe each of them.

2.2 Electronic structure

While solving for the electronic energy of molecules is in general a hard problem, in this thesis we work with molecules for which the solution is conceptually relatively simple. This is not a coincidence: in order for laser cooling to be practical for a molecule, it should ideally behave in a manner similar to that of an atom, meaning that mixing of the constituent atoms' electronic orbitals should be limited to the extent possible. In our case, we will see that the valence electronic orbitals of CaOH inherit much of the character of a bare Ca^+ ion, with relatively mild perturbations from the ligand (OH in this case) to which it is bound.

The qualitative picture is as follows, and applies to a number of molecules with the structure ML, where M is

an alkaline-earth (AE) or AE-like atom, and L is a ligand that will become a singly-charged anion after filling its valence shell (e.g. F, OH, OCH_3, NH_2, etc.) [212]. Because of the low ionization energy of the metal compared to the electron affinity of the ligand, the configuration that minimizes the energy of an ML molecule is for the metal atom to donate one electron to the ligand. The result is a molecule with a closed-shell, $M^{2+}L^{-}$ ionically bonded core, plus a single valence electron.[1] To minimize its energy, the valence electron will remain centered near the metal ion, so that the molecule's electronic states are derived from a free M^+ ion and perturbed by the nearby anionic ligand. The primary effect of the ligand is to polarize the valence electronic wavefunction away from the bond (further minimizing its energy via electrostatic repulsion), which is achieved quantum mechanically by mixing low-lying M^+ electronic orbitals to remove their spherical symmetry. This picture, where the electronic states are described using a basis of M^+ electronic orbitals that are mixed by the interaction with the ligand, is called ligand field theory and yields fairly good agreement with the observed electronic structure [212, 235].

In the case of Ca-containing molecules like CaOH, the low-lying electronic states of Ca^+ are $4s$, $4p$, and $3d$. However, the cylindrical symmetry of the molecule lifts the M_L degeneracy of these states, leading to corresponding molecular orbitals with symmetry σ, π, and so on [236].[2] Interactions with the ligand can then mix molecular orbitals of the same symmetry. It turns out that the $\widetilde{X}^2\Sigma^+$ state of CaOH arises from mixing of $4s\sigma$ and $4p\sigma$ orbitals, the $\widetilde{A}^2\Pi$ state comes from mixing of $4p\pi$ and $3d\pi$, and the $\widetilde{B}^2\Sigma^+$ state arises from mixing of $4p\sigma$ with $3d\sigma$ [212, 235]. See Refs. [212, 214] for figures illustrating the way this mixing affects the shape of the molecular orbitals and perturbs the electronic energies of the Ca^+ atom into those of the molecule. Fig. 2.1 shows the observed

[1] While the valence electron is what makes electronic transitions accessible in these molecules, it also means that they are highly-reactive radicals that need to be studied in gas phase.

[2] This process can be thought of as a Stark effect that conserves the projection of $\vec{L}$ onto the internuclear axis but does not conserve $\vec{L}$ itself [236].

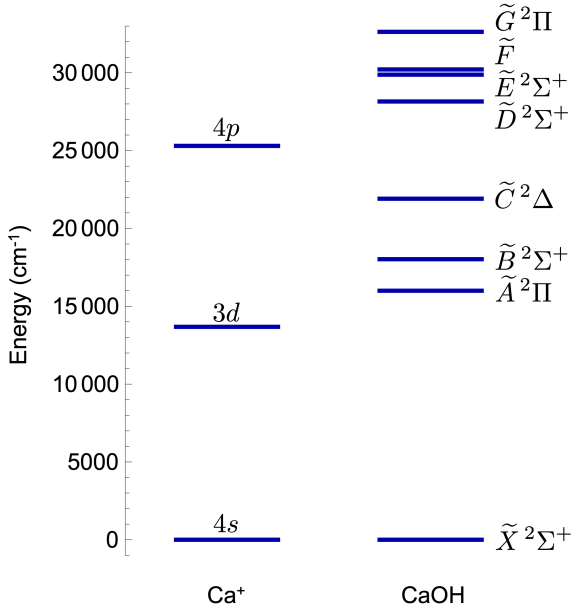

Figure 2.1: Electronic states of CaOH and Ca^+. Observed CaOH electronic state energies are from Refs. [93, 237–242]. Ca^+ electronic states are mixed by the electric field from the OH^- ligand to deform into the CaOH electronic states. The higher-energy CaOH states also include contributions from Ca^+ $5s$, $4d$, and $5p$ states [241, 243]. Note that the $\widetilde{F}$ state is bent [240] and is therefore not given a symmetry label.

electronic states of CaOH, alongside low-lying electronic levels of Ca^+.

Aside: electronic state notation

The electronic states of linear molecules are labeled with term symbols similar to those used for atoms. The term symbol is ${}^{2S+1}\Lambda_\Omega$, where S is the electron spin, Λ is the projection of the electronic angular momentum onto the internuclear axis, and Ω is the sum of the projections of the electron spin and electronic angular momentum onto the internuclear axis.[3] These angular momenta are described in more detail below. The electronic angular momentum projection Λ is given a capital greek letter in the term symbol, with $\Lambda = 0$ corresponding to Σ,

[3] Ω is only included in the term symbol in states for which it is well defined, namely those in which the electron spin has a definite projection onto the molecular axis.

$|\Lambda| = 1$ to Π, $|\Lambda| = 2$ to Δ, and so on. For states with $|\Lambda| > 0$, electronic states of both parities $\pm$ are allowed, since linear combinations $|\Lambda, \pm\rangle \propto |\Lambda\rangle \pm |-\Lambda\rangle$ are parity eigenstates. However, for Σ states the electronic parity is instead denoted by a superscript, either Σ^+ or Σ^-. Capital letters are used to label the electronic states, in particular to distinguish different states of the same symmetry.[4] Typically $\widetilde{X}$ refers to the ground state, and excited electronic states are labeled $\widetilde{A}$, $\widetilde{B}$, etc. The tilde is omitted for diatomic molecules but is necessary for polyatomic species to distinguish the state label from its term symbol (see below).

The linear molecule labels are a special case of the more general symmetry labeling used for nonlinear molecules. Linear molecules belong to the $C_{\infty v}$ molecular symmetry group, the irreducible representations of which are Σ^+, Σ^-, Π, Δ, and so on. Therefore, their term symbols turn out to be of the general form ${}^{2S+1}\Gamma$, where Γ is the irreducible representation of the molecular point group that describes the symmetry of the electronic state. This notation applies to any molecule, including nonlinear species. For example, the symmetric top molecule $CaOCH_3$ (described later in this thesis) belongs to the C_{3v} point group, whose irreducible representations are A_1, A_2, and E. Its lowest-lying states are $\widetilde{X}^2A_1$, $\widetilde{A}^2E$, and $\widetilde{B}^2A_1$, which correspond closely to states in CaOH.[5] See Ref. [244] for a detailed discussion of molecular symmetry.

2.3 Vibrational structure

As we saw above, within each electronic state there is a vibrational potential $V(\boldsymbol{R})$ (where $\boldsymbol{R}$ describes the nuclear coordinates) due to changes in the electronic energy as function of the nuclear configuration. (Recall that in the Born-Oppenheimer approximation we assume that the electronic wavefunction instantaneously minimizes

[4] This because the principal quantum number used for this purpose in atoms is no longer defined, due to orbital mixing.
[5] Note that A_1 correlates to Σ^+, A_2 to Σ^-, and E to any degenerate state Π, Δ, ... in the linear case.

its energy in response to changes in $\boldsymbol{R}$.)

For a polyatomic molecule, the potential energy is a multidimensional surface, which depends on the $3N$ nuclear coordinates q_i describing the 3-dimension motion of all N nuclei. Near the bottom of the potential, the potential energy surface can be Taylor expanded as [234, 236]

$$V = V_0 + \frac{1}{2}\sum_{i=1}^{3N}\sum_{j=1}^{3N}\left(\frac{\partial^2 V}{\partial q_i \partial q_j}\right)_{q_i=q_j=0} q_i q_j + \frac{1}{3!}\sum_i\sum_j\sum_k\left(\frac{\partial^3 V}{\partial q_i \partial q_j \partial q_k}\right)_0 q_i q_j q_k + \ldots \tag{2.4}$$

Here we have defined the coordinates so that the equilibrium geometry corresponds to $q_i = 0$. To a good approximation, the low-lying vibrational states in this potential may be described within the harmonic approximation, in which case the vibrational Hamiltonian is [234, 236]

$$H_v = \sum_{i=1}^{3N-6(5)}\left(-\frac{\hbar^2}{2}\frac{\partial^2}{\partial Q_i^2} + \frac{1}{2}\lambda_i Q_i^2\right) \tag{2.5}$$

where Q_i is a mass-weighted normal coordinate describing the ith normal mode of vibration and $\sqrt{\lambda_i}$ is the vibrational frequency of the mode. Notice that for a polyatomic molecule there are $3N - 6$ (or $3N - 5$ for a linear molecule) normal vibrational coordinates; the other 6(5) normal coordinates are taken up by the 3 translational and 3(2) rotational degrees of freedom of the molecule.

Vibrations along each of the normal coordinates are fully separable in the harmonic approximation, so the

vibrational wavefunction can be expressed as

$$\psi(Q_1, Q_2, \ldots, Q_{3N-6}) = \prod_{i=1}^{3N-6} \psi_{v_i}(Q_i) \tag{2.6}$$

where $\psi_{v_i}(Q_i)$ is the simple harmonic oscillator wavefunction [236] with vibrational quantum number v_i. The energy of the state in the harmonic approximation is

$$E_v = \sum_{i=1}^{3N-6} \hbar\omega_i \left(v_i + \frac{1}{2}\right) \tag{2.7}$$

Reintroducing the anharmonic terms in the potential energy surface has two effects. The first is to couple the harmonic oscillator eigenstates from Eq. 2.6, as discussed below. The second effect is to alter the state energies, which can be expressed as [234, 245]

$$G(v_1, v_2, \ldots, v_p) = \sum_i \omega_i \left(v_i + \frac{d_i}{2}\right) + \sum_i \sum_{k \geq i} x_{ik} \left(v_i + \frac{d_i}{2}\right)\left(v_k + \frac{d_k}{2}\right) + \sum_i \sum_{k \geq i} g_{ik} \ell_i \ell_k + \ldots \tag{2.8}$$

where ω_i is the frequency of the ith mode, d_i is its degeneracy, x_{ij} and g_{ij} are anharmonicity constants, and ℓ_i is a quantum number describing the vibrational angular momentum along the molecular axis.

In molecular spectroscopy, it is usually convenient to refer all energies to the lowest energy level, which has an energy $G(0, 0, \ldots)$. In this case, the combined electronic and vibrational energy of the molecule is $T_{ev} =$

$T_0 + G_0(v_1, v_2, \ldots)$, where T_0 is the energy of the lowest vibrational state and

$$G_0(v_1, v_2, \ldots) = \sum_i \omega_i^0 v_i + \sum_i \sum_{k \geq i} x_{ik}^0 v_i v_k + \sum_i \sum_{k \geq i} g_{ik} \ell_i \ell_k + \ldots \tag{2.9}$$

The effective vibrational frequency in this equation is $\omega_i^0 = \omega_i + x_{ii} d_i + \frac{1}{2} \sum_{k \neq i} x_{ik} d_k + \ldots$ [245, 246].

Anharmonic terms in the potential not only change the energies but also mix harmonic oscillator wavefunctions. For example, a cubic term acting on normal mode i of the form $V_{iii} = k_{iii} Q_i^3 \propto k_{iii} (a_i^\dagger + a_i)^3$ will mix states differing by $|\Delta v_i| = 1$ or $|\Delta v_i| = 3$. Here k_{iii} is an anharmonic force constant, Q_i is a mass-weighted normal coordinate, and $a_i^\dagger$ (a_i) is a raising (lowering) operator. The most important terms are those coupling vibrational states of the same symmetry that are near-degenerate, causing significant perturbations to the vibrational energies of eqn. 2.9.[6] This effect is well understood, and is known as the Fermi resonance interaction [247, 248]. Fermi resonance interactions are important in CaOH because the Ca–O stretching frequency is approximately double the Ca–O–H bending frequency, leading to many accidental near-degeneracies that are important for understanding vibrational branching ratios for laser cooling (see chapter 4).

2.3.1 Vibrational structure of CaOH

CaOH is a linear triatomic molecule with 4 normal vibrational modes.[7] One of these, the bending mode, is doubly degenerate. The vibrational state of CaOH is labeled by $(v_1 v_2^\ell v_3)$, where v_1 is the quantum number for the symmetric stretching mode, v_2 describes the bending mode, v_3 describes the antisymmetric stretching mode, and

[6] Note that anharmonic terms only couple vibrational states of the same symmetry. For a more detailed discussion of symmetry in polyatomic molecules, see [244].

[7] Linear molecules have $3N - 5$ normal modes, where N is the number of atoms. Nonlinear polyatomic molecules have $3N - 6$ normal modes – one fewer than a linear molecule due to the extra rotational degree of freedom.

ℓ gives the vibrational angular momentum in the bending mode.[8] The vibrational angular momentum arises because linear combinations of the degenerate bending vibrations along two perpendicular (linear) axes can be formed which have elliptical trajectories. This can be thought of as producing a nuclear orbital angular momentum about the molecular axis. Doubly degenerate bending modes such as this one are formally described by the 2D harmonic oscillator, and ℓ can take the values $v_2, v_2 - 2, \ldots, -v_2 + 2, -v_2$ [236]. The symmetry of the vibrational state is set by its ℓ value, with $\ell = 0$ corresponding to Σ^+ symmetry, $|\ell| = 1$ to Π symmetry, and so on [236].

Energies of low-lying vibrational states in the CaOH $\widetilde{X}^2\Sigma^+$ ground state potential are shown in Table 2.1. This includes states we have spectroscopically observed in this thesis work at high resolution, along with previous values from the literature. A few of these states were observed at high resolution for the first time in our laboratory, including (110), (03^10), (12^00), and (12^20).

2.3.2 Measured CaOH vibrational constants

In principle, the vibrational energy measurements from Table 2.1 can be used to fit the $\widetilde{X}^2\Sigma^+$ state vibrational constants (eqn. 2.9). However, this process is complicated by the presence of significant Fermi resonance interactions. This can be accounted for using a deperturbation analysis similar to the one described in Ref. [250].

The relevant anharmonic term describing Fermi resonance in CaOH is $V_{122} = k_{122}Q_1Q_2^2$, where k_{122} is an anharmonic force constant and Q_1 and Q_2 are normal coordinates associated with Ca–O stretching and Ca–O–H bending, respectively. This perturbation mixes states with $|\Delta v_1| = 1$ and $|\Delta v_2| = 2$, many of which are

[8] Because of the large mass imbalance between hydrogen and calcium, the symmetric stretching mode corresponds primarily to Ca–O stretching, while the antisymmetric stretching mode is primarily O–H stretching.

Table 2.1: CaOH $\widetilde{X}^2\Sigma^+$ vibrational state origin energies, in cm^{-1}. All values are rounded to the nearest 0.01 cm^{-1} (300 MHz). "This work" refers to the state energies determined from high resolution spectroscopy in our lab (Appendix E). Our measurements neglect the variation of the rotational constant with vibrational state, which could lead to corrections of up to $\sim$0.02 cm^{-1} for the higher-energy states [249].

State	Literature	This work
(000)	0	0
(010)	352.93[a]	352.93
(100)	609.02[b]	609.02
(02^00)	688.67[b]	688.66
(02^20)	713.04[b]	713.01
(110)	952[c]	950.71
(03^10)	–	1032.47
(200)	1210.15[b]	1210.16
(12^00)	1286[c]	1282.17
(12^20)	–	1302.49
(300)	1803.05[b]	1803.02
(400)	2387.27[b]	–
(001)	3778[c]	–

[a] Ref. [93]
[b] Ref. [249]
[c] Ref. [240] (low resolution)

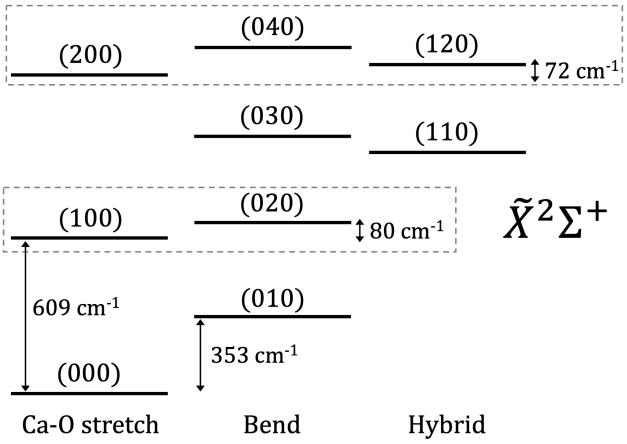

Figure 2.2: Low-lying vibrational states in the CaOH $\widetilde{X}^2\Sigma^+$ potential. Near-degenerate groups of states with significant Fermi resonance interactions are indicated with dashed boxes. Reproduced from Ref. [251].

nearly degenerate in CaOH, as depicted in Fig. 2.2. For example, (100) mixes with (02^00); (110) with (03^10); (200) with (12^00) and (04^00); and so on. The relevant matrix elements of V_{122} are [248]

$$\langle v_1+1, v_2, v_3; l|V_{122}|v_1, v_2+2, v_3; l\rangle = W\left[(v_1+1)(v_2+2-l)(v_2+2+l)\right]^{1/2} \tag{2.10}$$

where

$$W = \frac{k_{122}}{2\sqrt{2}}\left(\frac{\hbar}{2\pi c\omega_2}\right)\left(\frac{\hbar}{2\pi c\omega_1}\right)^{1/2} \tag{2.11}$$

is the Fermi resonance parameter, and ω_1, ω_2 are the vibrational frequencies in cm^{-1}.

Following Ref. [250], if we know W and the measured frequencies of a set of states perturbed by a Fermi resonance interaction, we can back out the unperturbed frequencies. For example, for the resonance between (100) and (02^00) in CaOH, we can work out the unperturbed frequencies by solving the system of eigenvalue equa-

tions

$$\begin{vmatrix} G^{(0)}(100) - G(100) & 2W \\ 2W & G^{(0)}(02^{0}0) - G(100) \end{vmatrix} = 0 \tag{2.12a}$$

$$\begin{vmatrix} G^{(0)}(100) - G(02^{0}0) & 2W \\ 2W & G^{(0)}(02^{0}0) - G(02^{0}0) \end{vmatrix} = 0 \tag{2.12b}$$

where $G^{(0)}(i)$ is the unperturbed state energy, $G(i)$ is the observed energy, and the vertical bars indicate the determinant. The Fermi resonance parameter W has not been measured for the $\widetilde{X}$ state of CaOH but is known for the $\widetilde{A}$ state [250]. Because the potentials are similar for the two states, we assume the same k_{122} and scale by the difference in the vibrational frequencies, which gives $|W| \approx 10.7\ \mathrm{cm}^{-1}$ [251]. We then estimate the unperturbed energy of states in the Fermi groupings $(100)/(02^{0}0)$, $(110)/(03^{1}0)$, $(200)/(12^{0}0)/(04^{0}0)$, and $(12^{2}0)/(04^{2}0)$ using equations similar to eqns. 2.12 along with the measured vibrational frequencies (Tab. 2.1). Since we have not observed (040) at high resolution, we used the low-resolution value from Ref. [240] as an estimate for the energy of $(04^{0}0)$ and added $4g_{22}$ to that value as an estimate for the $(04^{2}0)$ energy. The resulting estimates for the unperturbed energies are $G^{(0)}(100) = 615.3\ \mathrm{cm}^{-1}$, $G^{(0)}(02^{0}0) = 682.4\ \mathrm{cm}^{-1}$, $G^{(0)}(110) = 964.1\ \mathrm{cm}^{-1}$, $G^{(0)}(03^{1}0) = 1019.1\ \mathrm{cm}^{-1}$, $G^{(0)}(200) = 1224.1\ \mathrm{cm}^{-1}$, $G^{(0)}(12^{0}0) = 1287.3\ \mathrm{cm}^{-1}$, and $G^{(0)}(12^{2}0) = 1315.8\ \mathrm{cm}^{-1}$.

Fitting these values (along with the (000), (010), and $(02^{2}0)$ energies from Table 2.1) to eqn. 2.9 gives the vibrational constants shown in Table 2.2. We excluded (300) from the fit, since it is expected to be perturbed by Fermi resonance with (220), (140), and (060). Our results are in reasonable agreement with the literature,

Table 2.2: CaOH $\widetilde{X}^2\Sigma^+$ state vibrational constants, in cm^{-1}. Measurements from this work removed the effect of Fermi resonance on the vibrational energies, as described in the text.

Parameter	Ref. [249]	Ref. [250]	Ref. [240]	This work
ω_1^0	612.822	–	610.4	619.4
ω_2^0	–	349.34	350.0	350.3
x_{11}^0	−3.747	–	−3.7	−3.7
x_{22}^0	–	−3.95	−0.8	−4.4
x_{12}^0	–	–	−7.1	−5.9
g_{22}	6.092	7.53	–	7.4

but to our knowledge represent the first time that Fermi resonance has been accounted for in all states included in the fit. From these measurements, we estimate the true vibrational frequencies of the $\widetilde{X}^2\Sigma^+$ potential to be $\omega_1 \approx \omega_1^0 - x_{11}^0 - x_{12}^0 \approx 629.0\,\mathrm{cm}^{-1}$ and $\omega_2 \approx \omega_2^0 - 2x_{22}^0 - \frac{1}{2}x_{12}^0 \approx 361.9\,\mathrm{cm}^{-1}$ (see discussion around eqn. 2.9).

2.4 Rotation and spin

2.4.1 Rotational structure

The rotational structure of molecules is approximately described by a rigid rotor Hamiltonian. The most general structure is that of an asymmetric molecule with three distinct moments of inertia – I_a, I_b, and I_c – corresponding to its three molecule-frame principal axes. These are conventionally ordered so that $I_a \leq I_b \leq I_c$. Classically, the energy of the rigid rotor is

$$E = \frac{1}{2}I_a\omega_a^2 + \frac{1}{2}I_b\omega_b^2 + \frac{1}{2}I_c\omega_c^2 = \frac{L_a^2}{2I_a} + \frac{L_b^2}{2I_b} + \frac{L_c^2}{2I_c} \tag{2.13}$$

where in the second equality we used the definition of the classical angular momentum along axis k, $L_k = I_k \omega_k$.

In the quantum treatment, we replace the classical angular momentum $\boldsymbol{L}$ with an analogous quantum operator, which we will call $\hat{\boldsymbol{R}}$ for "rotational angular momentum". The rigid-rotor Hamiltonian then becomes

$$\hat{H}_{\text{rot}} = A\hat{R}_a^2 + B\hat{R}_b^2 + C\hat{R}_c^2 \tag{2.14}$$

where $\hat{R}_k$ is the projection of the rotational angular momentum onto the k principal axis in the molecule frame, and we have defined the rotational constants $A = 1/2I_a$, $B = 1/2I_b$, and $C = 1/2I_c$. These are ordered such that $A \geq B \geq C$. Details on the rotational Hamiltonian for asymmetric molecules can be found elsewhere, e.g. in Ref. [252]. In this thesis, however, we focus exclusively on molecules with higher symmetry, namely symmetric top molecules and linear molecules.

For linear molecules, such as CaOH in the vibrational ground state, there is no rotational degree of freedom about the a axis, and $B = C$. In this case, the rotational Hamiltonian takes the simple form

$$H_{\text{rot}} = B\boldsymbol{R}^2 \tag{2.15}$$

The eigenstates of this Hamiltonian are spherical harmonics $|R, M\rangle$, which obey the eigenvalue equation $\boldsymbol{R}^2|R, M\rangle = \hbar^2 R(R+1)|R, M\rangle$. Here R is the rotational quantum number and M is its projection onto the laboratory Z axis.[9] The eigenvalues of the Hamiltonian are therefore

$$E_{\text{rot}} = BR(R+1) \tag{2.16}$$

[9] Here upper case Z refers to the lab frame and lower case z refers to the molecule frame.

where we absorbed a factor of $\hbar^2$ into the rotational constant.[10] In CaOH, the rotational constant is $B/h \approx 10$ GHz. The lowest-lying rotational states therefore have energies of 0 GHz ($R = 0$), 20 GHz ($R = 1$), 60 GHz ($R = 2$), and so on.

In symmetric top molecules (e.g. $CaOCH_3$), two of the principal axes have the same moment of inertia. For *oblate* symmetric top molecules, $C > B = A$, whereas for *prolate* symmetric top molecules (like $CaOCH_3$), $A > B = C$. In the latter case, the rotational Hamiltonian reduces to

$$H_{\text{rot}} = B\boldsymbol{R}^2 + (A - B)R_z^2 \quad \text{(prolate symmetric top)} \tag{2.17}$$

where R_z is the projection of $\boldsymbol{R}$ onto the molecule-frame z axis (the symmetry axis).[11] In the oblate case, A and C should be swapped.

The eigenfunctions of this Hamiltonian are symmetric top wavefunctions $|R, K, M\rangle$, where K is the projection of $\boldsymbol{R}$ onto the molecule-frame z axis and M is its projection onto the lab-frame Z axis.[12] The rotational energies for a symmetric top are

$$E_{\text{rot}} = BR(R + 1) + (A - B)K^2 \tag{2.18}$$

In $CaOCH_3$, $A/h \approx 163$ GHz and $B/h \approx 3.5$ GHz. This means that the structure is divided into a number of K manifolds split by hundreds of GHz, each of which contains a rotational ladder with states split by much

[10] In general, we ignore factors of $\hbar$ in this section for simplicity. Practically speaking, it is usually convenient to think of the rotational constants as having units of energy or frequency, with the operators and quantum numbers being unitless. The appropriate factors of $\hbar$ can then be inserted as appropriate.

[11] Note that for prolate symmetric tops and linear molecules, the z axis is often used interchangeably with a.

[12] The symmetric top wavefunctions are closely related to rotation matrices, and their form can be found in many references, e.g. Ref. [236]. However, for most purposes all that is needed is to know that they are simultaneous eigenfunctions of $\boldsymbol{R}^2$, R_z, and R_Z obeying $\boldsymbol{R}^2|RKM\rangle = \hbar^2 R(R+1)|RKM\rangle$, $R_z|RKM\rangle = \hbar K|RKM\rangle$, and $R_Z|RKM\rangle = \hbar M|RKM\rangle$.

lower energies (10 GHz scale).

The rotational structure of CaOH will be considered in much more detail below, when we describe the structure of specific states. The rotational structure of $CaOCH_3$, meanwhile, will be described in chapter 10.

2.4.2 Fine and hyperfine structure

Along with electronic, vibrational, and rotational structure, CaOH also has a valence electron with spin $S = 1/2$ and a hydrogen nucleus with spin $I = 1/2$, both of which introduce additional angular momentum structure. The primary interactions that these introduce are

1. Spin-orbit interactions, between the electron spin $\boldsymbol{S}$ and the electronic angular momentum $\boldsymbol{L}$. This creates a large ($\sim$2 THz) first-order splitting in electronic states with $L \neq 0$ (i.e. "degenerate" electronic states, like $\widetilde{A}^2\Pi$). Because of the strength of this interaction, it can also significantly mix different electronic states, leading to effects like Λ doubling, as described later in this chapter.
2. Spin-rotation interactions. These are interactions between the electron spin and the molecular rotation, and they appear in the Hamiltonian as a coupling between these two angular momenta. Splittings due to this spin-rotation term are around $10 - 100$ MHz in the CaOH ground state (though a large fraction of that energy is actually due to spin-orbit mixing with excited states, as described below).
3. Hyperfine interactions, between the hydrogen nuclear spin and the electronic degrees of freedom. In the ground state, the dominant interaction is between the nuclear spin $\boldsymbol{I}$ and the electron spin $\boldsymbol{S}$. Because the valence electron cloud is centered near the Ca atom and polarized away from the bond, there is very little overlap with the hydrogen nucleus. Consequently, the hyperfine interaction in CaOH is quite weak, with an energy of about 1 MHz. This is much smaller than in CaF, whose F nuclear spin is closer to the electron cloud, leading to hyperfine interactions on the 50-100 MHz scale.

In addition to these interactions, there are a few more that we will encounter below. For example, Λ doubling leads to GHz splittings between opposite-parity levels in degenerate electronic states, and ℓ-type doubling causes MHz splittings between opposite-parity levels in degenerate vibrational states. We will also see that vibronic coupling – interactions between electronic and vibrational angular momenta – can cause large energy shifts in states

Structure	Energy scale (cm^{-1})	Energy scale (Hz)
Electronic	$\sim$15000	$\sim$500 THz
Vibrational	$\gtrsim$300	$\gtrsim$10 THz
Spin-orbit[a]	67	2 THz
Rotational	$\sim$0.3	$\sim$10 GHz
Spin-rotation[b]	$\sim 10^{-3}$	$\sim$10-100 MHz
Hyperfine	$\sim 10^{-4}$	$\sim$2 MHz

[a] Only present at first-order in degenerate electronic states (e.g. $\widetilde{A}^2\Pi$).
[b] Slightly larger ($\sim$GHz) in excited electronic states.

Table 2.3: Summary of (approximate) structural energy scales in CaOH.

with nonzero electronic *and* vibrational angular momentum (e.g. $\widetilde{A}^2\Pi(010)$). These effects (and others) will be described in further detail below.

2.4.3 Summary

Table 2.3 summarizes the structures described in the preceding sections, along with their corresponding energy scales in CaOH. The angular momentum structures will be described in more detail in the following sections.

2.5 Structure of states relevant to this work

In the following sections, we describe the angular momentum structure of specific states used for laser cooling and quantum control of CaOH. This includes vibrational states of various symmetries in both the $\widetilde{X}^2\Sigma^+$ electronic ground state and in the $\widetilde{A}^2\Pi$ excited state.

2.5.1 Aside: Effective Hamiltonian treatment

Before describing the angular momentum structure of individual electronic and vibrational states in CaOH, it is interesting to step back and consider what even allows us to treat individual states this way. In general, the full molecular Hamiltonian contains terms that couple all manner of different electronic and vibrational states. For instance, let's choose a natural set of molecular basis states $|\eta, v, J\rangle$ describing the unperturbed electronic (η), vibrational (v), and angular momentum (J) degrees of freedom. To pick a convenient starting point, let's say that $|\eta\rangle$ is an eigenstate of the nonrelativistic electronic Hamiltonian H_e^0 (eigenstates of which are $\eta = \widetilde{X}^2\Sigma^+$, $\widetilde{A}^2\Pi$, $\widetilde{B}^2\Sigma^+$, etc.) and $|v\rangle$ is an eigenstate of the harmonic oscillator Hamiltonian H_v^0 (eqn. 2.5). These two effects are combined into the zero-order Hamiltonian $H^0 = H_e^0 + H_v^0$, whose eigenvalues are $H^0|\eta v J\rangle = E_{\eta,v}^0|\eta v J\rangle$. All other terms in the Hamiltonian – e.g. molecular rotation, spin-orbit interactions, hyperfine structure, and so on – are included in a perturbing Hamiltonian H'.

If we write out the total Hamiltonian $H = H^0 + H'$ as a matrix in this unperturbed basis, we get something

that looks like

$$H = \begin{pmatrix} \begin{bmatrix} E^0_{X(000)}\boldsymbol{I} + H'_{X(000)} & H'_{X(000),X(010)} & \cdots \\ H'_{X(000),X(010)} & E^0_{X(010)}\boldsymbol{I} + H'_{X(010)} & \cdots \\ \vdots & \vdots & \ddots \end{bmatrix} & \boldsymbol{H'}_{XA} & \\ \boldsymbol{H'}_{XA} & \begin{bmatrix} E^0_{A(000)}\boldsymbol{I} + H'_{A(000)} & H'_{A(000),A(010)} & \cdots \\ H'_{A(000),A(010)} & E^0_{A(010)}\boldsymbol{I} + H'_{A(010)} & \cdots \\ \vdots & \vdots & \ddots \end{bmatrix} & \\ & & \ddots \end{pmatrix} \tag{2.19}$$

where we have divided the matrix into blocks (square brackets) corresponding to different electronic states, each of which contains an entry for each vibrational state. Each of these entries is itself a matrix describing the rotational structure (contained in $H'_{\eta,v}$), plus an energy offset $E^0_{\eta,v}$ ($\boldsymbol{I}$ is the identity matrix). There are a large number of off-diagonal entries coupling different states, which would nominally mean that the *entire* Hamiltonian needs to be included, even if one is just interested in, say, a single vibrational level of a single electronic state.

This problem is solved in molecular spectroscopy by using "effective Hamiltonians" to describe individual states. The idea is to apply several orders of perturbation theory to make the Hamiltonian approximately block

diagonal, with each block being an effective Hamiltonian $H^{\text{eff}}_{\eta,v}$ describing the vibronic state $|\eta, v\rangle$:

$$H \approx \begin{pmatrix} H^{\text{eff}}_{X(000)} & 0 & 0 & 0 & 0 & 0 \\ 0 & H^{\text{eff}}_{X(010)} & 0 & 0 & 0 & 0 \\ 0 & 0 & \ddots & 0 & 0 & 0 \\ 0 & 0 & 0 & H^{\text{eff}}_{A(000)} & 0 & 0 \\ 0 & 0 & 0 & 0 & H^{\text{eff}}_{A(010)} & 0 \\ 0 & 0 & 0 & 0 & 0 & \ddots \end{pmatrix} \tag{2.20}$$

Each effective Hamiltonian contains both the first-order and the off-diagonal effects of the perturbing Hamiltonian H' up to a reasonable order in perturbation theory. Techniques used for obtaining the effective Hamiltonian include the contact transformation and the Van Vleck transformation [253].

The effective Hamiltonian will typically include first-order effects along with the effect of coupling to different electronic and vibrational states. These effects all get combined into spectroscopic parameters that be measured without having to explicitly consider these couplings, and can still be used to describe the state with a high level of accuracy.[13] The effective Hamiltonian approach is described in great detail in Ref. [253].

2.5.2 Angular momentum quantum numbers: Hund's cases

Once we've written down the effective Hamiltonian for a vibronic state, we need to diagonalize it to find energies and eigenstates. To do this, we need to choose a basis of angular momentum quantum numbers with which

[13] Below, we will sometimes explicitly consider coupling to different electronic and vibrational states, e.g. when understanding the origin of terms in the effective Hamiltonian, or when describing perturbations that affect branching ratios. But for the most part, the effective Hamiltonian approach is sufficient for describing relevant molecular structure.

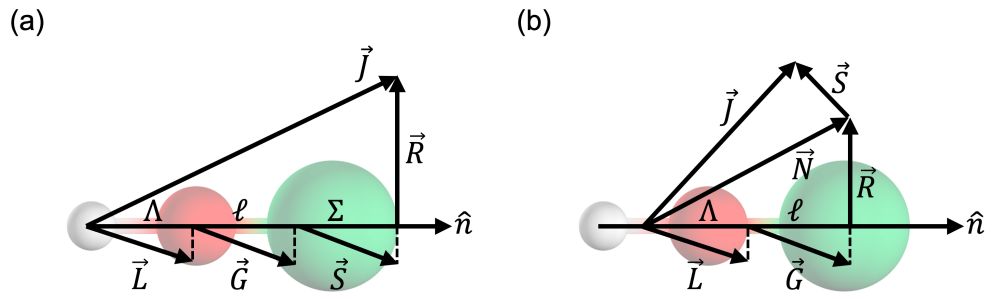

Figure 2.3: Illustration of Hund's case (a) and case (b) angular momentum coupling schemes.

to work. The best choice of basis set depends on the angular momentum coupling in the state of interest. For molecules, there are a number of different angular momentum coupling schemes that provide natural starting points. These are referred to as Hund's cases. In CaOH, most states are well described by either Hund's case (a) or Hund's case (b). These two coupling cases are illustrated in Fig. 2.3 and described in this section.

Hund's case (a) applies to cases where the electron spin couples strongly to the electronic angular momentum and has a definite projection on the molecular symmetry axis. This appliess to the CaOH $\widetilde{A}^2\Pi$ state due to its nonzero electronic angular momentum and large spin-orbit interactions. The electronic orbital angular momentum $\vec{L}$, vibrational angular momentum $\vec{G}$, and electron spin angular momentum $\vec{S}$ have well-defined projections onto the molecular symmetry axis, Λ, ℓ and Σ, respectively. The rigid body rotation $\vec{R}$ is perpendicular to the molecular axis and therefore has no projection. The total angular momentum $\vec{J} = \vec{R} + \vec{L} + \vec{G} + \vec{S}$ also has a well-defined projection quantum number, $P = \Lambda + \Sigma + \ell$. The related projection quantum number $\Omega = \Lambda + \Sigma$ is often also defined, and is useful for describing spin-orbit interactions. For states with $\ell = 0$, P and Ω are equivalent.[14]

[14] Typically P is used for nonlinear molecules and Ω for linear molecules. We have chosen to use P as the projection of J here since it is a more general notation. One should be aware, however, that they are often used interchangeably for linear polyatomics.

Description	Vector label	Projection onto molecular axis
Rigid body rotation	$\vec{R}$	–
Vibrational angular momentum	$\vec{G}$	ℓ
Electronic orbital angular momentum	$\vec{L}$	Λ
Total spinless angular momentum	$\vec{N} = \vec{J} - \vec{S}$	$K = \ell + \Lambda$
Electron spin angular momentum	$\vec{S}$	Σ
Total angular momentum (no hyperfine)	$\vec{J}$	$P = \ell + \Lambda + \Sigma$
Nuclear spin angular moment	$\vec{I}$	–
Total angular momentum (with hyperfine)	$\vec{F} = \vec{J} + \vec{I}$	–

Table 2.4: Quantum numbers used to describe linear polyatomic molecules. Note that Σ and P are only good quantum numbers in Hund's case (a), while $\vec{N}$ (and K) is good in Hund's case (b).

In Hund's case (b), which applies to the $\widetilde{X}^2\Sigma^+$ and $\widetilde{B}^2\Sigma^+$ states, the electron spin $\vec{S}$ does not couple to the molecular axis, but the other relevant angular momenta do. The total angular momentum *excluding* spin is therefore conserved: $\vec{N} \equiv \vec{J} - \vec{S} = \vec{R} + \vec{L} + \vec{G}$. The projection of $\vec{N}$ onto the axis is $K = \Lambda + \ell$. $\vec{N}$ and $\vec{S}$ ultimately add to form the total angular momentum $\vec{J}$.

Table 2.4 gives a summary of the quantum numbers described above. In both cases, for CaOH we also define a total angular momentum *including* the hydrogen nuclear spin, $\vec{F} = \vec{J} + \vec{I}$.

Converting between case (a) and case (b)

The relationship between the case (a) and case (b) basis states is [252]

$$|NKSJM\rangle = \sum_{\Sigma,P} (-1)^{-J+P+2S} (2N+1)^{1/2} \begin{pmatrix} J & N & S \\ P & -K & -\Sigma \end{pmatrix} |JPM\rangle |S\Sigma\rangle \tag{2.21}$$

This is useful, for instance, when describing the $\widetilde{A}^2\Pi$ state in a case (b) basis in order to calculate transition dipole moments for $\widetilde{X}^2\Sigma^+ \rightarrow \widetilde{A}^2\Pi$ transitions.

2.5.3 Calculating energies and eigenstates

The general prescription for calculating the energies of a vibronic manifold in CaOH is as follows. First, one needs to choose a set of basis states, typically either the case (b) basis $|N, \Lambda, \ell, S, J, I, F, M\rangle$ or the case (a) basis $|\Lambda, \ell, \Sigma, S, J, I, F, M\rangle$, and then write the effective Hamiltonian in that basis.[15] This is done by calculating matrix elements $\langle i|H^{\text{eff}}|j\rangle$ so that

$$H^{\text{eff}} = \sum_{i,j} |i\rangle\langle i|H^{\text{eff}}|j\rangle\langle j| \tag{2.22}$$

where $|i\rangle$ and $|j\rangle$ are basis states. The Hamiltonian can then be numerically diagonalized, yielding eigenvalues E_α and eigenvectors $|\alpha\rangle = \sum_i c_i|i\rangle$, where the sum is over basis states $|i\rangle$. The eigenvalues E_α are the molecular state energies, and the eigenvectors provide information about the quantum numbers describing each molecular state. They are also important for calculating transition dipole moments (TDMs) between states, since matrix elements of the dipole operator can be calculated in the case (a) or case (b) basis, then sandwiched between two eigenvectors in the same basis to evaluate the TDM. All of the information about the molecular structure is therefore encapsulated in the matrix elements $\langle i|H^{\text{eff}}|j\rangle$. These can be calculated using spherical tensor algebra, and they are given for many of the relevant states in CaOH in Appendix A.[16]

While evaluating matrix elements and diagonalizing the Hamiltonian is the most general approach for calculat-

[15] The chosen basis should ideally make the Hamiltonian as close to diagonal as possible (typically case (b) for nondegenerate electronic states and case (a) for degenerate electronic states). This isn't mathematically necessary since we will ultimately just take the eigenvalues and eigenvectors of the Hamiltonian, but choosing a "nice" basis helps when assigning quantum numbers to each state.

[16] Hamiltonian matrix elements are described for a variety of molecular structures in Refs. [252, 253], among others.

ing molecular state energies, we can describe most of the states in CaOH with closed-form expressions, provided an appropriate choice of basis is made. In the following sections, we describe the structure of CaOH from this perspective. However, for the most quantitatively accurate calculations, it is recommended that the reader use the matrix elements from Appendix A to diagonalize the full effective Hamiltonian.

2.6 The $\widetilde{X}^2\Sigma^+$ ground state of CaOH

The $\widetilde{X}^2\Sigma$ state is a nondegenerate electronic state with electronic angular momentum projection quantum number $\Lambda = 0$, electron spin $S = 1/2$, and nuclear spin $I = 1/2$. The vibrational angular momentum ℓ depends on the vibrational state, and all states with the same value of ℓ have a similar structure. In this section, we describe the structure of (1) nondegenerate vibrational states ($\ell = 0$, e.g. (000), (100), (02^00), etc.); (2) states with $|\ell| = 1$ [e.g. (010), (110), (03^10)], and (3) states with $|\ell| = 2$ [e.g. (02^20), (12^20)].

2.6.1 Nondegenerate vibrational states ($\ell = 0$)

The effective Hamiltonian for nondegenerate vibrational states in the CaOH $\widetilde{X}^2\Sigma^+$ manifold is

$$H_X^{\text{eff}} = H_{\text{rot}} + H_{\text{sr}} + H_{\text{hf}} \tag{2.23}$$

where H_{rot} is the rotational Hamiltonian, H_{sr} describes the spin-rotation interaction, and H_{hf} describes hyperfine structure. This Hamiltonian applies to the absolute vibronic ground state of CaOH, $\widetilde{X}^2\Sigma^+(000)$, along with other vibrational states used for laser cooling, e.g. $\widetilde{X}^2\Sigma^+(100)$ and $\widetilde{X}^2\Sigma^+(02^00)$. As mentioned above, because this is a nondegenerate electronic state, the electron spin is not coupled to the molecular axes, and the state is well

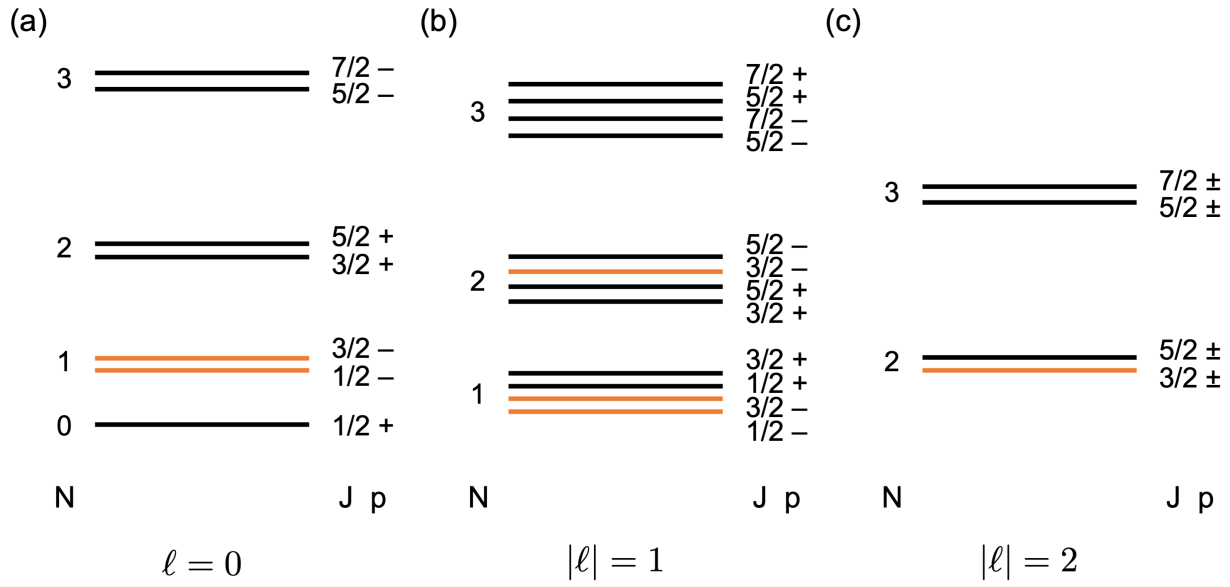

Figure 2.4: Rotational structure of states with different vibrational angular momentum ℓ within the $\widetilde{X}^2\Sigma^+$ electronic manifold. Rotational spacings are approximately to scale, but spin-rotation and parity-doublet splittings are exaggerated. Hyperfine structure is not shown. States that are populated during rotationally-closed optical cycling are highlighted in orange. The quantum numbers are N (rotational angular momentum), J (total angular momentum excluding nuclear spin), p (parity), and ℓ (vibrational angular momentum projection). (a) Nondegenerate vibrational states, e.g. $\widetilde{X}(000)$, $\widetilde{X}(100)$, and $\widetilde{X}(02^00)$. (b) States with $|\ell| = 1$, e.g. the $\widetilde{X}(01^10)$ bending mode. (c) States with $|\ell| = 2$, e.g. the $\widetilde{X}(02^20)$ level.

described using the Hund's case (b) basis $|NSJIFM\rangle$. The structure of this state is illustrated in Fig. 2.4(a).

The rotational part of the Hamiltonian is

$$H_{\text{rot}} = B\boldsymbol{N}^2 - D\boldsymbol{N}^4 \tag{2.24}$$

where B is the rotational constant and D is the centrifugal distortion constant. Our case (b) basis states are eigenstates of $\boldsymbol{N}^2$, so the rotational energies are just

$$E_{\text{rot}}(N) = BN(N+1) - DN^2(N+1)^2 \tag{2.25}$$

In the $\widetilde{X}^2\Sigma^+(000)$ ground state of CaOH, $B = 10.023$ GHz and $D_X = 12$ kHz [93, 242, 254]. The latter term (centrifugal distortion) can safely be ignored when considering the low-lying rotational states used for laser cooling. The parity of each state is $p = (-1)^N$, since the rotational wavefunctions are spherical harmonics $|NM_N\rangle$, which transform like $\hat{P}|N, M_N\rangle = (-1)^N|N, M_N\rangle$ when the parity inversion operator $\hat{P}$ is applied. Note that this is the parity of the full state, not just the rotational part, since the electronic state has $+$ parity. (By comparison, a Σ^- electronic state has $-$ parity, so that the total state would instead follow $p = -(-1)^N$.)

The spin-rotation part of the Hamiltonian describes a coupling between the electron spin and the rotational angular momentum,

$$H_{\text{sr}} = \gamma \boldsymbol{N} \cdot \boldsymbol{S} \tag{2.26}$$

where γ is the spin-rotation constant. For CaOH (which has $S = 1/2$), this interaction splits each rotational state N into two levels, $J = N \pm 1/2$. The energies of these two states are[17]

$$E_{\text{sr}}(J = N + 1/2) = BN(N+1) - DN^2(N+1)^2 + \frac{\gamma}{2}N \tag{2.27a}$$

$$E_{\text{sr}}(J = N - 1/2) = BN(N+1) - DN^2(N+1)^2 - \frac{\gamma}{2}(N+1) \tag{2.27b}$$

where $\gamma = 34.76$ MHz in the vibrational ground state of CaOH [93, 242, 254].[18] The spin-rotation splitting in

[17] These can be derived from the spherical tensor expressions in Appendix A. Alternatively, one can use the standard trick of noting that $2\boldsymbol{N} \cdot \boldsymbol{S} = \boldsymbol{J}^2 - \boldsymbol{N}^2 - \boldsymbol{S}^2$, so that $E_{\text{sr}}(J, N, S) = \gamma/2[J(J+1) - N(N+1) - S(S+1)]$. Plugging in $J = N \pm 1/2$ and $S = 1/2$ gives the correct energies.

[18] γ includes a first-order contribution from the actual spin-rotation coupling in the $\widetilde{X}$ state, but it also includes a significant contribution from 2nd-order coupling to the $\widetilde{A}$ state (absorbed into γ when constructing the effective Hamiltonian). Coarsely speaking, this arises from a cross term between the spin-uncoupling [$\sim B(N_+L_- + N_-L_+)$] and spin-orbit [$\sim A(S_+L_- + S_-L_+)$] interactions (see sec. 2.7), giving a second order contribution $\gamma^{(2)} \sim AB/\Delta E_{XA} \sim 10^{-3}$ cm^{-1} [253], which is actually quite similar to the measured value of γ.

Table 2.5: Values of the CaOH $\widetilde{X}^2\Sigma^+(000)$ effective Hamiltonian parameters.

Parameter	Value	Ref.
B	10023.0841 MHz	[254]
D	11.54 kHz	[254]
γ	34.7593 MHz	[254]
b_F	2.602 MHz	[254]
c	2.053 MHz	[254]
$\lvert\mu\rvert$	1.465 D	[256]

rotational level N is therefore $\Delta E_{\text{sr}} = \gamma/2(2N+1)$, i.e. it is approximately 52 MHz in $N = 1$, 87 MHz in $N = 2$, and so on. Of course, $N = 0$ only has a single level, $J = 1/2$.

The hyperfine Hamiltonian is

$$H_{\text{hf}} = b_F \boldsymbol{I}\cdot\boldsymbol{S} + \frac{c}{3}(3I_zS_z - \boldsymbol{I}\cdot\boldsymbol{S}) \tag{2.28}$$

where the first term is the Fermi contact interaction, and the second is the dipole-dipole hyperfine interaction. In the CaOH $\widetilde{X}^2\Sigma^+(000)$ state, $b_F = 2.602$ MHz and $c = 2.053$ MHz [254], both of which are below the natural linewidth of the excited electronic states ($\Gamma_A \approx 2\pi \times 6.4$ MHz [255]). Therefore, hyperfine structure is optically unresolved, and often reasonable to ignore. In the $N = 1$ state used for CaOH laser cooling, the $J = 3/2$ spin-rotation level splits into $F = 2$ and $F = 1$ hyperfine components spaced by 1.5 MHz, and $J = 1/2$ splits into $F = 0$ and $F = 1$ components spaced by only about 7 kHz (due to cancellation between the Fermi contact and dipolar terms).

The $\widetilde{X}^2\Sigma^+(000)$ state constants are tabulated in table 2.5.

Note that the $\widetilde{B}^2\Sigma^+(000)$ state of CaOH has the same Hamiltonian as $\widetilde{X}^2\Sigma^+(000)$. While the rotational

constant $B = 10.17$ GHz is similar to that of the $\widetilde{X}$ state, the spin-rotation constant $\gamma = -1.30$ GHz is much larger (and negative!) due to strong mixing with the nearby $\widetilde{A}$ state [238].[19]

External fields

We are often interested in the behavior of the molecule under the influence of applied DC electric and magnetic fields (we will consider AC Stark shifts later, in chapter 6).

Ignoring rotational and nuclear spin magnetic moments, the effective Zeeman Hamiltonian for a molecule in a $^2\Sigma^+$ state is [257]

$$H_{\text{Zeeman}} = g_S \mu_B \boldsymbol{S} \cdot \boldsymbol{B} + g_l \mu_B \left(S_x B_x + S_y B_y \right) \tag{2.29}$$

where the first term is the electron spin Zeeman interaction and the second term is an anisotropic Zeeman interaction. In the effective Hamiltonian, g_S is typically close[20] to the electron-spin g-factor of 2.0023, and the anisotropic g-factor g_l is approximately given by the Curl relationship

$$g_l \approx \gamma / 2B \tag{2.30}$$

where γ is the spin-rotation constant and B is the rotation constant [257]. This is roughly three orders of magnitude smaller than g_S in CaOH and can generally be ignored. Matrix elements are found in appendix A, and a plot of the $N = 1$ energies in the $\widetilde{X}^2\Sigma^+(000)$ state of CaOH is found in Fig. 2.5(a).

[19] The spin-rotation splitting in $\widetilde{B}$ is similar in size to Λ-doubling in the $\widetilde{A}$ state. This is not a coincidence, as both effects arise from the same term(s) in the full Hamiltonian. However, they are called different things since $\widetilde{A}$ is a good case (a) state with nonzero electronic angular momentum.

[20] This may not be exact due to the effective Hamiltonian formulation, whereby mixing between electronic states could change the effective value of the Hamiltonian parameters.

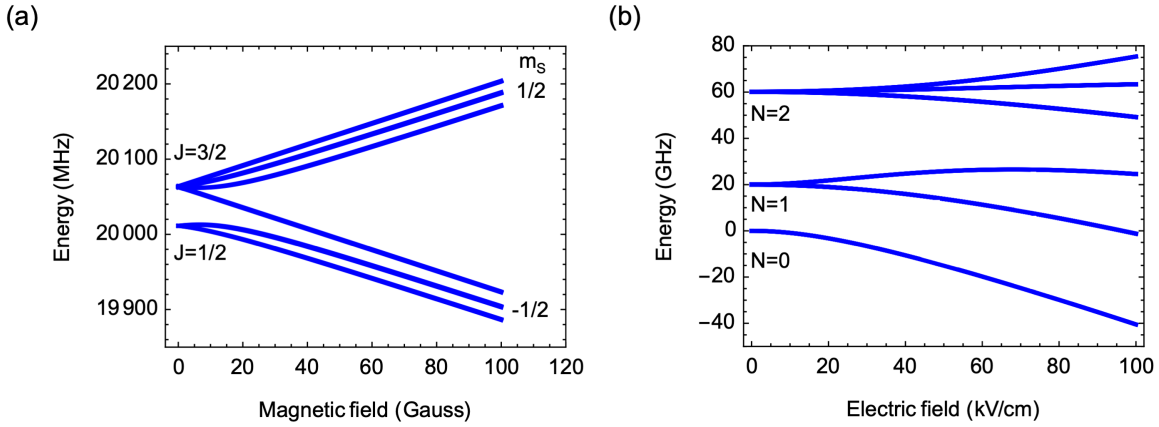

Figure 2.5: (a) Zeeman shifts of the $\widetilde{X}^2\Sigma^+(000)(N = 1)$ state. (b) Stark shifts of low-lying rotational states in $\widetilde{X}^2\Sigma^+(000)$.

The Stark Hamiltonian, describing the influence of external electric fields, is

$$H_{\text{Stark}} = -\boldsymbol{\mu} \cdot \boldsymbol{E} \tag{2.31}$$

where $\boldsymbol{\mu}$ is the molecule-frame electric dipole moment ($|\mu| = 1.465$ D for the $\widetilde{X}^2\Sigma^+(000)$ state of CaOH [256]), and $\boldsymbol{E}$ is the applied electric field. Matrix elements of this Hamiltonian are found in appendix A, and the structure of low-lying rotational levels in the $\widetilde{X}^2\Sigma^+(000)$ state is shown in Fig. 2.5(b). The effect of the electric field is to mix adjacent rotational manifolds of opposite parity, which eventually aligns the molecule in the laboratory frame. This alignment occurs when the dipolar interaction is comparable to the rotational spacing, $\mu E/2B \sim 1$. For CaOH, this occurs at electric fields around 30 kV/cm, as seen in Fig. 2.5(b).

2.6.2 States with $|\ell| = 1$

Vibrational bending modes with $\ell \neq 0$ have angular momentum along the molecular symmetry axis, which complicates the rotational structure, making it look closer to that of a symmetric top molecule. The primary practical difference is that each rotational level contains states of both parities, and those opposite-parity states can be split by a finite energy.

The origin of the nonzero vibrational angular momentum and the opposite parity states is the fact that the bending vibration can occur in two perpendicular planes in the molecule frame, i.e. along the x and y axes, where z is the axis of cylindrical symmetry (Fig. 2.6(a)). In a classical picture, linear combinations of x and y-axis vibrations, when 90° out of phase with each other, lead to motion where the molecule appears permanently bent and rotates about the z axis. This is what causes the vibrational angular momentum ℓ to appear for certain bending modes. See Ref. [258] for a more detailed discussed of bending modes in triatomic molecules.

While the x and y vibrations are nominally degenerate, this degeneracy is lifted by a Coriolis interaction when the molecule's end-over-end rotation is added to the picture [234].[21] As shown in Fig. 2.6(b), bending vibrations in the plane of rotation are perturbed by Coriolis interactions, which couple the bending vibrational mode with stretching vibrational modes. The out-of-plane bending vibration, meanwhile, is unperturbed.

To describe the bending mode quantum mechanically, we once again start by choosing a Hund's case (b) basis, but this time including the vibrational angular momentum ℓ. The case (b) basis states are $|N, \ell, S, J, I, F, M\rangle$. As described in Refs. [252, 253], the action of the parity inversion operator $\hat{P}$ on a symmetric top wavefunction $|NKM\rangle$ is to pull out a phase of $(-1)^{N-K}$ and also flip the sign of K, which is the projection of $\vec{N}$ onto the

[21] Generally speaking, there is always some mechanism that splits opposite-parity states in molecules, though it is often orders of magnitude smaller than in CaOH [92].

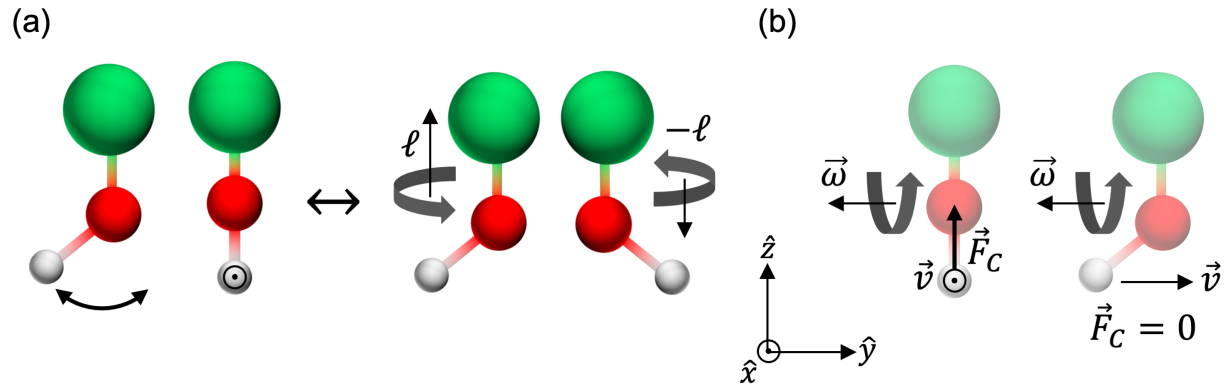

Figure 2.6: Illustration of the vibrational bending mode in CaOH. (a) In the molecule frame, the primary motion in the bending mode is the hydrogen atom moving off axis. This bending can occur in either the x or y plane, leading to two degenerate vibrational modes. Linear combinations of out-of-phase x and y vibrations lead to states with nonzero vibrational angular momentum ℓ, where the molecule appears permanently bent and rotates about the z axis. (b) Lifting of degeneracy due to Coriolis interactions. When the molecule has end-over-end rotational angular momentum $\vec{\omega}$, Coriolis interactions perturb bending vibrations in the plane of rotation but not out of plane. The Coriolis force $\vec{F}_C \propto \vec{\omega} \times \vec{v}$ for the in-plane vibrational mode (where $\vec{v}$ is the velocity of the vibrating atoms) is along the bond axis, thereby coupling the in-plane bending mode with stretching vibrational modes. This lifts the degeneracy of in-plane and out-of-plane bending vibrations.

molecule-frame z axis. In the bending mode, this projection quantum number is $K \equiv \ell$, so that $\hat{P}|N, \ell, S, J, I, F, M\rangle = (-1)^{N-\ell}|N, -\ell, S, J, I, F, M\rangle$. Therefore, we can construct parity eigenstates $|N, |\ell|, S, J, I, F, M, \pm\rangle \equiv \frac{1}{\sqrt{2}}\left(|N, \ell, S, J, I, F, M, \rangle \pm (-1)^{N-\ell}|N, -\ell, S, J, I, F, M\rangle\right)$. Accordingly, each rotational manifold N contains states of both parities, corresponding to linear combinations of states with $\ell = \pm 1$. These states are split by the ℓ-type doubling interaction, whose physical origin is the Coriolis interactions described above [259].

The effective Hamiltonian for $|\ell| = 1$ vibrational states in the CaOH $\widetilde{X}^2\Sigma^+$ manifold is

$$H^{\text{eff}}_{X(010)} = H_{\text{rot}} + H_{\ell\text{d}} + H_{\text{sr}} + H_{\text{hf}} \tag{2.32}$$

where H_{rot} is the rotational Hamiltonian, $H_{\ell\text{d}}$ is the ℓ-type doubling interaction, H_{sr} is the spin-rotation interaction, and H_{hf} is the hyperfine interaction.

Rotational Hamiltonian

The form of the rotation and ℓ-doubling terms can be derived by starting with the *true* rotational Hamiltonian, $H_{\text{rot}} = B\boldsymbol{R}^2$, where $\boldsymbol{R}$ is the rigid body rotational angular momentum. In the vibrational ground state we had $\boldsymbol{N} = \boldsymbol{R}$, but in the bending mode $\boldsymbol{N}$ also includes the vibrational angular momentum $\boldsymbol{G}$ [259]. Substituting in and expanding, we get

$$\begin{aligned} H_{\text{rot}} &= B(\boldsymbol{N} - \boldsymbol{G})^2 \\ &= B\{(N_x - G_x)^2 + (N_y - G_y)^2 + (N_z - G_z)^2\} \\ &= B(N_x^2 + N_y^2) + B(G_x^2 + G_y^2) - 2B(N_x G_x + N_y G_y) \\ &= \underbrace{B(\boldsymbol{N}^2 - \ell^2)}_{\text{rotation}} - \underbrace{B(N_+ G_- + N_- G_+)}_{\ell\text{-type doubling}} + \underbrace{B(G_x^2 + G_y^2)}_{\text{vibrational correction}} \end{aligned} \tag{2.33}$$

where we used $N_z = G_z = \ell$ and $N_\pm = N_x \pm iN_y$.

The first term is what we will call H_{rot} in the effective Hamiltonian, and is reduced by ℓ^2 from the typical $B\boldsymbol{N}^2$ expression to account for the on-axis angular momentum encapsulated by ℓ. The third term is a constant that can be absorbed into the origin energy of the vibrational state. It can be viewed as a correction to the anharmonic constants of the vibrational potential [259].

ℓ-type doubling

The second term in eqn. 2.33 couples different vibrational states, leading to ℓ-doubling. This is the quantum analogue of the classical picture described above, where we saw that Coriolis interactions couple different vibrational

modes to lift the degeneracy of the bending mode. Indeed, the matrix elements of $G_\pm$ are proportional to Coriolis coupling coefficients [259]. Without going into specifics, we can infer the form of the effective ℓ doubling Hamiltonian by looking for combinations of N_+G_- and N_-G_+ that return to the same vibrational state. The vibrational angular momentum operators $G_\pm$ can raise and lower ℓ by 1, while also changing vibrational quantum numbers by 1 [259]. Therefore, these terms can couple the degenerate $\ell = \pm 1$ states in the bending mode at *second order*. In particular, if we start in a state with $\ell = \pm 1$, two applications of $G_\mp$ will connect to a state with $\ell = \mp 1$ in the same vibrational level.[22] Two applications of $N_\pm$ come along for the ride, and operate on the rotational degrees of freedom. The effective ℓ-type doubling Hamiltonian for a state with $|\ell| = 1$ is therefore

$$H_{\ell \mathrm{d}} = \frac{q}{2}(N_+^2 + N_-^2) \tag{2.34}$$

where the ℓ doubling parameter q absorbs the 2nd order coupling to other vibrational states [259]:

$$q = \frac{2B^2}{\omega_2}\left(1 + 4\sum_{k\neq 2}\frac{\zeta_{2k}^2\omega_2^2}{\omega_k^2 - \omega_2^2}\right) \tag{2.35}$$

Here $k = 1, 3$ correspond to the symmetric and antisymmetric stretching modes, $k = 2$ is the bending mode, ω_k is the vibrational frequency of mode k, and ζ_{2k} is a Coriolis coupling coefficient.

The action of the ladder operators $N_\pm$ on the (non-parity) case (b) basis states is $N_\pm|N, \ell, S, J, I, F, M\rangle = [N(N+1) - \ell(\ell \mp 1)]^{1/2}|N, \ell \mp 1, S, J, I, F, M\rangle$.[23] Using this relationship and writing everything in the

[22] There are a number of intermediate states through which this coupling can occur, e.g. $(010) \rightarrow (001) \rightarrow (010)$, $(010) \rightarrow (120) \rightarrow (010)$, etc.

[23] Note that N_+ actually *lowers* ℓ since it acts in the molecule frame – this is what is referred to as an "anomalous" commutation relation [253].

parity basis, we find that $H_{\ell\mathrm{d}}$ is diagonal in the parity basis, with eigenvalues $\pm q(-1)^{N-1}N(N+1)/2$, where $\pm$ corresponds to states with positive and negative parity. In the $\widetilde{X}^2\Sigma^+(010)$ state of CaOH, $q \approx 21.5$ MHz [93, 94][24], so the splitting between opposite parity states in the $N = 1$ bending mode is approximately 42 MHz, with the positive parity state being higher in energy.

Spin-rotation interaction

Replacing $\boldsymbol{N}$ with $\boldsymbol{N} - \boldsymbol{G}$ as above, the spin-rotation Hamiltonian in the bending mode is

$$\begin{aligned} H_{\mathrm{sr}} &= \gamma(\boldsymbol{N} - \boldsymbol{G}) \cdot \boldsymbol{S} \\ &= \gamma[(N_x - G_x)S_x + (N_y - G_y)S_y + (N_z - G_z)S_z] \\ &= \gamma(N_x S_x + N_y S_y) - \gamma(G_x S_x + G_y S_y) \\ &\approx \frac{1}{2}\gamma(N_+ S_- + N_- S_+) \end{aligned} \tag{2.36}$$

where we used that $N_z = G_z$. We dropped the $\gamma(G_x S_x + G_y S_y)$ term because it will mix vibrational levels [259], but negligibly compared to the much larger ℓ-doubling term discussed above (which is proportional to B rather than γ). Matrix elements of this Hamiltonian are found in appendix A.

[24] Note that both of these references used the parity phase convention $(-1)^N$ rather than $(-1)^{N-\ell}$ as used here, so there is a sign difference in our definition of q.

Analytic expressions for the energies when $S = 1/2$ can be found in, e.g., Refs. [245, 260].[25] They are

$$E_{sr}(F_1) = \frac{\gamma}{2}\left[1 - \frac{\ell^2}{N(N+1)}\right] N \tag{2.37a}$$

$$E_{sr}(F_2) = -\frac{\gamma}{2}\left[1 - \frac{\ell^2}{N(N+1)}\right] (N+1) \tag{2.37b}$$

where F_1 and F_2 refer to the upper and lower spin-rotation components in rotational manifold N. Notice that when $N \gg \ell$, these reduce to the standard spin-rotation energies for a linear molecule (eqn. 2.27b). However, for small N there is a noticeable correction. In particular, for $N = 1$ in an $|\ell| = 1$ bending mode, the spin-rotation splitting is $3\gamma/4$, which is a factor of 2 smaller than the $N = 1$ spin-rotation splitting in an $\ell = 0$ state. For the $N = 1$ level in $\widetilde{X}^2\Sigma^+(010)$, this works out to a spin-rotation splitting of approximately 26 MHz.

[25] Note that the spin-rotation energies are those of a symmetric top molecule, but with zero $N_z S_z$ interaction. There can, in principle, be an $N_z S_z$ interaction in the bending mode, which is proportional to γ' in Ref. [259]. However, this interaction has not been observed in CaOH and is presumed to be small.

Combined energies

Combining the above, the energies of rotational states in an $|\ell| = 1$ bending mode (e.g. $\widetilde{X}^2\Sigma^+(010)$), excluding hyperfine interactions, are [259]

$$E(J = N + 1/2, \pm) = B\left[N(N+1) - \ell^2\right] - D\left[N(N+1) - \ell^2\right]^2 \pm (-1)^{N-\ell}\frac{q}{2}N(N+1) + \frac{\gamma}{2}\left[1 - \frac{\ell^2}{N(N+1)}\right]N \tag{2.38a}$$

$$E(J = N - 1/2, \pm) = B\left[N(N+1) - \ell^2\right] - D\left[N(N+1) - \ell^2\right]^2 \pm (-1)^{N-\ell}\frac{q}{2}N(N+1) - \frac{\gamma}{2}\left[1 - \frac{\ell^2}{N(N+1)}\right](N+1) \tag{2.38b}$$

where the two equations refer to the upper and lower spin-rotation components in each manifold (the F_1 and F_2 components), while $\pm$ refers to the parity of the state. The constants for the $\widetilde{X}^2\Sigma^+(010)$ bending mode of CaOH are listed in table 2.6. The structure of low-lying rotational states is shown in Fig. 2.4(b).

The hyperfine Hamiltonian is the same as for the $\ell = 0$ states (eqn. 2.28), and its matrix elements are in appendix A. Hyperfine interactions cause each J state to split into two F states separated by 1-2 MHz. The structure of the $\widetilde{X}^2\Sigma^+(010)$ bending mode is shown with all hyperfine splittings in Fig. 7.1, later in this thesis.

External fields

The Zeeman and Stark Hamiltonians for the bending mode are the same as in the vibrational ground state (eqns. 2.29 and 2.31). Zeeman shifts and Stark shifts of the $N = 1$ manifold in $\widetilde{X}^2\Sigma^+(010)$ are shown in Fig. 2.7.

As discussed in section 1.2.1, the parity-doublet structure of the bending mode means that the molecule is

Table 2.6: Values of the CaOH $\widetilde{X}^2\Sigma^+(010)$ effective Hamiltonian parameters used in this thesis.

Parameter	Value	Ref.
B	9996.82 MHz	[93][a]
D	11.7818 kHz	[93]
γ	35.4954 MHz	[93]
q	21.5281 MHz	[93]
b_F	2.45 MHz	This work[b]
c	2.6 MHz	This work
$\lvert\mu\rvert$	1.465 D	[256][c]

a Parameters for $\widetilde{X}(010)$ were also measured in Ref. [94]. Though they were not used in this thesis, they appear to agree slightly better with our measurements and are recommended for use in future work.

b Estimated by fiting a limited data set of microwave transitions observed in this work. The constants differ by a few hundred kHz from the values for $\widetilde{X}(000)$ from Ref. [254].

c Measured for the $\widetilde{X}(000)$ vibrational state and assumed to be the same for $\widetilde{X}(010)$ (in good agreement with our data).

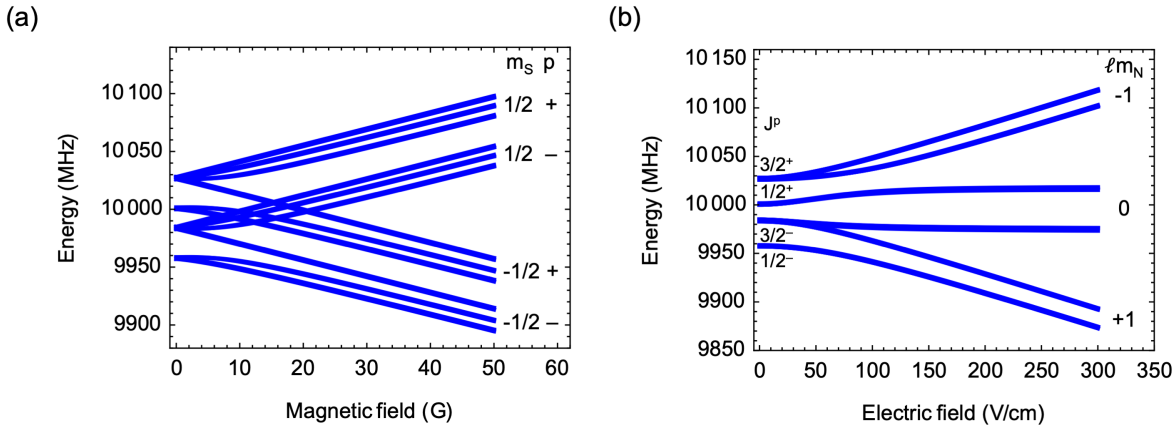

Figure 2.7: (a) Zeeman shifts of the $\widetilde{X}^2\Sigma^+(010)(N = 1)$ state. (b) Stark shifts of the $\widetilde{X}^2\Sigma^+(010)(N = 1)$ state.

aligned in the lab frame at low electric fields, in this case only around 150 V/cm. The sign and magnitude dipole moment is determined in part by the sign of ℓm_N, as discussed in Ref. [140], where m_N is the projection of N onto the lab frame quantization axis (defined by the electric field). At high field, the $N = 1$ state splits into three distinct manifolds grouped by the value of ℓm_N, as shown in Fig. 2.7. These manifolds are further split by spin-rotation, ℓ-type doubling, and hyperfine interactions.

2.6.3 States with $|\ell| = 2$

While we are mostly interested in states with $\ell = 0$ and $|\ell| = 1$ in this work, a few of the repumping transitions used for CaOH laser cooling address states with $|\ell| = 2$, specifically $\widetilde{X}(02^20)$ and $\widetilde{X}(12^20)$. The effective Hamiltonian contains the same terms as for $|\ell| = 1$ states, namely rotation, ℓ-type doubling, spin-rotation, and hyperfine. The rotation, spin-rotation, and hyperfine Hamiltonians are the same as those discussed above. However, the ℓ-type doubling in this state is different. As we saw, the ℓ-doubling interaction mixes states with $\Delta\ell = 2$, which can directly couple $\ell = \pm 1$ in the $\widetilde{X}(010)$ bending mode. However, for an $|\ell| = 2$ state, this interaction couples $\ell = \pm 2$ to $\ell = 0$, which is an energy $4g_{22}$ away (sec. 2.3). For instance, the ℓ-doubling interaction mixes $\widetilde{X}(02^20)^2\Delta$ with $\widetilde{X}(02^00)^2\Sigma$ in CaOH. In second order perturbation theory, the energy shift of the $|\ell| = 2$ states is therefore on the order of $q^2/4g_{22} \sim 1$ kHz.[26] Accordingly, the parity doubling in $|\ell| = 2$ states is significantly smaller than in $|\ell| = 1$ states.

[26] Another way to think about this is that the $|\ell| = 1$ states are mixed at second order, after two applications of $G_\pm$, while for $|\ell| = 2$ a fourth order vibrational mixing is required.

The energies of $|\ell| = 2$ vibrational states in the CaOH ground state (e.g. $\widetilde{X}(02^20)$) are

$$E(J = N + 1/2, \pm) \approx B\left[N(N+1) - \ell^2\right] - D\left[N(N+1) - \ell^2\right]^2 + \frac{\gamma}{2}\left[1 - \frac{\ell^2}{N(N+1)}\right] N \tag{2.39a}$$

$$E(J = N - 1/2, \pm) \approx B\left[N(N+1) - \ell^2\right] - D\left[N(N+1) - \ell^2\right]^2 - \frac{\gamma}{2}\left[1 - \frac{\ell^2}{N(N+1)}\right] (N+1) \tag{2.39b}$$

where we have approximated the ℓ-doublets as degenerate and neglected hyperfine interactions. The structure of low-lying rotational states is shown in Fig. 2.4(c). In the lowest rotational level, $N = 2$, the spin-rotation splitting is $5\gamma/6 \approx 29$ MHz.

Fig. 2.8 shows energies of the $\widetilde{X}(02^20)(N = 2)$ as a function of applied electric field, calculated using the Hamiltonian from Refs. [250, 259]. Because of the small parity doubling (calculated to be ∼15 kHz using the Hamiltonian from Refs. [250, 259]), linear Stark shifts occur even at very small applied electric fields. Practically speaking, this probably means that molecules populate states of both parities during optical cycling due to stray electric fields. However, the same stray fields make it straightforward to repump both states (which are optically unresolved), so this presents no problems for the closed cycling transitions discussed later.

Finally, while we did not explore this state during this thesis work, the linear Stark shifts in $\widetilde{X}(02^20)$ could potentially be useful for quantum science applications that rely on linear Stark shifts near zero field.

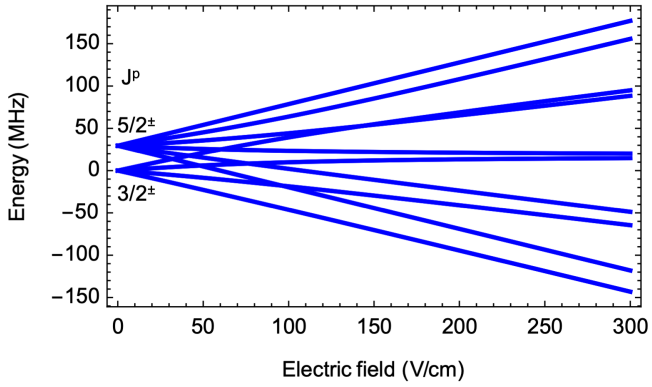

Figure 2.8: Stark shifts of the $\widetilde{X}^2\Sigma^+(02^20)(N=2)$ state in CaOH. The parity doubling is approximately 15 kHz, and so the state has linear Stark shifts even at very small electric fields.

2.7 The $\widetilde{A}^2\Pi$ excited state

The $\widetilde{A}^2\Pi$ state of CaOH has electronic angular momentum $|\Lambda| = 1$, which qualitatively changes its structure compared to the nondegenerate $\widetilde{X}^2\Sigma^+$ and $\widetilde{B}^2\Sigma^+$ states. In nondegenerate vibrational levels ($\ell = 0$), this introduces spin-orbit and Λ-doubling interactions to the Hamiltonian, in addition to molecular rotation and hyperfine interactions. In degenerate vibrational states ($\ell \neq 0$), the combination of electronic and vibrational angular momentum also allows strong *vibronic* mixing to occur. Below, we will discuss the structure of relevant vibrational levels in the $\widetilde{A}^2\Pi$ electronic state of CaOH, including states with $\ell = 0$ [$\widetilde{A}(000)$, $\widetilde{A}(100)$, ...], $|\ell| = 1$ [$\widetilde{A}(010)$], and $|\ell| = 2$ [$\widetilde{A}(020)$].

2.7.1 Nondegenerate vibrational states

The $\widetilde{A}^2\Pi$ state is best described by a Hund's case (a) basis, since the electronic angular momentum helps the electron spin also coupled to the internuclear axis. The bare case (a) basis states are $|\Lambda; S, \Sigma; J, P, M\rangle$.[27] The corresponding parity basis states (which are closest to the true molecular eigenstates), are $||\Lambda|; S, |\Sigma|; J, |P|, M; \pm\rangle = 2^{-1/2}[|\Lambda; S, \Sigma; J, P, M\rangle \pm (-1)^{J-S}|-\Lambda; S, -\Sigma; J, -P, M\rangle]$. Note that we will not consider the hyperfine structure of the $\widetilde{A}^2\Pi$ state, which is optically unresolved and has not been measured.[28]

Coarse derivation of the effective Hamiltonian

To gain an understanding of where the interactions in the $\widetilde{A}^2\Pi$ state come from, we will take a similar approach to the $\widetilde{X}(010)$ bending mode and start by writing the spin-orbit and rotation Hamiltonians in terms of the pure rotational quantum number $\boldsymbol{R} = \boldsymbol{J} - \boldsymbol{S} - \boldsymbol{L}$.[29] This allows us to directly see the effect of coupling between electronic states, which ultimately manifests itself as Λ doubling in the effective Hamiltonian for the $\widetilde{A}$ state only. Writing out the spin-orbit and rotational interactions and expanding, we have:

$$H = A\boldsymbol{L}\cdot\boldsymbol{S} + B\boldsymbol{R}^2 = A\boldsymbol{L}\cdot\boldsymbol{S} + B(\boldsymbol{J}-\boldsymbol{S}-\boldsymbol{L})^2$$

$$= (A+2B)\boldsymbol{L}\cdot\boldsymbol{S} + B\boldsymbol{J}^2 - 2B\boldsymbol{J}\cdot\boldsymbol{S} - 2B\boldsymbol{J}\cdot\boldsymbol{L} + B\boldsymbol{S}^2 + B\boldsymbol{L}^2$$

[27] Note that in diatomic molecules, $\Omega = \Lambda + \Sigma$ is often used in place of P. However, for generality we will use P in our discussion of polyatomic molecules, which is the projection of J onto the molecular axis even in the presence of contributions besides Λ and Σ. ($P = K + \Sigma = \Lambda + \ell + \Sigma$.)

[28] Hyperfine structure in the $\widetilde{A}^2\Pi$ state of CaF is described in Ref. [261]. Even in CaF, which has order-of-magnitude larger hyperfine splittings than CaOH in the ground state, hyperfine structure was unresolved in the $\widetilde{A}$ state. Therefore, it is likely that the hyperfine structure is quite small in the CaOH $\widetilde{A}$ state.

[29] This section is based on Brown & Carrington section 8.5 [253].

where A is the spin-orbit constant and B is the rotational constant. This can be split into "diagonal" and "off-diagonal" contributions, where the diagonal part acts within the $\widetilde{A}$ state and the off-diagonal contributions couple to different states, which will have to be accounted for in order to build an effective Hamiltonian acting within the $\widetilde{A}$ state only.

The diagonal part and its energy eigenvalues are

$$\begin{aligned} H_{\text{diag}} &= (A+2B)L_zS_z + B\boldsymbol{J}^2 + B\left[\boldsymbol{S}^2 + L_z^2 - 2J_z(S_z+L_z)\right] \\ E_{\text{diag}} &= \underbrace{(A+2B)\Lambda\Sigma}_{\text{spin-orbit}} + \underbrace{BJ(J+1)}_{\text{rotation}} + \underbrace{B\left[S(S+1)+\Lambda^2-2P^2\right]}_{\text{constant energy offset}} \end{aligned} \tag{2.40}$$

The diagonal spin-orbit term leads to a splitting $(A+2B)$ between states with $\Omega = \Lambda + \Sigma = 1/2$ and $3/2$. This is quite large, around 2 THz for CaOH. We label these two spin-orbit manifolds with a subscript denoting the value of $|\Omega|$, i.e. as the $\widetilde{A}^2\Pi_{1/2}$ and $\widetilde{A}^2\Pi_{3/2}$ states. The second term is the normal rotational rotational energy, and the third term is a constant that can be absorbed into the origin energy of the state.

The off-diagonal part is

$$\begin{aligned} H_{\text{off-diag}} = &\overbrace{\frac{1}{2}(A+2B)(L_+S_- + L_-S_+) - B(J_+L_- + J_-L_+)}^{\Lambda-\text{doubling}} \\ &- \underbrace{B(J_+S_- + J_-S_+)}_{\text{spin uncoupling}} - \underbrace{B(L_x^2+L_y^2)}_{\text{constant energy offset}} \end{aligned} \tag{2.41}$$

The spin-uncoupling term mixes the ${}^2\Pi_{1/2}$ and ${}^2\Pi_{3/2}$ spin-orbit manifolds, and (as its name suggests) is responsible for the spin becoming decoupled from the molecular symmetry axis as the molecule rotates faster. This

means that the eigenstates slowly transition from good case (a) towards case (b) at higher J. Moreover, this term means that the effective rotational constant is different for the $\widetilde{A}^2\Pi_{1/2}$ and $\widetilde{A}^2\Pi_{3/2}$ components, as we will see below. The final term is a constant energy offset, which we can absorb into the origin energy of the state.

The first term couples $\widetilde{A}^2\Pi$ to other electronic states, and is responsible for Λ doubling, which lifts the degeneracy between opposite parity states $|\pm\rangle = 2^{-1/2}\left(|\Lambda\rangle \pm (-1)^{J-S}|-\Lambda\rangle\right)$. The basic argument for why this occurs (at least in a quantum mechanical picture), is that the Λ-doubling operator couples each rotational level in the $\widetilde{A}^2\Pi$ state to a corresponding rotational level in a nearby $^2\Sigma$ state (primarily $\widetilde{B}^2\Sigma^+$). However, since the Λ-doubling operator conserves parity, and each rotational level in a $^2\Sigma$ state has just a single parity, only one of the two opposite parity states in $\widetilde{A}$ is shifted by this coupling. This lifts the degeneracy.[30]

Following the same argument as for ℓ-doubling in our discussion of the $\widetilde{X}(010)$ state, the form of the effective Hamiltonian can be derived by finding combinations of terms that couple back to the same electronic state at 2nd order. Since $L_\pm$ is a raising/lowering operator for the electronic angular momentum Λ, applying $L_\pm^2$ takes $\Lambda = \mp 1$ to $\Lambda = \pm 1$ via an intermediate Σ state. Taking all combinations of such terms gives [253]

$$H_{\Lambda\mathrm{d}}^{\mathrm{eff}} = \frac{1}{2}(o_v + p_v + q_v)(S_+^2 + S_-^2) - \frac{1}{2}(p_v + 2q_v)(J_+S_+ + J_-S_-) + \frac{1}{2}q_v(J_+^2 + J_-^2) \tag{2.42}$$

where the Λ-doubling parameters incorporate the 2nd-order sum over intermediate states.[31] For example, the dominant Λ-doubling parameter in the CaOH $\widetilde{A}^2\Pi_{1/2}$ state is p_v, which is on the order of $BA/\Delta E_{AB}$, where B is the rotational constant, A is the spin-orbit constant, and ΔE_{AB} is the energy splitting between the $\widetilde{A}^2\Pi_{1/2}$

[30] This argument is explained in more detail in section 7.4.5 of Ref. [253].

[31] Also implicit in this Hamiltonian is a condition that it only couple states with $\Delta\Lambda = \pm 2$.

and $\widetilde{B}^2\Sigma^+$ states.[32]

In the $\widetilde{A}^2\Pi_{1/2}$ state, the second term in eqn. 2.42 is the dominant interaction, since it directly couples the (initially degenerate) $\Omega = P = \pm 1/2$ components. Meanwhile, the first term vanishes when $S = 1/2$, and the third term couples $^2\Pi_{1/2}$ to $^2\Pi_{3/2}$.[33] In the case (a) parity basis, the eigenvalues of the 2nd term are $\pm(-1)^{J+S}(p+2q)(J+1/2)/2$, where $\pm$ refers to the positive and negative parity states.

Energy level expressions

Combining the above results, and grouping constants into effective Hamiltonian parameters, the energies of the $\widetilde{A}^2\Pi$ state may be written analytically as follows [236, 237]:

$$\begin{aligned} E(^2\Pi_{1/2}, \pm) &= T_{\text{eff}} - \frac{1}{2}A_{\text{eff}} + B_{1/2}J(J+1) \pm (-1)^{J+1/2}\frac{1}{2}(p+2q)\left(J+\frac{1}{2}\right) \\ E(^2\Pi_{3/2}, \pm) &= T_{\text{eff}} + \frac{1}{2}A_{\text{eff}} + B_{3/2}J(J+1) \end{aligned} \tag{2.43}$$

The first term is the electronic and vibrational origin energy, the second term is the spin-orbit splitting, the third term is the rotational structure, and the final term is the Λ doubling. Here we neglect Λ-doubling in the $^2\Pi_{3/2}$ state, which is small. The upper (lower) sign refers to states with $+$ ($-$) parity.

[32] Meanwhile, q_v is proportional to $B^2/\Delta E_{AB}$ and is therefore a much smaller contribution.

[33] Note that the Λ doubling is much smaller in the $^2\Pi_{3/2}$ component because the *only* contribution is from mixing with $^2\Pi_{1/2}$.

Table 2.7: Values of the CaOH $\widetilde{A}^2\Pi(000)$ parameters.

Parameter	Value (cm^{-1})	Value (Hz)	Ref.
T	15998.122	479.612 THz	[93][a]
A	66.8181	2.003 THz	[93]
B	0.341220	10.230 GHz	[93]
$p+2q$	−0.04352	−1.305 GHz	[93]
g_l'		−0.065	[166]
$\lvert\mu\rvert(\widetilde{A}^2\Pi_{1/2})$		0.836 D	[256]
$\lvert\mu\rvert(\widetilde{A}^2\Pi_{3/2})$		0.766 D	[256]

[a] Note that Ref. [237] measured the effective Hamiltonian parameters (eqn. 2.44), which are in agreement with the "true" parameters from Ref. [93] after transforming appropriately.

The effective Hamiltonian parameters are defined in terms of the "true" parameters as [236]

$$T_{\text{eff}} = T - \frac{3}{4}B \tag{2.44a}$$

$$A_{\text{eff}} = A - 2B \tag{2.44b}$$

$$B_{1/2} \approx B - \frac{B^2}{A} \tag{2.44c}$$

$$B_{3/2} \approx B + \frac{B^2}{A} \tag{2.44d}$$

where T is the electronic and vibrational origin energy, A is the spin-orbit constant, and B is the rotational constant. The constants for the $\widetilde{A}^2\Pi(000)$ state of CaOH are given in Tab. 2.7. Note, as usual, that these energies can also be calculated by building and diagonalizing the Hamiltonian, using matrix elements from appendix A.

Energy levels of the $\widetilde{A}^2\Pi$ state are shown in Fig. 2.9. The state is split into two spin-orbit manifolds, $\widetilde{A}^2\Pi_{1/2}$ and $\widetilde{A}^2\Pi_{3/2}$, split by approximately 2 THz. Within each manifold, there is a rotational ladder of states split by multiples of the rotational constant, $B \approx 10$ GHz. Each rotational state is split into two opposite parity (Λ-

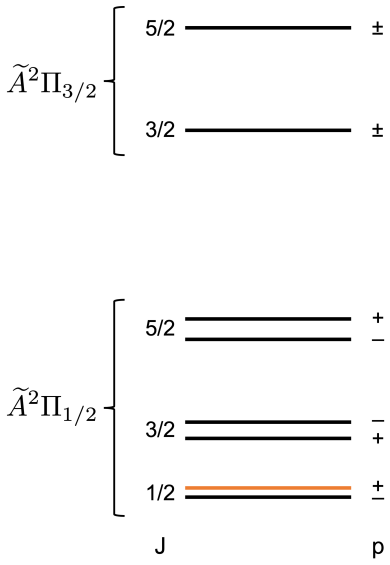

Figure 2.9: Low-lying rotational structure of the $\widetilde{A}^2\Pi(000)$ state (not to scale). The state used for optical cycling is highlighted.

doublet) states, with the splitting around 1 GHz.

External fields

The Stark Hamiltonian is the same as for the ground state (eqn. 2.31). The electric dipole moments of the $\widetilde{A}^2\Pi_{1/2}$ and $\widetilde{A}^2\Pi_{3/2}$ components are given in Tab. 2.7. The primary effect of applied electric fields is to mix the opposite-parity Λ-doublet states, which are approximately 1 GHz apart. This occurs when $\mu E/p \sim 1$ for $J = 1/2$ in the $\widetilde{A}^2\Pi_{1/2}$ state, which happens at electric fields $E \sim 3$ kV/cm. Parity mixing in the excited state will interfere with closed optical cycling when laser cooling CaOH, so we need to be careful to avoid applying large electric fields to the molecules.

The Zeeman Hamiltonian is [257]

$$H_Z = g_S \mu_B \boldsymbol{S} \cdot \boldsymbol{B} + g'_L \mu_B \boldsymbol{L} \cdot \boldsymbol{B} + g_l \mu_B \left(S_x B_x + S_y B_y\right) + g'_l \mu_B \left(e^{-2i\phi} S_+ B_+ + e^{+2i\phi} S_- B_-\right) \quad (2.45)$$

where g_S is the electron g factor, g'_L is the electron orbital g-factor, and g_l and g'_l are parity-independent and parity-dependent anisotropic g factors. In the $\widetilde{A}^2\Pi_{1/2}$ state, $\Sigma = \pm 1/2$ and $\Lambda = \mp 1$. Therefore, the first two terms approximately cancel, since $g_S\Sigma + g_L\Lambda \approx 0$ [262]. The dominant contribution thus turns out to come from the g'_l term, where g'_l can be estimated from a Curl relationship as $g'_l \approx p/2B \approx -0.063$ [166, 214, 257]. This is in excellent agreement with the measured value of $g'_l = -0.065(4)$. In the $J = 1/2$ state (which we use for laser cooling), the corresponding shift of the $M_J = \pm 1/2$ states is $\Delta E = \pm \frac{1}{3} g'_l \mu_B B_Z \approx \mp 0.022 \mu_B B_Z$. This very small Zeeman tuning is one reason magneto-optical trapping is difficult for molecules, as discussed in section 5.4.1.

2.7.2 The $\widetilde{A}(010)$ manifold

The $\widetilde{A}(010)$ manifold is strongly influenced by vibronic interactions, due to the coupling of the electronic and vibrational angular momentum ($|\Lambda| = |\ell| = 1$), and it therefore looks fairly different from the nondegenerate vibrational state(s) described above. This state is used frequently in this thesis work, both for laser cooling and for preparation and manipulation of molecules in the $\widetilde{X}(010)$ vibrational bending mode. In this section, we provide an overview of the structure of the $\widetilde{A}^2\Pi(010)$ state in CaOH. More general details on these states can be found in Refs. [93, 252, 263].

Fig. 2.10 shows the high-level structure of the state, which is split into four vibronic components by spin-orbit

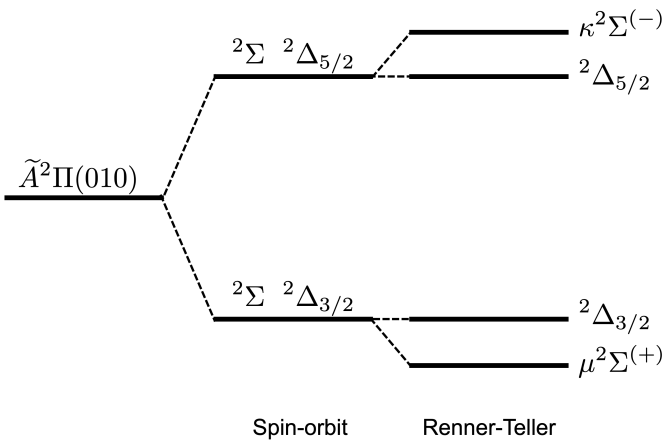

Figure 2.10: Vibronic components of the $\widetilde{A}^2\Pi(010)$ state in CaOH. The state is split by spin-orbit and vibronic interactions into four manifolds.

and vibronic interactions (specifically Renner-Teller interactions [252]). The states are labeled using the general vibronic state notation

$$^{2S+1}\Lambda(v_1v_2v_3)^{2S+1}K$$

where the electronic ($\Lambda = \Sigma, \Pi, \ldots$) and vibronic ($K = \Sigma, \Pi, \ldots$) symmetry are both indicated. The two vibronic $^2\Delta$ states are differentiated by the value of $P = \Lambda + \ell + K$, while the two $^2\Sigma$ states are conventionally distinguished with the labels μ and κ, where μ refers to the lower energy state and κ refers to the higher energy state. Finally, we note that the vibronic symmetry labels $^2\Sigma^{(\pm)}$ are meant to indicate that the two states look approximately, but not exactly, like $^2\Sigma^+$ and $^2\Sigma^-$ states.

The $\widetilde{A}(010)$ state in CaOH has been previously observed at high resolution. The Hamiltonian and fit parameters are described in Ref. [93], which should be used for quantitative energy level calculations. In the remainder of this section, we describe the vibronic interactions that appear in this state and describe the way they, along with the spin-orbit interaction, determine the energy of the four manifolds seen in Fig. 2.10.

Renner-Teller interaction

The Renner-Teller interaction is one of several effects that can occur in polyatomic molecules due to vibronic coupling – i.e. interactions between vibrational and electronic degrees of freedom that violate the Born-Oppenheimer approximation [252]. In linear polyatomic molecules, vibronic coupling occurs in states with nonzero electronic and vibrational angular momentum. For example, in a Π electronic state of a linear polyatomic like CaOH, vibronic interactions occur when a vibrational bending mode breaks cylindrical symmetry, thereby lifting the double-degeneracy between the two degenerate components of the electronic Π state wavefunction.[34] The resulting Hamiltonian consists of terms arising from a multipolar expansion of the electrostatic interaction between the nuclei and the valence electron [251, 252, 264–268],

$$H_{\mathrm{RT}} = \frac{V_{11}}{2}(q_+ L_- + q_- L_+) + \frac{V_{22}}{2}(q_+^2 L_-^2 + q_-^2 L_+^2) + \dots \tag{2.46}$$

where $L_\pm$ and $q_\pm$ are ladder operators for the electronic angular momentum Λ and the vibrational angular momentum ℓ, respectively. $q_\pm$ connects states satisying $q_\pm|\ell\rangle \propto |\ell \pm 1\rangle$, while $L_\pm$ connects states satisfying $L_\pm|\Lambda\rangle \propto |\Lambda \pm 1\rangle$.

The first, dipolar, term of H_{RT} has matrix elements between *different* electronic states, and couples pairs of states like $\widetilde{A}^2\Pi(000)$ and $\widetilde{B}^2\Sigma^+(010)$ (for example). This perturbation allows nominally symmetry-forbidden vibrational decays to occur when optically cycling CaOH, as discussed in chapter 4. It is sometimes referred to as the Herzberg-Teller interaction [252] or linear vibronic coupling [269].

[34] For instance, a bending vibration along x will break the degeneracy of the x and y lobes of the Π state electronic wavefunction.

The second, quadrupolar, term supports matrix elements within a single Π state.[35] This term causes Renner-Teller splittings in degenerate vibrational levels of the $\widetilde{A}^2\Pi$ electronic state, e.g. in $\widetilde{A}(010)$ as discussed here. Working with the case (a) basis set $|\Lambda, \ell, \Sigma\rangle$ (ignoring end-over-end rotation for now), we see that application of the V_{22} term gives $q_{\pm}^2 L_{\mp}^2 |\Lambda, \ell, \Sigma\rangle \propto |\Lambda \mp 2, \ell \pm 2, \Sigma\rangle$. Therfore, in the $\widetilde{A}(010)$ state, where $|\Lambda| = |\ell| = 1$, the nonzero matrix elements of $H_{\rm RT}$ are those that couple $|\pm 1, \mp 1, \Sigma\rangle$ to $|\mp 1, \pm 1, \Sigma\rangle$. Specifically, it turns out that $\langle \pm 1, \mp 1, \Sigma | H_{\rm RT} | \mp 1, \pm 1, \Sigma\rangle = \epsilon\omega_2$, where ϵ is the Renner parameter and ω_2 is the bending frequency [93, 252].[36]

Ultimately, this means that $H_{\rm RT}$ mixes the ${}^2\Sigma$ (i.e. $K = \Lambda + \ell = 0$) components in the $\widetilde{A}(010)$ manifold, while leaving the ${}^2\Delta$ states unperturbed.

Energies including Renner-Teller and spin-orbit

Here we will describe the $\widetilde{A}(010)$ vibronic states using the case (a) parity basis

$$|\Lambda, \ell, \Sigma, \pm\rangle = \frac{1}{\sqrt{2}}\big(|\Lambda, \ell, \Sigma\rangle \pm (-1)^{J-S}|-\Lambda, -\ell, -\Sigma\rangle\big)$$

The spin-orbit interaction couples Λ and Σ, while the vibronic interaction couples Λ and ℓ (while conserving $K = \Lambda + \ell$). The diagonal spin-orbit interaction is the same as described earlier, $H_{\rm SO} = A_{\rm eff}\Lambda\Sigma$. As shown in Fig. 2.10, this splits the $\widetilde{A}(010)$ state into two spin orbit manifolds, with the upper one having $|\Lambda + \Sigma| = 3/2$ and the lower manifold having $|\Lambda + \Sigma| = 1/2$. At this point, the Δ and Σ vibronic states are still degenerate: the upper spin-orbit manifold contains the ${}^2\Delta_{5/2}$ state $|1, 1, 1/2, \pm\rangle$ and the $\kappa^2\Sigma$ state $|1, -1, 1/2, \pm\rangle$, and the

[35] Since it can couple $\Lambda = +1$ to $\Lambda = -1$.

[36] The Renner parameter is related to matrix elements of the Hamiltonian parameters, e.g. $\epsilon\omega_2 \sim \langle -\Lambda | V_{22} L_-^2 | \Lambda\rangle$.

lower spin-orbit manifold contains the $^2\Delta_{3/2}$ state $|1, 1, -1/2, \pm\rangle$ and the $\mu^2\Sigma$ state $|1, -1, -1/2, \pm\rangle$.

When the Renner-Teller (RT) interaction is added, it mixes the two $^2\Sigma$ states but not the $^2\Delta$ states. Just considering the $^2\Sigma$ states, we can write the Hamiltonian $H = H_{\text{SO}} + H_{\text{RT}}$ as a 2x2 matrix in the basis defined by the two $^2\Sigma$ states:

$$H = \begin{pmatrix} \frac{1}{2}A_{\text{eff}} & \epsilon\omega_2 \\ \epsilon\omega_2 & -\frac{1}{2}A_{\text{eff}} \end{pmatrix} \tag{2.47}$$

Diagonalizing this Hamiltonian gives the energies

$$E(\mu^2\Sigma^{(+)}) = -\frac{1}{2}\sqrt{A_{\text{eff}}^2 + 4(\epsilon\omega_2)^2} \tag{2.48a}$$

$$E(^2\Delta_{3/2}) = -\frac{1}{2}A_{\text{eff}} \tag{2.48b}$$

$$E(^2\Delta_{5/2}) = +\frac{1}{2}A_{\text{eff}} \tag{2.48c}$$

$$E(\kappa^2\Sigma^{(-)}) = +\frac{1}{2}\sqrt{A_{\text{eff}}^2 + 4(\epsilon\omega_2)^2} \tag{2.48d}$$

This explains the state orderings and relative splittings seen in Fig. 2.10. In the CaOH $\widetilde{A}(010)$ state, $A_{\text{eff}} = 67.0951\ \text{cm}^{-1}$, and $\epsilon\omega_2 = -36.2634\ \text{cm}^{-1}$ [93].

The eigenstates in the parity basis, $|\Lambda, \ell, \Sigma, \pm\rangle$, are

$$|\widetilde{A}^2\Pi(010)\mu^2\Sigma^{(+)}\rangle = \cos\beta|1,-1,-1/2,\pm\rangle - \sin\beta|1,-1,1/2,\pm\rangle \tag{2.49a}$$

$$|\widetilde{A}^2\Pi(010)^2\Delta_{3/2}\rangle = |1,1,-1/2,\pm\rangle \tag{2.49b}$$

$$|\widetilde{A}^2\Pi(010)^2\Delta_{5/2}\rangle = |1,1,1/2,\pm\rangle \tag{2.49c}$$

$$|\widetilde{A}^2\Pi(010)\kappa^2\Sigma^{(-)}\rangle = \sin\beta|1,-1,-1/2,\pm\rangle + \cos\beta|1,-1,1/2,\pm\rangle, \tag{2.49d}$$

where

$$\beta = \frac{1}{2}\arcsin\left(\frac{2\epsilon\omega_2}{\sqrt{A_{\text{eff}}^2 + 4(\epsilon\omega_2)^2}}\right) \tag{2.50}$$

is the mixing angle between the two $^2\Sigma$ states. In the CaOH $\widetilde{A}(010)$ state, $\cos^2\beta \approx 0.84$.

As discussed in detail in Ref. [263], the mixing angle also determines the degree to which the rotational structure looks like a case (a) or case (b) state.[37] The figure of merit is $\sin 2\beta$, which is 0 in the case (a) limit and ± 1 in the case (b) limit. In CaOH, $\sin 2\beta \approx -0.74$, so the states are intermediate between case (a) and (b) but slightly closer to (b). This means (among other things), that N is an approximate quantum number, and can be used to gain intuition for the relative strength of rovibronic transitions but does not enforce strict selection rules. The structure of low-lying rotational states in the $\mu^2\Sigma^{(+)}$ and $\kappa^2\Sigma^{(-)}$ manifolds is shown in Fig. 7.1, from which it can be seen that the energy splittings are indeed intermediate between those of a good case (a) or case (b) $^2\Sigma$ state.

[37] Recall that in the case (a) limit, states are grouped by J with a small parity-doubling, while in the case (b) limit states are grouped by N, such that the two opposite-parity J states are split by a rotational energy scale.

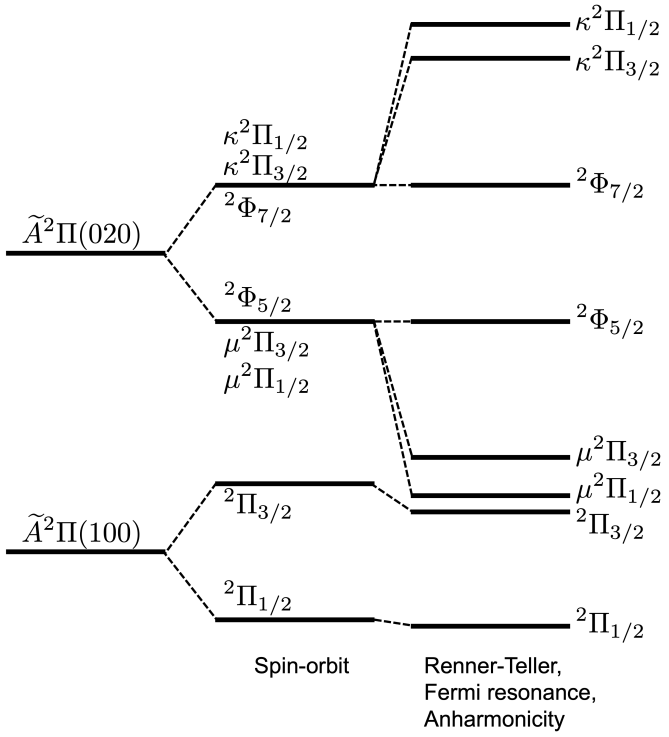

Figure 2.11: Structure of the $\widetilde{A}^2\Pi(100)$ and $\widetilde{A}^2\Pi(020)$ states in CaOH. They are split by spin-orbit and vibronic interactions into a number of manifolds. There is a strong interaction between the $\widetilde{A}(100)^2\Pi_{3/2}$ and $\widetilde{A}(020)\mu^2\Pi_{3/2}$ states due to Fermi resonance, which mixes vibronic states of the same symmetry.

2.7.3 The $\widetilde{A}(100)$ and $\widetilde{A}(020)$ states

The final set of states relevant to laser cooling CaOH are the excited $\widetilde{A}^2\Pi(100)$ and $\widetilde{A}^2\Pi(020)$ states. These are grouped together because they are nearby in energy, and experience significant Fermi resonance mixing. These states have been studied in detail in Ref. [250], and the parameters and Hamiltonian from that work should be used for quantitative energy level calculations. Here, we give a brief overview of their structure.

As shown in Fig. 2.11, the $\widetilde{A}(100)$ state is split into a $^2\Pi_{1/2}$ and $^2\Pi_{3/2}$ component by the spin-orbit interaction (just like the $\widetilde{A}(000)$ state discussed above). $\widetilde{A}(020)$ is also split into two components by the spin-orbit

interaction, but these states are then further split up by Renner-Teller interactions. In the end there are six resolved vibronic components, which are separated due to a combination of spin-orbit interactions, Renner-Teller interactions, and the anharmonic spitting between (02^00) and (02^20) vibrational states ($4g_{22}$). Finally, there are strong Fermi resonance interactions between these states (section 2.3). The Fermi resonance interaction conserves vibronic symmetry, so it mixes the $^2\Pi_{1/2}$ components with each other, and the $^2\Pi_{3/2}$ components with each other. The strong mixing between these states is helpful for vibrational repumping when laser cooling CaOH, since it makes it possible to repump the $\widetilde{X}(02^00)$ and $\widetilde{X}(02^20)$ states through $\widetilde{A}(100)$.

Eigenstates and mixing fractions

As with the $\widetilde{A}(010)$ state, it is useful to write down the vibronic components of $\widetilde{A}(100)$ and $\widetilde{A}(020)$ in a case (a) parity basis

$$|v_1, v_2; \Lambda, \ell, \Sigma, \pm\rangle = \frac{1}{\sqrt{2}}\big(|v_1, v_2; \Lambda, \ell, \Sigma\rangle \pm (-1)^{J-S}|v_1, v_2; -\Lambda, -\ell, -\Sigma\rangle\big)$$

where we have also now included the vibrational quantum numbers v_1 and v_2. The relationship between the vibronic labels and the pure case (a) parity basis states is:

$$|\widetilde{A}(100)^2\Pi_{1/2}\rangle^{(0)} = |1,0;1,0,-1/2\rangle \tag{2.51a}$$

$$|\widetilde{A}(100)^2\Pi_{3/2}\rangle^{(0)} = |1,0;1,0,1/2\rangle \tag{2.51b}$$

$$|\widetilde{A}(02^00)\mu^2\Pi_{1/2}\rangle^{(0)} = |0,2;1,0,-1/2\rangle \tag{2.51c}$$

$$|\widetilde{A}(02^20)\mu^2\Pi_{3/2}\rangle^{(0)} = |0,2;1,-2,-1/2\rangle \tag{2.51d}$$

$$|\widetilde{A}(02^00)\kappa^2\Pi_{3/2}\rangle^{(0)} = |0,2;1,0,1/2\rangle \tag{2.51e}$$

$$|\widetilde{A}(02^20)\kappa^2\Pi_{1/2}\rangle^{(0)} = |0,2;1,-2,1/2\rangle \tag{2.51f}$$

$$|\widetilde{A}(02^20)^2\Phi_{5/2}\rangle^{(0)} = |0,2;1,2,-1/2\rangle \tag{2.51g}$$

$$|\widetilde{A}(02^20)^2\Phi_{7/2}\rangle^{(0)} = |0,2;1,2,1/2\rangle \tag{2.51h}$$

where the (0) superscript refers to the fact that these are pure case (a) basis states, meaning they do not include the effects of Renner-Teller and Fermi resonance mixing. To include these effects, one can write down the Hamiltonian in this basis and diagonalize it to get the molecular eigenstates, as done in Refs. [250, 270].

For repumping in CaOH, we are specifically interested in the $^2\Pi_{1/2}$ components, since they have $J = 1/2^+$ rotational states that are necessary for rotationally closed optical cycling (as discussed in chapter 4). Diagonalizing the Hamiltonian, we find that the admixture of the case (a) basis states in the $J = 1/2^+$ rotational level of each of the $^2\Pi_{1/2}$ states is:

	$\lvert(100)^2\Pi_{1/2}\rangle^{(0)}$	$\lvert(02^00)\mu^2\Pi_{1/2}\rangle^{(0)}$	$\lvert(02^20)\kappa^2\Pi_{1/2}\rangle^{(0)}$
$\lvert\widetilde{A}(100)^2\Pi_{1/2}\rangle$	89.1%	9.8%	1.0%
$\lvert\widetilde{A}(020)\mu^2\Pi_{1/2}\rangle$	10.7%	74.0%	15.3%
$\lvert\widetilde{A}(020)\kappa^2\Pi_{1/2}\rangle$	0.1%	16.1%	83.7%

We see that $\mu^2\Pi_{1/2}$ has dominantly $\ell = 0$ character and $\kappa^2\Pi_{1/2}$ has dominantly $\ell = 2$ character. When discussing these states in later chapters, we will sometimes just refer to them as $\widetilde{A}(02^00)$ and $\widetilde{A}(02^20)$, respectively. These two states are used for repumping the $\widetilde{X}(12^00)$ and $\widetilde{X}(12^20)$ states, respectively.

Based on these mixing fractions, it should be possible to repump both $\widetilde{X}(02^00)$ and $\widetilde{X}(02^20)$ through $\widetilde{A}(100)^2\Pi_{1/2}$, and this is indeed what we do for laser cooling CaOH.

2.8 Electric dipole transitions

We will frequently be interested in driving transitions between different molecular states using lasers or microwaves. Electronic, vibrational, and rotational transitions in molecules are all electric-dipole allowed, so we will just consider these electric dipole transitions here.

Let's say our laser or microwave radiation has an electric field $\boldsymbol{E}(t) = \frac{1}{2}\mathcal{E}_0\hat{\epsilon}\left(e^{i\omega t} + e^{-i\omega t}\right)$, where $\mathcal{E}_0$ is the electric field amplitude, $\hat{\epsilon}$ is the polarization unit vector, and ω is the frequency. The Hamiltonian describing the interaction of this field with the molecule is $H' = -\boldsymbol{\mu}\cdot\boldsymbol{E}(t)$, where $\boldsymbol{\mu}$ is the electric dipole operator. This can drive transitions between molecular states $|i\rangle$ and $|j\rangle$ with a strength $|\langle i|H'|j\rangle|^2 \propto |\langle i|\hat{\epsilon}\cdot\boldsymbol{\mu}|j\rangle|^2|\mathcal{E}_0|^2$. Therefore, calculating transition strengths requires evaluating matrix elements of the electric dipole operator $\hat{\epsilon}\cdot\boldsymbol{\mu}$.

We will describe our molecule using the separable basis states $|\eta, v, J, M\rangle$, where $|\eta\rangle$ is the electronic state,

$|v\rangle$ is the vibrational state, and $|J, M\rangle$ is the rotational state. This basis (and this section) assumes the Born-Oppenheimer separation of electronic, vibrational, and rotational degrees of freedom.

Rotational transitions

Rotational transitions can be driven at microwave frequencies, and are electric dipole allowed as long as the molecule is polar, since the microwaves can couple to the molecule-frame electric dipole moment. Because the electronic and vibrational states are unchanged, we have

$$\begin{aligned}\langle \eta, v, J, M|\hat{\epsilon}\cdot\boldsymbol{\mu}|\eta, v, J', M'\rangle &= \langle\eta|\eta\rangle\langle v|v\rangle\langle J, M|\hat{\epsilon}\cdot\boldsymbol{\mu}|J', M'\rangle \\ &= \langle J, M|\hat{\epsilon}\cdot\boldsymbol{\mu}|J', M'\rangle\end{aligned}$$

These can be calculated by evaluating matrix elements of the electric dipole operator in a basis of rotational states, as described in appendix A. Generally speaking, allowed transitions are between states with opposite parity and obey $\Delta J = 0, \pm 1$. The strength is proportional to the molecule-frame dipole moment (1.465 D in the $\widetilde{X}^2\Sigma^+$ state of CaOH).

In the literature, reference is often made to the line strength, which sums over all polarizations and projection quantum numbers [236, 271, 272]:

$$S_{J'J} = \sum_{q,M,M'} \left|\langle J, M|\mu_q|J', M'\rangle\right|^2 \tag{2.52}$$

where μ_q is a component of the dipole operator (in the spherical basis). The sum over q is equivalent to a sum

over all polarizations. Again, these line strengths can be calculated using matrix elements of the dipole operator, but they are also often tabulated in the molecule literature.

Vibrational transitions

For a vibrational transition, both v and J can change:

$$\begin{aligned}\langle \eta, v, J, M|\hat{\epsilon}\cdot\boldsymbol{\mu}|\eta, v', J', M'\rangle &= \langle\eta|\eta\rangle\langle v, J, M|\hat{\epsilon}\cdot\boldsymbol{\mu}|v', J', M'\rangle \\ &\approx \langle v|\boldsymbol{\mu}|v'\rangle\langle J, M|\hat{\epsilon}|J', M'\rangle\end{aligned}$$

where in the second line we made the approximation that the vibrational and rotational wavefunctions are separable. The vibrational matrix element sets the overall strength of the transition, with the intensity divided between rotational states according to the rotational matrix elements. These can once again be calculated using angular momentum algebra (appendix A). The total line strength of a vibrational transition is [236]

$$S_{J'J} = \sum_{q,M,M'} \left|\langle v, J, M|\mu_q|v', J', M'\rangle\right|^2 = |M_{vv'}|^2 S_J^{J'} F(J) \approx |M_{vv'}|^2 S_J^{J'} \tag{2.53}$$

where $|M_{vv'}|^2 \equiv |\langle v|\boldsymbol{\mu}|v'\rangle|^2$ is the vibrational transition strength and $S_J^{J'} = \sum_{q,M,M'} |\langle J, M|\epsilon_q|J', M'\rangle|^2$ is the Hönl-London factor, which sets the relative strength of different rotational lines. Hönl-London factors can be calculated using matrix elements of the dipole operator (appendix A), or looked up in tables in the literature [236]. $F(J)$ is called the Herman-Wallis factor and corrects for errors in the separation of the vibrational and rotational degrees of freedom [236]. In the final expression we made the approximation $F(J) \approx 1$.

At a first approximation, we can estimate the vibrational line strength $|M_{vv'}|^2$ using the *double harmonic approximation* [236]. The molecule frame electric dipole moment depends in general on the vibrational coordinates $\mu(r)$ (since, e.g., increasing the bond length will change the molecular dipole moment). If we Taylor expand $\mu(r)$ about the equilibrium position r_e and also assume that the vibrational states are pure harmonic oscillator wavefunctions, we get [236]

$$|M_{vv'}|^2 = |\langle v|\boldsymbol{\mu}|v'\rangle|^2 \approx \left|\langle v|\left(\mu(r_e) + (r-r_e)\frac{d\mu}{dr}\Big|_{r=r_e} + \dots\right)|v'\rangle\right|^2 \approx \left(\frac{d\mu}{dr}\right)^2 \left|\langle v|r|v'\rangle\right|^2 \tag{2.54}$$

The matrix elements of r can be evaluated using harmonic oscillator algebra.[38] Therefore, we see that to a first approximation, vibrational transition strengths are proportional to the derivative of the molecular dipole moment with respect to the vibrational coordinate.

We will come back to this later in this thesis when studying how blackbody radiation can drive vibrational transitions in CaOH (chapter 6).

Electronic transitions

For an electronic transition, it is possible to change the electronic, vibrational, and rotational state. We first consider just the electronic and vibrational wavefunctions and make the Born-Oppenheimer approximation (section 2.1) $\psi_{ev}(\boldsymbol{r}, \boldsymbol{R}) \approx \psi_e(\boldsymbol{r}; \boldsymbol{R})\psi_v(\boldsymbol{R})$, where $\boldsymbol{r}$ describes the electronic coordinates and $\boldsymbol{R}$ describes the nuclear coordinates. The electronic wavefunction depends only parametrically on the nuclear coordinates. The transition

[38] E.g. using $r \propto (a + a^\dagger)/\sqrt{2}$ for a 1D harmonic oscillator, where a and $a^\dagger$ are raising and lowering operators.

dipole moment integral, in this approximation, is [236]

$$\begin{aligned}\boldsymbol{M}_{ev} &= \int \psi^*_{ev}(\boldsymbol{r},\boldsymbol{R})\boldsymbol{\mu}\psi_{e'v'}(\boldsymbol{r},\boldsymbol{R})d\tau \\ &\approx \int \psi^*_{v}(\boldsymbol{R})\left(\int \psi^*_{e}(\boldsymbol{r};\boldsymbol{R})\boldsymbol{\mu}\psi_{e'}(\boldsymbol{r};\boldsymbol{R})d\tau_e\right)\psi_{v'}(\boldsymbol{R})d\tau_n \\ &\equiv \int \psi^*_{v}(\boldsymbol{R})\boldsymbol{R}_e(\boldsymbol{R})\psi_{v'}(\boldsymbol{R})d\tau_n \end{aligned} \tag{2.55}$$

where $d\tau_n$ and $d\tau_e$ denote integration over nuclear and electronic coordinates. In the last line we defined the electronic transition dipole moment $\boldsymbol{R}_e \equiv \langle\eta|\boldsymbol{\mu}|\eta'\rangle$. If we neglect the dependence of $\boldsymbol{R}_e$ on the nuclear coordinates $\boldsymbol{R}$ (i.e. by Taylor expanding about the equilibrium geometry and taking only the first term [236]), this means that we can factor it out of the integral:

$$|\boldsymbol{M}_{ev}|^2 \approx |\boldsymbol{R}_e|^2 \left|\int \psi^*_{v}(\boldsymbol{R})\psi_{v'}(\boldsymbol{R})d\tau_n\right|^2 \equiv |\boldsymbol{R}_e|^2\, q_{vv'} \tag{2.56}$$

where we defined the Franck-Condon factor (FCF), $q_{vv'} = |\langle v|v'\rangle|^2$.

Adding back the rotational dependence in analogy with eqn. 2.53 above, the line strength of a rovibronic transition is [236]

$$S_{J'J} \approx |M_{ev}|^2 S_J^{J'} \approx |\boldsymbol{R}_e|^2\, q_{vv'} S_J^{J'} \tag{2.57}$$

where $|\boldsymbol{R}_e|^2$ is the electronic transition strength, $q_{vv'}$ is the Franck-Condon factor (FCF), and $S_J^{J'}$ is the Hönl-London factor. The electronic transition strength sets the overall intensity of the transition, which is divided into rotational and vibrational branches by the FCFs and Hönl-London factors. These factors will be discussed

further in chapter 4.

3

A Cryogenic Buffer Gas Beam of CaOH

The complex rotational and vibrational structure of molecules means that thousands of internal states are occupied at room temperature, and the fractional population in the low-energy rotational states used for laser cooling is very small. Working with molecules near the ground state therefore requires cooling their internal degrees of freedom to low temperatures, typically below 10 K. Moreover, laser cooling and trapping of

molecules is aided by having a slow and translationally cold molecular beam as a starting point. We achieve both of these aims using cryogenic buffer gas cooling. In this technique, molecules are collisionally cooled by an inert buffer gas (here we use ^{4}He) in a cryogenically cooled copper cell (the "buffer gas cell"). This cools the translational motion and also effectively thermalizes the rotational degrees of freedom (while leaving the vibrational distribution relatively hot). The molecules are then extracted through an aperture at the front of the cell to produce a bright, slow molecular beam [137, 138]. This provides a good starting point for laser cooling and trapping, and is our method of choice for this work. In this chapter we describe our cryogenic buffer gas beam (CBGB) source for CaOH molecules.

3.1 Overview of the CaOH beam box

The cryogenic chamber, or "beam box," used for CaOH was described in detail in a prior thesis, by Louis Baum [273]. Here we give a brief overview of the essential features.

The beam box is made from a rectangular, o-ring-sealed aluminum vacuum chamber. It is pumped on with a$\sim$250 l/s turbomolecular pump and also via cryopumping when cold, resulting in base pressures around 10^{-7} Torr (measured in the room temperature portion of the chamber) when cold. The beam box houses a Cryomech PT415 1K pulse tube cryocooler. The 40 K and 4 K cooling stages are used to cool two sets of radiation shields. The 40K radiation shields are made from aluminum, and the 4K shields are made from copper. Layers of aluminized mylar (NRC-2) "superinsulation" are placed outside the 40 K shields and in between the 40 K and 4 K shields to reduce radiative heat loads on the shields.[1] The inside of the 4 K shields contains a large surface area

[1] Note that our beam box was assembled in 2018, at which time superinsulation was standard in Doyle group beam boxes. Since then, Doyle group beam box design has shifted towards using gold-plated copper for both the 40 K and 4 K shields [274].

of coconut charcoal sorbs, used to cryopump helium [273, 275]. Many of these sorbs are "protected," meaning they do not have direct line of sight to the buffer gas cell aperture and are therefore less susceptible to degradation caused by certain chemicals used for (or produced as byproducts of) molecule production. The sorbs that do have line-of-sight to the cell, notably the sorb surfaces directly surrounding the aperture in the 4K shields used to extract the molecular beam from the beam box, need to be periodically replaced to maintain the brightest possible CaOH MOT. It was also found that moving the cell as far away as possible from the 4K aperture improves molecular beam extraction by preventing a buildup of helium density that could eject slow CaOH molecules from the beam [273]. It is likely that having fresh charcoal near the aperture further mitigates this effect by more effectively pumping the helium that could otherwise knock slow CaOH molecules from the beam.

The second component of the PT415 1K cryocooler is a closed-loop helium system. A copper pot at the bottom of the pulse tube is filled with liquid helium and pumped on by a scroll pump (Edwards XDS35i), which cools the helium to temperatures as low as ∼1.5 K. Gas-phase helium on the high-pressure side of the pump is then filtered and returned to the pot after being pre-cooled on the 40 K and 4 K stages of the pulse tube, then expansion cooled through an adjustable needle valve. The circulating helium system as shipped by Cryomech had extensive issues that made it initially unusable. A large number of fixes were implemented by Louis Baum to make it functional. The complete system is described in detail in his thesis [273]. See appendix C for technical notes on this system based on the last few years of operation.

The buffer gas cell used to produce and cool CaOH is connected to the helium pot via flexible copper 10100 heat links. The helium loop is able to provide up to ∼400 mW of cooling power, enabling us to run the experiment at cell temperatures below 2.5 K.

3.1.1 Extraction of the molecular beam

A challenge for cryogenic buffer gas beam sources is to extract the molecular beam from the beam box without being hindered by collisions with background helium buffer gas atoms. As was observed in early work in the CaOH dewar [273], if too high a helium density builds up anywhere along the path of the molecular beam, helium-CaOH collisions can kick slow CaOH molecules out of the molecular beam. In that earlier work, when the cell was too close to the 4 K aperture, there was a significant helium buildup near the aperture. The consequence was that the peak velocity of the molecular beam measured outside of the beam box was significantly faster than the velocity measured inside the 4 K radiation shields [273]. This was mostly solved by moving the cell further back from the 4 K aperture.

Helium buildup can also be a problem as the molecules travel from the 4 K region to room temperature, through apertures in the 4 K, 40 K, and 300 K shields. Optimizing the size of the apertures and the distance between them is not entirely obvious. For each aperture, if it is too small there will be significant amounts of helium bouncing backwards and colliding with the beam. Too large, and the helium escapes to the next region where it will likely be hotter if it collides with the molecules. A similar problem exists for the gap/distance between the apertures. Too narrow a gap, and the vacuum conductance is too low for the helium atoms to efficiently move away from the aperture, so large densities of helium build up near the molecules. However, if the gap is too wide, the molecules spend more time in the beam box and therefore have more opportunity to collide with helium. Moreover, collisions in regions near the 40 K and 300 K shields can be especially bad, since these helium atoms (which have typically bounced off the shields at least once) will be hot. These atoms can impart larger kicks to the molecules and also increase their rotational temperature, so that a lower fraction of the molecules that actually

make it out of the beam box are in the correct $N = 1$ rotational state needed for laser cooling.[2]

The geometry we ended up using to make a CaOH MOT is as follows. The aperture in the front 4 K shield has a 10 mm diameter and is approximately 4" (100 mm) away from the cell aperture. There is a 25 mm gap between the 4 K aperture and the 40 K aperture, which has a diameter of 25 mm. There is sorb on the outside of the 4 K shield surrounding the aperture to help cryopump helium in this gap region. The gap between the 40 K and 300 K shields is 38 mm, and the 300 K aperture size is defined by an in-vacuum shutter (Uniblitz VS14) with a 14 mm diameter aperture. A 250 l/s turbomolecular pump pumps on the region between the 40 K and 300 K shields (which is one reason we keep the gap relatively large).

3.2 Buffer gas cell and molecule production

Over the course of this thesis we iterated through a number of buffer gas cell designs in order to optimize the CaOH molecular beam properties important for loading a MOT, as described in the sections below. The essential figure of merit to optimize was the number of molecules produced at a sufficiently low velocity to be radiatively slowed to <10 ms. We expected to be able to scatter approximately $\bar{N} = 10,000$ photons, on average, from each CaOH molecule, with each photon removing approximately 11 mm/s of forward velocity from the beam (chapter 4). The fraction of molecules surviving after scattering N photons is $\exp(-N/\bar{N})$, so that 37% of the molecules remain after slowing by 110 m/s. This coarsely meant that our goal was to produce as many molecules as possible at velocities near 100 m/s. Notably, while there has been significant work in the Doyle group producing very slow molecular beams using two-stage buffer gas cells [214, 276, 277], we determined that the loss of flux

[2] Some of these ideas came from extensive direct simulation Monte Carlo (DSMC) simulations of our beam box conducted by Paige Robichaud and Loïc Anderegg.

associated with these cells was not worth the improvement in velocity. In particular, every extra 50 m/s in initial velocity corresponds to an additional ∼40% loss of molecules to dark states after laser slowing. Meanwhile a decrease of 50 m/s of the buffer gas beam velocity usually decreases the flux by a larger amount. Note that this reasoning is specific to radiative slowing and to our apparatus. For slowing methods that remove a fixed *energy* rather than a fixed momentum – e.g. optical loading [160] or Zeeman-Sisyphus deceleration [165, 166] – minimizing the beam velocity is typically much more important. The final parameters of our optimized beam were a mean velocity of approximately 140 m/s and a molecular flux of $\sim 5 \times 10^{10}$ molecules/sr/pulse in the $N = 1$ rotational state used for laser cooling.

In this section, we provide an overview the design of the buffer gas cell used to achieve these beam parameters. A previous version of the CaOH buffer gas cell, which was used for laser cooling and spectroscopy of a CaOH molecular beam [47, 220, 251], was described in Ref. [273]. Therefore, for the remainder of the chapter we will focus on the changes made in order to optimize our cell for radiative slowing and magneto-optical trapping of CaOH. This included a switch to chemically enhanced molecule production (section 3.3), alterations to the cell to make it compatible with our high power radiative slowing lasers (section 3.4), and tests of the cell geometry to optimize molecule flux and velocity (section 3.5). First, we provide an overview of the final setup used for making a CaOH MOT.

3.2.1 Overview

The buffer gas cell is shown in Fig. 3.1. It is similar to cells used in a number of previous experiments in the Doyle group, described for instance in Refs. [214, 273, 277, 278], though with some modifications specific to our apparatus. The cell is made of copper and consists of two stages. The first stage is 44.45 mm (1.75") long with a 43.18 mm

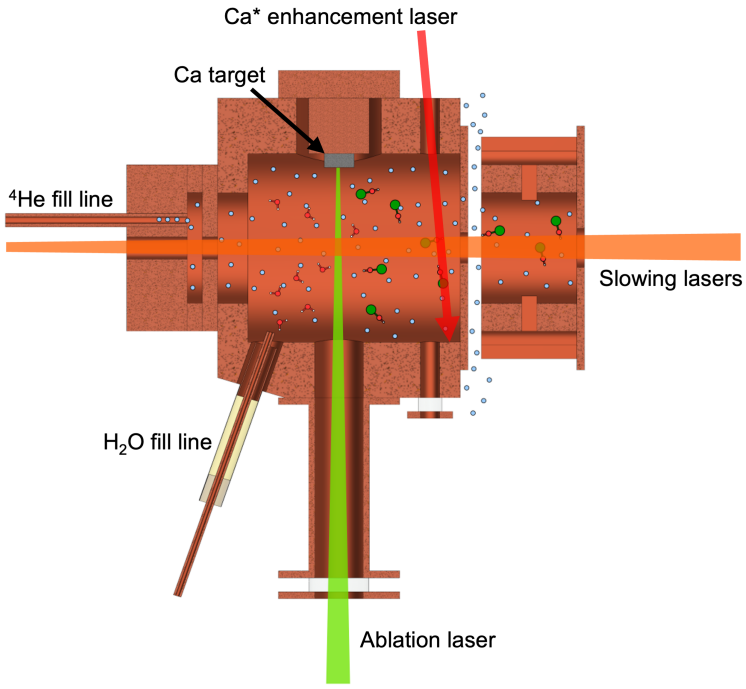

Figure 3.1: Diagram of the CaOH buffer gas cell, as described in the text.

(1.7") diameter inner bore. This is a larger diameter than what was used for previous Doyle group laser cooling experiments, and was increased to mitigate a beam speed-up caused by water ice (section 3.5) [214]. The front aperture is 7 mm in diameter, and there is also a a 12.7 mm long, 5 mm-diameter hole in the back of the cell through which laser slowing light can exit. This hole is designed to have a much higher impedance than the front aperture, as described in section 3.4.2. There is a 2.8 mm gap between the first and second stages, which helps to reduce the buffer gas density in the second stage cell compared to the first. The second stage cell is 20 mm long with a 25.4 mm inner diameter and a 9 mm-diameter exit aperture. There is no mesh on the exit aperture, which deviates from the design of previous second stage cells [214, 273, 276–278]. This is because we found that slowing light incident on the mesh dramatically reduced the molecular beam flux, as described in section 3.4.

Pre-cooled ^{4}He buffer gas is flowed in from the back of the cell, via a diffuser, at flow rates of typically 5-10 standard cubic centimeters per minute (sccm), leading to buffer gas densities of $\sim 10^{15}$ cm^{-3} in the first stage cell [138]. Molecules are produced by ablating a Ca metal target with a pulsed, frequency-doubled Nd:YAG laser (Amplitude/Continuum Minilite II, 532 nm, ~5 ns pulse duration, up to ~30 mJ pulse energy), focused to a spot size of around 40 μm, though we find that optimal molecule production often corresponds to the beam hitting the surface of the target up to a few inches away from the focus.[3] To improve stability of the molecule production, we typically raster the ablation beam position over the target using a motorized mirror mount, moving every 10-100 ablation shots.

Along with helium buffer gas, we also flow H_2O vapor into the cell via a copper fill line heated to 285 K at a flow rate of <1 sccm. The water vapor reacts with Ca atoms in the buffer gas cell to produce CaOH, as described

[3] Depending on how much ice and dust has accumulated in the cell, we sometimes find that focused beams with lower pulse energy are optimal, and sometimes that defocused ablation with higher pulse energy is best.

below. Details of the heated fill line are in Louis Baum's thesis [273]. We generally find that higher water vapor flow rates lead to better molecule production but also faster degradation of the cell performance due to a buildup of water ice. The flow rate we use is chosen to trade off between these two parameters, allowing us to run for 5 days a week without excessive degradation in CaOH MOT numbers. We then thermally cycle every weekend to melt off water ice and refresh the cell.

Along with the weekly water-ice buildup, we find longer term degradation of MOT numbers due to buildup of dust (e.g. Ca, $Ca(OH)_2$, and other Ca-containing compounds) in the cell. We find that opening the beam box to clean the cell approximately once a month is necessary to maintain high MOT numbers. Finally, every few months we replace the charcoal sorb plate surrounding the molecular beam aperture in the 4K radiational shields. This significantly improves the MOT number, likely by reducing helium buildup near the 4K aperture that limits molecule extraction from the beam box [273].

3.3 Chemically enhanced CaOH molecule production

Previous experiments in the Doyle group have shown that chemical production of molecules (by ablating Ca metal and reacting it with a partner gas) provides higher molecule beam flux and improved stability compared to ablating powder targets, making it a good choice for laser cooling experiments [273, 278]. For CaOH, the goal is to find a reaction partner that can donate an OH group to bond with the Ca atom. Two natural choices are methanol and water, both of which are liquids at room temperature with reasonable vapor pressures for flowing into the buffer gas cell. The chemical reactions of Ca with these vapors, and the corresponding reaction enthalpies

ΔH_0^0, are [279]

$$\mathrm{Ca}(^1S_0) + \mathrm{CH_3OH} \rightarrow \mathrm{CaOH}(\widetilde{X}) + \mathrm{CH_3} \qquad (\Delta H_0^0 = -2424\ \mathrm{cm}^{-1})$$

$$\mathrm{Ca}(^1S_0) + \mathrm{H_2O} \rightarrow \mathrm{CaOH}(\widetilde{X}) + \mathrm{H} \qquad (\Delta H_0^0 = 7356\ \mathrm{cm}^{-1})$$

$$\mathrm{Ca}(^3P_2) + \mathrm{CH_3OH} \rightarrow \mathrm{CaOH}(\widetilde{X}) + \mathrm{CH_3} \qquad (\Delta H_0^0 = -17722\ \mathrm{cm}^{-1})$$

$$\mathrm{Ca}(^3P_2) + \mathrm{H_2O} \rightarrow \mathrm{CaOH}(\widetilde{X}) + \mathrm{H} \qquad (\Delta H_0^0 = -7941\ \mathrm{cm}^{-1})$$

where negative ΔH_0^0 indicates that a reaction is exothermic. Based on these thermochemistry values, it would appear that reacting ground state $\mathrm{Ca}(^1S_0)$ with methanol could potentially enable production of CaOH, but promoting the Ca atoms to a metastable ^3P state should make both reactions exothermic and much more favorable. This was recently demonstrated as a viable method for improving the yield of YbOH molecules in a cryogenic buffer gas source [214, 280], where 556 nm light was used to promote Yb atoms to the metastable $^3P_1$ state inside the buffer gas cell.

In early experiments with CaOH in our lab, we found that we could produce CaOH via the $\mathrm{Ca} + \mathrm{CH_3OH}$ reaction without exciting the Ca to a metastable state [273]. Moreover, attempts to chemically enhance the molecular signal by exciting the $4s^2\,{}^1S_0 \rightarrow 4s4p\,{}^1P_1$ transition at 423 nm provided no increase in molecule production, while exciting the atoms on the 657 nm $4s^2\,{}^1S_0 \rightarrow 4s4p\,{}^3P_1$ transition improved the molecule signal by only a few percent [273]. We also directly measured the population in the $^3P_1$ state with an in-cell absorption probe monitoring the $4s4p\,{}^3P_1 \rightarrow 4s5s\,{}^3S_1$ transition at 612 nm, and confirmed that the population in the metastable state increased by well over an order of magnitude when using the 657 nm excitation light. Therefore, the lack of improved molecule production was not due to technical limitations in our ability to populate the metastable

state.

Following these observations, we consulted *ab initio* DFT calculations of the reaction pathways, performed by Jacek Kłos and Svetlana Kotochigova [281] using similar methods to those described in Ref. [280]. For reactions of Ca($^1S_0$) with methanol, it was found that, despite the overall exothermicity of the reaction, there is a transition state at around 8000 cm^{-1} that must be overcome to complete the reaction. Though the energy imparted by the ablation laser might help, it is likely that the reaction is significantly suppressed due to the need to tunnel through this barrier. For reactions of metastable Ca(^3P) with methanol, while the CaOH + CH_3 pathway is indeed >17000 cm^{-1} exothermic, it was found that the dominant reaction pathway actually leads to production of $CaOCH_3$, with an exothermicity of approximately 8000 cm^{-1}. To test this prediction, we flowed methanol into the cell and observed the number of CaOH and $CaOCH_3$ molecules in the molecular beam, with and without 657 nm enhancement light resonant with the Ca $4s^2\,{}^1S_0 \rightarrow 4s4p\,{}^3P_1$ transition. With 200 mW of 657 nm light sent through an absorption window into the first stage cell (see Fig. 3.1), we observed no change in the CaOH production but a 4× increase in $CaOCH_3$ production (Fig. 3.2).

Similar *ab initio* calculations for reactions of calcium and water painted a more promising picture. While it was predicted that reactions of Ca($^1S_0$) with H_2O to produce CaOH would be ∼7000 cm^{-1} endothermic, reactions of Ca(^3P) with water were predicted to produce predominantly CaOH with an exothermicity of 7800 cm^{-1} [281].

Fig. 3.3 shows data confirming the predicted chemical enhancement effect when promoting Ca to the metastable $^3P_1$ state. To do this, we locked a cw laser to the $4s^2\,{}^1P_0 \rightarrow 4s4p\,{}^3P_1$ transition at 657 nm and sent a collimated laser beam into the cell through an absorption window. The light was aligned to scatter off the inside of the cell, which was seen to be beneficial for chemical enhancement in previous work [214], and it was pulsed on for 10s of

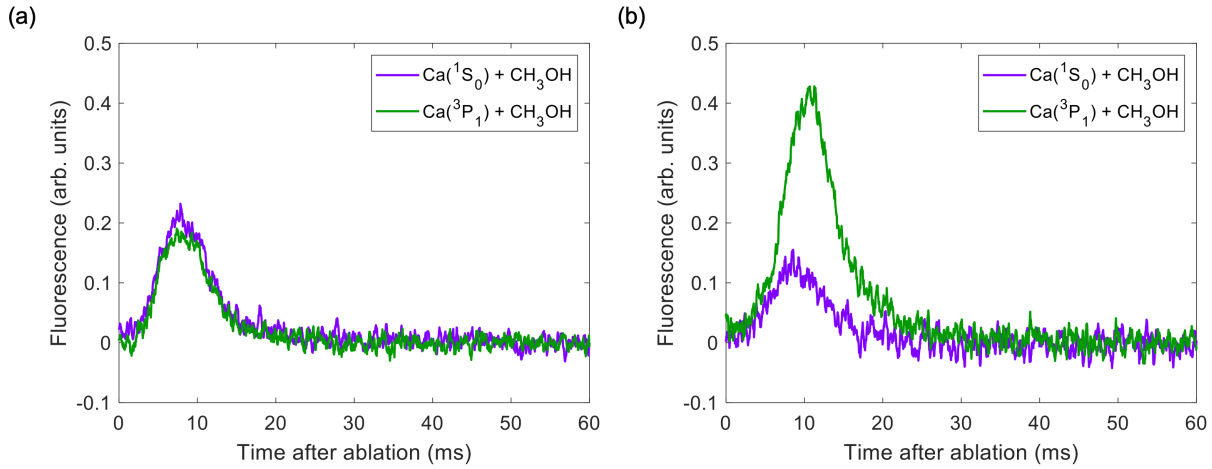

Figure 3.2: Production of (a) CaOH and (b) $CaOCH_3$ from reacting Ca with CH_3OH, with and without Ca($^3P_1$) enhancement.

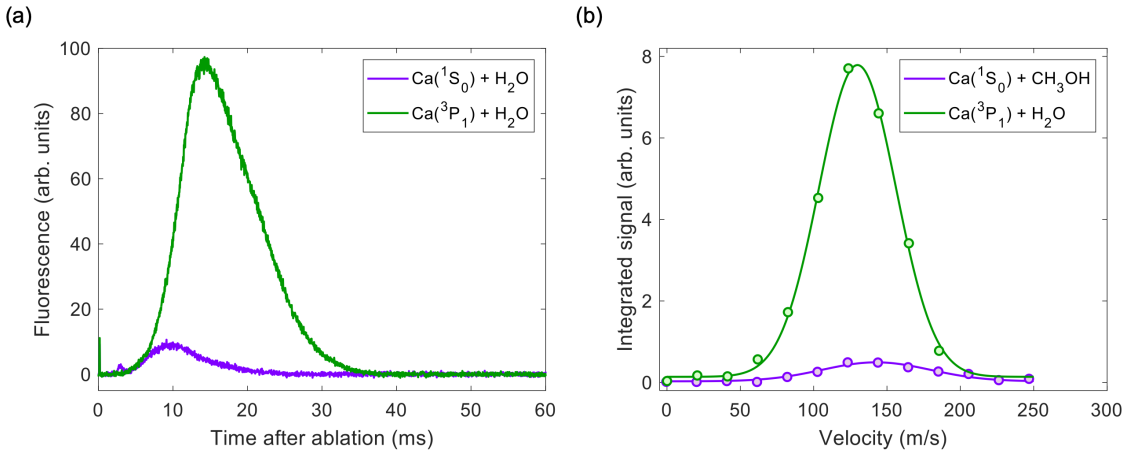

Figure 3.3: Chemical enhancement of the CaOH molecular beam by reacting metastable Ca($^3P_1$) with H_2O. (a) Molecular beam fluorescence vs. time after ablation, as recorded on a PMT approx. 65 cm downstream from the buffer gas cell. The two traces are for reactions of Ca metal with water vapor, with and without approx. 230 mW of 657 nm $^1S_0 \rightarrow {}^3P_1$ enhancement light incident in the cell. The total molecule number is improved by $>10\times$ with the enhancement light. Detection was with our standard "off-diagonal" technique, using lasers addressing the $\widetilde{X}(000) \rightarrow \widetilde{A}(000)$ and $\widetilde{X}(100) \rightarrow \widetilde{B}(000)$ transitions, while detecting 555 nm photons emitted on the $\widetilde{B}(000) \rightarrow \widetilde{X}(000)$ transition. (b) Molecular beam velocity and comparison to Ca + methanol production. Producing CaOH via chemically enhanced reactions with water produces approximately $10\times$ more molecules than the old production method using Ca and methanol, with a similar, but slightly slower, beam velocity.

ms around the time of ablation to avoid large heat loads on the cell. We found that optimal enhancement conditions occurred when the light was input through an absorption window towards the front of the cell (illustrated in Fig. 3.1). We also tried sending the enhancement laser copropagating with the ablation laser and in through the cell front aperture, neither of which worked as well. From Fig. 3.3, we see that the chemical enhancement improved the number of molecules in the CaOH molecular beam by over an order of magnitude compared to both the unenhanced Ca + H_2O production and the Ca + CH_3OH production.[4] The forward velocity of the beam also appears to have decreased slightly.

Because of the narrow ($\Gamma \approx 2\pi \times 400$ Hz) linewidth of the Ca intercombination transition used for enhancement, there was some question about how much population we were able to place in the metastable state. Scans of the enhanced molecule signal vs. laser power showed that the number of molecules in the molecular beam did not saturate even up to 1 W of enhancement light in the cell. We tried several techniques to attempt to improve this population. The first was to broaden the spectrum of the enhancement laser with an EOM to cover the inhomogeneous, Doppler-broadened linewidth of the molecules in the cell. This did not yield any improvement in the molecule numbers, though neither did it degrade the enhancement effect out to at least 100 MHz of broadening. We also tried to populate the state via the two-photon process $4s^2\,{}^1S_0 \rightarrow 4s4p\,{}^1P_1 \rightarrow 4s6s\,{}^1S_0$, using resonant lasers at 423 nm and 587 nm. Based on known branching ratios from $4s6s\,{}^1S_0$, this should have put at least 20% of the excited Ca molecules into the ${}^3P_1$ state. This did not work, likely for technical reasons. However, other work in the Doyle group has since shown that such two-photon methods do not improve the enhanced number beyond what is observed with direct intercombination line excitation.

[4] Depending the specific enhancement parameters and the amount of water ice and dust present in the cell, we have seen enhancement factors of up to 40-50× compared to Ca + H_2O production without enhancement.

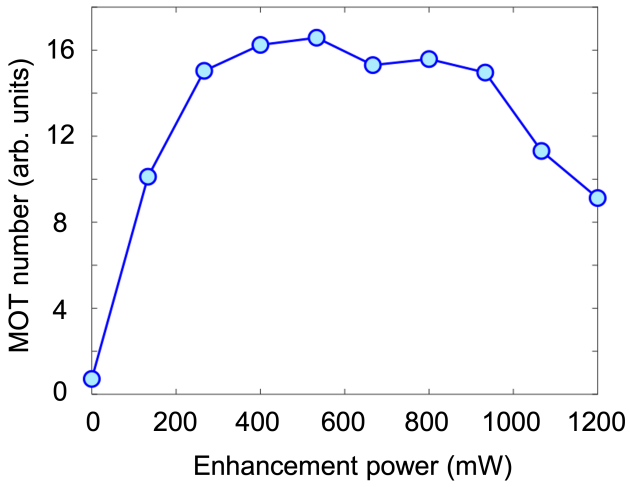

Figure 3.4: Number of molecules loaded in the CaOH MOT vs. 657 nm enhancement power. A $>10\times$ increase in the number of trapped molecules is observed for enhancement powers as low as 300 mW and up to approximately 1 W.

Ultimately, we found that for the CaOH MOT, approximately 600 mW was sufficient to optimize the enhancement effect (Fig. 3.4). This is likely due to a trade-off between enhanced molecule flux and beam speed-up from the increased heat load at higher powers. It is also possible that the increased enhancement seen in beam data for higher powers is specific to molecules that either leave the cell at the wrong time or have the wrong velocity to be captured in the MOT. For instance, it was seen in reactions of $\mathrm{Yb}(^3P_1) + \mathrm{H_2O}$ in the Doyle group that the largest enhancement factors came for molecules produced at late times [214].

3.4 Modifications to the cell for radiative laser slowing

In this section, we discuss changes made to the cell when we began trying to radiatively slow the beam, in response to the high-power slowing light incident on the cell.

3.4.1 Removal of mesh from second stage cell

As demonstrated previously in the Doyle group, adding a second stage "slowing" cell to a buffer gas source can significantly reduce the velocity of the atomic or molecular beam [138, 214, 276, 277, 282]. The first-stage cell is tuned to have a high enough helium density for efficient molecule thermalization and extraction, while the second stage has a significantly lower density (typically ∼10% that of the first stage), such that the molecules collide with the buffer gas only a few times and the resulting velocity distribution is nearly effusive. Adding a copper mesh on the output of the cell allows He atoms to bounce backwards off the mesh, helping to slow the molecules even further. It has been found in previous work that the specific transparency and pore size of the mesh is important for optimizing the performance of two-stage buffer gas cells [214, 277].

While it was our hope to use a second stage cell with a mesh in order to achieve the slowest possible CaOH beam for radiative slowing, we found that the mesh led to several challenges for stably producing and slowing CaOH. Ultimately, these led to the decision to remove the mesh from our cell.

Mesh clogging

The first problem occurred in some of our early tests of two-stage cells with a 1.7" first stage diameter and a 30% transparency, 0.15 mm pore size mesh on the exit of the 2nd stage cell. Over the course of a week, the molecule flux decreased by over an order of magnitude, and we observed that the mesh appeared to be clogged. It was initially suspected that the clog was methanol ice, but upon inspection we found that the mesh was filled with a white substance that remained solid at room temperature (Fig. 3.5). We had the sample analyzed using SEM/EDS (scanning electron microscope/ energy-dispersive X-ray spectroscopy), which found that the compound con-

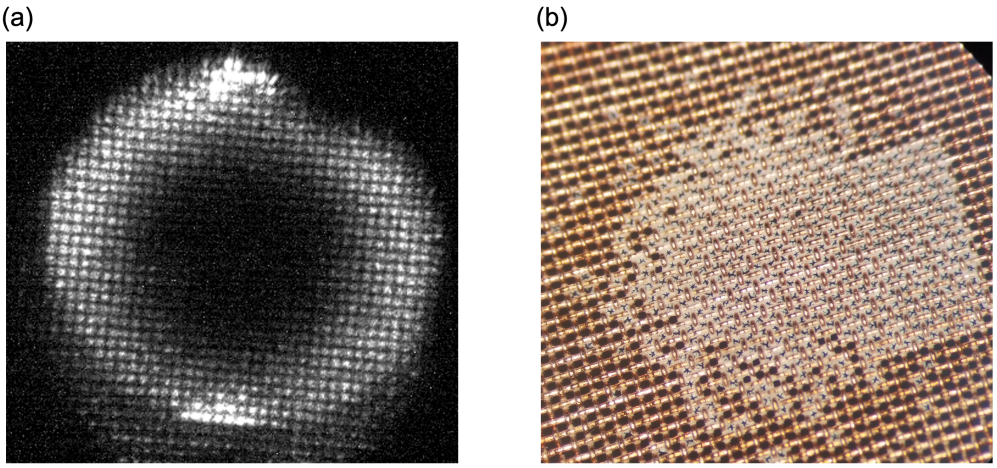

Figure 3.5: Clogging of a 30% transparency, 0.15 mm pore size mesh. (a) *In-situ* image of the mesh, looking from the front of the cell with the inside of the cell illuminated. The dark circle in the middle indicates the presence of an optically opaque material clogging the mesh. (b) Microscope image of the mesh after removing from the cell, indicating that the clog was due to a white substance accumulating on the copper. This clog resulted in an approximately 10× decrease in molecule flux over the course of a week.

tained Ca and O in an approximately 1:2 ratio, meaning that the substance was likely $Ca(OH)_2$ or a similar by-product of CaOH production (the analysis technique was insensitive to hydrogen). We tried gold plating the mesh to impede the substance's ability to bind to it, but saw similar clogging. We also were careful to avoid cleaning the mesh with Citranox, residue from which we thought might be able to react with Ca and/or methanol to generate clogs. To mitigate the clogging problem, we ultimately switched to a 36% transparency, 0.38 mm pore size mesh. This did not significantly change the molecule number or beam velocity, but it dramatically improved the timescale over which mesh clogging occurred. After nearly two months of running, we saw only some buildup of the $Ca(OH)_2$-like substance on the mesh after removing and inspecting the cell.

Mesh heating

Another problem we encountered was that when we began trying to radiatively slow CaOH, we found that hitting the cell with slowing slight immediately truncated the molecular beam, preventing any new molecules from leaving the cell once the light was on. This effect is demonstrated in Fig. 3.6(a), which shows 100 m/s molecules detected with 600 mW of $\widetilde{A}^2\Pi \rightarrow \widetilde{D}^2\Sigma^+$ light down the bore (used as part of two-photon detection, described in sec. 5.3), along with 3 W of repumping lasers. When the detection and repumping lasers are turned on before all molecules have left the cell, the detected molecular beam signal is truncated at a time corresponding to arrival of molecules that would have left the cell after the lasers were turned on. This indicates that lasers incident from the front of the cell immediately stop molecules from exiting.[5] The relatively sharp cutoff suggests that this effect is related to heating of the mesh on the exit aperture, since there would be a larger time delay if the molecule depletion arose from bulk cell heating.

To test this hypothesis, we tested a cell with a 4 mm hole cut in the middle of the mesh (the full 2nd-stage aperture has a 9 mm diameter), and we also tested a cell with no mesh at all on the 2nd-stage aperture. The 4 mm hole helped mitigate the observed effect, while removing the mesh entirely eliminated the problem. As can be seen in Fig. 3.6(b), while removing the mesh caused the molecular beam to speed up from approximately 90 m/s to 130 m/s, it also increased the molecular beam flux by over an order of magnitude. We therefore continued without a mesh for slowing and trapping CaOH.

Note that these effects seen in our experiment are somewhat extreme and do not appear to have been so pronounced on other apparatuses. For instance, CaF MOTs were made for years in the Doyle group with a mesh on

[5] Note that these are repumping lasers, so they will not slow the beam or pump molecules into dark states.

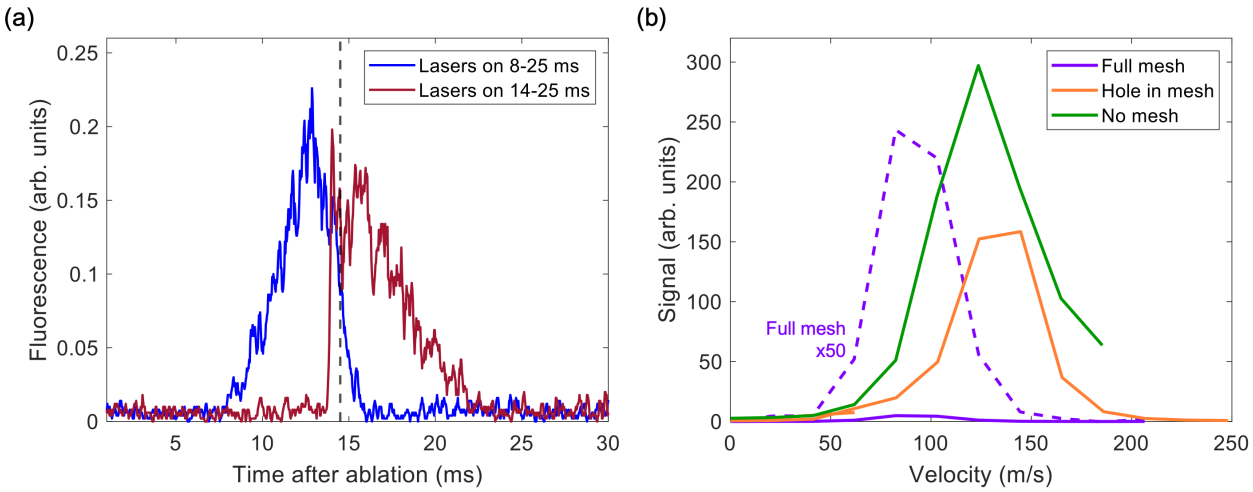

Figure 3.6: Effects of 2nd-stage cell mesh on CaOH production and velocity. (a) Loss of molecules with slowing lasers incident on the cell. For the blue trace, 3.6W of detection and repumping lasers are pointed down the bore into the cell and turned on between 8-25 ms. For the red curve, the same lasers (including detection) are turned on between 14-25 ms. The molecules are detected with velocity-sensitive two-photon detection (see sec. 5.3) tuned into resonance with 100 m/s molecules. The vertical dashed line is the time of arrival for 100 m/s molecules that would have exited the cell at 8 ms, when the lasers were turned on, indicating that no molecules leave the cell after this time. The red curve shows that in the absence of the lasers, molecules continue to arrive at later times. (b) Velocity distributions of molecules produced by a cell with a 36% transparency, 0.38 mm pore size mesh; with a 4 mm hole cut into the middle of the mesh; and with no mesh. The detection method was the same for these three curves and therefore the brightness should be comparable. However, note that the "full mesh" data was taken with an old cell that had a small clog in the mesh. Therefore, the increase in brightness from removing the mesh may be slightly exaggerated.

the 2nd-stage cell. It is unknown whether the issues we observed were fundamental (e.g. CaOH production behaving differently than CaF, higher slowing powers needed[6]), or experimental quirks (e.g. helium buildup due to our suboptimal beam box geometry [273], a poorly heat-sunk mesh, etc.).

3.4.2 Cell heating and slowing beam exit aperture

After removing the mesh, we found that the slowing light continued to cause problems by heating the bulk of the cell. These problems were less dramatic, causing increases in cell temperature and correspondingly faster beams, but they nonetheless hindered our ability to make progress in radiative slowing of CaOH. Fig. 3.7(a) shows velocity distributions of the CaOH molecular beam with and without heat load from the radiative slowing light. In the first curve (blue), the velocity distribution is scanned using two-photon detection (see sec. 5.3), with approximately 500 mW of 824 nm $\widetilde{A}^2\Pi_{3/2} \rightarrow \widetilde{D}^2\Sigma^+$ light pointed down the beamline and into the cell for 25 ms every ∼1 s. In the 2nd curve (red), approximately 3.5 W of laser power – from all slowing lasers except the $\widetilde{X}(000) \rightarrow \widetilde{A}(000)$ cycling laser – are also aligned into the cell and turned on for 25 ms every ∼1 s. The latter case corresponds to approximately 85 mW of extra steady-state power into the cell, causing the cell temperature to increase from 2.8 K to 3.3 K. More critically, the molecular beam velocity increased by approximately 40 m/s.

To solve this problem, we decided to allow the slowing light to exit the back of the cell, then dump the optical power onto the 40 K stage of the pulse tube (which has approx. 60 W of cooling power compared with the 500 mW of cooling power from the helium pot). Ideally we would want a window on the back of the cell to allow the slowing light to escape while keeping the cell sealed. However, we suspected that this window would

[6] The higher slowing powers are probably not the explanation; we saw similar beam truncation with only 600 mW (just the 824 nm two-photon detection light) incident on the cell.

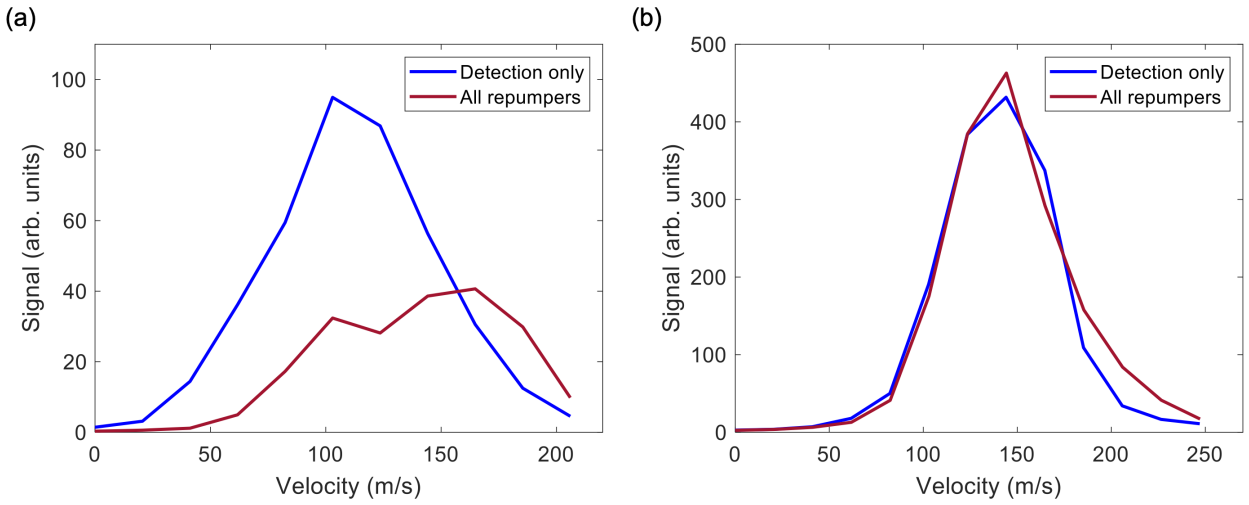

Figure 3.7: Effect of slowing lasers on CaOH beam velocity due to cell heating. Velocity distributions are shown with and without approximately 3.5 W of slowing light (all repumping lasers but no $\widetilde{X}(000) \rightarrow \widetilde{A}(000)$ cycling laser) incident on the cell. The lasers are pulsed on for 25 ms during each experimental shot, and the experimental repetition rate is approx. 1 Hz. (a) Cell with no slowing light exit hole. The steady-state cell temperature is observed to be approx. 2.8 K without the repumping lasers and 3.3 K with them. (b) Buffer gas cell with a 5 mm diameter, 12.7 mm long aperture in the back, allowing slowing light to exit the cell. In this case, turning on the slowing lasers did not cause an increase in beam velocity.

get covered with powder over time (this happens to all other windows on our cells, including the ablation and absorption windows), leading to absorption of laser power and heating of the cell, undermining the original purpose of the window. Therefore, we instead elected to put an open aperture on the cell, designed to have a significantly lower conductance than the front aperture, so that the vast majority of buffer gas and molecules would still exit through the front aperture and into the radiative slowing beamline. We ended up settling on a 12.7 mm long, 5 mm diameter tube at the back of the cell. The diameter is large enough to allow the focused slowing lasers to exit the cell without significant clipping, while the length helps to significantly decrease the gas conductance compared to the front aperture, which has a 7 mm diameter and a thickness of 1.6 mm (1/16"). From direct simulation Monte Carlo (DSMC) simulations of our cell with and without the rear aperture,[7] adding the rear hole reduces the steady-state buffer gas density by approximately 15%, implying that the conductance of the slowing hole is approximately one-sixth that of the front aperture.[8] While we would have preferred to have a conductance that was even lower, in practice we can slightly increase the buffer gas flow rate and take a small hit in our molecule extraction without impeding our ability to make a MOT of CaOH. Practically speaking, we saw that the optimal flow rate for our cell increased from approximately 4 sccm to 6 sccm after adding the slowing hole.

After the light exited the back of the cell, our initial idea was to reflect it out of the beam box using a mirror attached to the cell, which would not only get the heat load out of the beam box but also help for aligning the slowing light through the cell. However, when we tried this we found that the mirror began to get coated with dust exiting through the rear aperture, with the fractional slowing power directed out of the beam box decreasing

[7] These simulations were carried out using the DS2V program.

[8] The aperture and tube diameters D are both slightly larger than the helium mean free path $\lambda \sim 1$ mm, and since $D/\lambda > 1$, we are slightly outside of the molecular flow regime [283]. This makes calculating conductances imprecise, though the estimated ratio of molecular flow conductances is roughly consistent with the DSMC result.

from 85% to 10% over the course of two weeks. The remaining power was absorbed by the coated mirror, causing the cell to heat up.

To solve this problem, we instead built a cryogenic beam dump, which was mounted directly behind the cell but thermally anchored to the 40 K shield, whose ∼60 W of cooling power would have no problem absorbing the ∼100 mW of power dumped by the slowing lasers. The beam dump was machined out of a block of copper 101. A conical hole approx. 7 mm in diameter was machined into the copper where the slowing lasers would be dumped, and the hole and its surroundings were blackened by growing a copper(II) oxide black coating, using the procedure described in Ref. [284]. The copper piece was fixed to the 4 K radiation shields using an Ultem standoff to minimize conductive heat load onto the 4 K stage (the calculated heat load is ∼15 mW when the beam dump is at 50 K). Instead of going to 4 K, the heat load on the dump is carried away to the 40 K radiation shields using a 10 gauge copper wire. Photos of the beam dump are shown in Fig. 3.8.

After installing the hole in the cell, we found that the beam velocity no longer increased in the presence of the slowing lasers (Fig. 3.7(b)). Moreover, thermal anchoring to the 40 K shields appeared to work as intended, with the temperature of the beam dump increasing from approx. 39 K to <42 K with the slowing lasers on at their typical duty cycle.

3.5 Cell geometry optimization

In this section, we described work attempting to optimize the cell geometry in response to a beam speedup observed due to the presence of H_2O ice in the cell.

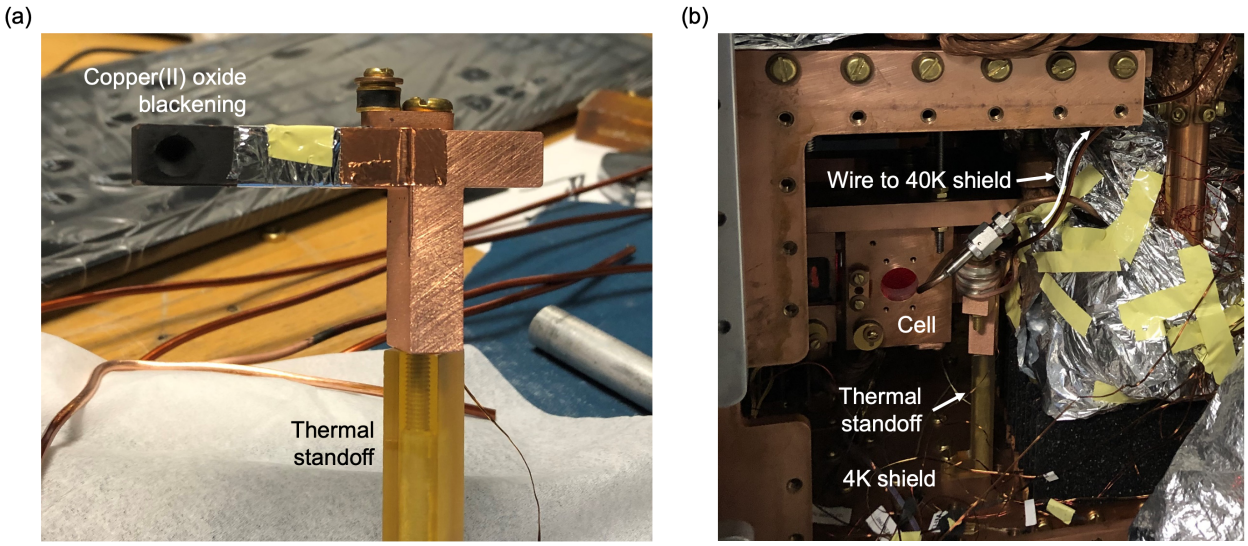

Figure 3.8: Beam dump used for slowing light exiting rear of cell. (a) Image of the beam dump outside the beam box. (b) Beam dump installed in beam box, with Ultem thermal standoff from the 4 K shields and copper wire carrying heat load to the 40 K shields highlighted.

3.5.1 Beam speedup due to water ice

While producing CaOH with H_2O instead of CH_3OH led to an order of magnitude increase in our molecule signal via chemical enhancement, an undesired side effect was that the water ice building up in the cell led to significant increases in the forward velocity of the CaOH molecular beam. A similar beam velocity speedup had previously been observed in the Doyle group for Yb atoms in a He buffer gas cell with methanol vapor (used to produce YbOH) flowed in. This speedup was almost entirely eliminated by increasing the first-stage cell diameter from 1.0" to 1.7", corresponding to a $\sim 3\times$ increase in the cell volume [214]. It was hypothesized that a layer of methanol ice building up on the walls of the cell had hindered the ability of the helium buffer gas to thermalize with the cell, leading to a significant increase in the buffer gas temperature after ablation (which dumps $\sim$10 mJ of energy into the cell). According to this hypothesis, increasing the cell volume meant that the energy was spread

out over more helium atoms (provided the buffer gas density was not changed), leading to a lower increase in buffer gas temperature and a correspondingly lower beam speedup [214]. While we did not observe this effect in the CaOH beam (perhaps because of the larger velocity of Ca compared to Yb), after these observations we nonetheless switched to a 1.7" bore cell.

In contrast to the methanol results, when we started flowing water vapor into our 1.7" large-bore cell, we observed a significant speedup in the beam's forward velocity, indicating that water ice has even less favorable properties than methanol ice.[9] Fig. 3.9 shows velocity distributions of a Ca atomic beam produced by our buffer gas cell after flowing in various amounts of water via the hot fill line, for the cell geometry described earlier (1.7" diameter first stage bore, a 7 mm first-stage aperture, 20 mm long 2nd stage, 9 mm 2nd stage aperture). With no water flowed into the cell, the Ca atomic beam has a peak velocity of 100 m/s. However, when we begin flowing water into the cell at a mass flow rate of approximately 0.1 sccm, we see that within 5 minutes the velocity has increased to 120 m/s, and within 20 minutes it has reached 140 m/s, where it ultimately saturates. Moreover, the velocity distribution starts to look less thermal as more water is flowed into the cell, with a pronounced tail at velocities >200 m/s.

3.5.2 Geometry scans and results

In an attempt to mitigate this speedup effect, we tested a number of cell geometries over a span of a few months, aiming to achieve a higher flux of CaOH molecules at velocities near 100 m/s. The primary idea was to attempt to increase the volume of the cell further, since a volume increase had been shown to mitigate the boosting effect from methanol ice in a cell for Yb atoms [214]. We tried increasing the volume by extending the length of the

[9] Similar observations were made with Yb/YbOH in a different apparatus in the Doyle group [214].

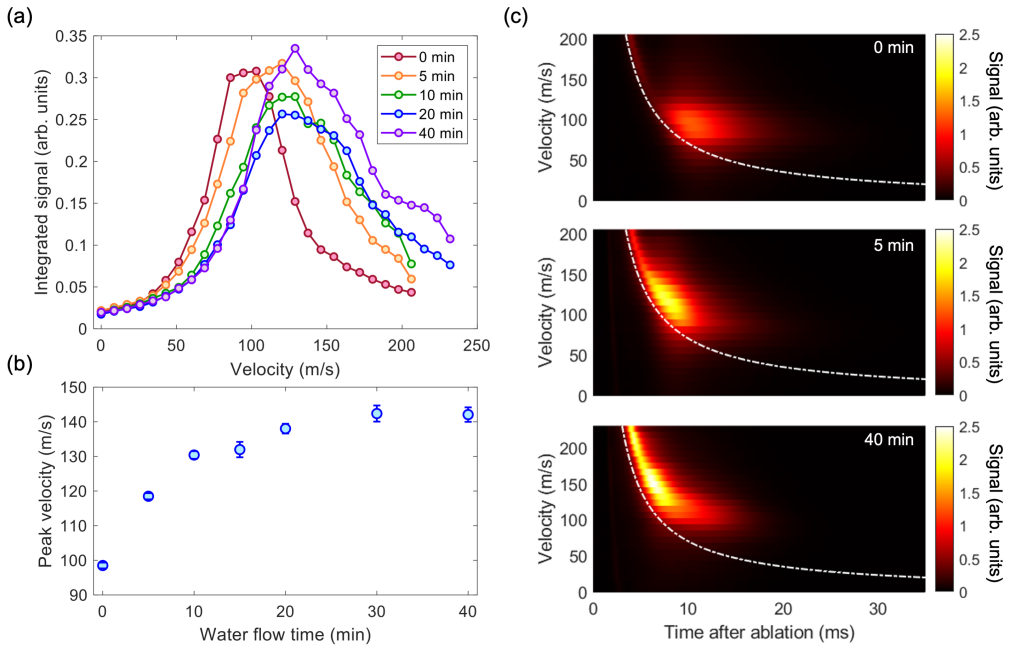

Figure 3.9: Speedup of Ca atomic beam after flowing water vapor into the buffer gas cell for varying amounts of time, at a flow rate of approximately 0.3 sccm. (a) Ca beam signal vs. velocity, after different integrated H_2O flow times. (b) Peak velocity of the Ca beam after different H_2O flow durations. (c) Atomic beam brightness as a function of beam velocity and arrival time. The white curve is the minimum time-of-flight for atoms at a given velocity to traverse the 71 cm distance between the cell and the detection region. The original Ca beam has a lobe near 100 m/s characteristic of well thermalized buffer gas beam production; this lobe disappears as water is flowed into the cell, and a fast tail begins to appear at velocities >200 m/s.

Configuration	First-stage	1st aperture	Gap	Second stage
A	1.0" diameter, 2" long	7 mm	2.8 mm	10 mm long No mesh
B	1.7" diameter, 2" long[a]	7 mm	2.8 mm	20 mm long No mesh
C[b]	1.7" diameter, 2" long	7 mm	2.3 mm	20 mm long 40% transparency, 0.27mm pore size mesh
D	1.7" diameter, 2" long 1.25" long, 1.7" diameter front extension	7 mm	2.8 mm	20 mm long No mesh
E	1.7" diameter, 2" long 1" long, 2x2" rear extension	8.5 mm	2.8 mm	20 mm long No mesh
F	1.7" diameter, 2" long 1/32" wide, 1/16" deep grooves	7 mm	N/A	None
G	3x3" cross section, 2" long	7 mm[c]	N/A	None

[a] More precisely, the back 0.25" of the cell has a 1.0" diameter, and the remaining 1.75" has a 1.7" diameter. Variations of this geometry apply to most of the cell in the table.
[b] Chosen to match a cell geometry that had been shown to produce slow YbOH beams at ∼35 m/s [214].
[c] Aperture located in upper third of the cell (not centered) due to geometric constraints in beam box.

Table 3.1: Summary of cell configurations tested in an attempt to reduce boosting of the molecular beam's forward velocity, due to water ice in the cell.

cell (by adding extensions either in front or in back) as well as by increasing the cross sectional area even further. A summary of the cell configurations tested is given in Table 3.1, with measured beam velocities and molecule numbers for each cell shown in Table 3.2. Photos some of the cell configurations are shown in Fig. 3.10.

From the cell geometries tested, we observed a few general trends. Most notably, we found that increasing the volume of the cell tended to reduce the magnitude of the H_2O-induced boosting of the beam's forward velocity. However, we also found that the larger cell geometries suffered by extracting a significantly lower number of molecules into the molecular beam. Therefore, despite the lower velocities supported by these cells, they nevertheless failed to produce high molecule numbers at velocities below 100 m/s. In an attempt to improve extraction while preserving the desirable lack of a water-induced speedup, we also tried two configurations without a 2nd

Configuration	Volume (cm^3)	Ca velocity (No H_2O)	Ca velocity (With H_2O)	CaOH velocity in beam	CaOH flux (molecules/sr/pulse)
Two-stage cells					
A (1.0" diameter)	26	130 m/s	>200 m/s	190 m/s	5×10^{10}
B (Normal 1.7" diam.)	68	100 m/s	140 m/s	130-140 m/s	5×10^{10}
C (2nd stage mesh)	68	80 m/s	140 m/s	100 m/s	2×10^{9}
D (Front extension)	115	95 m/s	115 m/s	120 m/s	3×10^{9} (Note[a])
E (Rear extension)	134	85 m/s	110 m/s	–	3×10^{9} (Note[b])
Single-stage cells					
F (Normal 1.7" diam.)	68	150 m/s	>150 m/s (Large high-velocity tail)	160 m/s	8×10^{10}
G (3x3" cross section)	261	130 m/s	130 m/s	130 m/s	6×10^{9}

[a] Poor Ca($^3P_1$) enhancement efficiency, likely due to light being far from front aperture

[b] Normal enhancement; suggests that enhancement near front aperture is important

Table 3.2: Summary of CaOH buffer gas cell configurations tested in an attempt to mitigate boosting of the CaOH beam from water ice in the cell. "Volume" refers to the volume of the first-stage cell, the Ca velocities with and without H_2O refer to the velocity before any water has been flowed into the cell, and after the cell has been seeded with enough water for the beam speedup to saturate, respectively. CaOH molecule flux is measured in a room temperature chamber 71 cm downstream from the cell, and assumes a 1 cm $\times$ 2 cm detection area (this is only approximate). The absolute number of molecules detected ranged from 9×10^5 to 3×10^7. This measurement only accounts for molecules in the $N = 1$ rotational state. Note that the helium flow and ablation energies were optimized for each cell, though they were typically in the ranges 5-10 sccm and $\sim$10-20 mJ, respectively.

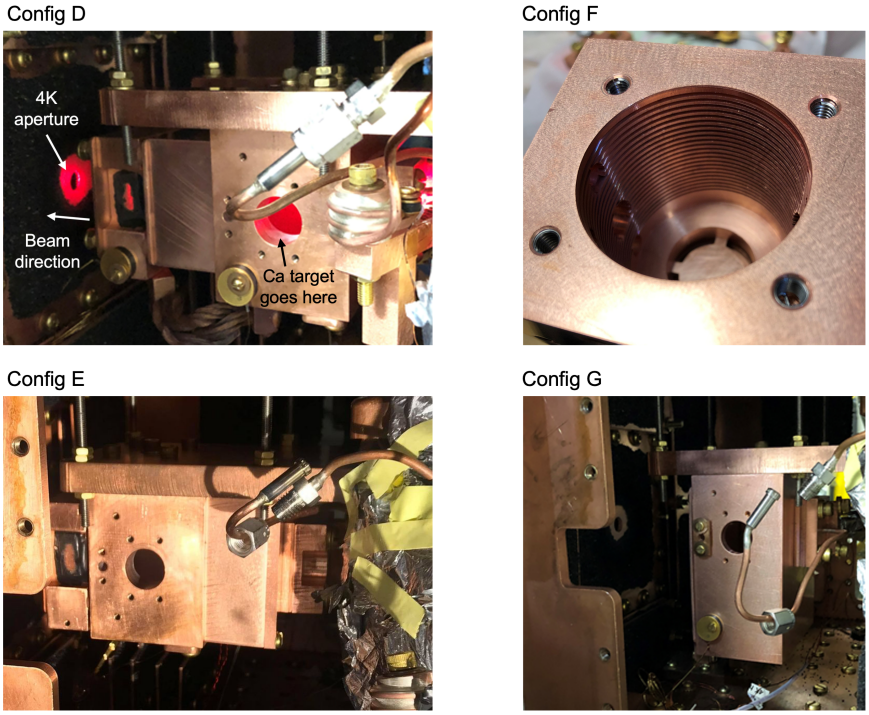

Figure 3.10: Photos of some of the cell geometries tested in this work. Configs D, E, and G show the cell mounted inside the 4K shields of the beam box, but without the Ca target installed. The target would normally fill and seal the large hole on the side of the cell facing the camera. The photo for config F is inside the first stage cell, which has 1/32" wide, 1/16" deep grooves spaced by 1/32". The idea of these grooves was to increase the surface area of the cell and therefore increase the amount of water required to coat the surface, potentially delaying the onset of water-induced boosting.

stage slowing cell. While these generally produced higher flux than their two-stage counterparts, the combination of higher forward velocities and only modestly improved fluxes once again led to little improvement in the number of slow molecules. Ultimately, we found that the original cell configuration (1.7" first-stage bore, no extension, 20 mm-long 2nd stage with no mesh) represented the best tradeoff between molecule flux and boosted velocity.

3.6 In search of the optimal MOT: techniques and observations

3.6.1 Ablation "prefire" pulse

When we first made a MOT of CaOH, our experimental repetition rates were relatively fast (around 1 Hz). However, as we went to longer sequence lengths once the molecules were trapped in an optical dipole trap (ODT), we discovered that the MOT signal became more temperamental. Returning to fast ($\sim$1 Hz) repetition rates typically recovered a good MOT.

While we were debugging this problem, we discovered that firing the ablation laser twice in succession, with the second shot being the one used to load the MOT, dramatically improved the molecule signal. This began by evenly spacing the ablation pulses (so as to mimic an experiment with an effectively faster repetition rate), but we found that moving the pulses close to each other, so that the "prefire" pulse occurred under 50 ms before the MOT loading pulse, led to optimal MOT loading. This "prefire" pulse was initially done by firing the 532 nm Nd:YAG ablation laser twice in succession, but we later switched to using several-ms-long pulses of 1064 nm light with similar total pulse energy as the YAG, suggesting that this effect was a thermal effect.

Fig. 3.11 shows some of our observations related to this phenomenon. We first noticed that the forward velocity

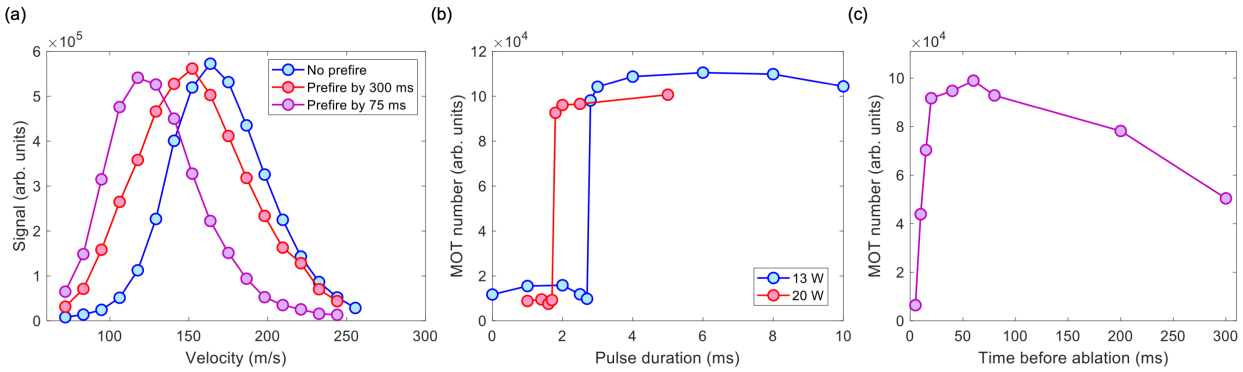

Figure 3.11: (a) CaOH beam velocity with two ablation pulses. Having two ablation pulses during each experimental repetition reduces the beam velocity compared to having just one, and the velocity is even lower when the pulse happens shortly before the ablation pulse used to load the MOT. (b) MOT number vs. pulse duration, using a 1064 nm laser with a power of 13 W (blue) or 20 W (red). For this data, the prefire happens 65 ms before ablation. (c) MOT number as a function of prefire pulse timing, using a 6 ms pulse at 13 W.

of the CaOH beam decreased when the prefire pulse was applied, and that the reduction in velocity was more pronounced as the time delay between the prefire pulse and the MOT loading pulse decreased. This time delay was limited by the maximum repetition rate of our ablation laser, so we couldn't move the delay below ~75 ms.

To gain access to shorter delays, we switched to a 1064 nm fiber amplifier that could be pulsed on for several ms at up to 50 W, which would be sufficient to apply 10s of mJ of energy the cell (comparable to the YAG ablation energy). We co-aligned this beam with the ablation laser but kept it collimated, rather than focused, onto the target. As shown in Fig. 3.11(b), we observed an apparent threshold behavior, where the MOT numbers increased by nearly an order of magnitude once approximately 30 mJ was applied to the cell. We also saw that the optimal MOT was obtained by firing the prefire laser between ~20-50 ms before the ablation pulse (Fig. 3.11(c)).

While we do not fully understand these observations, it is likely that the mechanism is related to the prefire laser desorbing a large amount of helium from the cell prior to the ablation pulse.[10] If the helium were instead

[10]It is likely that the helium density during ablation is significantly higher than the steady-state helium density in the cell. This is supported by measurements of the MOT chamber pressure, which increases 2-4x after ablation compared to the

desorbed by the ablation laser, this would lead to a large increase in the helium density in the cell, causing the velocity of the beam to be significantly boosted. Moreover, for longer sequence lengths helium has more time to adsorb back onto the cell in between ablation pulses, which may explain why the prefire pulse is more important for low repetition rates. It is possible that helium adsorption onto the cell is aided by water ice, but the prefire pulse was also later observed to help MOT numbers in the CaF experiment in the Doyle group, even though that experiment uses SF_6 rather than H_2O for molecule production.

Note that we do not always observe such a dramatic effect of the prefire pulse, and there is likely a complicated interplay between the ablation energy, YAG spot size, prefire power and timing, enhancement laser power and geometry, and so on. For example, at low prefire energies we can sometimes get a decent MOT using large ablation energies, while for high prefire energies the optimal ablation energy is often lower.

3.6.2 Other observations

Optimizing the molecule production is a persistent challenge, and we find that a number of parameters can be optimized to aid CaOH MOT numbers. These include:

- Ablation energy and spot size. We find that sometimes the best MOTs are obtained by moving the focusing lens towards the beam box, so that the ablation beam hits the target before reaching its focus (meaning that it has a larger spot size). Generally, higher pulse energies are required in this geometry. Other times (typically later in the week, when the cell is "dirtier"), the best MOTs are obtained by moving the lens back so the focus is closer to the surface of the target. Sometimes the pulse energy also needs to be reduced in this configuration.
- Ablation beam pointing/alignment. We generally move the spot every 10-100 shots during normal running, using a motorized mirror in the Nd:YAG optical path. The MOT signal is not always uniform

steady-state pressure when helium is flowing.

across the Ca target, and we often find that we have to restrict this automatic rastering to small regions of the target for optimal MOT numbers. This optimal region may vary with other ablation parameters.

- Prefire pulse energy and duration. The optimal prefire pulse duration is often seen to increase over the course of a week.
- Number of ablation pulses during sequence. For especially long sequences/low repetition rates, it is often helpful to have multiple evenly spaced ablation pulses during the sequence. The UHV shutter is closed for the later pulses so no molecules reach the MOT chamber, but this helps clear out helium from the cell the same way that we hypothesize the prefire pulse helps.
- Ca* enhancement beam alignment. Good MOTs are sometimes seen to correspond to the 657 nm beam clipping the edge of the entry window.

In addition to feeding back on the MOT or ODT signal, the real-time pressure in the MOT chamber (read by an ion gauge), is often a decent indicator of how good the MOT will be. There is an "optimal" height for the pressure spike after ablation, with the pressure being too high or too low potentially providing a clue as to the way in which the molecule production is suboptimal. We also monitor the in-cell CaOH absorption signal. This absorption tends to degrade over several weeks of running. Higher in-cell absorption corresponds to better MOTs in a broad sense, but the shape (i.e. time dependence) of the in-cell signal also seems to be important. Therefore, the in-cell signal is not necessarily a reliable indicator of MOT numbers, as also observed in Ref. [278].

4

A Closed Optical Cycle for CaOH Laser Cooling

The key challenge of laser cooling polyatomic molecules is to identify a set of electronic transitions that can be used to scatter a large number of optical photons from the molecule when resonantly excited by lasers. Paradigmatically, this consists of an "optical cycling" transition – typically a strong electronic line capable of scattering several photons by itself – accompanied by a number of "repumping" transitions which are used to return

lost population to the cycling line. In polyatomic molecules, the repumping transitions primarily address population lost to vibrational and rotational states outside the main cycling transition, though there are certain instances where other electronic states may also need to be addressed [214, 285].

The change in momentum Δp arising from a single scattered photon on the $\widetilde{X}^2\Sigma^+ \rightarrow \widetilde{A}^2\Pi_{1/2}$ transition in CaOH ($\lambda = 626$ nm, $m = 57$ u) corresponds to a change in velocity $\Delta v = \Delta p/m = \hbar k/m = 11 \times 10^{-3}$ m/s. Slowing the $\sim$140 m/s CaOH beam produced by the CBGB source (chapter 3) to rest therefore requires approximately 13000 photons to be scattered from each molecule. It turns out that the other steps in the laser cooling process, described later in this thesis, require similar or fewer photons. Therefore, our goal when constructing an optical cycling scheme for CaOH is to enable an average of $\gtrsim 10^4$ photons to be scattered from each CaOH molecule.

CaOH was chosen as a natural extension of prior work in our laboratory laser cooling CaF molecules. Though SrOH had already been optically cycled and laser cooled in one dimension [216–218], it was determined that the lighter mass of CaOH, among other properties, would be favorable for full three-dimensional laser cooling and trapping [286]. At the time, it was believed that approximately 5 lasers would be required to magneto-optically trap CaOH, due to its similar rotational structure and only modestly more complicated vibrational structure compared to CaF [33, 213, 286]. A major finding from the first few years of this thesis work was that more than double that number of repumping lasers would be required due to a number of small yet extremely important interactions occurring in even in the simplest polyatomic molecules [251, 269]. In this chapter, we describe the measurements and calculations used to understand these effects and build an optical cycling scheme capable of scattering $\gtrsim 10^4$ photons from CaOH.

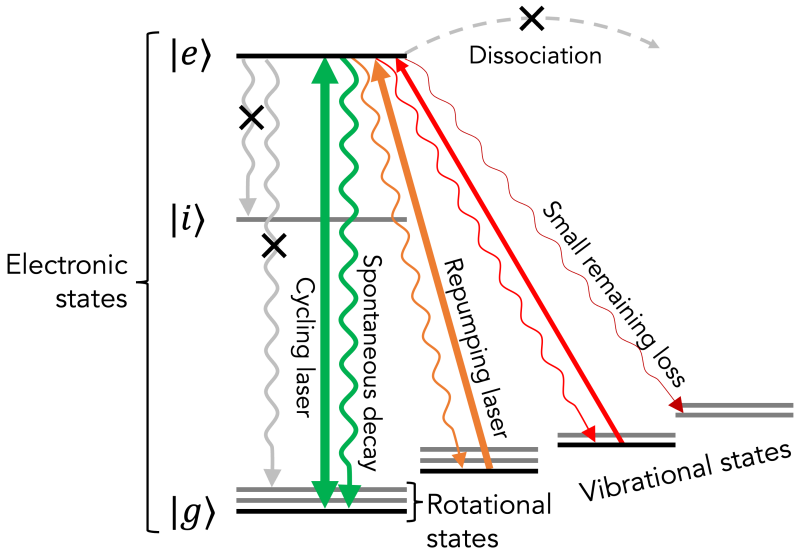

Figure 4.1: Schematic of an optical cycling transition for molecules. Solid lines denote cycling and repumping lasers, and wavy lines indicate spontaneous decay. Processes with black x's (dissociation/predissociation, electronic leakage, and rotational leakage) can and should be suppressed as much as possible. Vibrational leakage will always occur, and can be addressed with a finite number of repumping lasers provided the molecule is chosen to have favorable vibrational branching ratios. The allowable "small remaining loss" is determined by the number of photons that must be scattered, e.g. for 10^4 photons, the remaining fractional losses must total $<10^{-4}$.

4.1 Optical cycling of molecules: overview

For a molecule to be amenable to optical cycling it should have certain structural properties, illustrated schematically in Fig. 4.1. These broadly follow three main criteria regarding the electronic, vibrational, and rotational degrees of freedom:

1. The molecule must possess an electronic transition between two bound electronic states, one of which is stable or metastable and the other of which radiatively decays predominantly back to the initial state. The optical wavelength and the excited state lifetime determine how strong the laser cooling forces will be, with shorter wavelengths and shorter lifetimes leading to stronger forces. The excited state should be chosen to avoid radiative decay to electronic states besides the ground state, as well as to avoid non-radiative

processes such as molecular dissociation, predissociation [208], or internal state redistribution [52].[1]

2. The excited state should decay only to a manageable number of vibrational levels within the ground state potential – i.e. to few enough states that they may be repumped with a technologically feasible number of lasers. This criterion is quantified by the molecule's vibrational branching ratios (VBRs), described in detail below. Because of the large number of vibrational states in polyatomic molecules and the lack of strict selection rules on vibrational decay, only a small subset of molecules are expected to have favorable VBRs for optical cycling. Certain broad classes of polyatomic molecules have nonetheless been identified to have favorable VBRs, suggesting that a variety of molecular structures could potentially be laser cooled [33–38, 48, 49, 215].

3. The transition must be rotationally closed, meaning that the rotational, fine, and hyperfine states used for optical cycling should be chosen so that the excited state(s) decay back to the addressed ground state(s) with as small a number of laser frequencies as possible. Unlike electronic and vibrational branching, rotational branching is governed by strict angular momentum selection rules, meaning that closed cycles containing a small number of rotational states may be found for most molecular structures [37, 52, 190, 215].

These criteria, and other general features of optically cycling molecules, are described in more detail in this section.

4.1.1 Bernoulli Sequence and the "Photon Budget"

Optical cycling in molecules is well described as a Bernoulli sequence [189], with a probability p for the molecule to decay to a state outside the optical cycle during each scattering (absorption/emission) event. The probability p is approximately the sum of decay probabilities from the optical cycling excited state to all states that are not repumped (plus any nonradiative loss probability).

Our primary interest is in determining the probability of the first loss event occurring after N photon scattering events. This limit of the Bernoulli sequence corresponds to a geometric distribution, with X the number

[1] Note, however, that such effects are tolerable if sufficiently small, and optical cycling has been achieved in several molecules where these mechanisms were observed [195, 208, 214, 219, 285].

of photon scattering events before the first molecule loss event. The probability of the first loss event occurring after exactly N photons are scattered is $\Pr(X = N) = (1-p)^{N-1}p$, while the cumulative loss probability is $P_{\text{loss}}(N) = \sum_{n=1}^{N} \Pr(X = n) = 1-(1-p)^N$. Equivalently, the probability of a molecule remaining inside the optical cycle after N photon scattering events is $P_{\text{bright}}(N) = (1-p)^N$, which simplifies to $P_{\text{bright}}(N) \approx e^{-pN}$ if either $pN \ll 1$ or if $N \to \infty$.[2] Therefore, after a time sufficient for the bright molecules to have scattered p^{-1} photons, $P_{\text{bright}}(N = p^{-1}) \approx e^{-1} \approx 37\%$ of the molecules will remain in bright states. In the long-time limit $N \to \infty$, where each molecule has the opportunity to scatter $\gg p^{-1}$ photons, the average number of photons scattered is $N_{\text{avg}} = \sum_{n=1}^{\infty} n \times \Pr(X = n) = p^{-1}$.

The result of these calculations is that $\bar{N} = p^{-1}$ gives a characteristic measure of the number of photons that can be scattered by an optical cycle with total loss probability p per photon scattered. This number can be interpreted as (a) the number of photons scattered before $1/e \approx 37\%$ of the molecules remain in the optical cycle; and (b) the ensemble-average number of photons scattered by the molecules after an infinitely long optical cycling duration. We often refer to $\bar{N}$ as the "photon budget" of the optical cycle and use other imprecise language, but one should keep the precise definitions above in mind when interpreting photon scattering numbers. Importantly, it is possible to scatter many more photons than the photon budget of an optical cycle, provided one is willing to sacrifice molecule numbers. In a typical CaOH experimental sequence, many of the molecules scatter double or even triple the photon budget.

[2] In the $pN \ll 1$ limit we make the binomial expansion $(1-p)^N \approx (1-pN) \approx e^{-pN}$, where we also assumed that $p \ll 1$ because N is an integer. The $N \to \infty$ limit follows from the definition $e^x \equiv \lim_{n\to\infty}(1+x/n)^n$. We have $\lim_{N\to\infty} P_{\text{bright}}(N) = \lim_{N\to\infty}(1-p)^N = \lim_{N\to\infty}(1-pN/N)^N = e^{-pN}$. In practice, this approximation is least precise for $pN \approx 1$, and improves for smaller p. For CaOH, where $p \sim 10^{-4}$, this approximation is very good for all N.

4.2 Rovibronic branching

At its core, designing a closed optical cycling transition simply requires an understanding of where molecular population ends up after being initialized in and eventually decaying from a particular excited electronic state. As discussed above, we aim to avoid nonradiative processes when selecting laser coolable molecules, so we assume here that all losses are due to spontaneous, radiative decay.

The strength of generic, electric dipole-allowed spontaneous emission in molecules is given by the Einstein A coefficient [236]

$$A_{J' \to J''} = \frac{16\pi^3 \nu^3 |\langle \mu \rangle|^2}{3\epsilon_0 h c^3 (2J'+1)}, \tag{4.1}$$

where $|\langle \mu \rangle|^2 = \sum_{M'M''} |\langle \eta', v', J', M' | \boldsymbol{\mu} | \eta'', v'', J'', M'' \rangle|^2$ is the degeneracy-weighted line strength of an electric dipole transition, ν is the transition frequency, and $\boldsymbol{\mu}$ is the electric dipole operator. The rovibronic molecular states $|\eta, v, J, M\rangle$ consist of electronic, $|\eta\rangle$, vibrational, $|v\rangle$, and rotational, $|J, M\rangle$ components.[3] Single primes denote the excited state and double primes label the ground state. The transition strength may be approximately separated into electronic, vibrational, and rotational components as follows (see chapter 2) [236]:

$$|\langle \mu \rangle|^2 \approx q_{v'-v''} |\boldsymbol{R}_e|^2 S^{J'}_{J''}(\zeta', \zeta'') \tag{4.2}$$

[3] In this section we use $|J, M\rangle$ to represent a generic angular momentum state, though this should really be understood to mean all relevant angular momentum quantum numbers in a specific molecule, including e.g. the rotation, electron spin, and nuclear spin.

Here $|\boldsymbol{R}_e|^2$ is the electronic transition dipole moment and

$$q_{v'-v''} = |\langle v'|v''\rangle|^2 \tag{4.3}$$

is the Franck-Condon factor (FCF). $S^{J'}_{J''}(\zeta', \zeta'')$ is the Hönl-London (HL) factor, which characterizes the rotational line strength but depends in general not only on the rotational states $|J\rangle$ but also on the vibronic states involved, which we label $|\zeta\rangle = |\eta, v\rangle$ for notational convenience.

For qualitative descriptions of rovibrational branching, we next make the assumption that the electronic line strength $|\boldsymbol{R}_e|^2$ is constant for all rovibrational decays between two electronic states. This approximation is not exact because the nuclear coordinates, and therefore the electronic wavefunction, differ for different rovibrational states. However, this is a relatively small effect for the low-lying vibrational levels considered here, and this approximation dramatically improves our ability to understand and calculate branching ratios. Under this approximation, we can write down the *rovibrational branching ratio* from initial state $|\zeta', J'\rangle$ to final state $|\zeta'', J''\rangle$ as

$$P_{|\zeta',J'\rangle\to|\zeta'',J''\rangle} \approx \frac{\nu^3 q_{v'-v''} S^{J'}_{J''}(\zeta', \zeta'')}{\mathcal{N}}, \tag{4.4}$$

where

$$\mathcal{N} = \sum_i \nu_i^3 q_{v'-v_i''} S^{J'}_{J_i''}(\zeta', \zeta_i'') \tag{4.5}$$

is a normalization factor. The sum is over all final states $|\zeta_i'', J_i''\rangle$ to which the initial state may decay. Apparently, the branching ratios are predominantly determined by (1) the FCFs, $q_{v'-v''}$, and (2) the HL factors, $S^{J'}_{J''}(\zeta', \zeta'')$. These will be discussed in the following sections.

4.2.1 Vibrational Branching: FCFs and VBRs

The relative intensities of decay pathways from a laser cooling excited state to different ground vibrational levels are given by *vibrational branching ratios* (VBRs). These are the most important quantities to know for selecting a laser-coolable molecule: while rotational (and, to some extent, electronic) branching can typically be addressed with a small number of lasers, VBRs that do not quickly converge towards zero will generally preclude laser cooling.

VBRs are very similar to the rovibrational branching ratios defined above but they sum over all rotational decay pathways: $\mathrm{VBR}_{v'\to v''} = \sum_{J''} P_{|\zeta',J'\rangle\to|\zeta'',J''\rangle}$. This means that the Hönl-London factors disappear, and we are left with

$$\mathrm{VBR}_{v'\to v''} \approx \frac{\nu^3 q_{v'-v''}}{\sum_i \nu_i^3 q_{v'-v_i''}} \tag{4.6}$$

Therefore, the VBRs are proportional to the Franck-Condon factors (FCFs) with a correction due to the ν^3 scaling of the Einstein A coefficients. The FCFs, $q_{v'-v''} \equiv |\langle v'|v''\rangle|^2$, are defined as the overlap integral between the ground and excited state vibrational wavefunctions. Intuitively, electronic transitions occur on much faster timescales than the nuclear motion, so the vibrational wavefunctions $|v'\rangle$ and $|v''\rangle$ remain approximately unchanged during electronic excitation [234]. Their overlap integral thus sets the strength with which the transition will occur.

To a first approximation, the vibrational wavefunctions are products of simple harmonic oscillator wavefunctions corresponding to the normal modes of vibration of the molecule,

$$\langle Q|v\rangle = \psi_{\mathrm{vib}}(Q_1, Q_2 ... Q_n) \approx \psi_{v_1}(Q_1)\psi_{v_2}(Q_2)\dots\psi_{v_n}(Q_n), \tag{4.7}$$

where $\psi_{v_i}(Q_i)$ is the harmonic oscillator wavefunction corresponding to the ith normal mode with excitation quantum number v_i and normal coordinate Q_i. The number of normal modes n is $3N - 6$ for nonlinear molecules and $3N - 5$ for linear molecules, where N is the number of atoms in the molecule. Accordingly, the FCF can be rewritten as a product of 1D overlap integrals:

$$q_{v'-v''} = |\langle v'|v''\rangle|^2 \approx \left|\int \psi^*_{v'_1}\psi_{v''_1}dQ_1\right|^2 \left|\int \psi^*_{v'_2}\psi_{v''_2}dQ_2\right|^2 \dots \left|\int \psi^*_{v'_n}\psi_{v''_n}dQ_n\right|^2 \tag{4.8}$$

The integrals can be readily evaluated provided that the equilibrium coordinates (molecular bond lengths and bond angles) and vibrational frequencies are known. Methods for evaluating these overlap integrals have been extensively developed for molecules, and are described in appendix B. For real molecules, the harmonic oscillator basis described here does not perfectly describe the energy eigenstates, which are perturbed by a number of effects including anharmonicity in the molecular potential and breakdown of the Born-Oppenheimer approximation.

Fig. 4.2 illustrates the FCFs for a simple one-dimensional vibration, e.g. the Ca–O symmetric stretching mode in CaOH. From this illustration it is clearly desirable to have similar bond lengths and vibrational frequencies in both electronic states, with the FCFs being more sensitive to the bond length than to the frequency [214]. In the limit of identical potential energy surfaces, the vibrational wavefunctions are the same in the ground and excited states, $|v'\rangle = |v''\rangle$. By orthonormality of solutions to the Schrödinger equation for a given potential, we therefore have $\langle v'_i|v''_j\rangle = \delta_{ij}$. In this limit, the matrix of FCFs $q_{v'-v''}$ is diagonal, and so good laser cooling molecules are often referred to as "diagonal" or having "diagonal Franck-Condon factors."

Based on this understanding, having good FCFs requires that electronic excitation of a molecule leave the potential energy surface mostly unchanged. This can be achieved by building a molecule whose valence electron

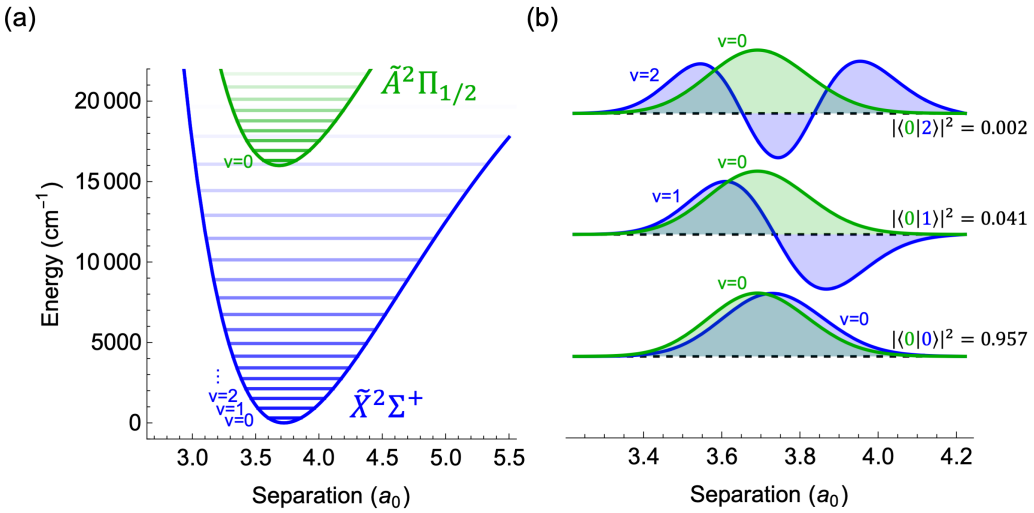

Figure 4.2: Franck-Condon factors for the symmetric, Ca–O stretching mode of CaOH. (a) Illustration of the $\widetilde{X}^2\Sigma^+$ and $\widetilde{A}^2\Pi_{1/2}$ potentials and their vibrational eigenstates, labeled with vibrational quantum number v. The potentials use the measured Ca–O stretch frequencies and bond lengths ($\omega_X = 615$ cm^{-1}, $\omega_A = 628$ cm^{-1}, $r_X = 1.973\ a_0$, $r_A = 3.69\ a_0$ [250]), and they assume a Morse potential with a dissociation energy of 4 eV [287] for illustrative purposes. (b) Comparison of the $\widetilde{A}^2\Pi_{1/2}(v=0)$ vibrational wavefunction (green) with the lowest three vibrational wavefunctions of the $\widetilde{X}^2\Sigma^+$ potential (blue). Because the center positions (bond lengths) and curvatures (frequencies) of the two potentials are similar, the FCFs are nearly diagonal. Calculated overlap integrals for these 1D wavefunctions confirm this intuition, and are actually relatively close to the measured VBRs for CaOH (sec. 4.3).

does not participate in the molecular bonding. In practice, the paradigm that has proven most successful for molecule laser cooling to date is to take an alkaline earth or alkaline-earth-like atom (e.g. Ca, Sr, Ba, Yb, ...) and ionically bind it to a ligand (F, OH, OCH_3, NH_2, ...), which accepts one electron to form a singly charged anion and leaves the remaining electron near the alkaline earth cation. As described in chapter 2, the electronic structure of such a "metal-ligand" (ML) molecule is derived from the electronic structure of the metal ion, and the valence electron wavefunction is generally repelled away from the molecular bond by the anion's electron cloud. Quantum mechanically, this occurs via orbital hybridization: in the $\widetilde{X}$ ground state, $s\sigma$ and $p\sigma$ orbitals mix to push the electron cloud away from the ligand, while in the $\widetilde{A}$ state the mixing is between $p\pi$ and $d\pi$ orbitals [212]. The lack of electron density between the metal and the ligand in either state means that the bonding should be relatively unperturbed.

While the FCFs are primarily determined by the molecule's geometry, there are some selection rules that arise from molecular symmetry arguments. Specifically, by the *vanishing integral rule* [244], the FCF

$$q_{v'-v''} = |\langle v'|v''\rangle|^2 = \left|\int \psi^*_{v'}\psi_{v''}d\tau\right|^2$$

is nonzero only if the integrand $\psi^*_{v'}\psi_{v''}$ contains the totally symmetric representation of the symmetry group to which the molecule belongs. If $\Gamma^{(v')}$ and $\Gamma^{(v'')}$ are the symmetry species of the two vibrational states, the requirement is that $\Gamma^{(v')} \otimes \Gamma^{(v'')} \supseteq \Gamma^{(s)}$, where $\Gamma^{(s)}$ is the totally symmetric representation. For linear molecules (symmetry group $C_{\infty v}$), the totally symmetry representation is Σ^+. Vibrational states with $\ell = 0$ have Σ^+ character, those with $\ell = \pm 1$ have Π character, and so on. This ultimately means that the symmetry selection rule for the FCFs is $\Delta\ell = 0$. However, as we will see, perturbations that couple electronic and vibrational angular

momentum relax these selection rules and introduce weak decays to bending modes with $\ell \neq 0$.

4.2.2 Rotational Branching and Rotational Closure

Returning to eqn. 4.4, the other contribution to rovibrational branching ratios is the Hönl-London (HL) factor $S^{J'}_{J''}(\zeta', \zeta'') = \sum_{M',M''} |\langle J', M'|\boldsymbol{\mu}|J'', M''\rangle|^2$, which characterizes rotational branching.[4] The HL factors follow a generally well-behaved set of selection rules governed by angular momentum algebra, meaning that rotational branching can typically be controlled to a higher degree than vibrational branching.[5] The HL factors can be calculated using angular momentum algebra by taking matrix elements of the dipole operator (appendix A), or looked up in tables, for instance in Refs. [236, 288]. Note that in this section, we will work primarily with the angular momentum quantum numbers N, K, and J, where N is the angular momentum excluding spin, K is its projection onto the molecular symmetry axis (in CaOH, $K = \Lambda + \ell$), and J is the angular momentum including the electron spin ($S = 1/2$).

The general formula for forming a closed cycling transition in molecules was first proposed by Ref. [190] (and extended to nonlinear molecules in Refs. [34, 37, 47, 215]), and relies on the rotational and parity selection rules $\Delta N = 0, \pm 1; \Delta p = \pm 1; N'' = 0 \nrightarrow N' = 0$.[6] The key observation was that, while a traditional "type-I" $N'' \rightarrow N'' + 1$ transition cannot be rotationally closed (since a rotational level with $N'' + 2$ necessarily exists in the ground state), driving the "type-II" $N'' = 1 \rightarrow N' = 0$ transition (or its closest analogue within the molecule of choice) forms a closed transition. One consequence of this choice of transition is that there are more

[4] Portions of this section have been modified from Ref. [52].

[5] Unless otherwise stated, in this section we consider only electric dipole (E1) transitions. Higher-order transitions (e.g. M1, E2, etc.) are significantly weaker and are typically irrelevant for molecular laser cooling.

[6] The selection rules on K depend on specifics of the molecule. For instance, in linear polyatomics like CaOH, $K = \Lambda + \ell$, and Λ, but not ℓ, can be changed by up to ± 1 by an electronic transition, as discussed below.

ground states M'' than excited states M', meaning that there will be dark states regardless of the laser polarization chosen. These can be remixed with magnetic fields or polarization modulation [289].

CaOH, like most molecules that have been laser cooled to date, has a single valence electron, so its states have an electron spin quantum number $S = 1/2$. In this case, the rotational angular momentum N couples to the electron spin to form a total angular momentum quantum number J, which takes half-integer values.[7] In such a system, the electric dipole selection rules $\Delta J = 0, \pm 1$ and $J = 0 \nrightarrow J' = 0$ always apply, as well as the requirement that the parity of the state changes, $\Delta p = \pm 1$. For transitions between states well described by Hund's case (b) coupling, N is an approximately good quantum number and the selection rule $\Delta N = 0, \pm 1$ also applies. As we will see, regardless of the angular momentum coupling, closed transitions in CaOH are formed by always exciting the $J = 1/2^+$ level of an excited electronic state, where the superscript denotes positive parity $p = +$.

Unlike the universal selection rules on J and parity, selection rules for the angular momentum projection quantum number K depend on the specific molecular geometry and transition type. These are described in Refs. [34, 37, 47, 215], with a summary in Ref. [52]. For molecules like CaOH with cylindrical symmetry, transitions can be either parallel or perpendicular, meaning the transition dipole moment is induced either along the principal molecular axis or perpendicular to it, respectively. In linear molecules specifically, parallel transitions do not change the electronic angular momentum projection, $\Delta\Lambda = 0$, while perpendicular transitions change it by $\Delta\Lambda = \pm 1$ (for example, $\widetilde{X}^2\Sigma^+ \rightarrow \widetilde{A}^2\Pi$ is a perpendicular transition and $\widetilde{X}^2\Sigma^+ \rightarrow \widetilde{B}^2\Sigma^+$ is a parallel transition). Electronic transitions do not couple to the vibrational angular momentum ℓ, so $\Delta\ell = 0$. These selection rules together give the change in $K = \Lambda + \ell$ for an electronic transition.

[7] Here we ignore hyperfine degrees of freedom, which are often unresolved in polyatomic molecules, though the selection rules discussed below can be easily generalized to include hyperfine structure. In CaOH, hyperfine structure due to the hydrogen nuclear spin $I = 1/2$ causes approx. 1 MHz splittings, which are smaller than the electronic transition linewidth.

Rotationally closed transitions for relevant manifolds in CaOH are shown in Fig. 4.3. In nondegenerate vibrational states (those with $\ell = 0$), the closed rotational transitions are the same as for diatomic molecules (Fig. 4.3(a)). A closed optical cycling transition is formed by driving the ${}^{P}Q_{12}(J = 1/2)$ and $P_1(J = 3/2)$ transitions, which address both spin-rotation components of the $\widetilde{X}\,{}^2\Sigma^+(N = 1^-)$ ground state and excite them to either the $\widetilde{A}\,{}^2\Pi_{1/2}(J' = 1/2^+)$ or $\widetilde{B}\,{}^2\Sigma^+(N' = 0, J' = 1/2^+)$ state.[8] The key ingredient for achieving rotational closure in this scheme is not the specific electronic state but the fact that it have a well-resolved $J' = 1/2^+$ level. In this case the transition is guaranteed to be closed by the E1 selection rules $\Delta J = 0, \pm 1$ and $\Delta p = \pm 1$. The two ground state SR components are split by approximately 52 MHz in CaOH, so we drive these transitions with two frequencies generated using an AOM. Hyperfine structure from the hydrogen nuclear spin is on the $\sim$1 MHz scale and is unresolved for these optical transitions.

Including hyperfine structure introduces the possibly of one more rotational leakage channel. By angular momentum and parity selection rules, the $(J' = 1/2, F = 1^+)$ level of the excited state may, in principle, decay to the $(N = 3, J = 5/2, F = 2^-)$ ground state level. However, this requires that the hyperfine interaction mix the $N = 1$ and $N = 3$ states. The mixing fraction is on the order of $\sim c^2/(10B)^2 \sim 10^{-10}$ for CaOH, where c is the dipolar hyperfine constant and B is the rotational constant. While this decay mechanism is negligible for CaOH and alkaline-earth monohydroxides with similar structure, it may be of some significance for species with large hyperfine structure, e.g., with a nuclear spin on the optical cycling center [291].

For nondegenerate vibrational states, we still use $J' = 1/2^+$ excited states but have more allowed decays due to parity doubling in the ground state (Fig 4.3(b-c)). Since $J = 1/2^+$ can decay to any ground state with $J =$

[8] The rotational branch notation used here is ${}^{\Delta N}\Delta J_{F_i' F_j''}(J'')$, where $\Delta N, J = -1, 0, 1$ are denoted by P, Q, and R, respectively. F_i' is a label for the spin component of the state (see, e.g. Ref [290]). For instance, in the ground state F_1 and F_2 correspond to the upper and lower spin-rotation component in each N level.

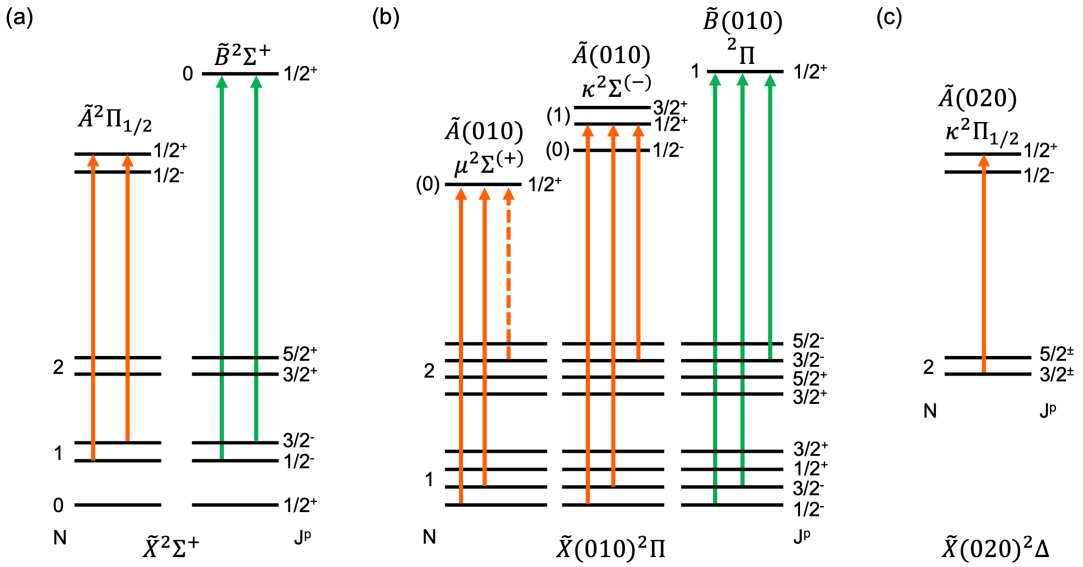

Figure 4.3: Rotationally closed transitions in CaOH. Adapted from Ref. [52].

$1/2$ or $J = 3/2$ and negative parity, decays to $(N = 2, J = 3/2^-)$ are now allowed. For $\ell = 1$ bending modes (e.g. (010), (110), (03^10)), this means that lasers must address the same ${}^PQ_{12}(1/2)$ and $P_1(3/2)$ transitions as for nondegenerate states, but also need to address the ${}^OP_{12}(3/2)$ transition from $N = 2$. The two $N = 1$ SR components are split by 26 MHz in the bending mode, which can be bridged by an AOM or broadened over with a single laser frequency, but the $N = 2$ component is 40 GHz away and needs to be bridged either with a high frequency EOM or a separate laser. In the experiment, we use separate lasers, providing more flexibility to repump the $N = 1$ and $N = 2$ components through different excited states. For $\ell = 2$ bending modes (e.g. (02^20), (12^20)), the lowest rotational state is $N = 2$, meaning that only $(N = 2, J = 3/2^-)$ needs to be repumped.

The excited states shown in Fig. 4.3 are those allowed by the $\Delta\ell = 0$ selection rule for electronic transitions. For some excited states, N' is at least an approximately good quantum number, and both N and J selection rules

must be followed. Most notably, this means that the $\widetilde{A}(010)\kappa^2\Sigma^{(-)}$ state should be chosen over the $\mu^2\Sigma^{(+)}$ component for repumping $N = 2$ in $\ell = 1$ bending modes, since approximate ΔN selection rules forbid the latter transition (dashed line in Fig. 4.3(b)).[9] Though not shown in the figure, in practice we will often repump bending modes on nominally forbidden transitions allowed by vibronic coupling, as described in section 4.4. In these cases we also need to heed ΔN selection rules; for instance, $N = 2$ cannot be repumped through nondegenerate vibrational components of the $\widetilde{B}^2\Sigma^+$ state.

4.2.3 Perturbations

In the above sections, we separated the electronic and vibrational degrees of freedom, and we also treated vibrational states in the harmonic approximation. Though these are good first approximations, there are additional terms in the molecular Hamiltonian that mix these states, leading to important corrections to vibrational branching at the level needed for laser cooling. Since these corrections are typically small, we will work with an unperturbed set of basis states $|\eta, v\rangle^{(0)}$ that treat the electronic (η) and vibrational (v) states as separable, with the vibrational states being separable into normal modes represented by simple harmonic oscillator eigenstates, $|v\rangle^{(0)} \equiv |v_1\rangle|v_2, \ell\rangle|v_3\rangle$. In the presence of a perturbing Hamiltonian H_{pert}, the unperturbed basis states are mixed and the vibronic states $|\zeta\rangle$ become

$$|\zeta_i\rangle = \sum_j c_{ij}|\eta_j v_j\rangle^{(0)} \approx |\eta_i v_i\rangle^{(0)} + \sum_{j\neq i} c_{ij}|\eta_j v_j\rangle^{(0)} \tag{4.9}$$

[9] In CaOH, this transition has a rotational branching ratio of approximately 6%.

where it is assumed that the total angular momentum J is conserved by any relevant perturbation. The coefficients can be determined either from perturbation theory or by diagonalizing the Hamiltonian including H_{pert}. The second (approximate) equality applies in the case where the perturbation is small.

Transition strengths between these perturbed states are

$$|\langle \zeta_i', J'|\boldsymbol{\mu}|\zeta_j'', J''\rangle|^2 \approx \Big| \overbrace{\langle \eta_i' v_i' J'|\boldsymbol{\mu}|\eta_j'' v_j'' J''\rangle}^{\text{unperturbed transition strength}} + \underbrace{\sum_{k''} c_{j''k''} \langle \eta_i' v_i' J'|\boldsymbol{\mu}|\eta_k'' v_k'' J''\rangle + \sum_{k'} c^*_{i'k'} \langle \eta_k' v_k' J'|\boldsymbol{\mu}|\eta_j'' v_j'' J''\rangle}_{\text{intensity borrowing}} \Big|^2 \tag{4.10}$$

where we have omitted terms proportional to $c_{ik}c_{jk}$ assuming $c_{ik} \ll 1$. We see that in the limit of small perturbations ($c_{ij} \ll 1$), the transition strength is primarily that of the unperturbed state, but that there are small modifications introduced by the perturbations. This effect is often referred to as "intensity borrowing." We find that this is a significant effect for CaOH branching ratios at or below the 10^{-3} level.

The primary perturbations that cause intensity borrowing relevant to CaOH laser cooling are vibronic coupling and anharmonicity in the vibrational potential. These are summarized in Fig. 4.4 and briefly described below. See Refs. [251, 269, 292] for a more detailed discussion of intensity borrowing effects relevant to laser cooling linear polyatomic molecules.

Note that rovibronic branching ratios including these effects may be estimated using measured spectroscopic parameters. Such calculations are described in appendix B and in Ref. [251].

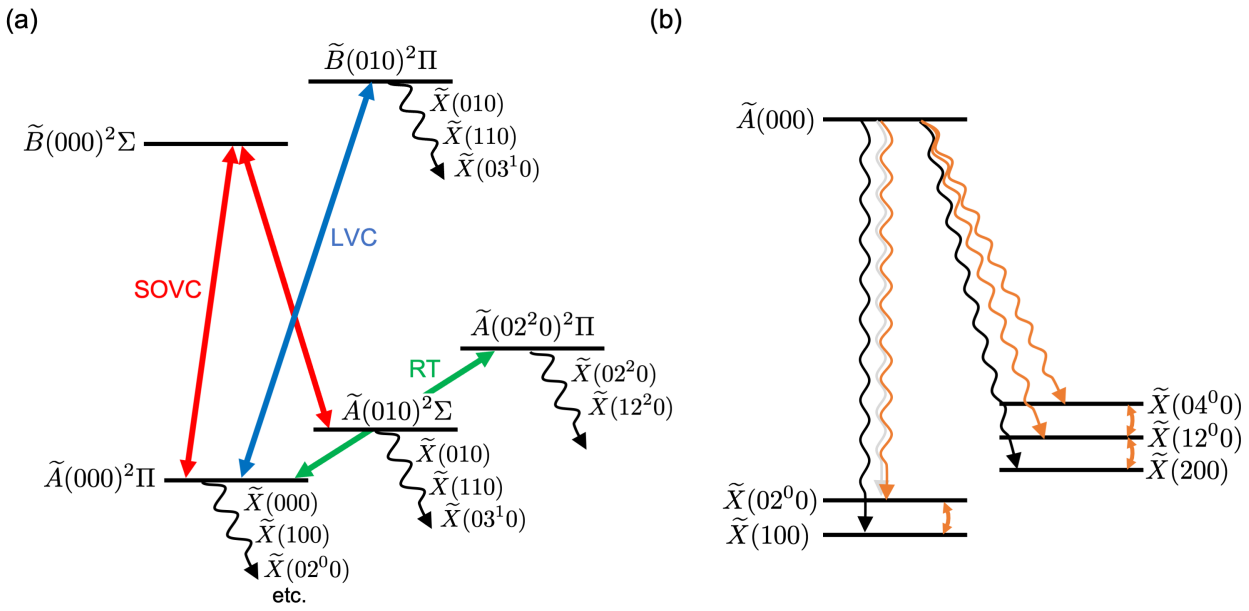

Figure 4.4: Summary of perturbations that contribute to vibrational branching in CaOH. (a) Vibronic coupling. The $\widetilde{A}(000)$ state couples to states with $\ell \neq 0$ in the $\widetilde{A}$ and $\widetilde{B}$ manifolds via several vibronic coupling mechanisms, including linear vibronic coupling (LVC), spin-orbit vibronic coupling (SOVC), and Renner-Teller interactions (RT). (b) Fermi resonance mixing between nearby bending and stretching modes causes increased decay from the $\widetilde{A}(000)$ state.

Vibronic interactions

As described in chapter 2, vibronic interactions are described by the Hamiltonian [252, 264–268]

$$H_{\text{vibronic}} = \frac{V_{11}}{2}(q_+ L_- + q_- L_+) + \frac{V_{22}}{2}(q_+^2 L_-^2 + q_-^2 L_+^2) + \dots \tag{4.11}$$

where $L_\pm$ and $q_\pm$ are ladder operators in the electronic angular momentum Λ and the vibrational angular momentum ℓ, respectively. The terms in this Hamiltonian describe a multipole expansion of the electromagnetic interaction between the electronic orbitals and the nuclei when the molecule is in a bending vibrational mode. These interactions can couple vibronic states in the $\widetilde{A}$ and $\widetilde{B}$ electronic manifolds, as shown in Fig. 4.4(a).

The first term has selection rules $\Delta\Lambda = \pm 1$, $\Delta\ell = \mp 1$. This means that it can directly couple $\widetilde{A}(000)$ to $\widetilde{B}(010)$, which has symmetry-allowed vibrational decays to ground states with $\ell = 1$. This mixing is therefore responsible for decays to e.g. $\widetilde{X}(010)$, $\widetilde{X}(110)$, and $\widetilde{X}(03^10)$ in CaOH. This term is the linear term in the vibronic Hamiltonian, and is therefore sometimes referred to as linear vibronic coupling (LVC). An additional effect that can occur is a second order process where LVC couples up to $\widetilde{B}(010)$ and a term in the spin-orbit Hamiltonian proportional to AL_-S_+ couples back down to $\widetilde{A}(010)$. We call this effect spin-orbit vibronic coupling (SOVC).[10] It has been shown that this effect is small compared to direct LVC even for molecules with large spin-orbit interactions, since there is a suppression in the energy denominator from spin-orbit splittings in the $\widetilde{A}$ state [269].

The second term in eqn. 4.11 mixes states with $\Delta\Lambda = \pm 2$, $\Delta\ell = \mp 2$. This can couple $\widetilde{A}(000)$ to $\widetilde{A}(02^20)$ (since it can take $\Lambda = 1 \to -1$ and $\ell = 0 \to 2$). The latter state has symmetry-allowed vibrational decays to

[10] A similar effect occurs via the $\widetilde{B}(000)$ state, as shown in Fig. 4.4(a).

$\ell = 2$. Therefore, this interaction is responsible for vibrational decay to $\widetilde{X}(02^20)$, $\widetilde{X}(12^20)$, and so on. This term is called the Renner-Teller (RT) interaction and is also responsible for large vibronic splittings in the $\widetilde{A}(010)$ and $\widetilde{A}(020)$ states (chapter 2).

Note that LVC affects both the $\widetilde{A}$ and $\widetilde{B}$ states, but RT interactions only affect the $\widetilde{A}$ state. Therefore, $\widetilde{B}^2\Sigma^+(000)$ would be expected to have significant vibrational decay to $\ell = 1$ bending modes but not to states with $\ell = 2$. Of course, this also means that $\ell = 2$ vibrational states must be repumped through the $\widetilde{A}$ manifold.

Vibrational anharmonicity

As shown in Fig. 4.4(b), anharmonic mixing between vibrational levels in the $\widetilde{X}$ state also contributes to increased VBRs. The most notable effect is Fermi resonance (described in chapter 2), which couples nearby vibrational states of the same symmetry. In CaOH, since the Ca–O stretching frequency is approximately double the bending frequency, sets of states like $(100) \leftrightarrow (02^00)$ and $(200) \leftrightarrow (12^00) \leftrightarrow (04^00)$ experience significant Fermi resonance interactions. As one example in CaOH, the harmonic estimate for branching to $\widetilde{X}(02^00)$ is at the 10^{-4} level, but the observed branching ratio is an order of magnitude stronger due to intensity borrowing from the much stronger $\widetilde{X}(100)$ decay (which is at the 5% level).

Note that in SrOH, the stretching and bending mode frequencies are not as similar in CaOH, resulting in substantially smaller branching ratios for decay to (02^00) and (12^00) [293].

4.3 Measurement of CaOH vibrational branching ratios

Prior to the construction of our experiment, vibrational branching ratios had been measured for CaOH using the dispersed laser-induced fluorescence (DLIF) technique with a noise floor of $\sim 2 \times 10^{-3}$, showing only three

observable decay channels from the $\widetilde{A}^2\Pi_{1/2}$ state [213]. However, early tests of optical cycling in our apparatus indicated that additional loss channels were limiting the number of photons that could be scattered, as described in Ref. [273]. These observations, combined with the realization that VBR measurements with a sensitivity of $<10^{-4}$ would be required to cycle the necessary $\gtrsim 10^4$ photons to make a MOT, motivated us to measure VBRs with higher sensitivity. We ultimately ended up pursuing two complementary methods to take these measurements.

The first method – depletion-revival spectroscopy – was natural to pursue in the early CaOH apparatus, which had been set up for optical cycling and laser cooling a molecular beam [220, 273]. This method, which relies on cycling photons until population accumulates in unaddressed states, then repumping those states and measuring the amount of population recovered, is advantageous because it constitutes a direct measurement of the performance of the optical cycle that will be used for laser cooling. Moreover, it is possible to calibrate the total remaining loss from an optical cycle by inferring the amount of unrecovered population, even without knowing the specific channels responsible for that loss. A disadvantage of the method is that every cycling and repumping transition must be known at high resolution, making it good at calibrating the branching ratios of known transitions, but bad at identifying new loss channels (which must be searched for by trying to repump each possible channel individually). Moreover, sensitivities well below 10^{-3} require cycling $\gtrsim 10^3$ photons, which is challenging given experimental constraints of finite interaction distance.

The second method was a variant of dispersed laser-induced fluorescence (DLIF) spectroscopy, whereby an optical cycling transition is driven, and the scattered photons are collected, dispersed on a diffraction grating, and imaged onto a high-sensitivity EMCCD. Compared to the earlier DLIF measurements [213], these measurements increased the sensitivity by two orders of magnitude from $\sim 10^{-3}$ to $\sim 10^{-5}$ by cycling $\sim$100 photons

per molecule [269]. This high-sensitivity DLIF approach is an excellent survey spectroscopy method for designing and building optical cycling schemes for new polyatomic molecules, since it reveals all (or nearly all) of the vibrational states will need to be repumped, and also has sufficient frequency resolution (typically a few cm^{-1}) to serve as a good starting point for high-resolution spectroscopy of repumping transitions. Following our CaOH work, this was used as the primary technique for building an optical cycle in SrOH [293]. This method was also recently used in our group to determine the feasibility of trapping certain nonlinear Sr-containing polyatomic molecules [215]. The primary disadvantage of the DLIF technique is that there is a possibility of uncontrolled errors that make it difficult to estimate the photon budget for a new optical cycling scheme. For instance, there could be unobserved decay channels, either below the noise floor or outside the wavelength range of the measurement, that contribute to reducing the expected photon budget. Moreover, this technique only provides information about radiatively emitted photons, so loss due to molecular dissociation, predissociation, or intra-vibrational relaxation (IVR) may not be noticed using DLIF alone [48, 51, 52]. Additionally, the frequency resolution is typically not sufficient to identify rotational leakage channels. Therefore, the optical cycle ultimately will need to be tested using depletion-revival or similar techniques to confirm the viability of laser cooling and trapping, even if the DLIF measurements look promising.

While the optimal method for a new laser-cooling experiment would be to perform high-sensitivity DLIF measurements and then test the optical cycle using depletion-revival methods, in the CaOH experiment we performed these measurements in the opposite order. This is because (1) the need for high-sensitivity DLIF was not readily apparent until the depletion-revival measurements showed more vibrational branching than expected, and (2) the experimental apparatus for depletion-revival measurements was available to us well before a DLIF setup was assembled in the Doyle group. We present these measurements in chronological order below.

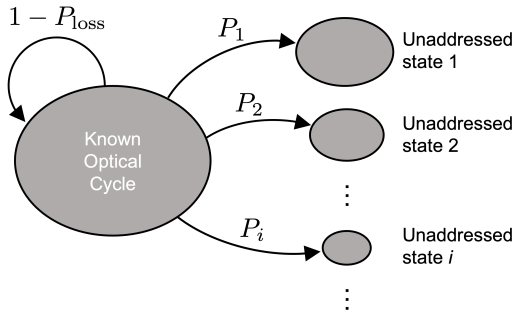

Figure 4.5: Schematic of the depletion-revival measurement. For a known, lossy optical cycling transition (which may contain several states), molecules are lost to unaddressed states with a probability P_{loss} after each photon scattering event. The probability of loss to each unaddressed state i is given by its branching ratio P_i, where normalization requires that $\sum_i P_i = P_{\text{loss}}$. After cycling $\gg P_{\text{loss}}^{-1}$ photons, nearly all population will be distributed in the unaddressed states. Repumping the population from state i and detecting the recovered population P_{rec} gives the branching ratio $P_i \approx P_{\text{rec}} \times P_{\text{loss}}$.

4.3.1 Method 1: Depletion-Revival Spectroscopy

Our early measurements of CaOH VBRs using depletion-revival techniques with a sensitivity of $\sim 5 \times 10^{-4}$ were described previously [251, 273].[11] For completeness, we will summarize those measurements again here, and also describe later efforts to measure VBRs with slightly better sensitivity.

The key idea of these measurements is shown schematically in Fig. 4.5. We begin with a set of states that is known to form a quasi-closed optical cycling transition, from which population is lost to unaddressed states with probability P_{loss} per photon scattering event. We then scatter photons on this cycling transition until nearly all population is pumped into the unaddressed levels, which occurs after $\gg P_{\text{loss}}^{-1}$ photons have been scattered. At this point, the molecular population is now distributed among the loss channels i according to the ratio of their branching ratios P_i, where $\sum_i P_i = P_{\text{loss}}$. The population of each of these states i is next repumped back into the optical cycle, and the fractional recovered population, P_{rec}, is measured by fluorescence detection of optically

[11] Portions of this section have been reproduced, with small modifications, from Ref. [251].

cycled photons. The branching ratio for state i can be determined by $P_i \approx P_{\text{rec}} \times P_{\text{loss}}$, up to small corrections accounting for natural state population and for imperfect depletion from the optical cycle.

In order for this method to work, P_{loss} must first be known for some optical cycling transition. In principle, this could be calibrated by deflecting a molecular beam using radiation pressure force, and inferring the number of scattered photons from the measured deflection angle and the known momentum imparted per scattered photon [216, 273]. However, this method is susceptible to a number of systematic errors and is therefore difficult to pin down with a high degree of precision.[12] Instead, we took advantage of the fact that DLIF measurements had already been performed for CaOH, albeit with a noise floor of $\sim 2 \times 10^{-3}$ [213]. While the limited sensitivity of this prior measurement prevented a precise determination of the absolute VBRs, the *relative* branching ratios to $\widetilde{X}^2\Sigma^+(000)$ and $\widetilde{X}^2\Sigma^+(100)$ were determined with good precision. This provided enough information to determine a starting value of P_{loss} from which to measure lower-level VBRs.

The experimental apparatus for these measurements, which were previously reported in Ref. [251], is depicted in Fig. 4.6. A cryogenic buffer gas beam (CBGB) of CaOH molecules was produced using the apparatus described in chapter 3 and Ref. [220],[13] then collimated with a 3×3 mm square aperture approximately 35 cm downstream to ensure that all molecules could be addressed by the applied laser light. We then applied light in three downstream regions: an interaction region, a clean-up region, and a detection region, as described below. We performed two measurements: the first was used to determine $\widetilde{X}(000)$ and $\widetilde{X}(100)$ branching ratios, and the

[12] We initially tried to use this technique to measure the loss probability when optically cycling with lasers addressing the $\widetilde{X}(000) \rightarrow \widetilde{A}(000)$ and $\widetilde{X}(100) \rightarrow \widetilde{B}(000)$ transitions [273]. However, due in part to the fact that our detection lasers were not retroreflected, we found that Doppler shifts of the deflected molecular beam's resonance frequency could impact both the measured amplitude and position of the beam in ways that were difficult to control.

[13] This was an early version of the apparatus, with some small differences from what we eventually used to make a MOT. These included producing CaOH by reacting Ca with methanol without Ca* chemical enhancement, and using a cell with a smaller, 1"-diameter bore.

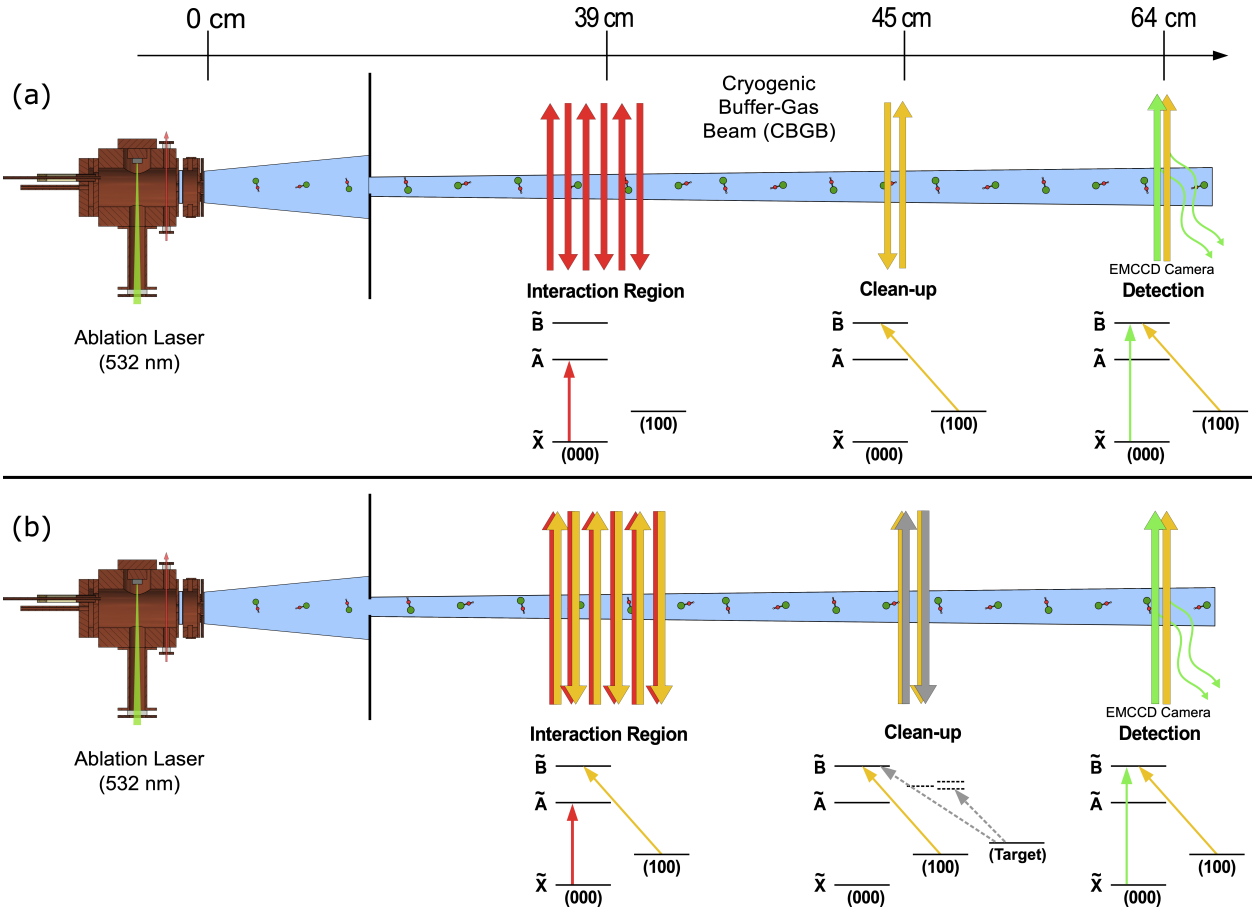

Figure 4.6: Experimental setup for depletion-revival branching ratio measurements. (a) Configuration for measuring $\widetilde{X}(000)$ and $\widetilde{X}(100)$ branching ratios. (b) Configuration for measuring branching ratios to $\widetilde{X}(200)$, $\widetilde{X}(02^{0}0)$, $\widetilde{X}(02^{2}0)$, and $\widetilde{X}(01^{1}0)$. Reproduced from Ref. [251].

2nd used these results as a starting point for determining $\widetilde{X}(200)$, $\widetilde{X}(02^00)$, $\widetilde{X}(02^20)$, and $\widetilde{X}(01^10)$ branching ratios.

Vibrational Branching Ratios to $\widetilde{X}(000)$ and $\widetilde{X}(100)$

In the first measurement, the $\widetilde{X}^2\Sigma^+\,(000) \rightarrow \widetilde{A}^2\Pi_{1/2}\,(000)$ laser was retroreflected through the interaction region as depicted in Fig. 4.6(a). Molecules interacted with this light field, cycling photons until >95% of the molecular population decayed to a dark vibrational state. The increase in molecular population in each excited vibrational state was directly proportional to the vibrational branching ratio to that state. A laser addressing the $\widetilde{X}^2\Sigma^+\,(100) \rightarrow \widetilde{B}^2\Sigma^+\,(000)$ transition recovered population lost to the $\widetilde{X}^2\Sigma^+(100)$ state. Molecules were detected with lasers addressing the $\widetilde{X}^2\Sigma^+\,(000) \rightarrow \widetilde{B}^2\Sigma^+\,(000)$ and $\widetilde{X}^2\Sigma^+\,(100) \rightarrow \widetilde{B}^2\Sigma^+\,(000)$ transitions, and the resulting laser-induced fluorescence was imaged onto an electron multiplying charged coupled device (EMCCD) camera. Absolute population drifts due to ablation fluctuations were mitigated by normalizing the recovered population with interleaved measurements of the total population taken with the light in the interaction region blocked. The fractional population recovered was P_{rec} = 85.2(6)%.

We model this process as a discrete Markov chain with two absorbing states corresponding to $\widetilde{X}(100)$ and to all other unaddressed states, respectively. Each discrete step corresponds to a spontaneous emission event which causes the population to evolve according to the expression

$$\begin{pmatrix} P^{n+1}_{(000)} \\ P^{n+1}_{(100)} \\ P^{n+1}_{\text{other}} \end{pmatrix} = \begin{pmatrix} T_a & 0 & 0 \\ T_b & 1 & 0 \\ T_c & 0 & 1 \end{pmatrix} \begin{pmatrix} P^{n}_{(000)} \\ P^{n}_{(100)} \\ P^{n}_{\text{other}} \end{pmatrix}. \tag{4.12}$$

In this expression the parameters T_a, T_b, and T_c correspond to the vibrational branching ratios from $\widetilde{A}(000)$ to $\widetilde{X}(000)$, $\widetilde{X}(100)$, and all other loss channels, respectively. $P^n_{(000)}$, $P^n_{(100)}$, and P^n_{other} are the molecular populations in $\widetilde{X}(000)$, $\widetilde{X}(100)$, and all other states, respectively, after n spontaneous decay events. This formula can be recursively applied with the resulting population at any step (n) described by the expression

$$\vec{P}_n = \begin{pmatrix} T_a & 0 & 0 \\ T_b & 1 & 0 \\ T_c & 0 & 1 \end{pmatrix}^n \vec{P}_0. \tag{4.13}$$

where $\vec{P}_0$ is a vector that represents the initial distribution of molecular population and is experimentally determined. In this first measurement, we do not measure the final population P^n_{other}, and as a result our model is insensitive to this quantity. We represent $\vec{P}_0$ as

$$\vec{P}_0 = \begin{pmatrix} P^0_{(000)} \\ P^0_{(100)} \\ P^0_{\text{other}} \end{pmatrix} = \begin{pmatrix} 0.92(1) \\ 0.08(1) \\ 0 \end{pmatrix}$$

where $P^0_{(000)}$ and $P^0_{(100)}$ are experimentally determined and P^0_{other} is set to zero to reflect the insensitivity of the model. As photons are scattered, the percentage of molecular population in excited vibrational states converges to an asymptotic limit. Previous measurements of vibrational branching in Ref. [213] have measured the VBRs to $\widetilde{X}(000)$ and $\widetilde{X}(100)$: $T_a = 0.957(2)$ and $T_b = 0.043(2)$. However, these values sum to 1, which is nonphysical given the known decay to higher vibrational states. To account for this, we use these measure-

ments to constrain the ratio $T_a/T_b = \frac{.957(2)}{.043(2)} = 22.3(1.0)$. In addition, conservation of probability demands that $T_a + T_b + T_c = 1$. These two constraints, combined with the experimental measurement of P_{rec} described above, allow the branching ratios to be uniquely determined. The values of T_a, T_b, and T_c are extracted from the model, and the combined vibrational branching ratio from $\widetilde{A}(000)$ to $\widetilde{X}(000)$ and $\widetilde{X}(100)$ is found to be $T_a + T_b = 0.9918(8)$. The uncertainty in this value is obtained by allowing each of P_{rec} and T_a/T_b to vary by up to 1 standard error in the model, computing the corresponding $T_a + T_b$ value, and taking one half the maximum difference found.

Vibrational Branching Ratios to $\widetilde{X}(200)$, $\widetilde{X}(02^00)$, $\widetilde{X}(02^20)$, and $\widetilde{X}(01^10)$

From the previous measurement, we knew that population decays from $\widetilde{A}(000)$ with a branching ratio of $T_c = 1 - T_a - T_b = 0.0082(8)$ to all states besides $\widetilde{X}(000)$ and $\widetilde{X}(100)$. The next step was to determine the specific states and branching ratios constituting that remaining loss. From previous calculations and measurements [33, 213], we expected $\widetilde{X}(200)$ and $\widetilde{X}(02^00)$ to contribute near the 10^{-3} level. However, early photon cycling tests in our experiment also indicated that there was significant decay to $\widetilde{X}(01^10)$ and to $\widetilde{X}(02^20)$, both of which are forbidden within the Born-Oppenheimer approximation (which enforces a $\Delta\ell = 0$ selection rule) and were not expected to appear at such a high level [286]. Once these four states were identified as the dominant next-order losses after $\widetilde{X}(000)$ and $\widetilde{X}(100)$, we pursued a measurement of their VBRs.

In order to measure the VBRs to these higher-lying vibrational states, we depleted population from the $\widetilde{X}(000)$ and $\widetilde{X}(100)$ states and directly measured the accumulation of molecules in other excited vibrational levels. In the interaction region (see Fig. 4.6(b)), photon cycling lasers addressing the $\widetilde{X}^2\Sigma^+(000) \rightarrow \widetilde{A}^2\Pi_{1/2}(000)$ and $\widetilde{X}^2\Sigma^+(100) \rightarrow \widetilde{B}^2\Sigma^+(000)$ transitions were retroreflected between two mirrors for a total of $\sim$ 12 cm of in-

teraction distance. This interaction length was sufficient to optically pump $\sim$ 90% of the population to higher vibrational states, corresponding to >250 scattered photons. Cycling multiple photons was crucial to this measurement as it allowed for substantial optical pumping (10% level population transfer) through small decay pathways. We selectively recovered population from the states of interest by applying appropriate repumping lasers in the clean-up region.

The decay probability to higher vibrational levels was assigned according to the fraction of population recovered from each state following the depletion-revival process, using the constraints that the total loss probability sums to 1 and the measured VBR to $\widetilde{X}(000)$ and $\widetilde{X}(100)$ accounts for 0.9918(8) of this total. [14] The experimental sequence for these measurements was designed to account for natural population in the repumped vibrational states and imperfect depletion from $\widetilde{X}(000)$ and $\widetilde{X}(100)$. We collected data in four different experimental conditions, interleaved to account for ablation drifts, allowing us to measure and correct for these factors and extract the "true" percentage of recovered population (P_{rec}). The four conditions are indicated below, where "interaction", "cleanup", and "detection" refer to the regions of optical access depicted in Figure 4.6(b):

(A) Detection Light only

(B) Detection Light and Cleanup Light

(C) Interaction Light and Detection Light

(D) Interaction, Cleanup, and Detection light

[14] In reality, the loss probability is slightly different here than in the $\widetilde{X}(000)/\widetilde{X}(100)$ measurement above, because here the $\widetilde{X}(100)$ state is repumped through $\widetilde{B}(000)$, which has slightly different branching ratios. Since 4.3% of the scattered photons are actually from the $\widetilde{B}(000)$ state, we can estimate the modified closure by combining our $\widetilde{A}$ state measurements with $\widetilde{B}$ state DLIF data from Ref. [213]. The result for the "effective" closure is $T_a^{\text{eff}} + T_b^{\text{eff}} \approx 0.957(T_a^A + T_b^A) + 0.043(T_a^B + T_b^B) \approx 0.957 \times 0.9918(8) + 0.043 \times 0.997(1) \approx 0.9920(8)$, which is within error of the value for cycling through $\widetilde{A}(000)$ only. Therefore, we will ignore this correction here.

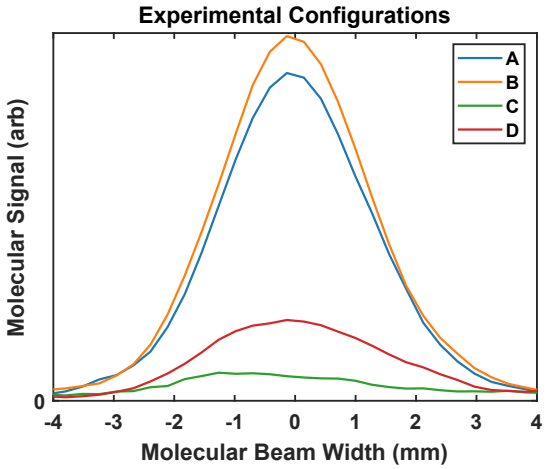

Figure 4.7: Depletion-revival data used to measure the branching ratio to $\widetilde{X}(010)(N'' = 1)$. The configurations are (A) detection only, (B) detection and repumping in clean-up region (which gives the natural population), (C) depletion and detection only (no cleanup; shows depleted fraction), and (D), depletion, cleanup, and detection (shows revival). Reproduced from Ref. [251].

These four measurement configurations allowed us to determine the population optically pumped into higher vibrational states (**A**-**C**), the natural population in higher vibrational states (**B**-**A**), and the population recovered from excited vibrational states (**D**-**C**-(**B**-**A**)), all while normalizing against ablation fluctuations. The recovered population, P_{rec}, is the percentage of depleted population that is recovered upon repumping one (or many) excited vibrational states and calculated as:

$$P_{rec} = \frac{\mathbf{D} - \mathbf{C} - (\mathbf{B}-\mathbf{A})}{\mathbf{A} - \mathbf{C}}. \tag{4.14}$$

An example of the data collected from this experimental sequence is given in Fig. 4.7, where each of the experimental conditions is indicated.

The final results from this measurement are shown in Table 4.1. Along with the measured VBRs, we also found that repumping all four states together recovered 87% of the population, meaning that 13(1)% of the de-

State	Measured branching ratio
$\widetilde{X}(000)$	$0.9492(27)$
$\widetilde{X}(100)$	$0.0426(19)$
$\widetilde{X}(200)$	$2.5(3) \times 10^{-3}$
$\widetilde{X}(02^{0}0)$	$3.3(4) \times 10^{-3}$
$\widetilde{X}(02^{2}0)$	$8.2(1.3) \times 10^{-4}$
$\widetilde{X}(01^{1}0)(N=1)$	$6.4(1.1) \times 10^{-4}$
Other	$1.1(3) \times 10^{-3}$

Table 4.1: Branching ratio measurements determined using the depletion-revival technique described in the text. These results were previously reported in Ref. [251].

pleted population was not recoverable. We attributed this loss to yet higher-lying states and assigned a corresponding VBR to all vibrational states not addressed. The measured VBRs were in agreement with previous results [213].

4.3.2 Depletion-revival measurements with 10^{-4} level sensitivity

Following our published measurements of branching ratios at the $\gtrsim 5 \times 10^{-4}$ level needed for transverse laser cooling [251], our next step was to begin pinning down the states that made up the remaining $\sim 1 \times 10^{-3}$ of unaccounted-for loss. The good news at this point is that we were developing a good semi-empirical understanding of the mechanisms responsible for rovibrational branching (see appendix B), so we had decent educated guesses for where the remaining population could be [251]. We therefore spent portions of the next year finding the next few expected repumping transitions and measuring their VBRs. While these measurements (and the ones described above) were eventually superseded by the DLIF measurements described in sec. 4.3.3 below, they have not previously been described and we will include them here for completeness. Moreover, these measurements have rotational resolution, so we used them in combination with the DLIF to estimate rotational

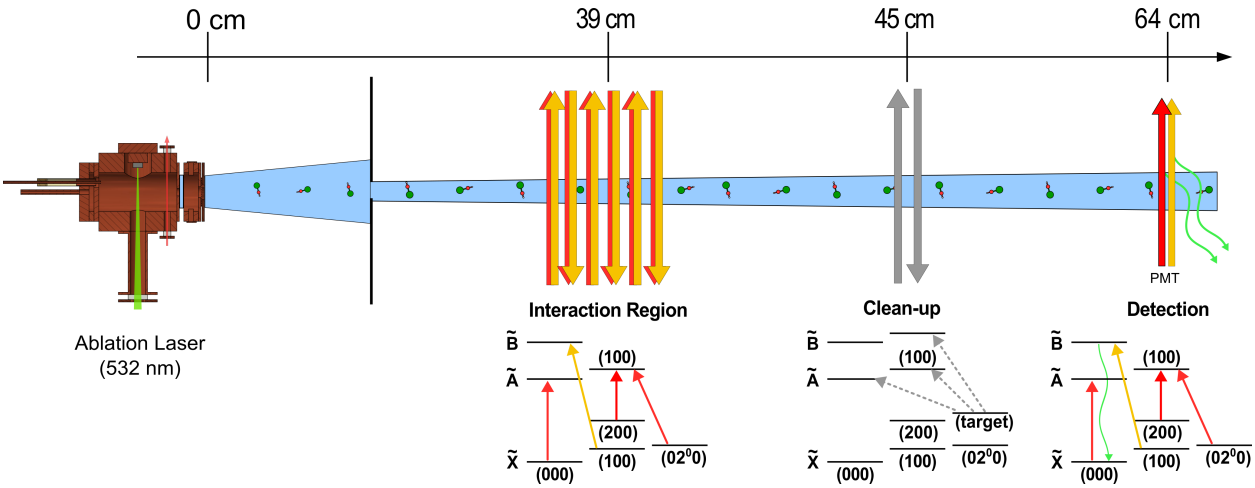

Figure 4.8: Experimental setup for depletion-revival branching ratio measurements with increased sensitivity.

branching fractions within a given vibrational manifold.

The experimental setup for these higher sensitivity measurements is shown in Fig. 4.8. It is similar to the one used for our earlier depletion-revival branching ratio measurements, with a few modifications. Molecules were produced in a buffer gas cell by reacting ablated Ca with methanol vapor, and the resulting CBGB was collimated with a 3×3 mm square aperture. In the interaction region, molecules were depleted by optically cycling with the first four repumping transitions: $\widetilde{X}(000) \rightarrow \widetilde{A}(000)$, $\widetilde{X}(100) \rightarrow \widetilde{B}(000)$, $\widetilde{X}(02^00) \rightarrow \widetilde{A}(100)$, and $\widetilde{X}(200) \rightarrow \widetilde{A}(100)$. The total loss out of the optical cycle should be $P_{\text{loss}} \approx 2.4 \times 10^{-3}$ based on our earlier measurements [251], assuming the $\widetilde{A}(100)$ state's branching ratios are well-behaved, as expected from calculations. Therefore, scattering approx. 1000 photons should cause >90% of the population to be depleted, and 10%-level repumping from loss channels will give branching ratio sensitivities in the low 10^{-4} range. To maximize the number of scattered photons, high optical powers of approx. 500 mW were used for each of the laser beams in the depletion region, each beam had 52 MHz spin-rotation (SR) sidebands added, and the polarzation

was modulated with a Pockels cell at ∼2 MHz to remix dark states [289].

To detect the lost population, molecules in the clean-up region were repumped back into the optical cycle using a repumping transition depending on the state to be measured. The repumping was done with typically ∼200-300 mW of laser power, with the relevant SR sidebands applied, and with a ∼2 G magnetic field applied to help remix dark states [289]. Then molecules were detected in the detection region using a background-free laser-induced fluorescence (LIF) technique. Photons were scattered using the same four optical cycling transitions used in the depletion region, and the 555 nm fluorescence emitted from $\widetilde{B}(000) \rightarrow \widetilde{X}(000)$ decay (approx. 1 out of every 18 scattered photons) was collected on a photomultiplier tube (PMT; Hamamatsu R7600U-200). The three red lasers had ∼10 mW of power while the $\widetilde{X}(100)$ laser had ∼100 mW of power. The lasers had the same SR sidebands and polarization modulation used in the depletion region. Because of this off-diagonal detection technique, the detection efficiency for molecules beginning in $\widetilde{X}(100)$ vs. $\widetilde{X}(000)$ was significantly different, since in the latter case approximately 18 photons would need to be scattered before detecting a single photon. To compensate for this effect, we attempted to ensure molecules were always in the same state when they entered the detection region.[15] We also included small correction factors in an attempt to compensate for any remaining discrepancy.

We measured branching ratios to six different states using the following repumping transitions in the cleanup region: $\widetilde{X}(02^20) \rightarrow \widetilde{A}(100)$, $\widetilde{X}(01^10)(N=1) \rightarrow \widetilde{A}(000)$, $\widetilde{X}(01^10)(N=2) \rightarrow \widetilde{A}(000)$, $\widetilde{X}(12^00) \rightarrow \widetilde{A}(100)$, $\widetilde{X}(300) \rightarrow \widetilde{B}(100)$, and $\widetilde{X}(12^20) \rightarrow \widetilde{A}(100)$. When taking data, we interleave experimental shots with the same four configurations (A-D) used in the earlier measurements. This is used to calibrate the depletion level and the natural population, and to normalize for ablation fluctuations. We calculate the effective recovered

[15] This was done, e.g., by intentionallly molecules in the "unperturbed" beam into $\widetilde{X}(100)$.

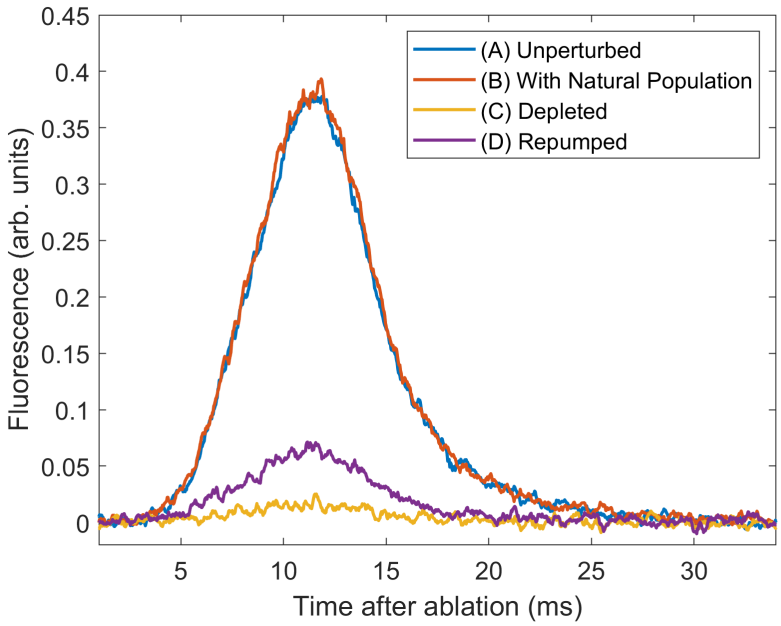

Figure 4.9: Depletion-revival data used to determine the branching ratio to $\widetilde{X}(010)(N=2)$. This state is repumped in the clean-up region using the $\widetilde{X}(010)(N=2) \rightarrow \widetilde{A}(000)$ transition at 641 nm. The four interleaved experimental configurations (A-D) are labeled in the legend.

fraction P_{rec} from these four configurations using eqn. 4.14. Example data for the $\widetilde{X}(010)(N=2)$ state is shown in Fig. 4.9. The recovered fraction for each state (calculated from eqn. 4.14) is shown in Table 4.2 along with the approximate corresponding VBR. As can be seen, we were able to deplete nearly all of the beam, corresponding to ∼1000 scattered photons, and resolve revival fractions of a few percent, corresponding to decays around 1×10^{-4}.

Measurement of $\widetilde{A}(100)$ branching ratios

We also undertook a measurement of the $\widetilde{A}(100)^2\Pi_{1/2}$ vibrational branching ratios, which play a role in CaOH optical cycling since we direct some of the repumping transitions through this state. We did not need high sensi-

State	Fraction recovered	VBR
$\widetilde{X}(02^20)$	0.25	6.2×10^{-4}
$\widetilde{X}(010)(N=1)$	0.20	4.9×10^{-4}
$\widetilde{X}(010)(N=2)$	0.11	2.7×10^{-4}
$\widetilde{X}(12^00)$	0.10	2.5×10^{-4}
$\widetilde{X}(300)$	0.04	9.9×10^{-5}
$\widetilde{X}(12^20)$	0.04	9.9×10^{-5}
Missing	0.26	6.4×10^{-4}

Table 4.2: Fraction of molecules recovered from each state after depleting population by optical cycling with the $\widetilde{X}(000)$, $\widetilde{X}(100)$, $\widetilde{X}(02^00)$, and $\widetilde{X}(200)$ lasers. Errors in the recovered fraction are approximately 1%. Calculated VBRs are also shown assuming $P_{\text{loss}} = 2.47 \times 10^{-3}$.

tivity for these measurements, since this state gets populated by lasers that repump 10^{-3} level (or lower) decays. To do this, we first drove the $\widetilde{X}(000) \rightarrow \widetilde{A}(100)$ transition. Afterwards, we could directly detect the population in $\widetilde{X}(100)$ to get the $\widetilde{X}(100)$ VBR, or drive the $\widetilde{X}(100) \rightarrow \widetilde{A}(100)$ transition and then detect $\widetilde{X}(000)$ to get the $\widetilde{X}(000)$ VBR (note that both of these measurements have the VBR to higher states as an unknown that can be solved for). To get VBRs to higher states, we drive $\widetilde{X}(000) \rightarrow \widetilde{A}(100)$ and $\widetilde{X}(100) \rightarrow \widetilde{A}(100)$ simultaneously, which cycles photons before depleting population into the higher states. These can then be recovered and the VBR inferred. The result of these measurements is shown in Tab. 4.3, along with a comparison to semiempirical calculations similar to those described in appendix B.

The $\sim$3% loss to other states is not especially concerning, since this state is not frequently populated, and most of the remaining decay is to states that will be repumped in the optical cycle anyway.

Table 4.3: Measured vibrational ranching ratios from $\widetilde{A}(100)^2\Pi_{1/2}$, determined using the depletion-revival technique.

State	Measured	Calc.[a]
$\widetilde{X}(000)$	0.043	0.046
$\widetilde{X}(100)$	0.856	0.869
$\widetilde{X}(200)$	0.068	0.072
$\widetilde{X}(02^00)$	0.006	0.003
Other	0.028	0.01

[a] Semiempirical calculations similar to those described in appendix B.

4.3.3 Method 2: Dispersed Laser-Induced Fluorescence (DLIF) Spectroscopy

The second method we used to measure vibrational branching ratios (VBRs) in CaOH was dispersed laser-induced fluorescence (DLIF) spectroscopy. The idea of this technique is to electronically excite molecules using a laser, then measure the optical spectrum of the spontaneously emitted photons, which conveys information about the decay transitions and their relative intensity. In practice, this is done by collecting molecular fluorescence and coupling it into a high-resolution spectrometer, which disperses the fluorescence on a diffraction grating, so that frequency information is converted into spatial information. Imaging the dispersed fluorescence on a camera then conveys information about the wavelength and relative intensity of each emission feature. Combined with some structural understanding of the molecule, these emission wavelengths can be assigned to different vibronic decay transitions originating from the initially populated state. In this way, information about all vibronic decays from a given excited state can be determined simultaneously, and without needing *a priori* knowledge of the frequency and expected strength of each possible decay channel. DLIF is a common technique in physical chemistry, and has been used to measure vibrational branching ratios for a number of laser-coolable molecules

in recent years [48, 49, 213–215, 293–296]. Our goal was to measure branching ratios with 10^{-5} sensitivity (sufficient to scatter $>10^4$ photons and make a MOT), which at the time was approximately two orders of magnitude lower than previous DLIF measurements. To do this, we needed a high molecular fluorescence signal, which we achieved using a chemically-enhanced cryogenic buffer gas beam and optical cycling. We also needed to be careful to excite the molecules with single rotational state resolution (using cw lasers) and to avoid collisions with background gas, which could transfer population to different electronic states [48, 49, 295].

In this section, we present DLIF measurements for three excited states used for laser cooling CaOH. We measured branching ratios from the $\widetilde{A}^2\Pi_{1/2}(000)$ state with 10^{-5} level sensitivity, sufficient to design an optical cycle capable of scattering $>10^4$ photons from this state. For the $\widetilde{B}^2\Sigma^+(000)$ state, which is populated more than an order of magnitude less frequently than $\widetilde{A}(000)$ during optical cycling, we measured VBRs at the 10^{-4} level. Finally we took DLIF data for the $\widetilde{A}(010)\mu^2\Sigma^+$ state with 10^{-3} level sensitivity. This state is only rarely populated during laser cooling, but branching ratios from $\widetilde{A}(010)$ are relevant for optical pumping into a single hyperfine state in the bending mode, described later in this thesis.

Branching ratios from $\widetilde{A}^2\Pi_{1/2}(000)$

The experimental setup used for measuring $\widetilde{A}^2\Pi_{1/2}(000)$ state VBRs (and the $\widetilde{B}^2\Sigma^+(000)$ data described below) is outlined in Fig. 4.10.[16] This apparatus was capable of producing two orders of magnitude improved sensitivity compared to previous DLIF measurements [213, 294, 296] by using a bright, cryogenic buffer-gas beam (CBGB) source, and by optically cycling to increase the number of photons emitted per molecule by over an order of magnitude. CaOH molecules were produced in the cryogenic beam source described in Refs. [214, 219] by

[16] Portions of this section have been published in Ref. [269].

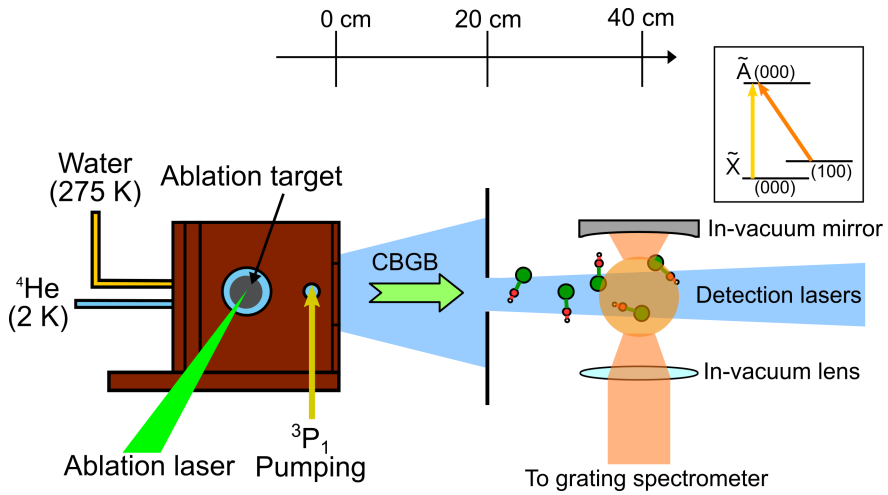

Figure 4.10: Experimental setup used for DLIF measurements, as described in the text. Reproduced from Ref. [269].

reacting ablated Ca metal with H_2O vapor in a ^{4}He buffer gas cell. The Ca atoms were excited to the metastable $4s4p\,^3P_1$ state using a 657 nm laser in the cell, which enhanced the molecule production by approximately $10\times$ [280]. The resulting molecular beam was collimated with a 7×7 mm aperture and allowed to propagate to a detection region approximately 40 cm downstream.

In the detection region, molecules were optically cycled using lasers addressing the rotationally-closed $^pQ_{12}(0.5)$ and $^pP_1(1.5)$ components of the $\widetilde{X}^2\Sigma^+(000) \rightarrow \widetilde{A}^2\Pi_{1/2}(000)$ and $\widetilde{X}^2\Sigma^+(100) \rightarrow \widetilde{A}^2\Pi_{1/2}(000)$ transitions. Since both lasers addressed the same excited state, this increased the fluorescence per molecule while ensuring that all fluorescence still originated from the same rovibronic state. Each molecule scattered approximately 30 photons on average, limited by finite interaction time. The fluorescence was collected using an in-vaccum lens and a spherical mirror, giving approximately 2% collection efficiency. It was then coupled (using free-space optics) into a 0.67 m Czerny-Turner style spectrometer (McPherson model 207A). The light was dispersed on a 300 grooves/mm, 120 mm $\times$ 140 mm Al-coated diffraction grating blazed at 500 nm. The dispersed fluorescence was

then imaged onto an EMCCD camera (Andor iXon 897). The DLIF spectrum at a single grating angle spanned approximately 35 nm with a resolution below 1 nm. To take a complete DLIF spectrum, we would average several thousand shots at each grating angle and "stitch" the spectra together by comparing peaks found in overlapping regions. The background signal from the detection lasers was subtracted out by interleaving data shots with and without molecule production.

To calibrate the wavelength and relative intensity response of the spectrometer, we injected small amounts of cw laser light at a number of different wavelengths, spanning the range 550-850 nm using an SFG system, dye lasers, and a titanium-sapphire laser. The wavelength axis was calibrated by comparing the position on the camera at a known grating angle to the absolute laser frequency as read on a wavemeter. The intensity axis was calibrated by coupling in a known laser power at a number of wavelengths and measuring the corresponding number of camera counts. The laser power for these measurements was calibrated by comparing the reading from several power meters and also calibrating the ND filters used to attenuate the light. Despite these efforts, the dominant measurement error for peaks well above the noise floor was an approximately 5% uncertainty in the intensity calibration. More details on the experimental apparatus and experimental protocol are found in Ben Augenbraun's thesis [214].

Our results for the $\widetilde{A}^2\Pi_{1/2}$ state are shown in Fig. 4.11. The two most prominent decay features are a $\sim$95% decay back to $\widetilde{X}(000)$ and a $\sim$5% decay to $\widetilde{X}(100)$, confirming that the VBRs for CaOH are nearly diagonal. Expanding the scale, we see approximately 10 resolvable decay features, to the first few excited states in the Ca–O stretch and Ca–O–H bending modes along with hybrid excitations of both modes. From this data, we extract vibrational energies and VBRs, which are summarized in Table 4.4 alongside *ab initio* calculations from Lan Cheng and Chaoqun Zhang. The calculations include a number of important perturbations (primarily spin-orbit

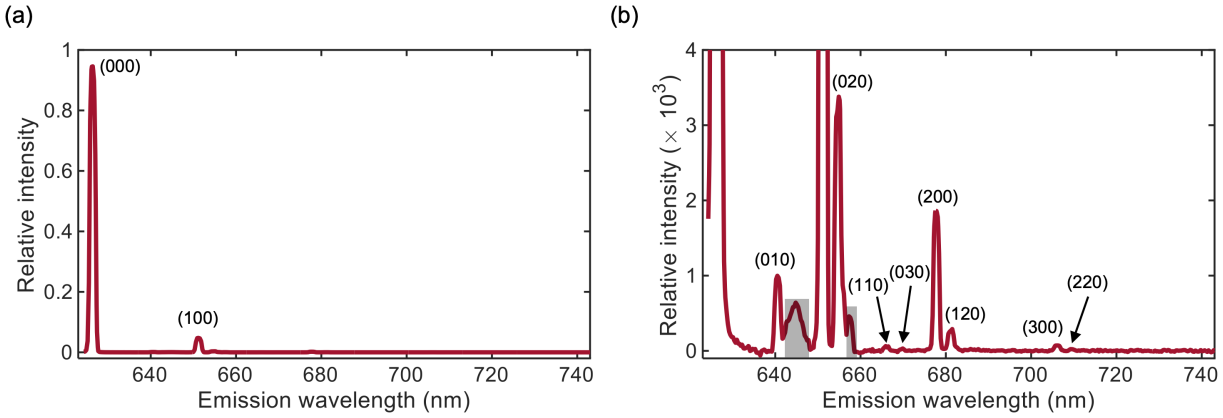

Figure 4.11: DLIF measurement of vibrational branching ratios from the $\widetilde{A}^2\Pi_{1/2}(000)(J = 1/2^+)$ state of CaOH. The state was populated by optically cycling with lasers addressing the $\widetilde{X}^2\Sigma^+(000) \rightarrow \widetilde{A}^2\Pi_{1/2}(000)$ and $\widetilde{X}^2\Sigma^+(100) \rightarrow \widetilde{A}^2\Pi_{1/2}(000)$ transitions at 626.4 nm and 651.2 nm, respectively. Panel (b) is the same data with an expanded scale to make the smaller decay features visible. Grey boxes indicate emission features from atomic calcium. This data was previously published in Ref. [269].

interactions and vibronic coupling) that are needed to accurately predict VBRs at the 10^{-5} level [269]. The good agreement between the calculations and measurements indicates a remarkable degree of understanding of the small molecular perturbations that contribute to these very weak vibronic decay pathways.

The measurements show that approximately 5 decay pathways show up above or near the 10^{-3} level, another 2 appear above the 10^{-4} level, and at least 6 more appear above a part in 10^5. Note that the DLIF measurements do not have rotational resolution, and they are also barely able to resolve the anharmonic splitting between $(02^00) - (02^20)$ and $(12^00) - (12^20)$. Therefore, we used a combination of calculations and depletion-revival measurements to determine the relative branching ratios to those states and to the $N = 1$ and $N = 2$ components of $\ell = 1$ bending modes [(010), (110), and (03^10)]. In order to scatter $> 10^4$ photons for CaOH, at least a few of the 10^{-5} level decays need to be repumped in addition to all branching pathways above 10^{-4}. The goal is for the sum of the remaining unaddressed branching ratios to be $<10^{-4}$. In the experiment, we leave (040),

Table 4.4: Summary of results from the $\widetilde{A}^2\Pi_{1/2}(000)$ DLIF measurements, sorted in order of increasing decay wavelength. The decay wavelengths are determined from the DLIF data and then converted into $\widetilde{X}^2\Sigma^+$ state vibrational energies ("Meas." column) by subtracting the excitation wavelength. These measured vibrational energies are compared to *ab initio* calculations by Lan Cheng and Chaoqun Zhang [269] ("Calc.") and to the vibrational energies derived from high-resolution spectroscopy conducted in our lab ("High Res."). The estimated uncertainty in the DLIF energy measurements is approximately ± 5 cm^{-1}. Also listed are the measured VBRs ("Expt."), which are compared with *ab initio* calculations ("Calc."). The majority of these results were previously published in Ref. [269].

	Decay	Energy (cm^{-1})			VBR (%)	
State	Wavelength	Meas.	Calc.	High Res.	Calc.	Expt.
(000)	626.4 nm	0	0	0	95.429	94.59(29)
(010)	640.6	354	355	353	0.063	0.099(6)
(100)	651.3	611	611	609	3.934	4.75(27)
(02^{0}0)	654.8	693	695	689	0.298	0.270(17)[a]
(02^{2}0)	–	–	718	713	0.079	0.067(12)[a]
(110)	666.2	953	954	951	0.003	0.0064(7)
(03^{1}0)	669.8	1035	1044	1032	<0.001	0.0034(8)
(200)	677.8	1211	1214	1210	0.157	0.174(16)
(12^{0}0)	681.4	1288	1293	1282	0.022	0.021(3)[a]
(12^{2}0)	–	–	1310	1302	0.005	0.005(1)[a]
(040)	686.6	1400	–	–	<0.001	0.0021(7)
(300)	706.4	1806	1815	1803	0.006	0.0068(8)
(22^{0}0)	709.8	1874	1890	–	0.002	0.0020(7)

[a] The $\ell = 0$ and $\ell = 2$ components were unresolved. Here we divided the total intensity according to the measured ratio of $\widetilde{X}(02^00)$ and $\widetilde{X}(02^20)$ decay in Ref. [251].

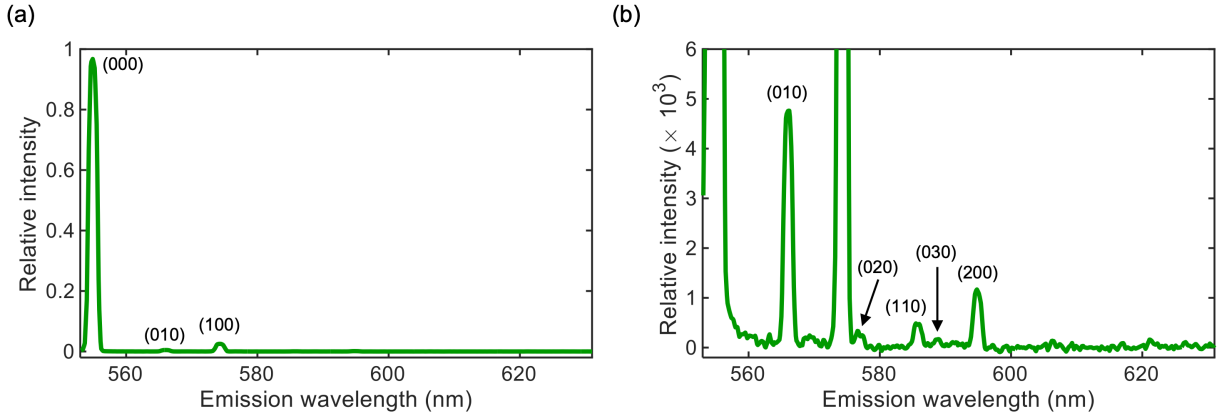

Figure 4.12: DLIF measurement of vibrational branching ratios from the $\widetilde{B}^2\Sigma^+(000)(N'=0)$ state of CaOH. The state was populated by optically cycling with lasers addressing the $\widetilde{X}^2\Sigma^+(000) \rightarrow \widetilde{B}^2\Sigma^+(000)$ and $\widetilde{X}^2\Sigma^+(100) \rightarrow \widetilde{B}^2\Sigma^+(000)$ transitions at 554.9 nm and 574.3 nm, respectively.

(22^00), and the $N=2$ level of (03^10) unaddressed, but repump all other decay pathways observed in the data.

We also compared the measured vibrational frequencies to high-resolution values determined from the rotationally resolved transitions observed with cw lasers in the lab (Appendix E). The DLIF values generally agree with the high resolution values to within 5 cm^{-1}, meaning that DLIF can be viably used as a starting point when searching for new repumping transitions at high resolution.

Because the frequencies and bond lengths for the asymmetric (O−H) stretch vibration are poorly known [250], we did not have a good theoretical bound on VBRs to these states. We searched for decays to $\widetilde{X}(001)$ and $\widetilde{X}(101)$ in the wavelength range from ∼800-880 nm and saw no resolvable features. Therefore we believe that these states do not significantly limit optical cycling in CaOH.

Branching ratios from $\widetilde{B}^2\Sigma^+(000)$

Fig. 4.12 shows the DLIF data taken for decays from the $\widetilde{B}^2\Sigma^+(000)$ electronic state. The experimental setup was identical to that used for the $\widetilde{A}^2\Pi_{1/2}(000)$ state, except that the optical cycling detection lasers drove rotationally closed transitions from $\widetilde{X}^2\Sigma^+(000) \rightarrow \widetilde{B}^2\Sigma^+(000)$ and $\widetilde{X}^2\Sigma^+(100) \rightarrow \widetilde{B}^2\Sigma^+(000)$. In the repumping scheme used to laser cool CaOH, every time a molecule decays from $\widetilde{A}(000)$ to any state besides $\widetilde{X}(000)$, it is eventually repumped through $\widetilde{B}(000)$. This happens after roughly 5.4% of photon scattering events, meaning that approximately 1 out of every 18 scattered photons decays from $\widetilde{B}(000)$. Therefore, it is sufficient to know the VBRs from this state with approximately an order of magnitude lower sensitivity than $\widetilde{A}(000)$ without hindering our ability to form a closed optical cycle. With that in mind, we only averaged the $\widetilde{B}(000)$ state data until 10^{-4} level sensitivity was achieved. From the data in Fig. 4.12, we see that the dominant off-diagonal decays are to (100) at the few percent level and to (010) at the 0.5% level. Also appearing above a part in 10^4 are decays to (02^00), (110), (03^10), and (200). The results are summarized in Table 4.5. There are no decays identified at this level that do not already appear in the $\widetilde{A}(000)$ measurements, so we do not expect repumping through $\widetilde{B}(000)$ to reduce our ability to form a highly closed optical cycling transition in CaOH.

Note that while we are unable to resolve anharmonic splittings between e.g. (02^00) and (02^20), or between (03^10) and (03^30), we have nonetheless assigned an ℓ value for these states. This is because decay to $\ell = 2$ is allowed by vibronic mixing that occurs within *degenerate* electronic states, so it is safe to say that branching to (02^20) from the *nondegenerate* $\widetilde{B}(000)$ state will be significantly suppressed compared to the symmetry-allowed (02^00) decay pathway. Meanwhile, the lowest rotational level in (03^30) is $N'' = 3$, so decay to that state from the $N' = 0$ rotational level populated in $\widetilde{B}(000)$ is rotationally forbidden.

State	Wavelength	VBR (%)
(000)	554.9 nm	96.78(15)
(010)	566.0	0.478(27)
(100)	574.3	2.53(13)
(02^{0}0)	577.2	0.034(4)
(110)	585.8	0.049(4)
(03^{1}0)	588.8	0.017(4)
(200)	594.9	0.117(7)

Table 4.5: Measured VBRs from $\widetilde{B}^2\Sigma^+(000)(N'=0)$ using DLIF spectroscopy.

Branching ratios from $\widetilde{A}(010)\mu^2\Sigma^+$

Branching ratios from the $\widetilde{A}(010)$ state were measured after we had already made a MOT of CaOH and were primarily of interest to determine the degree of optical cycling possible on the $\widetilde{X}(010) \rightarrow \widetilde{A}(010)$ transition. We use this transition to optically pump CaOH molecules into a single hyperfine state in the vibrational bending mode, which is an important state preparation technique needed for the coherent control experiments described later in this thesis. Note that for optical pumping we use the $\kappa^2\Sigma^{(-)}$ vibronic component of the $\widetilde{A}(010)$ state, whereas the data presented here measured VBRs for the $\mu^2\Sigma^{(+)}$ component. However, it is expected that the VBRs will be very similar for both states.

DLIF spectroscopy for the $\widetilde{A}(010)\mu^2\Sigma^{(+)}(J=1/2^+)$ state was performed using the apparatus described in Ref. [293].[17] CaOH molecules were produced in a He buffer gas cell at ∼6 K, then were extracted into a detection region immediately outside the cell and inside the 4 K shields of the beam source. Because we did not require high sensitivity, we relied on signal from molecules that were naturally populated in the $\widetilde{X}(010)$ state (typically 10% as much signal as for molecules in $\widetilde{X}(000)$ [273]). These molecules were excited using a laser addressing the

[17] Thanks to Ben Augenbraun for taking this data for us.

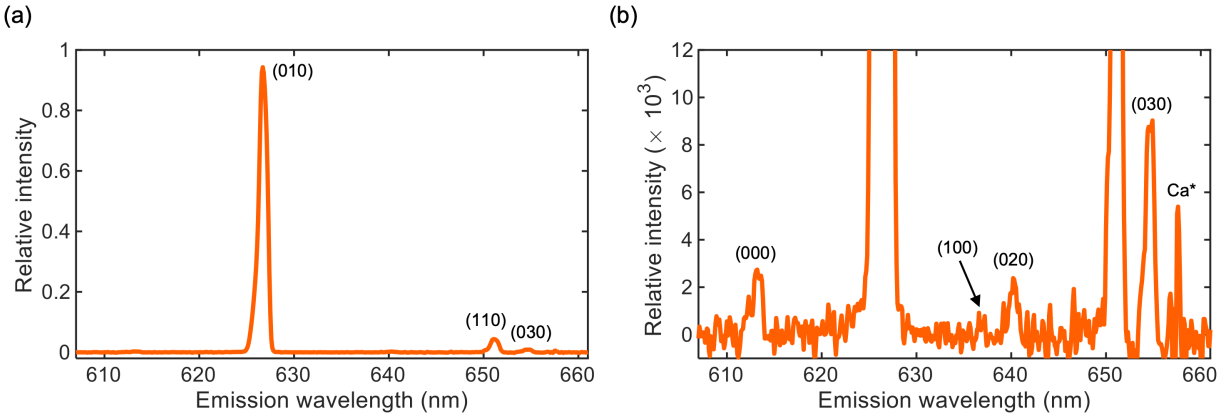

Figure 4.13: DLIF measurement of vibrational branching ratios from the $\widetilde{A}(010)\mu^2\Sigma^{(+)}$ state of CaOH.

State	Wavelength	VBR (%)
(000)	613.1 nm	0.28
(010)	626.7	94.30
(100)	636.9	0.06
(02^{0}0)	640.2	0.21
(110)	651.1	4.26
(03^{1}0)	654.7	0.88

Table 4.6: Measured $\widetilde{A}(010)\mu^2\Sigma^{(+)}(J = 1/2^+)$ state VBRs from DLIF spectroscopy.

$\widetilde{X}(010)(N'' = 1^-) \rightarrow \widetilde{A}(010)\mu^2\Sigma^{(+)}(J = 1/2^+)$ transition at 626.7 nm, and the resulting fluorescence was collected using in-vacuum optics and coupled into the spectrometer described above. The resulting spectrum is shown in Fig. 4.13, and the measured VBRs are listed in Table 4.6. The noise floor of the measurements is around the 10^{-3} level.

From the measurements, it appears that optical cycling on the $\widetilde{X}(010) \leftrightarrow \widetilde{A}(010)$ transition should work nearly as well as cycling on the $\widetilde{X}(000) \leftrightarrow \widetilde{A}(000)$ transition used for laser cooling. Approximately 18 photons can be scattered, on average, before molecules decay out of the cycling transition, and adding repumping lasers addressing $\widetilde{X}(110) \rightarrow \widetilde{A}(010)$ and $\widetilde{X}(030) \rightarrow \widetilde{A}(010)$ (both of which are already present in the optical cy-

cle used to cool and trap CaOH) should allow nearly 200 photons to be scattered. Note, however, that there are order-unity rotational decays to $N'' = 2$ in $\widetilde{X}(010)$, $\widetilde{X}(110)$, and $\widetilde{X}(03^10)$, so rotational repumping lasers are required. Since we don't have an $N'' = 2$ repumper for $\widetilde{X}(03^10)$ in the experiment, it is expected that this would reduce the average photon budget to approximately 150 photons when cycling through the $\mu^2\Sigma^{(+)}$ component and approx. 100 photons when cycling through the $\kappa^2\Sigma^{(-)}$ component (which decays more strongly to $N'' = 2$ than the μ state). The other observed decays are also to vibrational states contained in the main CaOH optical cycle, but these states are not repumped through $\widetilde{A}(010)$ so additional lasers would be needed to increase the photon budget further. Also note that a low 10^{-3} level decay to (210) would be expected near 678 nm,[18] which is outside the wavelength range of the data. It is therefore likely that the absolute photon budgets quoted here are slightly too optimistic.

4.3.4 Summary of branching ratio measurement results

Table B.2 compares the measured vibrational branching ratios from depletion-revival measurements vs. DLIF (where we have weighted the DLIF results from $\widetilde{A}(000)$ and $\widetilde{B}(000)$ to account for our photon cycling scheme, as described below). There is generally decent agreement between these results, with the primary discrepancy appearing to be that the depletion-revival measurements underestimated the VBR to $\widetilde{X}(010)$ compared to the DLIF. This in turn means that the depletion-revival measurements suggest a much higher fraction of the population is lost to other states than what is indicated by DLIF. This is likely from systematic errors in the depletion-revival measurement, and not due to a problem with the DLIF, since the DLIF measurements agree well with the

[18] This can be inferred by comparing the stretching mode decay ladder $\widetilde{X}(010)$, $\widetilde{X}(110)$, $\widetilde{X}(210)$, $\cdots$ to the equivalent ladder of decays from the $\widetilde{A}(000)$ state: $\widetilde{X}(000)$, $\widetilde{X}(100)$, $\widetilde{X}(200)$, $\cdots$

Table 4.7: Comparison of CaOH rovibronic branching ratio measurements.

State	Depletion-revival[a]	DLIF
$\widetilde{X}(000)$	0.9505	0.9471
$\widetilde{X}(100)$	0.0427	0.0463
$\widetilde{X}(200)$	0.0017	0.0017
$\widetilde{X}(02^00)$	0.0025	0.00257
$\widetilde{X}(02^20)$	6.2×10^{-4}	6.3×10^{-4}
$\widetilde{X}(010)(N=1)$	5.0×10^{-4}	12×10^{-4} (note[b])
$\widetilde{X}(010)(N=2)$	2.8×10^{-4}	–
$\widetilde{X}(12^00)$	2.4×10^{-4}	1.9×10^{-4}
$\widetilde{X}(12^20)$	8.9×10^{-5}	4.8×10^{-5}
$\widetilde{X}(300)$	8.9×10^{-5}	6.4×10^{-5}
Other	6.5×10^{-4}	1.7×10^{-4}

[a] Constrained so $\widetilde{X}(000)$ and $\widetilde{X}(100)$ VBRs add to the same value as in the DLIF, but all other VBRs are given by the fractional population recovered after photon cycling depletion.
[b] Sum of both rotational states (rotational states unresolved)

measured number of photons scattered in optically trapped CaOH.

Overall, the DLIF is more trustworthy at this level of precision, and we use it for calculating our final photon budgets. However, the depletion-revival measurements were still useful. For one, we used them to estimate the relative intensity of unresolved lines in the DLIF. These included $N = 1$ and $N = 2$ rotational decays in (010) and (110), and also the bending modes $(02^00)/(02^20)$ and $(12^00)/(12^20)$, which were too close in wavelength to be separately resolved by the DLIF spectrometer grating.

VBRs for the CaOH optical cycle

We ultimately used the DLIF measurements to determine branching ratios and associated photon budgets for CaOH optical cycling. As discussed above, the depletion-revival measurements were used to constrain the relative

State	Effective branching ratio	Approx. photon budget
(000)	0.9471	19
(100)	0.0463	150
(02^00)	2.57×10^{-3}	250
(200)	1.70×10^{-3}	430
$(010)(N=1)$	8.4×10^{-4}	680
(02^20)	6.3×10^{-4}	1200
$(010)(N=2)$	3.6×10^{-4}	2100
(12^00)	1.9×10^{-4}	3500
(300)	6.4×10^{-5}	4500
$(110)(N=1)$	6.3×10^{-5}	6300
(12^20)	4.8×10^{-5}	9100
$(03^10)(N=1)$	2.9×10^{-5}	12000
$(110)(N=2)$	2.4×10^{-5}	$\sim$14000
(040)	2.0×10^{-5}	–
(220)	1.9×10^{-5}	–
$(03^10)(N=2)$	1.2×10^{-5}	–

Table 4.8: Effective branching ratios and approximate photon budgets for CaOH optical cycling, obtained by weighting the DLIF measurements for $\widetilde{A}(000)$ and $\widetilde{B}(000)$ by the number of spontaneous decay events that originate from each state during optical cycling. In the experiment, we repump all states up through $(110)(N=2)$, indicated by a solid line in the table. As repumpers are added, the photon budget becomes increasingly sensitive to decays below the DLIF noise floor, so photon budgets are not quoted for the last few repumpers. The photon budget of approx. 14000 for the full optical cycle comes from experimental estimates.

strength of unresolved transitions in DLIF, e.g. rotational branching and $v_2 = 2$ bending modes.

Because the optical cycling scheme used for CaOH laser cooling primarily excites the $\widetilde{X}(000) \rightarrow \widetilde{A}(000)$ transition but eventually repumps all lost population through $\widetilde{B}(000)$, to a decent approximation we can estimate the "effective" or "average" branching ratios of the optical cycle by performing a weighted average of VBRs from the $\widetilde{A}(000)$ and $\widetilde{B}(000)$ states. The measured VBR from $\widetilde{A}(000)$ to $\widetilde{X}(000)$ is 0.946, so we can define the effective branching ratio of the CaOH optical cycle to state i as $P_i^{\text{eff}} \approx 0.946 P_i^A + 0.054 P_i^B$, where P_i^A and P_i^B

are the measured branching ratios from $\widetilde{A}(000)$ and $\widetilde{B}(000)$. The next-most populated state is $\widetilde{A}(100)$, which is repumped after approximately 0.5% of all photon scattering events. We will therefore ignore corrections due to this and other excited states that are populated even less frequently.[19] The effective branching ratios calculated using this method are shown in Table 4.8, along with the approximate photon budget after repumping each state and all previous decays.

4.4 Repumping scheme

The repumping scheme used for optical cycling and laser cooling CaOH is shown in Fig. 4.14, and has a photon budget of approximately 14000 photons.[20]

We decided which ground states to repump based on the measured branching ratios. The choice of excited state is guided by a few criteria. First, we wish to avoid repumping anything through $\widetilde{A}(000)$, which would reduce the scattering rate by coupling a larger number of ground states to the same excited state used for the main laser cooling transition [262]. Second, the excited state must predominantly decay to a state that is already repumped. As a rule of thumb, because CaOH has a relatively diagonal Franck-Condon matrix it is a good first approximation during this analysis to suspect that a vibrational level in the excited state will decay predominantly to the corresponding vibrational level in the ground state (e.g. $\widetilde{A}(100)$ decays predominantly to $\widetilde{X}(100)$).[21] Third, we try to repump using the strongest available transition, which reduces the required laser power. As a rule of

[19] To properly account for all excited state repumping pathways, one can use a discrete, absorbing Markov chain model [52, 251].

[20] This was experimentally determined by measuring the fluorescence of optically trapped CaOH as a function of the number of repumping lasers applied.

[21] Of course, it is also important to empirically verify that no substantial new loss channels are introduced by the choice of excited state.

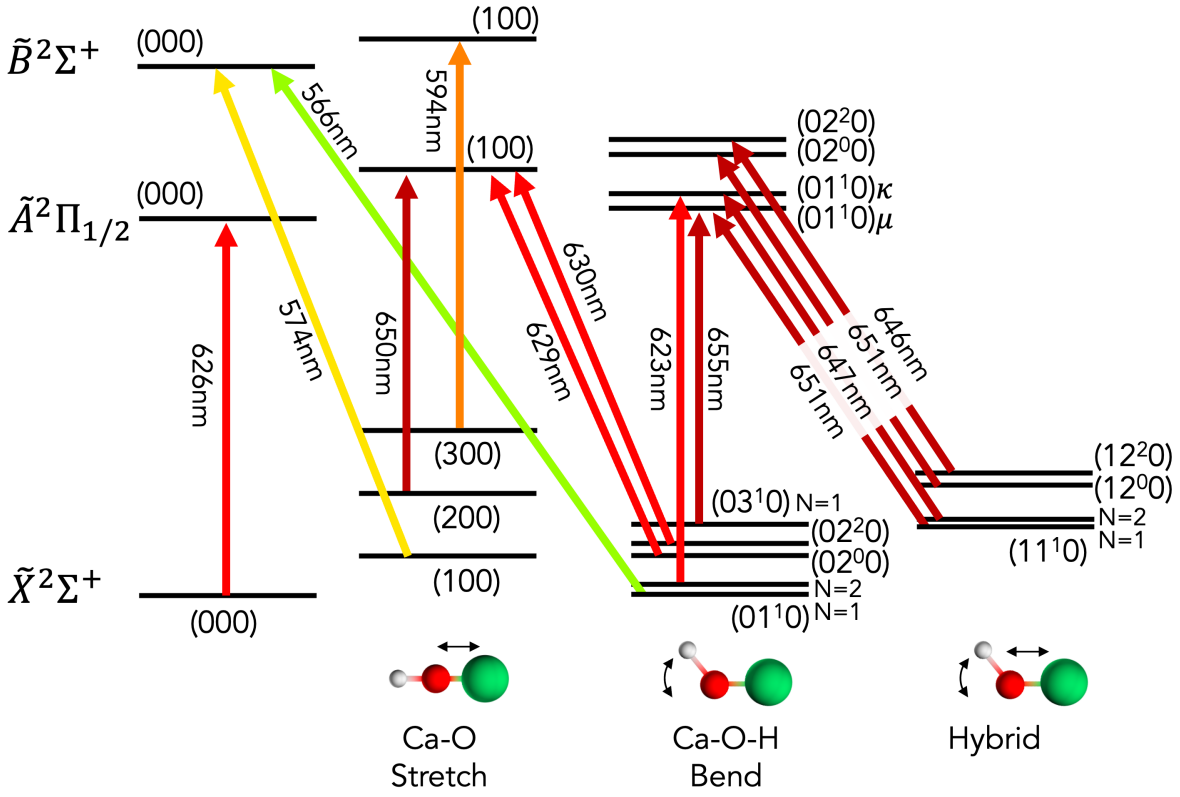

Figure 4.14: Repumping scheme used for optically cycling CaOH with a photon budget of ∼13000-15000 photons.

thumb, if (for example) the repumping transition is 10x stronger than the decay from the optical cycle, approximately 10x lower power will be needed for that repumper than the main line laser.[22] Fourth: all else being equal, we choose the technically simplest wavelength, e.g. the one whose frequency is already known, has more convenient laser technology, and/or is easier to combine with the other wavelengths.

We now briefly describe the decision making that went into each choice of repumping laser.

- $\widetilde{X}(000) \rightarrow \widetilde{A}(000)$. Main line cycling laser, chosen to go through the $\widetilde{A}$ state based on precedent and the fact that there are no electronic leakage pathways.
- $\widetilde{X}(100) \rightarrow \widetilde{B}(000)$. Chosen so as to avoid repumping through the same state used for main line optical cycling.
- $\widetilde{X}(200) \rightarrow \widetilde{A}(100)$. This decays primarily to $\widetilde{X}(100)$, which is already repumped. While $\widetilde{A}(100)$ or $\widetilde{B}(100)$ could work, 650 nm is diode accessible, and the high-power laser technology is not significantly better for either. Finally, repumping through $\widetilde{B}(100)$ would require a similar wavelength to the $\widetilde{X}(100) \rightarrow \widetilde{B}(000)$ repumper, making it harder to combine.
- $\widetilde{X}(02^{0}0) \rightarrow \widetilde{A}(100)$. This decays primarily to $\widetilde{X}(100)$, which is already repumped; Fermi resonance mixing means that the transition is not extremely weak; and 629 nm is at a convenient wavelength for SFG systems.
- $\widetilde{X}(02^{2}0) \rightarrow \widetilde{A}(100)$. Similar arguments to $\widetilde{X}(02^{0}0)$. The vibronic and Fermi resonance mixing in the $\widetilde{A}(100)(020)$ manifold makes the transition strength non-negligible.
- $\widetilde{X}(010)(N = 1) \rightarrow \widetilde{B}(000)$. $\widetilde{B}(000)$ has a relatively strong transition strength on this symmetry-forbidden line due to vibronic mixing with $\widetilde{A}(010)$.
- $\widetilde{X}(010)(N = 2) \rightarrow \widetilde{A}(010)\kappa^{2}\Sigma^{(-)}$. $\widetilde{A}(010)$ decays to $\widetilde{X}(010)(N = 1)$, which will get returned to the optical cycle via $\widetilde{B}(000)$. This is a diagonal transition so has a large transition strength.
- $\widetilde{X}(12^{0}0) \rightarrow \widetilde{A}(02^{0}0)$ (i.e. $\widetilde{A}(020)\mu^{2}\Pi_{1/2}$). This $\Delta v_1 = 1$ repumping transition is expected to have a strength of 5-10% of the main line, compared to a $\sim 10^{-4}$ level decay. Therefore, the power requirements should be modest. The excited state decays primarily to $\widetilde{X}(02^{0}0)$, which is already repumped.

[22] These rule-of-thumb power requirements may be checked against a rate-equation model of the full repumping scheme, e.g. using the model of Ref. [262].

- $\widetilde{X}(12^20) \rightarrow \widetilde{A}(02^20)$ (i.e. $\widetilde{A}(020)\kappa^2\Pi_{1/2}$). Similar arguments to above.
- $\widetilde{X}(300) \rightarrow \widetilde{B}(100)$. Neither $\widetilde{A}(200)$ or $\widetilde{B}(200)$ had been previously observed, so the next best option is a $\Delta v_1 = 2$ transition. Neither wavelength is especially good for lasers. However, 594 nm is more dye laser friendly than 670 nm, and we initially repumped the transition using a dye laser before switching to a frequency doubled Raman fiber amplifier.
- $\widetilde{X}(110)(N = 1) \rightarrow \widetilde{A}(010)\mu^2\Sigma^{(+)}$. This is a $\Delta v_1 = 1$ repumper, so should have a strong transition strength and require lower power. We picked the $\mu^2\Sigma^{(+)}$ manifold because it has a higher transition strength to $N = 1$.
- $\widetilde{X}(110)(N = 2) \rightarrow \widetilde{A}(010)\kappa^2\Sigma^{(-)}$. This is a $\Delta v_1 = 1$ repumper, so should have a strong transition strength and require lower power. We picked the $\kappa^2\Sigma^{(-)}$ manifold because it has a higher transition strength to $N = 2$.
- $\widetilde{X}(03^10)(N = 1) \rightarrow \widetilde{A}(010)\mu^2\Sigma^{(+)}$. This should be repumped through an $\ell = 1$ excited state, since symmetry-allowed transitions likely have the highest strength. We picked the $\mu^2\Sigma^{(+)}$ manifold because it has a higher transition strength to $N = 1$.

5

Radiative Slowing, Magneto-Optical Trapping, and Sub-Doppler Cooling of CaOH

Magneto-optical trapping is a workhorse technology of atomic and molecular physics. Magneto-optical traps (MOTs) use radiative optical forces to cool atoms or molecules to temperatures below 1 mK, while simul-

taneously trapping them in a mm scale region [2]. This is a powerful combination, creating a reservoir of cold, trapped particles that can be used as a starting point for a wide variety of experiments. Effectively all experiments that require cold, trapped neutral atoms begin with a MOT, and MOTs are responsible for a large fraction of the advances made in AMO physics over the last 30 years. Accordingly, loading polyatomic molecules into a MOT is likely the *key* technical step needed to enable quantum science experiments with polyatomic molecules.

In this chapter, we describe our work loading CaOH into a MOT. Compared to atomic MOTs, which can load relatively fast atomic beams and even hot vapors with some efficiency, molecular MOTs are significantly less efficient [262]. The capture velocity of molecular MOTs is typically around or below 10 m/s [297], meaning that we first need to slow our cryogenic buffer gas beam to this velocity. We describe radiative slowing of the CaOH molecular beam in section 5.3. In section 5.4, we describe our work loading, optimizing, and characterizing a MOT of CaOH. In anticipation of the need to reach lower temperatures and load optical traps for the quantum science experiments described in the rest of this thesis, in sec. 5.5 we describe our work cooling the trapped CaOH molecules to even lower temperatures, using sub-Doppler cooling techniques. Finally, in sec. 5.6 we describe our implementation of a blue-detuned conveyor belt MOT, which increased the density of our CaOH molecular MOT by two orders of magnitude, enabling the molecular collision experiments described in chapter 9 of this thesis.

5.1 Vacuum apparatus

The vacuum apparatus used for the CaOH MOT (and the work in optical traps described in the later chapters of this thesis) consists of the beam box (described in chapter 3), an approximately 81 cm-long beamline that provides

sufficient distance for the molecular beam to be slowed, and then a MOT chamber in which the molecules are trapped and interrogated. An overview of the apparatus is shown in Fig. 5.1.

Molecules are extracted from the cell and out of the beam box as described in chapter 3. An in-vacuum, UHV compatible shutter (Uniblitz VS14) is installed at the exit of the beam box, and is opened for approximately 15 ms following ablation to allow the molecular beam out of the beam box. The shutter prevents helium buildup in the MOT chamber; the pressure in the MOT chamber increases by a factor of 2-3 (from $< 3 \times 10^{-9}$ to $\sim 7 \times 10^{-9}$ Torr) if the shutter is left continuously open.

The beamline consists of a custom o-ring sealed rectangular aluminum chamber with rectangular windows on the top and bottom and a a 550 L/s turbomolecular pump on the side. The beamline is connected directly to the beam box, and the windows can be used for beam diagnostics, and potentially transverse cooling, directly outside the beam box. The large turbo provides differential pumping. Following the rectangular chamber is a gate valve, two differential pumping tubes and a 250 L/s turbo pump, then a CF bellows and a CF gate valve connected to the MOT chamber.

The MOT chamber (8.0" spherical square from Kimball Physics) has two 8.00" CF flanges on top and bottom for attaching vacuum pumps and the RF MOT coils (see below), four 2.75" flanges for the MOT beam viewports, and four 4.5" flanges. Three of these have viewports for slowing, molecule detection, and optical trapping beams, and the fourth is where the molecular beam enters the chamber. In addition, there are sixteen 1.33" flanges for small accessory beams, though these ports were unused during this thesis work. The chamber is pumped on with a 550 L/s turbo pump and a titanium sublimation pump (TSP, Gamma Vacuum). To reduce scattered light and improve molecule detection, the main chamber is blackened with Acktar Magic Black. The MOT beams are sent in through long CF nipples with copper(II) oxide blackened [284] tube inserts and machined baffles to further

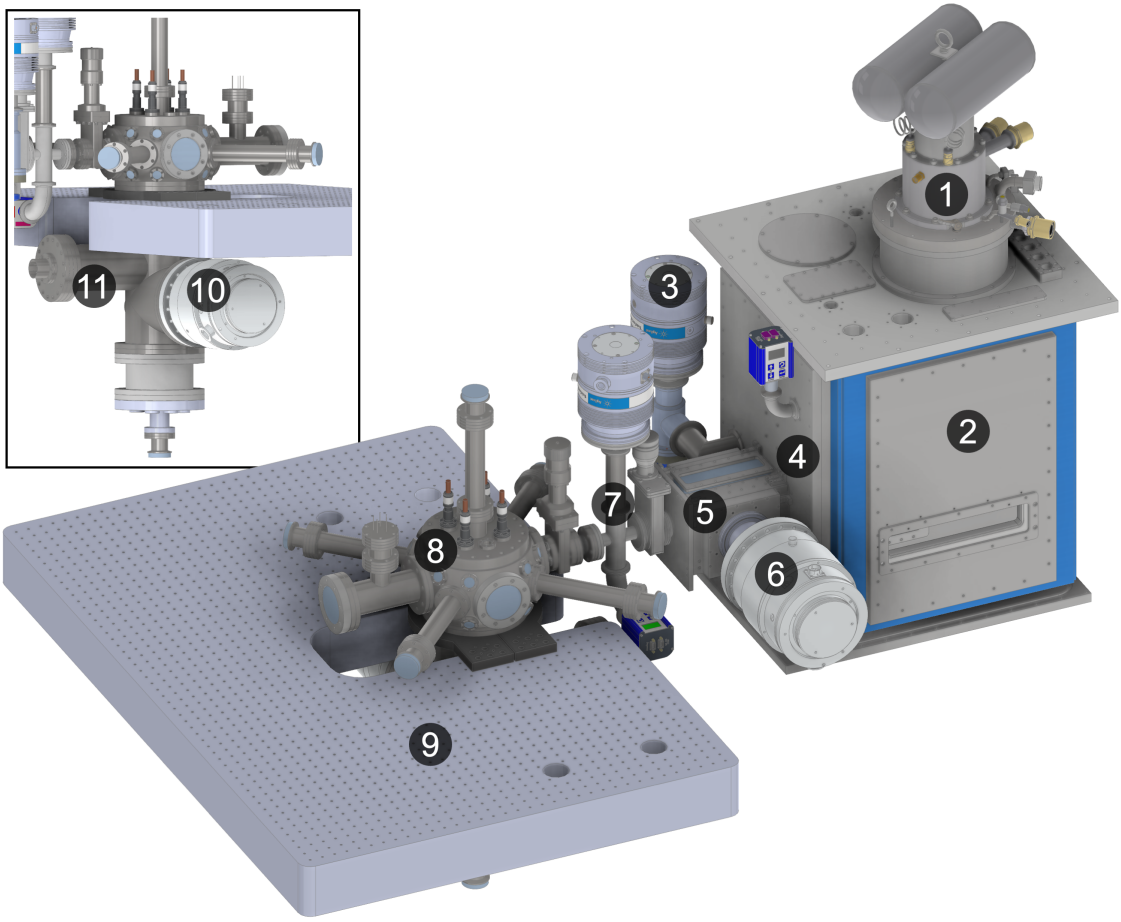

Figure 5.1: Overview of the experimental apparatus. (1) PT415 1K pulse tube. (2) Beam box. (3) Beam box front turbo pump. (4) UHV shutter (mounted on plate between beam box and rectangular beam line). (5) Transverse optical access. (6) Beam line turbo pump. (7) Differential pumping region. (8) MOT chamber. (9) Custom optical table. Inset: MOT chamber pumping below optical table. (10) MOT chamber turbo pump. (11) Titanium sublimation pump.

Ground state	Excited state	Wavelength	Laser system	Power for MOT	Approx. photons
$\widetilde{X}^2\Sigma^+(000)$	$\widetilde{A}^2\Pi_{1/2}(000)$	626.4 nm	SFG system # 1	1.3 W	18
$\widetilde{X}^2\Sigma^+(100)$	$\widetilde{B}^2\Sigma^+(000)$	574.3 nm	574 nm RFA	700 mW	150
$\widetilde{X}^2\Sigma^+(02^00)$	$\widetilde{A}^2\Pi_{1/2}(100)$	629.0 nm	629 nm RFA	400 mW	250
$\widetilde{X}^2\Sigma^+(200)$	$\widetilde{A}^2\Pi_{1/2}(100)$	650.4 nm	650 nm RFA	100 mW	440
$\widetilde{X}^2\Sigma^+(010)(N=1)$	$\widetilde{B}^2\Sigma^+(000)$	566.0 nm	566 nm RFA	150 mW	680
$\widetilde{X}^2\Sigma^+(02^20)$	$\widetilde{A}^2\Pi_{1/2}(100)$	630.0 nm	SFG system # 2	150 mW	1200
$\widetilde{X}^2\Sigma^+(010)(N=2)$	$\widetilde{A}(010)\kappa^2\Sigma^{(-)}$	622.9 nm	SFG system # 2	10 mW	2100
$\widetilde{X}^2\Sigma^+(12^00)$	$\widetilde{A}(020)\mu^2\Pi_{1/2}$	650.8 nm	650 nm RFA	20 mW	3500
$\widetilde{X}^2\Sigma^+(300)$	$\widetilde{B}^2\Sigma^+(100)$	594.3 nm	594 nm RFA	100 mW	4600
$\widetilde{X}^2\Sigma^+(110)(N=1)$	$\widetilde{A}(010)\mu^2\Sigma^{(+)}$	651.1 nm	ECDL	20 mW	6300
$\widetilde{X}^2\Sigma^+(12^20)$	$\widetilde{A}(020)\kappa^2\Pi_{1/2}$	645.9 nm	ECDL	20 mW	9100
$\widetilde{X}^2\Sigma^+(03^10)(N=1)$	$\widetilde{A}(010)\mu^2\Sigma^{(+)}$	654.6 nm	Dye	20 mW	$\sim$12000
$\widetilde{X}^2\Sigma^+(110)(N=2)$	$\widetilde{A}(010)\kappa^2\Sigma^{(-)}$	647.0 nm	ECDL	10 mW	$\sim$14000

Table 5.1: Summary of CaOH optical cycling transitions and lasers. Powers are the approximate minimum powers that were required for optimal white-light slowing and MOT (see Fig. 1 of Ref. [42]). A lower $\widetilde{X}(000) \rightarrow \widetilde{A}(000)$ main line power is required for chirped slowing. We typically run at higher powers for most repumpers to make the experiment less susceptible to power drifts.

reduce scattered light [273]. The RF MOT coils and other flanges and components are blackened using Alion MH2200 paint.

5.2 Laser systems

Table 5.1 summarizes the wavelength, approximate minimum power, and laser technology used for each of the cooling and repumping transitions in CaOH. The laser systems are described in this section.

Because of the large number of lasers needed, we tried to ensure that every system was as reliable as possible, meaning we avoided homebuilt diode lasers, tapered amplifiers, and injection lock systems, and attempted to

use solid-state lasers instead of dye lasers when possible.[1] The complete system includes several high power fiber amplifiers. To save resources, we attempted to reuse these for multiple visible wavelengths where possible. This included seeding fiber amplifiers with multiple wavelengths and "daisy-chaining" systems by reusing IR light to generate multiple visible wavelengths. Moreover, the large number of similar components – Yb and Er-doped fiber amplifiers and nonlinear crystals – in our system makes it relatively modular, so that we can back up a number of laser systems with only a few interchangeable components.

5.2.1 Sum frequency generation (SFG) systems

The first type of laser system we use is a sum-frequency-generation (SFG) system, where we combine high power light from two single-frequency fiber amplifiers on a nonlinear crystal (MgO-doped periodically poled lithium niobate, i.e. MgO:PPLN). When the crystal temperature is tuned near a quasi-phase-matching condition, a nonlinear process occurs where two IR photons are summed into a visible photon, producing the desired visible wavelength for CaOH laser cooling. See Ref. [273] for more details on the theory and alignment procedures for the sort of SFG system used in our lab.

When a Yb-doped fiber amplifier (YDFA) and an Er-doped fiber amplifier (EDFA) are used to produce the IR wavelengths, a range of visible wavelengths in the approximate range 610-650 nm can be generated, with the best range being near 630 nm (corresponding to 1064 nm and 1550 nm for the two pump beams). A number of our CaOH lasers fall in this range (including the main line 626 nm laser). Therefore, we use a few systems consisting of a 10 W YDFAs, 10 W EDFAs, and MgO:PPLN SFG crystals. We choose to build and align the SFG systems

[1] That said, our experience has been that cw dye lasers are reliable as long as they are well-built and periodically maintained.

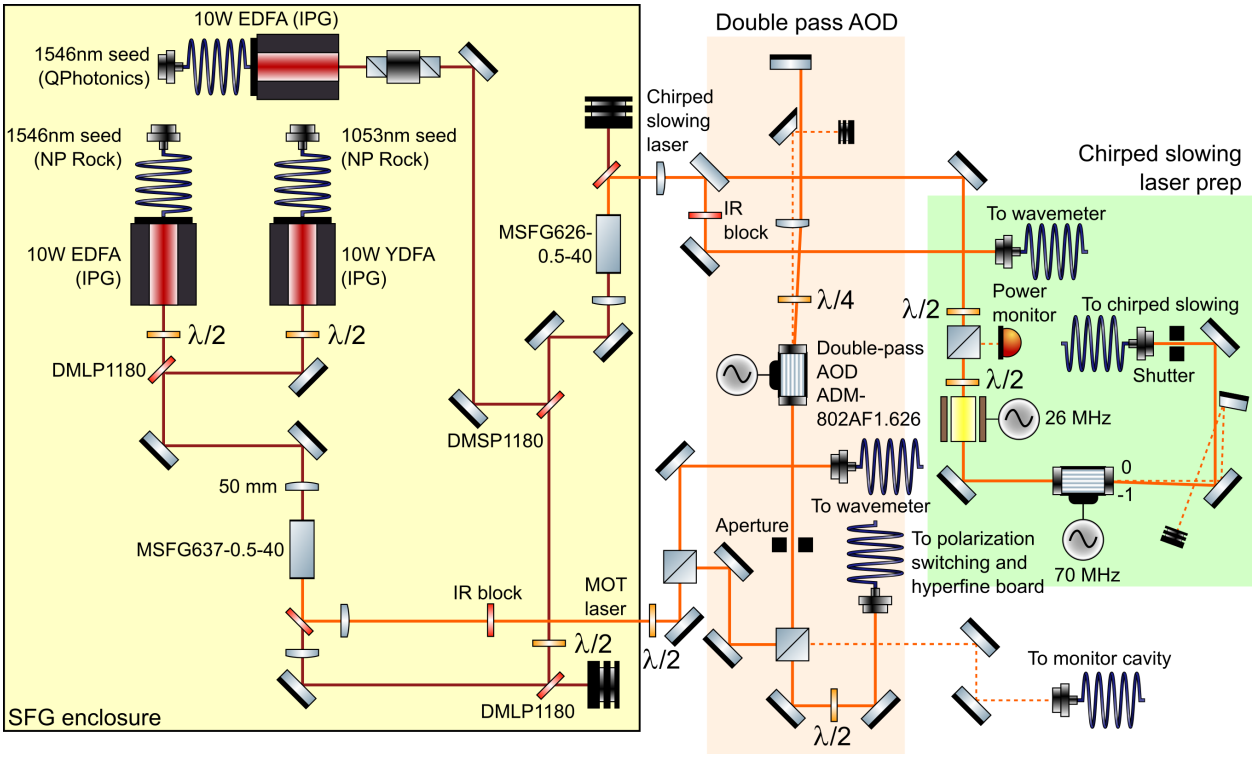

Figure 5.2: SFG laser system for the $\widetilde{X}(000) \rightarrow \widetilde{A}(000)$ main cooling and slowing lasers at 626 nm.

ourselves (using crystals from Covesion), since this improves modularity and makes it easier to troubleshoot any problems that may arise.

SFG system #1: $\widetilde{X}(000) \rightarrow \widetilde{A}(000)$ MOT and slowing lasers

The first SFG system is shown in Fig. 5.2 and is used to make the MOT and chirped slowing lasers at 626 nm. The MOT light is made from an SFG system consisting of 1053 nm and 1546 nm IR wavelengths. Two 10W fiber amplifiers (IPG) are seeded with NP Rock lasers[2], then combined on an SFG crystal (Covesion MSFG637-0.5-40)

[2]We occasionally noticed that these seeds would modehop or go multimode, so we monitor the SFG system on a cavity to ensure it is single mode. On the plus side, these lasers are very stable, so the linewidth is well below 1 MHz even with our slow wavemeter lock.

to produce up to approximately 7 W of visible light at 626 nm. The light is separated from the IR beams and sent to the MOT optics, while the IR beams are also separated, with the 1546 nm light being dumped. The 1053 nm light is then reused in a 2nd SFG system, where it is combined with another 1546 nm beam from a 10 W EDFA (IPG) seeded with a DFB laser diode (QPhotonics QDFBLD-1550-100NN). These beams are summed on another PPLN crystal (Covesion MSFG626-0.5-40), and the output visible light is separated from the IR and sent to the slowing setup.

To lock the SFG systems, we keep the 1546 nm NP Rock free-running, lock the 1053 nm laser feeding back on the frequency of the visible MOT laser, and lock the chirped slowing DFB feeding back on the visible slowing laser frequency.

Fig. 5.2 also shows some of the preparation optics for the MOT and slowing lasers, which are on the same table as the SFGs, before any fiber coupling. A portion of the MOT light is picked off and sent to the wavemeter for locking, while the remaining light is sent through a double pass AOM, which controls the frequency and power of the MOT, cooling, and imaging beams. We typically run the SFG below full power and send ∼2-3 W into the double pass AOM.

The chirped slowing beam is also picked off and sent to the wavemeter, while the remaining light is sent through an EOM which adds ± 26 MHz sidebands (to address the spin-rotation splitting in the CaOH ground state), then through a switching AOM and shutter before being fibered to the slowing path.

SFG system #2: $\widetilde{X}(02^20)$ and $\widetilde{X}(010)(N=2)$ repumping lasers

The second SFG system using YDFAs and EDFAs is shown in Fig. 5.3, and is used to produce light for the $\widetilde{X}(02^20)$ (630 nm) and $\widetilde{X}(010)(N=2)$ (623 nm) repumping lasers. The 630 nm light is produced by combining 1546 nm

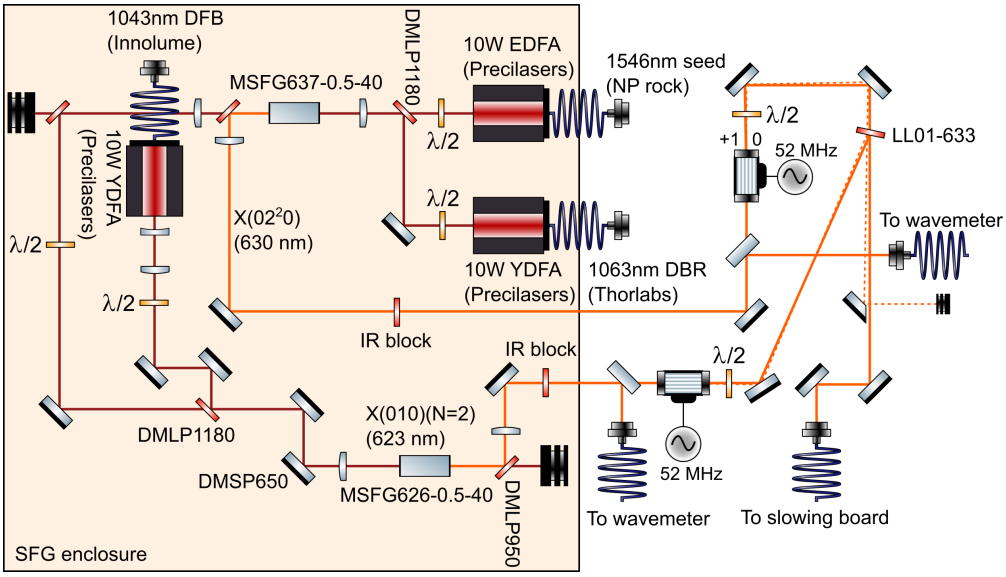

Figure 5.3: Laser system for the $\widetilde{X}(02^20) \rightarrow \widetilde{A}(100)$ and $\widetilde{X}(010)(N=2) \rightarrow \widetilde{A}(010)\kappa$ repumpers.

and 1063 nm light from 10 W Precilasers fiber amplifiers (seeded with an NP Rock[3] and Thorlabs DBR, respectively) on an SFG crystal (Covesion MSFG626-0.5-40). The 630 nm light is separated from the IR light, then the IR beams are separated and the 1063 nm light is dumped. The 1546 nm light is then combined with 1043 nm light (10 W Precilasers YDFA, seeded with an Innolume DFB-1043-PM-20-OI) on another SFG crystal to create 623 nm light for the $\widetilde{X}(010)(N=2)$ repumper. Both visible beams are sent through AOMs to switch them on and off, then combined on a dichroic and fiber coupled to the main experiment.

5.2.2 Raman fiber amplifier (RFA) systems

A number of our other repumping lasers are at wavelengths outside the convenient range for SFG systems, but they are accessible by frequency-doubled Raman fiber amplifiers (RFAs). We typically use commercial systems

[3] This is the same seed laser used for the 626 nm SFG system, and is split between the two setups.

that include the IR RFA system with an integrated second harmonic generation (SHG) crystal for frequency doubling. However, we have access to the IR light that wasn't frequency converted via a dump port, and in some cases we use this recycled light for additional visible frequencies.

RFA system #1 (574nm): $\widetilde{X}(100)$ repumper and Ca* enhancement laser

The first system is a 574 nm frequency-doubled RFA (4 W, MPB VRFA-P-4000-574.3-SF), seeded by a Toptica DL pro at 1148 nm. The visible light from this laser is split into two paths. The first is sent through a switching AOM and then fiber coupled to the slowing board, where it is combined with other repumping lasers. The second path goes through an AOM that adds 52 MHz spin-rotation sidebands, which are then combined and fiber coupled to the MOT chamber, where it is combined with the vertical MOT beam for MOT repumping.

The dumped, 1148 nm light from this RFA is combined with 1537 nm light (10 W IPG EDFA, seeded with a RIO Orion module) on an SFG crystal (Covesion MSFG647-0.5-40) to create several Watts of 657 nm light. This is used to excite the Ca $^1S_0 \rightarrow ^3P_1$ transition for CaOH chemical enhancement (chapter 3).

RFA system #2 (650nm): $\widetilde{X}(200)$ and $\widetilde{X}(12^00)$ repumpers

The second RFA system is a 650 nm frequency-doubled RFA (2 W, MPB VRFA-P-2000-650.38-SF-Plus), which was factory-set for $\widetilde{X}(200)$ repumping at 650.4 nm. However, we learned from MPB that it is possible to seed these RFAs with multiple wavelengths, provided they are near the design wavelength.[4] Therefore, we decided to seed the RFA with two wavelengths – 1300.8 nm and 1301.6 nm – to get 650.4 nm and 650.8 nm light for the

[4]Note that the spectrum when double-seeding an RFA does contain sidebands at multiples of the frequency spacing, but roughly 80% of the power was at the desired frequency based on data shared with us by MPB.

$\widetilde{X}(200)$ and $\widetilde{X}(12^00)$ repumpers. Both seed lasers were Innolume DFBs (DFB-13xx-PM-30-OI, where 13xx is the wavelength).[5]

To do this, we temperature-tuned the built-in SHG crystal in the MPB laser to frequency double the 1300.8 nm light, while leaving the 1301.6 nm light unaffected. This light was then dumped out of the laser, and we built our own SHG system outside the laser head, using a PPLN crystal (Covesion MSHG1320-0.5-40). Note that because of the nonlinearity of the SHG process, cutting the IR power in half means that we get 1/4 as much visible power, so our 2 W visible RFA was able to provide enough IR power to generate approximately 500 mW at each of the visible wavelengths. Another challenge we encountered was that stimulated Brillouin scattering (SBS) in the RFA became much worse at 1301.6 nm compared to the 1300.8 nm design wavelength.[6] Our power requirements for these lasers were sufficiently modest that this was acceptable, but it is worth keeping in mind when considering using a double-seeded RFA. Presumably this effect gets worse the farther one operates from the design wavelength.

The 650.4 nm and 650.8 nm visible wavelengths are too close together to be combined with dichroics. Instead, we combined them using volume Bragg gratings (Optigrate BP-650), which reflect a wavelength that meets the Bragg condition, with <0.15 nm selectivity. All other wavelengths are transmitted through the grating.[7] These wavelengths were also combined with the $\widetilde{X}(110)(N = 1)$ (651.1 nm) and $\widetilde{X}(03^10)(N = 1)$ (654.6 nm) repumpers using another grating and a dichroic beamsplitter. The combined wavelengths were then fiber coupled

[5]Note that we typically drive our DFBs using either Thorlabs temperature and current controllers or the Koheron CTL200-1-B-400 drivers. The latter is cheaper but also moderately less convenient.

[6]This appears to be slightly unpredictable. Originally it was low enough to still run the amplifier at full power. However, at one point we needed to send the RFA back to be repaired after a failure, and when the amplifier returned the SBS at 1301.6 nm was bad enough that we had to reduce the laser current.

[7]We found that we could get >90% reflection of 650.4 nm and ∼90% transmission of 650.8 nm using one of these gratings.

to the experiment to be combined with other repumpers for slowing.

Standalone RFA systems: $\widetilde{X}(02^{0}0)$, $\widetilde{X}(010)(N=1)$, and $\widetilde{X}(300)$ repumpers

We use frequency-doubled RFAs for three of the other repumping lasers. The $\widetilde{X}(02^{0}0)$ repumping light at 629 nm is generated with a doubled RFA system (4 W, MPB VRFA-P-4000-628.9-SF) seeded with a Toptical DL pro at 1258 nm. (In hindsight, this system was likely overkill, and we could have used a cheaper daisy-chained SFG system with noisier seeds. However, this system was purchased early on, before we had the opportunity to plan out the entire repumping scheme.) The $\widetilde{X}(010)(N=1)$ and $\widetilde{X}(300)$ repumping lasers, at 566 nm and 594 nm, respectively, are generated using Precilasers frequency-doubled RFAs. The 566 nm RFA is seeded with an 1132 nm cateye diode laser (MOGLabs CEL).[8] The 594 nm RFA is seeded with an Innolume DFB (1188.6-PM-30-OI).

5.2.3 Other laser systems

For three of the low-power repumping lasers near 650 nm, we use MOGLabs Littrow ECDLs, which contain 150 mW diodes (HL65014DG) and are able to produce close to 50 mW when the cavity is lasing.

For one of the repumpers (along with certain depletion and pumping lasers applied for microwave spectroscopy), we use Coherent 899 continuous wave dye lasers. These have been extensively described in previous Doyle group theses [278], and can reliably produce powers up to around 1 W over a range of visible wavelengths. They are outstanding resources for molecule spectroscopy and early-stage laser cooling experiments, though we have tried to slowly phase out dye lasers over the course of the experiment, once specific repumping wavelengths are known.

[8] Unfortunately, there are no DFBs available in this frequency range.

For our 609 nm $\widetilde{X}(000) \rightarrow \widetilde{A}(010)$ optical pumping light (used in chapters 8 and 9), we used a Vexlum VALO SHG SF laser.

5.2.4 Laser locking

We lock the lasers using a wavemeter lock. The wavemeter (High Finesse WS7-30) is passively pressure-stabilized inside a sealed ISO vacuum chamber (near 1 atm), in a "quiet" temperature and humidity controlled room. We also monitor a reference laser locked to a lithium oven, which helps correct for long-term drifts.[9] We use software PIDs and a DAQ card to apply locking voltages to the lasers.

For us, the primary challenge with wavemeter locking is the large number of lasers on our experiment. In addition to the 14 CaOH optical cycling lasers, we have several other lasers, including 657 nm Ca* enhancement light, a 609 nm laser for optically pumping molecules into the vibrational bending mode, and one or two dye lasers for assorted depletion and optical pumping tasks, plus the lithium reference laser. This means that we need close to 20 wavemeter channels. High Finesse sells 8 -channel switchers with the wavemeter, but this is insufficient (in addition to having a narrow wavelength range and finite lifetime).

To create more wavemeter channels, we use a galvanometer (Cambridge Technology) to switch, in rapid succession, a small amount of light from each laser into a fiber that is coupled into the wavemeter. This approach was described previously in Ref. [278] but for eight channels, which were switched using a single (horizontal) axis of the galvanometer. We expanded this setup to include 24 channels, by using three rows of eight beams each. The galvanometer position is controlled using an Arduino, and Python software is used to correlate the frequency

[9] We have recently found that the wavemeter is passively stable enough that the atomic reference is not necessary, with it being sufficient to occasionally adjust the global wavemeter offset by a few MHz to optimize the CaOH MOT or ODT signal.

read out by the wavemeter to the laser that was coupled in at the time. This setup is described in slightly more detail in Ref. [274].

5.3 Radiative slowing

The principle of radiative laser slowing is simple. We begin with a CaOH molecular beam produced by the buffer gas source with an initial forward velocity of $v_0 \approx 140$ m/s, propagating in the $\hat{x}$ direction. The goal is to slow the beam to below 10 m/s by pointing our optical cycling lasers along $-\hat{x}$, opposite the molecular beam's direction of propagation. By tuning the lasers to resonance and scattering thousands of photons from each molecule via optical cycling, we can remove momentum from the molecular beam. The mechanism underlying this process is as follows. Each time a counter-propagating photon is absorbed by a molecule, the molecule's momentum decreases by a constant amount $\Delta p = -\hbar k$, where $k = 2\pi/\lambda$ is the wavenumber of the photon and λ is its wavelength. A short time later[10], the molecule spontaneously emits a photon in a random direction, receiving another momentum kick. After a large number of photon scattering events, the momentum kicks from the spontaneously emitted photons average to zero (because the emission is isotropic), but the absorbed photons continue to slow the beam. As discussed in chapter 4, for the $\widetilde{X}(000) \rightarrow \widetilde{A}(000)$ transition in CaOH, $\hbar k/m \approx 1.1 \times 10^{-2}$ m/s, meaning that nearly 13,000 photons are needed to slow our ∼140 m/s molecular beam to rest.

The force applied to the molecules is the single-photon momentum times the *scattering rate* R_{sc}, which is the number of photons scattered per second. The scattering rate is just the excited state natural linewidth Γ times the population of the state. For a multi-level system with N_g ground states and N_e excited states, under the assump-

[10] The radiative lifetime of the $\widetilde{A}^2\Pi_{1/2}$ electronic excited state used in CaOH is approximately 25 ns [**?**]

tion all states are addressed with equal laser intensity, the scattering rate is approximately [298, 299]

$$F_{\text{rad}} = \hbar k R_{\text{sc}} \approx \frac{\hbar k \Gamma_{\text{eff}}}{2} \frac{s_{\text{eff}}}{1 + s_{\text{eff}} + 4\Delta^2/\Gamma^2} \tag{5.1}$$

where

$$\Gamma_{\text{eff}} = \frac{2N_e}{N_g + N_e}\Gamma \tag{5.2}$$

is the effective two-level linewidth, and $s_{\text{eff}} = I/I_{\text{sat, eff}}$ is the effective saturation parameter, where I is the total laser intensity and $I_{\text{sat, eff}}$ is the multi-level saturation intensity, which is typically much higher for a multi-level system than a two-level system [220, 298, 299]. The effective linewidth expression can be intuitively understood by noting that in the limit of high laser power, population will be equally distributed among all ground and excited states, and that the scattering rate is just the excited state population times the natural linewidth Γ. For example, for a saturated two-level system 50% of the population is in the excited state, leading to a maximum scattering rate of $\Gamma/2$. For a system with 3 ground states and 1 excited state, only 25% of the population is in the excited state when saturated. This explains why we designed our optical cycling scheme so that none of the repumping lasers couple to $\widetilde{A}(000)$. Repumping even a single vibrational state through $\widetilde{A}(000)$ would decrease the maximum scattering rate by a factor of two.

For CaOH optically cycled on the $\widetilde{X}^2\Sigma^+(000)(N = 1) \rightarrow \widetilde{A}^2\Pi_{1/2}(000)(J = 1/2^+)$ transition, there are $N_g = 12$ ground states and $N_e = 4$ excited states,[11] meaning that $\Gamma_{\text{eff}} = \Gamma/2$. At high saturation $s_{\text{eff}} \gg 1$ (which requires very high intensities for molecules), the scattering rate becomes $R_{\text{sc, max}} = \Gamma/4$, which is a factor

[11] The ground state has $J = 1/2$ and $J = 3/2$ spin-rotation components with hyperfine states $F = 1, 0$ and $F = 1, 2$, respectively, leading to 12 states when accounting for magnetic sublevels. The excited state is $J = 1/2$ and has hyperfine states $F = 0, 1$, leading to four sublevels.

of two lower than the two-level case. Because $\Gamma = 1/\tau = 1/(25\text{ ns})$ for CaOH, this means that the maximum scattering rate is theoretically around $1 \times 10^7\text{ s}^{-1}$. In practice it is typically only possible to get scattering rates up to around $2 \times 10^6\text{ s}^{-1}$.

The detuning in eqn. 5.1 is $\Delta = \delta - \vec{k} \cdot \vec{v}$, where $\delta = \omega_L - \omega_0$ is the laser detuning and $\vec{k} \cdot \vec{v}$ is the Doppler shift. Here $\vec{k}$ is the wavevector of the laser, $\vec{v}$ is the molecule velocity, ω_L is the laser frequency, and ω_0 is the resonance frequency. Achieving the maximum scattering rate during slowing requires that $\Delta = 0$ (or, equivalently, $kv = -\delta$)[12] be maintained across a range of molecule velocities from approximately 0-140 m/s. For atoms, this can be done using a Zeeman slower, which uses magnetic fields to tune the resonance frequency to match the atoms' velocity at each point in space [300]. Zeeman slowers are very efficient since the slowed atoms all reach the desired velocity at the same position, which can be chosen to be very close to the MOT region. However, Zeeman slowers are challenging for molecules due to their type-II structure and have not been demonstrated to date [301, 302].

Two alternative methods used in this work are (1) chirped slowing and (2) white-light slowing. In chirped slowing, the laser frequency is changed over time, so that the detuning $\delta(t)$ matches the molecules' velocity $v(t)$ throughout the slowing process. This means that molecules are slowed to the desired velocity at the right time, but not necessarily at the right position. In white-light slowing, the spectrum of the laser is broadened so that the full range of velocities are simultaneously resonant with some component of the laser's spectrum. This requires more laser power and is the least efficient method since it does not select the time or position at which slow molecules are produced, but it is also the simplest to optimize. The final velocity distribution from white-light slowing can be selected, at least to a degree, by the laser spectrum. For instance, if the laser spectrum is uniform

[12] Here and for the rest of this section we specify to counterpropagating laser beams, such that $\vec{k}$ is antiparallel to $\vec{v}$.

over the frequency range $[\omega_1, \omega_2]$, molecules will accumulate at velocities slightly below the "cutoff" velocity $kv_{\text{cutoff}} = \omega_0 - \omega_2$. For instance, for CaOH molecules slowed by 626 nm light, if the highest laser frequency is 30 MHz red-detuned from resonance, molecules will accumulate at velocities slightly below $v_{\text{cutoff}} \approx 19$ m/s, though the distribution is usually smeared out due to significant power broadening.

A useful graphical comparison between Zeeman slowing, chirped slowing, and white-light slowing can be found in Fig. 1 of Ref. [302].

For resonant slowing of CaOH, we find that we are able to achieve scattering rates of approximately $1 - 2 \times 10^6$ photons/s. Assuming $R_{\text{sc}} = 1.5 \times 10^6$ s^{-1}, it should take approximately 8 ms and 60 cm to slow a 140 m/s beam of CaOH to rest (using 626 nm slowing light on the $\widetilde{X}(000) \rightarrow \widetilde{A}(000)$ transition).

Note that there are alternative methods for slowing molecular beams that rely on fewer photons scattered, e.g. Zeeman-Sisyphus slowing [160, 165, 166]. However, these methods rely on constant *energy* removal rather than constant *momentum* removal, which makes them less robust to fluctuations in the velocity of the buffer gas beam source. Because we already had a large photon budget at our disposal for CaOH[13], we elected to stick with radiative slowing due to the relative experimental simplicity and robustness to drifts in the buffer gas source.

5.3.1 Two-photon velocity detection

To measure the velocity of the CaOH molecular beam, we send in a laser counter-propagating to the molecular beam and measure the signal as a function of laser frequency. Since the maximum signal corresponds to a detuning $\Delta = \delta + kv = 0$, where δ is the laser detuning and kv is the Doppler shift of the molecules, this can

[13] Having a photon budget $\gtrsim 10^4$ is important not just for slowing but also for loading the MOT and imaging molecules with high fidelity.

be used to extract the molecules' velocity v. When characterizing the velocity of the natural CaOH beam – e.g. for optimization of the cryogenic buffer gas beam production – we found that a background free scheme based on the optical cycling transitions worked well. In this approach, a photon cycling laser addressing the 626 nm $\widetilde{X}(000) \rightarrow \widetilde{A}(000)$ transition is introduced transverse to the molecular beam (with no velocity sensitivity), and a 574 nm $\widetilde{X}(100) \rightarrow \widetilde{B}(000)$ repumping laser is sent antiparallel to the molecular beam (maximum velocity sensitivity). The 626 nm laser pumps most molecules into the $\widetilde{X}(100)$ vibrational state after approximately 18 photons are scattered, and the 574 nm laser velocity-selectively pumps molecules into $\widetilde{B}(000)$, which then decays back to $\widetilde{X}(000)$ by emitting a 555 nm photon that can be detected with interference filters that block the laser light.

To optimize laser slowing, on the other hand, we would like to minimize inference from the slowing lasers, which means we would prefer a velocity detection method that (1) does not rely on the same optical cycling transitions used for slowing and (2) is background-free with regard to any light the molecules would already emit during laser slowing (for instance, molecules will naturally emit 555 nm photons during optical cycling). We therefore used a two-photon UV detection scheme similar to what was used to observe laser slowing in the CaF experiment [223, 278].

The scheme works as follows for CaOH. Molecules are excited from $\widetilde{X}^2\Sigma^+(000) \rightarrow \widetilde{A}^2\Pi(000) \rightarrow \widetilde{D}^2\Sigma^+(000)$ using two resonant lasers, where the "first-step" $\widetilde{X} \rightarrow \widetilde{A}$ laser is incident transverse to the molecular beam and the "second-step" $\widetilde{A} \rightarrow \widetilde{D}$ laser is counterpropagating to the molecular beam and detuned to be resonant with a chosen velocity. Molecules successfully driven to the $\widetilde{D}^2\Sigma^+$ state decay back to the $\widetilde{X}^2\Sigma^+$ state by emitting 355 nm UV photons, which can be detected background-free using optical filters (Semrock 360/23 and 390/SP interference filters with an Andover 005FG09 colored glass filter between) and a PMT (Hamamatsu R7600P-

200).[14] The PMT is operated in photon-counting mode, in that the signal is sent through a fast preamp (SRS SR445A) and then to a comparator, which sets a single-photon signal threshold. The output pulses from the comparator are counted by a DAQ card.[15]

To maximize signal, we installed in-vacuum optics to collect the UV photons (Fig. 5.4). We used two Thorlabs condenser lenses (ACL50832U-A, 2" diameter, 32 mm focal length) and a UV mirror (Newport 5120). The lens on the PMT side was placed such that the collected light was gently refocused back onto the PMT. Opposite the PMT side was a lens and a mirror, so that light emitted in that direction would be collimated, retroreflected off the mirror, focused back near the molecules and then collected by the PMT-side lens. The photon collection efficiency of this system was measured to be 9%, in excellent agreement with simulations.

The specific rotational transitions used for two-photon detection are shown in Fig. 5.5. The primary two-photon transition is driven by the lasers shown in the middle of the figure, which drive the $\widetilde{X}^2\Sigma^+(N'' = 1, J'' = 3/2) \rightarrow \widetilde{A}^2\Pi_{3/2}(J' = 5/2^+) \rightarrow \widetilde{D}^2\Sigma^+(N = 1, J = 3/2)$ transitions at 624 nm and 824 nm, respectively. The key to this scheme is that a $(J' = 5/2^+)$ rotational level is chosen in the intermediate $\widetilde{A}$ state. This means that only the $J = 3/2$ spin-rotation (SR) components of the $\widetilde{X}$ and $\widetilde{D}$ states can be excited, due to $\Delta J = 0, \pm 1$ angular momentum selection rules. The SR splittings are 52 MHz in $\widetilde{X}^2\Sigma^+(N'' = 1)$ and 38 MHz in $\widetilde{D}^2\Sigma^+(N = 1)$, which would lead to a number of peaks split by 30-40 m/s in our data if they could both be driven. While we could have chosen either the $\widetilde{A}^2\Pi_{1/2}$ or the $\widetilde{A}^2\Pi_{3/2}$ spin-orbit manifold as the intermediate state, we chose the latter due to a $\sim 3\times$ stronger rotational line strength on each step.[16]

[14] We tried several chilled PMT models that had lower dark-count rates than the room-temperature R7600P. However, we found that the signal-to-noise ratio of the R7600P was still superior, due to much higher signal levels.

[15] This setup is essentially identical to the one described in Ref. [278].

[16] We also tested a number of other two-photon transitions. If having only a single allowed SR transition is not important (e.g. for transverse beam detection), using the $\widetilde{A}^2\Pi_{1/2}(J' = 1/2^+)$ intermediate state gives the best signal, followed by

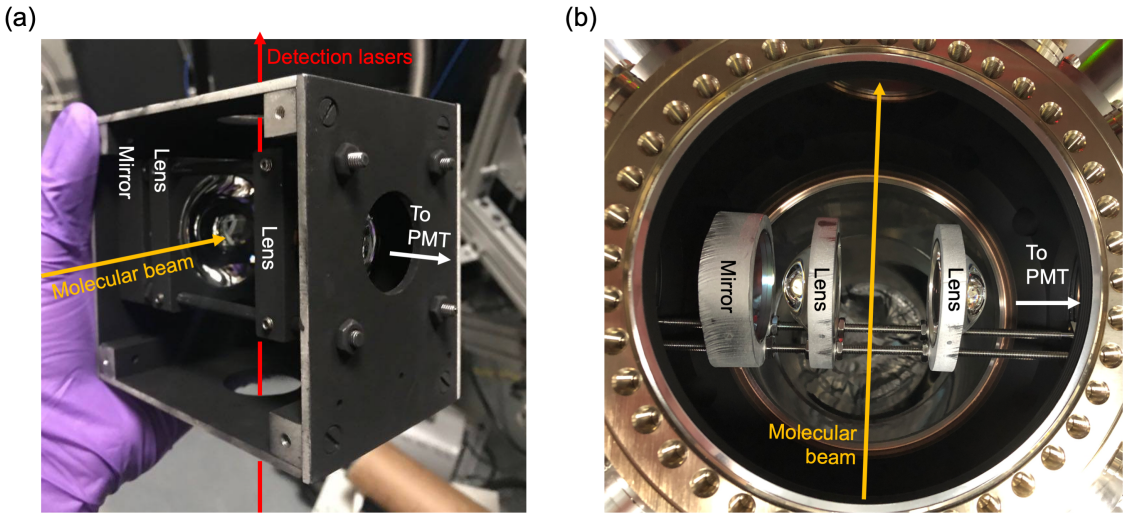

Figure 5.4: In-vacuum optics used for two-photon detection. The system consists of two aspheric condenser lenses (Thorlabs ACL50832U-A) and one flat UV mirror (Newport 5120). (a) In-vacuum optics mounted in a blackened box used for initial slowing tests in the o-ring sealed beamline that had previously been used for transverse cooling [220] and depletion-revival spectroscopy [251]. (b) In-vacuum optics mounted in the MOT chamber for slowing tests. The mounts are not blackened because two-photon detection is background free. Before making a MOT, we removed these optics and installed the RF MOT coils.

The 624 nm first-step transition was driven using either a cw dye laser (Coherent 899) or an external cavity diode laser (ECDL) (homebuilt, with an HL63163DG diode cooled to around -10°C), and the second-step, 824 nm transition was driven with a titanium-sapphire laser (Coherent 899). The first-step was always driven transverse to the molecular beam, and the second step was driven either transverse to the beam or co-linear with the slowing lasers for velocity-insensitive and velocity-sensitive measurements, respectively. For velocity scans, we typically kept the first-step laser around or below 1 mW and the second-step around 100 mW to avoid power-broadening of the velocity distribution. However, improved signal is observed for first-step powers above 10 mW and second-step powers above 500 mW. We generally operated with the first-step laser near resonant (so that

$\widetilde{A}^2\Pi_{3/2}(J'=3/2^+)$ and $\widetilde{A}^2\Pi_{1/2}(J'=3/2^+)$. The first case corresponds to the first step driving the photon-cycling $\widetilde{X} \rightarrow \widetilde{A}$ transition, which explains why it gives the best signal: here the IR laser has multiple changes to "grab" a molecule from $\widetilde{A}$ and excite it to $\widetilde{D}$.

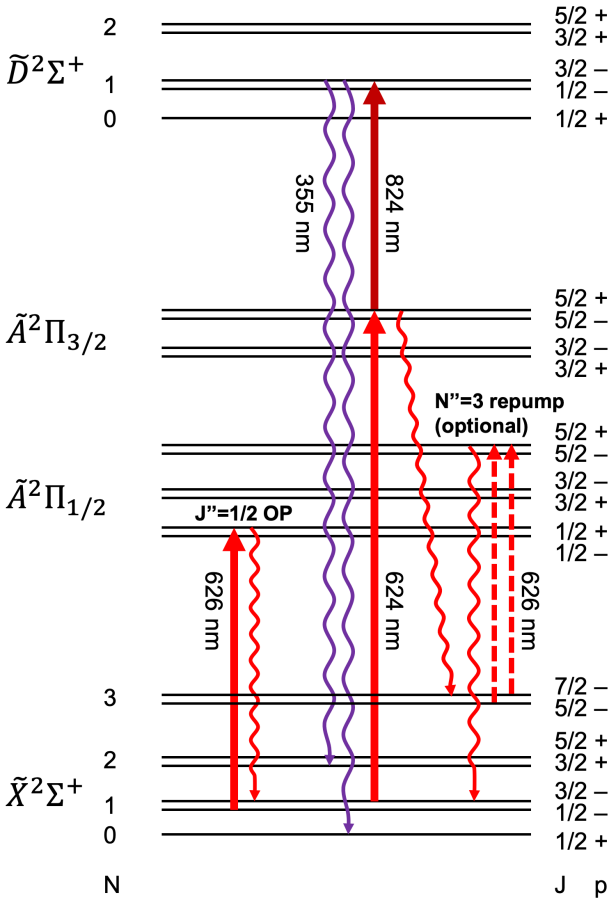

Figure 5.5: Two-photon detection scheme(s) used for CaOH velocity detection during radiative slowing. The 624 nm and 824 nm lasers are the main two-photon detection lasers, while the $J'' = 1/2$ OP laser is important for detecting all slowed molecules, and the $N'' = 3$ repump can be used to improve the signal by enabling a larger fraction of the molecules to be excited by the $\widetilde{X} \rightarrow \widetilde{D}$ laser.

the single-photon detuning is $\Delta \approx 0$), while the detuning of the second-step laser (which determines the two-photon detuning δ given a fixed first-step detuning) was used to select the resonant molecule velocity $v = -\delta/k$, where $k = 2\pi/(824\text{ nm})$.[17]

Also shown in Fig. 5.5 are two other lasers that we used for two-photon detection. These lasers address the molecular beam transversely, without velocity sensitivity. The first is a laser addressing the $\widetilde{X}^2\Sigma^+(N'' = 1, J'' = 1/2) \rightarrow \widetilde{A}^2\Pi_{1/2}(J' = 1/2^+)$ transition to optically pump population from $J'' = 1/2$ into $J'' = 3/2$. Without this laser, not all relevant molecules can be detected. This not only improves the detected signal, but it also prevents the measurements from being biased by state dependence in the slowing. For instance, the slowest molecules might be optically pumped into $J'' = 1/2$ by the slowing lasers because that state is further detuned [303]. These molecules would not be detected without the optical pumping laser. We use this laser for most of our slowing data. However, if slowing light is on while we are detecting we do not need this laser, since the slowing light itself transfers population between spin-rotation states.

Optionally, an $N'' = 3$ repumper can be used to improve the two-photon detection signal. This laser addresses both SR components of the $\widetilde{X}^2\Sigma^+(N'' = 3) \rightarrow \widetilde{A}^2\Pi_{1/2}(J' = 5/2^+)$ transition. This increases the two-photon signal by repumping molecules that decay from the $\widetilde{A}^2\Pi_{3/2}(J' = 5/2^+)$ intermediate state before they can be excited by the $\widetilde{A} \rightarrow \widetilde{D}$ laser. We found that this laser (which had 120 MHz sidebands introduced with an AOM) improved the two-photon signal by around a factor of 3. This laser was added to help observe signal at low velocities (~ 10 m/s) before we switched to look for a MOT.

[17] We sometimes found that the signal improved when operating at a single-photon detuning of a few 10s of MHz. This is possibly due to two-photon physics (e.g. Autler-Townes splitting). Alternatively, it is possible that when too close to resonance, molecules are depleted into $N'' = 3$ by the first-step laser before the second-step laser has the chance to drive them to the $\widetilde{D}^2\Sigma^+$ state.

5.3.2 Optical setup

The optics used for laser slowing are shown in Fig. 5.6 and accomplish two main goals. The first is to combine all of the slowing and repumping laser wavelengths, and the second is to prepare the lasers for slowing. Combining the 13 laser wavelengths needed for CaOH slowing and cooling is a bit complicated, not only due to the large number of lasers, but also because many of them are close in wavelength (within a few nm). All of the lasers are fiber coupled onto the board to clean up their beam shape[18], and they can be switched on and off by AOMs or shutters prior to the fiber coupling. Some of the wavelengths come fiber coupled to the slowing board pre-combined, as discussed above. Once on the slowing board, lasers are combined using Semrock filters and dichroics (part numbers given in Fig. 5.6), many of which have sharp edges and much be used at very specific angles. All of the red lasers ($\lambda > 620$ nm) are combined into one beam path and all of the yellow lasers ($\lambda < 600$ nm) are combined into another.

Once combined, the two composite beams (red and yellow) are focused through and broadened by two resonant electro-optic modulators (EOMs) to cover the ∼300 MHz frequency span needed to address all molecule velocities during slowing. The EOM design is from Yicheng Bao and was previously described in Ref. [274]. The EOMs are driven around 4.6 MHz (tuned to avoid piezo resonances[19]), which is less than the transition linewidth and so effectively creates a white-light spectrum on the lasers. The frequency spectra of the broadened lasers are shown in Fig. 5.7.

[18] We found that this was important for reliability of the system. We initially free-spaced the highest power lasers, but later found that it was more reliable to send them through very short single-mode fibers, which cleaned up the mode while still allowing high transmitted power. (Longer fibers would suffer from stimulated Brillouin scattering (SBS) limiting the power.)

[19] The signature of piezo resonances for us was a change in beam shape when the RF was turned on. Moving the EOM frequency by 100 kHz recovered the beam quality.

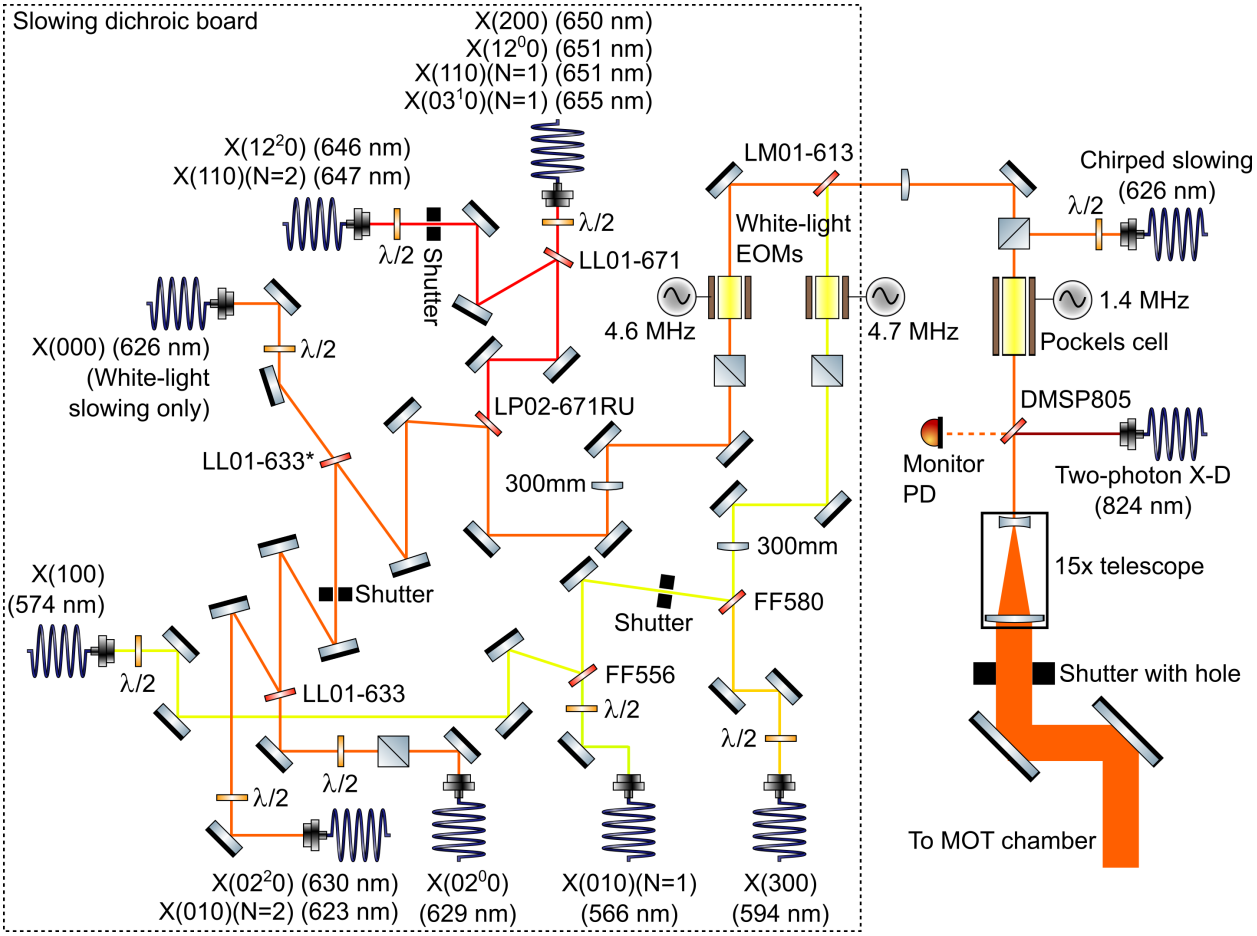

Figure 5.6: Slowing optics setup. A dichroic board is used to combine all of the slowing and repumping lasers, which are brought in from laser tables via optical fiber. The combined beams are white-light broadened using two homemade EOMs, with one EOM dedicated to the red lasers ($\lambda > 620$ nm) and the other used for the yellow lasers ($\lambda < 600$ nm). After broadening, the repumpers are combined with chirped slowing light (if used), polarization-modulated with a Pockels cell, and then expanded for slowing. A pick-off is used to monitor the laser powers in the experimental sequence. Optionally, 824 nm light can be combined with the slowing and repumping lasers for two-photon velocity detection. *This dichroic was replaced with a mirror when we switched from white-light to chirped slowing.

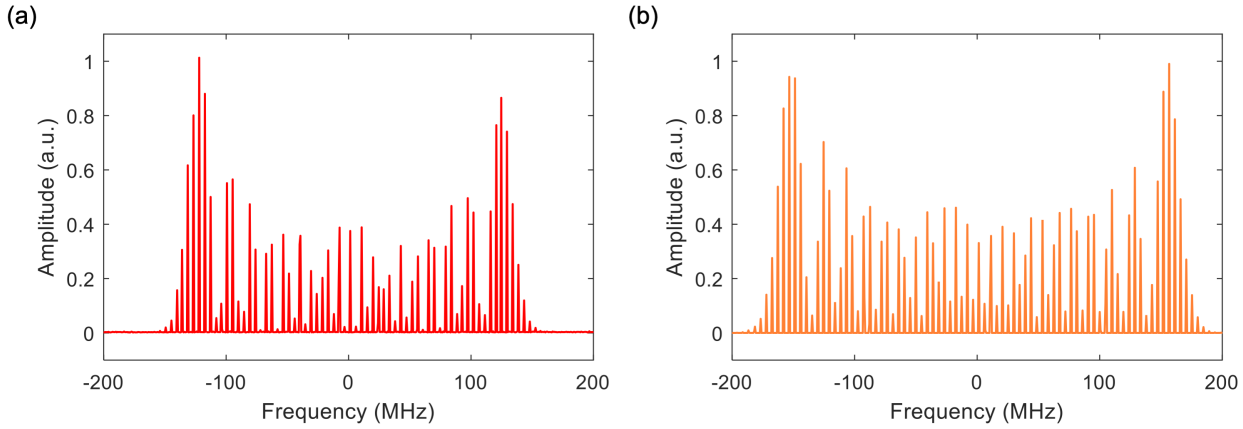

Figure 5.7: Frequency spectrum of slowing and repumping lasers from the white-light EOMs. (a) EOM 1 (red lasers) broadened to cover approximately 270 MHz. (b) EOM 2 (yellow lasers) broadened to cover approximately 330 MHz.

After the EOMs, the red and yellow beams are combined with the chirped slowing laser (if used), then sent through a Pockels cell (Conoptics Model 370), which is sinusoidally driven at approximately 1.4 MHz (via a resonant tank circuit) to rotate the laser polarization and remix dark states. A DC offset voltage is added to the RF drive and set to maximize the polarization contrast (by setting the crystal birefringence at zero RF amplitude). We set the Pockels cell drive voltage to rotate the polarization by a full 90° (i.e. between two orthogonal polarizations).

After the Pockels cell, the lasers are optionally combined with the 824 nm $\widetilde{A}^2\Pi_{3/2} \rightarrow \widetilde{D}^2\Sigma^+$ two-photon velocity-sensitive detection laser. The same dichroic reflects a small amount of slowing light, which is directed onto a photodiode and used to monitor the slowing powers. This monitoring is done at the start of every experimental sequence by turning on the lasers one at a time for 1 ms each and reading off the corresponding PD voltages. After the monitor pickoff, the beams are expanded with a $\sim 15\times$ telescope and directed down the slowing beamline. There is a shutter (Thorlabs SH1) with a hole drilled in it that was added during the optical tweezer

array project (chapter 8) to reduce scattered light from the repumpers for 626 nm ($\widetilde{A} \rightarrow \widetilde{X}$) imaging.

We set the beam size and alignment as follows. We first profiled all the slowing beams to ensure they had similar sizes and spatial overlap both at the entrance to the chamber and at the buffer gas cell.[20] The beam diameter is approximately 11 mm at the MOT position (this roughly matches the MOT beam diameter), and the beams gently focus down towards the cell, where they approximately fill the cell apertures and exit the hole in the back of the cell without significant clipping (5.5 mm diameter at the cell). We aligned the beams by centering them on the MOT chamber entrance viewport and on the cell, ensuring that they went straight through the cell, exiting the hole in the back with minimal clipping.[21] After this alignment procedure, we found that only very small changes to the alignment were needed to optimize the slowing and MOT.

Early in our slowing attempts, we found that leaving the slowing light on through the EOMs for prolonged durations led to thermal drift that decreased the reliability of the slowing. Therefore, we switch the lasers on and off before they reach the slowing board and EOMs, and attempt to keep them off when possible during the experimental sequence. Other improvements to reliability included adding the slowing power monitor described above, adding polarization cleanup optics before the EOMs, and using directional couplers to monitor the back-reflected power from the EOMs to ensure they are operating stably. Over time, we have added a number of shutters to the slowing board to block leaked light that could interfere with certain experiments.

[20] We checked the size at the buffer gas cell by installing a flip mirror in the slowing path and a beam profiler the correct distance away.

[21] We also confirmed that the slowing beams were centered on the cell by minimizing the heat load onto the cell from the slowing light. This was done by aligning the beams while monitoring the cell temperature.

5.3.3 Molecular beam depletion checks

Before looking for slowing of the molecular beam, we ran a number of depletion-revival checks to ensure that all repumpers were working properly. These tests could be used (1) to measure and optimize the scattering rate from the slowing lasers and (2) to ensure that each laser was repumping population appropriately. For these scans, we detuned the two-photon detection to be resonant with molecules near the peak of the molecular beam. After ablation, we kept the UHV shutter open for 4 ms to allow some molecules to escape the beam box, then closed the shutter to prevent late-arriving molecules from impacting the results. We waited some time (typically 3-5 ms) after the UHV shutter closed, then applied slowing light with various repumper configurations for long enough to pump >50% of the molecules into vibrational dark states. From the fraction of molecules depleted (measured by comparing experimental runs with and without the $\widetilde{X}(000) \rightarrow \widetilde{A}(000)$ laser on during the depletion time), we can estimate the average scattering rate. The experimental sequence is graphically depicted in Fig. 5.8(a).

As a first check, we confirmed that the Pockels cell was effectively remixing dark states. Fig. 5.8(b) shows depletion results after turning on the $\widetilde{X}(000) \rightarrow \widetilde{A}(000)$ laser (with no repumpers) for 10 μs at various Pockels cell frequencies, with the two-photon detection tuned to detect molecules around 165 m/s. With the Pockels cell running at 1 MHz, we see that approximately 33% of the molecules arriving in a 2 ms window after the depletion pulse survive. Given the photon budget of 18.5 when depleting with the $\widetilde{X}(000) \rightarrow \widetilde{A}(000)$ laser only, this corresponds to a scattering rate of 2.0×10^6 s^{-1}. When the Pockels cell frequency is increased to 2 MHz the scattering rate is unchanged. When the Pockels cell is run at 300 kHz, we see a decrease in the depletion level, corresponding to a reduced scattering rate of 1.7×10^6 s^{-1}, since dark states are no longer remixed fast enough to support the highest scattering rates. Using similar measurements, without the Pockels cell on we observe a scat-

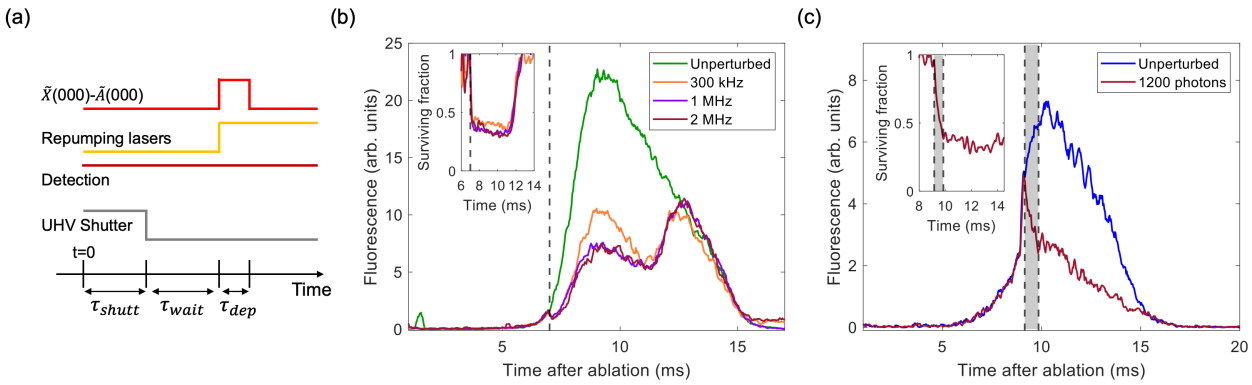

Figure 5.8: Depletion checks prior to radiative slowing. (a) Experimental sequence. Molecules are depleted for a time τ_{dep} using the $\widetilde{X}(000) \rightarrow \widetilde{A}(000)$ laser and some number of repumping lasers. The repumping lasers are then left on and the beam signal is compared with and without the $\widetilde{X}(000) \rightarrow \widetilde{A}(000)$ depletion pulse. The shutter is closed a time $\tau_{\text{shutt}} = 4$ ms after ablation, and there is an additional wait time τ_{wait} before depletion. (b) Depletion checks of the Pockels cell frequency. The $\widetilde{X}(000) \rightarrow \widetilde{A}(000)$ depletion light is turned on (with no repumping lasers) for 10 μs at $\tau_{\text{shutt}} + \tau_{\text{wait}} = 7$ ms after ablation with variable Pockels cell frequency. Inset: beam survival fraction (depleted signal divided by unperturbed signal) vs. time. (c) Depletion check with lasers addressing the $\widetilde{X}(000)$, $\widetilde{X}(100)$, $\widetilde{X}(02^{0}0)$, $\widetilde{X}(200)$, $\widetilde{X}(010)(N=1)$, and $\widetilde{X}(02^{2}0)$ states (photon budget of 1200) for $\tau_{\text{dep}} = 700$ μs, starting 9 ms after ablation. For the data in (b) and (c), the 824 nm two-photon detection laser is red-detuned by 200 MHz, corresponding to 165 m/s molecules being resonantly detected. The grey shaded regions denote the time when the depletion laser is on.

tering rate of only approximately 500×10^3 s^{-1}. Based on these measurements, we ended up using a Pockels cell frequency around 1.4 MHz for radiative slowing.

Next, we attempted to measure the scattering rate as we added sequentially more repumping lasers. Fig. 5.8(c) shows data with a 700 μs depletion pulse and a photon budget of 1200, corresponding to cycling and repumping lasers addressing the $\widetilde{X}(000)$, $\widetilde{X}(100)$, $\widetilde{X}(02^00)$, $\widetilde{X}(200)$, $\widetilde{X}(010)(N=1)$, and $\widetilde{X}(02^20)$ states. We observe an average molecule survival of 33% in a 2 ms window after the depletion pulse, which corresponds to a scattering rate of around 1.9×10^6 s^{-1}. We did similar checks for other combinations of repumping lasers, and also used the depletion level as a means of optimizing laser powers and alignment before directly looking for slowed molecules.

Note that this depletion method can only be used up to a point, since once the photon budget becomes too large, molecules will be slowed away from the detected velocity class (even in the 1200-photon case described above, the molecular beam would have been slowed by approximately 15 m/s). Even if we were to detect the beam transversely, the time of arrival would change for slowed molecules, so dividing the depleted signal by the unperturbed signal would be unreliable. Therefore, for the repumpers that come in after a large number of photons, the power can be scanned to ensure they are saturated, but the scattering rate cannot be directly inferred using this depletion method.

5.3.4 White-light slowing

After confirming that the slowing and repumping lasers were able to maintain a high scattering rate in the slowing region, the next step was to look for signatures of molecular beam slowing. This was done by measuring the velocity of the molecular beam (using two-photon detection) with and without the slowing lasers on. We initially used white-light slowing, with all the repumping lasers as well as the main $\widetilde{X}(000) \rightarrow \widetilde{A}(000)$ cycling laser

broadened using white-light EOMs (sec. 5.3.2) to cover molecule velocities between approximately 0-140 m/s.

For white light slowing, there are relatively few parameters to scan, which makes it a good choice for initial slowing and MOT loading. This is because the MOT – not the molecular beam velocity – is the best way to optimize slowing parameters.[22] The MOT is simpler to first obtain and optimize using white-light slowing, since there are fewer parameters to get right on the slowing side. Once the MOT is optimized, we can return to chirped slowing, which can be effectively tuned up by feeding back on the MOT brightness, as described in sec. 5.3.5

The primary parameters to tune for white-light slowing are (1) the wait time between ablation and the start of the slowing pulse, (2) the total duration of the slowing pulse[23], (3) the slowing power, and (4) the frequency spectrum of the slowing and repumping light, namely the center frequency and frequency broadening. In addition, it is important to optimize the beam size and alignment through the molecular beamline, as described above. The slowing duration is more important for MOT loading than for optimization of the beam velocity, since we continuously detect the beam during slowing. For most of our slowing data, we used a slowing duration of around 25 m/s, which was long enough for nearly all molecules exiting the cell to be slowed. The wait time is useful if the beamline is longer than the required slowing distance[24], because it lets the molecules get closer to the MOT region before we begin slowing. This helps prevent molecules from being prematurely slowed to rest and lets us using the minimum possible slowing distance, helping to minimize "pluming" [278]. We observed that the best accumulation of slow molecules occurred at wait times of around 2-4 ms, with longer wait times increasing the

[22] The dynamics of MOT loading are complicated, and predicting MOT loading from molecular beam measurements is nontrivial. Such predictions would likely require a precise understanding of the MOT capture velocity and loading dynamics, combined with precise measurements of the molecular beam velocity as a function of position and arrival time.

[23] For initial slowing checks, the total slowing time is not especially important, but it will be more important when loading a MOT. This is because the slowing light is strong enough to push molecules out of the MOT, and therefore it needs to be turned off as soon as the MOT is loaded.

[24] In our apparatus, the distance from the cell to the MOT is 81 cm, and the slowing distance is expected to be around 60 cm for a scattering rate of 1.5×10^6 s^{-1}.

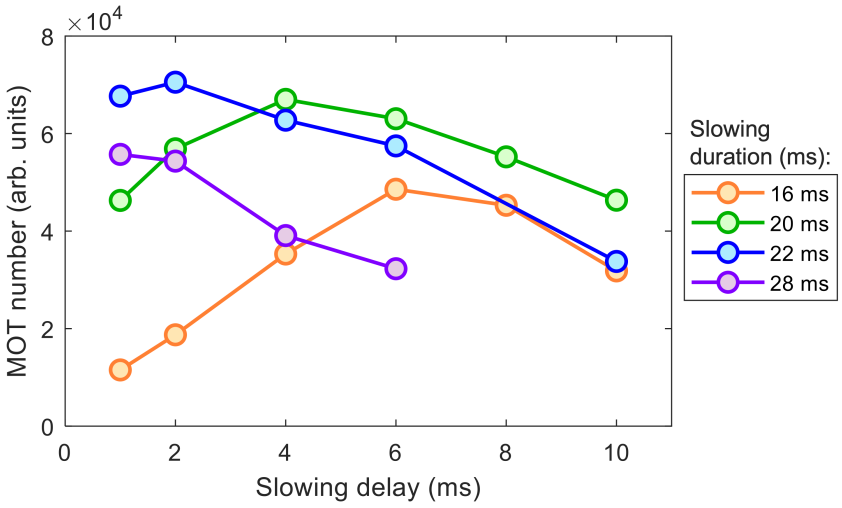

Figure 5.9: Optimization of MOT number vs. white-light slowing delay and slowing duration. Shorter slowing durations tended to require longer delay times. The optimal configuration for MOT loading was a slowing duration of 22 ms and a delay of 2 ms.

final velocity of the slowed molecules, as expected. After obtaining a MOT, we returned to these timing scans, with the results shown in Fig. 5.9.

Before optimizing slowing of molecules the MOT capture velocity, we first checked that we were able to slow to higher velocities, which are easier to detect. We did this both by changing the frequency spectrum of the slowing and repumping lasers, and also by reducing the power of the slowing lasers. As illustrated in Fig. 5.10 (and described in more detail below), the frequency spectrum of the slowing and repumping lasers can be adjusted to select a range of molecule velocities that will be optimally slowed. While we will eventually aim to cover all velocities between 0 m/s and the initial beam velocity, for early checks we reduced the frequency broadening to cover a narrower range and scanned the "velocity cutoff" (lowest resonant molecule velocity class) of the main $\widetilde{X}(000) \rightarrow \widetilde{A}(000)$ slowing laser (Fig. 5.11(a)). For these tests, all lasers were broadened to cover a velocity spread of 100 m/s, with the repumping lasers covering 40-140 m/s, and the main line laser being detuned further so as to

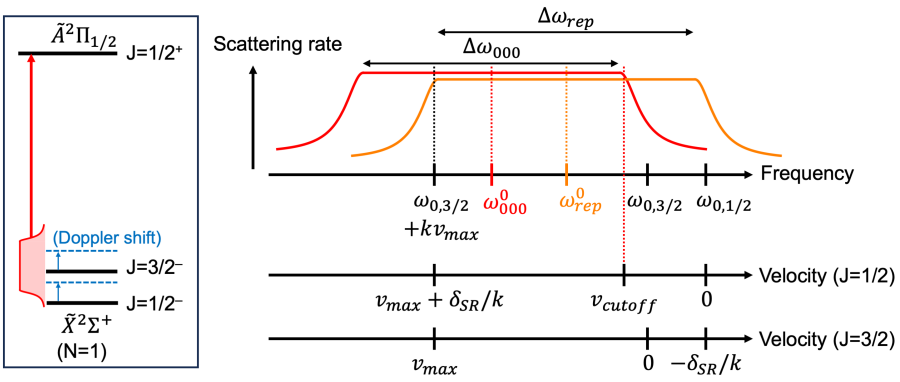

Figure 5.10: Schematic of white-light slowing laser frequencies. The system is divided into a main line $\widetilde{X}(000) \rightarrow \widetilde{A}(000)$ laser and a number of repumpers. The lasers are broadened over electronic transitions that contain two spin-rotation components split by $\delta_{\mathrm{SR}} = 2\pi \times 52$ MHz (inset). The main line laser has a center frequency of ω^0_{000} and a broadening of $\Delta\omega_{000}$, and the repumpers have a center frequency of ω^0_{rep} and a broadening of $\Delta\omega_{\mathrm{rep}}$. The repumpers are tuned to be resonant with zero-velocity molecules in $J = 1/2$ on the high-frequency side (this is a necessary condition to repump the MOT). The maximum slowed velocity v_{max} occurs when molecules in $J = 3/2$ are resonant with the low-frequency end of the repumping laser spectrum. While molecules in $J = 1/2$ can be slowed at higher velocities, they will rapidly be pumped into $J = 3/2$ and no longer be slowed. This means that the total velocity coverage is reduced by the spin-rotation splitting compared to the bare laser broadening, i.e. $v_{\mathrm{max}} = (\Delta\omega_{\mathrm{rep}} - \delta_{SR})/k$. The main slowing laser is detuned further, establishing a velocity cutoff $v_{\mathrm{cutoff}} \approx (\omega_{0,1/2} - (\omega^0_{000} + \Delta\omega_{000}/2))/k$, below which the scattering rate will decrease as molecules are pumped into the off-resonant $J = 1/2$ state. This cutoff can be used to help accumulate molecules at low velocity without overslowing [224].

address the velocity range v_c to $v_c + 100$ m/s, where v_c is the cutoff velocity. As shown in Fig. 5.11(a), reducing the velocity cutoff leads to accumulation of molecules at lower velocities, confirming that were are able to slow molecules and that the final velocity can be adjusted by tuning the white-light laser spectrum, as expected.

Next, we scanned the power of the main $\widetilde{X}(000) \rightarrow \widetilde{A}(000)$ while keeping the repumping powers constant, which allows us to reduce the scattering rate and therefore observe slowed molecules at easily detectable velocities (Fig. 5.11(b)). As we increase the power from 80 mW up to the "nominal" full slowing power of around 1.3 W, we see a decrease in the slowed molecule velocity and also an increase loss of molecules, largely due to optical pumping into vibrational dark states (note that we only had a budget of 6000 photons for this data, since the $\widetilde{X}(110)$

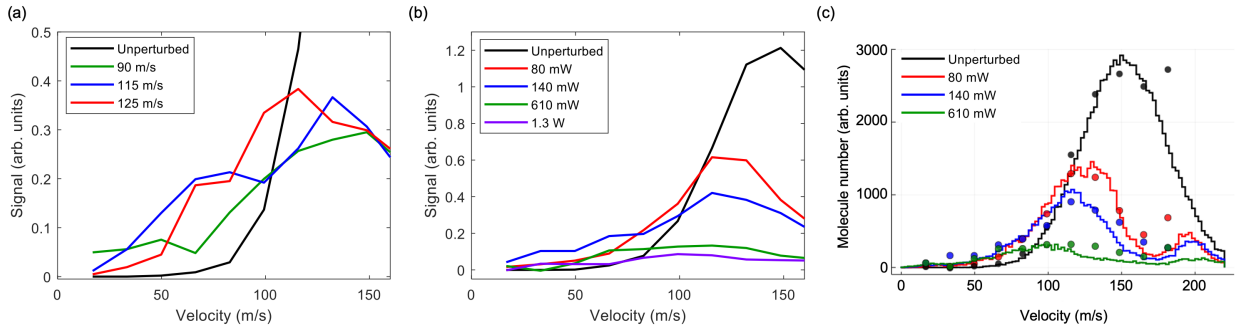

Figure 5.11: Initial slowing checks. (a) Slowed beam velocity as a function of the $\widetilde{X}(000) \rightarrow \widetilde{A}(000)$ main line laser velocity cutoff (i.e. the minimum resonantly addressed velocity). The data confirm that we can accumulate molecules at lower velocities as the cutoff is reduced. For this data, we used a wait time of 6 ms and set the repumping lasers to resonantly cover molecules from 40-140 m/s. (b) Power scan of the main $\widetilde{X}(000) \rightarrow \widetilde{A}(000)$ slowing laser, with all repumping powers fixed. This data was taken with the main line laser covering 40-180 m/s and the repumpers covering 20-160 m/s, with a 1 ms wait time and a 25 ms slowing pulse. (c) Monte Carlo simulation of slowing vs. main line power, including geometric losses and loss to vibrational dark states. Points are the data from part (b). The good agreement confirms that our slowing is working as expected, and is consistent with a maximum scattering rate of approximately 1.5×10^6 s^{-1} (at full >1W slowing power). Note that all data in this figure was taken without the $\widetilde{X}(110)$ repumpers, and so the photon budget was only approximately 6000.

repumpers had not yet been added). We compared the results to Monte Carlo simulations accounting for geometric and vibrational loss as well as the measured frequency spectrum of the laser (Fig. 5.11(c)). The data agree well with the simulations when assuming a scattering rate of around 1.5×10^6 s^{-1} at high power, which is consistent with out results from the depletion checks in sec. 5.3.3.

Having confirmed that we could accumulate molecules at velocities below 100 m/s, and that our data were consistent with Monte Carlo simulations, we proceeded to attempt slowing to lower velocities. As shown in Fig. 5.10, the range of molecule velocities covered by the slowing lasers is related to the center frequency and white-light EOM broadening of the lasers, and must take into account the fact that both ground-state spin-rotation components need to be resonantly addressed by some component of the frequency spectrum. To cover the full spread of molecule velocities during slowing, $\delta v \approx 140$ m/s, the frequency spectrum of each laser needs to have

a full width of roughly $\delta\omega = k\delta v + \delta_{\mathrm{SR}}$, where $\delta_{\mathrm{SR}} = 2\pi \times 52$ MHz is the spin-rotation splitting in the ground state.[25] For the red lasers ($\lambda = 2\pi/k \approx 620 - 650$ nm), this corresponds to a frequency broadening of $\delta\omega \approx 2\pi \times 270$ MHz. For the yellow lasers ($\lambda \approx 566 - 594$ nm), the required broadening is around 295 MHz. Broadening the repumpers further allows them to cover a wider range of velocities, but at the cost of a decreased power spectral density, which eventually reduces the scattering rate. Empirically, we found that a broadening of around 270 MHz for the red lasers and 295 MHz for the yellow lasers was, indeed, optimal for slowing to low velocities ($\lesssim 20$ m/s).

For our final slowing data, we set the center frequency of all the repumping lasers to approximately cover the velocity range $0 - 140$ m/s. Because these lasers are also used to repump the MOT, this is necessary to maintain a high scattering rate for those molecules. For laser slowing, we set the laser detunings based on our knowledge of the resonance frequency and frequency broadening, but once we achieved a MOT we found that some of the frequencies needed to be adjusted by 10s of MHz for optimal MOT brightness.

Unlike the repumpers, the main line $\widetilde{X}(000) \rightarrow \widetilde{A}(000)$ slowing laser frequency can be independently tuned (though with a broadening fixed to that of the repumpers since it shares the same EOM). We found that it is optimal to red detune this laser so that it is not resonant with 0 m/s molecules, and instead has a frequency cutoff at some finite velocity v_{cutoff}. The scattering rate will drop off for molecules below this velocity, which can potentially lead to accumulation near the capture velocity [224]. This may also improve MOT loading by reducing the force on the molecules in the MOT and making it possible to load some molecules even in the presence of slowing light. We optimized v_{cutoff} by monitoring molecule signal at 50 m/s and then 20 m/s, adjusting the laser

[25] The ground states with vibrational angular momentum $\ell \neq 0$ have smaller SR splittings, but this just means that the lasers will be slightly over-broadened for those states.

frequency to optimize the signal at each velocity class. We found that a cutoff velocity of $v_{\text{cutoff}} \approx 110$ m/s was approximately optimal for 50 m/s molecules, while a cutoff of $v_{\text{cutoff}} \approx 60$ m/s was optimal for accumulation of 20 m/s molecules. Molecules accumulate well below the cutoff velocity because of off-resonant scattering from the highly power-broadened slowing laser. This behavior was also observed in Ref. [224].

Up until this point, we had only been working with a photon budget of 6000, primarily because we did not have a laser repump $\widetilde{X}(110)$. Towards the end of our slowing work, we added the $\widetilde{X}^2\Sigma^+(110)(N=1) \rightarrow \widetilde{A}(010)\mu^2\Sigma^{(+)}$ repumping laser, first at several points transverse to the slowing beamline, and ultimately combined with the remaining lasers in the slowing path. This increased our photon budget to approximately 9100, improving the slowing efficiency considerably. Fig. 5.12 shows slowing data with and without the $\widetilde{X}(110)(N=1)$ and $\widetilde{X}(300)$ repumping lasers, allowing us to observe slowing at photon budgets ranging from ∼4600 up to ∼9100. The molecule survival after slowing improves by a factor of several with all repumpers added, and there appears to be nonnegligible population below the MOT capture velocity of ∼10 m/s. We also confirmed that there was significant slow molecule signal at 10 m/s, with both the $\widetilde{X}(110)(N=1)$ and $\widetilde{X}(300)$ repumpers (each of which plugs a vibrational leak at the 6×10^{-5} level) improving the slow molecule signal by a comparable amount (Fig. 5.13). At this point, we determined we had sufficient evidence of molecules below the MOT capture velocity, and that it was time to search for a MOT (sec. 5.4).

5.3.5 Chirped slowing

After obtaining a MOT, we decided to improve our slowing by switching from white-light slowing to chirped slowing. In chirped slowing, the main line $\widetilde{X}(000) \rightarrow \widetilde{A}(000)$ laser frequency is swept (or "chirped") over time in order to select which molecule velocities are optimally slowed. Compared to white-light slowing, where most

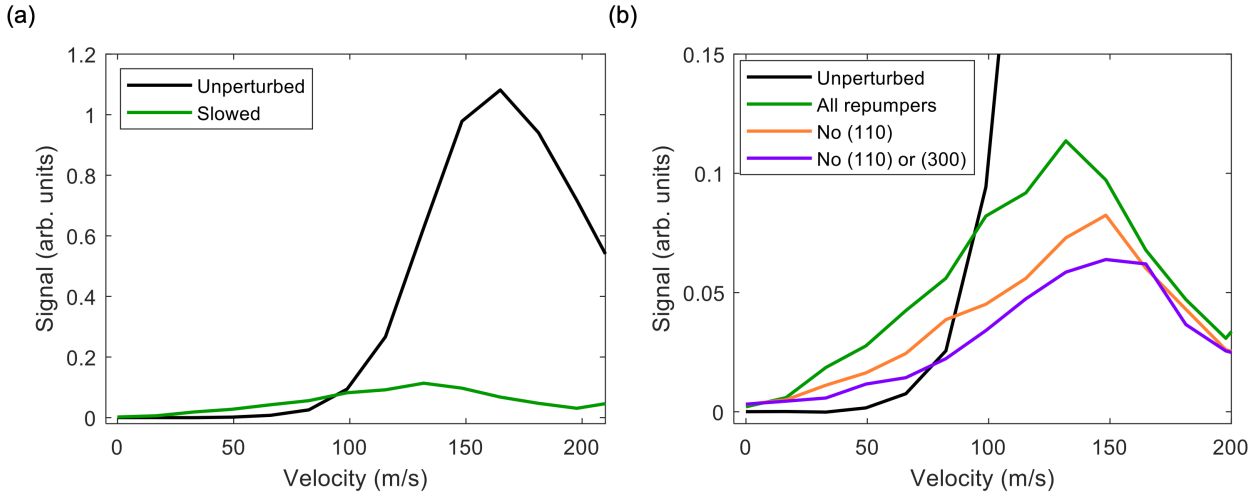

Figure 5.12: Slowing with all repumping lasers. (a) Comparison of unslowed and slowed molecular beams with all repumping lasers (photon budget of 9100). This data was taken with a 2 ms wait time after ablation, a 25 ms long slowing pulse, and a $\widetilde{X}(000) \rightarrow \widetilde{A}(000)$ cutoff velocity around 65 m/s. The $\widetilde{X}(110)(N=1)$ repumper was introduced in two regions transverse to the beam for this data. (b) Slowed beam velocities with all repumping lasers (∼9100) photons, with the $\widetilde{X}(110)(N=1)$ repumper removed (∼6000 photons), and with $\widetilde{X}(300)$ also removed (∼4600 photons).

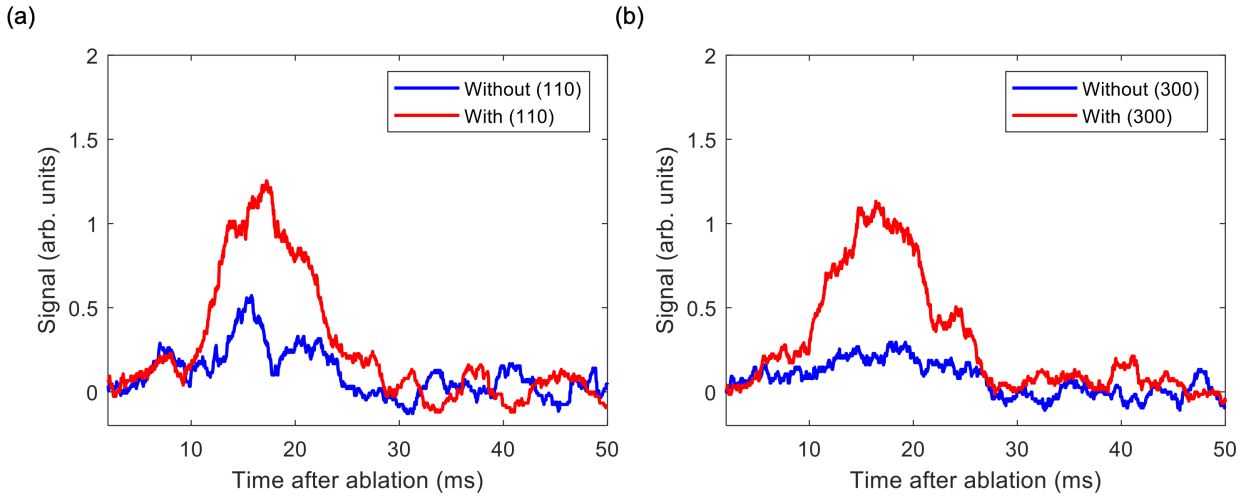

Figure 5.13: Accumulation of slow molecules at 10 m/s. (a) 10 m/s molecule signal with and without the $\widetilde{X}(110)(N=1)$ repumper. For this data, this repumper was combined with the other repumpers in the main slowing beam. (b) Same data with and without the $\widetilde{X}(300)$ repumper, which repumps a comparable vibrational decay channel. The accumulation of population in both cases indicates that molecules are being successfully slowed to low velocity, and that optimal slowing requires the full available photon budget. This data was taken with v_{cutoff} around 75 m/s.

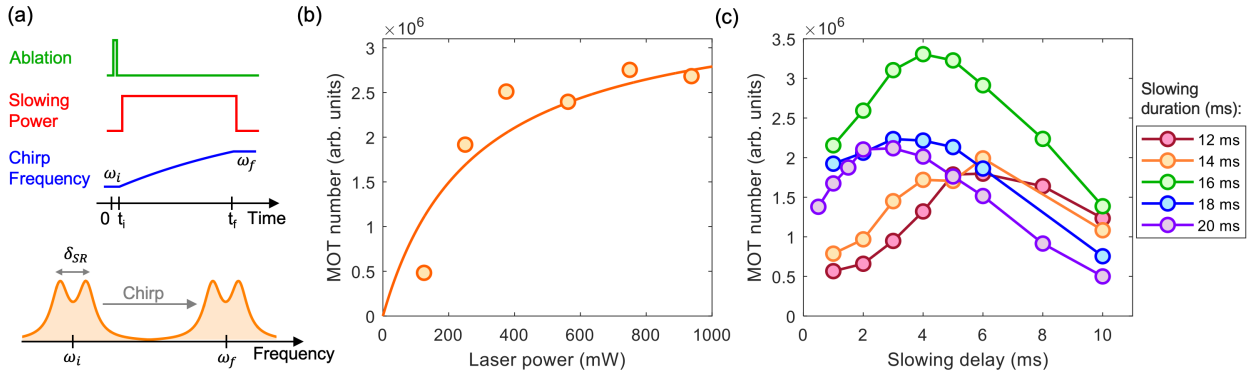

Figure 5.14: Chirped slowing of CaOH. (a) Outline of chirped slowing. After a short delay time after ablation, the slowing light is turned on and its center frequency is chirped from ω_i to ω_f over the slowing time, with the two frequencies chosen to roughly match the initial and final velocities of the molecular beam. The laser has two sidebands split by $\delta_{\mathrm{SR}} = 2\pi \times 52$ MHz to cover the spin-rotation splitting in the $\tilde{X}$ state. All repumpers are also on but are white-light broadened, not chirped. (b) Number of molecules in the MOT as a function of slowing power. The fit is to a saturation curve with a saturation power of approximately 300 mW. (c) MOT number as a function of slowing duration and slowing delay. An optimal MOT is achieved for a slowing duration of 16 ms and a slowing delay of 3 ms. (Note that the optimality of 16 ms data is likely exaggerated here due to ablation fluctuations. We typically observe 16 ms to be optimal, but not by as large a margin as seen in this data.)

molecules that are slowed to the MOT capture velocity get there at either the wrong position or the wrong time, chirped slowing slows the molecules to the desired velocity all at the same time. Chirped slowing can be very efficient for short molecular pulses because of the high correlation between position and time. This was experimentally demonstrated for CaF by the Tarbutt group, where a large gain over white light slowing was observed for the short molecular pulses produced by their buffer gas source [224]. In the Doyle group (whose buffer gas sources have longer pulse durations), the CaF experiment observed a $2\times$ increase in MOT numbers for chirped compared to white-light slowing [278]. An additional advantage of chirped slowing is that the main line slowing laser is less broadened, making it potentially more power efficient. Fig. 5.14(a) provides a schematic overview of the chirped slowing process.

To implement chirped slowing, we had to make a few upgrades to the experiment. Up until this point, we

had been using the same 626 nm SFG laser for both the white-light slowing and MOT. However, to implement chirped slowing, we needed a dedicated laser so that we could chirp its frequency without affecting the MOT detuning. Luckily, this was fairly straightforward because of the versatility of our SFG systems. As shown in Fig. 5.2, we took the dumped 1053 nm pump light from the MOT SFG system and combined it with 1546 nm light from a new 10 W fiber amplifier (IPG) on an SFG crystal (Covesion MSFG626-0.5-40) to make a separate 626 nm beam. By sweeping the frequency of the 1546 nm seed (QPhotonics QDFBLD-1550-100NN), we could chirp the slowing laser independently from the MOT laser. We chirp only the main slowing laser and leave all the repumping lasers white-light broadened. The chirped slowing beam was therefore combined with the repumpers after the white-light EOMs, and before the Pockels cell. To cover the 52 MHz spin-rotation splitting in the ground state, we modulate the laser using an EOM driven at 26 MHz, with an amplitude chosen to add only first-order sidebands.

To chirp the slowing laser, we modulated the current to the 1546 nm DFB seed by adding a chirp voltage (output from the Cicero control software) to the wavemeter locking voltage (output from Labview). We initially used a sample-and-hold circuit (similar to what was used in the CaF experiment [278]) to hold the locking voltage constant during the chirp and therefore prevent the wavemeter lock from interfering. However, we later added a threshold directly to the wavemeter locking software, wherein the laser lock would simply ignore frequencies sufficiently far from the setpoint. This worked sufficiently well to make the sample-and-hold unnecessary. Some fiber amplifiers are sensitive to fast seed frequency changes due to excessive back reflection in the fiber [278].[26] Luckily we observed no such effects for our chirped slowing IPG fiber amplifier.[27]

[26] For instance, we find that one of the IPG amplifiers used for the MOT SFG regularly shuts itself off if the seed frequency jumps.

[27] It is nonetheless a good idea to include a low-pass filter on the seed control voltage input as a precaution.

There are a number of parameters to optimize for chirped slowing. Along with the slowing duration, delay time, and laser power, we need to optimize the start and end frequencies and, potentially, the shape of the frequency sweep. We found that the optimal start and end frequencies for MOT loading corresponded to resonantly addressed velocities starting at $(\omega_0 - \omega_i)/k \approx 170$ m/s and ending at $(\omega_0 - \omega_f)/k \approx 20$ m/s. Here $k = 2\pi/(626\text{ nm})$, ω_0 is the molecule resonance frequency[28], and ω_i and ω_f are the slowing start and end frequencies, respectively. We ramped the frequency from ω_i to ω_f using a gentle exponential function, which was found to be slightly better than a linear ramp (and much better than an exponential with the wrong curvature).

We also scanned the slowing laser power and the chirped slowing timing to optimize the MOT loading, as shown in Fig. 5.14(b)-(c). We needed above around 500 mW of slowing power for optimal MOT loading (down from $\gtrsim$1 W required for white-light slowing). For the timing, we observed a correlation between the slowing duration and slowing delay, wherein shorter slowing durations required slightly longer delay times and vice versa. The optimal parameters appeared to be a wait time of 3 ms followed by a slowing duration of 16 ms.[29]

After implementing chirped slowing, we found that the MOT number improved by around 2x.[30]

5.4 Magneto-optical trapping

[28] Defined here as halfway between the two spin-rotation components.

[29] The optimal slowing timings and frequencies should be expected to change over time as the buffer gas source properties fluctuate. However, the slowing timings have been relatively stable over several years, with the slowing parameters as of the time of this writing (2.5 years after initial optimization) being a 2 ms delay and a 17 ms slowing duration. We find that tuning the start frequency ω_i of the laser, and sometimes the slowing duration, is usually sufficient to recover acceptable slowing performance over a range of molecule production conditions.

[30] Note that this is very approximate, since we did not do a careful back-to-back comparison with both slowing methods. However, this is in line with what was seen on the CaF experiment in Ref. [278].

5.4.1 Theory of molecular MOTs

A magneto-optical trap (MOT) uses radiative optical forces to simultaneously cool and trap atoms or molecules [304]. The essential idea is that red-detuned lasers are used to implement Doppler cooling, and a magnetic field gradient combined with carefully chosen laser polarizations adds spatial dependence, such that the atoms preferentially scatter photons from lasers that push them towards the center of the trap.

Atomic MOTs are typically implemented using type-I transitions, where the excited state has higher angular momentum than the ground state, $F' > F$. The principle is illustrated in Fig. 5.15(a), which shows a minimal model for a MOT in one dimension with a $F = 0$ ground state and a $F' = 1$ excited state. Two laser beams, both with frequency ω, are incident from either direction, with one laser having σ^- polarization[31] and driving atoms from $|F = 0, m_F = 0\rangle \rightarrow |F' = 1, m_F = -1\rangle$, and the other laser having σ^+ polarization and driving atoms to $m'_F = +1$. Because of the red-detuning of the lasers, atoms on the right side of the trap are closer to resonance with the left-pointing σ^- laser and preferentially scatter photons from it, pushing them towards the center of the trap. The same is true for atoms on the left side of the trap with the σ^+ laser. After being excited, atoms quickly decay back to $F = 0$ and start the process again.

For type-II systems like molecules, implementing a MOT is more challenging. As shown in Fig. 5.15(b) for a minimal model consisting of a $F = 1 \rightarrow F' = 0$ transition in one dimension, having more ground states than excited states means that molecules can fall into states that are dark to the trapping laser and only scatter photons from the anti-trapping laser (and the orthogonal lasers in a 3D MOT). As shown in Ref. [262], any type-II system with $F \geq F'$ and zero excited-state magnetic moment will have no net trapping force, since molecules are just as

[31] The polarization and magnetic field is defined relative to the $+z$ direction, so that $B_z > 0$ when $z > 0$ and $B_z < 0$ when $z < 0$.

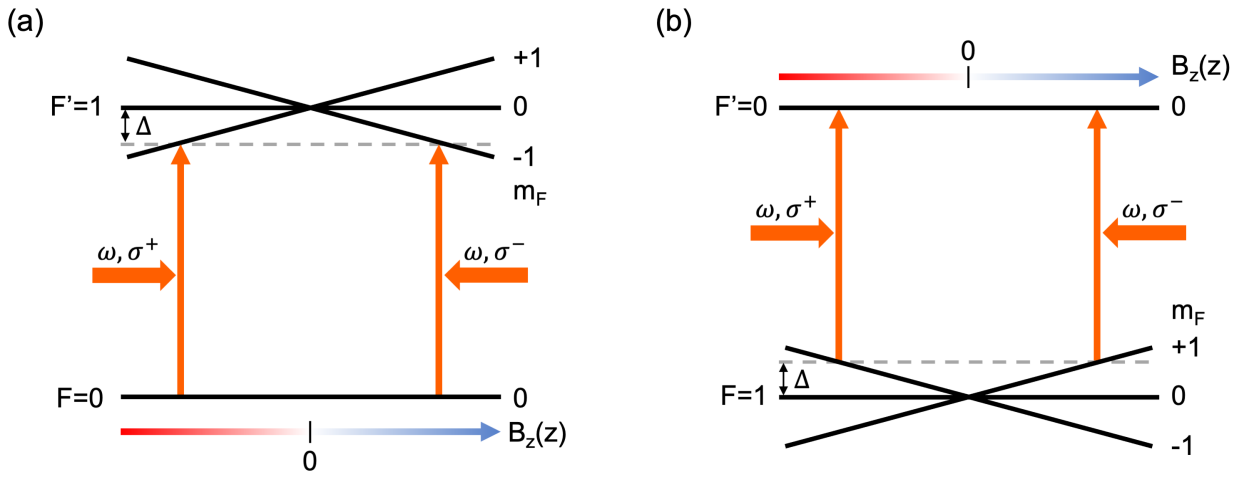

Figure 5.15: Illustration of type-I and type-II MOTs. (a) Type-I MOT with $F = 0$ and $F' = 1$. The magnetic field gradient splits the excited state into three m_F components as a function of position. Red-detuned lasers (detuning Δ) provide Doppler cooling, while their polarizations are chosen so that atoms preferentially scatter from the laser that tends to push them towards $z = 0$. For example, atoms on the right preferentially interact with the σ^- laser since $m_F = -1$ is closer to resonance than $m_F = +1$. (b) Type-II MOT with $F = 1$ and $F' = 0$. In this case, there is no net trapping force since molecules will be optically pumped into the lowest-energy m_F levels and, on average, end up scattering the same number of photons from both lasers regardless of their polarization [262].

likely to scatter from the trapping and anti-trapping lasers regardless of their polarization. Adding Zeeman shifts to the excited state breaks the ground state symmetry and turns on nonzero trapping forces, though they are still weak compared to type-I systems [262]. Unfortunately, CaOH has an extremely small excited state magnetic moment, with the Zeeman shift of the $m'_J = \pm 1/2$ components in the $\widetilde{A}^2\Pi_{1/2}$ state being approximately $\mp 0.022 \times \mu_B B_z$ [166]. The above argument therefore suggests that MOT forces for CaOH will be extremely weak.[32]

Luckily, as previously demonstrated for diatomic molecules with similar electronic structure [192–195, 299, 305], several techniques can be used to overcome these limitations, as shown in Fig. 5.16. The first (Fig. 5.16(a) is a "dual-frequency" mechanism, whereby a blue-detuned frequency with the opposite polarization is added to the MOT [261]. This provides a confining force for states that had previously been dark to the trapping laser, at the expense of adding a laser that contributes Doppler heating. However, provided the blue-detuned frequency is farther detuned than the red-detuned component, there is a net cooling force in addition to trapping. This scheme is naturally implemented in molecules like CaF, where the hyperfine spacing is small enough that a red-detuned laser addressing the second-highest hyperfine state ($F = 1$) naturally also provides a dual frequency effect for the highest ($F = 2$) hyperfine level [261]. In CaOH, the spin-rotation spacing is large enough ($\sim 8\Gamma$) that there is only a modest dual-frequency effect of this sort, so it is likely optimal to have two dedicated laser frequencies for at least the upper, $J'' = 3/2$ SR component.

The second approach is to remix magnetic sublevels that are dark to the trapping laser by modulating the magnetic field gradient and the laser polarization at a frequency on the order of the MOT scattering rate (Fig. 5.16(b)).

[32] Note that $\widetilde{B}^2\Sigma^+$ has a magnetic moment of order μ_B, so it is possible that DC MOTs would work better for that state, though then we would have to contend with undesired two-photon decays via the $\widetilde{A}$ state [224].

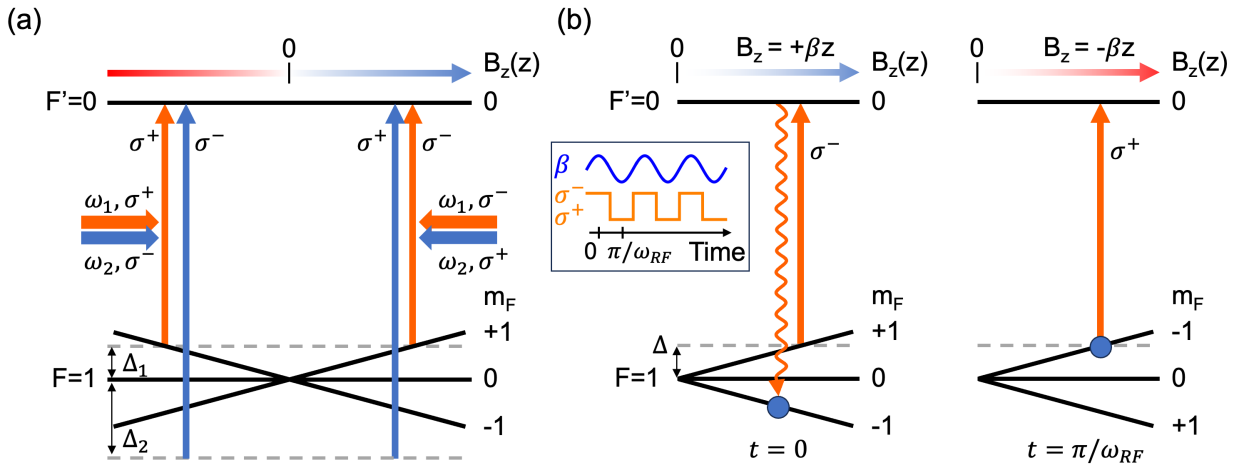

Figure 5.16: Dark state remixing techniques for molecular type-II MOTs. (a) Dual-frequency MOT. In addition to the red detuned frequency component ω_1, there is a blue detuned frequency components ω_2, which has opposite polarization and a larger detuning $|\Delta_2| > |\Delta_1|$. The second frequency provides a net trapping force for molecules pumped into the lowest-energy magnetic sublevels, while the higher detuning compared to the red component means that there is still net Doppler cooling. (b) Radio-frequency (RF) MOT. As shown in the inset, here the magnetic field gradient β and the laser polarization are modulated at a frequency ω_{RF}, which is on the order of the MOT scattering rate. Once molecules are optically pumped into anti-trapped states, the sign of the magnetic field and the polarization are reversed, remixing molecules back into trapped states and providing a net restoring force.

Changing the sign of the magnetic field remixes the magnetic sublevels, while changing the laser polarization maintains trapping after the magnetic field reversal. Note that the optimal way to do this is as proposed in Ref. [262], where the sign of the magnetic field is changed so quickly that the state cannot follow adiabatically, resulting in a change of internal state from m_F to $-m_F$, as shown in Fig. 5.16(b). In reality, the magnetic field spends a non-negligible time near zero when driven sinusoidally in the experiment,[33] so it is possible that nonadiabatic transitions will occur and slightly decrease the efficiency of the process. Nonetheless, it has been experimentally observed that RF molecular MOTs can obtain higher molecule densities than DC MOTs [194, 299].

MOT Forces

Provided dark states are properly remixed, the force on the molecules in the MOT (here focusing on the z axis) is the sum of the radiative forces from the two counter-propagating lasers [300]:

$$F_{\mathrm{MOT}}(z, v_z) = \frac{\hbar k \Gamma_{\mathrm{eff}}}{2}\left[\frac{s_{\mathrm{eff}}}{1 + s'_{\mathrm{eff}} + 4(\Delta - k v_z - \beta z)^2/\Gamma^2} - \frac{s_{\mathrm{eff}}}{1 + s'_{\mathrm{eff}} + 4(\Delta + k v_z + \beta z)^2/\Gamma^2}\right] \tag{5.3}$$

where Γ is the transition linewidth, Γ_{eff} is the effective linewidth accounting for the molecules' multi-level structure (eqn. 5.2), Δ is the detuning (defined so that $\Delta < 0$ for red detuning), $k = 2\pi/\lambda$ is the laser wavenumber, $\beta = \mu_{\mathrm{eff}}\langle B' \rangle/\hbar$ is the slope of the transition Zeeman shift, s_{eff} is the effective saturation parameter, and s'_{eff} is the modified saturation parameter accounting for the intensity of all lasers beams (2 beams in 1D, 6 beams in 3D). We have also defined an effective transition magnetic moment μ_{eff} that accounts for the many ground states with different g factors, and a time-averaged magnetic field gradient $\langle B' \rangle$. Linearizing F_{MOT} for small position and

[33] Because of the large voltages required to rapidly change the current, a sinusoid is the most experimentally feasible waveform.

velocity gives

$$F_{\mathrm{MOT}} \approx -\alpha v_z - \kappa z \tag{5.4}$$

where α is the damping coefficient and κ is the spring constant, defined as

$$\alpha = -\frac{8\hbar k^2 s_{\mathrm{eff}} \Gamma_{\mathrm{eff}} \Delta}{\Gamma^2 (1 + s'_{\mathrm{eff}} + 4\Delta^2/\Gamma^2)^2} \tag{5.5a}$$

$$\kappa = \frac{\beta \alpha}{k} \tag{5.5b}$$

Therefore, a working MOT should behave as a damped harmonic oscillator. Note that the effective scattering rate Γ_{eff} is typically below the value predicted by rate equations (e.g. eqn. 5.2), and both it and the effective magnetic moment μ_{eff} may be thought of as experimental fit parameters [220].

Implementing a MOT for CaOH

An overview of the MOT implementation for CaOH is shown in Fig. 5.17. Of course, the primary challenge for implementing a CaOH MOT is scattering the many photons required to apply significant optical forces. This is overcome using the vibrational repumping lasers shown in Fig. 5.17(a) and described at length earlier in this thesis. As described below, we measure an optimal oscillation frequency $\omega = \sqrt{\kappa/m} = 2\pi \times 59$ Hz and a photon scattering rate $R_{\mathrm{sc}} = 460 \times 10^3$ s^{-1} for the CaOH MOT, implying that nearly 8000 scattered photons are needed for a single trap oscillation. Therefore, the photon budget needed for the MOT is on the same order as that required for radiative slowing.

To remix dark states, we use the RF MOT approach for CaOH. As described above, an RF MOT was found

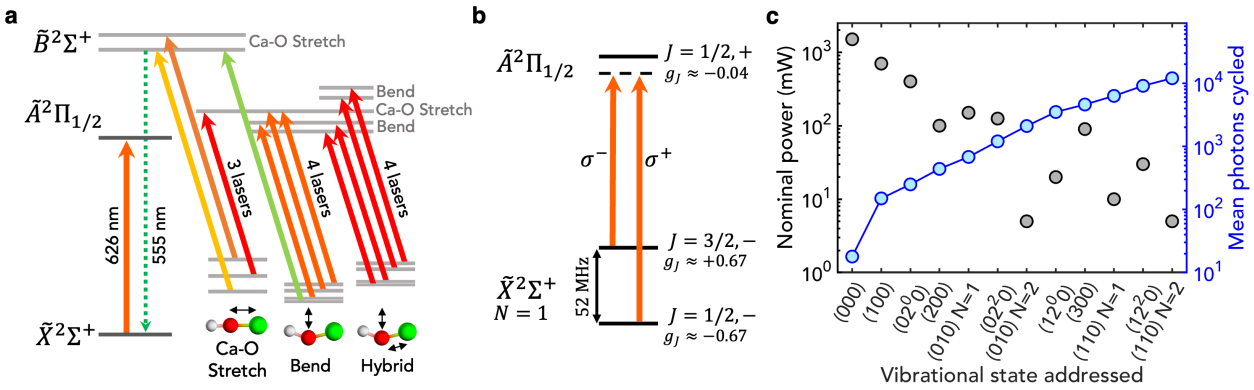

Figure 5.17: Laser cooling and repumping scheme. (a) The primary cycling transition for slowing and the MOT is the $\widetilde{X}\,^2\Sigma^+ \leftrightarrow \widetilde{A}\,^2\Pi_{1/2}$ transition at 626 nm. Spontaneous decay from the laser repumping the first Ca-O stretching mode is at 555 nm and is used for background free imaging. Decays to Ca-O stretch, bend, and hybrid vibrational modes in the electronic ground state are repumped though a number of excited vibronic states to attain a closure of ∼12,000 photons. (b) CaOH MOT polarization configuration. The MOT beams addressing the $\widetilde{X}(N'' = 1, J'' = 3/2, p'' = -)$ and $\widetilde{X}(N'' = 1, J'' = 1/2, p'' = -)$ ground states have opposite polarization due to their opposite g-factors. (c) Power of each slowing and repumping laser required to saturate the laser slowing and MOT efficacy (left axis; black). The right axis (blue) shows the mean number of photons, before $1/e$ loss of molecular population occurs, by adding all preceding repumping lasers (from left-to-right) [251, 269]. Lasers are labeled by the vibrational state repumped, notated as $(v_1 v_2^{\ell} v_3)$, where v_1, v_2, and v_3 are the vibrational quantum numbers for the Ca–O stretch, Ca–O–H bend, and O–H stretch modes, respectively, and ℓ is the projection of the vibrational angular momentum onto the molecular axis. Reproduced from Ref. [42].

to give higher density than a DC MOT for CaF [278]. If anything, the situation is expected to be worse for CaOH because there will be very little dual-frequency effect unless additional sidebands are added (due to the 52 MHz spin-rotation splitting in CaOH, which is roughly double the $F = 2 - F = 1$ hyperfine splitting that naturally provides dual-frequency trapping in CaF [261]). To make the RF MOT, we used two sidebands with opposite polarization addressing the $J = 3/2$ and $J = 1/2$ spin-rotation components of the ground state, as shown in Fig. 5.17(b). Opposite polarizations are used because the g-factors of the two states have opposite sign.

5.4.2 Optical setup

A schematic overview of the setup used to generate MOT light (along with cooling and imaging light for the experiments in later chapters) is shown in Fig. 5.18. The 626 nm $\widetilde{X}^2\Sigma^+(000) \rightarrow \widetilde{A}^2\Pi_{1/2}(000)$ SFG is locked to the wavemeter approximately 200 MHz below resonance. A double-pass AOD (IntraAction ADM-802AF1.626; optical setup shown in detail in Fig. 5.2) is used to bring the laser near resonance, globally tune the frequency and intensity of the cooling light, and also globally turn the light on and off. The light is then fiber coupled to a polarization switching board, which uses two AOMs to turn on and off beams of opposite linear polarization. (We previously used a Pockels cell (Conoptics 350-210-01-RP) for polarization switching, but moved to the AOM setup because of slow polarization drifts after turning off the Pockels cell, which prevented us from making a DC MOT.) The light is again fiber coupled to a sideband board (colloquially, the "hyperfine board"), which uses AOMs to add sidebands of various frequency, amplitude, and polarization. The sideband configuration depends on the type of cooling applied (RF MOT, DC conveyor-belt MOT, Lambda cooling, single frequency cooling, imaging, etc.). The sidebands are combined in a 4x4 PM fiber combiner (Evanescent Optics), and three of the output fibers are used for the MOT beams, which are expanded to a $1/e^2$ diameter of 10 mm, sent through $\lambda/4$

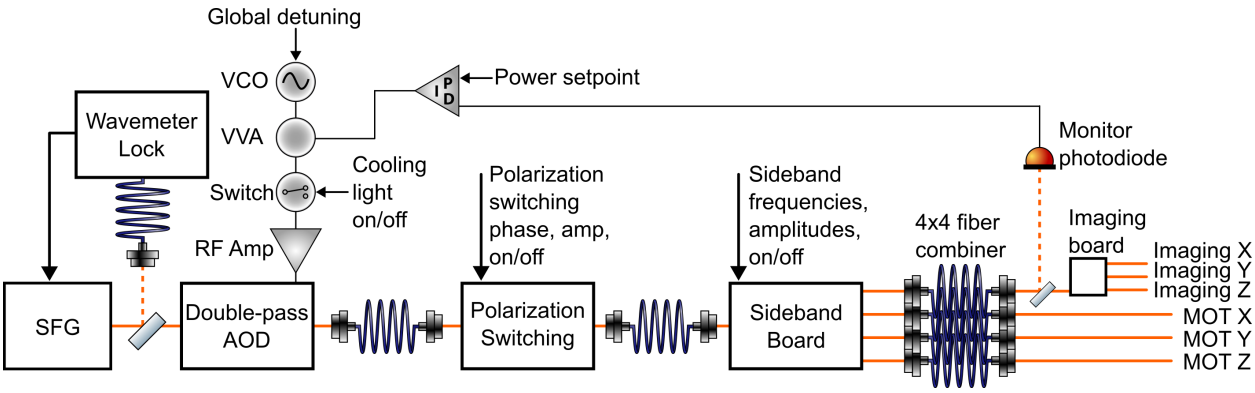

Figure 5.18: Overview of the setup used to prepare main line $\widetilde{X}(000) \rightarrow \widetilde{A}(000)$ light for the MOT, cooling, and imaging. The setup is described in the text.

waveplates and into the chamber, and retroreflected back from the far side of the chamber via another $\lambda/4$ waveplate. The fourth output fiber is evenly split using free space optics into three new beams, which are fiber coupled to the MOT chamber and used as small ($\sim$1.5 mm $1/e^2$ diameter) imaging beams for diagonal $\widetilde{A} \rightarrow \widetilde{X}$ detection, which we used for the optical tweezer and collision experiments described later in this thesis. Additionally, a portion of this fourth fiber output is picked off and sent to a photodiode. The PD signal is used to monitor the laser power and is also sent to a servo, which stabilizes the laser power by feeding back on the RF power to the double-pass AOD.

There are shutters installed in the path of each of the the three MOT beams and three imaging beams, which can be used to independently turn on one set of beams or the other. These are also closed when the molecules are held in an optical trap for long durations, to prevent leaked light through the AOD from weakly exciting the molecules. We also found that for very long hold times with MOT light off ($\gtrsim$1 s), it was helpful to close the shutters but leave the double-pass AOD on, which helped with thermal stability since the default configuration (i.e. when the experiment is not running) is to have the AOD continuously on.

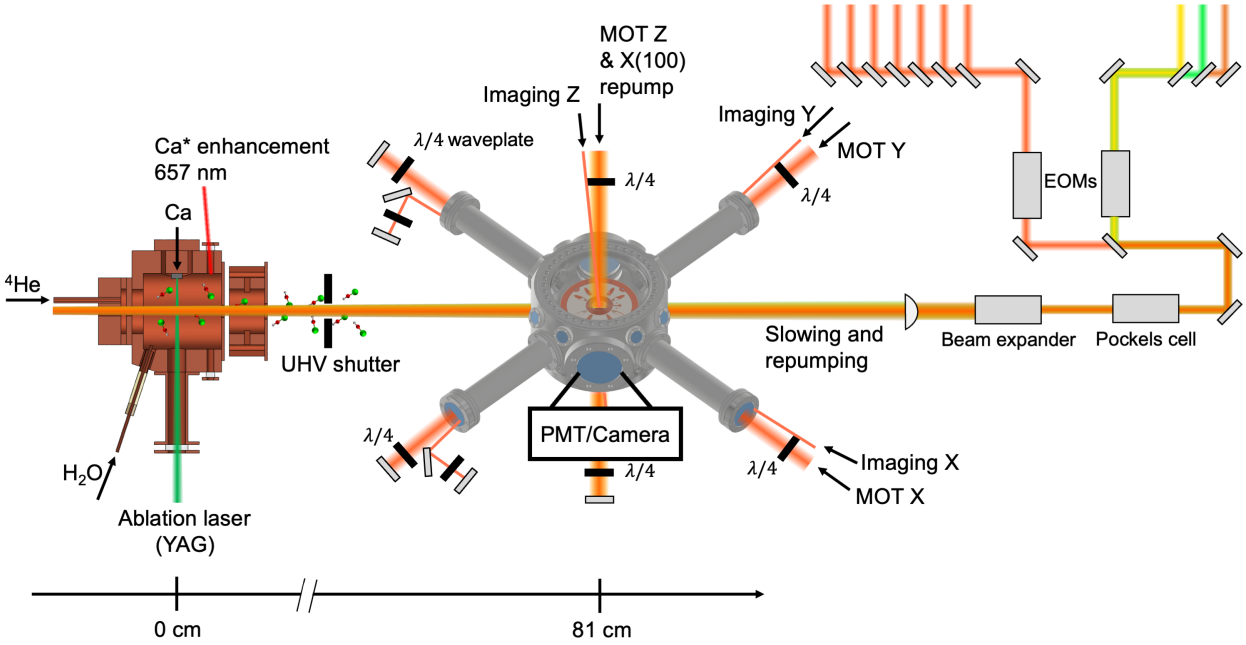

Figure 5.19: Overview of the experimental layout with slowing, cooling, and imaging laser beams.

The general layout of the MOT chamber with optics is shown in Fig. 5.19. Along with the slowing, MOT, and imaging beams (which were not added until the tweezer work), we include 574 nm $\widetilde{X}(100) \rightarrow \widetilde{B}(000)$ repumping light (with 52 MHz spin-rotation sidebands) in the vertical (Z) arm of the MOT chamber. This is because approximately one out of every 20 photons is scattered from this laser, so if it is only included in the slowing arm it provides a significant pushing force that moves the equilibrium MOT position. Adding this repumper in one of the MOT arms reduces the net force by a factor of 3, and we experimentally observed that this significantly reduced the MOT displacement. We often turn off the $\widetilde{X}(100)$ repumper in the slowing arm once the MOT is loaded, and just use the vertical repumping light. Note that all of the other MOT repumping is done using the slowing repumpers, which remain white-light broadened but still cover velocities around 0 m/s. The pushing force from these repumpers is negligible.

To detect molecules in the MOT, we use either an EMCCD camera (Andor iXon3) for spatial information, or a PMT (Hamamatsu R7600P-200) for temporal information. These can be interchangeably installed at the focus of the imaging system. The imaging system consists of four lenses: a 2" diameter lens with a focal length of 200 mm to collect the MOT fluorescence directly outside the chamber, followed by a 1:1 relay, with an iris installed at the intermediate focal plane for spatial filtering. The final lens, which focuses the image onto the camera or PMT, sets the magnification of the system. The measured collection efficiency of the imaging system was 0.15%.

For imaging the MOT, we collected 555 nm fluorescence from the $\widetilde{B}(000) \rightarrow \widetilde{X}(000)$ decay, which happens approximately once every 18 scattered photons. This wavelength is background-free with respect to the slowing and MOT lasers, scattered light from which would overwhelm the molecule signal if we detected main line $\widetilde{A}(000) \rightarrow \widetilde{X}(000)$ fluorescence. We used a filter stack consisting of Semrock 561RU and 554/23 filters, with a colored glass filter (Thorlabs FGL530) in between. This sufficiently attenuated all laser wavelengths, including the 566 nm $\widetilde{X}(010)$ repumper 11 nm away from the imaging transition.

5.4.3 RF MOT coils

To make an RF MOT, we need to apply magnetic field gradients that oscillate at frequencies around 1 MHz, with an RMS gradient on the order of 10 G/cm. This presents a significant challenge because of the large RF powers required. We use in-vacuum coils, which allow us to use relatively low currents to achieve the desired gradient, and also keep the inductance low. Using coils with a modest inductance of around 10 μH, if we try to apply a 2 Arms current to the coils at 1.4 MHz, the required voltage will be hundreds of volts, and the corresponding RF power will be hundreds of watts. When compressing the MOT, we need higher gradients and these numbers

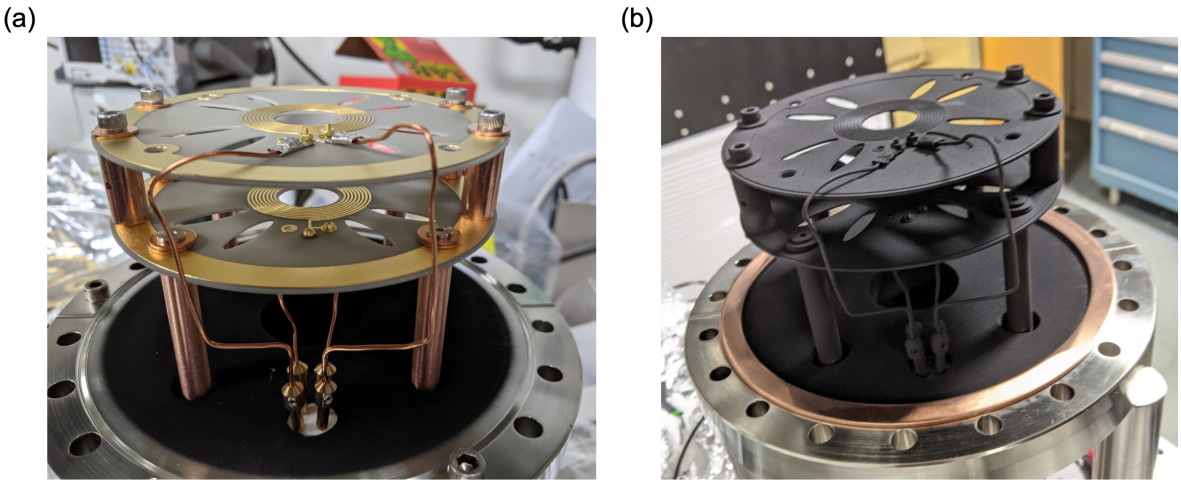

Figure 5.20: In-vacuum RF MOT coils (a) before and (b) after blackening with MH2200 paint. The coils are mounted on the CF flange used to install them in the MOT chamber.

increase significantly. Along with the challenge of generating these large RF powers, additional challenges include dissipating heat from the in-vacuum MOT coils and minimizing electric fields seen by the molecules. These problems and their solutions were discussed at length in Ref. [278]. In the CaOH experiment, our RF MOT coils are closely modeled after the ones designed for the CaF 2nd generation apparatus in our group, described in Ref. [274].

The in-vacuum RF MOT coils are shown in Fig. 5.20. Each coil consists of a pair of copper spirals bonded to a ceramic aluminum nitride board (Remtec). Each spiral has 8 turns, with an inner diameter of about 23 mm and an outer diameter of about 45 mm. The two boards are spaced by 25.4 mm, and the two spirals on each board are separated by 1.6 mm. The axial magnetic field gradient produced by the coils is 4.7 G/cm/A. Heat loads are effectively carried away by thick copper feedthroughs leading out of the chamber (these rods are also the structural mounts for the coils). The high thermal conductivity of the AlN substrate is also important for making this process effective. At our typical experimental duty cycles (MOT coils on for ∼10-20 ms every 1-2 seconds), we

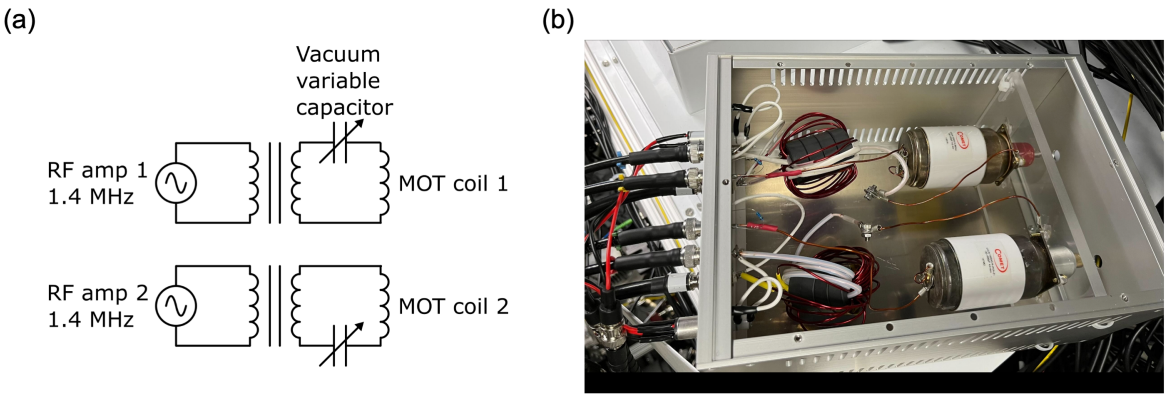

Figure 5.21: RF MOT tank circuit. (a) Schematic. Two independent RF amplifiers and tank circuits are used to drive the two MOT coils in a symmetric configuration. (b) Tank circuit installed on the experiment.

observe no significant heat management issues.

Each coil is driven using a series resonant tank circuit and a high-power RF amplifier. The tank circuit consists of a high voltage vacuum variable capacitor in series with the MOT coil (Fig. 5.21). A homemade transformer is used to impedance match the RF amp side to the side with the MOT coil and capacitor. The RF signals for the two coils are generated using two channels of an arbitrary waveform generator (Rigol), which is phase-locked to the signal generator used for polarization switching of the MOT light. The amplitude of these signals are controlled with an analog voltage from the experimental control software, which can be used to ramp the RF gradient during a sequence, e.g. for MOT compression. Each RF signal then passes through an RF switch, a 2W preamplifier, and then a high power, 1kW RF amplifier. The RF power amplifiers are based on LDMOS devices and are described in Ref. [274]. We initially used lower-power commercial amplifiers (ENI 550L), but switched to the 1 kW, home-built system once we needed to compress the MOT for ODT loading.

Because of the large voltages on the coils, we need to worry a bit about electric fields at the molecule location, which could mix opposite-parity Λ-doublets in the $\widetilde{A}^2\Pi_{1/2}$ state, turning on lossy decays to ground states of the

wrong parity [278]. Using independent tank circuits and amplifiers for the two coils allows us to manage electric fields as long as we're careful about their orientation. To see this, consider a simple model of the voltage and current on the coils. In anti-Helmholtz configuration, the current on coil 1 is $I_1(t) = I_0 \sin(\omega_{\mathrm{RF}} t)$ and the current on coil 2 is $I_2(t) = -I_0 \sin(\omega_{\mathrm{RF}} t)$. The voltage drop across the coils is therefore $\Delta V_{1,2}(t) = \pm V_0 \sin(\omega_{\mathrm{RF}} t)$, where $V_0 = L I_0 \omega_{\mathrm{RF}}$, L is the coil inductance, and $\pm$ refers to coils 1 and 2, respectively. If the tank circuit is oriented the same for both coils (i.e. if the capacitor is on the same end of both), the molecules will see an oscillating electric field with an amplitude of roughly $2V_0/d$, where d is the distance between the coils. However, if the tank circuits are symmetric, as shown in Fig. 5.21(a), the voltages on the two coils will be approximately equal, resulting in no electric field.

To tune the impedance matching once the coils are installed in the chamber, we monitor the current on both coils using current probes. The goal is to achieve as large an amplitude as possible while having the currents from the two coils equal in amplitude and 180° out of phase. To do this, we tune the amplitude and relative phase between the two channels on the RF signal generator, while also adjusting the vacuum variable capacitor in both tank circuits. Finally, we adjust the phase of the laser polarization switching to be aligned with the MOT coil currents by monitoring the polarization using a beamsplitter and photodiode. This provides a reasonable starting point for the RF MOT phase, but should ultimately be optimized by feeding back on the MOT signal after a MOT is obtained.

While the core RF MOT setup described here remained intact for all of the experiments described in this thesis, over time it was heavily accessorized to add the ability to apply more fields to the MOT coils. For instance, we added the capability to apply DC currents to make a blue-detuned conveyor belt MOT; DC electric fields to polarize CaOH molecules in the bending mode; and RF electric fields for driving transitions between molecules in

the bending mode. We also found that RF noise (both around 1 MHz and at higher frequencies associated with switching power supplies) from the high power RF amplifiers degraded the fidelity of some of our single-state control sequences for CaOH. To mitigate this problem, we eventually added a low-pass filter at the output of the power amplifiers to suppress high frequency noise, and a switchable short that suppressed low-frequency noise. These additions will be described later in this thesis.

5.4.4 Initial MOT signal

In our initial searches for the MOT, we compared data sets with the laser polarization switching in phase and 180° out of phase with the RF magnetic field gradient. In one configuration, the average spatial force would be trapping ("MOT configuration"), and in the other configuration, the average spatial force would be anti-trapping ("anti-MOT configuration"). Comparing data traces taken this way would allow us to isolate magneto-optical trapping effects from other parameters impacting our signal, e.g. from changes to the slowing or cooling parameters.

We initially searched for the MOT using a PMT collecting 555 nm $\widetilde{B}(000) \rightarrow \widetilde{X}(000)$ fluorescence. We observed a clear increase in beam brightness in the MOT vs. anti-MOT configuration even in the absence of slowing light. This demonstrated that we were able to apply magneto-optical forces to our beam, but at this point we were only compressing the molecular beam, not trapping molecules. When we increased the slowing time, fewer molecules survived, and the difference between MOT and anti-MOT configurations became less pronounced. We were unable to observe a clear signature of a MOT for a few days under these conditions.

At this point, we made a few small changes. On the molecule production side, we switched from a 10 mm-long 2nd-stage buffer gas cell to a 20 mm-long 2nd-stage cell, which was the optimal determined during our buffer gas

cell tests (sec. 3.5). (It is unclear how important this was for making the MOT.) We also installed an EMCCD and imaging system (described above) to look for spatial signatures of trapping. By comparing the imaged molecule signal with and without the MOT coils on, we were able to determine where the magnetic field zero was. We then aligned the three MOT beams one by one to maximize molecule fluorescence at that position. This ensured that the MOT beams were centered at the expected MOT location.

After optimizing the beam alignment, we switched back to the PMT, this time with spatial filtering (by partly closing an iris in an intermediate focal plane of the imaging system) to ensure it was only detecting molecule fluorescence from the region near the magnetic field zero. We then began to look at MOT/anti-MOT data as a function of slowing duration. We expected it to take only approximately 15 ms for slow molecules to arrive at the MOT chamber, but we nonetheless increased the slowing time well beyond this in hopes of observing some signal. As shown in Fig. 5.22, as we increased the slowing duration beyond 20 ms we began to observe a long-lived difference between the two traces. This feature was optimal at a slowing duration of 28 ms.

After obtaining this initial signal, we were able to quickly optimize it. We began by adding a $\sim$5 ms ramp to decrease the MOT beam power after a 5 ms hold at the full intensity. This had the effect of reducing the scattering rate and thereby increasing the MOT lifetime out to tens of ms after the end of slowing. We then switched to the EMCCD and were able to optimize the MOT to the point where it could be imaged in a single shot (with a 40 ms exposure). This was done by adjusting laser frequencies[34], beam alignment, and MOT beam collimation while monitoring the signal in real time.

[34] A number of repumper frequencies had been too red detuned and were adjusted by 10s of MHz. This is possibly because optimal slowing does not require the repumpers to resonantly cover all the way down to 0 m/s, but MOT loading will require even slightly negative velocities to be repumped.

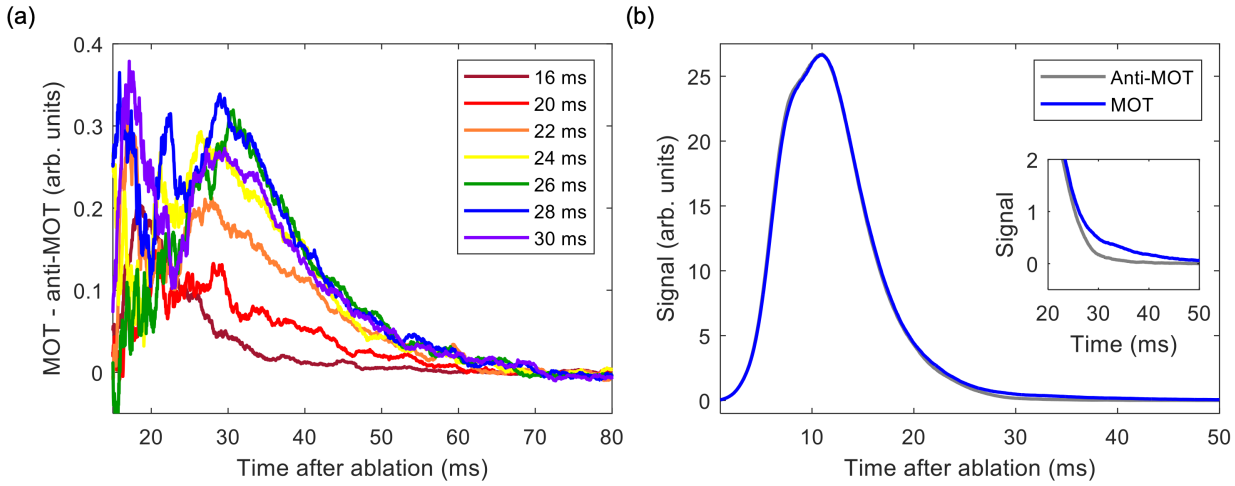

Figure 5.22: Initial signatures of a CaOH MOT. (a) Difference between MOT and anti-MOT signals as a function of slowing duration (with a wait time 1 ms). For this data, we had the MOT beams on continuously (until approximately 40 ms after slowing) at a power of 40 mW per beam and a detuning of approximately $-\Gamma$ ($\sim$6 MHz). (b) Full PMT traces for MOT and anti-MOT configurations at a slowing duration of 28 ms. The initial MOT signal appeared as a very small difference between MOT and anti-MOT signals (magnified in the inset) on the tail of the slowed beam.

5.4.5 MOT optimization

After getting the initial MOT signal, we systematically optimized a number of parameters. These included (roughly in the order they were optimized):

- Ablation energy and position (regularly optimized during normal running)
- MOT beam alignment and collimation
- Repumping laser frequencies
- White-light slowing delay and duration (Fig. 5.9)
- Slowing and repumping laser powers. Approximate minimum laser powers required in the slowing/repumping beam path are shown in Fig. 5.17(c).
- MOT loading detuning, intensity, and hold time (slightly higher detunings, and significantly higher intensities, were found to be optimal for MOT loading compared to the final MOT hold)

- Intensity ramp after MOT loading (ramp duration and shape, as well as the final hold power and detuning)
- Ca $^3P_1$ enhancement power, duration, and alignment
- Buffer gas flow rate
- Magnetic field gradient
- Relative phase between laser polarization and magnetic field gradient
- Pockels cell bias voltage and amplitude (sets the polarization cleanliness for the polarization switching MOT beams)
- Intensity ratio between $J = 1/2$ and $J = 3/2$ frequency components. Having approximately 2/3 of the power addressing $J = 3/2$ and 1/3 addressing $J = 1/2$ was found to be optimal.

After optimizing these parameters, we added the $\widetilde{X}(110)(N = 2) \rightarrow \widetilde{A}(010)\kappa^2\Sigma^{(-)}$ repumper, which increased our photon budget from approximately 9100 to 12000 photons. This improved the MOT number by approximately a factor of 2, as shown in Fig. 5.23.

After optimizing the MOT, the experimental sequence used to load the MOT was as follows. The slowing lasers are turned on 1 ms after ablation of the calcium target, and are held at constant power for a duration of 23 ms. During this time, the MOT beams are held at a power of 33 mW per beam with a detuning of -2.0Γ, where $\Gamma = 2\pi \times 6.4$ MHz is the natural linewidth of the cooling transition. When the slowing beam is turned off, the intensity in each MOT laser beam is ramped down to 3 mW over 5 ms, and the detuning is simultaneously ramped to -0.9Γ. All repumping lasers that are used for slowing (that is, all except for the main cycling laser at 626 nm) are kept on for the full MOT sequence to address vibrational and rotational dark states inside the MOT. Thus, the same frequency-broadened repumping lasers are used for repumping molecules during all three tasks of the experiment: slowing, magneto-optical trapping and sub-Doppler cooling (see below).

The complete MOT loading sequence is shown in Fig. 5.24.

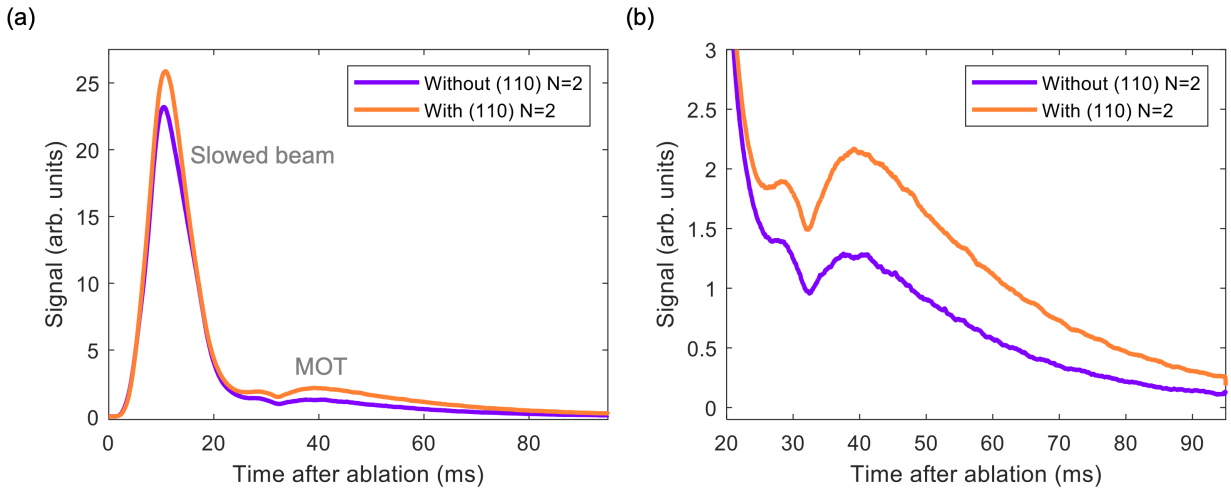

Figure 5.23: Comparison of the MOT fluorescence on a PMT with and without the $\widetilde{X}(110)(N = 2)$, which was added while optimizing the MOT to increase the photon budget from approximately 9100 to 12000 photons. (a) Full PMT trace, including the slowed beam for scale. (b) Zoom-in on the MOT portion of the PMT trace. Adding this repumper increases the MOT brightness by nearly a factor of 2 from a combination of improved slowing and MOT lifetime. Compare these PMT traces to Fig. 5.22 to see the improvement in MOT signal after the full optimization process.

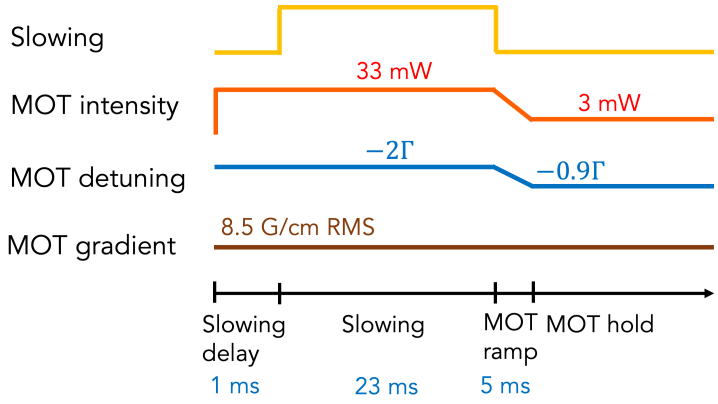

Figure 5.24: Sequence used for MOT loading. Immediately after slowing is turned off, the detuning and intensity are ramped to their final values, at which point the temperature and size equilibrate to the values discussed in sec. 5.4.6.

5.4.6 Optimized MOT properties

To characterize the MOT, we collect fluorescence photons emitted at 555 nm resulting from spontaneous emission on the $\widetilde{B}\,^2\Sigma^+ \rightarrow \widetilde{X}\,^2\Sigma^+$ transition. In our photon cycling scheme, approximately one out of every 18 photons scattered during laser cooling occurs at this wavelength (Fig. 5.17(a)). This imaging scheme enables background-free detection due to the absence of cooling or repumping lasers at 555 nm. As shown in Fig. 5.25(a), the MOT manifests itself as a persistence of molecular fluorescence (collected on a photomultiplier tube (PMT)) at long times after the slowed molecular beam has fully passed through the trapping region. The signal is observed to decay exponentially due to molecules being lost from optical cycling into higher vibrational dark states. By selectively removing repumping lasers during trapping, the average number of photon scatters during cooling may be varied. We observe that the MOT lifetime depends linearly on the number of photons scattered, as expected (Fig. 5.25(b)). We extract from the lifetime measurements a scattering rate of $4.6(1) \times 10^5$ s^{-1}. By decreasing the intensity of the MOT laser beams after initial loading, the overall scattering rate can be reduced, extending the MOT lifetime beyond 100 ms (Fig.5.25(a) inset).

Next, we measure the cooling of molecules and the damping of their motion in the MOT. The MOT forces may be approximated at low velocity and displacement as those of a damped harmonic oscillator, $F/m = -\beta v - \omega^2 r$. Here v and r are the velocity and position in the trap, and β and ω are the damping constant and trap frequency, respectively. To measure these properties, we observe the MOT after an intentional spatial displacement. After loading the MOT and ramping the MOT light to a power of 3 mW per beam, the slowing laser is turned on for 1 ms in order to displace the cloud of CaOH molecules from its equilibrium position. After a variable wait time, the molecules are imaged for 1 ms on an electron multiplying CCD (EMCCD) camera and the

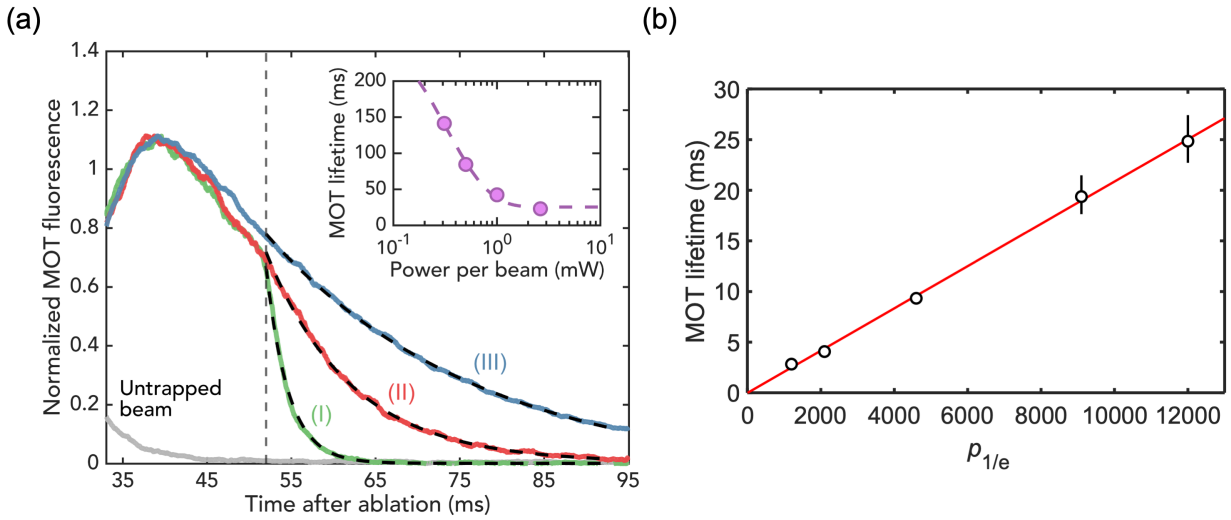

Figure 5.25: MOT lifetime versus number of states repumped. (a) CaOH fluorescence is plotted as a function of time for an untrapped molecular beam (grey curve), and for molecules trapped in the MOT, with select repumpers switched off at 52 ms (vertical dashed line; curves (I)-(III)). The configurations achieve $1/e$ population loss after (I) 1200 photons scattered (5 repumping lasers), (II) 4600 photons (8 repumpers), and (III) ∼12,000 photons (11 repumpers). (I)-(III) are normalized to their mean signal from 35 to 52 ms. The untrapped beam is normalized to the average of (I)-(III) from 1 to 35 ms (during which time fast, untrapped molecules pass through the MOT region). Dotted lines are exponential fits, from which we extract MOT lifetimes of 2.60(3) ms, 10.1(2) ms, and 25.7(6) ms for (I)-(III). Errors are 1σ fit errors. Inset: MOT lifetime versus power per MOT beam. The dotted line is a guide to the eye. (b) Fitted MOT lifetime vs. $1/e$ photon budget. The fit gives a scattering rate of approximately 460×10^3 s^{-1}. Modified from Ref. [42].

center position extracted (Fig. 5.26(a)). The observed maximum displacement increases with decreasing MOT intensity as the MOT forces weaken relative to the constant pushing force. Nonetheless, we find that the maximum displacement is $\lesssim$3 mm in all cases, implying that both the position, r, and velocity, $v = \dot{r}$, of the molecules is small enough that the MOT force may be Taylor expanded about $r = v = 0$ to yield [297]:

$$\ddot{r} + \beta\dot{r} + \omega^2 r = 0 \tag{5.6}$$

where β is the damping constant and ω is the oscillation frequency. We fit the center position of the CaOH molecular cloud, as a function of time, to the solution of eqn. 5.6 for an underdamped harmonic oscillator:

$$r(t) = r_0 + ae^{-\beta t/2}\sin(\sqrt{(\omega^2 - \beta^2/4)}t - \phi) \tag{5.7}$$

where r_0 is the equilibrium position, a is the amplitude, and ϕ is a phase.

At the optimal MOT power of 3 mW per beam, we measure a damping constant $\beta = 455(85)$ s^{-1} and an oscillation frequency $\omega = 2\pi \times 59(4)$ Hz. The observed damping constant and frequency are comparable to those achieved in MOTs of diatomic molecules [193, 194]. Moreover, the characteristic damping time $\beta^{-1} \approx 2.9$ ms at this intensity is much shorter than the $1/e$ MOT lifetime of 25.7(6) ms (Fig. 5.25), indicating that significant cooling and compression of the MOT is possible. The damping is lower for MOT laser powers both above and below the optimal (see Fig. 5.26(a)), as expected [297].

The temperature of the molecules in the MOT is measured by time-of-flight expansion. The MOT light is held at fixed power for ~15 ms following the initial ramp, and then the MOT lasers and anti-Helmholtz coils are

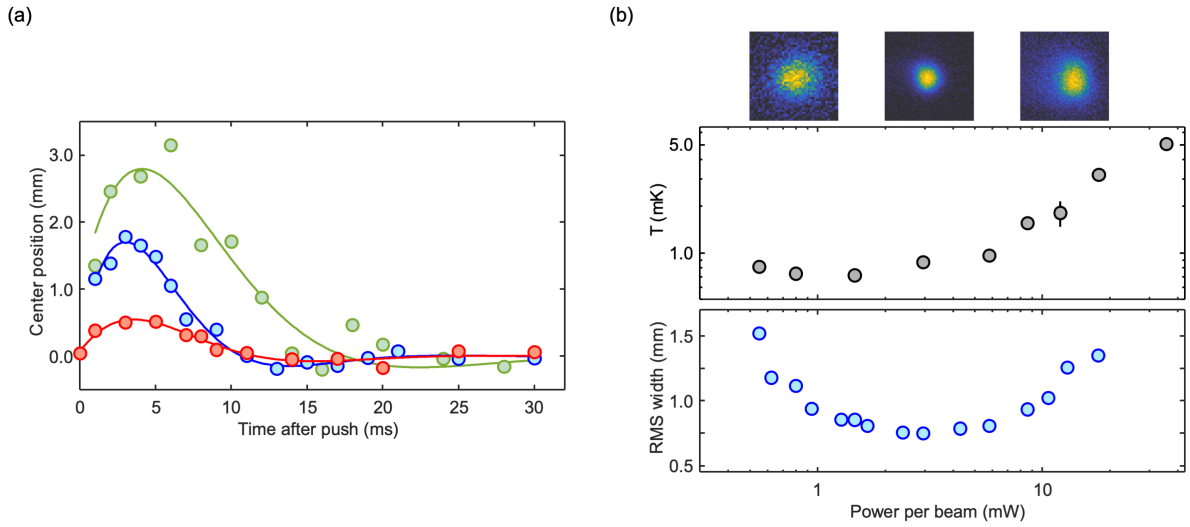

Figure 5.26: MOT dynamics and characteristics. **a,** CaOH cloud position as a function of time after a sudden displacement, for MOT powers of 1.2 mW (green; top curve), 3 mW (blue; middle curve), and 11.5 mW (red; bottom curve). Fitted MOT parameters are $\beta = \{310(90), 455(85), 340(100)\}$ s^{-1} and $\omega = 2\pi \times \{37(4), 59(4), 50(4)\}$ Hz for the three powers, respectively. **b,** Geometric mean temperature, $T = T_{\text{radial}}^{2/3} T_{\text{axial}}^{1/3}$ (middle plot; black) and geometric mean width (bottom plot; blue) of the CaOH MOT versus laser power in each MOT beam. Error bars are 1σ fit errors and are smaller than the plot markers for most points. CaOH MOT images are shown at top for representative powers of 0.5 mW, 3.0 mW, and 12.9 mW per MOT beam, from left to right. The MOT is imaged for 10 ms following a 15 ms wait time to fully thermalize. The image size is 7 × 7 mm. The three intensity axes are different due to changing numbers and scattering rates at each MOT power. Normalized to the center image, the maximum image intensity from left to right is 0.23, 1, and 0.38. Modified from Ref. [42].

simultaneously turned off. After a variable time τ_{TOF}, an image of the expanded molecular cloud is taken with a 1 ms pulse of resonant light, and its radial and axial widths, σ_ρ and σ_z, are fit from a 2D Gaussian model. The imaging time was chosen to be short compared to the time of flight (TOF), and it was verified, by comparing to images with even shorter exposures of 0.5 ms, that the imaged cloud size was unaffected by the imaging light. After ballistic expansion during TOF, the molecular cloud size along each axis is $\sigma^2 = \sigma_0^2 + k_B T \tau_{\mathrm{TOF}}^2/m$, where σ_0 is the initial size. Therefore, the radial and axial temperatures were determined by linear fits of σ_ρ^2 and σ_z^2 vs. τ_{TOF}^2 for each axis. The final MOT temperature depends strongly on the MOT power (Fig. 5.26(b)) due to sub-Doppler heating effects [306], as have been observed in other "type-II" MOTs [194, 299]. As the power is lowered, the temperature of the MOT reaches a minimum measured temperature of 720(40) μK.

Following the 5 ms loading ramp and a ∼15 ms hold at variable intensity, the diameter of the molecular cloud is determined by imaging the MOT with a 10 ms EMCCD exposure. The diameter is smallest at a power of 3 mW per MOT beam (Fig. 5.26(b)), increasing at both lower and higher intensities. After ∼15 ms of cooling at 3 mW per MOT beam, we observe approximately 20,000 molecules (Methods) with a temperature of 870(50) μK, a peak number density of $3.0(1.5) \times 10^6$ cm^{-3}, and a peak phase-space density of $1.4(7) \times 10^{-12}$. These values are all comparable to those achieved in the first MOTs of diatomic molecules [192–195]. The MOT could be further improved by repumping additional, known, vibrational loss channels [269].

5.4.7 Compressed RF MOT

To further compress the MOT and increase its density, we ramp up the gradient of the RF magnetic field after the intensity and detuning ramp, as shown in Fig. 5.27. We also scanned the intensity and detuning of the MOT laser during this ramp, but found that the previous values were already optimal, even at high gradient. We found that

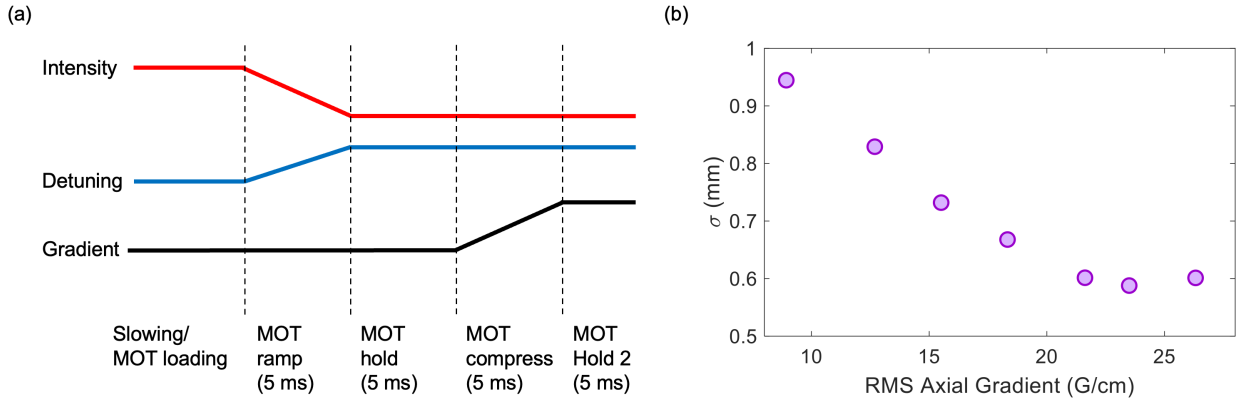

Figure 5.27: Compressed RF MOT of CaOH. (a) After loading the MOT and ramping the detuning and intensity, we ramp up the RF gradient. (b) We find that the MOT reaches a Gaussian width of $\sigma \lesssim 0.6$ mm at sufficiently high gradient.

the size of the MOT plateaued at RMS axial gradients above approximately 20-25 G/cm, with a Gaussian width of slightly below 600 μm. We also noticed a significant change (nearly 1 mm) in the center position of the MOT after compression. This could be due to misalignment of the MOT beams, which leads to extra pushing forces that shift the MOT's equilibrium position away from the magnetic field zero. In this scenario, the MOT moves closer to the magnetic field zero as the gradient is ramped up. We believe that this misalignment was improved in later work, when implementing the blue detuned MOT (section 5.6).

The decrease in size (and corresponding increase in density) achieved by compressing the RF MOT will be important for loading molecules into the ODT, described in chapter 6.

5.5 Sub-Doppler cooling

5.5.1 Overview of sub-Doppler cooling

In type-I atomic systems, sub-Doppler cooling occurs for red detuned light and relies on a polarization gradient, Sisyphus-type cooling mechanism arising from state-dependent AC Stark shifts and unequal transition strengths to different magnetic sublevels [300]. In contrast, sub-Doppler cooling in type-II systems is fundamentally different due to the presence of dark states, and requires blue detuned light [306].[35] In the cold atom community, this is often referred to as grey molasses cooling. The basic mechanism is illustrated in Fig. 5.28. In the presence of blue-detuned light, bright ground states are shifted up in energy by an amount that depends on the local laser intensity and polarization. Meanwhile, dark states remain unshifted. A molecule beginning in a bright state rides up a potential hill before scattering a photon and being optically pumped into the dark state, removing an energy equal to the difference in bright and dark state energies. Once in the dark state, the molecule can undergo a diabatic transition back into a bright state via motional remixing, since the local polarization and corresponding bright and dark states vary as a function of position.

In one dimension, it turns out that only certain polarization configurations work for cooling at zero magnetic field, as described in Ref. [306]. For an $F = 1 \rightarrow F' = 1$ system with counter-propagating beams in $\sigma^+\sigma^-$ and Lin$\perp$Lin configurations[36], the intensity is independent of position, and the AC Stark shifts are constant and there can be no cooling. For the Lin$\parallel$Lin configuration, the AC Stark shifts are maximized but the polarization does not vary, so there is no motional remixing (in this case adding a magnetic field remixes dark states – this is

[35] Note that type-II sub-Doppler cooling is not unique to molecules. In alkali atoms, type-II sub-Doppler cooling can be applied on the D1 line, and is used to achieve lower temperatures than type-I polarization gradient cooling for light species like Li and K.

[36] I.e. with the beams propagating along $+z$ and $-z$ having σ^+ and σ^- polarization in the former case, and orthogonal linear polarizations in the latter case.

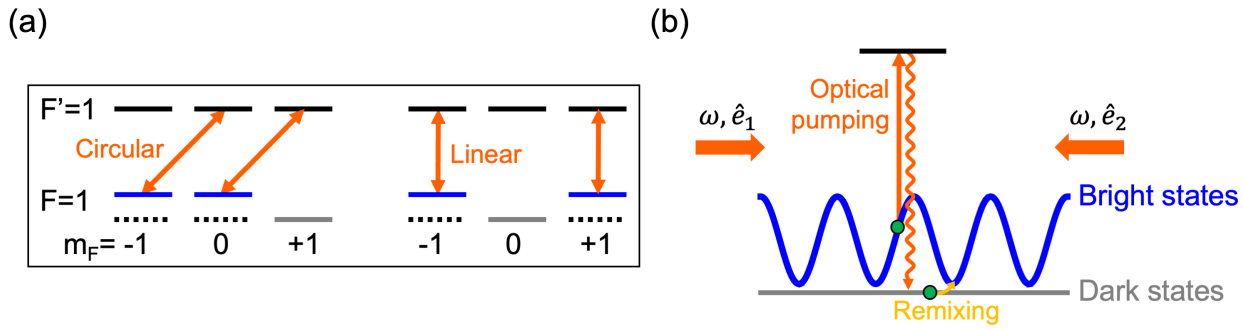

Figure 5.28: Sub-Dopper gray molasses cooling in type-II systems. (a) Example dark states for a type-II $F = 1 \rightarrow F' = 1$ system. For any laser polarization there is one dark state in this system. Other type-II systems have dark states that arise in a similar way [289]. (b) Illustration of the sub-Doppler cooling mechanism, which relies on non-adiabatic, polarization gradient, Sisyphus-type forces. Counter-propagating, blue-detuned lasers with frequency ω and polarizations $\hat{e}_1$ and $\hat{e}_2$ are incident on a type-II system. The bright states experience an AC Stark shifted standing-wave potential related to the lasers' intensity and polarization. Molecules in a bright state adiabatically follow this potential as they move, until they are optically pumped into a dark state, removing kinetic energy. They are then motionally remixed back into the bright state near the potential minimum and repeat the process.

called magnetically-assisted Sisyphus cooling and is an efficient technique for transverse cooling of molecular beams [47, 191, 217, 219, 307]). For configurations LinϕLin, where there is an angle $\phi \neq 0, \pi/2$ between the two linear polarizations, there is cooling in 1D since both the polarization and intensity of the laser field vary.

In three dimensions, the situation is more favorable. As shown in Ref. [306], having three orthogonal pairs of laser beams turns on polarization and intensity gradients even in the $\sigma^+\sigma^-$ and Lin$\perp$Lin configurations. The specifics of these effects will depend on the relative phase between the six lasers, but they persist after averaging over a number of such configurations [306]. Because of this, to implement sub-Doppler cooling in CaOH, we can simply turn off the magnetic field and cool using the MOT beams, which constitute a 3D $\sigma^+\sigma^-$ laser field.

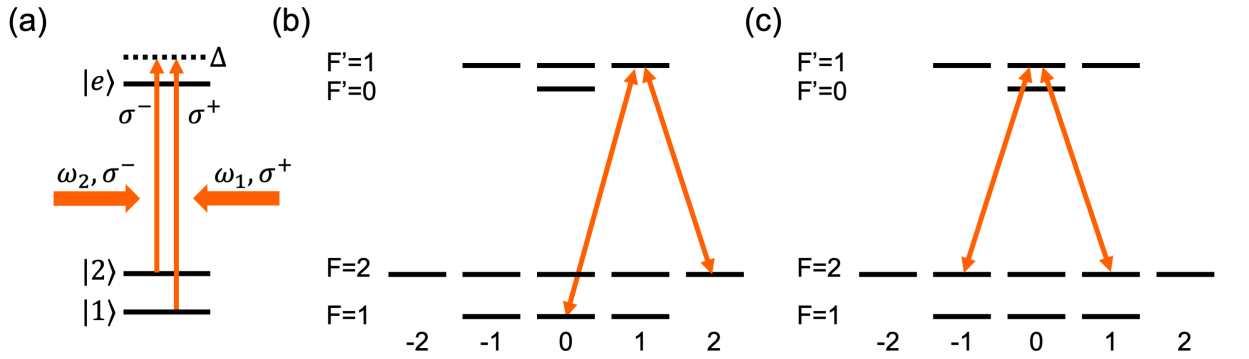

Figure 5.29: Velocity-selective coherent population trapping. (a) Sub-Doppler cooling is performed with two laser frequencies tuned into two-photon resonance with two ground hyperfine states. There is a coherent dark state formed between these two states when the velocity is zero. Away from zero, the two-photon detuning is Doppler shifted away from resonance and the molecules scatter photons until being cooled into the coherent dark state. (b-c) Example coherent dark states for a molecule like CaOH or CaF [232]. Configuration (b) corresponds to Λ cooling, and configuration (c) corresponds to single frequency cooling.

Coherent population trapping

Even lower temperatures can be achieved by creating coherent, velocity-selective dark states. This is done by applying two counterpropagating lasers on two-photon resonance with a transition between ground state hyperfine levels (Fig. 5.29). For properly chosen hyperfine states, there is a coherent dark state (which depends on the specific ground and excited state hyperfine structure of the system [289]) at zero velocity. At nonzero velocity, the lasers are Doppler shifted away from two-photon resonance. When the lasers are blue detuned, molecules are initially cooled by grey molasses cooling, then trapped in the dark state when they get sufficiently cold. This process (called velocity selective coherent population trapping, or VSCPT) can lead to extremely low temperatures, and has been used to cool atoms below the recoil limit [308, 309].

For molecules, two distinct schemes have been previously demonstrated [231, 232]. The first scheme, called Λ-enhanced grey molasses cooling [231, 310], has two lasers at different frequencies, tuned to address an $F = 1$ and

an $F = 2$ ground state hyperfine level (the excited states are $F' = 0$ and $F' = 1$ and are unresolved). These form a coherent dark state as shown in Fig. 5.29(b).[37] The second configuration has just a single laser frequency, the retroreflected beams of which forms a coherent dark state between two magnetic sublevels in the $F = 2$ ground state (Fig. 5.29(c)). This approach is referred to as single frequency (SF) cooling [232]. We pursue both cooling approaches for CaOH, finding that SF cooling is able to achieve slightly lower temperatures than Λ cooling in free space.

5.5.2 Grey molasses cooling

Our first attempt at sub-Doppler cooling was done with the two spin-rotation sidebands split by the amount used fo the initial MOT (52.1 MHz), which had ignored hyperfine structure and turned out to be in between the two Λ-enhanced cooling features we would later find (sec. 5.5.3). Therefore, this first attempt could be considered a demonstration of grey molasses cooling without significant VSCPT effects.[38]

We sub-Doppler cool the molecular cloud by applying a blue-detuned optical molasses. As demonstrated previously for diatomic molecules with the "type-II" $J \rightarrow J - 1$ transitions used here [193, 199, 311], the presence of dark states in the ground manifold leads to polarization gradient forces which result in strong sub-Doppler heating at red detuning and sub-Doppler cooling at blue detuning [306, 312]. After loading and cooling the MOT, we perform sub-Doppler cooling by turning off the MOT coils, MOT lasers, and the polarization switching in a time period of 130 μs, while simultaneously jumping both frequency components of the MOT lasers to a variable detuning Δ_{SD}. The cooling laser beams are then switched on for 1 ms at a power of 30 mW per beam. After this

[37] There are actually multiple coherent dark states; the one in the figure is an example [232].

[38] Note, however, that the two-photon detuning used here corresponds to one of the hotter regions of the Λ-enhanced cooling parameter space in Fig. 5.31, so it's possible there was some residual VSCPT heating in this data from being close to, but not on resonance with, two VSCPT features.

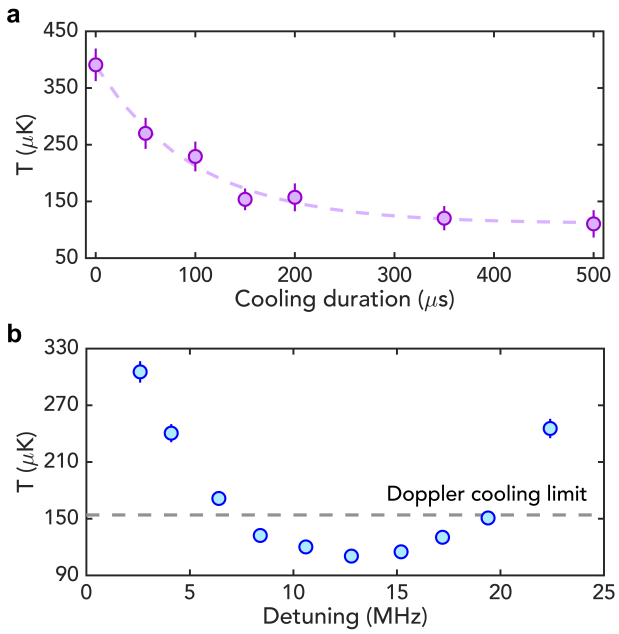

Figure 5.30: Sub-Doppler cooling. **a,** Temperature as a function of cooling duration. The dotted line is an exponential fit, from which we extract a $1/e$ cooling time of 98(15) μs. **b,** Temperature as a function of sub-Doppler detuning Δ_{SD}. The Doppler cooling limit for CaOH is shown as a dotted line. Error bars for both parts are 1σ fit errors derived from 2D Gaussian fits of the expanded molecular cloud widths. Reproduced from Ref. [42].

cooling pulse, the CaOH temperature is measured via time-of-flight expansion, as described above. The cooling occurs with a characteristic time of 98(15) μs (Fig. 5.30(a)) and a scattering rate of $7.7(4) \times 10^5$ s^{-1}, corresponding to only 75 photon scatters for a $1/e$ decrease in temperature. We find an optimal detuning of $\Delta_{\mathrm{SD}} = +13$ MHz (Fig. 5.30(b)). Since the lower frequency component of the sub-Doppler cooling light is red-detuned from the $\widetilde{A}(J' = 1/2, p' = +) \leftarrow \widetilde{X}(N'' = 1, J'' = 1/2, p'' = -)$ transition, sub-Doppler heating might be possible as the detuning increases. The minimum temperature acheived is 110(4) μK, which is comparable to the temperatures achieved in diatomic molecules using a similar cooling mechanism [193, 194, 232].

Magnetic field compensation

To implement sub-Doppler cooling, we had to add magnetic field compensation coils surrounding the MOT chamber (we did not have any compensation for the initial RF MOT). This is because sub-Doppler cooling works best with zero applied magnetic field, and earth's magnetic field will significantly reduce the effectiveness of the cooling. We installed three pairs of coils along the north/south, east/west, and vertical axes of the chamber. We optimized the current in each coil by minimizing the sub-Doppler cooling temperature, and found, as expected, that compensation fields on the order of earth's field were required along the north/south and vertical axes, while the east/west axis did not require compensation.

5.5.3 Dark-state-enhanced cooling

Our Λ-cooling and SF cooling implementations for CaOH molecules are both based on creating a blue-detuned optical molasses that addresses the same $\widetilde{X}^2\Sigma^+ \rightarrow \widetilde{A}^2\Pi_{1/2}$ transition as the MOT. This is a "type-II" transition (i.e., $J'' \geq J'$), which exhibits strong sub-Doppler cooling (heating) at blue (red) detuning due to polarization gradient forces that arise from the existence of dark states in the ground state manifold [306]. The experimental sequence for applying the molasses is as follows. Starting with CaOH molecules loaded into the MOT, the molecular cloud is compressed to about half its size by ramping the MOT gradient over 5 ms, from 8.3 G/cm (its value during MOT loading) to 23.6 G/cm. The MOT laser beams, MOT coils, and MOT light polarization switching (which is used to remix magnetic dark states) are then turned off in a time period of 130 μs. The two frequency components of the MOT beams—which separately address the spin-rotation components $\widetilde{X}^2\Sigma^+(N''=1, J''=1/2)$ and $\widetilde{X}^2\Sigma^+(N''=1, J''=3/2)$—are simultaneously tuned to the blue of the

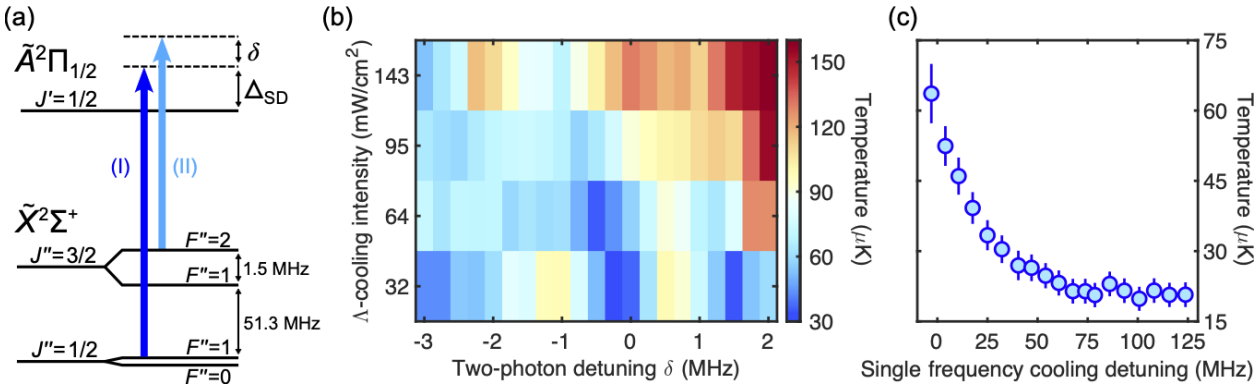

Figure 5.31: Λ-cooling and single frequency (SF) cooling of CaOH. (a) CaOH level structure and the two frequency components used for Λ-cooling (dark (I) and light blue (II) arrows), with a two-photon detuning of δ and single photon detuning of Δ_{SD}. For SF cooling, only the bluer component (I) is present. (b) Λ-cooling temperature as a function of δ and intensity per cooling beam, I_{SD}. (c) Temperature of SF cooling as a function of Δ_{SD} at $I_{SD} = 64$ mW/cm^2. Error bars include 1σ errors from the temperature fitting and systematic effects from imaging (described in the text). Figure reproduced from Ref. [43].

optical transition. The laser beams are then quickly turned back on to form the "blue-detuned molasses."

The blue-detuned molasses is configured for Λ-cooling by coupling two hyperfine levels in the $\widetilde{X}^2\Sigma^+(N''=1)$ manifold to the $\widetilde{A}^2\Pi_{1/2}(J'=1/2)$ excited state. To achieve this, the two frequency components of the molasses are tuned to nominally address the $\widetilde{X}^2\Sigma^+(J''=3/2, F''=2)$ and $\widetilde{X}^2\Sigma^+(J''=1/2)$ levels (Fig. 5.31(a)), with polarizations σ^- and σ^+, respectively. (Hyperfine levels in the $\widetilde{X}^2\Sigma^+(J''=1/2)$ state are unresolved in our experiment [254].) Both frequency components are blue-detuned by a common detuning Δ_{SD}, while the component addressing $\widetilde{X}^2\Sigma^+(J''=3/2, F''=2)$ is further detuned by δ, the two-photon detuning. We set $\Delta_{SD} = 12$ MHz, informed by our previous sub-Doppler cooling results in Ref. [42]. The peak cooling intensity, I_{SD}, is divided between the two frequency components, whose intensities are $I_{SD}/3$ for $\widetilde{X}^2\Sigma^+(J''=3/2, F''=2)$ and $2I_{SD}/3$ for $\widetilde{X}^2\Sigma^+(J''=1/2)$.

We investigate the dependence of Λ-cooling on both δ and I_{SD}, using ballistic expansion of the cooled molecules to measure their temperature after 1 ms of Λ-cooling (Fig. 5.31(b)). This cooling duration was chosen to be many

times longer than the characteristic time of the cooling. The lowest measured temperature, $T_{\text{min}} = 34(3)$ μK, occurs at $\delta \approx 0$ MHz and at the lowest cooling intensity used, $I_{\text{SD}} = 32$ mW/cm^2. A second, slightly higher local temperature minimum is observed at $\delta \approx 1.5$ MHz, which corresponds to the two-photon resonance for the Λ-system consisting of $\widetilde{X}^2\Sigma^+(J'' = 3/2, F'' = 1)$ and $\widetilde{X}^2\Sigma^+(J'' = 1/2)$. At higher intensities, the temperature is minimized at increasingly negative δ. We attribute this behavior to ac Stark shifts of the Λ-coupled hyperfine levels due to the cooling light: for higher intensities, the levels move further apart, and smaller δ is required to satisfy the two-photon resonance condition.

SF cooling is implemented similarly to Λ-cooling, except that the frequency component used to address the $\widetilde{X}^2\Sigma^+(J'' = 3/2, F'' = 2)$ state is removed. We find that the capture velocity of SF cooling is too low to cool molecules directly from the MOT temperature of $\sim$0.8 mK. We therefore start by cooling the molecular cloud with Λ-cooling, then apply SF cooling. For this sequence of cooling, Λ-cooling with parameters of $\Delta_{\text{SD}} = 10$ MHz, $\delta = 0.25$ MHz, and $I_{\text{SD}} = 32$ mW/cm^2 is applied for 2 ms, which cools the molecular cloud to $T \approx 50$ μK. The molasses is next reconfigured for SF cooling in a period of 1 ms, during which time the molasses light is turned off. SF cooling is then applied for 5 ms, resulting in a minimum temperature of $T_{\text{min}} = 20(3)$ μK, realized when $I_{\text{SD}} = 64$ mW/cm^2 and $\Delta_{\text{SD}} \gtrsim 70$ MHz (Fig. 5.31(c)). The cooling efficiency is insensitive to detuning above some threshold ($\Delta_{\text{SD}} \approx 70$ MHz), as has also been observed in SF cooling of CaF molecules [232].

Sub-Doppler cooling temperature measurements

The temperatures of sub-Doppler cooled CaOH molecules are determined from the standard ballistic expansion method. After the sub-Doppler cooling light has turned off, the cooled molecular cloud is allowed to expand

ballistically for a variable amount of time, τ_{exp}. An EMCCD camera image of the molecular cloud is then taken by applying resonant light on the $\widetilde{X}^2\Sigma^+(000)(N'' = 1) \rightarrow \widetilde{A}^2\Pi_{1/2}(000)(J' = 1/2)$ cycling transition with the MOT beams for 1 ms and collecting fluorescence decays from the $\widetilde{B}^2\Sigma^+$ state [42]. Radial and axial Gaussian widths, σ_ρ and σ_z, respectively, of the imaged cloud are fitted from a 2D Gaussian model and used to extract radial and axial temperatures from fits to $\sigma^2_{\rho,z} = \sigma^2_{0,\rho,z} + k_B T_{\rho,z}\tau^2_{\text{exp}}/m$, where $\sigma_{0,\rho,z}$ are the initial widths of the molecular cloud, k_B is the Boltzmann constant, T_ρ and T_z are the radial and axial temperatures, and m is the mass of CaOH. The temperature of the molecules is reported as the resulting geometric mean $T = T_\rho^{2/3} T_z^{1/3}$.

Resonant imaging of the molecular cloud causes heating that could lead to additional expansion of the molecular cloud. The imaging time of 1 ms was chosen to be short compared to the expansion times to minimize this effect, and it was verified by comparing to images with shorter exposures of 0.5 ms that the imaging did not significantly affect the size of the molecular cloud. The magnification of the imaging system was calibrated to be 1.16(3) by fitting the vertical position of a falling molecular cloud to $y = a\tau^2_{\text{exp}}/2$ and comparing the fitted acceleration a to the known acceleration due to gravity. The errors reported for the sub-Doppler cooling temperatures include both the statistical errors from the fitting procedure described above along with the error introduced from the uncertainty in the magnification.

5.6 Blue-detuned conveyor-belt MOT

Molecular MOTs are limited to relatively high temperatures and low densities in part due to the effect of sub-Doppler heating, which occurs in type-II systems with red-detuned light [306]. Sub-Doppler heating dominates

over Doppler cooling for sufficiently low molecule velocities, typically preventing red-detuned molecular MOTs from reaching the Doppler cooling limit. However, it has been proposed and demonstrated (with atoms), that type-II MOTs can be made with blue-detuned light [225]. This combines sub-Doppler cooling (so long as the starting temperature is below the sub-Doppler cooling capture velocity) with magneto-optical trapping forces for an appropriate choice of laser polarization. In the initial demonstration with rubidium atoms, a phase space density (PSD) orders of magnitude higher than comparable red-detuned type-II MOTs was achieved (the PSD was even slightly higher than that of normal type-I atomic MOTs) [225]. Because molecule laser cooling uses type-II transitions, this could be a promising approach for increasing the density and PSD of molecular MOTs. Over the last several years, blue-detuned MOTs have begun to be implemented with laser-cooled molecules, starting with YO [226] and followed by SrF [204] and CaF [227]. These experiments demonstrated that lower temperatures and higher densities were achievable with blue detuned MOTs compared to red-detuned molecular MOTs.

In this section, we describe our implementation of a blue-detuned MOT of CaOH molecules. Along with demonstrating a "naive" blue-detuned MOT of CaOH with comparable properties to prior demonstrations, we also discovered a new scheme based on a "conveyor-belt" mechanism, which provided significantly improved compression forces. This enabled us to achieve a density more than two orders of magnitude higher than our previous red-detuned RF MOTs, and an order of magnitude higher than the blue-detuned MOT without the conveyor-belt mechanism. These results were enabled in large part by Monte Carlo simulations of the MOT using a stochastic Schrödinger equation method, which very accurately matched the experiments and helped predict optimal MOT configurations. These simulations were implemented by Christian Hallas and Grace Li, and described in more detail in Refs. [228, 230].

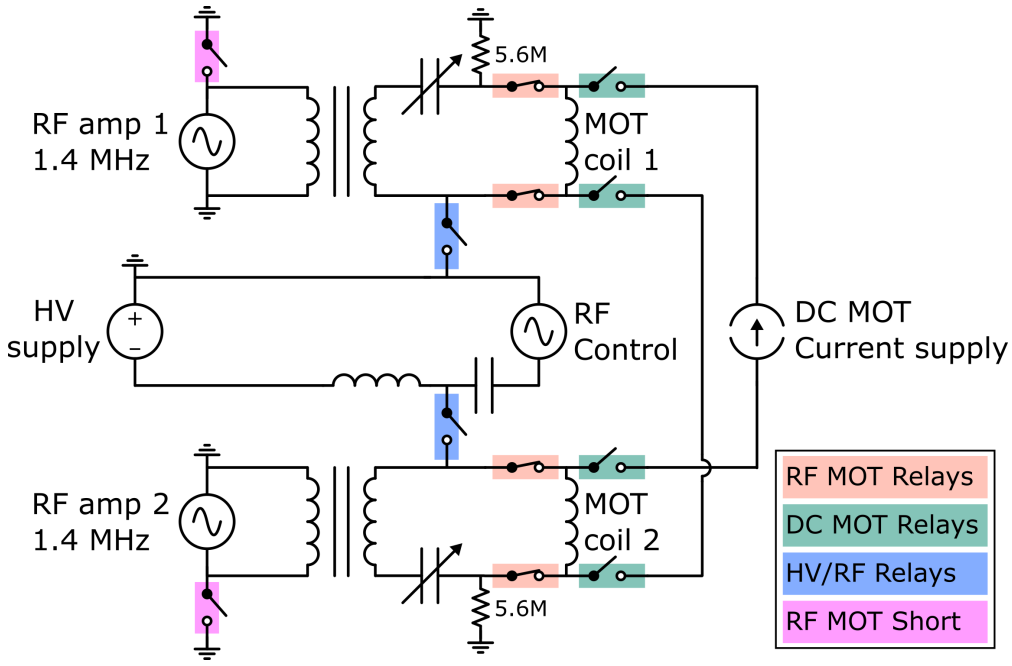

Figure 5.32: Connections to RF MOT coils. We use a number of latching, mechanical SPST relays (Kilovac K40P) to switch between RF MOT, DC MOT, and electric field configurations. The mechanical relays have an approx. 1 ms switching time and a specified lifetime of 10 million shots.

5.6.1 Experimental setup

Blue-detuned MOTs use a DC magnetic field gradient rather than an RF gradient. Therefore, we needed to be able to switch from the RF MOT to a DC MOT configuration in short succession, with the idea being to first load our RF MOT, and then transfer to the blue-detuned MOT for improved cooling and compression. This was done using a number of relays connected to the in-vacuum RF MOT coils, as shown in Fig. 5.32. This diagram also shows connections used to apply DC and RF electric fields to the coils for experiments described later in this thesis.

We use the in-vacuum MOT coils to apply AC currents and voltages near 1 kV for the RF MOT, DC currents

>30 A for the DC MOT, and DC voltages up to 2 kV to polarize CaOH molecules (described in later chapters). We elected to use mechanical high-voltage/high-current relays to switch between the different applied currents and voltages. To our knowledge, there are no solid state relay options that can satisfy all of these requirements. Because of the need for fast switching times, we elected to use latching SPST relays (Kilovac K40P), since corresponding SPDT Kilovac relay has a slower switching time. The switching time of the relays we use is approximately 1 ms, and they have a rated lifetime of 10 million shots. Because of the large number of relays in the system, this nonetheless means that one fails every few months, which as of this writing is one of the least reliable parts of the CaOH experiment.

To switch from the RF MOT to the DC MOT, we open the four relays connecting the RF tank circuits to the coils, and close the four relays connecting the DC MOT current supply to the coils. The DC current is provided by an analog programmable current supply (Delta Elektronika). Because we program the supply in constant current mode, when the relays are open the voltage is undefined, and sometimes floats to relatively high values, causing a voltage spike when the relays are closed. We found that this occasionally interfered with the clock signal in our experiment control hardware and caused buffer underruns. To prevent this issue, we installed a $\sim$100 Ω resistor across the output of the DC current supply. This is large compared to the impedance of the coils, but is small enough to significantly limit the voltage across the power supply when the Kilovac relays are open.

In addition to adding the ability to apply DC magnetic field gradients, we also had to reconfigure the MOT laser sideband board ("hyperfine board") to add sidebands for the conveyor-belt MOT. The layout of the hyperfine board is shown in appendix C.

5.6.2 Experimental sequence

To load the blue-detuned MOT, we start with our normal red-detuned RF MOT. After loading the RF MOT, we compress from an RMS gradient of 8.5 G/cm to 23.6 G/cm, then hold for 10 ms for the compression to occur. At this point, the Gaussian rms width of the MOT cloud is 0.53(3) mm and the peak number density is $2.0(6) \times 10^6$ cm^{-3}. To form the blue detuned MOT, we rapidly switch off the RF MOT light and magnetic field gradient, then apply 1 ms of free-space Λ cooling, which precools the molecules prior to turning on the blue detuned MOT. This also helps prevent the cloud from rapidly expanding during the time needed to switch the mechanical relays from the RF MOT to DC MOT configuration, so that we can begin applying DC magnetic field gradients. The blue-detuned MOT is then created by switching the laser detuning, power, and sideband configuration to the blue MOT configuration, and linearly ramping up a DC magnetic field in 4 ms. We observe negligible molecule loss during transfer to the blue MOT.

5.6.3 Demonstration and characterization of "1+1" and "1+2" blue MOTs

Fig. 5.33 shows the laser frequency configurations we use for the red detuned RF MOT and for the blue-detuned MOT. In the blue MOT laser configuration, a single frequency component (I), blue-detuned from the MOT transition by Δ, addresses the $|J = 1/2\rangle$ state while two closely-spaced frequency components of opposite polarization, denoted by (IIa) and (IIb), address the $|J = 3/2\rangle$ state. Referenced to the $F = 2$ hyperfine state, the detunings of (IIa) and (IIb) are $\Delta + \delta_{\mathrm{IIa}}$ and $\Delta + \delta_{\mathrm{IIb}}$, respectively, where δ_{IIa} and δ_{IIb} are the two-photon detunings for the (IIa) and (IIb) components with respect to (I). This configuration with both (I) and the (IIa)-(IIb) pair is referred to as the 1+2 scheme. We also create a blue MOT that employs laser frequency (I) and only

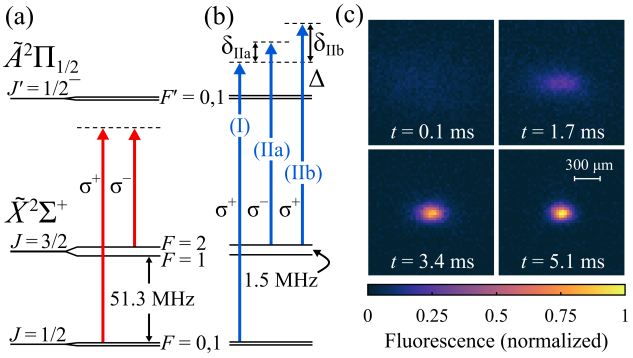

Figure 5.33: (a) Level structure and laser configuration for the CaOH red (RF) MOT. (b) CaOH blue (DC) MOT laser configuration. The single-photon detuning is denoted by Δ, and the two-photon detunings for the two MOT beams addressing the $|J = 3/2\rangle$ level are denoted by δ_{IIa}, and δ_{IIb}. (c) Images of the blue-detuned CaOH MOT taken with 2 ms in-situ images following a compression time of t. Reproduced from Ref. [228]

one of either (IIa) or (IIb) (1+1 scheme). We describe both of these configurations below.

1+2 frequency configuration: conveyor-belt MOT

Fig. 5.33(c) shows in-situ images taken throughout the compression of the molecular cloud while the 1+2 MOT light is applied. The ramped (axial) magnetic field gradient is $B'_z = 78$ G/cm (which corresponds to 16.6 A of current on the coils given our axial gradient of 4.7 G/cm/A). The frequency parameters for the MOT light are $\Delta = 7.4$ MHz, $\delta_{\mathrm{IIa}} = -1.0$ MHz, $\delta_{\mathrm{IIb}} = 0.75$ MHz and were chosen to maximize the compression of the molecular cloud. We note that, since the $|J = 3/2, F = 1\rangle$ state is only $\sim$1.5 MHz lower in energy compared to the $|J = 3/2, F = 2\rangle$ state, the two-photon detunings with respect to this state are of a similar scale, though negative for both (IIa) and (IIb). The total 1+2 MOT light intensity is ramped linearly from $I = 23.5$ mW/cm^2 to $I = 18.2$ mW/cm^2 during the magnetic field ramp. The fractions of the total intensity among the three frequency components are 37%, 28%, and 35% for (I), (IIa), and (IIb), respectively. The 1+2 MOT is fully compressed after 5 ms and reaches a final size of $\sigma = 59(5)$ μm. Using the time-of-flight expansion method,

the molecular temperature is measured to be $T = 170(10)\ \mu$K. After the 1+2 MOT compression, $\sim$60% of the molecules that were in the red MOT remain, corresponding to $\sim$2,900 molecules. With the measured final MOT size, this results in a peak number density of $n_0 = 8(2) \times 10^8$ cm^{-3}. The molecule loss is almost entirely from branching losses to vibrational dark states during photon cycling due to the finite photon budget. Given our scattering rate of $0.90(3)$ MHz and a photon budget of $13{,}500$ photons, this loss can be estimated theoretically as $e^{-0.9\ \text{MHz} \times 5\ \text{ms}/13{,}500} = 71\%$.

We quantify the cooling and trapping forces in the MOT by modeling the MOT as a damped harmonic oscillator with force $F = -\alpha v - kr$. Here r is position, v is velocity, α is the damping coefficient, and k is the spring constant. Using the equipartition theorem, the spring constant can be extracted from the size and temperature according to $k = k_B T/\sigma^2$ [225]. We find $k = 6(1) \times 10^{-19}$ N/m for the 1+2 MOT, which is more than an order of magnitude larger than spring constants achieved in previously demonstrated blue-detuned MOTs [204, 226, 227].

We also measured the temperature and width of the molecule cloud as a function of intensity and one- and two-photon detunings (see Ref. [228]). There were clear minima in the cloud size at specific single-photon detuning, total intensity, and intensity ratio, with the optimal values near the ones described above. The temperature was relatively insensitive to all parameters besides the single-photon detuning (too small a single-photon detuning led to significant heating). The most striking feature, however, is that when δ_{IIa} and δ_{IIb} are tuned close to each other, σ increases dramatically, i.e., the trapping force vanishes. The variation of the relative power ratio between (IIb) and (IIa) demonstrates that, as the intensity of (IIb) is increased from zero, the cloud size shrinks to the minimum size. The temperature is relatively insensitive to both δ_{IIa} and δ_{IIb} as well as the power ratio between (IIa) and (IIb).

Conveyor-belt trapping mechanism

Our observations suggest that having two distinct, closely spaced frequency components is critical to the significant compression seen in the 1+2 configuration. It turns out that this is a manifestation of a "conveyor-belt" MOT, which to our knowledge is a new form of MOT discovered during this work.

The conveyor-belt mechanism can be understood in a toy model using an $F'' = 1 \rightarrow F' = 0$ type-II system [230]. We apply two blue-detuned frequency components, with frequencies $\omega_1 = \omega_0 + \Delta$ and $\omega_2 = \omega_0 + \Delta + \delta$, where ω_0 is the resonance frequency, Δ is the single-photon detuning, and δ is the two-photon detuning. The polarizations of the two components are σ^+ and σ^-, and each component is retroreflected through a quarter waveplate, as would be the case in a typical MOT. The result is that we have four laser components, with the following properties:

- Component 1: frequency $\omega_1 + \delta$, polarization σ^-, wavevector $+k$
- Component 2: frequency $\omega_1 + \delta$, polarization σ^+, wavevector $-k$
- Component 3: frequency ω_1, polarization σ^+, wavevector $+k$
- Component 4: frequency ω_1, polarization σ^-, wavevector $-k$

Now, if we group these components by polarization, we find that components (1) and (4) combine to form a σ^- polarized standing wave moving with a velocity $v_{CB} = c\delta/2\omega_1$ in the lab frame. Similarly, beams (2) and (3) combine to form a σ^+ standing wave moving at a velocity $-v_{CB}$. We will call each pair of beams a "conveyor belt" for reasons that will become clear below. For the 1.75 MHz two-photon detuning used in the CaOH conveyor belt MOT, $v_{CB} \approx 0.55$ m/s.

Now, when a magnetic field gradient is applied, molecules will preferentially interact with the σ^+ or σ^- conveyor belt depending on their position in the trap. For instance, when molecules are closer to resonance with the

σ^+ standing wave, they will be sub-Doppler cooled (via the magnetically assisted Sisyphus effect [47, 191, 217, 307]) into the frame moving with the standing wave. In this way, the molecules will be dragged by a molasses moving with the conveyor belt towards the MOT center. Once they reach the center of the MOT, there will no longer be a clear preference for interacting with one conveyor belt or the other, and so the molecule will be deposited near the magnetic field zero (where it continues to be sub-Doppler cooled via normal grey molasses cooling).

Simulated molecule trajectories confirm the conveyor-belt effect by showing that molecules accumulate at velocities $\pm v_{CB}$ as they are being compressed. For more on the conveyor belt trapping effect and the simulations, see Refs. [228, 230].

Comparison to 1+1 frequency configuration

We also create a blue MOT without the conveyor-belt trapping effect, by applying laser frequency (I) and only one of either (IIa) or (IIb). We refer to these 1+1 schemes as (A) using (I) and (IIa), and (B) using (I) and (IIb). A difference between (A) and (B) is that the polarization for the component addressing the $|J = 3/2\rangle$ state is reversed. The 1+1 (A) MOT is the approach used in the blue MOTs created for YO and CaF and follows the conventional MOT configuration where the frequency separation between each of the components of the MOT light is significantly greater than the MOT transition linewidth [226, 227]. We find significantly reduced spatial compression in both of the 1+1 schemes. In Fig. 5.34, we compare the compressions of the 1+2 and 1+1 (A) MOTs. The compression predicted by the numerical simulations for the MOTs are shown as dashed curves and are in excellent agreement with the experimentally observed sizes and compression timescales. At optimal parameters for compression, the 1+1 (A) MOT achieves a final size of $\sigma = 110(4)$ μm after 15 ms of compression, which is

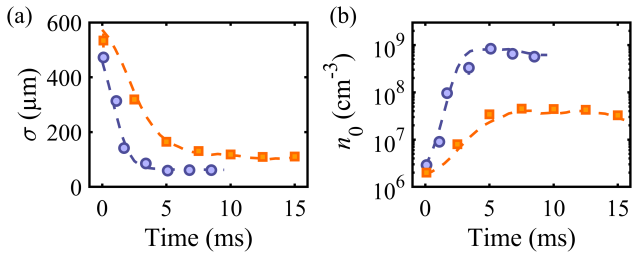

Figure 5.34: (a) MOT width σ and (b) MOT peak number density n_0 as a function of compression time for the 1+2 MOT (blue circles) and the 1+1 (A) MOT (orange squares). Dashed curves are simulation results. Reproduced from Ref. [228]

$\sim$2$\times$ larger than the size achieved with the 1+2 MOT. As with the 1+2 MOT, the gradient is ramped to $B'_z = 78$ G/cm over the first 4 ms. The temperature of the 1+1 (A) MOT is $T = 160(10)$ μK, which is similar to the temperature of the 1+2 MOT. For the 1+1 (A) MOT, $k = 1.8(1) \times 10^{-19}$ N/m, about $\sim$3.5$\times$ smaller than the spring constant for the 1+2 MOT. The scattering rate of the 1+1 (A) MOT is $0.7(1)$ MHz, only $\sim$20% smaller than that of the 1+2 MOT, so the large difference in spring constant implies that the 1+2 MOT achieves a significantly larger restoring force per photon scattered. The peak molecular density of the 1+1 (A) MOT is $n_0 = 5(1) \times 10^7$ cm^{-3}, a factor of $\sim$16 smaller compared to the 1+2 MOT.

6

Optical Trapping and Vibrational Lifetimes of CaOH

The next step towards quantum-controlled polyatomic molecules is to load them into a conservative trap, where they can be held without continuously scattering photons. In the MOT, the photon scattering required

for cooling and trapping constantly scrambles the molecules' internal state, precluding the possibility of full quantum state control. The lifetime of molecules in the MOT is also short (< 100 ms) due to our finite photon budget. By contrast, a molecule in a conservative trap can live for many seconds without its internal state changing. Molecules have previously been loaded into conservative magnetic [158–160, 170, 172–174, 197, 198], electrostatic [154, 168, 169, 176, 313–315], and optical traps [60, 179, 199, 202, 316–318], and any of these methods could be used to trap CaOH. However, magnetic and electric traps only work for certain low-field seeking states, and the large external fields they rely on can make achieving good internal state coherence challenging.[1] By contrast, optical traps can hold molecules in any internal state, can be tuned to allow good internal state coherence properties, and can be shaped to form a variety of potentials, including optical tweezer arrays. These features make optical trapping a natural choice for our goals of controlling the internal quantum states of CaOH (including single molecules), achieving high molecular densities and low temperatures, and ultimately allowing the molecules to coherently interact.

6.1 Theory: optical dipole trapping of molecules

An optical dipole trap (ODT) is a (nearly) conservative trap for neutral atoms and molecules formed from far-detuned laser beams, acting via electric dipole forces [320]. Classically, a far-detuned laser beam with frequency ω induces an oscillating electric dipole moment in the molecule, with a magnitude proportional to the AC polarizability $\alpha(\omega)$. If the electric field of the laser is $\boldsymbol{E}(\boldsymbol{r}, t) = \hat{e}\mathcal{E}_0(\boldsymbol{r})e^{-i\omega t} + \text{c.c.}$, the induced dipole moment is

[1] There have nonetheless been demonstrations of internal state coherence in magnetically and electrostatically trapped molecules [178, 319].

$\boldsymbol{\mu}(\boldsymbol{r},t) = \alpha(\omega)\boldsymbol{E}(\boldsymbol{r},t)$, leading to an energy shift [236, 320, 321]

$$U_{\text{dip}}(\boldsymbol{r}) = -\frac{\langle \boldsymbol{\mu}\cdot\boldsymbol{E}\rangle}{2} = -\alpha(\omega)\left|\mathcal{E}_0(\boldsymbol{r})\right|^2 = -\frac{1}{2\epsilon_0 c}\alpha(\omega)I(\boldsymbol{r}) \tag{6.1}$$

where $I = 2\epsilon_0 c\left|\mathcal{E}_0\right|^2$ is the laser intensity.[2] In the electronic ground state, wavelengths that are red-detuned from a strong electronic transition have $\alpha(\omega) > 0$, such that molecules are attracted to intensity maxima. Similarly, blue-detuned light has $\alpha(\omega) < 0$ and causes molecules to be repelled from regions of high intensity. Therefore, optical traps can be formed from shaped laser beams, e.g. by trapping molecules at the focus of a red-detuned Gaussian beam.

Quantum mechanically, the polarizability arises due to off-resonant coupling between electronic states driven by the laser. In 2nd-order perturbation theory, the polarizability is a sum of transition dipole matrix elements from the ground state $|i\rangle$ to all excited states $|j\rangle$ [320–322]:

$$\alpha_0(\omega) = \sum_j \left(\frac{1}{\hbar(\omega_{ij}-\omega)} + \frac{1}{\hbar(\omega_{ij}+\omega)}\right)\left|\langle i|\hat{e}\cdot\boldsymbol{\mu}|j\rangle\right|^2 \tag{6.2}$$

where (as above) $\hat{e}$ is the laser polarization, $\boldsymbol{\mu}$ is the dipole operator, ω is the laser frequency, and $\omega_{ij} = (E_j - E_i)/\hbar$ is the resonance frequency for the transition from state $|i\rangle$ to $|j\rangle$.

In atoms, the sum is over electronic states $|j\rangle$, but in molecules we also have to contend with vibrational and rotational structure. The dipole matrix elements can thus be written in terms of the combined rovibronic states

[2] Note that here we are only considering the real part of the polarizability. In general the polarizability is complex, with the real part describing the dipole force and the imaginary part describing dissipation (photon scattering) [320]. Additionally, in general α is a tensor that lets the induced dipole moment point in a different direction than the electric field. This allows the electric field to apply torque to the molecule, mixing internal states and causing state-dependent AC Stark shifts, considered later in this chapter [236].

$|j\rangle \equiv |\eta_j v_j J_j\rangle$ and separated (see chapter 2) as

$$|\langle i|\hat{e}\cdot\boldsymbol{\mu}|j\rangle|^2 \approx |\langle \eta_i|\hat{e}\cdot\boldsymbol{\mu}|\eta_j\rangle|^2 \, |\langle v_i|v_j\rangle|^2 \, |\langle J_i|\hat{e}|J_j\rangle|^2 \equiv \frac{|R_e^{ij}|^2}{3} q_{v_i v_j} S_{J_i}^{J_j} \tag{6.3}$$

Here $|R_e^{ij}|^2 \equiv |\langle \Lambda_i|\boldsymbol{\mu}|\Lambda_j\rangle|^2 \equiv |\langle \Lambda_i|\mu_x + \mu_y + \mu_z|\Lambda_j\rangle|^2$ is the total electronic transition dipole moment, and the factor of three in the denominator averages over all polarizations (since only a single component of the dipole operator in the molecule frame will drive a transition from Λ_i to Λ_j). The Franck-Condon Factor is $q_{v_i v_j} \equiv |\langle v_i|v_j\rangle|^2$, and the Hönl-London factors, ignoring electron spin, nuclear spin, and ℓ-type doubling[3] are [272]

$$S_{J_i}^{J_j} = (1 + \delta_{\Lambda_i 0} + \delta_{\Lambda_j 0} - 2\delta_{\Lambda_i 0}\delta_{\Lambda_j 0})(2J_i+1)(2J_j+1) \begin{pmatrix} J_i & 1 & J_j \\ -\Lambda_i & \Lambda_i - \Lambda_j & \Lambda_j \end{pmatrix}^2 \tag{6.4}$$

The prefactor involving Kronecker deltas enforces a $2\times$ increase in the line strength for transitions between a nondegenerate and a degenerate state (e.g. $\Sigma \leftrightarrow \Pi$) [271, 272]. Note that this expression has already been summed over the magnetic quantum numbers M_i and M_j; it will be important to account for this below.

Now, provided the laser is far-detuned compared to the excited-state rotational and vibrational energy scales, it

[3] While these structures are important when calculating individual line strengths, in the context of the sum rules discussed below, they simply add degeneracy factors that will eventually cancel out. This is because these structures are present in all electronic states and are not directly affected by electronic transitions. In the decoupled basis $|N\Lambda\ell M_N; SM_S; IM_I\rangle$, the quantum numbers ℓ, M_S, and M_I remain unchanged during an electronic transition.

is appropriate to sum over all rovibrational structure in the excited states. In that case, we use the sum rules

$$\sum_j q_{v_i v_j} = 1 \tag{6.5a}$$

$$\sum_j S_{J_i}^{J_j} = (1 + \delta_{\Lambda_i 0} + \delta_{\Lambda_j 0} - 2\delta_{\Lambda_i 0}\delta_{\Lambda_j 0})(2J_i + 1) \tag{6.5b}$$

for the Franck-Condon factors and Hönl-London factors, respectively [236, 271, 272]. The sum is over all states j connected by dipole transitions to the initial manifold with electronic angular momentum Λ_i and total angular momentum J_i. This manifold contains $(2 - \delta_{\Lambda_i 0})(2J_i + 1)$ states.

In the far-detuned limit, these sum rules allow the polarizability of the state $|\eta_i, v_i, J_i\rangle$ to be reduced to a sum over electronic states only:

$$\begin{aligned}\alpha_0(\omega) &\approx \sum_e \left(\frac{1}{\hbar(\omega_e - \omega)} + \frac{1}{\hbar(\omega_e + \omega)}\right) \frac{1}{(2J_i + 1)(2 - \delta_{\Lambda_i 0})} \frac{|R_e|^2}{3} \sum_{v_j, J_j} q_{v_i, v_j} S_{J_i}^{J_j} \\ &\approx \sum_e \left(\frac{1}{\hbar(\omega_e - \omega)} + \frac{1}{\hbar(\omega_e + \omega)}\right) \frac{|R_e|^2}{3} \frac{(1 + \delta_{\Lambda_i 0} + \delta_{\Lambda_e 0} - 2\delta_{\Lambda_i 0}\delta_{\Lambda_e 0})}{(2 - \delta_{\Lambda_i 0})}\end{aligned} \tag{6.6}$$

The factor of $(2J_i + 1)(2 - \delta_{\Lambda_i 0})$ in the denominator accounts for the degeneracy of the J_i manifold (magnetic and parity sublevels). Also recall that the factor of 3 in the denominator averages over all polarizations. It turns out that this polarization averaging gives the *scalar* polarizability, while state-dependent shifts, captured by the vector and tensor polarizability, appear when the trap polarization is considered. This polarizability anisotropy is considered below, in sec. 6.1.1.

It is convenient to convert the electronic transition dipole moment $|R_e|^2$ into the natural linewidth of the

electronic state [236],

$$\begin{aligned}\Gamma_e &= \frac{\omega_e^3}{3\pi\epsilon_0\hbar c^3(2-\delta_{\Lambda_e 0})(2J_e+1)}\sum_i |\langle \eta_i v_i J_i|\boldsymbol{\mu}|\eta_e v_e J_e\rangle|^2 \\ &= \frac{\omega_e^3}{3\pi\epsilon_0\hbar c^3(2-\delta_{\Lambda_e 0})}|R_e|^2(1+\delta_{\Lambda_i 0}+\delta_{\Lambda_e 0}-2\delta_{\Lambda_i 0}\delta_{\Lambda_e 0}) \end{aligned} \tag{6.7}$$

where we have summed over all ground states to which the excited level j can decay. Here, the factor of $(2-\delta_{\Lambda_e 0})(2J_e+1)$ accounts for the number of sublevels (magnetic and parity) in the excited manifold, and the radiative decay polarization is assumed to be isotropic (allowing the rate to be divided by 3). Substituting in above, the scalar polarizability thus becomes

$$\alpha_0(\omega) \approx \sum_e \frac{(2-\delta_{\Lambda_e 0})}{(2-\delta_{\Lambda_i 0})}\frac{\pi\epsilon_0 c^3\Gamma_e}{\omega_e^3}\left(\frac{1}{\omega_e-\omega}+\frac{1}{\omega_e+\omega}\right) \tag{6.8}$$

The Kronecker delta prefactor accounts for the $2\times$ increase in polarizability when coupling from a nondegenerate to a degenerate state (e.g. from $\widetilde{X}^2\Sigma^+ \rightarrow \widetilde{A}^2\Pi$).

Plugging back into eqn. 6.1 gives the isotropic (scalar) AC Stark shift of a ground-state molecule:

$$U_{\text{dip}}^{(0)}(\boldsymbol{r}) = -\sum_e (2-\delta_{\Lambda_e 0})\frac{\pi c^2\Gamma_e}{2\omega_e^3}\left(\frac{1}{\omega_e-\omega}+\frac{1}{\omega_e+\omega}\right) I(\boldsymbol{r}) \tag{6.9}$$

where we have specified $\Lambda_i = 0$, as in the $\widetilde{X}^2\Sigma^+$ ground state of CaOH.[4]

[4]Notice that there is a factor of 3 missing in this expression compared to the AC Stark shift of an atom (e.g. from Ref. [320]). This is because spherical symmetry allows electronic transitions in an atom to be driven by any laser polarization, while in molecules each electronic transition can be driven along only one axis in the molecule frame (or two axes for transitions from a nondegenerate to a degenerate state, hence the Kronecker delta factor). The factor of $1/3$ appears naturally in the scalar polarizability as defined by eqn. 6.12, below.

6.1.1 Polarizability anisotropy

We now account for the polarizability anisotropy, the fact that different ground states couple differently to the trap laser field, depending on the laser polarization. The anisotropy arises from the lack of spherical symmetry in most molecules, so that electronic transitions along different axes in the molecule frame can have varying strength. For linear molecules like CaOH, there are "parallel" transitions, which induce a dipole moment along the molecule-frame z axis (e.g. $\widetilde{X}^2\Sigma^+ \rightarrow \widetilde{B}^2\Sigma^+$), and "perpendicular" transitions, which induce a dipole moment perpendicular to that symmetry axis (e.g. $\widetilde{X}^2\Sigma^+ \rightarrow \widetilde{A}^2\Pi$). Classically, this means that the induced dipole moment is not necessarily parallel to the applied electric field, and is instead described using a polarizability tensor $\underline{\alpha}$, such that the induced dipole is $\boldsymbol{\mu} = \underline{\alpha}\boldsymbol{E}$. Since $\boldsymbol{\mu}$ is no longer parallel to $\boldsymbol{E}$, the field can exert a torque on the molecule, thereby coupling to the molecule's rotational degrees of freedom [236].[5]

Quantum mechanically, matrix elements of the AC Stark Hamiltonian between states $|i\rangle$ and $|i'\rangle$ within an electronic manifold can be written as [322, 323]

$$\langle i|H_{\mathrm{AC}}|i'\rangle = -|\mathcal{E}_0|^2 \sum_j \left(\frac{\langle i|\hat{e}\cdot\boldsymbol{\mu}|j\rangle\langle j|\hat{e}^*\cdot\boldsymbol{\mu}|i'\rangle}{\hbar(\omega_{ij}-\omega)} + \frac{\langle i|\hat{e}^*\cdot\boldsymbol{\mu}|j\rangle\langle j|\hat{e}\cdot\boldsymbol{\mu}|i'\rangle}{\hbar(\omega_{ij}+\omega)} \right) \tag{6.10}$$

This expression comes from combining eqns. 6.1 and 6.2, then generalizing to the case where the dipole operator can couple different ground states. The diagonal matrix elements $i = i'$ give the energy shifts considered above.

It is possible to explicitly calculate and sum over the dipole matrix elements above, and this gives a relatively simple way of understanding the origin of the differential AC Stark shifts. However, a more elegant approach is

[5] Similarly, if the polarizability changes as a function of a molecules' vibrational coordinates, the oscillating field can couple vibrational states [236]. These two effects are used for rotational and vibrational Raman spectroscopy, which are common techniques in physical chemistry.

to use spherical tensor notation, expressing all shifts in terms of the polarizability tensor. This is done in detail in Appendix A.6, following Ref. [322], with the approach briefly sketched here. The advantage of this approach is that the Stark shifts are quantified by the polarizabilities α_k, which encode the sum over excited electronic states but are ultimately just effective Hamiltonian parameters acting within a single electronic state. These can be spectroscopically measured (or calculated) and treated like any other parameter in the effective Hamiltonian.

Matrix elements of H_{AC} in the case (b) basis $|\Lambda, \ell, N, S, J, I, F, M\rangle$ are worked out in appendix A.6, following Ref. [322]. To a good approximation for far-detuned optical traps, all substructure within each electronic state can be ignored. In that case, the result is:[6]

$$
\begin{aligned}
&\langle \Lambda, \ell, N, S, J, I, F, M | H_{\text{AC}} | \Lambda, \ell, N', S, J', I, F', M' \rangle = \\
&\quad = -\frac{I}{2\epsilon_0 c} \sum_{k=0}^{2} \sum_{p=-k}^{k} (-1)^p \mathcal{P}_{-p}^{k} \\
&\qquad \times (-1)^{F-M} \begin{pmatrix} F & k & F' \\ -M & p & M' \end{pmatrix} (-1)^{J+I+F'+k} \sqrt{(2F+1)(2F'+1)} \begin{Bmatrix} J & F & I \\ F' & J' & k \end{Bmatrix} \\
&\qquad \times (-1)^{N+S+J'+k} \sqrt{(2J+1)(2J'+1)} \begin{Bmatrix} N & J & S \\ J' & N' & k \end{Bmatrix} \\
&\qquad \times (-1)^{N-K} \sqrt{(2N+1)(2N'+1)} \begin{pmatrix} N & k & N' \\ -K & 0 & K' \end{pmatrix} \alpha_k
\end{aligned}
\tag{6.11}
$$

where $K = \Lambda + \ell$ is the projection of N onto the molecular symmetry axis. The components of the polarization

[6] Note that here we neglect contributions that couple states with $\Delta\ell = \pm 2$. Such terms may arise due to vibronic coupling in CaOH and contribute parity-dependent AC Stark shifts in the $\widetilde{X}(010)$ ground state. See Appendix A.6 for details.

tensor, $\mathcal{P}_p^k$, describe the laser polarization and are defined in Appendix A.6. For linearly polarized light aligned along the laboratory Z axis, the nonzero components are $\mathcal{P}_0^0 = 1$ and $\mathcal{P}_0^2 = 1$. For X-polarized light, the $k = 0$ and $k = 1$ components are unchanged, while $\mathcal{P}_0^2 = -1/2$ and $\mathcal{P}_{\pm 2}^2 = \sqrt{3/8}$. The $k = 1$ components are zero for all linearly polarized light.

The polarizabilities, α_k, are[7]

$$\alpha_0(\omega) = \frac{1}{3}\left(\alpha_\parallel(\omega) + 2\alpha_\perp(\omega)\right) \quad \text{(scalar polarizability)} \tag{6.12a}$$

$$\alpha_1(\omega) \approx 0 \quad \text{(vector polarizability)} \tag{6.12b}$$

$$\alpha_2(\omega) = \frac{2}{3}\left(\alpha_\parallel(\omega) - \alpha_\perp(\omega)\right) \quad \text{(tensor polarizability)} \tag{6.12c}$$

where $\alpha_\parallel$ and $\alpha_\perp$ are the parallel and perpendicular polarizabilities, which encapsulate 2nd-order perturbation sums over parallel and perpendicular electronic transitions, respectively. For a Σ state (e.g. the ground state of

[7]Note that there is an arbitrary prefactor in these expressions that can be compensated in the definition of the polarization tensor, $\mathcal{P}_p^k$. Here we follow the convention of Caldwell [322]. Note that with this convention, α_0 is the mean polarizability, and α_2 is proportional to the polarizability anisotropy, $\gamma = \alpha_\parallel - \alpha_\perp$ [236].

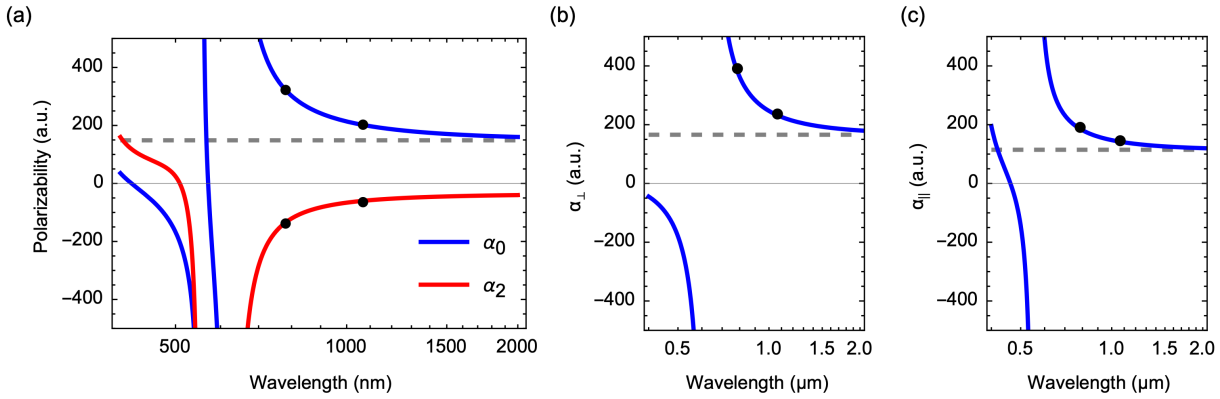

Figure 6.1: CaOH $\widetilde{X}^2\Sigma^+$ polarizability vs. optical wavelength. Shown are (a) the scalar (blue curve) and tensor (red curve) polarizabilities, (b) the perpendicular polarizability $\alpha_\perp$, and (c) the parallel polarizability $\alpha_\parallel$. Black dots are *ab initio* calculations at 1064nm and 780nm, and the grey dashed line is the calculated static ($\lambda \to \infty$) polarizability. Solid curves are calculated polarizabilities using eqns. 6.12 and 6.13 and approximate values of the state lifetimes, as described in the text.

CaOH) they are

$$\alpha_\parallel(\omega) = \sum_j \left(\frac{1}{\hbar(\omega_{ij}-\omega)} + \frac{1}{\hbar(\omega_{ij}+\omega)}\right) |\langle\Sigma|\mu|j,\Sigma\rangle|^2 \tag{6.13a}$$

$$= \sum_{e\in\Sigma} \frac{\pi\epsilon_0 c^3 \Gamma_e}{\omega_e^3}\left(\frac{1}{\omega_e-\omega} + \frac{1}{\omega_e+\omega}\right)$$

$$\alpha_\perp(\omega) = \sum_j \left(\frac{1}{\hbar(\omega_{ij}-\omega)} + \frac{1}{\hbar(\omega_{ij}+\omega)}\right) |\langle\Sigma|\mu|j,\Pi\rangle|^2 \tag{6.13b}$$

$$= \sum_{e\in\Pi} \frac{\pi\epsilon_0 c^3 \Gamma_e}{\omega_e^3}\left(\frac{1}{\omega_e-\omega} + \frac{1}{\omega_e+\omega}\right)$$

where the sum is over all excited Σ states for $\alpha_\parallel$ and over all Π states for $\alpha_\perp$. In the second line of each equation, we expressed the transition dipole moments in terms of the excited-state natural linewidth Γ, like in eqn. 6.8.

Fig. 6.1 plots the scalar and tensor polarizabilities, α_0 and α_2, and the perpendiular and parallel components $\alpha_\perp$ and $\alpha_\parallel$, as a function of wavelength for the CaOH $\widetilde{X}^2\Sigma^+$ ground state. Also shown are *ab initio* calculations

Wavelength	$\alpha_\perp$	$\alpha_\parallel$	α_0	α_2	α_2/α_0
Static	165.8	114.7	148.8	−34.1	−0.229
1064 nm	234.6	142.6	203.9	−61.3	−0.301
780 nm	393.2	186.5	324.3	−137.8	−0.425

Table 6.1: CaOH polarizabilities from *ab initio* calculations [43, 46, 324]. All polarizabilities are in a.u. We also tabulate the ratio α_2/α_0, which indicates how bad differential AC Stark shifts will be at the same average trap depth for different wavelengths.

from Lan Cheng and Chaoqun Zhang for specific wavelengths, which we use for calculating trap depths in this work [43, 46, 324]. These *ab initio* calculations are also shown in table 6.1.

For the plots of eqn. 6.13 in Fig. 6.1, the excited state linewidths Γ_e were chosen to approximately match the *ab initio* calculations at 1064 nm, 780 nm, and DC. For $\alpha_\parallel(\omega)$, we sum over the $\widetilde{B}^2\Sigma^+$ and $\widetilde{D}^2\Sigma^+$ states. For $\alpha_\perp(\omega)$, we only include the $\widetilde{A}^2\Pi$ state explicitly, but also add an offset $\alpha_{\perp,\mathrm{bg}}$ that captures the effect of higher lying electronic states (e.g $\widetilde{F}$ and $\widetilde{G}$ [240, 325]). We use $\Gamma_A = 2\pi \times 6.0\,\mathrm{MHz}$, $\Gamma_B = 2\pi \times 4.5\,\mathrm{MHz}$, $\Gamma_D = 2\pi \times 6.6\,\mathrm{MHz}$, and $\alpha_{\perp,\mathrm{bg}} = 42$ a.u., all of which were chosen to roughly match the *ab initio* calculations (black data points and dashed line). This value of Γ_A is consistent with the measured $\widetilde{A}$ state lifetime of $1/\Gamma_A = 25(2)$ ns [255], though this analysis should not be considered a precise determination of the state lifetimes.

Remarks

We now make a few general notes about the AC Stark Hamiltonian and its matrix elements. First, we find that the $k = 0$ matrix elements are diagonal and independent of the quantum numbers, with $\langle H_{\mathrm{AC}}^{k=0}\rangle = -(1/2\epsilon_0 c)\alpha_0 I$, which is just the isotropic AC Stark shift discussed above. Therefore, the scalar polarizability describes the common mode shift of all states in an electronic manifold.

The $k = 1$ terms (vector polarizability) are zero in the far-detuned limit since $\alpha_1 \to 0$, though they will ap-

pear once spin-orbit structure (e.g. in the $\widetilde{A}^2\Pi$ state) is taken into account [322, 323].[8] However, the components of $\mathcal{P}_p^1$ are all zero for linearly polarized trapping light, so this term can be made to vanish by appropriate choice of polarization (we use linearly polarized traps throughout this thesis).

The $k = 2$ terms (tensor polarizability) are non-vanishing even for linearly polarized trapping light, and their matrix elements are in general state-dependent and not diagonal (meaning they can mix the molecules' field-free eigenstates). A key challenge for experiments that require long coherence times with optically trapped molecules is to minimize the effect of these tensor polarizability contributions. This can be done either by tuning the tensor polarizability itself to zero, typically using a "magic wavelength" [64, 326] chosen so that $\alpha_{\parallel} = \alpha_{\perp}$ (and therefore $\alpha_2 = 0$), or by tuning the laser polarization so as to zero out these terms, using techniques such as magic angles [205] or magic ellipticities [327, 328]. Of course, another way to minimize the effect of the tensor polarizability is to cool to very low temperatures (or ideally to the motional ground state of the trap [30, 322]), so that the AC Stark shifts are the same for all molecules.

As mentioned earlier, only α_0 and α_2 are nonvanishing for the CaOH ground state when ignoring excited state structure. However, the largest interactions in degenerate electronic states – primarily spin-orbit and vibronic interactions – cause other terms in the polarizability tensor to become significant. For instance, at 1064nm, the vector polarizability α_1 is approx. 0.5% as large as the tensor polarizability [322, 323]. In the $\widetilde{X}(010)$ bending mode, there is an additional term that causes parity-dependent AC Stark shifts and is around 1% as large as α_2. This means that there are differential AC Stark shifts between opposite parity-doublet states in the CaOH bending mode, though they are much smaller than ordinary tensor Stark shifts. These effects are described in more detail in Appendix A.6.

[8] For instance, in the CaOH ground state, $\alpha_1 \approx 0.001\alpha_{\perp}$ at a wavelength of 1064 nm.

6.1.2 Photon scattering

For far-detuned optical trapping light, the dominant effect on the molecules is a conservative electric dipole force proportional to the gradient of the intensity. However, the trapping light also causes the molecules to slowly scatter photons. In the far detuned limit, this can be understood in a classical picture: the optical electric field induces an oscillating electric dipole moment in the molecule, which absorbs and re-radiates a small amount of energy. Quantum mechanically, this occurs because the molecular eigenstates in the presence of the trapping light include a small admixture of excited electronic states, which spontaneously emit photons when populated. There are two types of photon scattering. The first is Rayleigh (or elastic) scattering, where the emitted photon has the same energy as the trap photons, and the molecular state is unchanged. The second is Raman (inelastic) scattering, where the emitted photon energy differs from that of the trap photons, and the internal molecular state changes. In the context of quantum control experiments, Rayleigh scattering is a problem only insofar as it slowly heats the trapped molecules, while Raman scattering scrambles the molecules' internal states, limiting our ability to control them over long periods of time.

In the presence of far-detuned trap light, the initial molecular state $|i\rangle$ obtains an admixture of excited state population. In first-order perturbation theory, the state becomes[9]

$$|i\rangle \to |i^{(1)}\rangle \approx |i\rangle + \mathcal{E}_0 \sum_j |j\rangle \left(\frac{\langle j|\hat{e}\cdot\boldsymbol{\mu}|i\rangle}{\hbar(\omega_{ij}-\omega)} + \frac{\langle j|\hat{e}^*\cdot\boldsymbol{\mu}|i\rangle}{\hbar(\omega_{ij}+\omega)} \right) \equiv |i\rangle + \sum_j c_j|j\rangle$$

where the sum is over all excited states j, $\mathcal{E}_0$ is the electric field amplitude, $\hat{e}$ is the laser polarization unit vector,

[9] The counterrotating term can be thought of as arising from a laser with frequency $-\omega$ and polarization $\hat{e}^*$, see section 5.9 of Ref. [321]

and $\boldsymbol{\mu}$ is the electric dipole operator. When the molecule scatters a photon, it decays back to ground state $|i'\rangle$, which is not necessarily the same as the initial ground state, i.e. it could be a different rotational or vibrational level (Rayleigh scattering corresponds to $|i'\rangle = |i\rangle$, and anything else is Raman scattering). The rate at which this happens is proportional to the transition dipole matrix element squared (just as the natural linewidth Γ is proportional to $|\langle g|\boldsymbol{\mu}|e\rangle|^2$), and the actual operator corresponding to a spontaneous decay event projects the excited state onto the ground state according to dipole selection rules, $P_{i'} = \sum_j |i'\rangle\langle i'|\hat{e}_s \cdot \boldsymbol{\mu}|j\rangle\langle j|$, where $\hat{e}_s$ is the polarization of the spontaneous decay photon. Adding prefactors to convert the transition dipole into a scattering rate[10] gives for the photon scattering rate from state $|i\rangle$ to $|i'\rangle$

$$\begin{aligned} R_{ii'} &\approx \frac{\omega^3}{3\pi\epsilon_0\hbar c^3}\left|\sum_j \langle i'|P_{i'}|j\rangle c_j\right|^2 \\ &\approx \frac{\omega^3|\mathcal{E}_0|^2}{3\pi\epsilon_0\hbar c^3}\left|\sum_j\left(\frac{\langle i'|\hat{e}_s^*\cdot\boldsymbol{\mu}|j\rangle\langle j|\hat{e}\cdot\boldsymbol{\mu}|i\rangle}{\hbar(\omega_{ij}-\omega)}+\frac{\langle i'|\hat{e}_s\cdot\boldsymbol{\mu}|j\rangle\langle j|\hat{e}^*\cdot\boldsymbol{\mu}|i\rangle}{\hbar(\omega_{ij}+\omega)}\right)\right|^2 \\ &\equiv \frac{\omega^3 I}{6\pi\epsilon_0^2\hbar c^4}|\langle i'|\mathcal{S}_{\mathrm{AC}}|i\rangle|^2 \end{aligned} \tag{6.14}$$

Notice that the dipole matrix elements are summed before squaring, meaning interference effects can modify the scattering (for instance, we will see that Raman scattering is significantly suppressed compared to Rayleigh scattering due to destructive interference [329]).[11]

In the third line, we defined an operator $\mathcal{S}_{\mathrm{AC}}$ that encompasses the sum over excited states. Comparing eqn. 6.14

[10] I.e. by taking the power radiated from the induced dipole and dividing by $\hbar\omega$. Note that the radiated photons are at the laser frequency, ω, not the resonance frequency.

[11] One way to understand why this interference occurs is to note that, by conservation of energy, the frequency of the scattered photon is just the laser frequency minus the change in the molecule's internal state energy [321]. Since the photon energy contains no information about the excited electronic state, measuring it does not collapse the superposition of excited states.

with the AC Stark Hamiltonian from eqn. 6.10, we see that $\mathcal{S}_{\text{AC}}$ is nearly identical to H_{AC}, with the difference being that the polarizations of the two photons can differ (since one photon is absorbed from the laser and the other is a spontaneous decay photon). By analogy with our discussion of AC Stark shifts above, Rayleigh scattering ($i = i'$) is related to the diagonal matrix elements and therefore to the scalar polarizability, while Raman scattering is related to the vector and tensor polarizabilities.

The Rayleigh scattering rate comes from setting $i = i'$ and $\hat{e}_s = \hat{e}$, so that

$$\begin{aligned} R_{\text{Rayleigh}} &\approx \frac{\omega^3 |\mathcal{E}_0|^2}{3\pi\epsilon_0 \hbar c^3} \left(\sum_j |\langle i|\hat{e}\cdot\boldsymbol{\mu}|j\rangle|^2 \left(\frac{1}{\hbar(\omega_{ij}-\omega)} + \frac{1}{\hbar(\omega_{ij}+\omega)} \right) \right)^2 \\ &\approx \frac{\omega^3 I}{6\pi\epsilon_0^2 \hbar c^4} \left(\sum_e \frac{(2-\delta_{\Lambda_e 0})}{(2-\delta_{\Lambda_i 0})} \frac{\pi\epsilon_0 c^3 \Gamma_e}{\omega_e^3} \left(\frac{1}{\omega_e - \omega} + \frac{1}{\omega_e + \omega} \right) \right)^2 \\ &\approx \frac{\omega^3}{6\pi\epsilon_0^2 \hbar c^4} \alpha_0(\omega)^2 I \end{aligned} \tag{6.15}$$

where we noted that the expression in parentheses in the first line is just the scalar polarizability from eqn. 6.2. Fig. 6.2 shows the Rayleigh scattering rate as a function of wavelength for CaOH, with a laser intensity similar to what we use in the optical trap described later in this chapter.

For a transition from a nondegenerate ground state to a nondegenerate excited state with linewidth Γ and resonance frequency ω_0, this reduces to

$$R_{\text{Rayleigh}} \approx \frac{\pi c^2 \Gamma^2}{6\hbar\omega_0^3} \left(\frac{\omega}{\omega_0} \right)^3 \left(\frac{1}{\omega_0 - \omega} + \frac{1}{\omega_0 + \omega} \right)^2 I \tag{6.16}$$

This is similar to the standard expression for an optically trapped atom [320], except it is lower by a factor of 9.

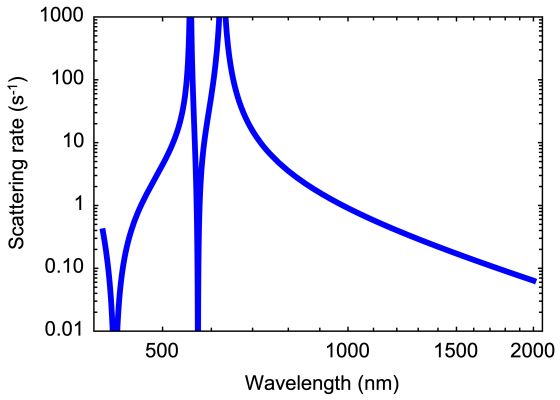

Figure 6.2: Rayleigh scattering rate as a function of wavelength, for molecules at the bottom of an optical trap with a power of 13.5 W and a waist of 25 μm (similar to the geometry of our ODT). The polarizability used for this calculation is the same as in Fig. 6.1.

This is because each electronic transition has 1/3 the transition strength of a corresponding atomic transition (or 2/3 the strength for transitions from a nondegenerate to a degenerate state), since it can only be driven along a single axis in the molecule frame.[12]

Whereas the Rayleigh scattering rate is proportional to $\alpha_0(\omega)^2$, the Raman scattering rate will be proportional to $\alpha_2(\omega)^2$ (assuming the vector polarizability is negligible). The strengths can be calculated in a similar way to the tensor Stark shift matrix elements (which are discussed above and in appendix A.6.) However, there are slight differences due to the fact that the two photons need not have the same polarization.

[12] This is due to the lifting of spherically symmetry when going from an atom to a molecule. However, if we sum over transitions along all three axes, e.g. over the $\widetilde{A}^2\Pi$ and $\widetilde{B}^2\Sigma$ states in the 2nd line of eqn. 6.15, we recover the Rayleigh scattering rate for an atom.

6.1.3 Trap properties for a Gaussian beam

In this thesis, we use focused Gaussian laser beams to form optical traps. The intensity of a (generally elliptical) Gaussian beam propagating along the z axis is

$$I(x,y,z) = I_0 \frac{w_{0x} w_{0y}}{w_x(z) w_y(z)} \exp\left(-\frac{2x^2}{w_x(z)^2}\right) \exp\left(-\frac{2y^2}{w_y(z)^2}\right) \tag{6.17}$$

where w_{0x} and w_{0y} are the beam waists ($1/e^2$ radii) along the x and y axes, $w_i(z) = w_{0,i}\sqrt{1+(z/z_{R,i})^2}$ is the beam size along axis i ($i = x, y$) as a function of axial position, $z_{R,i} = \pi w_{0,i}^2/\lambda$ is the Rayleigh range, and $I_0 = 2P/\pi w_{0x} w_{0y}$ is the peak intensity for a beam with optical power P.

The corresponding trapping potential is

$$U(x,y,z) = U_0 \left(1 - \frac{w_{0x} w_{0y}}{w_x(z) w_y(z)} \exp\left(-\frac{2x^2}{w_x(z)^2}\right) \exp\left(-\frac{2y^2}{w_y(z)^2}\right)\right) \tag{6.18}$$

where $U_0 \approx \alpha_0 I_0/(2\epsilon_0 c)$ is the average trap depth (ignoring state-dependent shifts).

For sufficiently low temperatures, such that the molecules only explore the bottom of the potential, a Gaussian

trap looks approximately harmonic. The harmonic trap frequencies are

$$\omega_x = \left(\frac{1}{m} \left. \frac{\partial^2 U}{\partial x^2} \right|_{x,y,z=0} \right)^{1/2} = \sqrt{\frac{4U_0}{m w_{0x}^2}} \tag{6.19a}$$

$$\omega_y = \left(\frac{1}{m} \left. \frac{\partial^2 U}{\partial y^2} \right|_{x,y,z=0} \right)^{1/2} = \sqrt{\frac{4U_0}{m w_{0y}^2}} \tag{6.19b}$$

$$\omega_z = \left(\frac{1}{m} \left. \frac{\partial^2 U}{\partial z^2} \right|_{x,y,z=0} \right)^{1/2} = \sqrt{\frac{U_0}{m z_{R,x}^2} + \frac{U_0}{m z_{R,y}^2}} \tag{6.19c}$$

so that $U(x,y,z) \approx m\omega_x^2 x^2/2 + m\omega_y^2 y^2/2 + m\omega_z^2 z^2/2 + \mathcal{O}(r^4)$.

The number density of molecules in the trap is $n(\boldsymbol{r}) = n_0 \exp(-U(\boldsymbol{r})/k_B T)$, where T is the temperature and n_0 is the peak density, which is determined by the requirement that integrating $n(\boldsymbol{r})$ over all space gives the total molecule number, N. Within the harmonic approximation, we find

$$n_0 \approx N \left(\int \exp\left(-\frac{m(\omega_x^2 x^2 + \omega_y^2 y^2 + \omega_z^2 z^2)}{2k_B T} \right) d^3\boldsymbol{r} \right)^{-1} = \frac{N\omega_x\omega_y\omega_z}{(2\pi k_B T/m)^{3/2}} \tag{6.20}$$

Notice, in particular, that for constant laser power, the trap frequencies scale with the beam waist (assuming a circular beam, $w_0 \equiv w_{0x} = w_{0y}$) as $\omega_x \propto 1/w_0^2$, $\omega_y \propto 1/w_0^2$, and $\omega_z \propto w_0^3$. Therefore, for fixed trap power, number, and temperature, the peak density scales as $1/w_0^7$ [278].

6.2 Optical trapping of CaOH

In this section, we describe our work loading CaOH into an optical dipole trap, formed from a high-power 1064 nm laser with a waist of approximately 25 μm.

6.2.1 Optical setup

To trap CaOH, we used a very similar setup to the CaF experiment, which was previously described in Ref. [278].[13] In particular, we chose to use a 1064 nm trapping laser due to the availability of high-power fiber amplifiers at this wavelength. As discussed previously, CaOH has a positive scalar polarizability at 1064 nm, enabling optical trapping at the focus of a Gaussian beam. Moreover, 1064 nm excitation from the $\widetilde{A}$ and $\widetilde{B}$ states is far detuned from any excited electronic manifolds, so it shouldn't interfere with imaging (by contrast, we saw that 780 nm light coupled $\widetilde{A}$ and $\widetilde{B}$ to the $\widetilde{D}$, $\widetilde{E}$, and $\widetilde{F}$ states, which interfered with molecule imaging in optical tweezers, as described in chapter 8).

We use a 50 W, 1064 nm fiber amplifier (Nufern) seeded with either a RIO Orion module or a Thorlabs DBR. The RIO has significantly better relative intensity noise (RIN) than the DBR, but we did not find that this mattered until going to very high trap depth for the collision work described in chapter 9. It is, however, critically important to use a single frequency trapping laser. As observed previously in the CaF experiment, using a multimode trapping laser causes severe problems [278]. The light from the fiber amplifier is sent through an AOM for switching and intensity stabilization, then coupled into a photonic crystal fiber (PCF) (LMA-PM-15) and sent to the MOT table. We observe that the alignment of the Nufern amplifier drifts over the first $\sim$30 minutes of running each day, with it sometimes being necessary to adjust the vertical alignment to maintain sufficiently high fiber coupling. However, this usually stabilizes later in the day. We also monitor the temperature of the input end of the PCF (with a temperature probe on the outside casing), since poor fiber coupling could cause the temperature to get very high. However, we never observe temperatures higher than $\sim$30°C.

[13] Most of our setup was, in fact, removed from CaF Gen I and reinstalled on our experiment once that experiment was decommissioned.

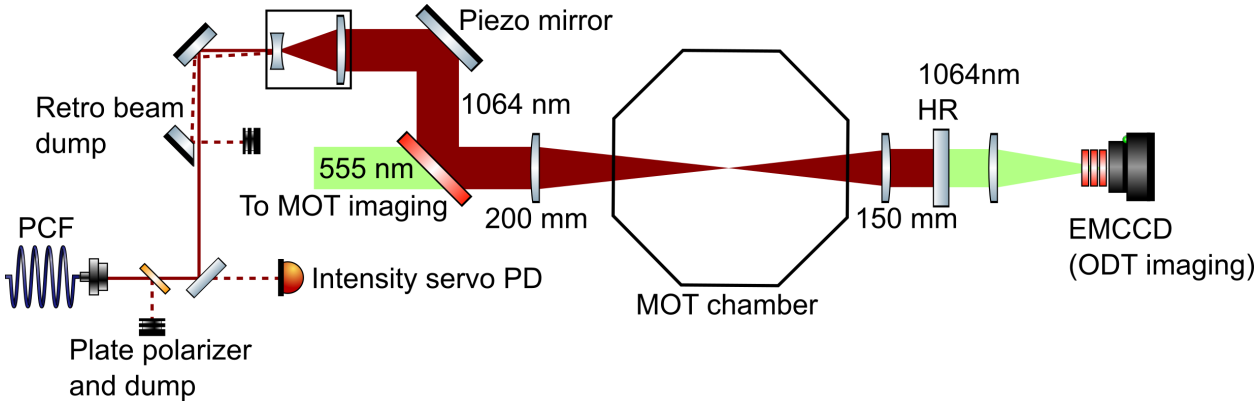

Figure 6.3: Overview of the optics used for forming and imaging the ODT.

An overview of the ODT setup near the MOT chamber is shown in Fig. 6.3. After the PCF, a small amount of light is picked off and sent to a photodiode for monitoring and intensity stabilization (the stabilization uses an SRS SIM960 PID box controlling the RF power into the AOM). The beam is expanded, combined with the MOT imaging path on a dichroic, and then focused into the chamber with a 200 mm lens, resulting in a focused beam waist of $w \approx 25\ \mu$m. The beam is retroreflected back through the chamber with a slight misalignment to avoid forming a lattice, then picked off and dumped back near the PCF fiber coupling. This is done because we found that dumping the light on the same side as the ODT imaging camera resulted in significant background light in the image. There are dichroics on both sides of the chamber to separate the 1064 nm ODT light from 555 nm molecule fluorescence. This fluorescence can be collected and imaged on either side, with the camera on the near side typically used for imaging the MOT and the camera on the far side being used to image molecules in the ODT. We use an Andor iXon 897 Ultra EMCCD to image the ODT. Note that for subsequent work, including what is described in chapters 7, 8, and 9, we installed an in-vacuum asphere on the far side of the MOT chamber. This was eventually used to project optical tweezers, but the initial use was to improve collection effi-

ciency when imaging molecules in the ODT. That setup looks similar to Fig. 6.3, but with the first lens after the ODT focus on the right hand side moved from outside the chamber to inside the chamber.

We use approximately 13.3 W of 1064 nm light for form the ODT, which combined with our ∼25 μm waist should give a trap depth around 620 μK, based on the *ab initio* polarizability calculations described above. This agrees well with trap frequency measurements described below. Because we can cool to 20 μK in free space using a single-frequency molasses, this depth should be more than sufficient for loading the trap.

Initial alignment and first signal

To initially align the ODT, we imaged the MOT with the ODT imaging camera (on the far side of the MOT chamber), and made sure the imaging system was well focused on the MOT. Next, we imaged the 1064 nm ODT beam on the same camera (by removing filters that would otherwise block it from reaching), and made sure it was centered at the imaged MOT position and approximately focused. We simulated that there would be an approx. 1 mm focal shift for imaging 1064 nm vs. 555 nm (the MOT imaging wavelength), so we also had to account for this when setting the focus position. For comparison, the Rayleigh range of our ODT is approximately 1.5-2 mm. Nonetheless, this ∼1 mm focal shift is important to account for to give ourselves the best possible chance of seeing an ODT.

Because the focal/axial position was less well constrained than the radial position, we began searching for an ODT by scanning the focus, using a translation stage to move the 200 mm focusing lens. We tried loading the ODT at full trap depth (∼600 μK) from a molasses using single-frequency (SF) cooling, then turning off the molasses for 40 ms to allow any untrapped molecules to fly away, and then imaging the molecules in the trap. With significant averaging, we were able to see a dependence on the focal position, which confirmed our initial

ability to load the ODT. From there, we began optimizing parameters, including the loading duration, loading cooling parameters, and imaging parameters. We also added the ability to compress the RF MOT (which we did not have when first loading the ODT), which provided a significant improvement.

For imaging the ODT, we initially used a short pulse of resonant light but soon switched to SF cooling. This allows the molecules to stay trapped during imaging, allowing significantly more photons to be scattered [231].[14] Note that if our imaging were not background free we might have a preference for imaging with Λ cooling (which is what we use for tweezer imaging in chapter 8), since the higher ratio of photon scattering rate to imaging laser power results in better signal-to-noise when the laser power is a limitation. However, SF imaging is more robust to drifts in laser detuning, and there is no downside when imaging background free other than the longer time needed to image.

6.2.2 Experimental overview

Once the various parameters were optimized, the ODT loading sequence and resulting number, density, and temperature were as follows. These results were previously reported in Ref. [43].

CaOH molecules are loaded into the ODT using a blue-detuned single-frequency (SF) molasses (see chapter 5). The experimental sequence is as follows. We begin by loading an RF MOT, and then we compress the MOT it by ramping the RMS axial gradient up to $\sim$24 G/cm (chapter 5). After switching off the MOT, the ODT is turned on and a 1 ms pulse of Λ-cooling ($\Delta_{\mathrm{SD}} = 12$ MHz, $\delta = 0$ MHz, $I_{\mathrm{SD}} = 64$ mW/cm^2) is used to cool the molecules to below the capture velocity of SF cooling. The molasses is then reconfigured for SF cool-

[14] It also prevents the cloud from expanding during imaging, improving SNR since the collected photons end up on fewer camera pixels.

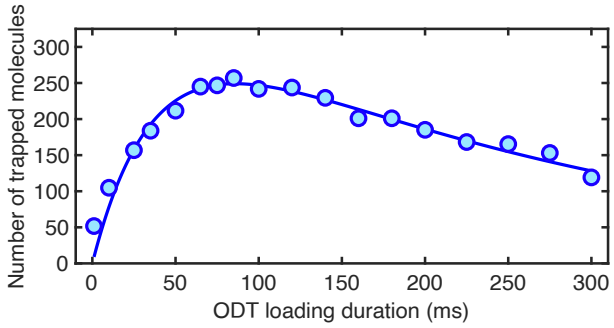

Figure 6.4: Number of molecules loaded into the optical dipole trap as a function of loading time with SF cooling on. The solid curve is a fit to a rate equation with constant loading and loss rates. The loss rate is consistent with photon scattering into vibrational dark states during SF cooling. Figure reproduced from Ref. [43].

ing ($\Delta_{\mathrm{SD}} = 74$ MHz, $I_{\mathrm{SD}} = 64$ mW/cm^2) to cool and load the molecules into the ODT. After loading the ODT, the molasses is turned off for 50 ms to allow untrapped molecules to escape the field of view of the EMCCD camera used to image the molecules. Trapped molecules are then imaged by turning SF cooling on again for 100 ms and collecting fluorescence decays from the $\widetilde{B}^2\Sigma^+$ state [42]. We find that a maximum number of 260(80) molecules are trapped in the ODT by loading with SF cooling for ∼80 ms (Fig. 6.4). Longer loading times decrease the number of loaded molecules due to loss to rovibrational dark states during SF cooling. An in-trap temperature of $T = 57(8)$ μK is determined by varying the ODT depth and observing the number of surviving molecules, as described below. We calculate a peak molecule number density of $3(1) \times 10^9$ cm^{-3} and a phase-space density of $9(5) \times 10^{-8}$ in the ODT.

6.2.3 Measurement of trap frequencies

The radial trap frequencies of the ODT are determined by the parametric heating method [320]. Following loading of the ODT, a first image is taken with 50 ms of SF cooling. The power of the ODT is then amplitude modulated from the nominal power (13.3 W) with a variable modulation frequency and a modulation depth of ∼29%

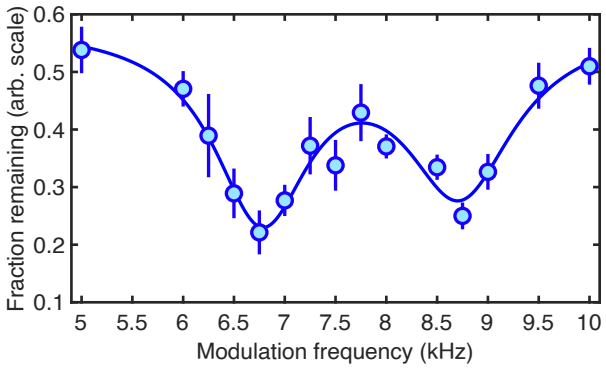

Figure 6.5: Molecule loss versus modulation frequency of the trap depth of the ODT. The fit is to two Lorentzian functions with centers located at $6.8(1)$ kHz and $8.7(2)$ kHz and an offset of 0.58(8). Reproduced from Ref. [43].

for a total of 500 modulation cycles.[15] A second 50 ms image is taken following the modulation sequence, with a short wait time (with the trap held at a constant depth) inserted between the end of the modulation and the second image to ensure that there is a constant total time between the two images. This normalizes out the effect of vacuum losses. Loss of molecules from the ODT due to parametric heating caused by the modulation appears as a decrease in the fraction of molecules remaining in the second image, normalized to the number in the first image (Fig. 6.5). Two resonant loss features are observed at modulation frequencies of $6.8(1)$ kHz and $8.7(2)$ kHz, from which we identify radial trap frequencies $\omega_x = 2\pi \times 3.4(1)$ kHz and $\omega_y = 2\pi \times 4.4(1)$ kHz. The axial trap frequency was not measured.

In section 6.1.3, we found that in the harmonic approximation, the trap depth is related to the radial frequencies by

$$U_0 = \frac{m w_{0,i}^2 \omega_i^2}{4} \tag{6.21}$$

where m is the mass, $w_{0,i}$ is the waist along axis i, and ω_i is the trap frequency along axis i. The harmonic ap-

[15] The SRS PID bandwidth is 100 kHz, so we just modulated the power setpoint of the PID box.

proximation applies in our experiment since the molecule temperature is approximately 1/10 the trap depth. The radial waists are measured to be $w_{0,x} = 27.5\ \mu$m and $w_{0,y} = 23.3\ \mu$m by imaging the focused ODT beam on a CCD camera. Combined with the trap frequencies reported above, the trap depth may be calculated from eqn. 6.21 using either $w_{0,x}$ and ω_x or $w_{0,y}$ and ω_y, resulting in two separate measurements of the trap depth of $\sim$592 μK and $\sim$704 μK. The $\sim$15% disagreement between these two values may be due to uncharacterized errors in the waist and/or frequency measurements or possible deviations of the trapping potential from an asymmetric Gaussian beam profile, for example, due to astigmatism, which is not modeled. For density measurements (see below), we use the geometric mean, i.e., $U_0 = m\overline{w_0}^2\overline{\omega}^2/4 = 645(87)\ \mu$K, where $\overline{w_0} = (w_{0,x}w_{0,y})^{1/2}$ and $\overline{\omega} = (\omega_x\omega_y)^{1/2}$. This is in very good agreement with the predicted trap depth using the measured ODT power and beam waist along with the *ab initio* scalar polarizability calculation. Therefore, the *ab initio* theory appears to be quite reliable.

6.2.4 Temperature measurement

We use a "shaving" method to determine the temperature of molecules in the ODT. The idea is to load the ODT, then diabatically drop the trap depth and hold for a sufficiently long duration that all molecules with an energy higher than the trap depth will escape. We then jump the trap depth back up and image the number of surviving molecules. The molecule survival as a function of shaving depth can then be fit to a model to extract the temperature.

Naively, one might imagine that this method directly measures the distribution of molecule energies in the

trap. The Boltzmann energy distribution for a harmonic trap is [330]

$$f_{\text{th}}(E) = \frac{1}{2(k_B T)^3} E^2 e^{-E/k_B T} \tag{6.22}$$

where T is the molecule temperature and E is the molecule energy. When we shave the trap down to a depth E_f, the molecule survival probability is just the integral of this distribution from 0 to E_f, which is [330]

$$P_{\text{surv}}(\eta_f) = 1 - \left[1 + \eta_f + \frac{1}{2}\eta_f^2\right] e^{-\eta_f} \tag{6.23}$$

where $\eta_f = E_f/k_B T$. It turns out that this is indeed the correct model for an *adiabatic* shave, where the trap depth is lowered very slowly [330]. However, for a fast shave like we use in the experiment, we are in the opposite limit. We find that in this case, fitting to eqn. 6.23 typically gets the temperature too low by approximately a factor of two. This is likely because an infinitely fast diabatic shave leaves each molecule's kinetic energy approximately unchanged, but reduces its potential energy by the change in trap depth at the molecule's position. Therefore, this method is primarily sensitive to the kinetic, but not potential, portion of the total energy distribution.

Ultimately, because of these issues, we use Monte Carlo simulations of the trap dynamics to properly extract the temperature from these shaving measurements. Nonetheless, the shaving protocol contains plenty of information about the molecules' temperature, so a fit to the Monte Carlo model is a reasonably reliable way to extract the temperature.

Our sequence for doing this is as follows. A first image of the trapped molecules is taken with 50 ms of SF cooling to measure the initial number of molecules loaded into the ODT. After a 40 ms wait time following this

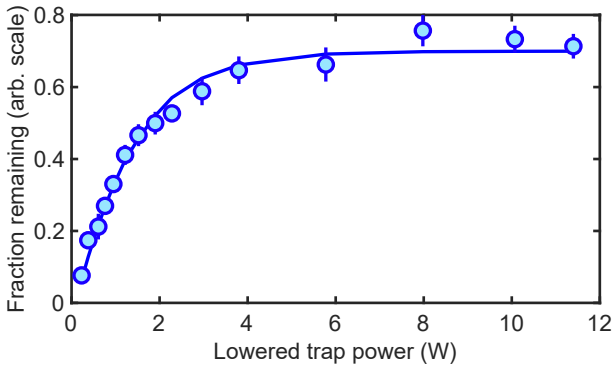

Figure 6.6: Molecule survival vs. lowered trap depth for shaving temperature measurements. The solid curve is a Monte Carlo simulation of losses of trapped molecules, initialized with a temperature 57 K, during the experimental sequence corresponding to the data shown. Reproduced from Ref. [43].

first image, the trap depth is lowered by decreasing the ODT power to a variable fraction of the initial power (13.3 W). The ODT power is controlled by an AOM and is changed with a response time of ∼10 μs. The ODT is kept at this lower power for 30 ms before increasing the power back to its initial value. Following a 30 ms wait, a second 50 ms image is taken and the surviving fraction of molecules is determined by comparison to the first image (Fig. 6.6). In order to extract the in-trap temperature from the experimentally observed survival, the trap losses are modeled by a Monte Carlo simulation of trapped CaOH molecules undergoing the experimental sequence. The model is described in Ref. [43]. The fit is shown in Fig. 6.6 and gives a temperature of $T = 57(8)$ μK.

6.2.5 Density

With the temperature estimate above, we estimate the peak density of the ODT as

$$n_0 = \frac{N\omega_x\omega_y\omega_z}{(2\pi k_B T/m)^{3/2}} = 3(1) \times 10^9, \tag{6.24}$$

where $\omega_z \approx 2\pi \times 37(3)$ Hz is estimated from eqn. 6.19, using the measured trap depth U_0 and Rayleigh ranges $z_{R,x} = 2.2$ mm and $z_{R,y} = 1.6$ mm determined from the measured beam waists. The corresponding peak phase-space density is

$$\rho_0 = n_0 \lambda_{\mathrm{dB}}^3 = 9(5) \times 10^{-8}, \tag{6.25}$$

where $\lambda_{\mathrm{dB}} = (2\pi\hbar^2/mk_BT)^{1/2} = 3.0(2) \times 10^{-8}$.

6.3 Transfer into the bending mode

After loading CaOH molecules into the optical dipole trap, the next step was to promote the molecules to the "science state," namely the $\widetilde{X}(010)$ vibrational bending mode. The key feature of this state is that, because the nuclei bend off axis while vibrating, there is a moment of inertia about the symmetry axis of the molecule and a corresponding angular momentum quantum number about this axis. In effect, the molecule looks nonlinear and takes on the key properties a nonlinear molecule would.

To study the $\widetilde{X}^2\Sigma^+(010)(N'' = 1^-)$ vibrational bending mode, we optically pump molecules into this state by simply turning off the corresponding repumping laser (Fig. 6.7). To quantify the transfer, we first load the ODT and image the trapped molecules with 50 ms of SF cooling, as described above. This first image serves as a normalization signal to account for shot-to-shot variations in the number of molecules loaded into the ODT. The molecules are then SF cooled for a variable time with the $\widetilde{X}^2\Sigma^+(010)(N'' = 1^-)$ repumping laser turned off. The vibrational branching ratio (VBR) from the optical cycle into this state is $v_{\mathrm{bend}} = 8.2 \times 10^{-4}$, while the VBR into dark rovibrational states is $v_{\mathrm{dark}} \approx 8.5 \times 10^{-5}$ [42]. We therefore expect the fraction of molecules pumped into the vibrational bending mode to be at most $v_{\mathrm{bend}}/(v_{\mathrm{bend}} + v_{\mathrm{dark}}) \approx 91\%$. The timescale for optical

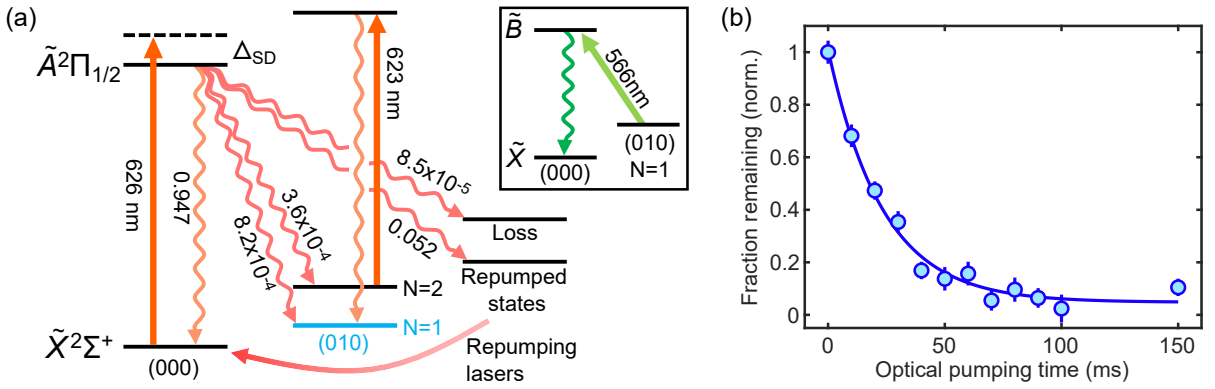

Figure 6.7: Populating the $\widetilde{X}^2\Sigma^+(010)(N'' = 1)$ vibrational bending mode. (a) The optical pumping scheme. The bending mode repumping laser is turned off while all other cycling and repumping lasers remain on. Vibrational repumping lasers for other states are shown schematically by the "repumping" arrow connecting back to (000). Vibrational branching ratios are labeled for each decay channel. The main cooling laser is blue-detuned by a frequency Δ_{SD} to perform SF cooling of the molecules during population transfer. For more details on the optical cycling lasers used, see Ref. [42]. Inset: repumping transition driven to optically detect molecules in the bending mode. (b) Transfer into the bending mode versus optical pumping time. The solid curve is an exponential fit with a time constant of $\tau = 23.4(2.2)$ ms. Figure reproduced from Ref. [43].

pumping, τ_{bend}, corresponds to $1/v_{\text{bend}} \approx 1200$ photons scattered at the SF cooling scattering rate, R_{SF}. At the measured scattering rate of $R_{\text{SF}} = 45 \times 10^3\ \text{s}^{-1}$ (see below), this results in a calculated optical pumping timescale of ~26 ms. After optical pumping, the surviving ground-state molecules are imaged with the bending mode repumping laser turned off (Fig. 6.7(b)). We observe $\tau_{\text{bend}} = 23.4(2.2)$ ms, which is consistent with the calculated value. A short repumping pulse on the $\widetilde{X}^2\Sigma^+(010)(N'' = 1^-) \rightarrow \widetilde{B}^2\Sigma^+(000)(N' = 0)$ transition is used to recover molecules from the bending mode (Fig. 6.7(a), inset). We observe 80(3)% survival after two-way transfer into and out of the bending mode, normalized to the number of surviving molecules after an equal hold time in the $\widetilde{X}^2\Sigma^+(000)$ ground state. There is no measurable change to the in-trap temperature due to the optical pumping, hence the density in the trap has decreased by at most ~20% after the transfer.

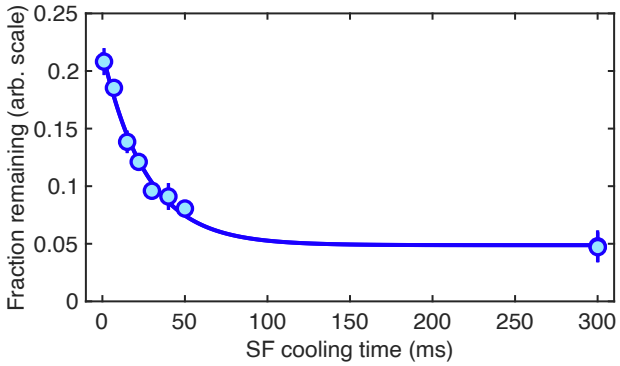

Figure 6.8: Molecule loss versus cooling time for SF cooling in the ODT, with repumping lasers removed so that the molecules scatter only 1200 photons before $1/e$ loss occurs. The fit is to an exponential decay with a time constant $\tau_{\text{scatt}} = 26.7(2.3)$ ms and an offset of $0.049(4)$. Reproduced from Ref. [43].

Measurement of SF scattering rate in the ODT

To measure the scattering rate for SF cooling in the ODT (which is useful for characterizing the *in situ* imaging and optical pumping into the bending mode), we load molecules into the ODT and image for 60 ms for normalization of the initial number. The SF imaging/cooling parameters are $I_{\text{SD}} = 64\ \text{mW/cm}^2$ and $\Delta_{\text{SD}} = 74$ MHz. We then cool the molecules for a variable time with the same SF cooling parameters, but with several repumping lasers removed so that only 1200 photons are scattered before $1/e$ loss of molecules occurs. The cycling and repumping lasers used for the measurement address $\widetilde{X}(000)$, $\widetilde{X}(100)$, $\widetilde{X}(02^00)$, $\widetilde{X}(200)$, $\widetilde{X}(02^20)$, and $\widetilde{X}(010)(N'' = 1^-)$ only. After cooling, the surviving molecules are imaged (with the high-level repumpers still turned off), and the signal is divided by the number in the first image to determine the survival fraction. A fit to an exponential function with an offset is shown in Fig. 6.8. The offset arises primarily from molecules which are transferred from dark to bright rovibrational states due to vibrational thermalization between cooling and imaging. The fitted exponential decay time is $\tau_{\text{scatt}} = 26.7(2.3)$ ms, corresponding to a scattering rate of

$R_{SF} = 45(4) \times 10^3\ s^{-1}$.

6.4 Vibrational state lifetimes

One challenge of working with trapped polar molecules is their susceptibility to loss from blackbody radiation in the environment, which incoherently drives rovibrational transitions out of the internal quantum state of interest.[16] This mechanism has been theoretically studied [90, 331, 332] and experimentally observed [171, 197, 333, 334] for trapped diatomic molecules, where it can limit lifetimes to $\lesssim$ 10 s at room temperature. The specific sensitivity of diatomic molecules to blackbody radiation has also been proposed as a tool for blackbody thermometry, with the capability for much longer interrogation times compared to Rydberg atoms [90]. Because of the increased quantity of rovibrational states in polyatomic molecules (the number of vibrational modes scales as $\sim 3N$, where N is the number of atoms in the molecule), they have the potential for significantly increased sensitivity to blackbody radiation compared to diatomic species. Although blackbody lifetimes of trapped polyatomic molecules have received some attention in the literature [174, 335, 336], they have been less thoroughly explored.

In addition to blackbody loss, excited vibrational states in polar molecules have finite lifetimes due to spontaneous, radiative decay. A number of proposed experiments with polyatomic molecules rely on population in excited vibrational levels, and the radiative lifetimes of these states are therefore critical for these experiments. In particular, the low-lying vibrational bending modes of linear polyatomic molecules like CaOH, SrOH, and YbOH are expected to be useful for experiments including quantum simulation and computation [101, 109, 110], electrostatic shielding of collisions [131], and precision searches for ultralight dark matter and the electric dipole moment of the electron [45, 89, 140]. Radiative decay lifetimes for excited vibrational states have been previ-

[16] This section has been reproduced, with modifications, from Ref. [44].

ously measured in diatomic molecules [334, 337, 338], but these measurements are more challenging in polyatomic molecules due to their increasingly complex vibrational structure.

In this section, we describe the effect of blackbody radiation (BBR) on trapped molecule lifetimes, and present a measurement of these lifetimes for CaOH in the ODT. In section 6.4.1, we provide an overview of the effect of BBR on optically trapped polar molecules. The key idea is that blackbody radiation and spontaneous decay can redistribute molecules into dark states that remain trapped, so that there is often a significant background of undetectable molecules in our experiments. In section 6.4.2, we make these arguments more quantitative by using rate equations to describe the internal state dynamics. In section 6.4.3, we describe our measurement of the lifetime of the $\widetilde{X}(000)$, $\widetilde{X}(010)$, and $\widetilde{X}(100)$ states in optically trapped CaOH. From this, we extract a few key parameters of the rate equation model that can be used to describe dynamics of a number of low-lying vibrational states. This model can then be applied towards understanding the effect of BBR in experiments later in this thesis.

6.4.1 Overview: blackbody dynamics of polar molecules

In typical experiments with cold, trapped molecules, the molecules are prepared in a single internal quantum state, embedded in a large landscape of states arising from hyperfine, rotational, vibrational, and electronic structure. This highly nonthermal initial distribution can be affected by the room temperature environment. The thermalization process, during which the internal state distribution of the molecule comes into thermal equilibrium with the environment, is mediated by blackbody radiation. Microscopically, thermalization occurs when the tendency for blackbody radiation to drive transitions up the rovibrational ladders is balanced by radiative decay, as first described by the A and B rate coefficients of Einstein.

In polar molecules, electric dipole transitions between rotational or vibrational levels can be strongly driven by room temperature blackbody radiation, which has a maximum power spectral density near 600 cm^{-1}. Because vibrational frequencies in laser coolable molecules are often near this energy, blackbody-driven vibrational transitions can be a significant source of incoherent population transfer in trapped molecules on experimentally relevant timescales, typically on the order of 1 s [171, 197, 333].

Fig. 6.9 schematically illustrates these dynamics using CaOH molecules as an example. The Ca–O stretching mode and the bending mode both have vibrational frequencies near the peak of the blackbody spectrum at 300K (inset). Blackbody radiation drives transitions at a rate R_{bbr} between vibrational states obeying the electric dipole selection rules $\Delta v_1 = \pm 1$ or $\Delta v_2 = \pm 1$; $\Delta \ell = 0, \pm 1$; $\Delta N = 0, \pm 1$; and $\Delta p = \pm 1$, where v_1 and v_2 are the vibrational quantum numbers for the Ca–O stretch and Ca–O–H bending modes, ℓ is the projection of the vibrational angular momentum onto the molecular axis, N is the rotational quantum number, and p is the parity of the state. Excited states spontaneously decay according to the same selection rules at a rate A_{rad}.

In typical laser cooling experiments, the population is initially prepared in the $N = 1$ level of the vibrational ground state, as shown in Fig. 6.9. Vibrational populations thermalize after a few transitions according to the selection rules highlighted above, while rotational populations take many transitions to fully thermalize, as the populations "walk" up the rotational ladder via repeated transitions between vibrational states. The timescale for rotational thermalization is therefore significantly longer than for vibrational thermalization. (Note that pure rotational transitions are driven by the blackbody environment much more slowly due to their low energy.)

Note that for molecules in optical traps, all states near the bottom of the ground electronic potential are trapped. However, in magnetic and electrostatic traps, some states are anti-trapped. In this case, it is possible for BBR to cause molecules to exit the trap by transferring them to an anti-trapped level. Here the focus is on optical

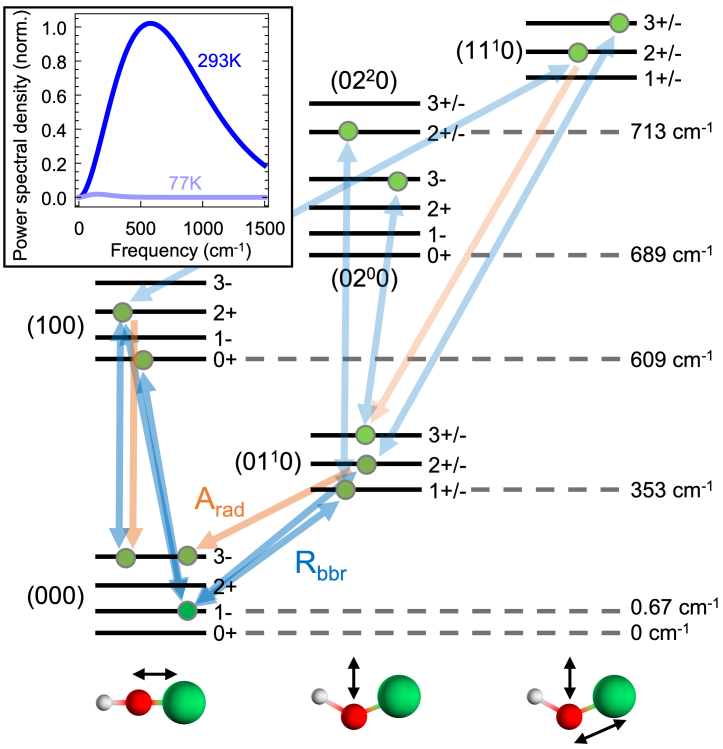

Figure 6.9: Schematic level diagram illustrating rovibrational thermalization dynamics in low-lying vibrational levels of CaOH, with all population initially prepared in the $N = 1$ level of the (000) state. Populations are represented by green circles, while blackbody transitions and radiative decay are represented by blue and orange arrows, respectively. For clarity, only some representative transitions are shown. All rovibrational transitions are driven following the selection rules (within the harmonic approximation) $\Delta v_1 = \pm 1$ or $\Delta v_2 = \pm 1$, $\Delta N = 0, \pm 1$, and $\Delta p = \pm 1$. Transition rates for the blackbody transitions, R_{bbr}, are determined by the power spectral density of blackbody radiation at the transition frequency (inset). The antisymmetric (O–H) stretching mode in CaOH has a frequency of $\sim$3700 cm^{-1} [250] and is therefore neglected. Figure reproduced from Ref. [44].

traps, and we therefore assume that all internal states remain trapped.

6.4.2 Rate equation model

We model the internal state dynamics of conservatively trapped polyatomic molecules using a set of rate equations that capture the effects of radiative decay and blackbody excitation between vibrational manifolds within the electronic ground state. The rate equations are sufficient to capture these dynamics due to the incoherent nature of the blackbody radiation, though we mention in passing that in high-lying vibrational levels of large polyatomic molecules, near-degenerate states may give rise to coherent dynamics not captured by the rate equations [339–341]. These effects are negligible when analyzing the lifetimes of low-lying vibrational states, as done here.

We consider rovibronic states described by the quantum numbers $|\{v\}_i, N, K, p\rangle$, where $\{v\}_i \equiv \{v_{1i}, v_{2i}, \ldots\}$ is the set of quantum numbers describing excitation of the vibrational normal modes, N is the rotational quantum number, K is the projection of N onto the molecule-frame z axis, and p is the parity of the state. Spin-rotation and hyperfine structure can be readily included in the equations below using standard angular momentum algebra, but they do not affect the primary results of this section.

The spontaneous decay rate, A_{ij}, and the blackbody excitation rate, R_{ij}, from initial state i to final state j are [236]

$$A_{ij} = \frac{\omega_{ij}^3}{3\pi\varepsilon_0\hbar c^3(2N_i+1)} S_{ij}, \tag{6.26}$$

$$R_{ij} = \frac{1}{6\varepsilon_0\hbar^2(2N_i+1)} \frac{2\hbar\omega_{ij}^3}{\pi c^3} \frac{1}{e^{\hbar\omega_{ij}/k_BT}-1} S_{ij}, \tag{6.27}$$

where $S_{ij} = |\langle i|\mu|j\rangle|^2$ is the rovibrational transition strength, N_i is the angular momentum quantum number of the initial state, ω_{ij} is the transition frequency, and T is the temperature of the environment.

The rovibrational transition strengths can be separated into vibrational and rotational components:

$$\begin{aligned} S_{ij} &= |\langle \{v\}_i, N_i, K_i, p_i|\mu|\{v\}_j, N_j, K_j, p_j\rangle|^2 \\ &= |\langle \{v\}_i|\mu|\{v\}_j\rangle|^2 \, |\langle N_i, K_i, p_i|\mu|N_j, K_j, p_j\rangle|^2 \\ &\equiv S_{ij}^{\text{vib}} S_{ij}^{\text{rot}}, \end{aligned} \tag{6.28}$$

where S_{ij}^{rot} and S_{ij}^{vib} are the rotational and vibrational line strengths, respectively. The rotational line strengths, or Hönl-London factors, are [252, 272]

$$\begin{aligned} S_{ij}^{\text{rot}} =& \delta_{p_i,-p_j}(1 + \delta_{K_i 0} + \delta_{K_j 0} - 2\delta_{K_i 0}\delta_{K_j 0}) \\ & \times (2N_i + 1)(2N_j + 1) \begin{pmatrix} N_i & 1 & N_j \\ -K_i & K_i - K_j & K_j \end{pmatrix}^2, \end{aligned} \tag{6.29}$$

where we emphasize that since we have chosen a basis where the parity is defined for each state, K is always a positive number. The Kronecker delta terms enforce a $2\times$ increase in the line strength for transitions from nondegenerate ($K = 0$) to degenerate ($K \neq 0$) states [271].

For the vibrational line strengths, we make the "double harmonic" approximation [236], wherein the vibrational potential is assumed to be that of a perfect harmonic oscillator, and the electric dipole moment is assumed to be a linear function of the internuclear spacing near the equilibrium geometry of the molecule. Within this

approximation, we expand the vibrational line strength as follows:

$$\langle\{v\}_i|\mu|\{v\}_j\rangle \approx \sum_n^{3N-6(5)} \left(\left| \frac{d\vec{\mu}_e}{dQ_n} \right|_{Q_{n,\mathrm{eq}}} \langle v_{n,i}|Q_n|v_{n,j}\rangle \prod_{k\neq n} \langle v_{k,i}|v_{k,j}\rangle \right), \tag{6.30}$$

where the sum is over all $3N-6$ ($3N-5$ in a linear molecule) vibrational modes, $\vec{\mu}_e$ is the electric dipole moment of the molecule, Q_n is a normal coordinate describing the nth mode, and $Q_{n,\mathrm{eq}}$ is its equilibrium value.[17] The product enforces the fact that the transition can change just a single vibrational mode at a time (at this level of approximation). Within the harmonic approximation, we can use harmonic oscillator algebra to write the vibrational matrix elements. For nondegenerate vibrational modes the matrix elements are

$$|\langle v_n+1|Q_n|v_n\rangle|^2 = \frac{v_n+1}{2}, \tag{6.31}$$

while for degenerate modes we use higher-dimensional harmonic oscillator algebra. For instance, for vibrational bending modes with vibrational angular momentum ℓ (as found in, e.g., linear triatomic molecules), the degeneracy is 2 and the matrix elements are

$$\begin{aligned} &|\langle v_n+1, \ell\pm 1|Q_n|v_n,\ell\rangle|^2 \\ &= \frac{1}{4}(1+\delta_{\ell,0}+\delta_{\ell\pm1,0}-\delta_{\ell,0}\delta_{\ell\pm1,0}) \left(\frac{v_2\pm\ell}{2}+1\right). \end{aligned} \tag{6.32}$$

The advantage of the double-harmonic approximation is that it allows every vibrational transition moment to

[17] Our units are chosen so that $d\vec{\mu}_e/dQ_n$ has units of debye; this can be achieved by making Q_n unitless by scaling by the harmonic oscillator length $\sqrt{\hbar/(\mu\omega_n)}$, where μ is the reduced mass of the vibration.

be expressed in terms of just the dipole moment derivatives along each of the normal coordinates. For low-lying vibrational states this approximation is expected to be reasonably appropriate. If deemed necessary, anharmonicity can be included by expanding eqn. 6.30 to higher order. The matrix elements $\langle v_{n,i}|Q_n^k|v_{n,j}\rangle$ can be calculated using standard harmonic oscillator algebra and will be able to connect states with $|\Delta v| \leq k$, where k is the expansion order. The additional dipole moment derivatives can be fit to data or calculated by *ab initio* methods.

The internal state dynamics under the influence of blackbody excitation and radiative decay are determined by a set of rate equations for the population, n_i, of rovibrational state i:

$$\frac{dn_i}{dt} = -\sum_j R_{ij} n_i - \sum_{j<i} A_{ij} n_i + \sum_j R_{ji} n_j + \sum_{j>i} A_{ji} n_j, \tag{6.33}$$

where $\sum_{j<i}$ implies a sum over all states lower in energy than state i.

Fig. 6.10 compares the solution to eqn. 6.33 for CaOH in a 300K environment including both bending and stretching vibrations (see Fig. 6.9), with a diatomic analogue which has the same stretching vibrational constants but no bending vibration. For comparison, we also plot the equilibrium vibrational populations given by

$$P(\{v\}_i) = \frac{1}{Z} d_i \exp\left(\frac{\sum_n v_{ni}\hbar\omega_n}{k_B T}\right), \tag{6.34}$$

where

$$Z = \sum_i d_i \exp\left(\frac{\sum_n v_{ni}\hbar\omega_n}{k_B T}\right) \tag{6.35}$$

is the partition function, i sums over all vibrational states $\{v\}_i$, d_i is the degeneracy of the ith vibrational state, n sums over the vibrational modes, and ω_n is the frequency of the nth mode. As shown in Fig. 6.10, after an

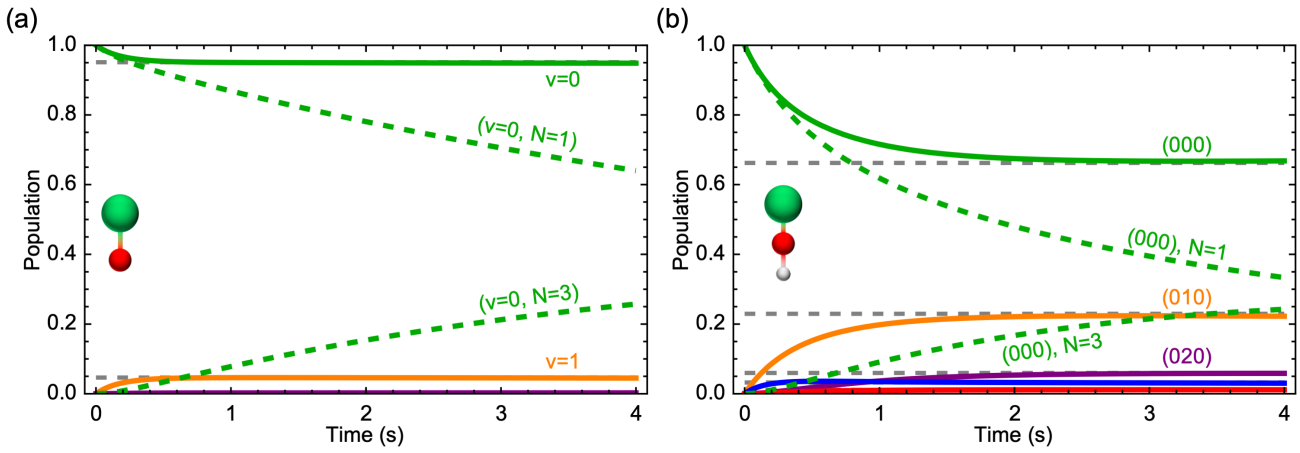

Figure 6.10: Generalized calculations of vibrational thermalization dynamics for (a) diatomic molecules and (b) linear triatomic molecules. For these plots, the molecular constants are matched to those of CaOH, but with the bending vibration removed in the diatomic case (resulting in a molecule similar to CaF). The inclusion of one additional vibrational mode significantly decreases the lifetime of the ground state $N = 1$ level and increases the time required to achieve vibrational thermalization. Dashed gray lines correspond to the equilibrium vibrational populations. Reproduced from Ref. [44].

initial equilibration time the vibrational populations (including population in all rotational levels of a vibrational state) converge to these equilibrium values. The individual rotational levels (dashed curves) take much longer to equilibrate.

Note that even after the populations reach steady state, individual molecules will continue to undergo transitions between rovibrational states. At any time, individual state lifetimes are given by the rate at which population leaves the state due to blackbody excitation and radiative decay. In terms of the rates in eqn. 6.33, the lifetime of a single rovibrational state i is $\tau_i = (\sum_j R_{ij} + \sum_{j<i} A_{ij})^{-1}$.

Other experimental limitations to lifetime

In addition to blackbody thermalization and radiative decay, there are other sources of population loss in experiments with trapped molecules. One possible mechanism is trap loss due to collisions with background gas in the vacuum chamber, which generally leads to exponential population decay on typical timescales of 1 to 100 s in experiments with optically or magnetically trapped molecules. In addition, collisions with other trapped molecules can give density-dependent losses [69, 71, 72, 117], though these were not considered in this work due to the relatively low molecule number densities in the ODT used for these measurements. Our recent measurements of CaOH–CaOH collisional loss rates (Chapter 9 of this thesis) give $k_{(000)} = 0.7(2) \times 10^{-10}$ cm^3 s^{-1} for $\widetilde{X}(000)$ and $k_{(010)} = 2.9(9) \times 10^{-10}$ cm^3 s^{-1} for $\widetilde{X}(010)$ [342]. At the measured CaOH ODT density of $3(1) \times 10^9$ cm^{-3} used for the lifetime measurements, this gives a collisional lifetime of approximately 5 s for molecules in $\widetilde{X}(000)$ and 1 s for molecules in $\widetilde{X}(010)$. These are both longer than the measured lifetimes by a factor of several, confirming the assumption that collisions would not be a dominant process.

Another potential loss mechanism is photon scattering from optical traps, as described earlier in this chapter. This can change the internal state of optically trapped molecules in a process known as Raman scattering. While a single Raman scattering event manifests as loss from the rotational state of interest, Raman scattering may be suppressed by a large margin compared to Rayleigh scattering, which preserves the internal state [329]. For linearly polarized trapping light, Rayleigh scattering arises from state-preserving terms proportional to the square of the scalar polarizability of the molecule, α_0, while Raman scattering arises from state-changing terms related to the tensor polarizability, α_2. Therefore, the ratio of Raman to Rayleigh scattering is on the order of $(\alpha_2/\alpha_0)^2$, which is $\sim$10% for CaOH in a 1064 nm trap. Because the Rayleigh scattering rate is $\sim$1 Hz for the op-

tically trapped CaOH as described below, Raman scattering occurs on timescales of $\sim$ 10 s and is neglected from the model.

6.4.3 CaOH lifetime measurement

We measure the lifetime of low-lying CaOH vibrational states using optically trapped molecules in an ODT, as described above. This is achieved by fitting experimental state lifetime data to a rate equation model of the full experimental sequence. We specifically measure the blackbody lifetime of the $\widetilde{X}^2\Sigma^+(000)$ vibrational ground state of CaOH, as well as blackbody and radiative lifetimes of the $\widetilde{X}^2\Sigma^+(01^10)$ and $\widetilde{X}^2\Sigma^+(100)$ states. Measuring all three states helps to isolate the values of dipole moment derivatives $|d\vec{\mu}_e/dQ_1|$ and $|d\vec{\mu}_e/dQ_2|$, as well as the vacuum lifetime τ_{vac}. Each of these three parameters contributes differently to the three states, with the two dipole derivatives dominating for the $\widetilde{X}(100)$ and $\widetilde{X}(010)$ states, respectively, and the vacuum lifetime being most important for the ground state. [18] For these measurements, we cooled the in-vacuum RF MOT coils to $\sim$ 0 °C by connecting cooled copper plates to the copper MOT coil feedthrough rods. This slightly reduced the temperature of the blackbody environment, and also significantly improved outgassing from the aluminum nitride boards, which in turn improved the vacuum lifetime during the measurement. This is somewhat important since we measure for hold times of up to 3 s.

The experimental sequence is as follows. We load the ODT for 100 ms using SF cooling, then hold the molecules for 30 ms to allow untrapped population to fly away. Next, we image the loaded molecules in the trap with 50 ms of SF imaging. This allows us to normalize against shot-to-shot fluctuations in the number of molecules loaded

[18] Here Q_1 is the normal coordinate for the Ca–O stretching vibration and Q_2 is the normal coordinate for the Ca–O–H bending vibration.

into the trap. Next, we prepare the internal state. For $\widetilde{X}(000)$ we do nothing, so that the molecules are initialized primarily in $(N = 1, J = 3/2)$. For $\widetilde{X}(010)$, we optically pump the molecules into the bending mode $[\widetilde{X}(010)(N = 1^-)]$ by turning off the $\widetilde{X}(010)(N = 1) \rightarrow \widetilde{B}(000)$ repumping laser and applying SF cooling for 100 ms, as described in sec. 6.3. For $\widetilde{X}(100)$, we instead turn off the $\widetilde{X}(100) \rightarrow \widetilde{B}(000)$ repumper and apply SF cooling for 2 ms.

After state preparation, we hold the molecules in the dark for a variable amount of time,[19] then image them in the trap using 50 ms of SF imaging light. The fractional molecule survival (final image brightness divided by initial image brightness) is shown in Fig. 6.11 for the three states. The solid curves are fits to the rate equation model described below. Note that the surviving molecules are not just those in the target vibrational states but also any other detectable state in our optical cycle [42]. This means that we have to careful to (a) limit the hold times in the experiment as much as possible to avoid buildup of population in undesired states and (b) model the entire experimental sequence when fitting the data in order to account for this population buildup.

We fit the data using a modified version of the rate equation model presented in sec. 6.4.2. The primary modifications are that we included a finite vacuum lifetime τ_{vac}, and that we include the angular momentum J in the basis. The latter change is because there are some cases where we can detect only a single J level in a rotational state N. Additionally, to account for background population introduced between the ODT loading and the lifetime hold, we model the complete experimental sequence, including ODT loading, the first image, and the state preparation time. To fit the lifetimes, we perform a simultaneous fit of the rate equations to the data for all

[19] Because of the long hold time in this measurement, we were careful to install shutters to block leaked light through AOMs that could deplete molecules over long periods of time. Specifically, these shutters were used to block leaked light from the MOT beams as well as the $\widetilde{X}(100)$ and $\widetilde{X}(010)$ repumpers. All other repumpers should be far off resonance and their AOMs are off, so the very small amount of leaked optical power is insignificant.

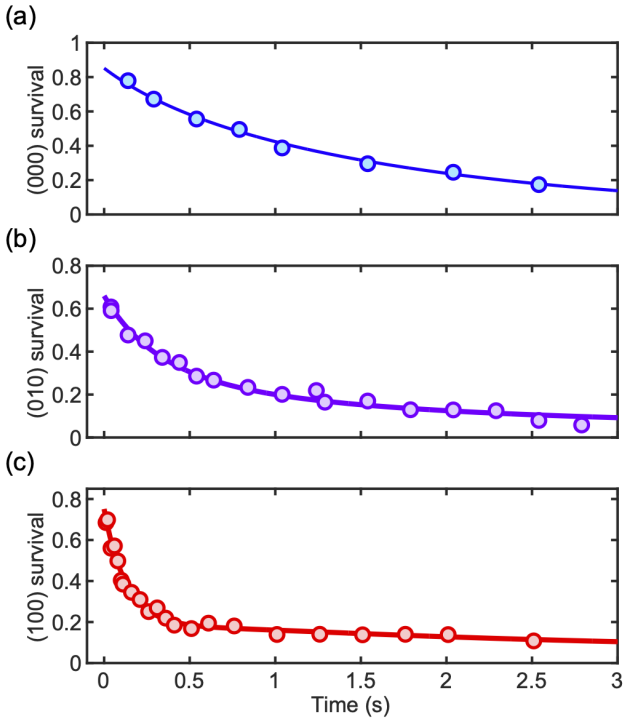

Figure 6.11: Lifetime measurements of the (a) $\widetilde{X}^2\Sigma^+(000)$, (b) $\widetilde{X}^2\Sigma^+(010)$, and (c) $\widetilde{X}^2\Sigma^+(100)$ states in optically trapped CaOH. Points are experimental data, and curves are fits to the rate equation model described in Sec. D.1. Figure reproduced from Ref. [44].

State	τ_{spont}	τ_{bbr}	τ_{tot}
$\widetilde{X}(000)$	–	$1.3^{+0.3}_{-0.2}$	$0.90^{+0.20}_{-0.16}$
$\widetilde{X}(010)$	$0.72^{+0.25}_{-0.13}$	$0.95^{+0.26}_{-0.16}$	$0.36^{+0.11}_{-0.07}$
$\widetilde{X}(100)$	$0.19^{+0.03}_{-0.03}$	$0.81^{+0.09}_{-0.08}$	$0.14^{+0.02}_{-0.02}$

Table 6.2: State lifetimes and 68% confidence intervals determined from the rate equation fit. The vacuum lifetime is constant for all states and fits to $\tau_{\text{vac}} = 3.0^{+0.4}_{-0.7}$ s. Table reproduced from Ref. [44].

three vibrational states. The rate equation modeling of the CaOH sequence and the fitting procedure are both described in appendix D.

The results of the fit are shown in Tab 6.2. The table is divided into contributions from spontaneous decay and from blackbody radiation. The total lifetime comes from the sum of both effects. In future experiments, cooling the environment to cryogenic temperatures would reduce the BBR contribution and allow us to reach the spontaneous decay-limited lifetime.

We see that the lifetime of the $\widetilde{X}(010)$ bending mode is approximately 360 ms at room temperature, and could made as high as approximately 720 ms if we were to cool the surrounding environment. The ground state has a BBR lifetime of around 1.3 s, with the total lifetime of 900 ms being also limited by vacuum lifetime. The $\widetilde{X}(100)$ has a shorter spontaneous decay lifetime of approximately 190 ms due to its higher energy than the bending mode.

Vibrational	$\lvert\vec{\mu}_v\rvert$		$\lvert d\vec{\mu}_e/dQ\rvert$		τ_{sp}			τ (300 K)	
state	Calc. (H)	Calc.	Calc.	Exp.	Calc. (H)	Calc.	Exp.	Calc.	Exp.
(010)	0.301	0.284	0.426	0.440	0.78	0.88	0.72	0.41	0.41
(100)	0.262	0.295	0.370	0.384	0.20	0.16	0.19	0.14	0.15
(000)	-	-	-	-	-	-	-	1.14	1.3

Table 6.3: Calculated transition dipole moments $|\vec{\mu}_v|$ (in debye), calculated and experimentally determined derivatives of the electronic dipole moment $d\vec{\mu}_e/dQ$ (in debye), spontaneous lifetimes (in s), and overall lifetimes at 300 K (in s) for the $\widetilde{X}^2\Sigma$ state of CaOH. "(H)" denotes results obtained using the harmonic approximation. Experimental results quoted here ignore vacuum loss and are drawn from Tab. 6.2 for the lifetimes. The experimental values of $|d\vec{\mu}_e/dQ|$ are determined using the harmonic approximation as described in appendix D. Table reproduced from Ref. [44].

6.4.4 Comparison to theory

We compared our results to *ab initio* calculations performed by Lan Cheng's group. These calculations are described in Ref. [44]. The results are shown in Tab. 6.3. We observe excellent agreement between our measurements and the theory, lending confidence that we understand the limitations to the CaOH vibrational state lifetimes. This also suggests that the calculations have some predictive power. In chapter 11, we briefly describe what these calculations suggest about vibrational lifetimes of even larger polyatomic molecules for future work.

7

Coherent Control of CaOH and the "eEDM Pathfinder" Experiment

Ultracold polyatomic molecules are promising candidates for experiments in quantum science, quantum sensing, ultracold chemistry, and precision measurements of physics beyond the Standard Model. While we

have realized many of the initial requirements for these experiments by loading CaOH into a conservative optical trap at temperatures below 100 μK, the next step is to achieve full quantum control over the complex internal structure of the molecules. In this chapter, we describe methods for establishing coherent control over individual quantum states in the $\widetilde{X}(010)$ bending mode of CaOH. This is done by optically pumping the molecules into a single hyperfine state, and then using microwave pulses to coherently transfer population between rotational and hyperfine states in the bending mode. As an application of these techniques, we demonstrate a method for searching for the electron electric dipole moment (eEDM) with ultracold polyatomic molecules in parity doublet states. We identify an eEDM sensitive state with tunable, near-zero magnetic field sensitivity, which could be a useful resource for suppressing decoherence that could limit future eEDM searches with these molecules. We perform an electron spin precession measurement using this "zero-g factor" eEDM state, and identify the dominant sources of decoherence in the experiment. Because of the relatively light mass of CaOH, our states do not have inherently high sensitivity to the eEDM. However, a similar protocol could be applied in heavier polyatomic molecules with otherwise very similar structure, e.g. SrOH, YbOH, or RaOH. These results therefore present a pathway towards improved experimental sensitivity to time-reversal-violating physics using trapped polyatomic molecules.

7.1 Overview: microwave manipulation of CaOH in the bending mode

We begin where we left off in the previous chapter (chapter 6), with CaOH molecules loaded into an optical dipole trap and optically pumped into the $\widetilde{X}(010)$ bending mode. The experimental setup is substantially similar to what was described there. In brief, we start by loading several hundred CaOH molecules into a 1064 nm ODT with a Gaussian waist of $\sim$25 μm and an initial trap depth around 600 μK. After loading the ODT, we

image the molecules *in situ* using single-frequency imaging, which establishes an initial molecule number that can be used to normalize for MOT fluctuations when performing spectroscopy and coherent control. After the initial image, we pump molecules into the $\widetilde{X}(010)(N = 1)$ bending mode by applying SF cooling with the $\widetilde{X}(010)(N = 1) \rightarrow \widetilde{B}(000)$ repumping laser turned off. We then apply a short "pushout" pulse, which uses resonant $\widetilde{X}(000) \rightarrow \widetilde{A}(000)$ light, along with all repumpers besides $\widetilde{X}(010)(N = 1) \rightarrow \widetilde{B}(000)$, to push detectable molecules out of the trap if they did not make it into the bending mode. At this point, all trapped molecules in detectable states are in an incoherent mixture of 12 hyperfine states within the $(N = 1, J = 1/2^-)$ and $(N = 1, J = 3/2^-)$ states in $\widetilde{X}(010)$. For reference, the structure of low-lying rotational and hyperfine states in the $\widetilde{X}(010)$ bending mode, along with the $\widetilde{A}(010)\mu^2\Sigma^{(+)}$ and $\widetilde{A}(010)\kappa^2\Sigma^{(-)}$ states, is shown in Fig. 7.1.

In the following sections, we describe our microwave manipulation of molecules in the bending mode, which is done by driving microwave transitions on the 40 GHz transition between $N = 1$ and $N = 2$. Combined with depletion and optical pumping lasers, this can be used for hyperfine, Zeeman, and Stark spectroscopy; for optically pumping population into a single hyperfine state; and for coherently manipulating the population by driving Rabi oscillations and transferring molecules between internal states. We ultimately use these techniques to prepare molecules in an eEDM sensitive, "zero-g factor" state and perform a spin precession measurement.

7.2 Experimental setup

For the experiments in this chapter (and the following chapters), we had to add the ability to apply 40 GHz microwave radiation to drive hyperfine-state resolved transitions between rotational states in the bending mode.

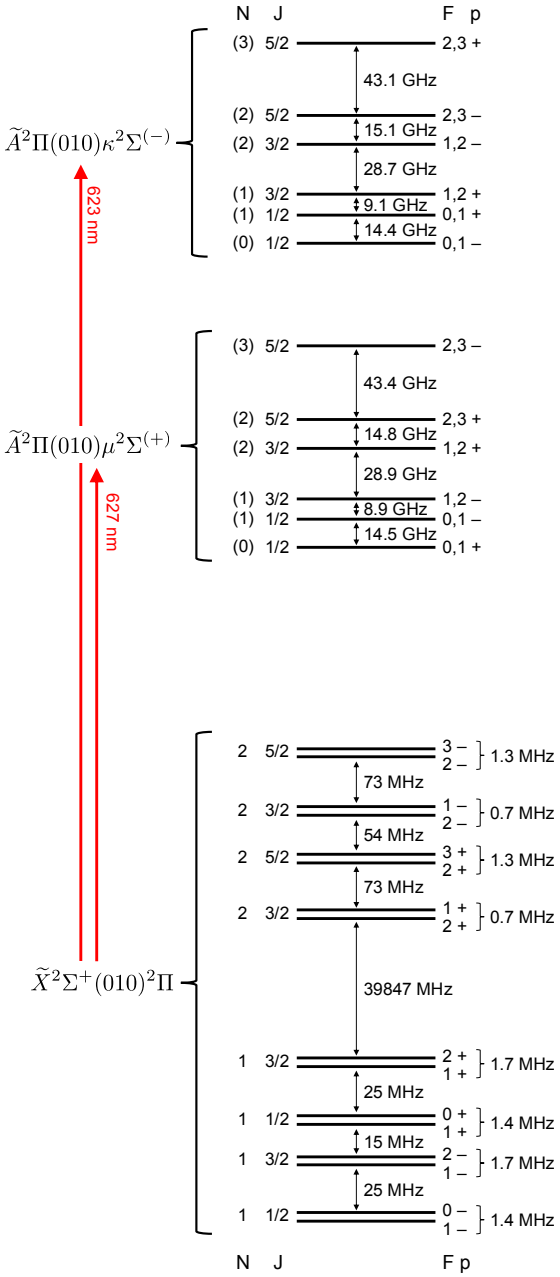

Figure 7.1: Rotational structure of the CaOH $v_2 = 1$ bending modes. The $\widetilde{A}(010)$ states are intermediate between case (a) and case (b) due to the similar strengths of spin-orbit and vibronic coupling. This means that N is only an approximately good quantum number, as denoted by parentheses. Energy splittings are calculated using the spectroscopic parameters listed in Table 2.6 and Ref. [93].

We also added the ability to apply external electric and magnetic fields for manipulating the structure of the molecules. Finally, we added a few upgrades designed to stabilize electric and magnetic fields in the MOT chamber. We found that without stabilization, we would see drifts in microwave transition frequencies, and this would also affect the coherence time of the eEDM states studied later in the chapter.

7.2.1 40 GHz microwaves

We apply 40 GHz microwave radiation to the molecules using two horn antennas, installed outside the 4.5" CF viewports used for imaging and ODT projection. The two microwave horns are installed on opposite sides of the chamber, and one is aligned to deliver Z polarized microwaves (where Z is the vertical axis in the lab), and the other is rotated to deliver X (i.e. horizontally) polarized microwaves.[1] These two polarizations were needed for different steps in the eEDM sequence described later. We use the same microwave path for both horns, and have a 40 GHz switch as the last element (after a high-power amplifier), which switches between the two.

To generate the microwaves, we used a 20 GHz signal generator and frequency doubled the signal up to slightly below 40 GHz (at a frequency that is not resonant with any transition). To apply resonant microwave frequencies during the experimental sequence, we used a mixer to mix in RF frequencies, which could be applied by switching between channels on RF AWGs (frequencies <500 MHz). This generated first-order sidebands above and below the microwave carrier frequency, and we typically used the first-order positive frequency sideband to apply resonant microwaves to the molecules. We were careful to confirm on a spectrum analyzer that there were no sidebands (e.g. the -1 order, or other higher-order frequencies) that were accidentally on resonance

[1] Note that it is important to ensure that the horn is pointed straight at the molecules without clipping the edge of the viewport. We initially had one of the horns pointed too close to the edge, and all of the power ended up being deflected at a large angle away from the molecules, even though the majority of the horn appeared to have direct line-of-sight (and was pointing straight at) the molecule position.

with an undesired transition in the molecule. In general, it was best to use relatively high RF frequencies (ideally >100 MHz) to reduce the density of the spectrum and lower the likelihood of having power at a "bad" frequency.

7.2.2 DC electric and magnetic fields

We apply DC electric fields using a high-voltage, analog-controllable power supply (Kepco BHK 500-0.4MG). The voltage supply is connected directly to the in-vacuum RF MOT coils, using high-voltage relays (Kilovac K40P) as shown in Fig. 5.32 (chapter 5).[2] Due to a peculiarity of the analog control for this supply, we ground the positive terminal and MOT coil, and apply a negative voltage to the other coil. The voltage difference between the two MOT coils generates an electric field of 0.3 (V/cm)/V at the molecules.[3] Therefore, we can apply electric fields up to 150 V/cm with our 500 V supply.

To apply magnetic bias fields, we wound small coils around the vertical axis of the MOT chamber in Helmholtz configuration. These coils are driven with a small 5 A power supply, and apply a field of approximately 1 G/A to the molecules.

7.2.3 Stabilizing external fields in the MOT chamber

We found during microwave spectroscopy that there was evidence of significant drifts of the electric field in the chamber over time. Our hypothesis was that this was due to charges accumulating on the insulating surfaces near the molecules, namely the aluminum nitride RF MOT coil boards and the in-vacuum asphere, which we used to image the ODT with high collection efficiency (this lens is described in more detail in chapter 8 in the context

[2] The high-voltage Kilovac relays are closed whenever we apply electric fields but open otherwise, to prevent significant RF power or DC current from the RF and DC MOTs from reaching the high voltage supply.

[3] This number was obtained from simulations but agrees well with our spectroscopy, assuming the dipole moment from the literature for the $\widetilde{X}(000)$ state [256].

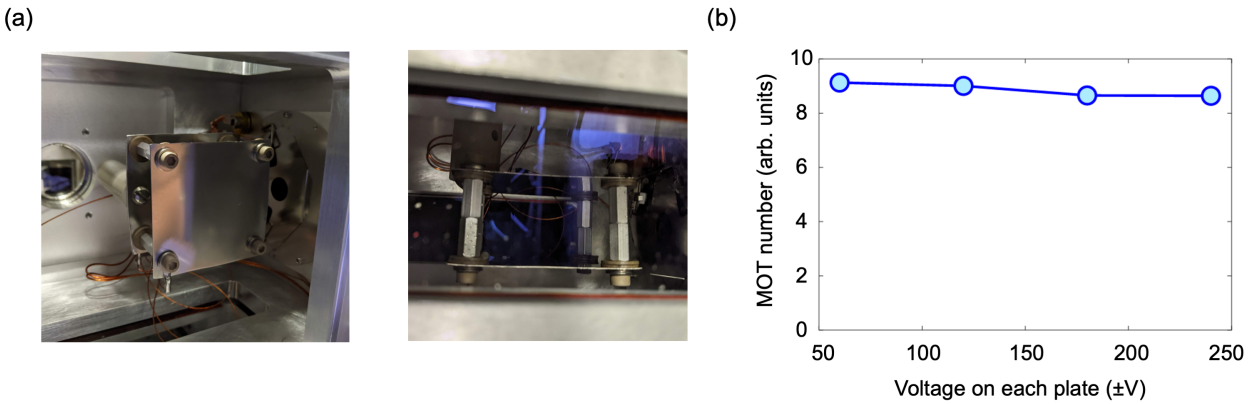

Figure 7.2: (a) Photos of the ion sweeper installed on the experiment. (b) MOT number as a function of voltage on the ion sweeper plates. We typically run at ± 150 V on the two plates.

of optical tweezers). In Rydberg atom experiments (e.g.), it has been seen that UV light can be used to stabilize electric fields in setups with insulating surfaces. We therefore applied UV light during the dead time between each experimental shot. The UV sources were pointed into the chamber with the intention of hitting both inner MOT board surfaces as well as the asphere. Adding UV light appeared to improve the electric field drift but did not eliminate the problem. We also turned off the ion gauge in our chamber in hopes of removing a potential source of charges.

The more important effect, however, is likely that the buffer gas beam contains ions that can potentially make it all the way to the MOT chamber and land on an insulating surface near the molecules. To eliminate this problem, we installed an "ion sweeper" in the beamline right after the UHV shutter. This consists of two parallel metal plates approximately 1" apart (Fig. 7.2). We apply a voltage of ± 150 V to the two plates, corresponding to an electric field of approximately 120 V/cm. This is more than enough to deflect even heavy ions out of the beam before they reach the MOT chamber, but still low enough that we saw no impact on the MOT number.[4]

[4] At higher voltages, we would expect Λ doublets in the $\widetilde{A}$ state to mix, causing optical cycling losses during slowing.

We also apply active compensation to stabilize slow drifts in the magnetic field. This was not critical for microwave state preparation, but it was key for achieving long coherence times in the spin precession measurements described in section 7.6. To do this, we installed a 3-axis fluxgate magnetometer outside the MOT chamber and wound three large coils around the optical table. These are sufficiently large that the different in position between the magnetometer and the molecules is negligible. At the end of each experimental shot, we read out the magnetic field on the fluxgate and stabilize it to a setpoint by feeding back on the current to the three coils.[5]

Note that we also trigger our experiment on the 60 Hz mains in the lab, so any 60 Hz noise sources will be phase stable in our experiment.

7.3 Microwave spectroscopy

We began by performing hyperfine-resolved spectroscopy of rotational transitions between $N = 1$ and $N = 2$ in the $\widetilde{X}(010)$ bending mode. This served as a check on our ability to drive microwave transitions in CaOH, and could be used to confirm our understanding of the bending mode Hamiltonian and fit the unknown hyperfine constants. Spectroscopy also provides a method for state-selective detection of population in specific hyperfine states, and is important for finding microwave transitions that we ultimately want to coherently drive.

The simplest way to perform spectroscopy is to start with molecules in a detectable state (i.e. one that is repumped in the optical cycle), then apply microwaves driving population to an undetectable state. If the microwaves are applied on resonance for a sufficiently long time (typically around 1 ms), population will decohere and then equilibrate to an incoherent mixture of initial and final states. The corresponding loss of population

[5] Note that we actually take 5 readings spaced by multiples of 60 Hz over ∼100 ms and feed back after each reading. This helps stabilize up the PID process, which would be quite slow and potentially prone to oscillation if it could only rely on a single data point every 1.5 s at the end of each shot.

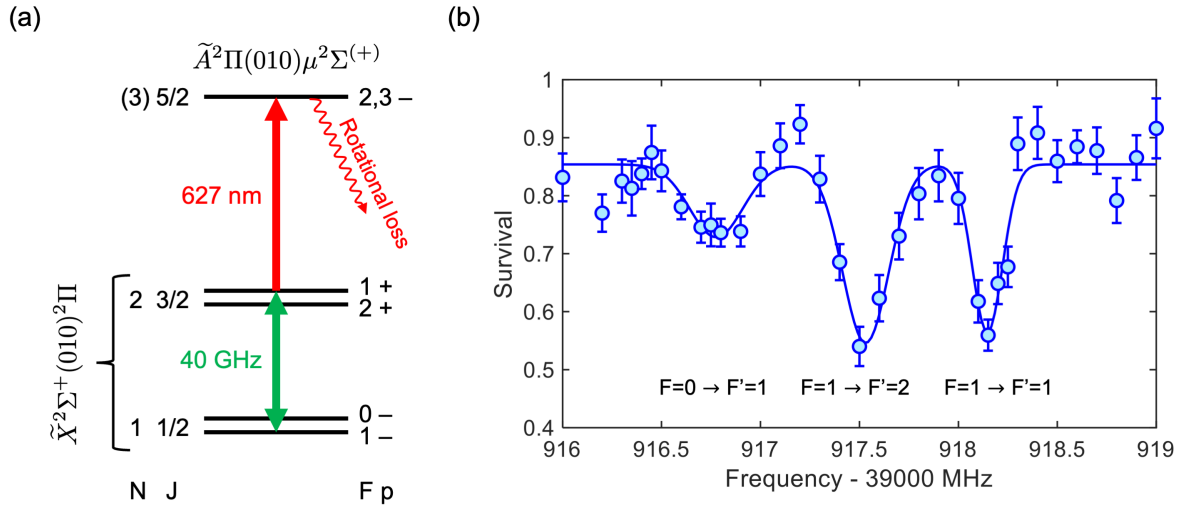

Figure 7.3: Microwave spectroscopy of the $(N = 1, J = 1/2^-) \leftrightarrow (N' = 2, J' = 3/2^+)$ hyperfine transitions at an ODT trap depth of approximately $k_B \times 90$ μK. (a) Spectroscopy configuration. Microwaves drive population from $N = 1$ to $N' = 2$, and a laser rotationally depletes the $N' = 2$ population. (b) Spectroscopy results, showing three distinct depletion features corresponding to the three transitions allowed at zero field. Also plotted is a fit to the sum of three Gaussians. The fitted frequencies, from left to right, are 916.78 MHz, 917.54 MHz, and 918.14 MHz.

can then be observed when the molecules are detected.

To improve on this method, we can also deplete the final state with a laser that either drives a lossy rotational transition or pushes the molecules out of the trap. Because the laser constantly depopulates the final state, this allows all molecules addressed by the microwaves to be depleted, thereby increasing the contrast of the spectroscopy signal.[6]

Fig. 7.3 shows microwave spectroscopy of the $(N = 1, J = 1/2^-) \leftrightarrow (N' = 2, J' = 3/2^+)$ transition in the bending mode. This set of transitions is particularly important to characterize because $(N = 1, J = 1/2^-)$

[6]Specifically, the contrast is doubled when driving a transition between two states. For more states (e.g. driving from $F = 1$ to $F' = 2$ at zero field), the population is distributed equally among all states. In this example, 3/8 of the population would remain in $F = 1$.

is significantly populated after pumping into the bending mode, and we will ultimately want to pump all population into the $F = 0$ state, as described below (sec. 7.4). To perform this spectroscopy, we load and nondestructively image CaOH molecules in the ODT using SF imaging, then optically pump them into the bending mode using SF cooling with the $\widetilde{X}(010)(N = 1)$ repumper turned off (as described in chapter 6). At this point, population is distributed in a hyperfine mixture within the detectable $(N = 1, J = 1/2^-)$ and $(N = 1, J = 3/2^-)$ states. We next ramp the ODT trap depth down to approx. $k_B \times 90\ \mu$K to minimize AC Stark shifts. Finally, we turn on $\hat{X}$-polarized microwaves near resonant with $(N = 1, J = 1/2^-) \leftrightarrow (N' = 2, J' = 3/2^+)$, while rotationally depleting the molecules that are successfully excited to $N' = 2$ using a laser (Fig. 7.3(a)). After 5 ms, we turn off the microwaves, ramp the trap back up to ∼600 μK, then detect the molecules remaining in $N = 1$ (along with all other bright states in the CaOH optical cycle). The number of molecules surviving in the final image, divided by the number in the first image, is shown in Fig. 7.3(b).

We observe three peaks in the data, corresponding to the three allowed hyperfine transitions at zero field. (We also see hints of a fourth peak corresponding to $F = 0 \rightarrow F' = 2$, which is allowed by AC Stark mixing from the trap.) The two $F = 1$ features are 3 times larger than the $F = 0$ feature, confirming that the four hyperfine states are equally populated. By comparing the data to simulated spectra using the bending mode Hamiltonian with all but the hyperfine constants held fixed, we estimate that the hyperfine parameters are $b_{F,(010)} \approx 2.45$ MHz and $c_{(010)} \approx 2.6$ MHz. These differ somewhat significantly from the hyperfine constants of the $\widetilde{X}(000)$ ground state, which were measured in Ref. [254] to be $b_{F,(000)} = 2.602$ MHz and $c_{(000)} = 2.053$ MHz.

7.4 Optical pumping into a single hyperfine state

Before we can begin to coherently control CaOH molecules, we must first prepare the molecules in a pure internal state.[7] This is in contrast to the incoherent mixture they are in after laser cooling and optical pumping into the bending mode, which distributes molecules over a number of hyperfine states in the $(N = 1, J = 1/2^-)$ and $(N = 1, J = 3/2^-)$ manifolds. The simplest way to do this is to just push all molecules in the wrong internal state out of the trap (or at least pump them into spectator dark states) though this comes with the obvious downside of causing a large fraction of the molecules to be lost. A better approach is to pump all the molecules into a single energy eigenstate (or some other pure state, e.g. a coherent superposition state that is dark to an applied laser field). The primary challenge for doing this with CaOH is that there are a large number of internal states relatively close together in energy.[8] Following previous work with CaF [31, 69, 205], we take the approach of pumping into an $F = 0$ state in the bending mode, which contains only a single m_F sublevel and can therefore be optically pumped even with no applied magnetic field.

The relevant bending mode structure is shown in Fig. 7.1. Our goal is to pump molecules from a mixture of hyperfine states in the $(N = 1, J = 1/2^-)$ and $(N = 1, J = 3/2^-)$ states into the $(N = 1, J = 1/2^-, F = 0)$ state. As we can see, one challenge with this approach is that $F = 0$ is separated from $F = 1$ by only 1.4 MHz, which is not optically resolvable. Therefore, we rely on microwaves to resolve the hyperfine states and drive

[7] Or, at least, all molecules that are detectable or in a relevant manifold must be put into a single state. Molecules in, e.g., dark vibrational states are typically spectators, so long as there are no molecule-molecule interactions and these states don't decay to a relevant manifold via blackbody radiation on experimental timescales. Practically, we find that BBR dynamics make some such background molecules impossible to avoid.

[8] In atoms, the same problem exists when considering magnetic sublevels at low magnetic fields, but the atoms can be easily optically pumped into a polarization dark state using, e.g. σ^+ polarized light. The same can in principle be done for CaOH (and has been demonstrated for CaF [32]), but is more challenging due to molecules' type-II structure.

	$\mu^2\Sigma^{(+)}(J'=1/2^+)$	$\kappa^2\Sigma^{(-)}(J'=1/2^+)$
$(N''=1, J''=1/2^-)$	0.109	0.558
$(N''=1, J''=3/2^-)$	0.826	0.008
$(N''=2, J''=3/2^-)$	0.065	0.434

Table 7.1: Rotational branching ratios from the two $\widetilde{A}(010)$ optical cycling states to the ground $\widetilde{X}(010)$ state.

$F=1$ population to a separate, optically-resolvable level. An optical pumping laser then excites these molecules to provide the dissipation (via spontaneous decay) required for optical pumping to work. To design the optical pumping scheme, it is also important to know the rotational branching ratios from the excited $\widetilde{A}(010)$ states, which are given in Tab. 7.1.

We first attempted a scheme that required the optical pumping laser to be able to resolve the $J=1/2^-$ and $J=3/2^-$ states, which are split by 26 MHz (by comparison, the natural linewidth of the $\widetilde{A}$ state is $\Gamma \approx 2\pi \times 6.4$ MHz). Two microwave frequencies were used to couple molecules from $(N=1, J=1/2^-, F=1)$ up to $(N=2, J=3/2^+)$ and then back down to $(N=1, J=3/2^+)$. From there, a 627 nm laser would excite molecules to $\widetilde{A}(010)\mu^2\Sigma^{(+)}(J=1/2^+)$. These would then decay back to $F=0$ with an approx. 3% probability, and the remaining decays could be pumped again, with an average of 30 scattered photons required to complete the optical pumping. This approach never worked, which was likely due to a combination of heating from the large number of scattered photons, off-resonant coupling of the OP laser back to $F=0$, and off-diagonal vibrational branching (which occurs around 6% of the time if no states are repumped; see chapter 4).

The method that ended up working improved upon the first attempt by (1) requiring fewer microwave frequencies, (2) having more favorable branching ratios so that fewer scattered photons were required, and (3) not requiring the optical pumping laser to be able to resolve states only 10s of MHz apart. Another benefit of this approach is that the OP laser is just the $\widetilde{X}(010)(N=2)$ repumping laser that was already installed on the experi-

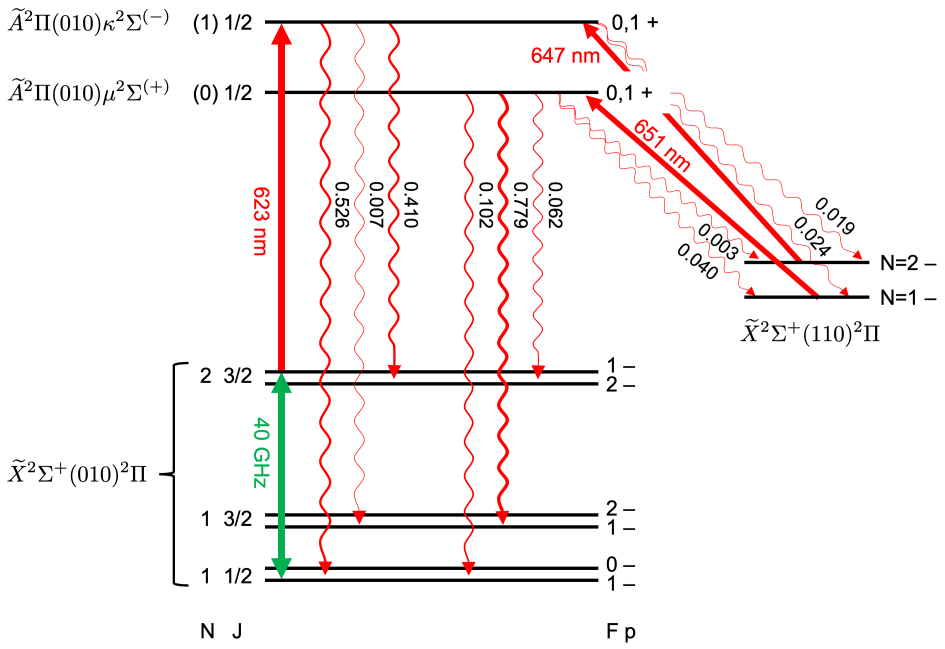

Figure 7.4: Optical pumping into the $(N = 1, J = 1/2^-, F = 0)$ state in the CaOH $\widetilde{X}(010)$ bending mode. Branching ratios are calculated at $E = 0$ V/cm but do not significantly change at the OP field of $E = 7.5$ V/cm. Loss to other vibrational states is around 1% and is not shown. The lasers do not resolve hyperfine structure, and branching ratios are averaged over all hyperfine states in each N or J manifold.

ment, meaning that the optical pumping could be done "for free".

The optical pumping scheme is illustrated in Fig. 7.4. A microwave resonantly couples population in $(N = 1, J = 1/2^-, F = 1)$ to $(N = 2, J = 3/2^-)$, with a Rabi frequency chosen so that there is negligible off-resonant coupling to the $F = 0$ OP target state 1.4 MHz away. The $\widetilde{X}(010)(N = 2)$ repumping laser is used to excite the $(N = 2, J = 3/2^-)$ population to $\widetilde{A}(010)\kappa^2\Sigma^{(-)}(J = 1/2^+)$, which decays back to each of $(N = 1, J = 1/2^-)$ and $(N = 2, J = 3/2^-)$ with around 50% probability (decay to $(N = 1, J = 3/2^-)$ is negligible[9]). Approximately 25% of the decay to $(N = 1, J = 1/2^-)$ goes to the $F = 0$ hyperfine level, meaning

[9]This is called a "satellite" branch in the limit where both states are good case (b) [245, 343]. The satellite branches ($\Delta J \neq \Delta N$) are typically quite weak (and get increasingly suppressed as N increases) since they require flipping the electron spin. (To see this, note that these transitions couple the upper spin-rotation level in one state to the lower SR level in

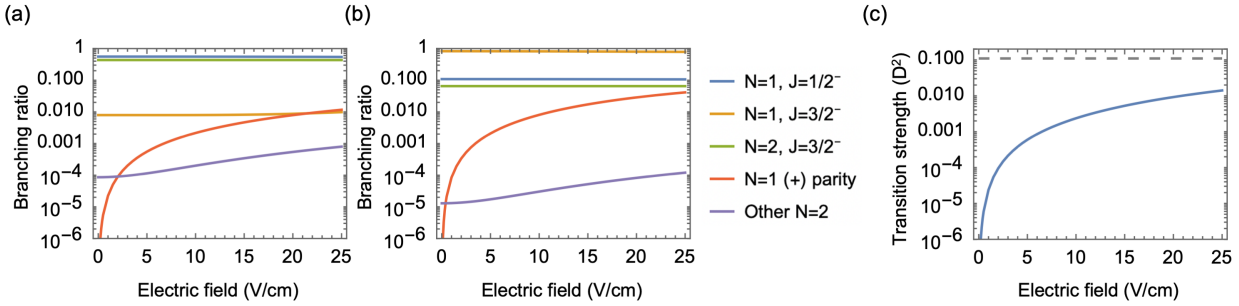

Figure 7.5: Optical pumping branching ratios and transition strengths vs. applied electric field. (a) Rotational branching ratios from $\widetilde{A}(010)\kappa^2\Sigma^{(-)}(J=1/2^+)$ to different states within $\widetilde{X}(010)$ as a function of electric field. Vibrational branching is ignored (i.e. the VBR is assumed to be 1). (b) Branching ratios from $\widetilde{A}(010)\mu^2\Sigma^{(+)}(J=1/2^+)$. (c) OP microwave transition strength $\sum_{m_F,F',m'_F}|\langle N=1,J=1/2^-,F=1,m_F|\vec{\mu}|N'=2,J'=3/2^-,F',m'_F\rangle|^2$ vs. applied electric field, calculated for $\hat{x}$ polarized microwaves. The grey dashed line is the asymptotic strength when parity is fully mixed (around 100 V/cm). At $E=7.5$ V/cm, losses to $(+)$ parity states are around 0.1% for the κ state and 0.5% for the μ state (which is populated significantly less often). The microwave transition strength is around 1% of the value reached when parity is fully mixed.

that an average of 8 photons are required to pump population into $F=0$.

Because the microwave transition is parity-forbidden, we apply a small electric field $E=7.5$ V/cm to mix parity just enough for the transition to be allowed, but not enough for significant branching into $+$ parity states to occur during the optical decay. Fig. 7.5 shows calculated branching ratios and microwave transition strengths as a function of applied electric field, indicating that our field of $E=7.5$ V/cm does not induce significant losses.

Because the $\widetilde{A}(010)\rightarrow\widetilde{X}(010)$ vibrational branching ratio is only 94.3% (chapter 4), significant population will be lost to vibrational dark states during optical pumping if no vibrational repumping lasers are used. Luckily, the dominant decay pathways are to $\widetilde{X}(110)$ (4.3% VBR) and $\widetilde{X}(03^10)$ (0.9% VBR), which are already repumped through $\widetilde{A}(010)$ in our experiment. By turning on these repumping lasers, we can reduce the vibrational loss to <1% and therefore improve the optical pumping efficiency. However, as shown in

the other.)

Fig. 7.4 (which only shows the $\widetilde{X}(110)$ repumpers for simplicity), some of the repumpers couple through the $\widetilde{A}(010)\mu^2\Sigma^{(+)}$ state, whose rotational branching ratios are much less favorable and cause population to accumulate in $(N = 1, J = 3/2^-)$. Therefore, for maximum optical pumping efficiency we need to intersperse normal optical pumping with $J = 3/2$ repumping, wherein the microwaves are instead tuned to address the $(N = 1, J = 3/2^-) \leftrightarrow (N = 2, J = 3/2^-)$ transitions. Note that in this case there are two hyperfine states separated by 1.7 MHz that must be addressed by the microwaves in $(N = 1, J = 3/2^-)$. We did not do this in this thesis, but it would likely lead to improvements of optical pumping in future work.

Fig. 7.6 shows the results of a discrete Markov chain model of the optical pumping process. We account for all rotational and vibrational branching effects, but assuming no off-resonant microwave coupling to $F = 0$. We find that without any vibrational repumping lasers the maximum optical pumping efficiency is 75%, which increases to 82% with vibrational repumping and to around 94% when interspersing $J = 3/2$ repumping stages, at which point the efficiency is limited by the remaining ∼1% vibrational branching. Note that these fidelities may be difficult to achieve experimentally due to small off-resonant coupling to $F = 0$, as well as the need to effectively couple to all hyperfine sublevels (some of which are split by AC Stark shifts) with the microwaves.

Note that a laser addressing the 609 nm $\widetilde{X}(000) \rightarrow \widetilde{A}(010)\kappa^2\Sigma^{(-)}$ transition (which we used to populate the bending mode in experiments described in chapters 8 and 9) could be added to repump the 0.3% branching to $\widetilde{X}(000)$. However, this still represents less than 1/3 of the remaining loss.

7.4.1 Experimental implementation

To apply optical pumping to the molecules, we proceeded as follows. First, we ramped the trap depth down to approximately 180 μK to minimize differential AC Stark shifts, and also turned on an electric field of of 7.5 V/cm

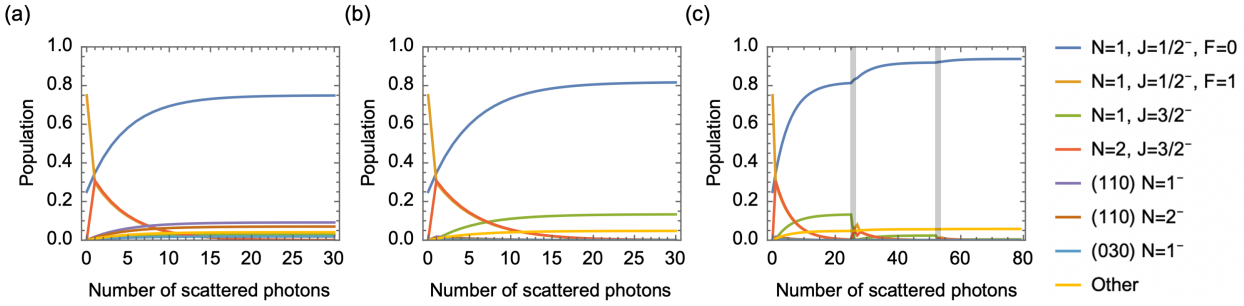

Figure 7.6: Markov chain model of rovibrational branching during optical pumping, with population starting in a thermal mixture of hyperfine states in $(N = 1, J = 1/2^-)$, and assuming perfect microwave coupling of the desired rotational and hyperfine states. (a) No vibrational repumping. (b) With $\widetilde{X}(110)(N = 1)$, $\widetilde{X}(110)(N = 2)$, and $\widetilde{X}(03^10)(N = 1)$ repumping lasers. (c) With repumpers and two $J = 3/2$ repumping pulses (shaded regions).

to mix parity enough for the OP transitions to be driven (see above). To transfer $J = 3/2^-$ molecules to $J = 1/2^-$, we drove the $(N = 1, J = 3/2^-) \rightarrow (N = 2, J = 3/2^-)$ microwave transition (with the X-polarized horn) while applying $\widetilde{X}(010)(N = 2) \rightarrow \widetilde{A}(010)\kappa^2\Sigma^{(-)}(J = 1/2^+)$ repumping light. This excited state decays predominantly to $(N = 1, J = 1/2^-)$, so this step pumps population into that state. We applied this stage for approximately 3 ms, while continuously sweeping the microwave frequency over a $\sim \pm 500$ kHz range to address both hyperfine states in $J = 3/2^-$.

Next, to pump molecules into $F = 0$, we drove the $(N = 1, J = 3/2^-, F = 1) \rightarrow (N = 2, J = 3/2^-)$ microwave transition while applying the same $\widetilde{X}(010)(N = 2) \rightarrow \widetilde{A}(010)\kappa^2\Sigma^{(-)}(J = 1/2^+)$ repumping light, which pumps molecules into $F = 0$ after approximately 8 photons are scattered, as discussed above. This stage was applied for approximately 5 ms. Because of differential AC Stark shifts, the m_F sublevels in the $F = 1$ state are split apart. To broaden over all these features and make sure all molecules are addressed by the microwaves, we modulate the microwave frequency over a range of around ± 100 kHz (at a modulation frequency of $\sim$10 kHz, so that the spectrum is swept many times during the OP pulse).

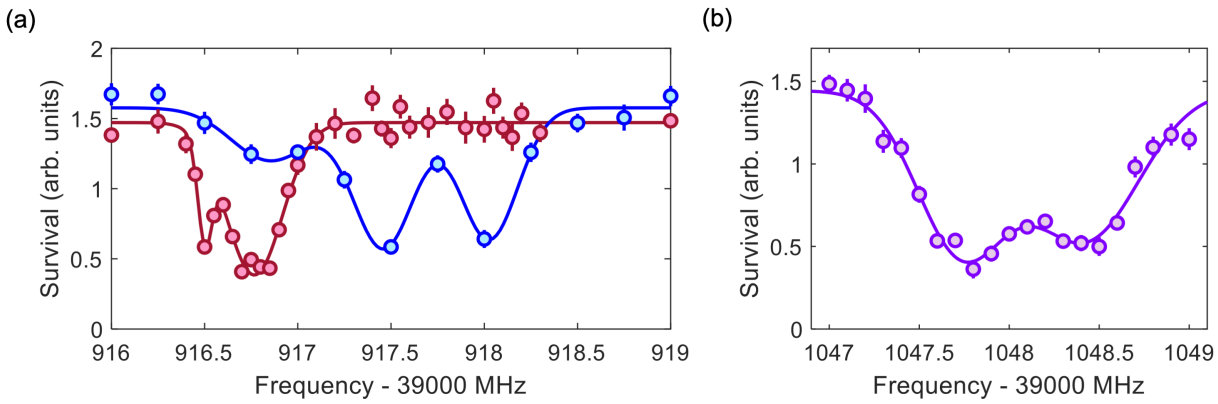

Figure 7.7: Optical pumping into $F = 0$. (a) Microwave spectroscopy of the $(N = 1, J = 1/2^-) \rightarrow (N' = 2, J' = 3/2^+)$ transition with (red) and without (blue) optical pumping. The two peaks on the left are $F = 0 \rightarrow F' = 2$ and $F = 0 \rightarrow F' = 1$ (the first transition is weak, but allowed by AC Stark mixing in the trap). The two peaks on the right are the $F = 1 \rightarrow F' = 2$ and $F = 1 \rightarrow F' = 1$ transitions. (b) Frequency scan of the optical pumping microwaves. Detection is done after depleting population on the $F = 0$ feature in part (a), so lower survival corresponds to better optical pumping. The two peaks correspond to the $(N = 1, J = 1/2^-, F = 1) \rightarrow (N' = 2, J' = 3/2^-, F' = 2, 1)$ optical pumping transitions. The upper state hyperfine splitting is 0.7 MHz. For this data, the microwaves are broadened over ∼100 kHz by frequency modulation.

Fig. 7.7 shows optical pumping data.[10] We see that after optical pumping, nearly all population is transferred out of the $F = 1$ state and into $F = 0$. Separate data indicates that there is a small amount of residual population in $J = 3/2^-$, as expected from the model. Fig. 7.7(b) shows a scan of the optical pumping microwave frequency, which shows two transitions corresponding to the two hyperfine states in $(N = 2, J = 3/2^-)$. Both transitions provide optical pumping with similar efficiency. The higher frequency transition is farthest away from off-resonantly driving $F = 0$ population, but ultimately either line works well.

We estimate that the efficiency of our optical pumping is typically around 70%, since there is still significant population remaining in detectable states even after depleting $F = 0$ (as evidenced by the nonzero baseline in Fig. 7.7). Some of this baseline is likely due to blackbody radiation/population shelving effects, but some of it is from molecules left in $J = 3/2^-$ after optical pumping.

7.5 Coherent state transfer

Once molecules are in $F = 0$, we can begin coherently transferring them to different rotational and hyperfine states using microwave sweeps and π pulses.

As a first test of our ability to apply coherent pulses, we added a small magnetic field to split m_F sublevels and tried to drive the three $(N = 1, J = 1/2^-, F = 0) \rightarrow (N = 2, J = 3/2^+, F = 1, m_F)$ transitions. We observed Rabi oscillations (with Rabi frequencies between 500-1000 kHz) on the transitions to $m_F = \pm 1$, but only saw slow decoherence on the transition to $m_F = 0$. This confirms that our microwaves are mostly horizontally polarized, with only a small Z polarized component.

[10] This data was taken during the collision experiments described in chapter 9, and is similar to, but slightly better than, what we observed during the eEDM work). One reason for this is that we did not need the initial $J = 3/2$ pumping stage in the collision data, due to the way we populated the bending mode.

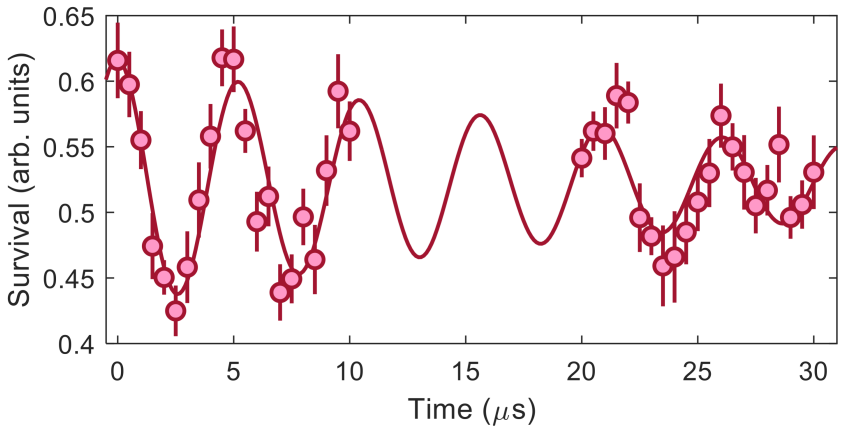

Figure 7.8: Rabi oscillations on the $(N = 2, J = 3/2^-, F = 2, m_F = 0) \rightarrow (N = 1, J = 1/2^+, F = 1, m_F = \pm 1)$ transition at 39997.12 MHz. The electric field is 61.5 V/cm and the magnetic field is ∼5 mG. This transition is used for preparing the eEDM sensitive state, described in section 7.6.

For the eEDM experiment (described below), we need to prepare molecules in the $(N = 1, J = 1/2^+)$ state at an electric field near 60 V/cm. To do this, we first transfer population up to $(N = 2, J = 3/2^-, F = 2, m_F = 0)$ by applying an electric field of 150 V/cm to mix states of opposite parity. This transition is driven with the Z polarized microwave horn. We initially tried to use an adiabatic rapid passage (ARP)/Landau -Zener (LZ) sweep to do this population transfer, but we found that the relatively dense spectrum made it challenging to do this without accidentally driving into the wrong state. Therefore, we used a microwave π pulse.

To prepare the eEDM state, we drove a transition down to $(N = 1, J = 1/2^+, F = 1, m_F = \pm 1)$ using another microwave π pulse (this time with the X polarized horn). Rabi oscillations on this transition are shown in Fig. 7.8.

The main challenge for observing Rabi oscillations was drifts in external electric and magnetic fields, which would cause the transition frequency to change so that Rabi oscillations would degrade over time. Our efforts to stabilize these fields are described in section 7.2. Additionally, the spread of the molecules in the trap (Rayleigh

range ∼1.5-2 mm) is not negligible compared to the microwave wavelength of 7.5 mm. Therefore, there is some decoherence in our Rabi oscillations due to inhomogeneity in the applied microwave power (simulations show that the microwaves form a standing wave inside our metal chamber).

7.6 The "EDM pathfinder" experiment

This section is reproduced, with small modifications, from Ref. [45].

Parity-doublet states in trapped polyatomic molecules are expected to be an invaluable tool for systematic error rejection in precision measurements of physics beyond the Standard Model (BSM) [140]. One powerful avenue for tabletop BSM searches is probing for the electric dipole moment of the electron (eEDM) [11, 344–347], d_e, which violates time-reversal (T) symmetry and is predicted by many BSM theories to be orders of magnitude larger than the Standard Model prediction [11, 345]. Current state-of-the-art eEDM experiments are broadly sensitive to T-violating physics at energies much greater than 1 TeV [83–87, 348]. All such experiments use Ramsey spectroscopy to measure an energy shift due to the interaction of the electron with the large electric field present inside a polarized molecule [84–87, 349]. Molecular beam experiments have achieved high statistical sensitivity by measuring a large number of molecules over a $\approx$ 1 ms coherence time [84, 86], while molecular ion-based experiments have used long Ramsey interrogation times ($\approx$ 1 s) though with lower numbers [85, 87, 349]. Measurements with trapped neutral polyatomic molecules can potentially combine the best features of each approach to achieve orders-of-magnitude improved statistical sensitivity [140].

In this section, we demonstrate full quantum control over the internal states of a trapped polyatomic molecule in a vibrational bending mode with high polarizability in small electric fields. The method starts with preparing

ultracold, optically trapped molecules in a single hyperfine level, after which a static electric field is applied to polarize the molecules. The strength of the polarizing electric field is tuned to obtain near-zero g-factor spin states, which have strongly suppressed sensitivity to magnetic field noise while retaining eEDM sensitivity. Microwave pulses are applied to create a coherent superposition of these zero g-factor spin states that precesses under the influence of an external magnetic field. The precession phase is then read out by a combination of microwave pulses and optical cycling.

We observe spin precession over a range of electric and magnetic fields and characterize the current limitations to the coherence time of the measurement. With readily attainable experimental parameters, coherence times on the order of the state lifetime (>100 ms) could be realistically achieved. We therefore realize the key components of an eEDM measurement in this system. The eEDM sensitivity arises from the relativistic motion of the electron which is enhanced by higher mass nuclei. Although the light mass of CaOH precludes a competitive eEDM measurement [350], the protocol demonstrated here is directly transferable to heavier laser-cooled alkaline earth monohydroxides with identical internal level structures, such as SrOH, YbOH, and RaOH, which have significantly enhanced sensitivity to the eEDM [140, 217, 219, 350**?**].

In eEDM measurements with polarized molecules, the electron spin $\vec{S}$ precesses under the influence of an external magnetic field B_Z and the internal electric field of the molecule, $\mathcal{E}_{\text{eff}}$, which can be large due to relativistic effects. Time evolution is described by the Hamiltonian

$$\begin{aligned} H &= g_S \mu_B B_Z \vec{S} \cdot \hat{Z} - d_e \mathcal{E}_{\text{eff}} \vec{S} \cdot \hat{n} \\ &= g_S \mu_B B_Z M_S - d_e \mathcal{E}_{\text{eff}} \Sigma. \end{aligned} \tag{7.1}$$

Here, $g_S \approx 2$ is the electron spin g-factor, μ_B is the Bohr magneton, B_Z points along the lab $\hat{Z}$ axis, and the internal field $\mathcal{E}_{\text{eff}}$ points along the molecule's internuclear axis $\hat{n}$. We define the quantities $M_S = \vec{S} \cdot \hat{Z}$ and $\Sigma = \vec{S} \cdot \hat{n}$ to describe the electron's magnetic sensitivity and EDM sensitivity, respectively. The effect of the eEDM can be isolated by switching the orientation of the applied magnetic field or, alternatively, by switching internal states to change the sign of M_S or Σ. Performing both switches is a powerful technique for suppressing systematic errors [85, 86].

Current EDM bounds rely on specific states in diatomic molecules that have an unusually small g-factor, reducing sensitivity to stray magnetic fields [84, 85]. However, CaOH, like other laser-coolable molecules with structure amenable to eEDM searches [33, 34, 140**?**], has a single valence electron, which results in large magnetic g-factors. In this work, we engineer reduced magnetic sensitivity by using an applied electric field E_Z to tune M_S to a zero-crossing, while maintaining significant eEDM sensitivity Σ. This technique is generic to polyatomic molecules with parity-doublets. Details of a specific $M = \pm 1$ pair of zero g-factor states are shown in Figure 7.9 (a)-(b). We emphasize that near the zero g-factor crossing, the eEDM sensitivity is nearly maximal due to the large projection of the electron spin onto the internal electric field of the molecule. Sensitivity to transverse magnetic fields is also suppressed in these zero g-factor states. See the Supplemental Material of Ref. [45] for more details on the zero g-factor states. The magnetic field and eEDM sensitivities in Fig. 7.9(b) are calculated using the $\widetilde{X}(010)$ Hamiltonian described in chapter 2 and appendix A.

7.6.1 Experimental overview

The experiment begins with laser-cooled CaOH molecules loaded from a magneto-optical trap [42] into an optical dipole trap (ODT) formed by a 1064 nm laser beam with a 25 μm waist size, as described in previous work

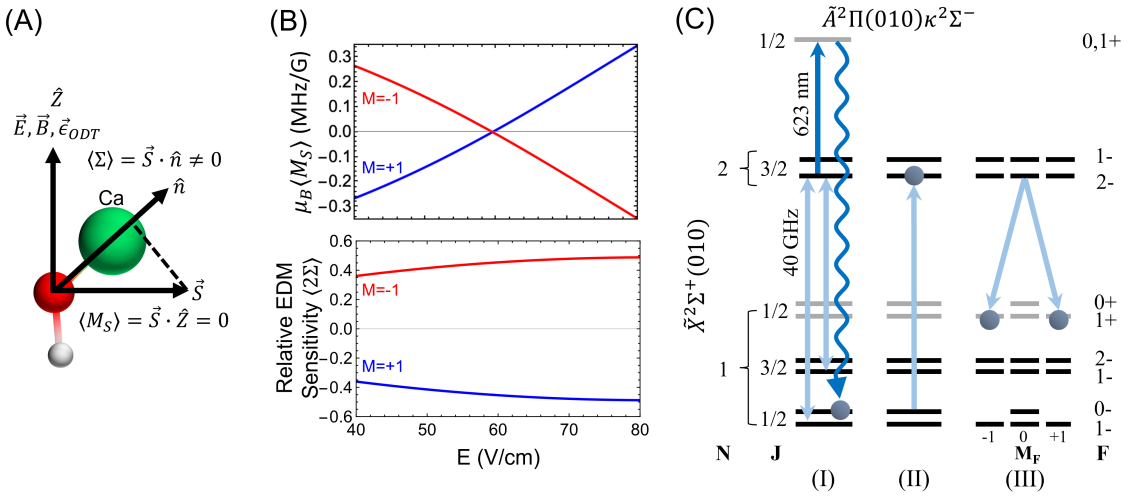

Figure 7.9: (a) A geometric picture of the bending molecule at the zero g-factor crossing. The electron spin ($\vec{S}$) has a finite projection on the molecule axis ($\hat{n}$), giving eEDM sensitivity. However, the electron spin ($\vec{S}$) is orthogonal to the magnetic field ($\vec{B}$), resulting in suppressed magnetic field sensitivity. (b) The magnetic sensitivity (upper plot) and eEDM sensitivity (lower plot) for a pair of zero g-factor states ($N = 1, J = 1/2^+, F = 1, M_F = \pm 1$) are shown as a function of the applied electric field. (c) Experimental sequence to prepare the eEDM sensitive state. First, the molecules are pumped into a single quantum state ($N = 1, J = 1/2^-, F = 0$) with a combination of microwave drives and optical pumping (I). Next, a microwave π-pulse drives the molecules into the $N = 2, J = 3/2^-, F = 2, M_F = 0$ state (II). Lastly, the eEDM measurement state is prepared as a coherent superposition of the $N = 1, J = 1/2^-, F = 1\ M_F = \pm 1$ states with a microwave π-pulse (III). The states which are optically detectable with the detection light are shown in black, while those not addressed by the detection light are in grey. Reproduced from Ref. [45].

[43]. The ODT is linearly polarized and its polarization vector $\vec{\epsilon}_{\mathrm{ODT}}$ defines the $\hat{Z}$ axis, along which we also apply magnetic and electric fields, $\vec{B} = B_Z\hat{Z}$ and $\vec{E} = E_Z\hat{Z}$, respectively, as depicted in Figure 1(a). We first non-destructively image the molecules in the ODT for 10 ms as normalization against variation in the number of trapped molecules. The molecules are then optically pumped into the $N = 1^-$ levels of the $\widetilde{X}^2\Sigma^+(010)$ vibrational bending mode [43] (Figure 1(c)), and the trap depth is adiabatically lowered by $3.5\times$ to reduce the effect of AC Stark shifts from the trap light and to lower the temperature of the molecules to 34 μK. Any molecules that were not pumped into $N = 1^-$ levels of the bending mode are heated out of the trap with a pulse of resonant laser light.

Following transfer to the $\widetilde{X}^2\Sigma^+(010)(N = 1^-)$ state, the molecular population is initially spread across twelve hyperfine Zeeman sublevels in the spin-rotation components $J = 1/2$ and $J = 3/2$. To prepare the molecules in a single hyperfine state, we use a combination of optical pumping and microwave pulses, as shown in Figure 7.9(c) (and described in section 7.4). We first apply microwaves from the $(N = 1, J = 3/2^-)$ state up to the $(N = 2, J = 3/2^-)$ state. As this transition is parity-forbidden, we apply a small electric field $E_Z = 7.5$ V/cm to slightly mix the parity of the $N = 1$ levels and provide transition strength. From the $N = 2$ state, we drive an optical transition to the excited $\widetilde{A}^2\Pi(010)\kappa^2\Sigma^{(-)}, J = 1/2^+$ state. This state predominately decays to both $F = 0$ (the target state) and $F = 1$ states in the $N = 1, J = 1/2^-$ manifold. After 3 ms of optical pumping, the microwaves are switched to drive the accumulated $N = 1, J = 1/2^-, F = 1$ population to the same $N = 2, J = 3/2^-$ state in $\widetilde{X}(010)$, where they are excited by the optical light and pumped into the target $F = 0$ state. Once this optical pumping sequence is complete, we adiabatically ramp the electric field to $E_Z =$150 V/cm to significantly mix parity, then drive population up to the $N = 2, J = 3/2^-, F = 2, M = 0$ state with a microwave π-pulse (Figure 7.9(c)(II)). We clean out any remaining population in the $N = 1$ state

with a depletion laser that resonantly drives population to undetected rotational levels.

To perform spin precession in the eEDM sensitive state, we first adiabatically ramp the electric field to a value E_Z, then turn on a small bias magnetic field B_Z. We measure the electron spin precession frequency using a procedure analogous to Ramsey spectroscopy [84, 86]. The molecules are prepared by driving a π-pulse (2.5 μs), with microwaves linearly polarized along the lab $\hat{X}$ axis, into the "bright" superposition state $|B\rangle = (|M = 1\rangle + |M = -1\rangle)/\sqrt{2}$ within the $N = 1, J = 1/2^+, F = 1, M = \pm 1$ eEDM sensitive manifold (Figure 7.9(c)). The state begins to oscillate between the bright state and the "dark" state $|D\rangle = (|M = 1\rangle - |M = -1\rangle)/\sqrt{2}$ at a rate $\omega_{SP} = \mu_{\text{eff}} B_Z$, where the effective magnetic moment $\mu_{\text{eff}} = \mu_B g_{\text{eff}} = g_S \mu_B (\langle M_S \rangle_{M=1} - \langle M_S \rangle_{M=-1})$ is tuned via the applied electric field E_Z (Figure 7.9(b)). The contribution from the $d_e \mathcal{E}_{\text{eff}}$ term in eqn. 7.1 is negligible in CaOH, but could be measured in heavier molecules with much larger $\mathcal{E}_{\text{eff}}$. After a given time, a second π-pulse is applied to stop spin precession and transfer the bright state to the optically detectable $N = 2, J = 3/2^-$ level. Once the electric field is ramped down, the population remaining in the eEDM manifold, which has the opposite parity, is not optically detectable. We then image the ODT again and take the ratio of the first and second images (Figure 7.10). At long spin precession times (> 10 ms), losses from background gas collisions ($\sim$1 sec), blackbody excitation ($\sim$1 sec), and the spontaneous lifetime of the bending mode ($\sim$0.7 sec) lead to an overall loss of signal, as characterized in Refs. [43, 44]. This effect is mitigated with a fixed duration between the first and second images, making the loss independent of the precession time.

7.6.2 Zero g-factor states

To map out the location of the zero g-factor crossing, we perform spin precession measurements at a fixed magnetic field $B_Z = 110$ mG for different electric fields (Figure 7.11). The spin precession frequency corresponds

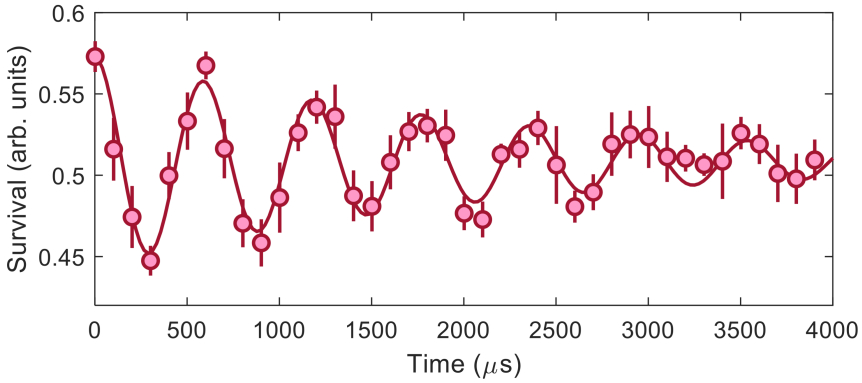

Figure 7.10: Spin precession of the eEDM sensitive state in the presence of a bias magnetic field. This data is taken at an electric field of $E_Z = 61.5$ V/cm, corresponding to a magnetic field sensitivity of 0.06 MHz/G. The bias magnetic field is $B_Z = 30$ mG.

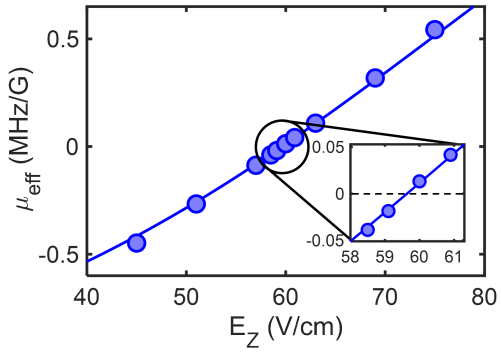

Figure 7.11: Magnetic field sensitivity of the eEDM state in CaOH as a function of electric field. The field sensitivity is determined by measuring the spin precession frequency at different electric fields with an applied magnetic field of $B_Z = 110$ mG. Error bars are smaller than the markers. The solid curve is the calculated magnetic field sensitivity in the presence of trap shifts using known molecular parameters. Adapted from Ref. [45].

to an effective g-factor at that electric field. We find that the zero g-factor crossing within the $N = 1, J = 1/2^+, F = 1, M = \pm 1$ eEDM manifold occurs at an electric field of 59.6 V/cm, in agreement with theory calculations.[11] We note that there is another zero g-factor crossing for the $N = 1, J = 3/2^+, F = 1$ manifold at ≈ 64 V/cm, which has a smaller eEDM sensitivity but the opposite slope of g_{eff} vs. E_Z, thereby providing a powerful resource to reject systematic errors related to imperfect field reversals (see Supplemental Material of Ref. [45].). We emphasize that while the location of these crossings is dependent on the structure of a specific molecule, their existence is generic in polyatomic molecules, which naturally have parity-doublet structure [140].

7.6.3 Optimizing coherence time of eEDM-sensitive states

A critical component of the spin precession measurement is the coherence time, which sets the sensitivity of an eEDM search. Figure 7.12(a) shows the measured coherence time of our system at different applied fields B_Z and E_Z. We characterize two dominant limitations that wash out oscillations at long times. Variations in the spin precession frequency can be linearly expanded as $\delta\omega_{\text{SP}} = \mu_{\text{eff}}(\delta B_Z) + (\delta\mu_{\text{eff}})B_Z$. The first term describes magnetic field noise and drift of the applied bias field, given by δB_Z. The second term describes noise and drifts in the g-factor, δg_{eff}, which can arise from instability in the applied electric field, E_Z, or from AC Stark shifts (described below). Drifts in the bias electric field E_Z are found to be negligible in our apparatus.

Decoherence due to magnetic field noise, δB_Z, is independent of the applied magnetic field but is proportional to μ_{eff}, and can be mitigated by operating near the zero g-factor crossing. As shown in Fig. 7.12(b), at an electric field of 90 V/cm, corresponding to a large magnetic moment of $\mu_{\text{eff}} = 1.0$ MHz/G, we realize a magnetic

[11] The calculations use the Hamiltonian from chapter 2 and appendix A. They are also described in the Supplemental Material of Ref. [45].

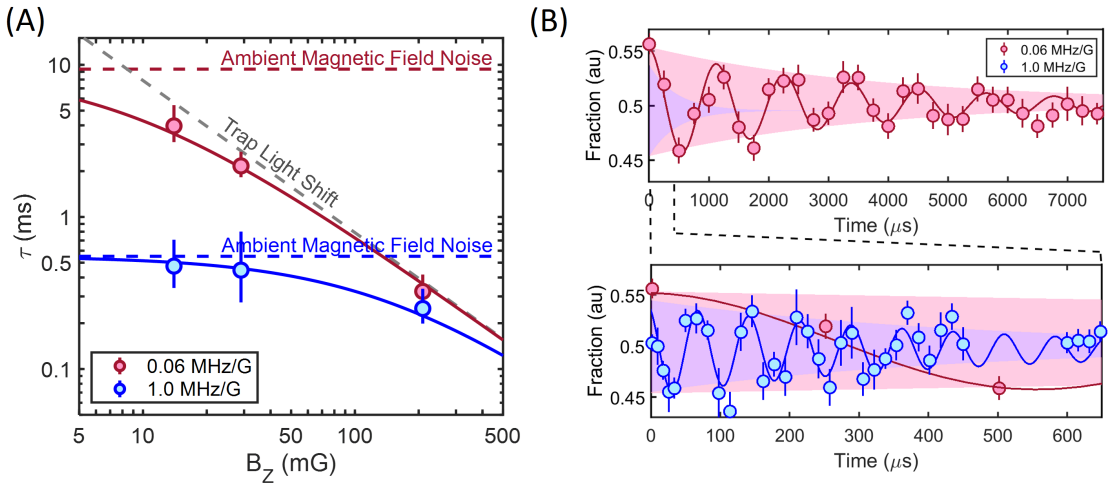

Figure 7.12: Coherence time of the spin precession signal. (a) Measured coherence times τ versus B_Z at different electric fields (red and blue markers, corresponding to different magnetic field sensitivity). The coherence time scales as $1/B_Z$ due to AC Stark shift broadening, then plateaus at a limit set by the magnetic field instability δB. This limit increases as the g-factor approaches zero. Solid and dashed curves are fit to the data. The ambient magnetic field noise determined from the fit is $\delta B = 4^{+2}_{-1}$ mG, while the fitted decoherence time due to light shifts is $\tau = (1/B_Z) \times 80^{+20}_{-10}$ ms×mG. (b) The spin precession coherence time at $B_Z = 15$ mG is extended by 16× by approching the zero g-factor point. Reproduced from Ref. [45].

field noise-limited coherence time of 0.5 ms at $B_Z \approx 15$ mG. At an electric field of 61.5 V/cm, corresponding to $\mu_{\text{eff}} = 0.06$ MHz/G, much closer to the zero g-factor location, we find a coherence time of 4 ms at the same B_Z.

At higher magnetic fields, the primary limitation to the coherence time is due to AC stark shifts from the optical trapping light (Fig. 7.13). The intense Z-polarized ODT light leads to a shift in the electric field at which the zero g-factor crossing occurs. Due to the finite temperature of the molecules within the trap, they will explore different intensities of trap light and hence have different values of g_{eff}. The spread δg_{eff} causes variation of ω_{SP}, which leads to decoherence. In contrast to the magnetic field noise term, this effect is independent of the electric field E_Z but decreases monotonically with B_Z, which scales the frequency sensitivity to g-factor variations, $\delta\omega_{\text{SP}} = B_Z \delta\mu_{\text{eff}}$. The insensitivity of g-factor broadening to the exact value of g_{eff} is demonstrated in Fig. 7.13(c). Decoherence due to AC Stark shifts can be reduced by cooling the molecules to lower temperatures or by decreasing B_Z. The bias magnetic field can be reduced arbitrarily far until either transverse magnetic fields or magnetic field noise become dominant. From the decoherence rates measured in this work, it is expected that AC Stark shift-limited coherence times $\sim$1 s could be achieved at bias fields of $B_Z \sim 100$ μG.

From the above discussion, it is expected that the longest achievable coherence times will occur for very small g-factors, $g_{\text{eff}} \approx 0$, and very small bias fields, $B_Z \approx 0$. Minimizing B_Z requires reducing the effects of both magnetic field noise and transverse magnetic fields to well below the level of the bias field energy shifts. We cancel the transverse magnetic fields to below 1 mG by maximizing the spin precession period under the influence of transverse B fields only (as described below), and actively monitor and feedback on the magnetic field along each axis to minimize noise and drifts in B_Z. Note that the stainless steel vacuum chamber has no magnetic shielding, leading to high levels of magnetic field noise which would not be present in an apparatus designed for an eEDM search. Even under these conditions, we achieve a coherence time of 30 ms at an electric field of 60.3 V/cm

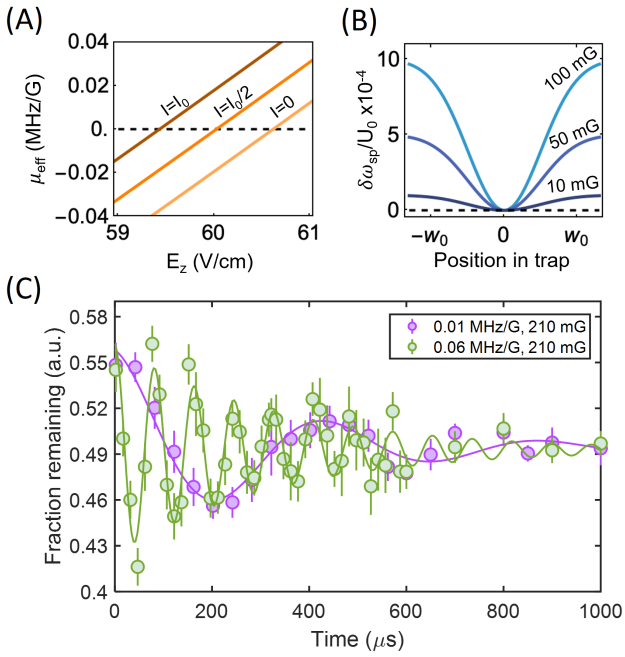

Figure 7.13: Effect of trap light on coherence time. (a) The trap light shifts the location of the zero crossing in μ_{eff}. As a result, molecules at a finite temperature explore different magnetic field sensitivities μ_{eff}. (b) Dependence of the spin precession frequency (scaled by the trap depth U_0) on position within the trap. At lower magnetic fields, the relative change in spin precession frequency is reduced. (c) Two spin precession curves taken at the same magnetic field ($B_Z = 210$ mG) but at different electric fields, showing that the AC Stark shift limitation is independent of the effective g-factor, since AC Stark shifts dominate the coherence time for large bias fields. Reproduced from Ref. [45].

(corresponding to $\mu_{\text{eff}} = 0.02$ MHz/G) and a bias field of $B_Z \approx 2$ mG (see below). However, at such a low bias field, the molecules are sensitive to 60 Hz magnetic field noise present in the unshielded apparatus, which is on the same order as the bias field. Since the experiment is phase stable with respect to the AC line frequency, this 60 Hz magnetic field fluctuation causes a time-dependent spin precession frequency. Nevertheless, our prototype experiment confirms that long coherence times are possible. Any future eEDM experiment would have magnetic shielding that would greatly suppress nefarious magnetic fields from the environment. Such shielding could readily enable coherence times exceeding that of the ~ 0.5 s lifetime of the bending modes of similar linear polyatomic molecules with larger eEDM sensitivity [43].

Zeroing magnetic fields

When transverse magnetic fields are dominant, the electron will be quantized along the transverse axis and there is minimal spin precession by the bias B_Z field. The transverse coupling results in eigenstates given by $(|M_F = 1\rangle \pm e^{i\phi}|M_F = -1\rangle)/\sqrt{2}$, where the phase ϕ is set by the direction of $\vec{B}$ in the transverse plane. If $\phi = 0$ or π, only one of these states is bright to the $\hat{X}$-polarized state preparation microwaves, which means the initial state is stationary under the transverse fields. For all other orientations, the transverse field causes spin precession with varying contrast, depending on the specific value of ϕ.

We are able to use transverse spin precesion to measure and zero transverse fields to the mG level. We do so by operating with minimal bias field $B_Z \approx 0$ and operating E_Z near the zero g-factor crossing, such that $g_{\text{eff}} B_Z < g_\perp B_\perp$. We then apply a small transverse magnetic field to perform transverse spin precession. Here, the dynamics are dominated by the transverse fields rather than the Z fields. We obtain field zeros by iteratively minimizing the precession frequency by tuning the bias fields B_X and B_Y. See Fig. 7.14 for an example of one such iteration,

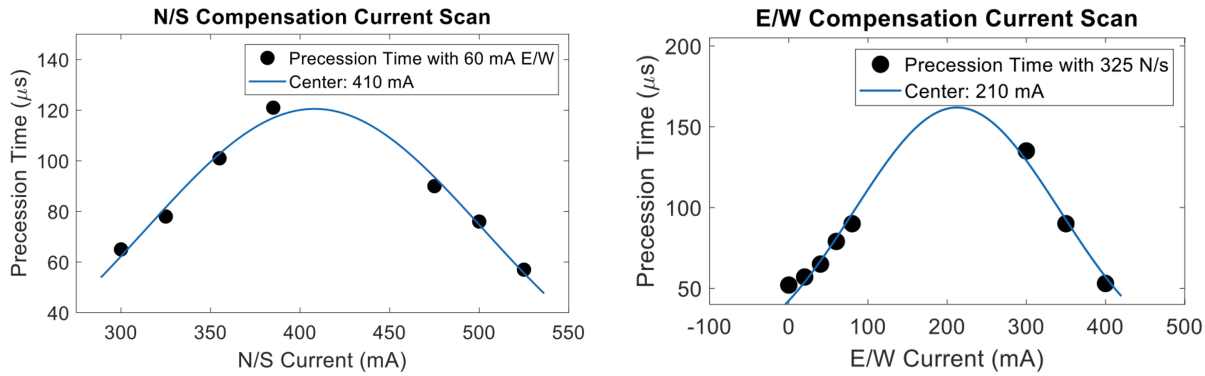

Figure 7.14: Cancellation of transverse magnetic fields along the north/south and east/west axes of the lab. The current refers to the current of the compensation coils mounted just outside the MOT chamber. Later, we applied another round of cancellation by adjusting the setpoint of the magnetic field active compensation PID, which allowed us to achieve even longer spin precession times, with corresponding transverse fields at the mG level.

where we maximize the precession time by scanning each transverse field.

Spin Precession Near Zero g-Factor

As discussed above, the longest achievable coherence times occur at at combination of low effective g-factors (which suppress δB_Z decoherence) and low magnetic bias fields (which suppress $\delta\mu_{\text{eff}}$ decoherence). These low g-factors and bias fields only very weakly enforce a quantization axis along Z, enhancing the potential for transverse magnetic fields $B_\perp$ to contribute. Such fields have the effect of (a) reducing the spin precession contrast and (b) altering the observed precession frequency. To avoid these effects, the condition $g_{\text{eff}}B_Z > g_\perp B_\perp$ must therefore be satisfied. To achieve this, we zero the transverse magnetic fields by intentionally taking spin precession data at $B_Z \approx 0$ and $g_{\text{eff}} \approx 0$ while varying the transverse fields B_X and B_Y. By minimizing the spin precession frequency as a function of the transverse fields, we reduce $B_\perp$ to approximately 1 mG. In addition, long-term drifts in the dc magnetic field along all three axes are compensated by actively feeding back on the magnetic field

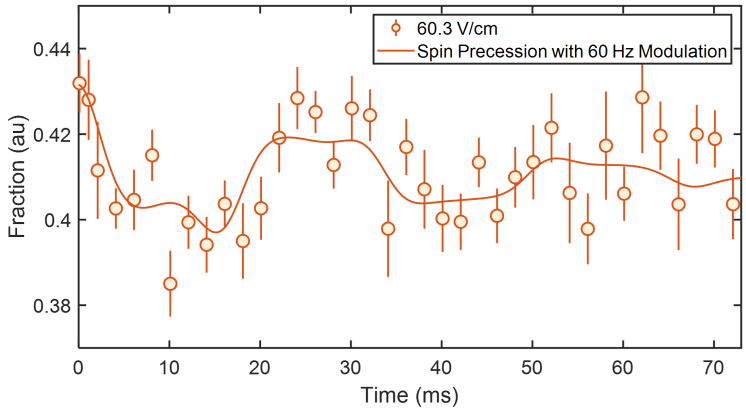

Figure 7.15: Spin precession at $E_Z = 60.3$ V/cm and $B_Z = 2$ mG. The fit includes a 60 Hz time-varying magnetic field whose amplitude and phase are measured with a magnetometer. The coherence time fits to 30 ms. Reproduced from Ref. [45].

as measured with a fluxgate magnetometer. Under these conditions, at an electric field of 60.3 V/cm (corresponding to $\mu_{\text{eff}} = 0.02$ MHz/G) and a bias field of $B_Z \approx 2$ mG, we achieve a coherence time of 30 ms (Fig. 7.15).

At these very low bias fields, the molecules are also sensitive to 60 Hz magnetic field noise present in the unshielded apparatus, whose amplitude is on the same order as B_Z. Since the experiment is phase stable with respect to the AC line frequency, this 60 Hz magnetic field fluctuation causes a time-dependent spin precession frequency. A fluxgate magnetometer is used to measure the amplitude and phase of this 60 Hz field, which are then used as fixed parameters in the fit shown in Figure 7.15.

7.6.4 Conclusion

In summary, we have realized coherent control of optically trapped polyatomic molecules and demonstrated a realistic experimental roadmap for future eEDM measurements. By leveraging the unique features of the quantum levels in polyatomic molecules, we achieve a coherence time of 30 ms for paramagnetic molecules in a stainless

steel chamber with no magnetic shielding. With common shielding techniques employed in past EDM experiments, there is a clear path to reducing stray fields and extending coherence times to > 100 ms. At such a level, the dominant limitation becomes the finite lifetime of the bending mode [43, 44]. Even longer coherence times are possible with the right choice of parity doublet states, as found in symmetric or asymmetric top molecules [37, 47, 140, 351].

Following our established roadmap with heavier trapped polyatomic molecules has the potential to provide orders-of-magnitude improvements to current bounds on T-violating physics. Using a recent study of the $\widetilde{X}(010)$ state in YbOH [352], we have identified similar $N = 1$ zero g-factor states for eEDM measurements with significantly improved sensitivity. In addition to the g-factor tuning demonstrated in this work, polyatomic molecules provide the ability to reverse the sign of Σ without reversing M_S - a crucial feature of recent experiments that have greatly improved the limit on the eEDM [86, 87]. For example, in the $N = 1$ manifold of CaOH, there is another zero g-factor crossing at a nearby electric field value, with 69% smaller values of Σ and opposite sign. Since the ratio of eEDM sensitivity to g-factor vs. E_Z slope differs between these two crossings, measurements at both points could be used to suppress systematics due to non-reversing fields coupling to the electric field dependence of the g-factor [86].

This work provides a first experimental demonstration of the advantages of the rich level structure of polyatomic molecules for precision measurements. While we have focused here on spin precession with T-reversed states ($M = \pm 1$), many levels of interest can be favorably engineered for precision measurement experiments. In a recent proposal [146], parity-doublets, magnetically tuned to degeneracy in optically trapped polyatomic molecules, were shown to be advantageous for searches for parity violating physics. In another recent work [89], a microwave clock between rovibrational states in SrOH was proposed as a sensitive probe of ultra-light dark

matter, utilizing transitions tuned to electric and/or magnetic insensitivity. In other recent work, it was shown that many pairs of states with suppressed sensitivity to magnetic and electric fields can be found in polyatomic molecules [145]. In these proposals, and now experimentally demonstrated in our work, coherent control and state engineering in polyatomic molecules can mitigate systematic errors and enable robust searches for new physics.

8

An Optical Tweezer Array of CaOH

A natural goal in the quest for quantum control of molecules is to be able to manipulate the motion, position, and internal states of *single* molecules in the quantum regime. Once this ability is established, it is possible to begin building quantum systems *from the ground up*, adding each constituent part with the ability to precisely influence and observe its role as part of the larger collective. Optical tweezer arrays have blossomed

within the atomic physics community over the last decade due to their ability to lend exactly this kind of control to AMO systems.[1]

Optical tweezers are tightly focused beams of light that can be used to trap single atoms and molecules.[2] In fact, in an AMO context the key distinction between a tweezer and a generic optical dipole trap is that a tweezer traps *only* one atom or molecule. This relies on a "collisional blockade" effect, first demonstrated in Refs. [353, 354], where light assisted collisions rapidly cause pairs of molecules to collide, meaning that only 0 or 1 atoms can be loaded (since 2 initially loaded molecules collide to become 0, 3 become 1, etc.).

Since this initial work, arrays of optical tweezers have found numerous quantum science applications. It has been shown that defect-free arrays of loaded optical tweezers can be assembled by imaging the initial, stochastically loaded array, and then rearranging to remove empty traps. This has allowed for positioning of individually trapped particles in arbitrary geometries, as well as dynamic rearrangement of their positions [355–357]. Optical tweezer arrays have already proven to be extremely successful for ultracold atoms [358, 359], enabling the realization of high-fidelity quantum processors [105, 357, 360, 361] and quantum simulators [362–365] based on Rydberg interactions, as well as the development of tweezer-based optical clocks for precision metrology [366–368] and the study of ultracold collisions [369]. Tweezer arrays of diatomic molecules have also been achieved [180, 202, 370], as has the observation of dipolar interactions and two-molecule entangling gates [31, 32, 63]. Recently, Raman sideband cooling of these molecules to the motional ground state of the trap has demonstrated full quantum control of both internal and external states of laser cooled diatomic molecules [30, 206].

There are a large number of promising applications for polyatomic molecules, described elsewhere in this the-

[1] Portions of this chapter have been reproduced from Ref. [46].

[2] They have also found significant application manipulating macroscopic objects for biology applications. This was the original context in which optical tweezers were developed, culminating in the 2018 Nobel Prize for Arthur Ashkin.

sis. All of these applications could either be enabled by, or benefit from, isolating and controlling individual polyatomic molecules in optical tweezer arrays. Towards these scientific goals, polyatomic molecules have been laser cooled [42, 52, 217] and trapped in electrostatic [154, 176], magnetic [174], and optical [43, 45] traps, but they have not previously been controlled at the single particle level.

In this chapter, we describe our work trapping polyatomic molecules in an array of optical tweezers. Laser-cooled CaOH molecules are trapped in a magneto-optical trap (MOT) and transferred into a large optical dipole trap (ODT), and then single molecules are loaded into optical tweezers. During loading, a collisional blockade occurs [353], ensuring that each tweezer contains at most one molecule. The molecules are non-destructively imaged in the tweezers, enabling identification of loaded tweezers and re-imaging later in the experimental sequence. We observe that the loading and imaging efficiencies depend strongly on the tweezer light wavelength due to the rich spectrum of excited states in CaOH. We characterize this dependence and determine optimal parameters to control these effects. Finally, we prepare individually trapped CaOH molecules in a single quantum state within the lowest lying parity-doubled vibrational bending mode, an identified resource for many quantum science goals.

8.1 Initial setup and challenges

8.1.1 Optical setup

To project optical tweezers, we need to build a near-diffraction-limited imaging system with high numerical aperture (NA). Ideally we need a tweezer waist below 2-3 μm, which is where CaF molecules were observed to enter the collisional blockade regime in previous experiments in the Doyle lab [278]. This presents a bit of a geometrical challenge in our MOT chamber, since the in-vacuum RF MOT coils are 1" apart, limiting optical access from

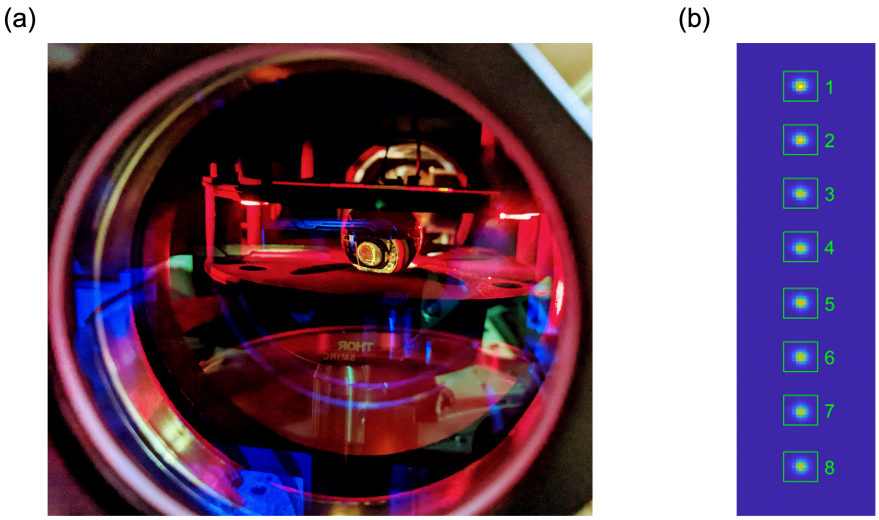

Figure 8.1: (a) In-vacuum asphere mounted in the MOT chamber, between the in-vacuum RF MOT coils. (b) Image of the projected 780 nm array on a beam profiler. The imaged beam waists are approximately 2 μm.

the side. We elected to achieve a high NA by using a 25 mm diameter in-vacuum aspheric lens placed between the MOT coils and close to the molecules (Edmund Optics #16-979, 25 mm diam., 0.40 NA, AR coated 600-1050 nm). A photo of the asphere mounted in the chamber is shown in Fig. 8.1(a).

We elected to form the tweezers using a 780 nm laser, as was previously done with CaF [202]. As discussed in chapter 6, the polarizability of CaOH in the ground state is higher at 780 nm than at 1064 nm, meaning we will need less power per tweezer. The diffraction limit is also slightly smaller for 780 nm. However, as discussed below, there were unforeseen challenges with this wavelength in CaOH. We initially used a frequency-doubled 1550 nm fiber amplifier (NKT, with RIO Orion seed) to form tweezers near 775 nm. However, the fiber amplifier failed midway through the experiment, and we switched to using a Coherent 899 titanium sapphire (Ti-Sapph) laser we already had in the lab. This turned out to be advantageous, because the frequency tunability of the Ti-Sapph allowed us to choose an optimal wavelength for loading and imaging, as discussed below.

The optical setup is shown in Fig. 8.2. We created a small 1D tweezer array using an AOD (AA DTSX-400-780AO), followed by a telescope and a set of relay lenses before projecting the array via the in-vacuum asphere. The optical setup was designed, built, and tested by Paige Robichaud and Loïc Anderegg. An image of the projected array (imaged on a beam profiler) is shown in Fig. 8.1(b). We drove the AOD using up to 8 RF tones near 100 MHz. The waveform is precomputed (with the relative phases chosen to minimize the peak amplitude of the summed waveform), and a 500 MHz AWG (Siglent) is programmed to continuously output the waveform. The powers were balanced to $\lesssim$10% across the array by using a beam profiler to feed back on the intensity of each beam. Afterwards, we measured the trap frequencies using molecules in the array and confirmed that they were roughly uniform. For our final tweezer data, we used a 1.875 MHz frequency spacing, corresponding to a tweezer separation of 11 μm. We found that spacings <1.5 MHz caused significant molecule loss due to heating.

To image molecules in the tweezer array, we collect molecule fluorescence at 555 nm or 626 nm via the asphere, separate it from the tweezer path with a dichroic, and then image it onto an EMCCD (Andor iXon Ultra 897). Because we image with a single asphere, there are chromatic shifts between 780 nm and the imaging wavelength that cause spherical aberration. To correct for this, we use 3x -1.00λ spherical aberration correction plates (Edmund Optics) in the imaging path. The collection efficiency is expected to be approximately 1%, limited by the effective numerical aperture of the imaging optics ($\sim$3% collection efficiency) and by transmission losses from the optical elements in the imaging path ($\sim$40%). In practice, we find by comparing the observed histograms to simulations that the collection is slightly lower, likely due to imperfect alignment. Images are acquired by binning the fluorescence from each tweezer onto a single EMCCD pixel at the hardware level, minimizing the effect of camera readout noise. This procedure applies to all of the tweezer data presented below, except for the averaged image in Fig. 8.9(a), which uses no binning.

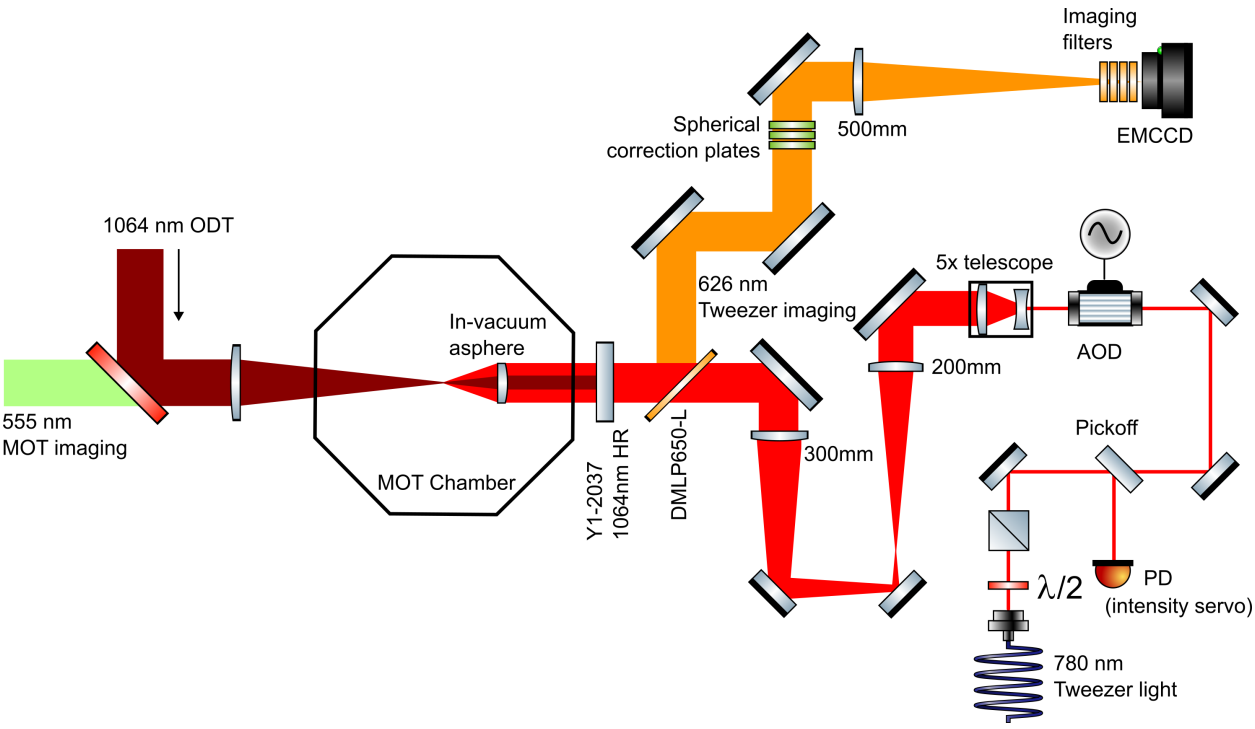

Figure 8.2: Optics used for loading, projecting, and imaging 780 nm optical tweezers.

When we initially aligned the tweezer beam path, we did not open the vacuum chamber[3], and instead used an auxiliary, green laser beam as an alignment aid. The spot size of the projected tweezers is extremely sensitive to the position and angle on the asphere, with even a 0.1° tilt being enough to significantly increase the spot size. The idea was to send in an auxiliary beam (we chose a green wavelength since it's easy to see and is not in the AR coating band of the asphere) from the ODT side of the chamber. This beam could be aligned to the asphere by looking at the reflected spots from the two surfaces of the asphere. Reflections from the flat surface provide information about the tilt angle, and reflections from the curved surface provide information about the centering. By overlapping both spots with the incident green beam, we could ensure that it was well aligned. We then carefully overlapped the 780 nm tweezer light with the portion of the green beam that was transmitted through the asphere. This procedure was initially tested offline and appeared to perform well. However, as we will see, there were problems with the initial alignment. It is unclear whether this was a failing of the alignment procedure or whether an optic was later bumped.

Pros and cons of the in-vacuum asphere

Compared to using a high-NA objective, the in-vacuum asphere approach was sufficient for our initial work with optical tweezers, but is not necessarily an ideal setup. On the plus side, this approach is inexpensive, straightforwardly compatible with our existing MOT chamber and with the RF MOT, and can potentially achieve quite high NA if one is willing to put a lens very close to the molecules. On the other hand, the use of a single asphere means most of the advantages of a multi-element objective are lost. As already mentioned, the spot size is highly sensitive to alignment. The field-of-view is also quite small since the performance degrades for tweezers projected

[3] The asphere had been installed 6 months earlier for ODT imaging.

off-axis, limiting the size of the array that can be formed. Additionally, using a single asphere means that it is diffraction limited for only one wavelength, so diffraction-limited imaging of molecule fluorescence requires correction optics, as described above. Finally, the asphere is an insulating surface fairly close to the molecules, which can potentially cause stray electric fields that affect state preparation and coherence times.

8.1.2 Initial tweezer loading

Before looking for tweezer loading, we made a small ODT with the 780 nm laser and attempted to load molecules into it from the 1064 nm ODT. We were not able to observe much loading initially. Interestingly, we also saw that attempting to image molecules in the 1064 nm ODT in the presence of the 780 nm light dramatically reduced the signal. To see if this was a wavelength-dependent effect, we switched from the NKT fiber amplifier (which had a fixed wavelength of 777.4 nm) to the Ti-Sapph. We found that at most Ti-Sapph wavelengths between 776-781 nm the molecule imaging was unaffected, but there was a significant loss feature around 777 nm, which is very close to the wavelength we had initially been using. We tracked this down to 777 nm being resonant with the $\widetilde{A}(000) \rightarrow \widetilde{D}(100)$ transition in CaOH, which can deplete molecules that are promoted to $\widetilde{A}(000)$ state during imaging. We moved the wavelength to 780.2 nm and found that we were able to load the 780 nm trap from the 1064 nm ODT as expected. At this point we switched back to the tweezer configuration.

The MOT density is too low to load directly, so we have to first load into the ODT and then cool into the tweezers [202, 278]. After some effort to get the ODT aligned to the tweezer position, we eventually saw signatures of molecules in the tweezer (at this point we were projecting just a single tweezer, not an array). However, the measured trap frequency was much lower than expected for what we thought should be a 2 μm beam. After some debugging, we decided that the most likely explanation was that the tweezers were misaligned.

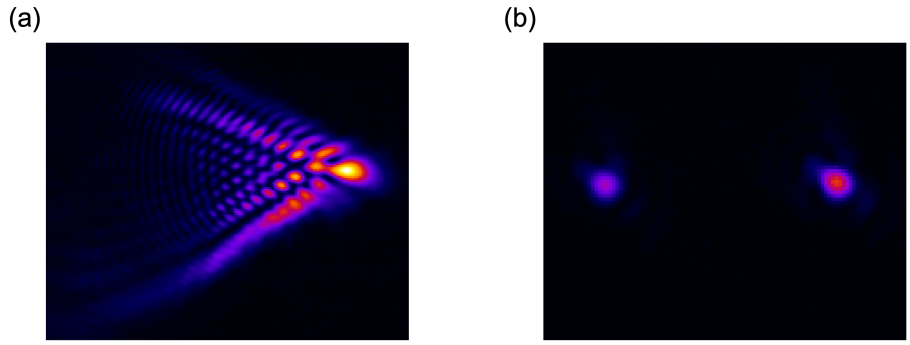

Figure 8.3: (a) *In situ* image of the tweezer beam after initial alignment. (b) Image of an array of two tweezer beams after *in situ* realignment.

We opened the chamber and profiled the trap *in situ*. As shown in Fig. 8.3(a), the beam appeared to be severely misaligned, with a shape that roughly corresponded to simulations at a tilt of $\sim 0.4^\circ$. We then realigned the beam *in situ* by looking at the beam profiler. The beam shape after realignment (for an array of two tweezers) is shown in Fig. 8.3(b).

After pumping out the chamber and loading a MOT again, we discovered that this time the tweezer position (as imaged on the MOT camera) was 1 mm away from the center of the MOT. We spent a few days attempting to make a red-detuned DC MOT and then shim it over to the tweezer position by applying a magnetic field, but the DC MOT was not good enough to get reliable signal.[4] Therefore, we opened up the chamber and realigned the tweezer again. This was done by putting the beam profiler on a translation stage, moving it over by the known distance between the tweezer and the MOT, and then realigning the tweezer to the new beam profiler location. Moving the position while maintaining a Gaussian, diffraction-limited beam required us to adjust the alignment of the in-vacuum asphere along with the optics further upstream.

Having confirmed that the tweezer was now overlapped with the MOT, we started by intentionally increasing

[4] It is probably possible to make a decent DC MOT of CaOH, but doing so would require significantly more time, and likely some laser cooling simulations.

the size of the trap to ∼8 μK by changing the beam size out of the fiber coupler (using a zoom collimator on the fiber output), and also swapping the 200 mm and 300 mm relay lenses. Once we had molecules loaded into this larger trap (which required having the ODT well overlapped with it), we focused the imaging system and then went back to the normal 2 μm trap size. We were able to load molecules into this trap (at this point probably a tweezer) and focus it on the camera. However, our imaging histograms showed no separation between loaded and empty traps (just a shift in the mean number of counts). This was attributed to the fact that we were still using 555 nm $\widetilde{B}(000) \rightarrow \widetilde{X}(000)$ "off-diagonal" imaging, which meant we were throwing away 95% of our scattered photons. To get well-separated histograms where we could distinguish empty from loaded traps in a single shot would require switching to diagonal, 626 nm $\widetilde{A}(000) \rightarrow \widetilde{X}(000)$ imaging.

8.1.3 Diagonal 626 nm imaging

While diagonal imaging increases the number of photons that can be detected by nearly a factor of 20, the cost is that it is sensitive to scattered light from the 626 nm cooling and imaging beams. The MOT beams are large enough to clip on the in-vacuum coils and on the asphere, meaning that they create too much scattered light to be useful. Therefore, following the first-generation CaF experiment [278], we installed small, 1.5 mm diameter "imaging beams." These were aligned at a small angle to the MOT beams, as shown in Fig. 5.19, and they were generated using the fourth port of the 4x4 fiber combiner in the MOT laser setup (Fig. 5.18). We also installed homemade low-scatter viewports similar to those used in Ref. [278]. The imaging beams took some effort to align, with certain angles causing very bad background scatter for somewhat mysterious reasons (likely reflections of reflections inside the chamber). We therefore had to walk the angle of the beams to minimize scattered light while still being well centered on the tweezers. The initial alignment was done by trying to deplete molecules

from the ODT with resonant light. Once the beams were hitting the ODT and tweezers with relatively low scatter, we optimized the pointing by walking each beam to maximize the tweezer brightness when imaging.

In addition to the imaging beams, we had to reduce other sources of scattered light. There was a significant amount of scatter from the 626 nm SFG setup on the other side of the MOT table making it to the camera, so we installed blackened panels at a number of points in between. In addition, several of the repumping lasers are at wavelengths close enough to 626 nm that they are difficult to filter out.[5] To help with this issue, we drilled a $\sim$5 mm hole in a shutter (Thorlabs SH1) and installed it in the slowing/repumping beam path. For slowing and MOT loading, we open the shutter, allowing the full slowing beam to pass. During tweezer imaging we close the shutter so that the repumping beams are reduced to a few-mm diameter. This significantly improved the scattered light. After doing this, the repumpers at 629 nm and 630 nm did not contribute any background, but there was still some background light from the 623 nm, $\widetilde{X}(010)(N = 2)$ repumping laser. Luckily, this laser has a very low saturation power, so we simply attenuate it during tweezer imaging by reducing the RF power to its switching AOM.

Because we are still somewhat limited by background scattered light (though at a fairly low level), we decided to use Λ cooling for imaging molecules in tweezers. This is because the scattering rate is higher, so we get a higher number of signal photons per background photon. Note that this is in contrast to experiments in the ODT, where we used SF cooling.

In addition to minimizing background scatter, we also made an effort to reduce noise introduced by the EMCCD. At high EM gain, the primary source of noise in the EMCCD is from clock-induced charge (CIC). We

[5] We used a filter stack containing a FF01-615/20 and a FF01-635/18 filter along with several colored glass filters. Combined, these cut out all but a very small range of wavelengths around 626 nm.

minimized this as much as possible by adjusting readout settings. We also aligned the imaging system so that the image of the array is near the bottom of the sensor, where the CIC is lowest.

To help understand our imaging and its limitations throughout the tweezer project, we also compared our data to simulated imaging histograms. These were made by modeling the EMCCD according to Ref. [371], and also accounting for the estimated photon collection efficiency and the photon budget during imaging.

8.1.4 Evidence for a low photon budget during imaging

After aligning the diagonal imaging, our histograms could still not sufficiently resolved loaded from empty traps. As we continued diagnosing the imaging, we realized that we were unable to scatter anywhere near the full photon budget's worth (∼14000) of photons before molecules were lost. Fig. 8.4(a) shows the fluorescence from the tweezer as a function of imaging duration for two configurations. In the first configuration, we image normally with all repumping lasers. In the second configuration, we intentionally limit the photon budget to 460 photons by imaging with only the first four repumping lasers [(000), (100), $(02^{0}0)$, and (200)]. The fitted asymptotic values are only a factor of 2 different, indicating that we are only able to scatter at most approximately 1000 photons, even with all repumpers.

For comparison, we took the same data in the 1064 nm ODT (Fig. 8.4(b)), finding that the ratio of fitted asymptotic signals was consistent with a photon budget of approximately 14000 photons.

This data could be consistent with the imaging beams heating molecules out of the tweezer due to misalignment, or to a problem with the 780 nm wavelength compared to 1064 nm. We continued to optimize the alignment of the imaging beams and saw no improvement. However, when we *reduced* the tweezer trap depth the imaging fluorescence improved. This was an extremely strong indication that the problem is with the trapping

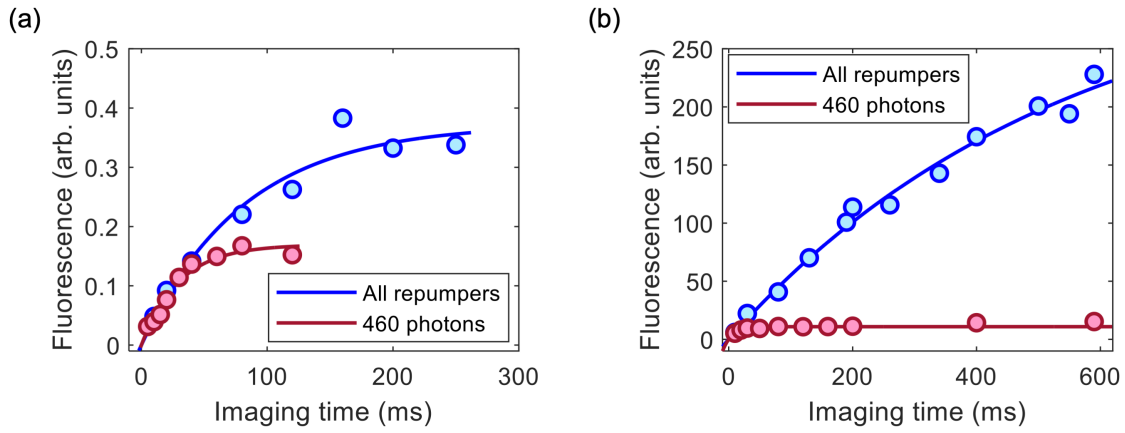

Figure 8.4: (a) Comparison of tweezer imaging fluorescence with all repumpers vs. a repumper-limited photon budget of 460 photons. (b) Same comparison for imaging in the 1064 nm ODT.

light itself. This led us to start investigating the effect of the trapping wavelength.

8.2 Wavelength dependence and excited state coupling

A general challenge of optically manipulating and trapping polyatomic molecules is the relatively large density of excited states compared to atoms and diatomic molecules. This shows up specifically in our experiment as molecular loss dependent on the wavelength of the tweezer light. We characterize the manifold of excited states near the tweezer wavelength, model the interactions of the molecules with the tweezer light, and are then able to tune the wavelength of the tweezer light to control loss.

8.2.1 Calculated excited state AC Stark shifts

Energy levels relevant to molecular imaging are shown in Fig. 8.5. The high-lying electronic potentials $\widetilde{D}^2\Sigma^+$, $\widetilde{E}^2\Sigma^+$, and $\widetilde{F}$ [240] are coupled to the $\widetilde{A}^2\Pi_{1/2}$ and $\widetilde{B}^2\Sigma^+$ states by the tweezer light. This has the effect of

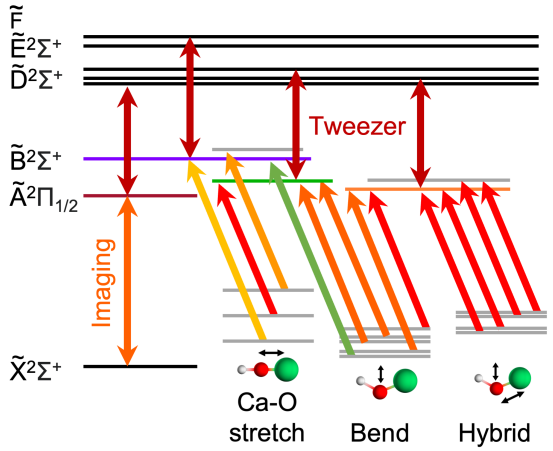

Figure 8.5: Level diagram showing the cooling and repumping lasers used for Λ imaging (arrows connecting $\widetilde{X}^2\Sigma^+$ to the $\widetilde{A}^2\Pi_{1/2}$ and $\widetilde{B}^2\Sigma^+$ manifolds), as well as the high-lying electronic states to which the ∼780 nm tweezer light (dark red arrows) couples. Modified from Ref. [46].

(a) shifting cooling and repumping imaging lasers out of resonance due to AC Stark shifts and (b) sometimes directly exciting molecules to these electronic states, which can lead to loss from imaging excitation. We model these effects as follows.

In the large detuning limit ($\Delta \gg \Omega$, where Δ is the tweezer detuning and Ω is the Rabi frequency), the effect of these couplings on the energy of excited state i is given by

$$\Delta E_i/\hbar \approx \sum_j \frac{\Omega_{ij}^2}{4(\omega_{ij} - \omega_L)} + \frac{\Omega_{ij}^2}{4(\omega_{ij} + \omega_L)} \tag{8.1}$$

where Ω_{ij} is the Rabi frequency for the transition from state i to state j, ω_L is the laser frequency, $\omega_{ij} = (E_j - E_i)/\hbar$ is the transition frequency, and the sum is over all molecular states j that can couple to state i.[6]

A number of vibrational levels have previously been observed in CaOH, in electronic states from $\widetilde{X}$ state all

[6]Note that this equation is identical to the scalar trap shift expressions from chapter 6 assuming an appropriate definition of the Rabi frequency.

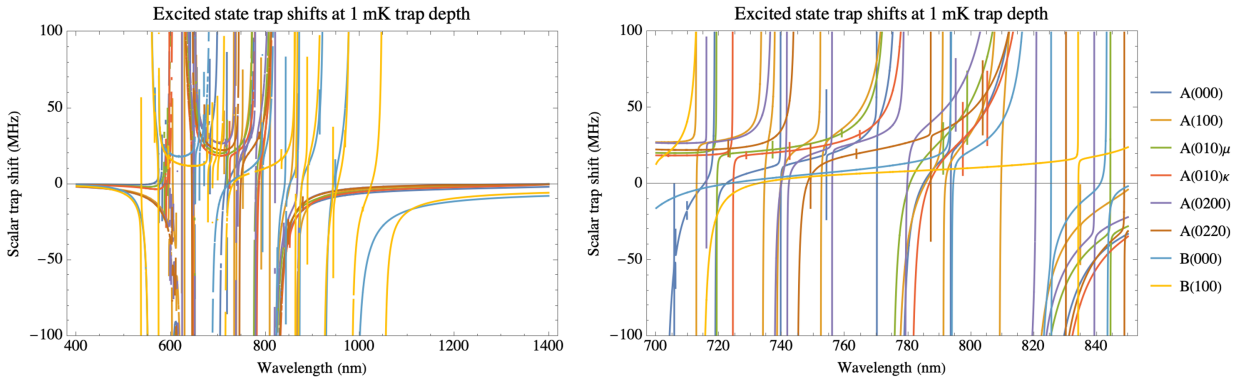

Figure 8.6: Calculated AC Stark shifts of excited states used for CaOH optical cycling. All previously observed vibronic states of CaOH are included in the calculation, and the laser intensity is held constant at the intensity corresponding to a 1 mK tweezer trap depth at 780 nm.

the way up to the $\widetilde{G}$ state [93, 238–241, 249, 250]. We use eqn. 8.1 to calculate the AC Stark shift of the laser cooling excited states (vibrational levels in $\widetilde{A}^2\Pi$ and $\widetilde{B}^2\Sigma^+$) arising from coupling to all known vibronic states in CaOH. To estimate the Rabi frequency of these transitions, we use transition dipole moments calculated for the corresponding electronic states in CaF [372], and estimate relative transition strengths to different vibrational states by assuming that the Franck-Condon matrix is similar to that of the $\widetilde{X} \rightarrow \widetilde{A}$ transition. The calculations should not be considered quantitatively accurate, but they give a sense of the density of transitions at different tweezer wavelengths and also likely get the right order-of-magnitude on the width of the features. Calculated AC Stark shifts for the laser cooling excited states are shown in Fig. 8.6.

From the calculations, we see that there should not be significant problems near 1064 nm, but that there is a forest of lines around our tweezer wavelength of 780 nm. However, the density is low enough that it may be possible to find workable tweezer wavelengths. We therefore return to the experiment and scan the tweezer wavelength, looking at the tweezer imaging brightness and also directly measuring the excited-state AC Stark shifts.

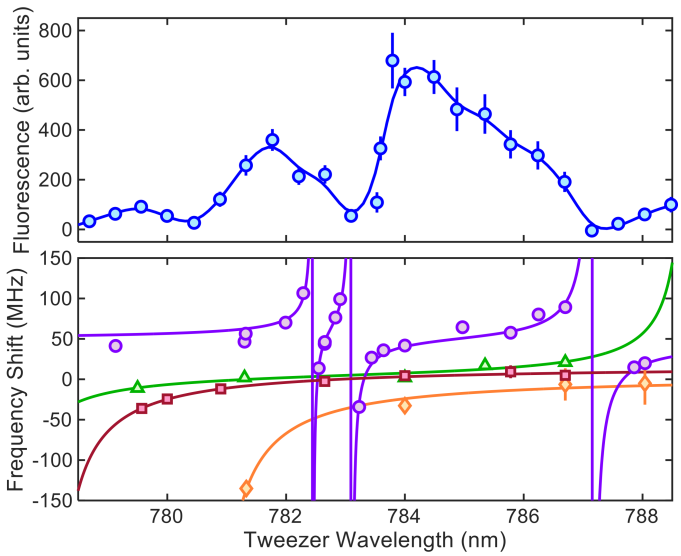

Figure 8.7: Wavelength dependence of CaOH trapping. Top plot: average tweezer fluorescence vs. wavelength for 50 ms array images. The solid curve is a guide to the eye. Bottom plot: measured relative AC Stark shifts of the $\widetilde{A}^2\Pi_{1/2}(000)$ (red squares), $\widetilde{B}^2\Sigma^+(000)$ (purple circles), $\widetilde{A}^2\Pi_{1/2}(100)$ (green triangles), and $\widetilde{A}(010)\kappa^2\Sigma^{(-)}$ (orange diamonds) states. Solid curves are fits used to extract line positions and coupling strengths. Error bars represent 68% confidence intervals. Modified from Ref. [46].

8.2.2 Measured tweezer brightness and AC Stark shifts

Fig. 8.7 (top plot) plots the overall brightness of molecules in the tweezers (a combination of loading fraction and imaging efficiency) as a function of tweezer light wavelength over the range 779-788 nm. This was done using fixed imaging and repumping frequencies chosen to optimize the signal at 784 nm. While bright tweezers are observable around 784 nm and 782 nm, they are very dim in several wavelength regions, notably around 783 nm, above 787 nm, and below 780 nm.

To characterize the wavelength dependence, we measure the AC Stark shifts of the laser cooling excited states as a function of tweezer wavelength (Fig. 8.7, bottom plot). Specifically, we study the $\widetilde{A}(000)$, $\widetilde{B}(000)$, $\widetilde{A}(100)$, and $\widetilde{A}(010)$ states, which are the most important excited states used for CaOH optical cycling [42].

The excited state AC Stark shifts are measured by imaging molecules in the tweezer array with one of the repumping lasers replaced by a separate frequency-tunable beam. At each tweezer wavelength, the frequency of the repumping beam is scanned near resonance, and the AC Stark shift is determined by comparing the repumping frequency that maximizes the image brightness with the known free space resonance for the repumping transition. Because the tweezer is far detuned from all transitions out of the $\widetilde{X}$ manifold, the wavelength dependence is assumed to arise from Stark shifts of the excited states only, while the ground state AC Stark shifts contribute a constant offset.

The specific transitions used are $\widetilde{X}^2\Sigma^+(100) \rightarrow \widetilde{B}^2\Sigma^+(000)$, $\widetilde{X}^2\Sigma^+(02^00) \rightarrow \widetilde{A}^2\Pi_{1/2}(100)$, and $\widetilde{X}^2\Sigma^+(010)(N=2) \rightarrow \widetilde{A}(010)\kappa^2\Sigma^{(-)}$. For the $\widetilde{A}^2\Pi_{1/2}(000)$ state AC Stark shifts, the $\widetilde{X}^2\Sigma^+(000) \rightarrow \widetilde{A}^2\Pi_{1/2}(000)$ cooling light was instead tuned during tweezer imaging, and the AC Stark shift was determined by comparing the optimal tweezer imaging detuning with the optimal free space Λ imaging detuning. This approach is susceptible to common mode offsets in the measured AC Stark shift due to the need to compare with a free space resonance frequency. However, relative frequencies and resonance wavelengths are insensitive to such offsets, meaning that the extracted transition wavelengths and transition strengths (Rabi frequencies) are robustly determined, in turn leading to accurate loss rate calculations (see below).

We fit the observed Stark shifts to analytic lineshapes to determine the position and strength of the excited state couplings (solid curves in Fig. 8.7). Starting with eqn. 8.1, if we restrict ourselves to a small range of wavelengths $\Delta\lambda$ near the tweezer wavelength λ_0, we can make the approximation that only a small number of near-detuned states k are responsible for the wavelength dependence, and that the remaining states contribute an approximately constant energy offset $\Delta E_{\text{off}}/\hbar$ as long as they are far detuned compared to $\Delta\lambda$. Furthermore, we can make the rotating wave approximation and drop the second, counter-rotating term in eqn. 8.1. We find that

the wavelength dependence of the energy of state i in the range $\Delta\lambda$, which contains N near-detuned states k, is

$$\Delta E_i/\hbar \approx \sum_{k=1}^{N} \frac{\Omega_{ik}^2}{8\pi c(1/\lambda_L - 1/\lambda_{ik})} + \Delta E_{\text{off},i}/\hbar \tag{8.2}$$

where $\lambda_L = 2\pi c/\omega_L$ and $\lambda_{ik} = 2\pi c(1/\omega_i - 1/\omega_k)$. This expression is used to fit the AC Stark shift data in Fig. 8.7, where the Rabi frequencies Ω_{ik}, center wavelengths λ_{ik}, and energy offsets $\Delta E_{\text{off},i}$ are fit as free parameters. We use this model-fitting approach due to a lack of complete spectroscopic data for the excited states.

The measured transition wavelengths determined from the fit to eqn. 8.2 are as follows. The energy of the $\widetilde{A}^2\Pi_{1/2}(000)$ excited state exhibits a resonance at $777.9(6)$ nm, which is consistent with the expected wavelength for coupling from $\widetilde{A}^2\Pi_{1/2}(000) \rightarrow \widetilde{D}^2\Sigma^+(100)$ [240]. $\widetilde{A}^2\Pi_{1/2}(100)$ contains resonances at 777 nm and 789 nm (consistent with coupling to $\widetilde{D}^2\Sigma^+(200)$ and $\widetilde{D}^2\Sigma^+(110)$, respectively), while $\widetilde{A}(010)\kappa^2\Sigma^{(-)}$ displays a strong resonance at 780.6 nm due to coupling with the $\widetilde{D}^2\Sigma^+(110)$ state. Three features are observed in the $\widetilde{B}^2\Sigma^+(000)$ data, at $782.4(1)$ nm, $783.1(1)$ nm, and $787.2(1)$ nm, corresponding to high-lying features at $30804(2)$ cm^{-1}, $30792(2)$ cm^{-1}, and $30726(2)$ cm^{-1}, respectively. These features fall slightly above the origin energy of the $\widetilde{E}^2\Sigma^+$ and $\widetilde{F}$ electronic potentials, in a frequency range not covered by previous spectroscopic literature [240].

Based on this data, we choose an optimal tweezer wavelength of 784.5 nm, which is well separated from the observed resonances and results in minimal loss.

8.2.3 Modeling losses due to excited state coupling

Losses arising from coupling of state i (in the laser cooling scheme) to a lossy excited state j occur at a rate $R_{ij} = |c_{ij}|^2 \Gamma_j \rho_{ii}$, where c_{ij} is the admixture of state j into i due to tweezer coupling, Γ_j is the decay rate of state j (assumed to be purely to nondetectable states), and ρ_{ii} is the molecular population in state i during tweezer imaging [203]. In the large detuning limit $\Delta_{ij} \gg \Omega_{ij}$, the admixture is $c_{ij} \approx \Omega_{ij}/(2\Delta_{ij})$, where $\Delta_{ij} = \omega_L - \omega_{ij}$. The population of the laser cooling excited state i is approximately $\rho_{ii} \approx \Gamma_{\text{scatt}}/\Gamma_i \times r_i$, where $\Gamma_{\text{scatt}} = 250 \times 10^3\ \text{s}^{-1}$ is the photon scattering rate during imaging and r_i is the fraction of photon scattering events that originate from state i. The latter quantity is set by the vibrational state repumping scheme used in the experiment [42].

The total observed molecule loss rate during tweezer imaging is a combination of excited state loss R_{ij}, vacuum loss $R_{\text{vac}} = 1/690\ \text{ms}^{-1}$ (see below), and loss to dark (i.e., not repumped) vibrational states, $R_{\text{vib}} = \Gamma_{\text{scatt}}/N_{\text{phot}}$, where $N_{\text{phot}} = 1.6 \times 10^4$ is the vibrational repumping-limited average number of photons scattered per molecule. The total loss rate $R_{\text{loss}} = R_{ij} + R_{\text{vib}} + R_{\text{vac}}$ is calculated as a function of tweezer wavelength using the fitted Rabi frequencies and center wavelengths from the AC Stark shift data.

Fig. 8.8 shows the number of photons scattered per molecule in the experiment (measured as in Fig. 8.4) as a function of tweezer wavelength. We also plot the calculated photon number determined from the loss rate calculations, $N_{\text{im}} = \Gamma_{\text{scatt}}/R_{\text{loss}}$ (blue, solid curve). Here we have used the known loss rates R_{vac} and R_{vib} as well as the measured Rabi frequencies and wavelengths for tweezer-induced excited-state loss. The only unknown parameter is Γ_j, the loss rate from the high-lying states to which the tweezer couples, which was assumed to be constant for all excited states and varied to match the measured photon number data. We find reasonable agree-

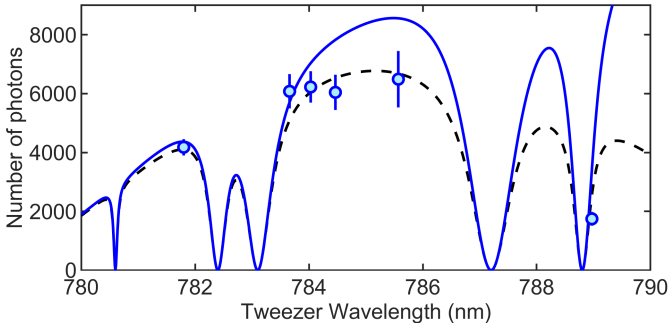

Figure 8.8: Imaging photon budget vs. tweezer wavelength. Calculated (curves) and measured (points) number of imaging photons that can be scattered during molecule imaging in the tweezer array, as a function of the trapping wavelength. Calculations include the effect of vacuum loss, loss to vibrational dark states, and trap-wavelength-dependent excitation to lossy excited electronic levels. The solid blue curve accounts for excitation only to those states observed using AC Stark shift data, while the black, dashed curve additionally includes $\widetilde{A}^2\Pi_{1/2}(000) \leftrightarrow \widetilde{D}^2\Sigma^+(010)$ excitation predicted at 793.6 nm. Reproduced from Ref. [46].

ment with the experimental data using an excited state loss rate $\Gamma_j \approx 2\pi \times 75$ MHz, corresponding to a lifetime of $\Gamma_j^{-1} \approx 2.1$ ns. The remaining disagreement, particularly in the 784-786 nm range, may be attributed to the effect of other excited state resonances that were not considered in the AC Stark shift data. For example, there is a known resonance from $\widetilde{A}^2\Pi_{1/2}(000) \leftrightarrow \widetilde{D}^2\Sigma^+(010)$ at 793.6 nm [240]. Including this state, assuming the same Rabi frequency measured for the $\widetilde{A}^2\Pi_{1/2}(000) \leftrightarrow \widetilde{D}^2\Sigma^+(100)$ transition at 777.9 nm, results in better agreement with the experimental data (black, dashed curve).

The inferred ∼2 ns lifetime of the high-lying electronic states is an order of magnitude shorter than the radiative lifetime of the lower-lying $\widetilde{A}^2\Pi$ and $\widetilde{B}^2\Sigma^+$ states in CaOH. This could indicate non-radiative loss mechanisms for these states, as hypothesized for similar states in tweezer-trapped diatomic molecules [203, 373].

8.3 Overview of the optimized experimental sequence

For the remainder of this chapter, we park at the optimal tweezer wavelength of 784.5 nm and characterize the tweezer properties.

The experiment begins with $\sim 10^4$ laser-cooled CaOH molecules loaded in a magneto-optical trap (MOT) at $\sim$1 mK [42]. The molecules are next cooled into an optical dipole trap (ODT) [43], and then into six optical tweezer traps projected inside the ODT. The ODT and optical tweezers are loaded using a 5 ms Λ-enhanced grey molasses cooling pulse followed by 80 ms of single-frequency (SF) cooling [43]. The ODT is necessary to achieve sufficient density for efficient tweezer loading [202], and the ODT and tweezers remain on for the full cooling duration. The $\sim$600 μK deep ODT is generated from a 13.3 W, 1064 nm laser beam focused down to a $\sim$25 μm waist in the center of the molecular MOT [43]. During loading, we raster the ODT position along the tweezer array axis at a frequency of 100 Hz using a piezo-actuated mirror mount in the 1064 nm beam path. The tweezer trap depth during loading is 1.6 mK, corresponding to approximately 150 mW of optical power per trap. After loading, a 4 ms pulse of Λ-imaging light [43, 231] is applied to induce light-assisted collisions in tweezers with more than one molecule loaded, ensuring a collisional blockade, wherein each tweezer contains at most one single molecule [353]. Finally, the trap depth is reduced to 1.4 mK, which optimizes the imaging fidelity.

Molecules in the tweezers are imaged using Λ-enhanced grey molasses cooling, which allows thousands of photons to be scattered [43, 231]. Fluorescence from the $\widetilde{A}^2\Pi_{1/2}(000) \rightarrow \widetilde{X}^2\Sigma^+(000)$ cooling transition at 626 nm is collected via the lens used to project the tweezers, and then imaged onto an EMCCD camera. We find that optimal imaging occurs only at specific tweezer wavelengths and requires several of the vibrational repumping lasers used for imaging to be tuned by $\sim$100 MHz from their free-space values, as discussed in detail below. Fig. 8.9(a)

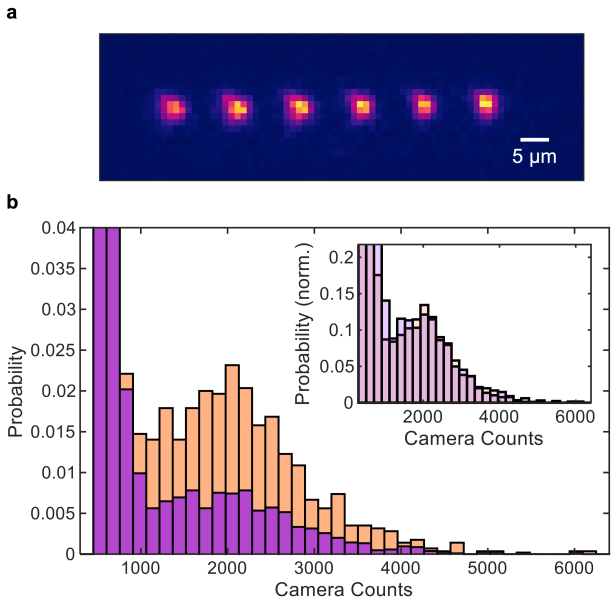

Figure 8.9: An optical tweezer array of CaOH molecules. **a**, Averaged image of the CaOH tweezer array, attained by imaging the molecules for a 50 ms duration and averaging over hundreds of iterations of the experimental sequence. **b**, Histograms of collected fluorescence for 15 ms duration tweezer images at average loading probabilities of 31% (orange) and 13% (purple). Inset: histograms normalized by loading rate, indicating that the shape of the loaded molecule peak does not change with the loading probability. Reproduced from Ref. [46].

shows an averaged image of the tweezer array.

Histogram analysis of the intensity of fluorescence from the molecules reveals single molecule trapping in the tweezers. Fig. 8.9(b) shows histograms of camera counts attained from fluorescence imaging of the molecules in tweezers. Histograms are shown for 15 ms images and for two average tweezer loading probabilities of 31% (orange) and 13% (purple), tuned by varying the number of molecules loaded in the MOT. The narrow peak on the left corresponds to empty tweezers, while the broader peak on the right corresponds to loaded tweezers; choosing a threshold value between the two peaks enables classification of single shot images as corresponding to loaded or empty tweezers. As shown in the inset of Fig. 8.9(b), rescaling the histograms by their respective loading rates

shows that they have identical shapes. This is only possible if single molecules are loaded; otherwise, reducing the loading rate would lower the average number of molecules loaded, and thereby decrease the average brightness while altering the qualitative shape of the histograms. From quantitative analysis of the histograms, we identify the residual fraction of loaded traps containing more than one molecule to be $5 \pm 5\%$ (see Ref [46] for details).

8.3.1 Tweezer trap frequencies, trap depth, and inferred trap geometry

The oscillation frequencies of molecules in the optical tweezer array are measured using the parametric heating method. After loading the array, molecules are imaged for 7 ms to detect loaded traps. The trap intensity is then modulated at a variable frequency ω_{mod} for 5 ms, causing parametric heating loss when $\omega_{\text{mod}} \approx 2\omega_i$, where $\omega_{i=x,y,z}$ are the trap frequencies. The tweezers are briefly shut off for 6 μs to allow heated molecules to escape, then the remaining molecules are imaged for 15 ms. The molecule survival exhibits loss features at $\omega_{\text{mod}} = 2\pi \times 119(4)$ kHz and $\omega_{\text{mod}} = 2\pi \times 167(5)$ kHz, corresponding to radial trap frequencies of $\omega_x = 2\pi \times 59(2)$ kHz and $\omega_y = 2\pi \times 84(2)$ kHz. Using the calculated 780 nm dynamic polarizability for the ground state of CaOH ($\alpha_0 = 324.3$ a.u., see chapter 6) and the known laser power per trap ($\sim$125 mW), these frequencies imply a tweezer trap depth of $U_0 = k_B \times 1.4$ mK, an axial frequency of $\omega_z \approx 7$ kHz, and slightly elliptical tweezer beams with waists $w_x \approx 2.4$ μm and $w_y \approx 1.7$ μm.

We confirmed that the trap frequencies were approximately uniform across the array.

8.4 Tweezer imaging

We image CaOH molecules in the tweezer array using grey molasses cooling light in a Λ configuration [43, 231], as shown in Fig. 8.10(a).

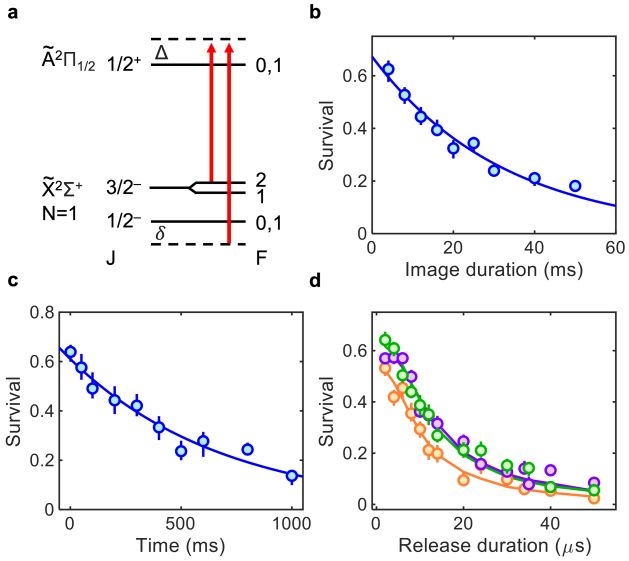

Figure 8.10: Tweezer array imaging and characterization. **a**, Laser configuration used for Λ imaging of the tweezer array, where Δ is the single-photon detuning and δ is the two-photon detuning. **b**, Lifetime of CaOH molecules during imaging, measured to be 32(3) ms. **c**, Tweezer hold lifetime, measured to be 690(70) ms, limited predominantly by background gas and blackbody excitation [43, 44]. **d**, Release-recapture temperature measurements for single-photon detunings of $\Delta = 16$ MHz (orange), 22 MHz (purple), and 28 MHz (green). Solid curves show Monte Carlo fit results, indicating ratios of trap depth to temperature $\eta = 6(2)$, $12(1)$, and $9(1)$, respectively. Error bars represent 68% confidence intervals. Reproduced from Ref. [46].

The optimal parameters for tweezer imaging are as follows (detunings are referenced relative to free space resonance). The single-photon detuning is $\Delta = 22$ MHz, the two-photon detuning is $\delta = 1.25$ MHz, the sideband intensity ratio is $I_{1/2}/I_{3/2} \approx 2$, and the total intensity is approximately 9 mW cm^{-2} per beam. The tweezer trap depth used for imaging is 1.4 mK. Additionally, four of the repumping laser frequencies are tuned from the free-space optimal used for radiative slowing, the MOT, and tweezer loading, to AC Stark-shifted frequencies optimized for tweezer imaging brightness. Specifically, the $\widetilde{X}^2\Sigma^+(100) \rightarrow \widetilde{B}^2\Sigma^+(000)$ repumping laser is tuned approximately 60 MHz to the blue; the $\widetilde{X}^2\Sigma^+(010)(N = 1) \rightarrow \widetilde{B}^2\Sigma^+(000)$ repumping laser is tuned approximately 140 MHz to the blue; the $\widetilde{X}^2\Sigma^+(02^00) \rightarrow \widetilde{A}^2\Pi_{1/2}(100)$ repumping laser is tuned approximately 40 MHz to the red; and the $\widetilde{X}^2\Sigma^+(010)(N = 2) \rightarrow \widetilde{A}(010)\kappa^2\Sigma^{(-)}$ repumping laser is tuned approximately 140 MHz to the blue.[7] Note that the frequency spectrum of each repumping laser is broadened by $\sim$300 MHz to the red of free-space resonance for radiative slowing [42]. This broadening remains on throughout the experimental sequence, therefore reducing the precision requirements for the tweezer repumping frequencies.

The imaging lifetime, τ, is the average time the molecules survive during imaging before being lost from the tweezer or falling into a molecular dark state. To measure τ and the photon scattering rate of the molecules, Γ, we image for a variable duration, then wait 50 ms and image a second time (15 ms duration). The molecule survival (defined as the conditional probability that a molecule is detected in the second image, given that it was present in the first image) is plotted in Fig. 8.10(b) as a function of the first image duration. The data are fit to an exponential decay with a $1/e$ imaging lifetime of $\tau = 32(3)$ ms. We also find for long imaging times $t \gg \tau$ that each molecule scatters $N_{\text{im}} = 8(1) \times 10^3$ photons, on average, before going dark to the imaging light (Fig. 8.11).

[7] The frequencies are jumped by adding a voltage from Cicero (our experiment control software) to the Labview laser locking voltage. Similar to chirped slowing, we included a threshold in the laser locking software that ignores frequency readings $\gtrsim 20$ MHz from resonance, so that the lock doesn't attempt to compensate for the frequency jump.

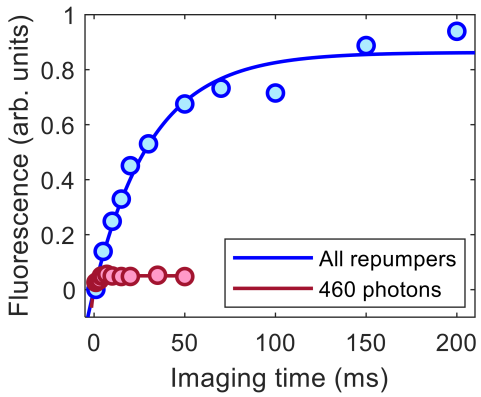

Figure 8.11: Comparison of tweezer fluorescence vs. imaging duration with all repumpers vs. just the first four repumpers (photon budget of 460). The ratio of asymptotic values indicates a photon budget of 8000 for tweezer imaging.

Combining these measurements, we determine that the photon scattering rate is $\Gamma = 250(40) \times 10^3\ \mathrm{s}^{-1}$ during imaging. We measure the molecule lifetime in the absence of imaging light to be 690(70) ms, which is determined predominantly by imperfect vacuum and by blackbody excitation (Fig. 8.10c) [43, 44].

The average number of photons scattered during long imaging pulses, N_{im}, is slightly less than the expected limit of approximately $\sim 1.4 \times 10^4$ photons from loss to known dark vibrational states [42]. We attribute the additional loss primarily to scattering from the tweezer light during imaging, which we model using the AC Stark shift data, as described above.

We measure the temperature of the molecules in tweezers after imaging using the release-recapture method (Fig. 8.10(d)) [330], which we briefly describe here. After loading the tweezer array, we image the molecules for 7 ms to identify loaded tweezers. We then quickly switch off the tweezers, wait a variable time (on the order of 10 μs), switch the tweezers back on, and then image a second time (15 ms imaging duration) to determine the fraction of molecules recaptured into the tweezers. The molecule survival probability vs. release time is fit to a Monte Carlo simulation to extract the temperature. The results are plotted in Fig. 8.10(d). For optimal imaging param-

eters, we measure the molecule temperature to be $T = 120(10)$ μK, corresponding to a ratio of trap depth to molecule temperature of $\eta = 12(1)$. Increasing the single-photon detuning by 6 MHz increases the temperature ratio to $\eta = 9(1)$ but causes no decrease in the maximum number of photons scattered. This suggests that the imaging lifetime is not limited by the molecule temperature.

One key feature of the optical tweezer platform is the ability to image molecules nondestructively, for example in order to postselect data on loaded tweezers or to rearrange the molecules into ordered arrays [355]. Doing so requires the ability to distinguish loaded from empty tweezers with high fidelity while minimizing molecule loss. We find that an imaging duration of 7 ms achieves a satisfactory balance between these requirements. Using a background subtraction procedure described below, we determine that the imaging fidelity after 7 ms of imaging is $0.94^{+0.02}_{-0.03}$ for a tweezer loading rate of 34%, while the probability of the molecule surviving after the image is 80%. Higher molecule survival probabilities can be attained by imaging for even shorter durations, at the cost of more frequently misidentifying loaded traps as empty. The detection fidelity is limited by the finite molecule imaging lifetime in combination with our photon collection efficiency, and does not increase significantly for longer imaging durations.

8.4.1 Imaging fidelity

The imaging fidelity is defined as the probability of correctly identifying whether a trap is initially empty (0 molecules) or loaded (1 molecule in the collisional blockade regime). Specifically, it may be defined in terms of the error rates ϵ_{01} (incorrectly identifying an empty trap as loaded; "false positive") and ϵ_{10} (incorrectly identifying a loaded trap as empty; "false negative") as follows: $f(p) = 1 - p\epsilon_{10} - (1-p)\epsilon_{01}$, where p is the tweezer loading probability [203].

The error rates depend on the threshold number of counts, θ, used to distinguish loaded and empty traps. The false positive rate, $\epsilon_{01}(\theta)$, is determined by analyzing histogram data for empty traps, which can be collected by taking images of tweezers guaranteed to be empty by, e.g., turning off the molecule source. The histogram data, $h_0(n)$, is a function of the number of image counts n, and is normalized so that $\sum_n h_0(n) = 1$. Moreover, we define a cumulative probability distribution for the histogram data, $g_0(\theta) = \sum_{n=0}^{\theta} h_0(n)$. Following these definitions, the false positive rate $\epsilon_{01}(\theta)$ is simply the probability of collecting greater than θ counts from an image of an empty trap, i.e. $\epsilon_{01}(\theta) = 1 - g_0(\theta)$.

To determine the false negative rate $\epsilon_{10}(\theta)$, we must infer the histogram of image counts collected from loaded traps, $h_1(n)$. Because the loading rate is much less than 1 in the experiment, this requires subtracting out the effect of empty traps from $h_{\text{exp}}(n)$, the measured histogram data. This is done by scaling the empty trap histogram data $h_0(n)$ by a factor of $(1-p)$ (the probability of a trap being empty), subtracting this from the experimental data to remove the background contribution, and renormalizing the result: $h_1(n) = \left[h_{\text{exp}}(n) - (1-p)h_0(n)\right] p^{-1}$. We discuss how p is determined below. The cumulative probability distribution for loaded traps is defined as $g_1(\theta) = \sum_{n=0}^{\theta} h_1(n)$, and the false negative error rate is the probability of collecting fewer than θ counts from a loaded tweezer, $\epsilon_{10}(\theta) = g_1(\theta)$.

Determining p, the tweezer loading probability, is equivalent to finding the scale factor to apply to $h_0(n)$ so that the empty trap background is appropriately subtracted from $h_{\text{exp}}(n)$ in the procedure above. To perform this background subtraction, we take advantage of the tall ($\sim$80% of the counts in $h_0(n)$), zero-photoelectron peak generated by the EMCCD camera, which is approximately Gaussian in shape with a standard deviation of $\sigma_r \approx 4$ digital counts (given by the camera readout noise), and is centered at zero photoelectron counts (far left side of the histogram). We isolate this peak in both the signal and background histograms, then apply a scale

factor of $(1 - p)$ to the empty histogram data and calculate the sum of squared differences between the two, $S(p) = \sum_{n=n_i}^{n_f} \left[h_{\text{exp}}(n) - (1-p)h_0(n)\right]^2$, where n_i and n_f are the lower and upper edges of the peak. The value of p that minimizes $S(p)$ is the inferred loading probability for the experimental data and is used to determine $h_1(n)$ via the procedure defined above.

A necessary assumption of the background subtraction procedure is that the zero-photoelectron peak in the experimental data arises purely from empty traps, meaning that we can rescale the background histogram to match the height of this peak and assume that the result accurately reflects the distribution of empty trap counts in the experimental data. This approximation is justified by the fact that the *average* number of counts arising from loaded traps, $\bar{n}$, is hundreds of counts above the zero-photon peak ($\bar{n} \gg \sigma_r$), so that any residual tail at low count numbers is negligible compared to the contribution from empty traps. By benchmarking the background subtraction procedure against simulated histogram data with varying fractions of the zero-photon counts arising from loaded traps, we conservatively estimate that this approximation could bias the calculated fidelity up to 2% above the true value for our experimental parameters. Systematic errors due to differing scattered light and camera noise environments between the experimental datasets $h_0(n)$ and $h_{\text{exp}}(n)$ contribute at the 1% level.

Fig. 8.12 illustrates the fidelity results for 7 ms tweezer images, chosen to be short enough for reasonably high molecule survival after imaging. Fig. 8.12(a) shows the signal and background histograms ($h_{\text{exp}}(n)$ and $h_0(n)$, respectively) from which the error probabilities $\epsilon_{01}(\theta)$ and $\epsilon_{10}(\theta)$ are inferred using the procedure described above. These error rates are plotted as a function of the threshold value θ in Fig. 8.12(b). Higher choices of threshold reduce the probability of misidentifying empty traps as loaded (ϵ_{01}, blue curve), at the expense of increasing the likelihood of misidentifying loaded traps as empty (ϵ_{10}, red curve). Fig. 8.12(c) shows the imaging fidelity, $f(p, \theta) = 1 - p\epsilon_{10}(\theta) - (1-p)\epsilon_{01}(\theta)$, as a function of detection threshold for various loading probabil-

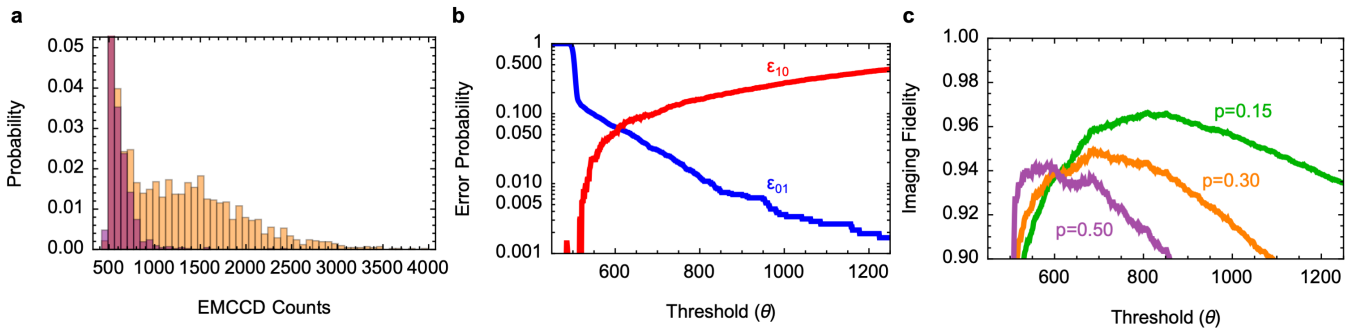

Figure 8.12: Determination of tweezer imaging fidelities. (a) Signal (orange) and background (purple) histogram data, $h_{\text{exp}}(n)$ and $h_0(n)$, for 7 ms tweezer images. The average tweezer loading probability in the signal histogram is $p = 0.34$. (b) Misidentification error rates $\epsilon_{01}(\theta)$ and $\epsilon_{10}(\theta)$ for 7 ms tweezer images, inferred from the experimental data as described in the text. (c) Imaging fidelities $f(p)$ for several average tweezer loading probabilities p, as described in the text. Reproduced from Ref. [46].

ities. Each curve exhibits a peak corresponding to the optimal tradeoff between the two misidentification error sources. For higher loading probabilities, a lower threshold optimizes the fidelity, since reducing the likelihood of misidentifying loaded traps as empty becomes more important at higher loading rates. For all loading rates, fidelities $f \gtrsim 0.94$ are possible for an appropriate choice of threshold.

Combining the systematic error sources above with a statistical error of ∼1.5% obtained using a bootstrapping procedure, we determine that the imaging fidelity is $f = 0.94^{+0.02}_{-0.03}$ for the 7 ms tweezer images at an optimal threshold of $\theta \approx 700$ and a measured loading rate of $p = 0.34$.

8.5 Single quantum state control in optical tweezers

8.5.1 Experimental setup

The experimental setup for coherently controlling internal states of CaOH in the $\widetilde{X}(010)$ bending mode is similar to what was used in chapter 7. We apply microwaves, electric fields, and magnetic fields in the same way, and

use the ion sweeper, UV light, and magnetic field compensation coils to stabilize electric and magnetic field drifts.

The primary changes and additions to the setup were the ability to drive the molecules with RF electric fields, the ability to pump molecules into the bending mode using a single photon (using a Vexlum laser addressing the 609 nm $\widetilde{X}(000) \rightarrow \widetilde{A}(010)\kappa^2\Sigma^{(-)}$ transition), and a few upgrades to reduce RF noise that interferes with the molecules.

We apply RF electric fields using the MOT coils. As shown in Fig. 5.32, this is done by connecting an RF source and amplifier to the coils via a bias tee in the path used for applying DC electric fields. The idea is that one coil remains grounded while the other coil has an oscillating voltage, corresponding to an RF electric field at the molecules. In reality, there is significant coupling between the two coils and the system is not impedance matched to the RF source, so we find that the response of the coils is highly dependent on the drive frequency. Despite its shortcomings, this approach is nonetheless sufficient to drive the necessary RF transitions in CaOH (described below).

During our work to apply the optical pumping technique from chapter 7, we discovered that there was significant RF noise from the high power RF MOT amplifiers leaking into the coils and disrupting our ability to keep molecules in a single state. The first problem is that the RF MOT coil drive frequency is 1.4 MHz, which is, coincidentally, the same as the splitting between the $F = 0$ and $F = 1$ states relevant for optical pumping. Therefore, any leaked RF at this frequency could significantly disrupt the optical pumping efficiency. To solve this problem, we use two high-voltage relays to short the output of the RF MOT amplifiers to ground whenever they are off (see Fig. 5.32). This serves as a low-pass filter (shorter wavelengths/higher frequencies are imperfectly attenuated due to reflections) and attenuates frequencies $\lesssim 10$ MHz by over an order of magnitude.

We also find that there is significant noise at higher frequencies (up to at $\sim$100 MHz) that is likely attributable

to the switching power supplies in the high power RF amplifiers.[8] We reduced this noise by installing high-power low-pass filters at the output of the RF MOT amplifiers.

These upgrades (especially the RF MOT short) significantly improved the fidelity of our optical pumping into $F = 0$.

8.5.2 Optical pumping and coherent state control

Next, we demonstrate coherent control of the internal states of CaOH molecules in the optical tweezer array. We begin by optically transferring molecular population into the $\widetilde{X}^2\Sigma^+(010)$ vibrational bending mode, whose ℓ-type parity doublet structure is useful for many quantum science applications [45, 101, 110, 131, 140]. Unlike in our previous work with CaOH in an ODT, where ∼1200 photons were scattered during this step [43], here with tweezers we optically pump using only ∼2 photons by exciting the $\widetilde{X}^2\Sigma^+(000)(N = 1^-) \rightarrow \widetilde{A}^2\Pi(010)\kappa^2\Sigma^{(-)}(J = 1/2^+)$ transition at 609 nm. The excited state decays to the $N = 1, J = 1/2^-$ and $N = 2, J = 3/2^-$ states in the bending mode with approximately equal probability, and the $N = 2, J = 3/2^-$ population is repumped back through $\widetilde{A}(010)$ and into $N = 1$. After optical transfer, the tweezer trap depth is reduced by 80% (to approximately 280 μK) in preparation for further state manipulation.

After transfer into the vibrational bending mode, population is predominantly contained in the 4 hyperfine sublevels of the $N = 1, J = 1/2^-$ manifold, which we label $|0\rangle$, $|1\rangle$, $|2\rangle$, and $|3\rangle$ (Fig. 8.13a). We optically pump the majority of this population into $|0\rangle \equiv (F = 0, m_F = 0)$ using the microwave-optical pumping scheme outlined in Fig. 8.13(a), as demonstrated in previous work with CaOH molecules in an ODT [45]. A microwave

[8] The noise has a bizarre spectrum consisting of many discrete frequencies, which we believe may be a method used by the power supply manufacturer to distribute the switching noise so it remains below certain RF emission compliance thresholds.

field at ∼40 GHz resonantly couples states $|1\rangle$, $|2\rangle$, and $|3\rangle$ to $N = 2, J = 3/2^-$ in the presence of a small electric field (7.5 V/cm), while state $|0\rangle$ is sufficiently detuned (by ∼1.4 MHz) to remain dark to the microwaves. A 623 nm laser drives the $N = 2, J = 3/2^-$ population to $\widetilde{A}(010)\kappa^2\Sigma^{(-)}(J = 1/2^+)$, which spontaneously decays to $|0\rangle \ldots |3\rangle$ with ∼55% probability, and back to $N = 2, J = 3/2^-$ otherwise (with a small ∼1% fraction lost to unaddressed levels). Population therefore accumulates in $|0\rangle$ after approximately 7 photons are scattered. Finally, we perform microwave spectroscopy to read out the hyperfine state populations. As shown in Fig. 8.13(b), we find that the molecular population is predominantly contained in the near-degenerate $F = 1^-$ states ($|1\rangle$, $|2\rangle$, and $|3\rangle$) in the absence of optical pumping (orange data), while a majority of the molecular population is transferred into $|0\rangle$ after optical pumping is applied (purple data).

After optical pumping, we demonstrate coherent control of CaOH molecules in the optical tweezer array by driving Rabi oscillations on a parity-doublet transition in the bending mode. We choose the hyperfine stretched states $|+\rangle \equiv (F = 2^+, m_F = 2)$ and $|-\rangle \equiv (F = 2^-, m_F = 2)$ due to their large transition dipole moment, which would enable strong dipolar spin-exchange interactions between adjacent molecules and make them promising qubit states. We begin by transferring population from $|0\rangle$ to $|+\rangle$ with an rf π pulse in the presence of a small magnetic field $B = 2$ G. We then resonantly drive the $|+\rangle \leftrightarrow |-\rangle$ parity-doublet transition with a 43 MHz rf field. The population detected in $|-\rangle$ as a function of drive time is shown in Fig. 8.13(c), demonstrating clear Rabi oscillations with a frequency $\Omega = 2\pi \times 180$ kHz.

8.5.3 Attempts to measure coherence time

After observing Rabi oscillations between the $|+\rangle$ and $|-\rangle$ qubit states, we attempted to measure their coherence time. These states were expected to have a very long coherence time. This is because they have identical quan-

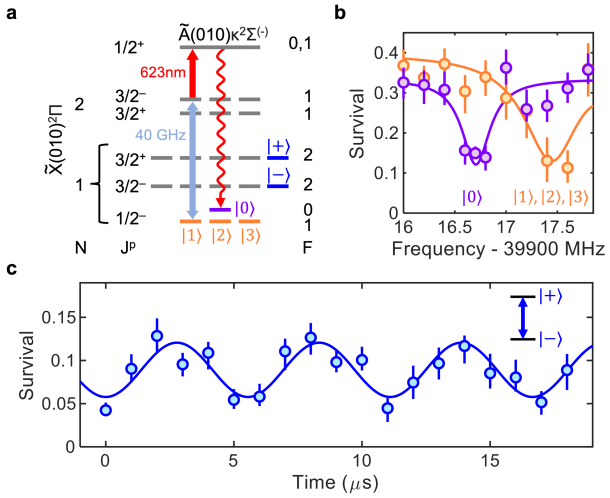

Figure 8.13: Single-state control of CaOH in optical tweezers. **a**, Microwave-optical scheme for pumping population into the single quantum state $|0\rangle$ ($F = 0^-$) in the $\tilde{X}(010)$ bending mode. Microwave radiation at 40 GHz resolves $|0\rangle$ from the nearby states $|1\rangle$, $|2\rangle$, and $|3\rangle$, while a 623 nm laser dissipatively returns population to states $|0\rangle$ through $|3\rangle$. Also shown are the parity-doublet states $|+\rangle$ ($F = 2^+, m_F = 2$) and $|-\rangle$ ($F = 2^-, m_F = 2$). Nearby hyperfine levels are omitted from the figure for clarity. **b**, Depletion spectroscopy of the $N = 1, J = 1/2^- \rightarrow N = 2, J = 3/2^+$ microwave transitions before (orange) and after (purple) optical pumping, demonstrating accumulation of population in $|0\rangle$ (leftmost peak). **c**, Rabi oscillations on the $|-\rangle \leftrightarrow |+\rangle$ parity-doublet transition at 43 MHz. Error bars represent 68% confidence intervals. Reproduced from Ref. [46].

tum numbers besides parity, which means that they should have identical magnetic field sensitivity and only be quadratically sensitive to electric fields. We also expected them to have identical AC Stark shifts, again due to their identical angular momentum quantum numbers and the fact that the AC Stark Hamiltonian conserves parity. However, when we measured the coherence time of these states (using a Ramsey sequence similar to Ref. [205]), we observed a bare coherence time <100 μs. With a spin echo, the coherence time was still <1 ms.

We initially thought that the dominant source of decoherence would be from electric fields, with an imperfectly zeroed electric field allowing small first-order shifts between the two states. We intentionally applied voltages to the coils but saw nothing to suggest that the electric field should have actually been a problem. However, when we increased the trap depth from 280 μK to 600 μK, we observed a $\sim$120 kHz shift in the resonance frequency of the parity-doublet transition. We did not have a model that explained the differential AC Stark shift at the time, and decided to move on to the next project while working to better understand the Hamiltonian on the side. This decision was also partially due to the difficulty of doing spectroscopy in the tweezers, primarily due to the low data rate.[9]

Since then, we found that there is a parity-dependent term in the AC Stark Hamiltonian, as described in chapter 6 and appendix A.6. This is still much smaller than the "normal" tensor polarizability for non-parity-doublet states (e.g. rotational qubits in CaF [205]). Therefore, with magic angle trapping [205] it is likely that very long coherence times can be achieved for these qubit states. This is a topic for future work.

[9] By contrast, we found that spectroscopy in the ODT (described in chapter 9) was substantially faster with much higher data quality. This suggests that an ODT is the best place to work when performing spectroscopy to understand the states of interest, before then moving to tweezers for measurements that specifically rely on single-molecule control.

8.6 Summary and outlook

In summary, we have realized an array of single CaOH molecules by directly loading laser-cooled molecules into tightly focused optical tweezer traps at 785 nm. We directly and nondestructively image individual trapped molecules and achieve fidelities greater than 90% for distinguishing loaded from empty traps. We have characterized the trap wavelength dependence of the tweezer imaging, which is found to be limited by tweezer light-mediated coupling to high-lying electronic states in CaOH. Finally, we prepared CaOH molecules in the tweezer array in single quantum states and observed coherent Rabi oscillations on a parity-doublet transition in the vibrational bending mode.

These results pave the way for numerous experiments in quantum information science [100, 101], quantum simulation [109, 110], ultracold collisions [69, 77, 131], and precision measurements [45, 89, 140] that require (or could benefit from) the combination of full internal and external state control of individual polyatomic molecules, as provided by the optical tweezer platform. The platform demonstrated here can be used in the near term to realize dipolar interactions between molecules in adjacent optical tweezers in parity doublet states and for cooling of the molecules' motion to the quantum regime [30, 206]. The imaging fidelities achieved here could be increased in future work by using longer tweezer light wavelengths, e.g. 1064 nm, which we successfully used to optically trap CaOH in larger optical dipole traps [43]. Finally, this work is expected to be extendable to larger and/or more complex polyatomic molecules amenable to direct laser cooling techniques, including symmetric and asymmetric top molecules [37, 47].

9

Controlled Collisions of Optically Trapped CaOH Molecules

Collisions between molecules at ultracold temperatures are a rich topic of experimental and theoretical study [56, 58]. While such collisions are well described by the Schrödinger equation in the quantum mechanical

regime, the complex structure of molecules means that solving the collisional problem for even two molecules is extremely challenging due to the very high density of states present. Nonetheless, approximation methods can be used to make some collisional calculations tractable, and the results, in combination with experimental observations, reveal a variety of interesting phenomena occurring in ultracold molecular collisions.[1]

Ultracold molecular collisions were first observed around 2010 with the advent of coherently associated bialkali molecule experiments [65, 80]. Since then, there has been a large amount of activity studying cold and ultracold collisions between diatomic molecules. However, observing collisions between polyatomic molecules is an even harder experimental challenge, with only a few experiments having previously reported collisions between cold polyatomic molecules [122–124], none of which were at ultracold temperatures.

In this chapter, we report on the observation of collisions between optically trapped, bosonic CaOH molecules at temperatures $\sim$100 μK. Compared to previous experiments at $\gtrsim$0.1 K, the molecules are colder than all rotational energy scales, parity doublet splittings included, and are in the few-partial-wave regime. We observe inelastic collisional loss for CaOH prepared in both the vibrational ground state and in the lowest-energy vibrational bending mode. The measured collisional loss rate in the bending mode is higher than in the ground state, which we attribute to the parity doublet structure of the bending mode. We also measure collisional loss rates of molecules in single quantum states in the bending mode, including as a function of applied electric field. We compare the measurements to calculations that include long-range dipolar interactions and universal short-range loss, and use these comparisons to build physical understanding of the collisional behavior of parity-doublet molecules. Certain parity-doublet states are identified that have repulsive long-range interaction potentials, which are calculated to have high ratios of elastic to inelastic collision rates at lower temperature.

[1] Portions of this chapter have been reproduced from Ref. [342].

9.1 Overview of prior work

To date, the majority of the work with cold and ultracold molecular collisions has occurred with diatomic molecules. In the realm of cold collisions, trapping is not necessarily an essential requirement. A significant field of research exists in studying cold collisions of molecules using crossed molecular beams – in this case, cold collisional temperatures can be achieved by merging the beams at a small angle, such that the relative velocity of the two beams is low [374].

Trapping molecules provides another avenue for exploring cold molecular collisions. Sub-Kelvin temperatures have been achieved for molecules held in magnetic and electric traps, enabling a number of experiments to observe cold collisions between diatomic molecules and atoms. Cold molecule-molecule collisions have also been observed, including between O_2 molecules in a superconducting magnetic trap at temperatures <1 K [173]. Recently, dipolar collisions were observed between electrically trapped CH_3F molecules at 350 mK [124].

The application of laser cooling techniques to molecules (either by direct cooling or association of laser cooled atoms) enabled reaching the ultracold temperature regime ($\lesssim$ 1 mK), where rich quantum mechanical collision effects can be more readily observed, especially in the regime where one or few partial waves are present. Pioneering work in this direction was done at JILA with optically trapped, fermionic KRb molecules at temperatures <1 μK. Notably, it was seen that quantum statistics could dramatically impact collision rates: while molecules in identical internal states could only collide via p-wave interactions (due to Fermi statistics), hyperfine state mixtures of molecules collided at an orders-of-magnitude higher rate due to s-wave collisions being "turned on" [80]. It was also observed that applying an electric field to align the molecular dipole moments in the laboratory frame dramatically increased the collision rate by helping to overcome the zero-field p-wave barrier [65]. Notably, these

collisions were seen to result primarily in molecule loss, a result that was attributed to the chemical reaction KRb + KRb $\rightarrow$ K_2Rb_2 being energetically favorable. Note that this is a qualitatively different result than for collisions of ultracold atoms, where elastic collisions can be easily made to dominate over inelastic collisions and/or atom loss.

Subsequent experiments with ultracold diatomic molecules – including nonreactive species – observed collisional inelastic loss rates near the universal limit, in which the probability of loss after a collision at short range is unity [67–69, 74, 80, 114, 118]. It was proposed that this could be the result of "sticky collisions," whereby two molecules that approach short-range separations form a long-lived complex due to the very high density of molecular states in this region of the potential [116, 118]. These complexes could then be lost due to a number of processes. In particular, it was suggeested that excitation by optical trapping light could be a dominant mechanism driving loss of collisional complexes [117]. These predictions were verified the following year via experiments with KRb [72] and RbCs [71]. See Ref. [118] for a much more detailed review of sticky collisions in molecules. Regardless of the specific mechanism, it seems that universal loss is the norm for collisions between ultracold molecules.

Of course, lossy collisions are undesirable for many experiments (most notably those aiming for quantum degeneracy in bulk gases). Accordingly, in the past few years a number of techniques have been developed and demonstrated for leveraging the long-range dipolar interactions between polar molecules to engineer repulsive potentials [75–78]. Such a potential "shields" the molecules from ever reaching short range and therefore can increase collisional lifetimes by orders of magnitude. Recently, these collisional shielding techniques have been used to achieve quantum degeneracy in molecular gases [29, 75, 79, 155].

A number of other phenomena have been observed in collisions between ultracold diatomic molecules. These include tuning of inelastic collision rates by applying electrostatic and microwave fields, observations of state-

dependent collisions, and the observation of collision resonances, most notably a Feshbach resonance between two ultracold NaLi molecules [65, 66, 70, 73, 80].

Compared to diatomic molecules, polyatomic molecules generically contain structures, most notably the presence of closely-spaced states of opposite parity [52, 96], that are expected to result in qualitatively distinct collisional properties [125–127, 131]. Examples include electrostatic shielding methods for evaporative cooling [130, 131], and field-linked states that can be used to tune collision rates and assemble larger polyatomic molecules [126, 131–133]. Experimentally, collisions between polyatomic molecules have been previously observed in the $0.1 - 1$ K temperature regime [123, 124], where dipolar relaxation was the dominant collisional effect [124]. Despite decades of theoretical studies [125–127, 130, 131, 375], collisions between molecules with parity doublet structure, including polyatomic species, have not previously been observed at ultracold temperatures (<1 mK).

9.2 Overview of the experiment

Observing collisions of trapped molecules requires sufficiently high number densities that the collision rate is significantly faster than the background loss rate due to single-molecule effects, e.g. blackbody and vacuum lifetimes. The overall lifetime of CaOH molecules in the $\widetilde{X}(000)$ vibrational ground state is approximately 1 s in our experiment, limited predominantly by room temperature blackbody radiation, while for CaOH in the $\widetilde{X}(010)$ bending mode the lifetime is approximately 350-400 ms, limited by blackbody radiation and spontaneous radiative decay back to the ground state (see chapter 6).

Molecular collision processes can be elastic (where the internal state of the molecules remains unchanged but their momentum vectors are altered), inelastic (where the internal state of the molecules changes), or lossy. For

our purposes, lossy collisions refer to short-range loss, where the molecules undergo chemical reactions or form a long-lived complex that is ultimately lost from the trap [118]. In practice, we usually cannot experimentally distinguish whether a collision was inelastic or lossy as long as we detect only a single internal state, and for brevity we will often refer to both of these processes as "inelastic."[2]

The elastic, inelastic, and lossy collision rates are parameterized by collision cross sections $\sigma_{\text{el}}(E)$, $\sigma_{\text{in}}(E)$, and $\sigma_{\text{loss}}(E)$, which depend in general on the collision energy E. The corresponding collision rate coefficients come from multiplying the cross section by the molecule velocity v, so that $k_{\text{loss}} = \sigma_{\text{loss}} v$ and so on. For a thermal energy distribution of molecules at temperature T, we instead use the two-body rate constants $k_{\text{loss}} = \int_0^\infty \sigma_{\text{loss}}(E) v(E) f(E,T) dE$, where $v(E) = \sqrt{2E/\mu}$ is the molecular velocity, μ is the reduced mass of the two-molecule system, and $f(E,T)$ is the Maxwell-Boltzmann energy distribution at temperature T. For molecules with local number density n, the rate at which collisions occur is $R_{\text{loss}} = k_{\text{loss}} n$ (and so on for the elastic and inelastic rates). As discussed more below, in the universal loss regime we expect the collisional loss rate to be $k_{\text{loss}} \sim 10^{-10}$ cm^{3}s^{-1}, meaning that achieving a collisional loss timescale $\tau_{\text{loss}} = R_{\text{loss}}^{-1}$ faster than the single-body lifetime requires number densities $n \sim 10^{11}$ cm^{-3}. This is the goal for our experiment.

Up to this point, the maximum number density we had achieved for CaOH in an ODT was $\sim 10^9$ cm^{-3} (chapter 6), several orders of magnitude too low to observe collisions. However, our implementation of a blue-detuned conveyor belt MOT (chapter 5) provided the opportunity to load an ODT at substantially higher density. This is the approach we followed for the experiments in this section.

An alternative approach that has been used to measure collisions of laser cooled molecules is merged tweez-

[2] Also note that most (but not all) state-changing collisions impart enough kinetic energy to the molecules that they are lost from the trap.

ers [69, 77]. This provides a highly controlled, high-density environment where only two molecules can collide. However, we elected to use a bulk sample in an ODT due to the higher signal, as well as the possibility of pursuing evaporative cooling (though we did not end up doing so in the work described here).

9.3 Experimental setup

The setup for the collision experiment is very similar to what we used to load an ODT for the experiments in chapters 6, 7, and 8. However, for this experiment we added the blue-detuned conveyor belt MOT (chapter 5) in order to achieve higher density. To load the ODT, we first made a conveyor MOT as described earlier, then switched off the magnetic field and loaded the ODT from a free space single-frequency (SF) molasses. We also attempted to load the ODT directly from the conveyor MOT, but found that the loading efficiency was worse than with the SF molasses, even after adjusting the laser detuning to account for the differential AC Stark shift between the $\widetilde{X}$ and $\widetilde{A}$ states. This approach merits more attention in the future, but it seems plausible that differential AC Stark shifts in the ground state fundamentally limit the efficacy of the conveyor MOT in the presence of the trap.

We began the collision work by trying to load a similar ODT to what was used previously (1064 nm, waist $\sim$25 μm). However, the molecule densities we achieved were not high enough to observe fast collisions. Noting from section 6.1.3 that the molecule density scales as $1/w_0^7$ at constant trap power, molecule number, and temperature, we tried reducing the waist size to increase the density.[3] Despite the reduced loading efficiency due to the smaller trap volume, this proved successful, and we ultimately settled on a trap with a waist of approximately 9 μm. This was done by replacing the beam expander in the ODT optical path (chapter 6). We found that

[3] Of course, the molecule number will decrease and the molecule temperature will increase in a small, deep trap of this sort, but the scaling is still more than enough to overcome these reductions.

optimal loading occurred using 20 ms of SF cooling.[4] During loading, we also raster the ODT in a circle at a frequency of 200 Hz, using a piezo mirror in the beam path. This helps the trap to collect more molecules from the molasses that otherwise might not diffuse to the right position. In the future, higher densities could be obtained by first loading a large ODT, then transferring into the smaller volume trap, as was done in Ref. [51].

At this trap size, we have significant power overhead, with the trap depth at our maximum 1064 nm power (13 W) being 4.5 mK, well above the trap depth needed to hold and image the molecules.[5] In the experiment, we vary the molecule density by up to an order of magnitude by ramping the trap depth, which provides a convenient method of turning fast collisions on and off as needed.[6]

9.3.1 Molecule imaging and light assisted collisions

We image molecules using "diagonal imaging," i.e. by collecting fluorescence from the 626 nm $\widetilde{A}(000) \rightarrow \widetilde{X}(000)$ transition, as was done for the tweezer experiment. We used the same 1.5 mm imaging beams that were used for tweezers, which needed only a small amount of realignment to be used with the collision ODT. Note that we started the collision project using the 555 nm "off-diagonal" scheme, but later decided that having the best signal-to-noise ratio possible would be important for accurately fitting two-body collision curves.

A problem with imaging molecules in the 9 μm ODT was that light-assisted collisions occur rapidly due to the high densities involved, even at relatively low trap depth. We measured the light-assisted collisional loss rate during Λ imaging to be $k_\Lambda \approx 3 \times 10^{-9}$ cm^{3}s^{-1}, which limited the molecule lifetime to under 10 ms when imaging

[4] The cloud quickly expands during the molasses, leading to diminishing returns for longer loading times.

[5] We typically image at trap depths between 600-1000 μK, and do state preparation at a depth around 250 μK.

[6] The density scales as $n \sim (U_0/T)^{3/2}$, where U_0 is the trap depth and T is the temperature. When the trap depth is ramped adiabatically, $T \sim \sqrt{U_0}$, so the density scales as $U_0^{3/4}$ in this case. (The adiabatic temperature scaling can be derived by noting that the phase space density, $\rho = n\lambda_{\mathrm{dB}}^3 \sim n/T^{3/2} \sim (U_0/T^2)^{3/2}$, is constant for an adiabatic ramp.)

at a typical trap depth of ∼900 μK. The SF light-assisted collision rate was estimated from imaging lifetime data to be a more modest $k_{SF} \approx 2 \times 10^{-10}$ cm^{3}s^{-1}, making in-trap SF imaging feasible.

Even with the manageable SF imaging light-assisted collision rate, collisions during imaging have the potential to bias our measurements. If the imaging duration is long enough for appreciable light-assisted collisions to occur, the collected fluorescence will no longer linearly depend on the number of molecules that were in the trap at the start of imaging. Simulations indicated that for the collision measurement sequences we were using, light assisted collisions during the image could bias the measured collision rates at the 10% level, even with only 10 ms of imaging. To avoid these issues, we instead chose to image the molecules in free space at the end of the collision measurement sequence, by turning off the trap and applying a 40 ms pulse of Λ cooling light.

9.3.2 Molecule number, temperature, and density

Calibration of molecule number

To image molecules in the ODT, we used the in-vacuum asphere (see chapter 8) to collect 626 nm fluorescence. The fluorescence was then sent through a relay consisting of a 75 mm lens followed by a 100 mm lens,[7] and then focused onto the EMCCD (Andor iXon 897 Ultra) using an 80 mm lens. There were three filters (Semrock FF01-615/20, Semrock FF01-635/18, Thorlabs FGS-900) in front of the camera, as well as a back-polished 1064 nm high-reflector just outside the chamber, which retroreflects the ODT light but mostly transmits visible fluorescence.

The collection efficiency of the imaging system was estimated to be $C = 0.55(12)\%$ for molecules trapped in the ODT. This was done by comparing a couple of methods. We measured the signal collected when imaging

[7] These relay lenses were added during the blue-detuned conveyor belt MOT project to increase the field of view of the imaging system.

approximately 1 molecule in the optical trap (i.e. by treating it like a "tweezer"), and also compared to measurements of the collection efficiency from the conveyor-belt MOT and optical tweezer experiments, which utilized a very similar imaging system [46, 228].[8] Note that all of these measurements indicate that the effective collection efficiency of our imaging system is lower than what would be nominally expected based on ray tracing. We do not know where the loss of signal comes from.

For the collision data, the molecules were imaged in a free-space molasses after turning off the trap, changing the collection efficiency compared to trapped molecules due to the larger size of the cloud and nonuniform imaging beam intensities. To account for this effect, the signal obtained from *in situ* imaging of a small number of molecules in the optical trap (with a known scattering rate) was compared to the signal obtained from imaging the same number of molecules in free space. The combined fractional uncertainty in the molecule number, including estimated errors in the collection efficiency, *in situ* imaging scattering rate, and free-space imaging conversion factor, is approximately 25%.

Molecule temperature

The molecule temperature was measured using time-of-flight (TOF) expansion. After loading the molecules into the ODT, an SF cooling pulse (single-photon detuning $\Delta \approx 90$ MHz, peak intensity $I_0 \approx 35$ mW/cm^2) was applied to set the initial temperature. The ODT intensity was then ramped up to the collision trap depth ($U_0 \approx k_B \times 4.5$ mK), held there for 1 ms, and then instantaneously shut off. The molecules were allowed to expand for a variable amount of time, before being imaged with a 10 ms pulse of Λ-cooling light using the large,

[8] In the tweezer experiment, the effective collection efficiency was determined by comparing our tweezer histograms to simulated histograms including the known EMCCD readout parameters. In the blue MOT experiment, the number was calibrated using the MOT camera on the other side of the chamber, whose NA is simpler to calibrate because it does not include an in-vacuum optic.

10 mm $1/e^2$-diameter MOT beams. To avoid scattered light from these large beams, fluorescence was collected using the "off-diagonal" $\widetilde{B}(000) \rightarrow \widetilde{X}(000)$ transition at 555 nm. For the TOF measurements, the magnification of the imaging system was calibrated by dropping the cloud and ensuring its position as a function of time was consistent with gravitational acceleration.

We at various points also tried to measure the temperature using shaving or release-recapture (described in chapters 6 and 8) [330]. However, we determined that these methods were too susceptible to systematic effects due to the trap geometry and collisions during the sequence. However, shaving in particular was able to provide a reasonable diagnostic of our temperatures, even if we couldn't rely on it to accurately measure the absolute temperature.

Measured TOF temperatures at 260 μK and 4.5 mK trap depths are shown in Fig. 9.1. For molecules in hyperfine mixtures (Fig. 9.2 below), no state preparation was done after the SF cooling pulse, and the temperature was measured to be 80 μK at high trap depth. For molecules in single hyperfine states in $\widetilde{X}(010)$ (Fig. 9.16 below), after the SF cooling pulse the molecules were optically pumped into the bending mode and then microwave-optically pumped into the $(J = 1/2^-, F = 0)$ hyperfine state. The temperature of these molecules was measured to be 100 μK during the collision time. It is likely that most of this heating occurs during the optical pumping, which scatters an average of $\sim$10 photons per molecule.

For measurements of the collision rate constant vs. temperature (Fig. 9.18 below), we adiabatically ramp the trap depth to different values between $U_0 = k_B \times 960\ \mu$K and $U_0 = k_B \times 4.5$ mK. The temperature scales as $T \propto \sqrt{U_0}$ when adiabatically ramping the trap depth, which we confirmed using TOF temperature measurements.

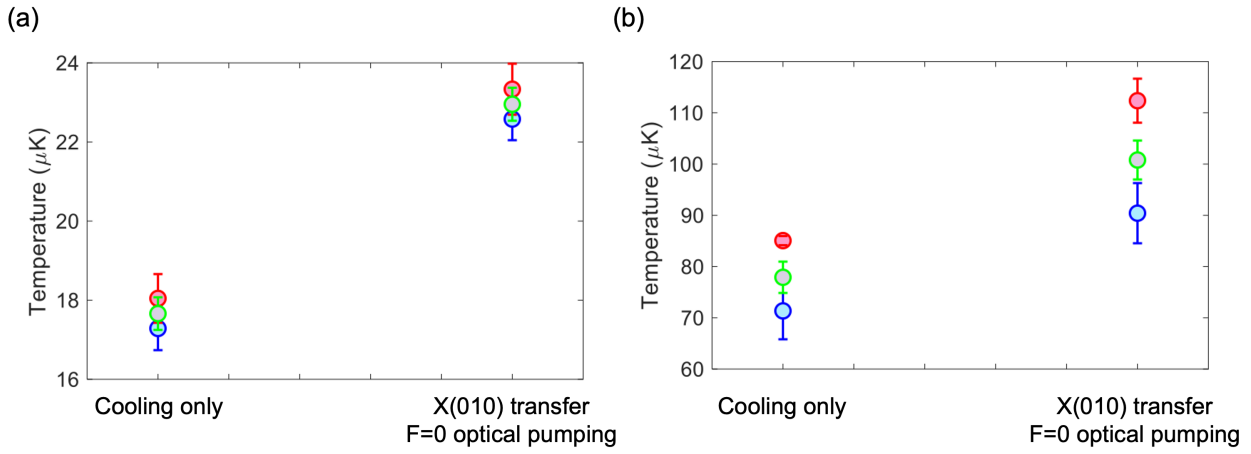

Figure 9.1: Time-of-flight temperature measurements with and without bending mode transfer and $F = 0$ optical pumping at a trap depth of (a) 260 μK and (b) 4.5 mK. SF cooling is performed at a trap depth of $U_0 \approx 650$ μK, and bending mode transfer and optical pumping are at a depth of 260 μK. The trap depth is then ramped to the value used for temperature measurements, with the temperature measured after a 1 ms hold at that depth. Red and blue points correspond to the fitted time-of-flight temperature along the two radial directions, and the green point is the mean.

Optical trap geometry

The ODT trap frequencies were measured using parametric heating spectroscopy, whereby the trap laser intensity was modulated to induce heating, and the resulting molecule loss was recorded as a function of the modulation frequency. Three loss features were observed, corresponding to approximately $2\times$ the motional frequency along each principal axis of the trap. These measurements were taken at relatively low trap depth to minimize the influence of collisions on the measurement, then scaled up using $\omega_i \propto \sqrt{U_0} \propto \sqrt{P}$, where ω_i is the trap frequency along axis i, U_0 is the trap depth, and P is the laser power (this scaling was experimentally verified). At the trap depth used for the collision measurements ($P = 12.6$ W), the scaled trap frequencies were $\{\omega_x^{\text{meas}}, \omega_y^{\text{meas}}, \omega_z^{\text{meas}}\} = 2\pi \times \{30.4, 26.2, 0.45\}$ kHz. However, Monte Carlo simulations of the parametric heating procedure (using the Gaussian trap geometry described below) indicate that the molecules' finite temper-

ature causes our measurement to underestimate the axial trap frequency, ω_z, by ∼20%. Accounting for this effect gives "corrected," zero-temperature frequencies $\{\omega_x, \omega_y, \omega_z\} = 2\pi \times \{30.4, 26.2, 0.55\}$ kHz.

Next, we infer the trap geometry from the measured frequencies. The trapping laser is modeled as an elliptical Gaussian beam, whose waists (w_x, w_y), Rayleigh range (z_R), and trap depth (U_0) are related to the trap frequencies and laser power by

$$\omega_x = \sqrt{\frac{4U_0}{mw_x^2}}, \quad \omega_y = \sqrt{\frac{4U_0}{mw_y^2}}, \quad \omega_z = \sqrt{\frac{2U_0}{mz_R^2}},$$
$$U_0 = \frac{1}{2\epsilon_0 c}\alpha_0 I_0, \tag{9.1}$$

where $I_0 = 2P/(\pi w_x w_y)$ is the peak laser intensity and $\alpha_0 = 204$ a.u. is the scalar polarizability of CaOH at 1064 nm [43]. Using the corrected frequencies from above, the trap parameters are estimated to be $w_x = 8.4\ \mu$m, $w_y = 9.8\ \mu$m, and $z_R = 330\ \mu$m, implying a trap depth of $U_0/k_B = 4.5$ mK at the trap power used for the collision data. Note that the modeled Rayleigh range, z_R, is slightly larger than the idealized Rayleigh ranges ($z_{R,x} = \pi w_x^2/\lambda \approx 210\ \mu$m, $z_{R,y} = \pi w_y^2/\lambda \approx 280\ \mu$m) that would correspond to the modeled beam waists. This could be due to aberrations (e.g. astigmatism) that are not captured in the model. Such aberrations should not significantly affect the final density determination since $\eta = U_0/k_B T \approx 45$, so the molecules see only the very bottom of the trap.

9.3.3 Number density

The average number density of molecules in the ODT is

$$\langle n \rangle = \frac{N\omega_x\omega_y\omega_z}{\xi(T)(4\pi k_B T/m)^{3/2}} \equiv \frac{N}{V_{\text{eff}}(T)} \tag{9.2}$$

where N is the molecule number, $V_{\text{eff}}(T) = \xi(T)(4\pi k_B T/m)^{3/2}(\omega_x\omega_y\omega_z)^{-1}$ is the effective trap volume, and $\xi(T)$ is a correction factor accounting for deviations from the harmonic approximation at finite temperature ($\xi = 1$ for a purely harmonic trap). $\xi(T)$ is just the ratio between the average number densities calculated in the harmonic approximation and for the actual trap geometry, and can be computed by integrating the number density over space. For the Gaussian trap model described above, we calculate $\xi(T = 80\ \mu\text{K}) \approx 1.07$ and $\xi(T = 100\ \mu\text{K}) \approx 1.09$.

Using the Gaussian model, for a temperature of $T = 100\ \mu$K and $N = 100$ molecules in the trap, we calculate a peak number density $n_0 \approx 3.7 \times 10^{11}$ cm^{-3}, an average number density $\langle n \rangle \approx 1.3 \times 10^{11}$ cm^{-3}, and a peak phase space density $\rho_0 = n_0\lambda_{\text{dB}}^3 \approx 5 \times 10^{-6}$, where $\lambda_{\text{dB}} = h/\sqrt{2\pi m k_B T}$ is the thermal de Broglie wavelength.

The dominant uncertainty in the number density is the ∼25% fractional uncertainty in the molecule number calibration. The uncertainties in the trap volume and molecule temperature are comparatively small. Therefore, we estimate that the total fractional uncertainty (standard error) in the molecule number density is 25%.

9.4 Observation of collisions between CaOH molecules

In this section, we describe our initial observation of inelastic collisions between CaOH molecules. We observed and measured inelastic collision rates in the $\widetilde{X}(000)$ state and the $\widetilde{X}(010)$ bending mode, with the molecular population in a mixture of hyperfine states in both cases.

9.4.1 Experimental sequence

Here we provide a brief summary of the experimental sequence, details of which were already described above.

The starting point of the experiment is a conveyor-belt blue-detuned magneto-optical trap (MOT) of CaOH [228, 230]. Compared to previously realized red-detuned MOTs of CaOH [42, 43], the conveyor MOT has approximately two orders of magnitude higher density, directly enabling ultracold collision experiments for laser-cooled polyatomic molecules. After forming the conveyor MOT, CaOH molecules are then loaded into an optical dipole trap (ODT), which is formed from a 1064 nm laser with a Gaussian beam waist of $\sim$9 μm and a trap depth of $\sim$650 μK. The number of molecules initially loaded into the ODT is measured using a short ($\leq$ 5 ms), nondestructive *in situ* single-frequency (SF) imaging pulse [43], followed by a 2 ms recooling pulse. Next, the molecules are prepared in the desired internal state (using a process described later).

To increase the density so that collisions occur on a faster timescale than single-molecule loss (which is due to thermalization of vibrational state population [43, 44]), the trap is adiabatically ramped up to a trap depth (U_0) of $U_0/k_B \approx 4.5$ mK. The initial temperature of the molecules after the ramp is $T_0 = 80$-100 μK, which depends on the prepared internal state. The trap frequencies are $\{\omega_x, \omega_y, \omega_z\} = 2\pi \times \{30.4, 26.2, 0.55\}$ kHz, corresponding to a peak number density of $n_0 \gtrsim 10^{11}$ cm^{-3} for the approximately 100 molecules in the trap.

At high density in the trap, molecules undergo elastic collisions, inelastic state-changing collisions, and short-range losses (e.g. chemical reactions [80, 131] or complex formation [118]). Elastic collisions thermalize the molecules. At the ratio of the trap depth to the molecule temperature in the experiment, $\eta = U_0/k_B T_0 \approx 45$, all observed collisional losses will be from inelastic and short-range processes (for brevity, we will refer to both of these processes as "inelastic"). Our experiments are designed to only detect molecules remaining in the initial state, meaning that all inelastic collisions will appear as loss in our data (some inelastic collisions will also impart enough kinetic energy to physically eject molecules from the trap).

After holding the molecules for a variable amount of time, the surviving molecules are detected by switching off the trap and imaging the cloud in free space using a 40 ms pulse of Λ-cooling light [43, 231]. The imaging is performed in free space to avoid systematic effects due to light-assisted collisions in the trap.

9.4.2 Collisions in $\widetilde{X}(000)$ and $\widetilde{X}(010)$

Fig. 9.2(a) depicts the low-lying rotational and vibrational states of CaOH in the $\widetilde{X}^2\Sigma^+$ ground electronic potential. In our first set of experiments, we prepare CaOH molecules in a mixture of hyperfine states within a single rotational state. This is done, separately, for molecules in either the ground vibrational state [$\widetilde{X}(000)$] or the vibrational bending mode [$\widetilde{X}(010)$]. Vibrational states are labeled with $(v_1 v_2 v_3)$, where v_1 is the vibrational quantum number for the Ca–O stretching mode, v_2 is for the bending mode, and v_3 is for the O–H stretching mode. Each rotational level in the $\widetilde{X}(010)$ bending mode contains opposite parity (parity-doublet) states spaced by tens of MHz, which correspond to bending vibrations in two perpendicular planes in the molecule frame. Their degeneracy is broken by Coriolis interactions [96].

To prepare molecules in $\widetilde{X}(000)$, we do nothing after SF cooling and imaging, which prepares most molecules

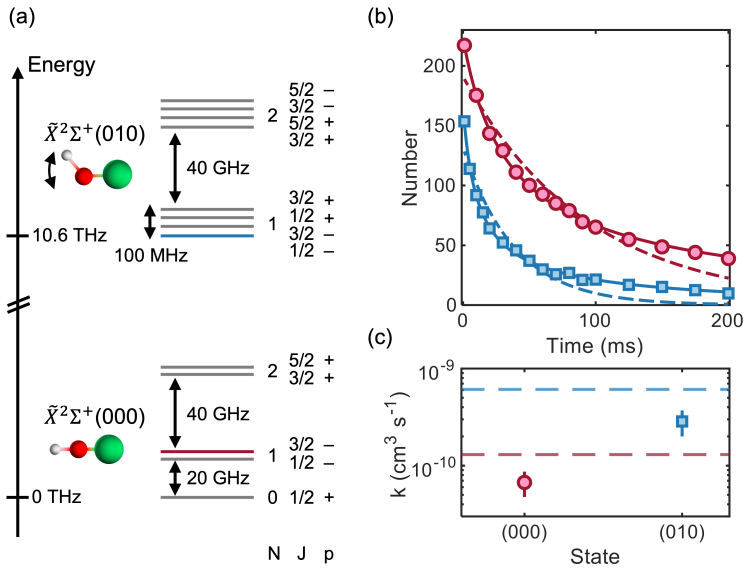

Figure 9.2: Observation of collisions between optically trapped CaOH molecules. (a) Rotational structure of CaOH in the vibrational ground state, $\widetilde{X}(000)$, and vibrational bending mode, $\widetilde{X}(010)$. Opposite-parity states, which must be mixed to turn on dipolar interactions, are spaced by approx. 20 GHz in the ground state and by approx. 40 MHz in the bending mode. States are labeled by the rotational quantum number N, total angular momentum (excluding nuclear spin) J, and parity p. (b) Molecule number vs. hold time in the ODT for molecules prepared at $T = 80$ μK in $\widetilde{X}(000)(N = 1, J = 3/2)$ (red circles) and in $\widetilde{X}(010)(N = 1, J = 1/2^-)$ (blue squares). Solid curves are fits to the two-body collision model described in the text, and dashed curves are fits to a single exponential timescale. (c) Fitted collisional loss rate constants, k, for the two vibrational states. Dashed lines are the universal loss rates calculated for these states. Reproduced from Ref. [342].

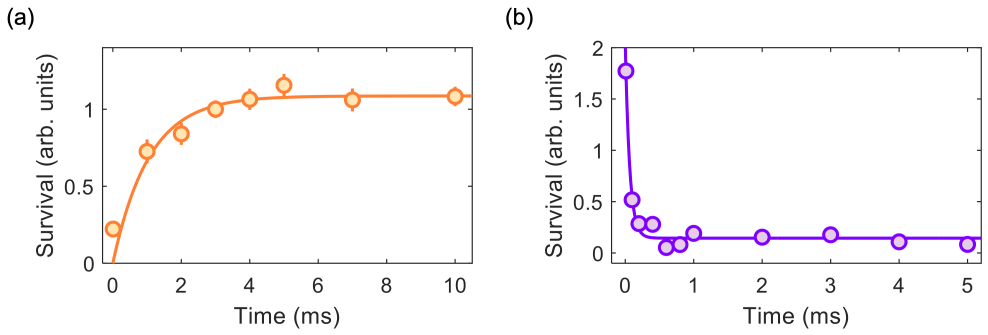

Figure 9.3: (a) Transfer into the bending mode by driving the 609 nm $\widetilde{X}(000) \rightarrow \widetilde{A}(010)\kappa^2\Sigma^{(-)}$ transition. (b) Pushout pulse. Detectable molecules are pushed out of the trap using a resonant pulse of slowing light. We typically use a 1 ms pushout pulse in the experiment.

in the $(N = 1, J = 3/2)$ state due to it being the farthest detuned ground state. To prepare $\widetilde{X}(010)$, we apply a 5 ms pulse of 609 nm $\widetilde{X}(000) \rightarrow \widetilde{A}(010)\kappa^2\Sigma^{(-)}$ light (along with all repumpers except $\widetilde{X}(010)(N = 1)$). The $\widetilde{A}(010)\kappa^2\Sigma^{(-)}(J = 1/2^+)$ state decays primarily to $(N = 1, J = 1/2^-)$ and to $(N = 2, J = 3/2^-)$, which is repumped back into $(N = 1, J = 1/2^-)$ (see chapter 7). Following the bending mode transfer, we push all other detectable molecules out of the ODT using a "pushout" pulse of resonant slowing light, along with all repumpers besides $\widetilde{X}(010)(N = 1)$. These two steps are shown in Fig. 9.3. In both cases, molecules are distributed among several hyperfine states but in a single J manifold.

Fig. 9.2(b) shows the molecule number as a function of hold time for molecules prepared in either the $\widetilde{X}(000)(N = 1, J = 3/2^-)$ level of the vibrational ground state (red circles) or the $\widetilde{X}(010)(N = 1, J = 1/2^-)$ level of the vibrational bending mode (blue squares). In both cases, the molecules are in an incoherent mixture of hyperfine states arising from the hydrogen nuclear spin $I = 1/2$. The data fit very well to two-body decay curves (solid lines) while fitting very poorly to exponential one-body curves (dashed lines), showing that CaOH-CaOH collisions dominate.

To determine the CaOH-CaOH collision rate constant, we fit the data to a rate equation model that includes the two-body loss rate constant k and the single-molecule background lifetime τ. We also account for molecular heating due to a mechanism where the coldest molecules are the most likely to collide and be lost from the trap. The coupled rate equations for the molecule number N and temperature T are (see Ref. [68] and sec. D.3)

$$\frac{dN(t)}{dt} = -k\frac{1}{V_{\text{eff}}(T)}N(t)^2 - \frac{1}{\tau}N(t) \tag{9.3a}$$

$$\frac{dT(t)}{dt} = \frac{1}{4}k\frac{1}{V_{\text{eff}}(T)}N(t)T(t) \tag{9.3b}$$

where $V_{\text{eff}}(T) = \xi(T)(4\pi k_B T/m)^{3/2}(\omega_x\omega_y\omega_z)^{-1}$ is the effective trap volume, and $\xi(T) \approx 1.1$ is a factor that accounts for the finite temperature of the molecules (see above). The single-molecule lifetimes τ are much longer than the observed collision timescales, and are held fixed in the fit to the measured values of $\tau_{000} \approx 900$ ms and $\tau_{010} \approx 360$ ms for the ground state and bending mode, respectively [43, 44]. Fits to the rate model of eqn. 9.3 are shown as solid curves in Fig. 9.2(b). The measured collision rate constants are $k_{(000)} = 0.7(2) \times 10^{-10}$ cm^3 s^{-1} and $k_{(010)} = 2.9(9) \times 10^{-10}$ cm^3 s^{-1}, plotted in Fig. 9.2(c). These values include a small (∼10% level) correction that accounts for collisions with molecules trapped in the wrong state (see below).

The inelastic loss rate constant k for molecules in the bending mode is $\sim 4\times$ higher than in the vibrational ground state. We attribute this difference to an increased interaction strength from the parity doublet structure in the bending mode. Molecules interact via a van der Waals (vdW) potential $V(r) = -C_6/r^6$ arising from electric dipole interactions, wherein the electric field from one molecule induces a dipole moment in the second molecule by mixing states of opposite parity. In the ground state, the nearest opposite-parity states are rotational levels split by the rotational constant $B = h \times 10.023$ GHz, while in the bending mode the opposite-parity states

are split by the ℓ-doubling parameter $q_\ell \approx h \times 21.5$ MHz. Ignoring electronic contributions, in second order perturbation theory the vdW coefficient is $C_{6,(000)} \approx \frac{1}{6B}\frac{d^4}{(4\pi\epsilon_0)^2}$ in the ground state and $C_{6,(010)} \approx 0.85 \times \frac{1}{24q_\ell}\frac{d^4}{(4\pi\epsilon_0)^2}$ in $J = 1/2^-$ of the bending mode, where $d = 1.465$ D is the molecule frame dipole moment [256] and the numerical prefactor accounts for substructure from the electron spin (see below and Ref. [342] for details on the calculation of vdW coefficients). The closely-spaced parity doublets therefore increase the van der Waals interaction strength by $C_{6,(010)}/C_{6,(000)} \sim B/q_\ell \sim 10^2$.

9.4.3 Calculated universal loss rates

In the universal limit, where molecules are lost whenever they collide at short range (for instance due to the chemical reaction CaOH + CaOH $\rightarrow$ $Ca(OH)_2$ + Ca [131]), k depends only on the form of the long-range potential, the collision energy, and the mass. For both the $\widetilde{X}(000)$ state and $\widetilde{X}(010)$ state, the long range potential has the form $V(r) = -C_6/r^6$, as discussed above. The value of C_6 for each potential is calculated in second-order perturbation theory using

$$\Delta E = \sum_{\eta' L' M'_L} \frac{\langle \eta L M_L | H_{\text{ddi}} | \eta' L' M'_L \rangle \langle \eta' L' M'_L | H_{\text{ddi}} | \eta L M_L \rangle}{E^{(0)}_\eta - E^{(0)}_{\eta'}} \tag{9.4}$$

where H_{ddi} is the dipolar interaction Hamiltonian, η describes the internal quantum numbers of the molecule, and $|L, M_L\rangle$ is the collision partial wave. Details of the calculations are described in Ref. [342]. The matrix elements of H_{ddi} are proportional to $\langle \eta_1 | d_1 | \eta'_1 \rangle \langle \eta_2 | d_2 | \eta'_2 \rangle$, where d_i is the dipole operator acting on molecule i and η_i describes the internal state of molecule i. Therefore, H_{ddi} couples channels $|\eta L M_L\rangle$ and $|\eta' L' M'_L\rangle$ only when both molecules have nonvanishing dipole matrix elements. The selection rules for the partial wave quantum

numbers are $\Delta L = 0, \pm 2$; $\Delta M_L = 0, \pm 1, \pm 2$, $L = 0 \not\leftrightarrow L' = 0$.

For two molecules in the $\widetilde{X}(000)(N = 0)$ state (i.e. the $|N_1 = 0, N_2 = 0\rangle$ collision channel), the interaction is dominated by second-order coupling to $|N_1 = 1, N_2 = 1\rangle$, where N_1 and N_2 are the rotational quantum numbers of the two molecules. This results in a vdW potential [342]

$$V_{(000)}(r) = -\frac{1}{6B}\left(\frac{d^2}{4\pi\epsilon_0}\right)^2 \frac{1}{r^6} \tag{9.5}$$

where $B = h \times 10.023$ GHz is the rotational constant and $d = 1.465$ D is the dipole moment. The potential is similar for molecules in the $|N_1 = 1, N_2 = 1\rangle$ channel (this time from coupling to $|N_1 = 0, N_2 = 0\rangle$, $|N_1 = 2, N_2 = 2\rangle$, and $|N_1 = 0, N_2 = 2\rangle$), resulting in the same average vdW interaction but with anisotropy depending on the angular momentum projection m_N. Fig. 9.4(a)-(b) shows the full calculated DDI potentials [342] (solid grey curves), along with the 2nd-order potential from eqn. 9.5 (dashed curves). We see that this describes $N = 0$ very well, but also is a decent approximation to the $N = 1$ potential if the dependence on magnetic sublevel is ignored.

Neglecting spin-rotation structure for the moment, for two molecules in $\widetilde{X}(010)(N = 1^-)$ (the $|N_1 = 1^-, N_2 = 1^-\rangle$ channel) the dominant 2nd-order interaction is with the upper parity-doublet state $|N_1 = 1^+, N_2 = 1^+\rangle$, which is higher in energy by $4q_\ell$. In this case, the 2nd order interaction energy is

$$V_{(010)}(r) = -\frac{1}{24q_\ell}\left(\frac{d^2}{4\pi\epsilon_0}\right)^2 \frac{1}{r^6} \tag{9.6}$$

as described in Ref. [342]. Accounting for spin-rotation structure (which is similar in energy to the parity dou-

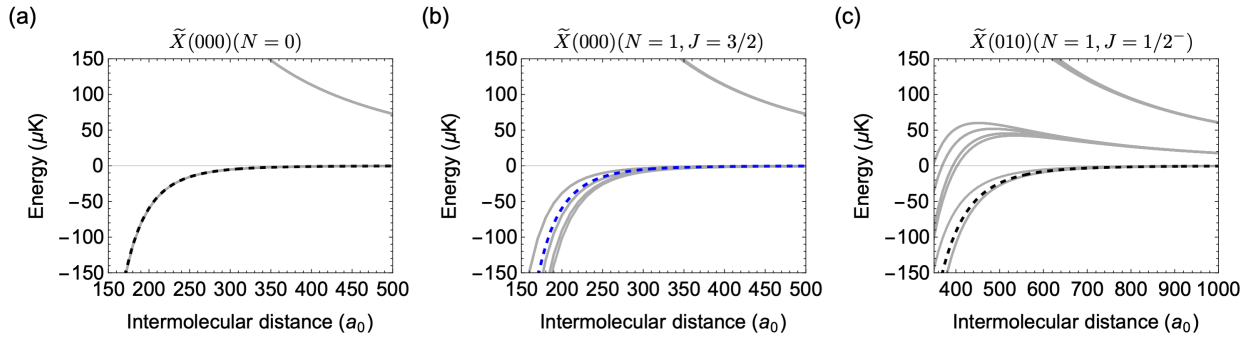

Figure 9.4: Calculated dipolar interaction potentials (solid curves) and 2nd-order approximations (dashed curves) for two molecules in (a) $\widetilde{X}(000)(N = 0, J = 1/2)$, (b) $\widetilde{X}(000)(N = 1, J = 3/2)$, and (c) $\widetilde{X}(010)(N = 1, J = 1/2^-)$. Note the different horizontal axis in part (c). Only even partial waves $L = 0$, 2, and 4 are shown.

blet splitting) adds small corrections to this value, described in Ref. [342], such that for the $J = 1/2^-$ state, $V_{1/2^-}(r) \approx 0.85 \times V_{(010)}(r)$. Fig. 9.4(c) shows dipolar interaction potentials for two molecules in $\widetilde{X}(010)(N = 1, J = 1/2^-)$, with the black dashed curve being the 2nd-order calculation including spin-rotation structure. Once again, there is anisotropy in the potential, with different combinations of M_J levels experiencing slightly different interaction strengths.

With these values of C_6 for the two states in hand, we now calculate universal loss rates. At low temperatures, k is expected to be proportional to the van der Waals length $r_{\mathrm{vdW}} = \frac{1}{2}(2\mu C_6/\hbar^2)^{1/4}$ [114]:

$$k_{\mathrm{loss}} = 2g\frac{h}{\mu}\frac{4\pi r_{\mathrm{vdW}}}{\Gamma(1/4)^2} \tag{9.7}$$

where $g = 1$ for distinguishable particles (which is the case in our experiment due to the hyperfine mixture), $\mu = (57\ \mathrm{u})/2$ is the reduced mass, and $\Gamma(z)$ is the gamma function. Using the C_6 values above, we estimate $r_{\mathrm{vdW},(000)} \approx 94\, a_0$ and $r_{\mathrm{vdW},(010)} \approx 297\, a_0$, implying a $\sim 3\times$ higher collisional loss rate in the bending mode

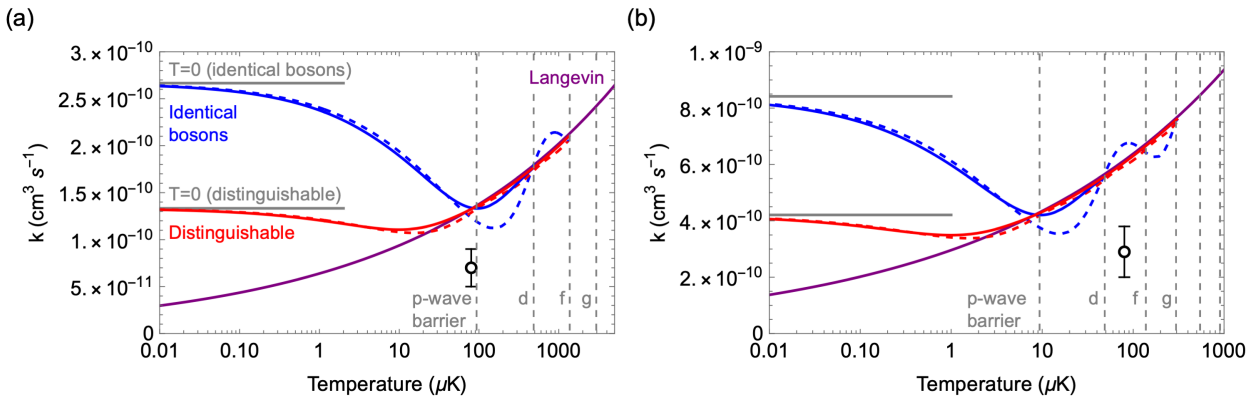

Figure 9.5: Calculated universal loss rate constants for (a) the $\widetilde{X}(000)$ state and (b) the $\widetilde{X}(010)(N = 1, J = 1/2^-)$ state. The low-temperature limit (horizontal grey lines) uses the expressions from Ref. [114], and the high-temperature Langevin limit (purple curve) uses the expression from Ref. [376]. Calculated rates in the intermediate temperature regime (blue and red curves) use the single-channel model from Ref. [115]. Dashed curves are single-energy calculations, and solid curves are thermally averaged values. Data points are the experimental measurements from Fig. 9.2. Reproduced from Ref. [342].

compared to the ground state.

At high temperatures, universal loss is well described by the Langevin capture model, which for a $-1/r^6$ potential gives a rate [376, 377]

$$k_{\text{loss}}(T) = 2^{11/6}\Gamma(2/3)\left(\frac{\pi}{\mu}\right)^{1/2} C_6^{1/3}(k_B T)^{1/6} \tag{9.8}$$

The calculated universal loss rates are shown as a function of temperature in Fig. 9.5. At temperatures well below the p-wave barrier, the universal loss rate approaches a constant value given by eqn. 9.7. At temperatures high enough for several partial waves to contribute, the universal loss is accurately described by a classical Langevin capture model [376, 377] (eqn. 9.8). At intermediate temperatures, universal loss rates may be calculated using a single-channel model based on analytic quantum defect theory (QDT), as described in Ref. [115].

We see from Fig. 9.5 that at our temperature (80 μK), the Langevin capture model accurately describes univer-

sal loss. The calculated universal loss rates at $T = 80\ \mu$K are $k^{\text{univ}}_{(000)} = 1.3 \times 10^{-10}$ cm^3 s^{-1} and $k^{\text{univ}}_{(010)} = 6.1 \times 10^{-10}$ cm^3 s^{-1}, shown as horizontal lines in Fig. 9.2(c). The calculated universal rate is $\sim$4.5$\times$ higher in the bending mode than in the ground state, and both measured rates are approximately 50% below the universal limit.

9.5 Single-state collisions in the vibrational bending mode

Having observed collisions with hyperfine state mixtures in the vibrational ground state and in the bending mode, our next goal was to prepare molecules in single hyperfine states in the $\widetilde{X}(010)$ bending mode. It had previously been predicted that certain states in the bending mode would exhibit favorable ratios of elastic to inelastic collisions at high electric field [131]. Moreover, there has been significant theoretical work examining ultracold collisions between parity doublet molecules [125–127, 129–131, 375, 378, 379], but very few experiments have been able to observe collisions between such molecules [124, 128], all of which were at much higher temperatures than our experiment. Therefore, we decided to map out the collisional loss rates for each manifold in the $N = 1$ bending mode as a function of electric field, hoping to shed light on the physics of parity-doublet collisions near the ultracold regime.

9.5.1 State preparation

Fig. 9.6 shows the structure of the $\widetilde{X}(010)(N = 1)$ bending mode as a function of applied electric field. At electric fields $E \gtrsim 150$ V/cm ("high field"), the structure splits into six resolved manifolds, labeled a-f in order of increasing energy. The a and b states are high-field seeking with quantum numbers $m_N \ell = +1$, and the two

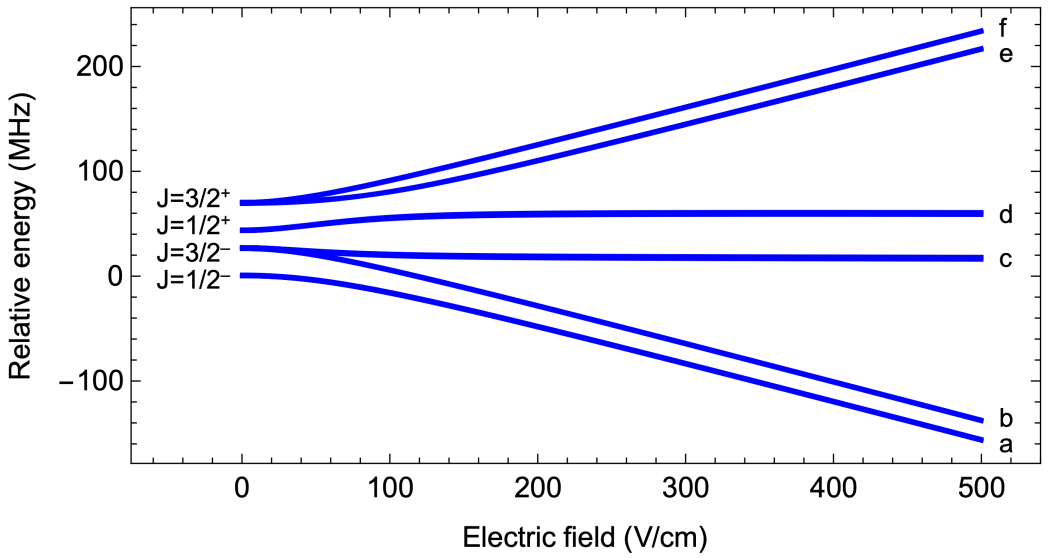

Figure 9.6: Structure of the CaOH $\widetilde{X}(010)(N=1)$ bending mode vs. applied electric field, with the high-field manifolds a-f labeled. Energies are reference to the lowest-energy, $J=1/2^-$ state at $E=0$ V/cm.

states are split by the spin-rotation interaction (based on the sign of $m_S m_N$).[9] The e and f states are low-field seeking with $m_N \ell = -1$, and they are split by the same spin-rotation interaction as a and b. The c and d states have zero lab-frame dipole moment (projection quantum number $m_N = 0$), and they are split by the ℓ-type doubling interaction. Each of the six manifolds contains four hyperfine states with splittings at the 1 MHz level. We expect the hyperfine states to be spectator degrees of freedom regarding collisions, but we nonetheless wish to prepare a single hyperfine state so that the molecules behave as identical bosons for collision purposes. We will choose the highest energy hyperfine state in each manifold as the collision state.

To prepare molecules in single hyperfine states, we load the ODT and then ramp the trap depth down to approximately 260 μK. We pump the molecules into the bending mode using the 609 nm $\widetilde{X}(000) \rightarrow \widetilde{A}(010)\kappa^2\Sigma^{(-)}$ transition (combined with $\widetilde{X}(010)(N=2) \rightarrow \widetilde{A}(010)\kappa^2\Sigma^{(-)}$ and $\widetilde{X}(110) \rightarrow \widetilde{A}(010)$ repumpers), which

[9] Here ℓ, m_N, and m_S are the projections of the vibrational angular momentum onto the molecule axis and the projections of the rotational angular momentum N and electron spin S onto the lab Z axis, respectively.

prepares most of the molecules in a hyperfine mixture within $\widetilde{X}(010)(N = 1, J = 1/2^-)$ after approximately 2 photons are scattered. We push all detectable molecules, besides those in $\widetilde{X}(010)(N = 1)$, out of the trap using a resonant pulse of slowing light. Such pushout steps are regularly employed throughout the sequence to minimize population in impurity states.

Next, we optically pump molecules into the $(J = 1/2^-, F = 0)$ hyperfine state, using the technique described in chapter 7, though without $J = 3/2^-$ microwave pulses. The optical pumping efficiency is around 70%, and we can push the remaining population out of the trap afterwards (as described below). Next, we coherently transfer the population into different hyperfine states using microwave and RF pulses. The state preparation uses a different method for each state, described below.

Along with being in the highest hyperfine state in each manifold, we also require that the state is resolved across a range of electric fields from 0-600 V/cm, which allows us to prepare the state at any convenient electric field and then adiabatically ramp to the desired field for the collision measurement. To do this, we typically apply a small magnetic field, listed in Tab. 9.1. Finally, we also need to ensure that the state does not undergo level crossings when ramping the trap depth from the state prep trap depth (typically 250 μK) up to the collision depth (4.5 mK). Note that the trap is linearly polarized along the laboratory X axis (orthogonal to the electric and magnetic fields along Z). This causes it to mix states with different M_F quantum numbers, which is helpful for some of the state preparation transitions used below, but also slightly complicates the spectrum at high trap depth due to large avoided crossings. Stark plots for each of the hyperfine states used for collisions, at the appropriate B field and trap depth, are shown in Fig. 9.7.

To ramp to electric fields of 600 V/cm, we need to be able to apply voltage differences up to 2 kV across the MOT coils. We use the same setup described in the previous chapters to apply these voltages to the MOT coils,

Manifold	B (G)	Hyperfine state
a	1.8	$(J = 1/2^-, F = 0, m_F = 0)$
b	2.9	$(J = 3/2^-, F = 2, m_F = 2)$
c	2.9	$(J = 3/2^-, F = 2, m_F = 1)$
d	0	$(J = 1/2^+, F = 0, m_F = 0)$
e	2.0	$(J = 3/2^+, F = 2, m_F = 0)$
f	1.8	$(J = 3/2^+, F = 2, m_F = 2)$

Table 9.1: Magnetic field and hyperfine state used for each collision manifold in the experiment.

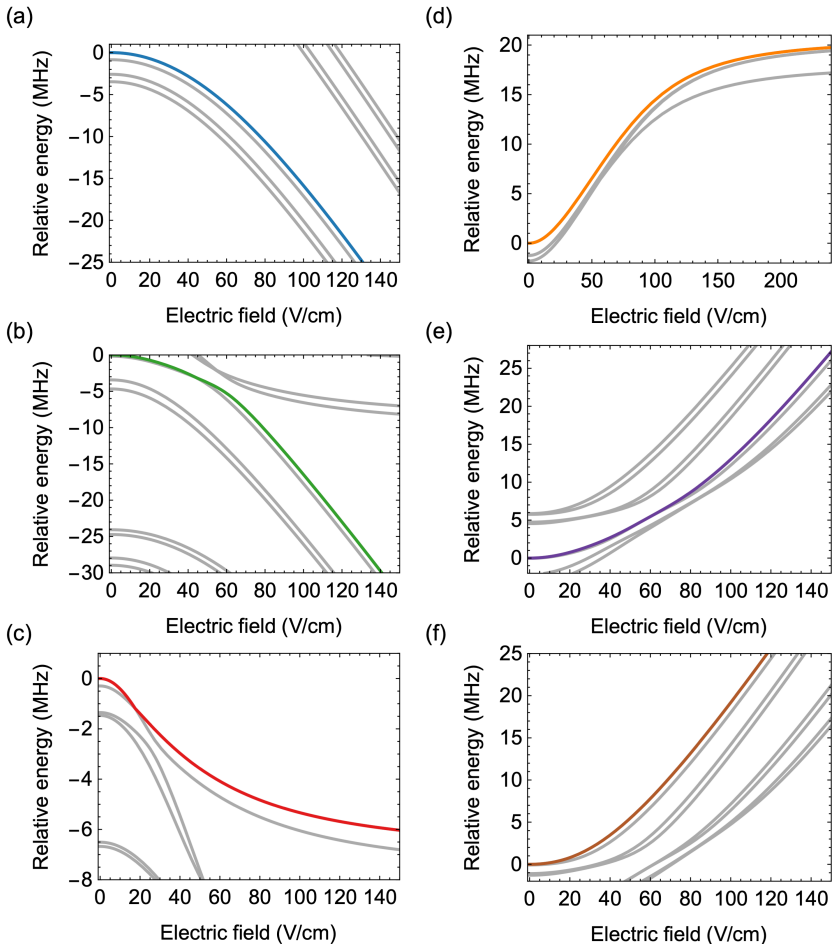

Figure 9.7: Stark plots of hyperfine states used for collision data in the a-f manifolds (panels (a)-(f)). The target hyperfine state is the highlighted curve, and energies for each plot are referenced to the energy of the target state at $E = 0$ V/cm. For these plots, the trap depth 4.5 mK, and the magnetic field is as listed in Tab. 9.1 for the target state.

but we replaced the 500 V supply with a 2 kV supply (Kepco BHK 2000-0.1MG) for these experiments.[10] The microwave and RF setups are also substantially unchanged from what was described in chapters 7 and 8, with the microwaves being linearly polarized along X, and the RF being linearly polarized along Z. To apply variable magnetic fields, we use a small homemade current amplifier (maximum current ∼3A) connected to small bias coils (magnetic field at the molecules of approximately 1 G/A) wound around the chamber. These are the same coils that were used for the previous experiments, except that previously we used a fixed-current power supply that could be switched on and off but not ramped during the sequence. The magnetic field and electric field are aligned in the same direction (laboratory Z axis). As in previous work, we turned off ion gauges, used an ion sweeper, and applied UV light to stabilize electric fields. We also used active compensation to stabilize the magnetic field against long term drifts. These were meant to improve the day-to-day repeatability of the state preparation.

Preparing the a and f states

To prepare the a and f states, we drive RF π pulses between the $(N = 1, J = 1/2^-, F = 0) \leftrightarrow (N = 1, J = 3/2^+, F = 2, m_F = 2)$ states at $E = 0$ V/cm and $B = 1.8$ G. Because this transition is only allowed by tensor AC Stark shifts (which mix states with $\Delta M_F = \pm 2$), we use a relatively high trap depth of ∼960 μK when driving this transition. Rabi oscillations on this transition are shown in Fig. 9.8. The typical π pulse efficiency is around 90%. For the a state, we drive a π pulse up to f (which is dark to the detection lasers), then push out all detectable molecules with a pulse of resonant slowing light, and then drive a second π pulse back down to a.

[10] The voltage noise from this supply is 4x worse, but this is not important since we don't need long coherence times for the collision measurements.

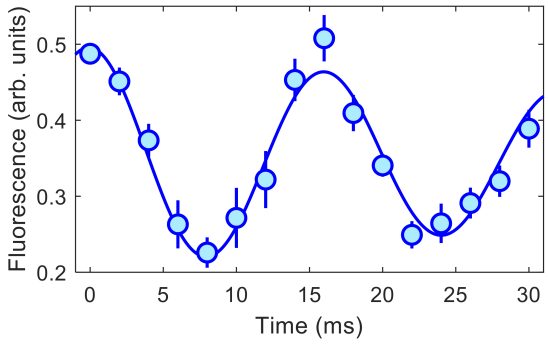

Figure 9.8: Rabi oscillations between the a and f states, at a magnetic field of 1.8 G and an RF frequency of 71.87 MHz.

This process is necessary to maximize the purity of the prepared state, by pushing out molecules that were not originally optically pumped into the correct state. For the f state, we apply a π pulse up and push out, but then leave the molecules in the upper state.

After the collision hold time, we reverse this process, being sure to apply another pushout pulse to remove molecules that may have appeared in bright states during the hold time. For the a state, we apply a π pulse up to f, then push out, then drive back down to a, which can be repumped and detected. For the f state, we simply push out and then drive down to a before detecting.

Preparing the b state

To reach the b state, we use two 40 GHz microwave transitions via $N = 2$, since direct RF transitions from a to b are electric dipole forbidden. This also allows us to shelve the molecules in a dark state ($N = 2^+$) to so that we can remove imperfectly prepared molecules from the trap. As seen in Fig. 9.7, there is a significant avoided crossing below around 60 V/cm, so we will only study the b state at higher fields. (At zero field, the b and c manifolds both become $J = 3/2^-$, so the zero-field collision rate will be determined by c state measurements.)

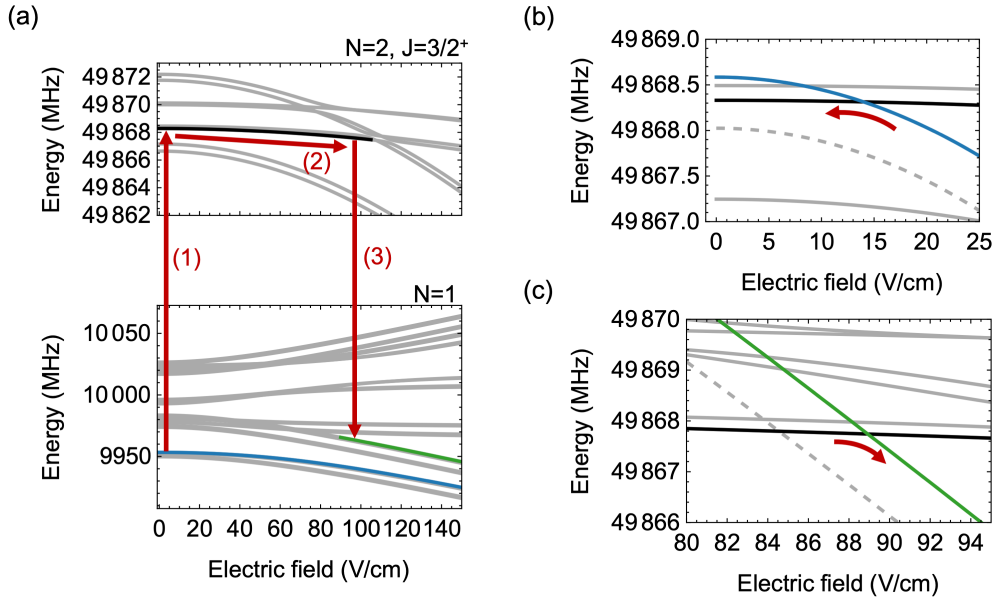

Figure 9.9: Preparation of the b state for collision measurements. (a) Illustration of the complete sequence. After optical pumping into $F = 0$ (blue state), we adiabatically transfer population into $(N = 2, J = 3/2^+)$ (black) around $E = 10$ V/cm (step 1). Next, we push out the remaining molecules in bright states, and ramp the electric field to approximately 90 V/cm (step 2). Finally, we transfer population back down to the b state (green) via another adiabatic sweep (step 3). (b) Adiabatic passage from $(N = 1, J = 1/2^-, F = 0)$ (blue) to $(N = 2, J = 3/2^+, F = 2, m_F = 1)$ (black). Solid black and grey curves are $N = 2$ state energies, while blue and dashed curves are dressed $N = 1$ state energies, i.e. the bare energy plus that of a 39915 MHz microwave photon. The microwave coupling opens up an avoided crossing between the two states (not shown), which allows us to transfer from the blue to black curve by sweeping the electric field across resonance. In the experiment, we sweep the electric field from 25 V/cm down to 0 V/cm. (c) Adiabatic passage from $(N = 2, J = 3/2^+, F = 2, m_F = 1)$ (black) to $(N = 1, J = 3/2^-, F = 2, m_F = 2)$ (green). Dashed and green curves are $N = 1$ states dressed by a 39902 MHz microwave photon. In this case, we ramp the electric field up from 87 V/cm to 92 V/cm. All plots in this figure are at a magnetic field of 2.9 G and a trap depth of 260 μK)

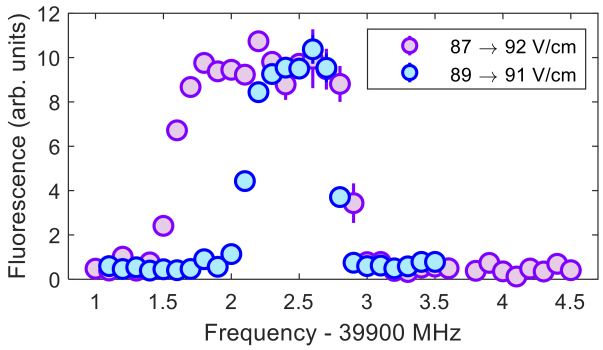

Figure 9.10: Spectroscopy of the "upleg" adiabatic passage transition from $(N = 1, J = 1/2^-, F = 0) \rightarrow (N = 2, J = 3/2^+, F = 2, m_F = 1)$, for two different electric field sweep ranges. The electric field sweep is linear and 1 ms in duration.

The state preparation protocol is illustrated in Fig. 9.9. We begin by turning on a 2.9 G magnetic field, then transfer population from $(N = 1, J = 1/2^-, F = 0) \rightarrow (N = 2, J = 3/2^+, F = 2, m_F = 1)$[11] via adiabatic passage, by adiabatically sweeping the electric field across resonance in the presence of microwave radiation (Fig. 9.9).[12] Spectroscopy of this transition is shown in Fig. 9.10.

Next, we push the remaining molecules in detectable states out of the trap using a resonant pulse of slowing light (note that $(N = 2, J = 3/2^+)$ is dark to the detection lasers, so correctly prepared molecules remain in the trap). After the pushout, we ramp the electric field to approximately 90 V/cm, and then use another ARP electric field sweep to transfer population down to the b state $(N = 1, J = 3/2^-, F = 2, m_F = 2)$.

Once in the b state, we can ramp the electric field anywhere from approximately 90-600 V/cm without encountering a level crossing, ramp up the trap depth, and measure collisional loss as a function of hold time. After

[11] Hyperfine states are significantly mixed at this magnetic field, so F is not a good quantum number. We label these states by their dominant F component at 2.9 G, but in reality the $(F = 2, m_F = 1)$ excited state correlates to $(F = 1, m_F = 1)$ at zero field.

[12] We will sometimes also refer to such a sweep as adiabatic rapid passage (ARP), or a Landau-Zener (LZ) sweep. See Ref. [321] for details.

the collision hold, we push out molecules in all states except $\widetilde{X}(010)(N = 1)$, then detect.[13]

Preparing the c state

As seen in Fig. 9.7, the c state undergoes a level crossing near 20 V/cm. Therefore, we prepare the state one way for 0 V/cm collision measurements, and a different way for all fields above around 50 V/cm. In both cases, we use a similar approach to the b state. We start by driving the same "upleg" microwave transition from $(N = 1, J = 1/2^-, F = 0)$ to $(N = 2, J = 3/2^+, F = 2, m_F = 1)$ at 2.9 G via an ARP electric field sweep, then push all detectable molecules out of the trap. Next, for the 0 V/cm data, we adiabatically transfer population down to the c state $(N = 1, J = 3/2^-, F = 2, m_F = 2)$ by using a 1 ms electric field sweep from 0→15 V/cm with microwaves at 39885.35 MHz. For collision data at higher fields ($E \gtrsim 50$ V/cm), we instead transfer population down to the c state ($N = 2, J = 3/2^-, F = 2, m_F = 1$ at these fields) by sweeping the electric field from 70→90 V/cm at a microwave frequency of 39891 MHz. As for the b state, after the collision hold we reverse the process in order to shelve the c state molecules and push any other detectable molecules out of the trap before imaging.

Preparing the d state

To prepare molecules in the d state, we again use two microwave transitions via $N = 2$.[14] This time, however, we need to deliberately apply an electric field to mix parity (since the a and d states have opposite parity at zero field).

[13] Note that the optimal way to do this would have been to shelve the molecules back into $N = 2^+$, then push out, then unshelve the molecules before detecting. However, it is unlikely that significant population builds up in impurity states in the bending mode during the collision hold.

[14] Even though the d state has opposite parity from the initial a state, our target state is also $F = 0$, so the direct RF transition is not dipole allowed.

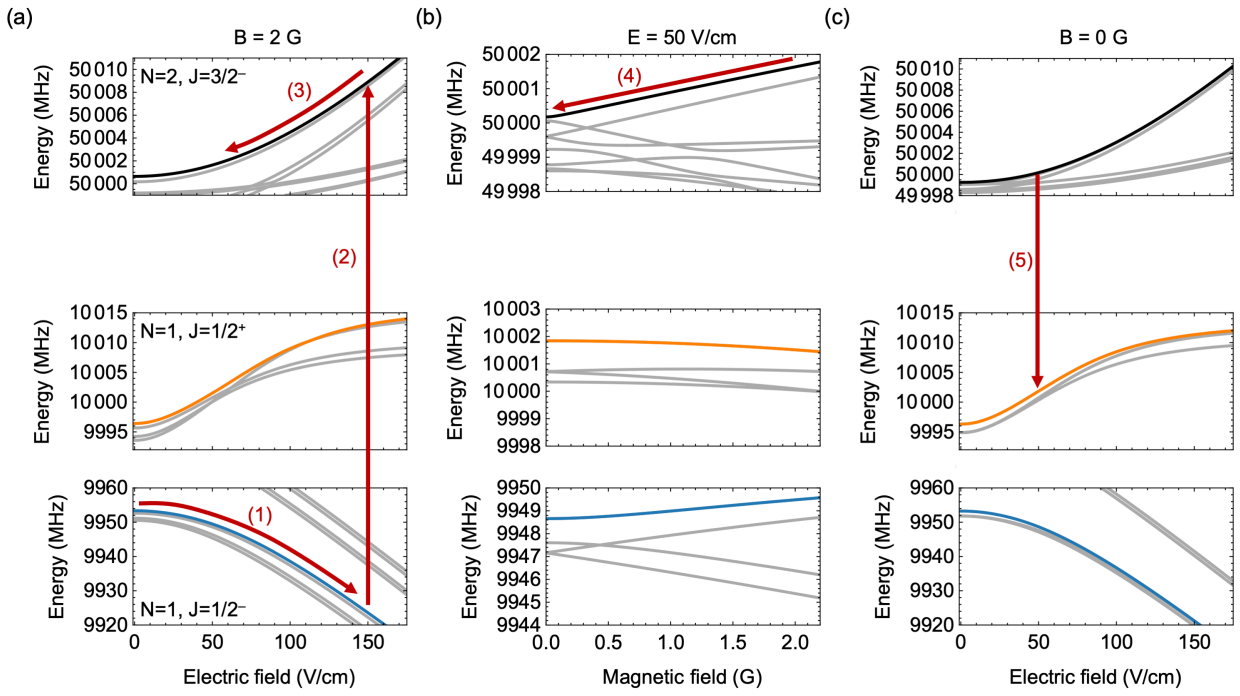

Figure 9.11: Preparation of the d state for collision measurements. (a) At a magnetic field of 2 G, we ramp the electric field to 150 V/cm (step 1) and drive a transition (via ARP) to $(N = 2, J = 3/2^-)$. (step 2) We then ramp the field down to 50 V/cm (step 3). (b) The magnetic field is ramped down to 0 G at an electric field of 50 V/cm (step 4). (c) We drive another microwave transition (via ARP), down to the d state at 50 V/cm and 0 G (step 5). All steps are performed at a trap depth of approximately 260 μK.

The state preparation procedure is shown in Fig. 9.11. The first transition is up to $(N = 2, J = 3/2^-)$, and we need an electric field to mix parity to make this transition electric dipole allowed, as well as a magnetic field to resolve magnetic sublevels. Therefore, we turn on a 2 G magnetic field and ramp the electric field up to approximately 150 V/cm with population in $(N = 1, J = 1/2^-, F = 0)$. We then use adiabatic passage to transfer population to $(N = 2, J = 3/2^-, F = 1, m_F = -1)$ (microwave frequency 40085.9 MHz, 1 ms sweep from 148.2 V/cm to 151.8 V/cm). Next we need to turn off the magnetic field, since at our initial 2 G field the d state crosses other hyperfine levels near 100 V/cm (see Fig. 9.11(a)).[15] Unfortunately, at 150 V/cm the $m_F = \pm 1$ states are nearly degenerate in the upper state, so we first ramp the electric field down to 50 V/cm, then ramp the magnetic field down to 0 G. Finally, we drive a transition down to the d state $(N = 1, J = 1/2^+, F = 0)$ using ARP (39999.5 MHz microwaves, 1 ms electric field sweep from 45.6 V/cm to 54.0 V/cm).

Once in the d state, we need to push out molecules that were not successfully optically pumped or transferred (we haven't yet done that in this sequence). Therefore, we ramp the electric field to 0 V/cm, where the d state becomes $J = 1/2^+$, which isn't detectable. We can then apply a pushout pulse to remove molecules left in bright states.

After the collision hold, we ramp the electric field to 0 V/cm, apply another 1 ms pushout pulse, and then use ARP to transfer molecules back to $N = 2, J = 3/2^-$, where they can be detected.

Preparing the e state

The e state undergoes significant avoided crossings below around 90 V/cm (Fig. 9.7(e)), and at zero field is the same as the f state. Therefore, we only need to prepare the e state at fields above 90 V/cm.

[15] In contrast, at 0 G the d state $(N = 1, J = 1/2^+, F = 0)$ has no level crossings, as shown in Figs. 9.7(d) and 9.11(c).

We start the same way as for the d state, using ARP to populate $(N = 2, J = 3/2^-, F = 1, m_F = -1)$ at $E = 150$ V/cm and $B = 2$ G. Next, we ramp the electric field down to 0 V/cm and apply a pushout pulse for all detectable states except $\widetilde{X}(010)(N = 2)$ (which is where our population is shelved). Next, we ramp the electric field back up to approximately 100 V/cm (keeping the magnetic field at 2 G), and drive an ARP transition down to the e state $(N = 1, J = 3/2^+, F = 2, m_F = 0)$ (39971.0 MHz, 1 ms sweep from 96 V/cm to 105 V/cm).

After the collision sequence, we repump population from $N = 2$ into $N = 1$,[16] then drive an ARP transition back up to $N = 2$, ramp down the electric field, and push out all detectable molecules except those in $\widetilde{X}(010)(N = 2)$. We then repump the molecules in $N = 2$ and detect.

9.5.2 Background collisions due to molecules in dark states

As discussed in chapter 6 and Ref. [44], blackbody radiation (BBR) and spontaneous, radiative decay processes redistribute molecular population into different vibrational and rotational states on timescales of hundreds of ms for CaOH. We saw effects of this in prior experiments, where there was typically background population in the final image that we could not get rid of by depleting all detectable molecules earlier in the experimental sequence. This suggests that after the ODT is loaded, molecules that were initially in bright states are transferred into dark states, sit there for a while during the experimental sequence, but then return to another bright state before the final molecule image.[17] In our spin precession and optical tweezer experiments (chapters 7 and 8) these effects were relatively unimportant, since we were only interested in single-molecule physics. However, background molecules in dark states present a more significant problem in the context of the collision measurements, since

[16] This is done so that we can push out any molecules that had accumulated in $N = 2$ during the collision sequence.

[17] For purposes of this section, "bright" states are those states addressed by our optical cycling and repumping lasers, and "dark" states are all others (including unaddressed rotational and vibrational levels).

they can still collide with molecules in bright states, causing spurious collisional loss. We therefore attempted to minimize the effect of BBR dynamics as much as possible.

One effect we noticed early on was that a significant contribution to background population is from molecules that were left in excited vibrational states after optical cycling, either (1) in a bright vibrational state that quickly decays to a dark state or (2) in dark vibrational states due to our finite photon budget. The first issue can be mitigated by applying a short repumping pulse after turning off optical cycling light, which prevents molecules from being left in excited bright vibrational states for too long. The second problem can only be mitigated by cycling as few photons as possible while in the trap. As an example, we load the ODT using 20 ms of single-frequency (SF) cooling light. Assuming a typical SF scattering rate of 50 kHz and a photon budget of 14000 photons, this means that approximately 7% of molecules are pumped into dark vibrational states during loading. Another ∼1-2% are lost to dark states during our 3-5 ms initial ODT image. Molecules in these dark vibrational states (e.g. $\widetilde{X}(220)$, $\widetilde{X}(040)$) can collide with molecules in bright states, and some will also decay over experimental timescales into (possibly bright) lower-lying vibrational levels. Fig. 9.12 shows evidence for these effects occurring in the ODT.

On top of these effects that arise from photon cycling, there are other effects that occur in the dark, even if we had not populated excited vibrational levels. For instance, after loading the trap, molecules initially in $\widetilde{X}(000)(N = 1^-)$ can be excited by BBR to positive-parity states in $\widetilde{X}(010)$ or $\widetilde{X}(100)$, which are not detectable. After some time in these states (during which they cannot be optically addressed, and therefore cannot be pushed out of the trap), they can return to a detectable state (e.g. $\widetilde{X}(000)(N = 1)$, $\widetilde{X}(110)(N = 1^-)$, etc.), or collide with a detectable molecule causing excess loss.

A final effect that is sequence-specific is that BBR dynamics can make the effective single-molecule lifetime look very different depending on the populated state. For instance, when molecules are prepared in a negative

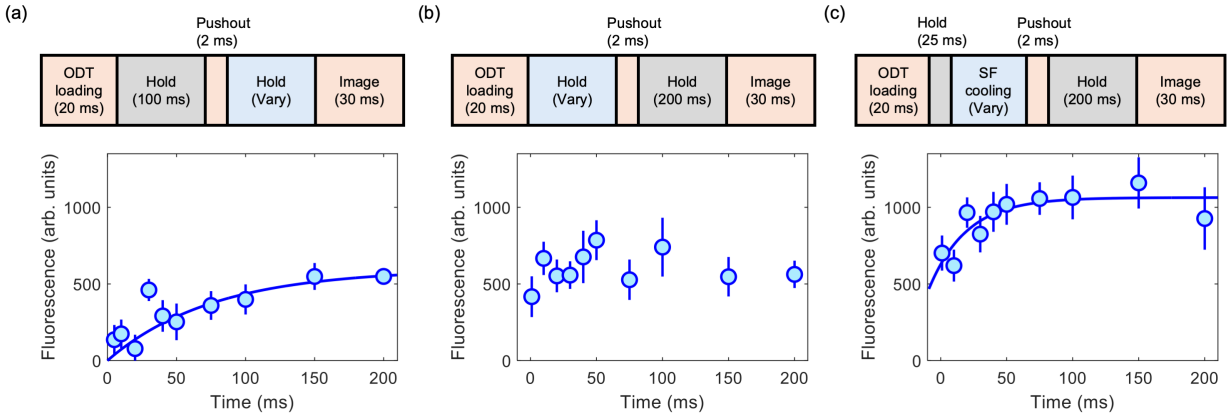

Figure 9.12: Characterizing molecular population in dark rovibrational states. (a) Revival of population in detectable states. Here we load the ODT, wait 100 ms (during which time the rovibrational state populations begin to thermalize), and then push all detectable molecules out of the trap. We observe a recovery of detectable signal over ∼100 ms after the pushout as dark molecules return to bright states. (b) Accumulation of background molecules when held in the dark. Here, molecules are prepared in $\widetilde{X}(000)$ in the ODT and held for a variable time. Detectable molecules are then pushed out of the trap, and the molecules are imaged after a 200 ms wait for population to return to bright states. In this case there is no significant increase in detectable population vs. wait time. This shows that a significant number of molecules are already in dark states after ODT loading, and that BBR dynamics after loading do not significantly increase the number of molecules that survive the pushout. (c) Accumulation of dark molecules during SF cooling. Here, we apply SF cooling for a variable duration, then push out and wait for dark molecules to return to bright states. We see that SF cooling significantly increases the number of dark state molecules that survive the pushout. For comparison, the signal is ∼10000 counts after a 200 ms hold with no pushout.

parity level in the bending mode (e.g. the a, b, and c states at zero field), any BBR decay from this state will be to a positive-parity, undetectable state (e.g. $\widetilde{X}(000)(N = 0, 2)$). Therefore, the lifetime of the detectable molecules will look very similar to the true bending mode lifetime, ∼350 ms. On the other hand, when molecules are prepared in a positive-parity state in the $N = 1$ bending mode (d, e, f at zero field), nearly *all* of the decays will be to detectable states (primarily transitions from $\widetilde{X}(010)(N = 1^+)$ to $\widetilde{X}(000)(N = 1^-)$, $\widetilde{X}(02^00)(N = 1^-)$, $\widetilde{X}(02^20)(N = 2^-)$, and $\widetilde{X}(110)(N = 1, 2^-)$).[18] In this case, the molecule lifetime will look more like that of the ground vibrational state. Finally at high electric fields when parity is mixed in the bending mode, there are a mix of BBR transitions to bright and dark states, giving an effective single-molecule lifetime somewhere in between. To account for this effect, we added pushout pulses for all molecules in bright states (except the desired collision state) immediately before and after the collision hold time. The first pushout helps maximize the fraction of trapped molecules that are in the intended collision state, and the final pushout ensures that nearly all of the detected molecules were in the collision state, rather than other bright states populated during the hold time.

To more quantitatively understand the effect of BBR dynamics on our collision measurements, we use the rate equation model from section 6.4 and appendix D to simulate the full experimental sequence (Fig. 9.13). This model is described in more detail in the supplemental material of Ref. [342] and in appendix D, and we benchmarked it against experimental data where we intentionally allowed more molecules to accumulate in vibrational dark states.

As seen in the model, around 80% of trapped molecules are in the correct state during the collision hold time. This is limited by (1) pumping into vibrational dark states during ODT loading and imaging (due to the finite

[18] Recall that the nominally allowed transitions (in the double harmonic approximation) are those that change a single vibrational quantum number by 1 while also obeying rotational angular momentum selection rules.

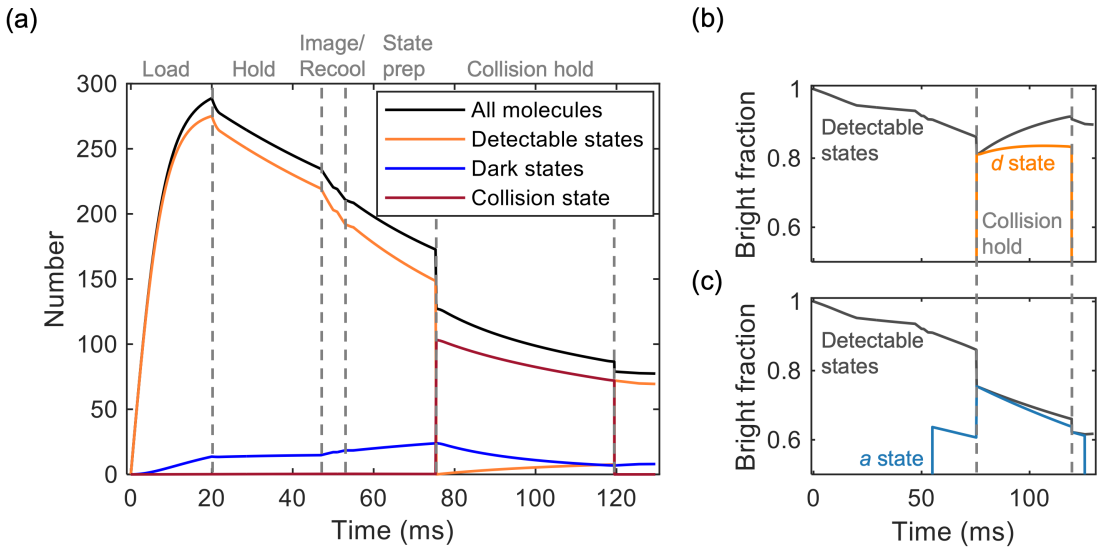

Figure 9.13: Rate equation model of dark-state population during the experimental sequence. (a) Modeled state populations during the sequence used for collisions in the d state at an electric field $\mathcal{E} = 0$. The total number of trapped molecules, the molecules in optically detectable states, the number in undetected (dark) states, and the number in the target collision state (d in this case) are plotted as a function of time after trap loading. (b) Fraction of molecules in detectable states and in the d state, for the d state collision sequence at $\mathcal{E} = 0$. (c) Fraction of molecules in bright states and in the a state during the a state collision sequence at $\mathcal{E} = 0$. Reproduced from Ref. [342].

photon budget) (2) finite hold times during state preparation (during which time BBR/spontaneous decay drives molecules from bright states into dark states) and (3) imperfect state preparation (primarily the ∼70% $F = 0$ optical pumping efficiency), which reduces the number of bright molecules but not the number of dark molecules. For the collision data, we were careful to minimize hold times in the trap, particularly once the molecules were in the bending mode. We also limit the collision measurement time to a maximum of 40 ms, to limit excess accumulation of molecules in undesired states. In the future, it will be necessary to improve the optical pumping efficiency (and either improve the photon budget or further reduce the number of scattered photons) to achieve better state purities.

Determining "background" collision rates

From the above, we know that not all molecules are prepared in the correct state. We model the effect of these molecules on the measured rate constants as follows. Suppose the molecules are imperfectly prepared in the target hyperfine state, such that the total number density n in the trap is the sum of the density of molecules in the target state, n_1, and that of molecules in impurity states, n_2. The rate equation describing two-body collisions of molecules in the target state is

$$\begin{aligned}\dot{n}_1 &= -k_{11}n_1^2 - k_{12}n_2n_1 = -\left(k_{11} + k_{12}\frac{n_2}{n_1}\right)n_1^2 \\ &\equiv -\left[k_{11} + k_{\text{bg}}(n_1, n_2)\right]n_1^2 \\ &\equiv -k_{\text{eff}}(n_1, n_2)n_1^2 \end{aligned} \tag{9.9}$$

where k_{11} is the loss rate constant for collisions between two molecules in the target state and k_{12} is the rate constant for collisions between a target molecule and an impurity molecule. We have rewritten the equation for $\dot{n}_1$ in terms of an effective collision rate, $k_{\text{eff}} = k_{11} + k_{\text{bg}}$, which is the effective, instantaneous two-body collision rate for molecules in state 1. In the experiment, we wish to measure k_{11} but have to contend with background collisions due to impurity molecules, described by the "background" rate constant k_{bg}. Even if collisions between molecules in the target state are fully suppressed ($k_{11} = 0$), we will measure a nonzero collision rate $k_{\text{bg}} = k_{12}n_2/n_1$. Generalizing to the case where there are many impurity states i, the background loss rate is a sum over all impurity states, $k_{\text{bg}} = \sum_i k_{1i}n_i/n_1$.

Molecules end up in background, impurity states due to rovibrational state redistribution from blackbody

radiation and spontaneous decay, and from losses to vibrational dark states during optical cycling. These effects are modeled using rate equations, as described above. For the single-state collision measurements, we estimate that $78(8)\%$ of molecules are in the target state during the collision hold time, and that the average collision rate between target molecules and impurity molecules is $\langle k_{1i} \rangle \approx 2.5(5) \times 10^{-10}$ cm^3 s^{-1}. This gives a background collision rate $k_{\mathrm{bg}} \approx 7(3) \times 10^{-11}$ cm^3 s^{-1}. This same background rate constant is also used for the temperature scans described below, since the background rate constants are assumed to be near the Langevin capture limit, which depends only weakly on temperature [376, 377].

For the hyperfine mixture data in Fig. 9.2 above, the state preparation is better since no optical pumping into a single hyperfine state is required and overall hold times are shorter. For these measurements, the rate equation model indicates that the background collision rates are $k_{\mathrm{bg},(000)} \approx 0.5(5) \times 10^{-11}$ cm^3 s^{-1} and $k_{\mathrm{bg},(010)} \approx 3(2) \times 10^{-11}$ cm^3 s^{-1} for $\widetilde{X}(000)$ and $\widetilde{X}(010)$, respectively.

Accounting for background collisions in measured rate constants

To account for background collisions, we subtract off the estimated k_{bg} from the measured rate and account for the corresponding error. In detail, we first fit the rate constant from the experimental data using eqn. 9.3, which has a mean value k_{meas} and statistical uncertainty (standard error) σ_{meas}. We then subtract off the estimated background collision rate to obtain a mean and standard error for the "corrected" collision rate:

$$k = k_{\mathrm{meas}} - k_{\mathrm{bg}}$$

$$\sigma \approx \sqrt{\sigma_{\mathrm{meas}}^2 + (k_{\mathrm{meas}}\sigma_n)^2 + \sigma_{\mathrm{bg}}^2}$$

where $\sigma_n = 0.25$ is the error in the density calibration and σ_{bg} is the error in k_{bg} (described above).

9.5.3 Other technical challenges

We encountered a number of technical issues in this experiment, due to the combination of long hold times, high trap depths, and high electric fields needed. (The background population described above was one of the major challenges.) We describe a few other issues here.

Single-molecule lifetime

In order to measure collision rates, we also need to know the single-molecule background lifetime. This was already known from previous work (expected to be approximately 350-400 ms from section 6.4 and Refs. [43, 44], limited by BBR and spontaneous decay). To be safe, we wanted to confirm that this lifetime still applied in the present experiment.

To measure the single-body lifetime, we loaded only a few molecules into the trap so as to (mostly) turn off collisions, then measured the survival as a function of time. As shown in Fig. 9.14, what we discovered was that at high trap depth, the lifetime of the collision hyperfine state was much shorter than expected. Moreover, the lifetime of a *single* hyperfine state was much shorter than the lifetime of *all* hyperfine states in the bending mode. Finally, we saw that this effect depended linearly on the trap depth.

These observations all point to the culprit being the ODT light driving Raman transitions between hyperfine states. From section 6.1.2, the Rayleigh scattering rate at our 4.5 mK trap depth is approximately 5 s^{-1}, with the Raman scattering rate being over an order of magnitude lower. Therefore, DC Raman scattering is likely not an issue. However, if there is intensity noise in the trap spectrum, it can resonantly drive transitions between

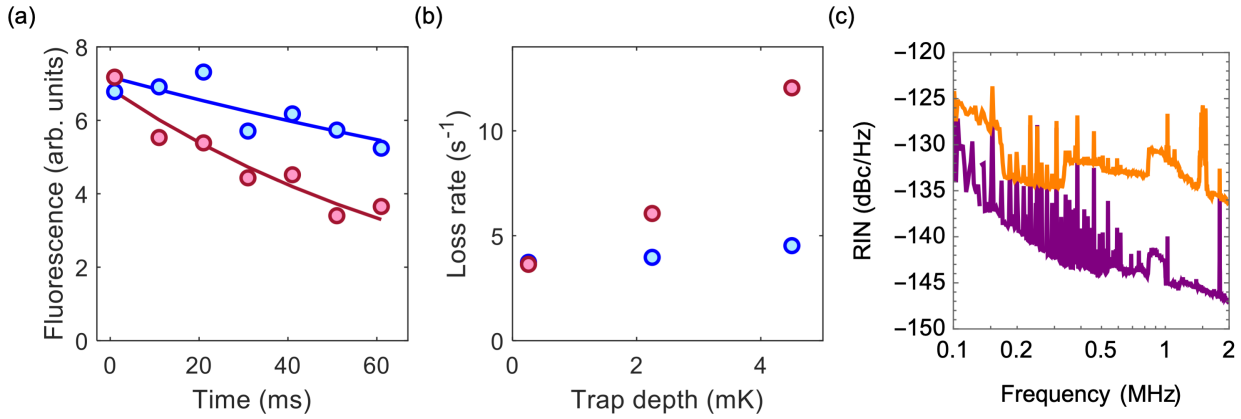

Figure 9.14: Raman transitions driven by ODT light with a noisy seed laser. (a) Molecule lifetime curves at 4.5 mK trap depth and low molecule number, for molecules initially prepared in the a state $(N = 1, J = 1/2^-, F = 0)$. The red curve is the lifetime detecting the a state only, and the blue curve is the lifetime detecting *all* molecules in the bending mode. The curves fit to lifetimes of ∼80 and ∼220 ms, respectively. We later confirmed that the extra population appears to be in other hyperfine states in $J = 1/2^-$. (b) Loss rate (1/lifetime) from the a state only (red points) and all detectable bending mode states (blue points) as a function of trap depth. (c) ODT RIN spectrum using a 1063 nm Thorlabs DBR seed (orange) and a 1064 nm RIO Orion seed (purple). Both seeds are amplified with a 50 W Nufern fiber amplifier. Switching to the RIO seed caused the curves in parts (a)-(b) to become identical.

hyperfine states. To see this, consider a three-level Λ system, following Refs. [380, 381]. The ODT laser couples hyperfine states $|1\rangle$ and $|2\rangle$ to excited state $|e\rangle$, where ω_{12} is the splitting between $|1\rangle$ and $|2\rangle$ in the absence of trap light, Δ is the single-photon detuning, and Ω_1 and Ω_2 are the Rabi frequencies. In the rotating frame, the Hamiltonian is

$$H/\hbar = \omega_{12}|2\rangle\langle 2| + \Delta|e\rangle\langle e| - \frac{\Omega_1}{2}|e\rangle\langle 1| - \frac{\Omega_2}{2}|e\rangle\langle 2| + \text{h.c.} \tag{9.10}$$

Adiabatically eliminating the excited state (when $\Delta \gg \Omega_1, \Omega_2$) gives an effective two-level Hamiltonian

$$H_{\text{TLS}} \approx \omega'_{12}|2\rangle\langle 2| - \frac{\Omega_{\text{eff}}(t)}{2}|1\rangle\langle 2| + \text{h.c.} \tag{9.11}$$

where ω'_{12} accounts for differential AC Stark shifts between states $|1\rangle$ and $|2\rangle$. The effective two-level Rabi frequency is

$$\Omega_{\text{eff}} = \frac{\Omega_1\Omega_2^*}{2\Delta} = \frac{\langle 1|\vec{d}\cdot\hat{\epsilon}|e\rangle\langle e|\vec{d}\cdot\hat{\epsilon}|2\rangle}{2\hbar^2\Delta}|\mathcal{E}(t)|^2 = \frac{\langle 1|\vec{d}\cdot\hat{\epsilon}|e\rangle\langle e|\vec{d}\cdot\hat{\epsilon}|2\rangle}{4\epsilon_0 c\hbar^2\Delta}I(t) \tag{9.12}$$

where $\mathcal{E}$ is the electric field amplitude, $\hat{\epsilon}$ is the polarization, and I is the intensity of the trapping laser. Therefore, if $I(t)$ has a frequency component oscillating at ω'_{12}, it can resonantly drive transitions between hyperfine states $|1\rangle$ and $|2\rangle$.

As shown in Fig. 9.14(c), we measured the relative intensity noise (RIN) spectrum of the ODT laser and found that it had significant RIN out to several MHz, which is sufficient to couple hyperfine states in the CaOH bending mode (splitting ∼1-2 MHz). We then switched the seed from a Thorlabs DBR to a RIO Orion module, which reduced the RIN by an order of magnitude at MHz frequencies. After making this switch, we no longer observed a difference between the single hyperfine state lifetime and the overall bending mode lifetime.

One challenge we encountered when measuring the single-body lifetime is that it is very difficult to entirely turn off collisions in our trap, especially since we want to measure at high trap depth to ensure there are no trap-induced losses. For instance, for the a state, the lifetime will be reduced from 350 to 300 ms even if only two molecules are loaded in the trap. However, we were able to confirm that the one-body lifetimes were consistent with the 350 ms expectation by taking data at low molecule numbers and accounting for these residual collision rates. We also note that the collision lifetimes in the high-density measurements are typically <100 ms, so the single-body lifetime barely affects the fitted collisional loss rates at the end of the day.

Effect of high electric fields

When applying high electric fields for long periods of time, we discovered that our microwave transition frequencies would significantly shift, as shown in Fig. 9.15. For instance, if we repeatedly run a sequence that at some point applies an electric field of 150 V/cm for 600 ms (as we would do during a long collision measurement), we find that the microwave transition frequencies measured at another point in the sequence shift by the equivalent of $\sim$1 V/cm compared to the case with no high field applied. After waiting a long time, however, the frequency returns to its original value. It therefore seems that the experiment has a residual "memory" of the high electric fields that were previously applied.

To see how long this "memory" lasts, we next check how long it takes for transition frequencies to recover after applying a 150 V/cm electric field continuously for 2 minutes. As shown in Fig. 9.15(b), we find that it takes more than five minutes for the microwave transition efficiency to recover when driving at the initial frequency.

Our model for this phenomenon is that when a large electric field is applied to the coils, the dielectric AlN material from which the MOT coil boards are made also experiences a large electric field (Fig. 9.15(c)). The dipoles in

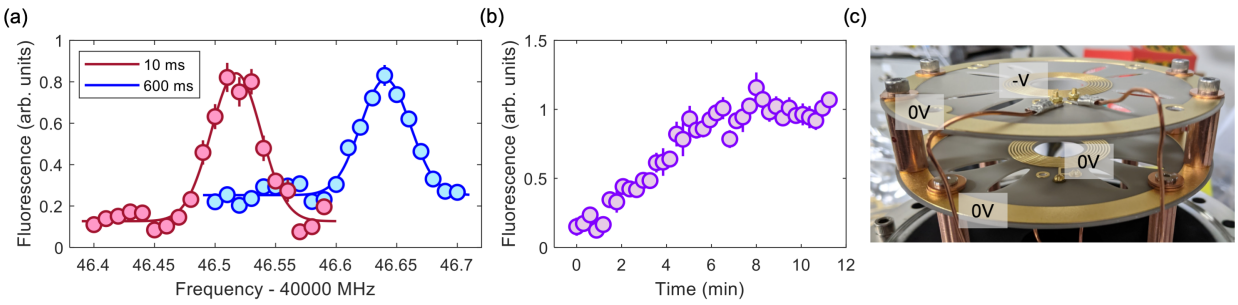

Figure 9.15: Electric field drift during long hold times at high field. (a) Measured frequency of the $(N = 1, J = 1/2^-, F = 0) \rightarrow (N = 2, J = 3/2^-, F = 2, m_F = 1)$ transition (at 2 G and 30 V/cm), after holding the electric field at 150 V/cm for 10 ms (red) or 600 ms (blue) every experimental shot (∼1.5 s total time per shot). The 120 kHz frequency shift corresponds to a ∼1 V/cm change in the electric field. (b) Molecule fluorescence when driving the transition at 40046.52 MHz as a function of time after applying an electric field of 150 V/cm for 2 minutes. (c) Photo of the MOT coils, with applied voltages labeled. Applying a voltage $-V$ to one of the coils while grounding the other one leads to an electric field $|E| = 0.3V$ on the molecules. The MOT coils boards are made of AlN (grey material).

the AlN align with the electric field, but have a time delay with a time constant of several minutes. This hysteresis in the response of the dielectric is well known, and is often referred to as "dielectric absorption" [382]. When the electric field is turned back off, the dipoles have a time delay before returning to their original, zero-field configuration, leading to the memory and slow recovery time of the residual electric field seen in the experiment.[19]

To account for this effect in the experiment, we need to ensure that the average electric field applied during each experimental shot is the same, despite the fact that we scan both the electric field and the collision hold time while taking data. To do this, we added an 80 ms "pad time" after the final molecule image in the sequence. During this time, we turn on an electric field whose value depends on the collision electric field and hold time used in that particular sequence.[20] Because the sequence length (∼1-2 s) is much shorter than the memory time of the

[19] Dielectric absorption is typically measured by applying voltage across a capacitor, then discharging it and disconnecting the contacts. Over time, a small voltage difference will reappear across the capacitor as the dielectric relaxes. We tried this with a single MOT coil board, looking at the voltage between the center coil and the ground plane on the outside, and observed a voltage reappear as expected.

[20] For instance, if no electric field was applied during the collision hold, the pad electric field will be 600 V/cm for 80 ms. If 600 V/cm was applied for 40 ms during the collision hold, the pad electric field will be 300 V/cm for 80 ms. Thus, the

MOT coils (∼minutes), making the average field constant in this way is sufficient to stabilize the state preparation.

9.5.4 Measured collision rates

To investigate the state and electric field dependence of CaOH-CaOH collisions in parity doublet states, we prepare the molecules in single quantum states within the $N = 1$ rotational manifold in the bending mode as described above, and then tune the interaction potential by applying an external electric field. The structure of this manifold is shown as a function of applied electric field in Fig. 9.16(a). At zero field, there are four well-resolved levels ($J = 1/2^-$, $J = 3/2^-$, $J = 1/2^+$, and $J = 3/2^+$ in order of increasing energy), split by the spin-rotation and ℓ-type parity doubling interactions. Under the presence of an applied electric field E, the opposite-parity states are mixed. For $E \gtrsim 150$ V/cm, the structure splits into 6 well resolved manifolds, which we label a-f in order of increasing energy [131]. In this "high-field" regime, the molecular dipole moment is aligned in the laboratory frame. Note that each manifold contains several hyperfine states, split by energies on the order of $k_B \times 100\ \mu$K, due to the hydrogen nuclear spin.

We prepare molecules in single quantum states as described earlier in this chapter. We measure collision rates over a range of electric fields $E = 0 - 600$ V/cm by recording the number of molecules vs. hold time at high density and fitting to eqn. 9.3 (Fig. 9.16(b)). To minimize redistribution of population into impurity states driven by blackbody radiation (BBR) [44], we record data only for hold times $\lesssim$40 ms, which is significantly less than the BBR-limited bending mode lifetime. We detect only the molecules in the target collision state, and push most of the molecules in other states out of the trap at several points during the sequence. Approximately 80% of the

total [electric field]×[hold time] is kept constant across scan parameters.

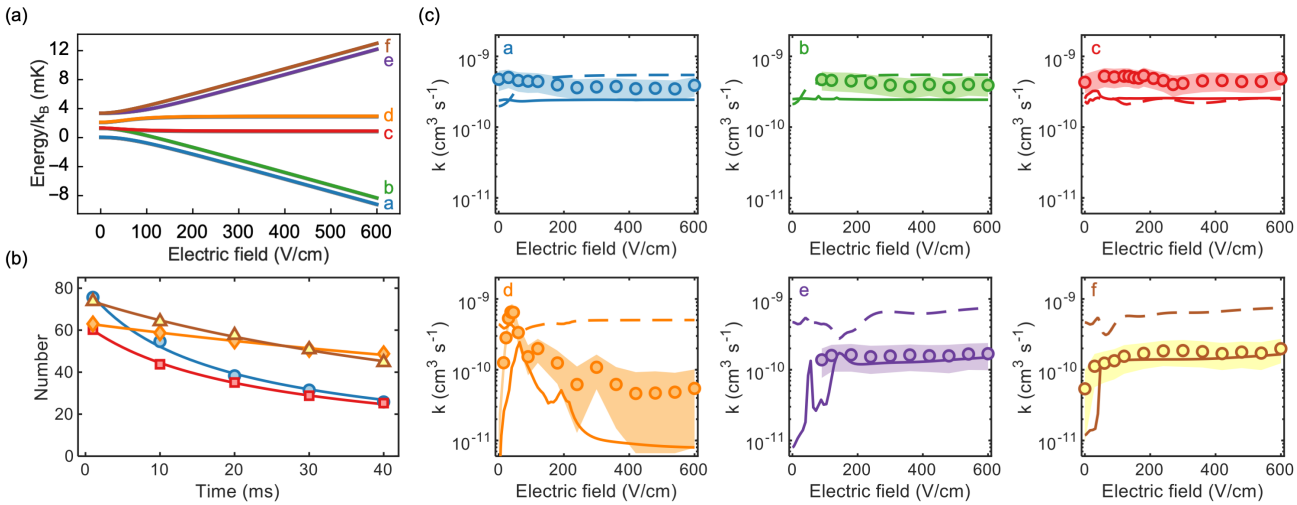

Figure 9.16: Electric field dependence of CaOH-CaOH collisions in the bending mode. (a) Single-molecule energies in the $\widetilde{X}(010), N = 1$ manifold of CaOH. At electric fields $\mathcal{E} \gtrsim 150$ V/cm, opposite parity-doublet states are mixed and the molecular dipole moment is aligned in the laboratory frame. In this regime, the structure separates into six manifolds, labeled a-f. (b) Collision lifetime curves for molecules prepared at $\mathcal{E} = 0$ in a single hyperfine state in the a (blue circles), c (red squares), d (orange diamonds), and f (brown triangles) manifold. Solid curves are fits to the rate equation model used to extract the two-body loss rate constant k. (c) Measured collisional loss rate constants k vs. electric field for single hyperfine states in the a-f manifolds. The shaded regions denote the experimental uncertainty (standard error), which accounts for statistical error, systematic uncertainty in the molecule number density, and uncertainty in the background loss rate from imperfect state preparation. Solid curves are calculated loss rate coefficients assuming universal short range loss, and dashed curves are the calculated elastic collision rate coefficients. Reproduced from Ref. [342].

molecules in the trap during the collision time are prepared in the correct hyperfine state, with the remaining molecules being in undetectable rovibrational states due to BBR- and laser cooling-induced losses (as discussed above).

Fig. 9.16(c) shows measured collisional loss rate constants for the a-f manifolds as a function of applied electric field. Experimental uncertainties are denoted by shaded regions. At high collision rates, the error is dominated by uncertainty in the trapped molecule density (see above). At low collision rates, the dominant uncertainty is from undesired collisions with molecules trapped in dark rovibrational states. The effective rate of these "background" collisions is estimated to be $k_{\mathrm{bg}} \approx 7(3) \times 10^{-11}$ cm^3 s^{-1} (see above), and likely depends on the state and electric field. We subtract k_{bg} from the fitted rate constants to obtain the rates shown in Fig. 9.16(c), with a corresponding uncertainty accounted for in the shaded region.

We also perform close-coupling calculations of the rate coefficients accounting for long-range dipolar interactions and universal short-range loss, at a collision energy $E_c = k_B \times 100\ \mu$K. Details are provided in Ref. [342]. Calculated loss rate coefficients k are plotted as solid curves in Fig. 9.16(c), and the corresponding elastic collision rate coefficients k_{el} are shown as dashed curves. We observe generally good agreement between the measurements and the calculations, within experimental uncertainty.

9.5.5 Discussion

Several general features are apparent in the data of Fig. 9.16(c). The collision rates vary primarily over the electric field range $\mathcal{E} = 0-150$ V/cm, then plateau at higher fields once the molecules are aligned in the laboratory frame. The a-c manifolds have higher collisional loss rates than the d-f states at nearly all fields. The d manifold exhibits a peak in the collision rate around $\mathcal{E} \approx 40$ V/cm, with much lower collision rates on either side, at $\mathcal{E} = 0$ V/cm

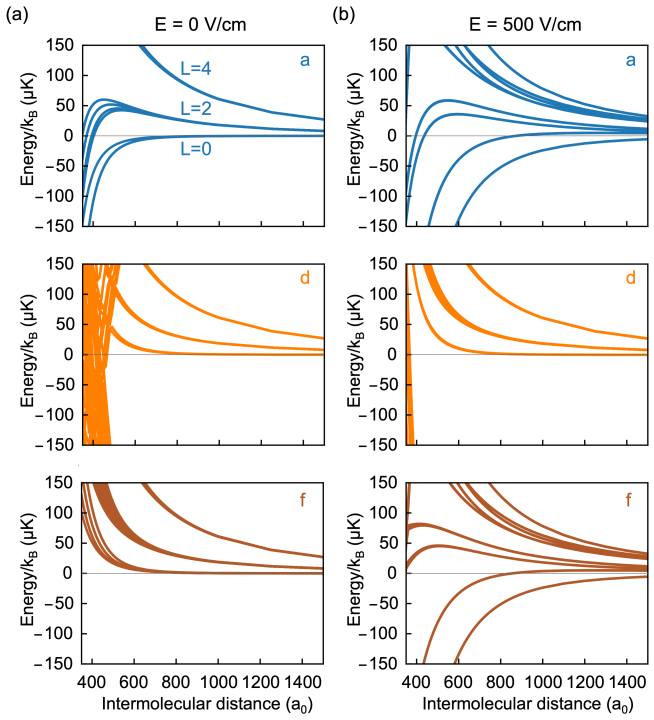

Figure 9.17: Adiabatic dipolar interaction potentials for the a, d, and f states at (a) $\mathcal{E} = 0$ V/cm and (d) $\mathcal{E} = 500$ V/cm. The first three even partial waves ($L = 0, 2, 4$) are shown. To reduce the density of states and improve visual clarity, these calculations do not include hyperfine structure, applied magnetic fields, or AC Stark shifts, none of which significantly influence the long-range interactions or qualitatively alter the shape of the potentials. Reproduced from Ref. [342].

and $\mathcal{E} \gtrsim 300$ V/cm. The rate constants vary by over an order of magnitude across the range of states and electric fields studied.

The observed collisional losses arise from two distinct effects: inelastic relaxation driven by dipolar interactions at long-range [375], and short-range losses (e.g. chemical reactions), which occur with high probability if the molecules are allowed to collide at short distance ($\lesssim 30\ a_0$). To help develop an intuition for these effects, in Fig. 9.17 we plot calculated adiabatic molecule-molecule interaction potentials for the a, d, and f manifolds at $\mathcal{E} = 0$ V/cm and $\mathcal{E} = 500$ V/cm.

At $\mathcal{E} = 0$ (Fig. 9.17(a)), molecules in the a state (as well as b and c) experience an attractive potential $-C_6/r^6$, with C_6 arising from second-order dipolar mixing with opposite parity states higher in energy, as described above. In contrast, the d, e, and f manifolds reside in the higher parity manifold, whereby the same mixing induces a repulsive C_6/r^6 interaction. The repulsive wall set up in the latter potentials prevents CaOH molecules at $T \approx 100\ \mu$K from reaching separations less than a few hundred Bohr radii (a_0), effectively shutting off short-range losses. The measured collisional loss rates for the d and f manifolds at zero field are $\gtrsim 5 - 10\times$ lower than the corresponding rates in the a and c manifolds. The remaining collisional loss in these states is from inelastic relaxation to the negative parity states, driven by dipolar interactions at long range [375].

At $\mathcal{E} = 500$ V/cm (Fig. 9.17(b)), opposite-parity states are mixed by the electric field, causing the molecular dipole moment to be aligned in the laboratory frame. In the a, b, e and f states, the dipole moment is aligned (or anti-aligned) with the applied electric field. These states therefore experience first-order dipolar interactions that qualitatively alter the interaction potentials. Collisional loss rates in these states are relatively high, with contributions from both short-range and inelastic losses. By contrast, molecules in the c and d states have zero lab-frame dipole moment even at $\mathcal{E} = 500$ V/cm, meaning that their interactions arise from second-order dipolar mixing.

The dominant mixing for molecules in the d state is with lower-energy channels, so these molecules experience a repulsive C_6/r^6 potential (the opposite is true for molecules in the c state). Molecules in the d state are therefore shielded from short-range loss at high field, with the remaining losses dominated by long-range dipolar relaxation.

In the intermediate-field range, loss rates for the e-f states rise rapidly, on the electric field scale over which the dipoles become polarized. This circumstance can be seen qualitatively in two effects, both given in terms of the dimensionless parameter $\beta \sim 2\langle d\mathcal{E}\rangle/2q_\ell$, where $2q_\ell$ is the ℓ-doublet splitting and $\langle d\mathcal{E}\rangle$ represents the matrix element of the Stark Hamiltonian between opposite parity states of the zero-field molecular Hamiltonian [125]. In the CaOH bending mode, $\beta \approx 1$ occurs at an electric field $\mathcal{E} \approx 60$ V/cm.

The first effect of turning on the electric field involves increasing the long-range, inelastic coupling to other scattering channels. This induced coupling scales as $\beta/(1+\beta^2)(1/r^3)$ [125] and is the dominant collisional loss mechanism in the electric field range $\beta \lesssim 1$. The second effect involves the direct long-range interaction. Even when the dipoles are partially or fully polarized, the dipole-dipole interaction vanishes in the s-wave channel. Nevertheless, second-order dipolar coupling to the d-wave channels leads to an effective interaction $-C_4/r^4$, with $C_4 \propto (\beta^2/(1+\beta^2))^2$ [125]. Thus as the molecules become polarized, the effective attraction in this channel grows, encouraging greater incoming flux to reach short range and react chemically. This effect becomes significant at higher fields ($\beta \gtrsim 1$), at which point the direct interaction strength C_4 approaches a constant value while the inelastic coupling falls off as $1/\beta$ (due to the increased spacing between Stark manifolds).

The calculations and measurements for the d-f states indeed show that inelastic relaxation initially dominates over short-range absorption, causing collisional loss rates to rise rapidly at fields $\mathcal{E} \sim 0 - 60$ V/cm as the dipoles become polarized. At higher fields $\mathcal{E} \gtrsim 150$ V/cm, the inelastic rate for the e-f states decreases while the short-

range loss rate grows, and these two rates eventually become comparable. For the d state at high field, inelastic relaxation remains the dominant effect due to the repulsive barrier discussed earlier. Plots showing the calculated contributions of inelastic and short-range losses to the total loss rate can be found in Ref. [342].

At intermediate fields, the d state experiences high collisional loss rates due primarily to long-range inelastic relaxation, which may be enhanced by level crossings between collision channels in this range of fields [342]. The result of these many curve crossings appears to be a rich resonant structure revealing quasi-bound states at intermediate separations r. Analysis of these resonances remains a task for future investigations.

The temperature of the molecules in our experiment is well above the dipolar energy scale $E_d/k_B \sim 1\ \mu$K [378] (but significantly below the parity-doublet energy $2q_\ell/k_B \approx 2$ mK), suggesting that further cooling may improve the ratio of elastic to inelastic collisions. Fig. 9.18 shows measured and calculated rate constants as a function of temperature for molecules prepared in (a) the f state at $\mathcal{E} = 0$ and (b) the d state at $\mathcal{E} = 500$ V/cm, both of which are shielded from short-range loss but undergo dipolar relaxation at long range. To vary the molecule temperature in the experiment, we adiabatically lower the ODT trap depth, which cools the molecules and reduces the density. Note that the decreased AC Stark shifts at lower trap depth could also cause small changes in the rate constant. The calculations in Fig. 9.18 are carried out at the highest trap depth, $U_0 = k_B \times 4.5$ mK.

In the temperature regime of the experiment, the inelastic collision cross section is constant, leading to a predicted scaling $k \sim T^{1/2}$ of the collisional loss rate constant vs. temperature T, in qualitative agreement with our measurements. Meanwhile, the calculated elastic collision rates increase over the same range. At temperatures below around 10 μK, the collision rates enter the threshold regime, where for identical bosons the inelastic collision rate is constant, and the elastic rate decreases as $k_{\text{el}} \sim T^{1/2}$. The calculated maximum shielding factor reaches $\gamma = k_{\text{el}}/k \approx 200$ for both states at temperatures around 10 μK, which is favorable for evaporative cooling.

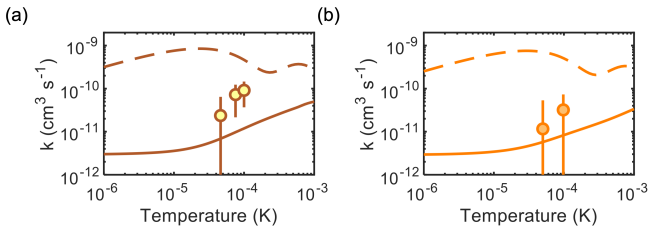

Figure 9.18: Temperature dependence of rate constants for states with repulsive long-range potentials. Collision rate constants are plotted vs. temperature for molecules prepared in (a) the f state at $\mathcal{E} = 0$ and (b) the d state at $\mathcal{E} = 500$ V/cm. Points are measured collisional loss rate constants with 1σ error bars. Solid curves are calculated collisional loss rate coefficients, and dashed curves are elastic collision rate coefficients. Reproduced from Ref. [342].

However, γ drops back below 100 at temperatures $\lesssim 1$ μK due to the threshold scaling laws [383].

The maximum low-temperature shielding factor γ_{max} depends on intrinsic molecular parameters, primarily the mass, dipole moment, and parity doublet splitting [375]. Most notably, higher shielding factors could potentially be obtained for polyatomic molecules with larger parity doublet splittings, which are expected to suppress inelastic loss [375].

9.6 Conclusion

We have observed and quantified collisions between ultracold CaOH molecules at temperatures near 100 μK, prepared the molecules in single quantum states within the parity-doubled vibrational bending mode, and measured the dependence of collisional loss rates on the internal state and the magnitude of the applied electric field. Our measurements are consistent with theoretical calculations that account only for long-range dipolar interactions and for universal short-range loss. We have identified certain parity-doublet states in the bending mode that have repulsive long-range potentials, which shield the molecules from short-range loss and reduce the measured collisional loss rates. For these states, the remaining collisional loss is dominated by inelastic dipolar relaxation at long

range [375]. The calculations indicate that the ratio of elastic to inelastic collisions in these states is sufficiently high for evaporative cooling of CaOH at temperatures $\lesssim 50\ \mu$K, though improved state preparation would also be required. Future experiments at even lower temperatures ($\sim$1 μK) may enable the observation of electrostatic field-linked states supported by parity-doublet structure [126, 131, 132]. These states could be harnessed to form $(CaOH)_2$ dimers [131, 133]. Reaching these temperatures remains a challenge for CaOH, but has been previously achieved for laser-cooled diatomic molecules [201, 231, 232].

Our observations and theory are expected to apply generally to molecules with parity-doublet structure [125, 127, 130], which exists generically in polyatomic molecules (and is also found in diatomic molecules with degenerate electronic ground states) [96]. For parity-doublet states with repulsive potentials, the shielding factor (which determines the feasibility of evaporative cooling) is expected to increase for molecules with larger parity doublet splittings and to also scale with the molecular dipole moment and mass [375], pointing the way to new molecules. There are a large number of polyatomic molecules that are amenable to direct laser cooling, including $CaOCH_3$, $CaNH_2$, and their analogues containing other alkaline-earth metals [34, 37, 47, 215], providing an opportunity to select a molecule with favorable properties for collisional shielding and quantum degeneracy in future work.

10

Direct Laser Cooling of Symmetric Top Molecules

Ultracold polyatomic molecules have potentially wide-ranging applications in quantum simulation and computation, particle physics, and quantum chemistry.[1] For atoms and small molecules, direct laser cooling has

[1] Portions of this chapter have been reproduced from Ref. [47].

proven itself a powerful tool enabling quantum science in the ultracold regime. However, the feasibility of laser cooling larger, nonlinear polyatomic molecules has remained unknown due to their complex structure. Here we laser cooled the symmetric top molecule calcium monomethoxide ($CaOCH_3$), reducing the temperature of $\sim 10^4$ molecules by a factor of 10 in one dimension, to 1.8 ± 0.7 mK, and state-selectively cooling two nuclear spin isomers. These results demonstrate that using proper rovibronic transitions makes laser cooling nonlinear molecules feasible, opening a path to efficient cooling of chiral molecules and, eventually, optical tweezer arrays of complex polyatomic species.

Laser cooling of atomic systems has enabled significant advances in quantum simulation, precision clocks, and quantum many-body physics [1, 7, 11, 57]. Extension to a diversity of complex polyatomic molecules would provide qualitatively new and improved platforms for these fields. For example, the parity doublets that result from rotations of a molecule around its principal axis, a general feature of symmetric top molecules, give rise to highly polarized states with structural features that are greatly desirable for both quantum science and precision measurement [101, 110, 140]. However, the same complexity that provides these advantages makes laser cooling nonlinear polyatomic molecules, including symmetric tops, challenging. Recent theoretical proposals have nonetheless suggested that laser cooling some nonlinear molecules is a practical possibility [33, 34, 37].

Laser cooling relies on repeatedly scattering photons from an atom or molecule via rapid optical cycling, removing energy and entropy with directed momentum kicks and spontaneous emission events. Although other direct [123, 154, 174, 384] and indirect [155, 179] methods of slowing, cooling, and trapping molecules have been used, direct laser cooling has successfully brought a number of diatomic [191, 193–195] and linear triatomic [217, 219, 220] molecules into the submillikelvin regime, with orders of magnitude increase in phase-space density. Critically, the ability to rapidly cycle photons, which is essential to laser cooling, naturally also allows for efficient

quantum state preparation and readout [202, 231], necessities for proposed quantum computation and simulation platforms using ultracold molecules, including those proposed for symmetric top molecules [101, 110].

The established recipe for achieving optical cycling and laser cooling of molecules requires three key ingredients: strong electronic transitions between two fully bound molecular states; diagonal Franck-Condon factors (FCFs), which limit branching to excited vibrational levels; and rotationally closed transitions. Here we satisfied these conditions for the symmetric top molecule $CaOCH_3$, using two distinct optical cycling schemes to enable rapid scattering of photons. We efficiently reduced the transverse temperature of a $CaOCH_3$ molecular beam from 22 ± 1 mK to 1.8 ± 0.7 mK and scattered over 100 photons while using only a few lasers, despite the presence of twelve vibrational modes. The state-selectivity of the cooling is intimately connected to both the nuclear spin statistics of the molecule, as well as its rigid-body angular momentum along the symmetry axis. These distinctive features of symmetric top molecules were not accessible to previously laser-cooled diatomic and triatomic molecules.

In this chapter we describe our work laser cooling $CaOCH_3$, including the spectroscopy and tests of optical cycling that led up to the final laser cooling results.

10.1 Overview of $CaOCH_3$ molecular structure

$CaOCH_3$ is a symmetric top molecule belonging to the C_{3v} molecular symmetry group. The irreducible representations of this group are A_1, A_2, and E. Comparing to $C_{\infty v}$ (which describes linear molecules like CaOH), A_1 is analogous to Σ^+, A_2 is analogous to Σ^-, and E is analogous to any degenerate state (e.g. Π, Δ, etc.). In this work we will work with states of A_1 and E symmetry. See Ref. [244] for a detailed discussion of molecular

symmetry.

10.1.1 Vibrational structure

For large polyatomic molecules, labeling vibrational states like we did for CaOH, i.e. using the notation $(v_1, v_2, \ldots, v_N)$, becomes unwieldy. Instead, we use the notation i_{v_i}, where i labels the vibrational mode and v_i is the vibrational quantum number for that mode. Only modes with $v_i \neq 0$ are labeled, and i is enumerated from 1 to n, where n is the total number of modes. Typically, the modes are ordered first by the symmetry of the vibrational mode and then in order of decreasing energy, as described in Ref. [245].

The vibrational modes in $CaOCH_3$ are depicted in Fig. 10.1. They are sorted by symmetry and in order of decreasing frequency. The first four modes are of A_1 symmetry, while the last four are of E symmetry and are doubly degenerate, giving a total of 12 modes. The modes are enumerated as $n = 1$: CH_3 symmetric stretch, $n = 2$: CH_3 symmetric bend, $n = 3$: C-O (asymmetric) stretch, $n = 4$: Ca-O (symmetric) stretch, $n = 5$: CH_3 asymmetric stretch, $n = 6$: CH_3 asymmetric bend, $n = 7$: O-CH_3 wag, and $n = 8$: Ca-O-C bend.

In this chapter, we only work with modes $n = 3$, 4 and 8. Decays to other vibrational modes are highly suppressed due to symmetry and diagonal branching ratios. Vibrational branching ratios were previously measured for the $\widetilde{A}^2E \rightarrow \widetilde{X}^2A_1$ and $\widetilde{B}^2A_1 \rightarrow \widetilde{X}^2A_1$ transitions with $\sim 5 \times 10^{-3}$ level sensitivity [213]. These measurements indicated that more than 100 photons can be scattered by repumping just the 4_1 and 3_1 states (corresponding to one excitation of the Ca–O stretching mode and one excitation of the O–C stretching mode).

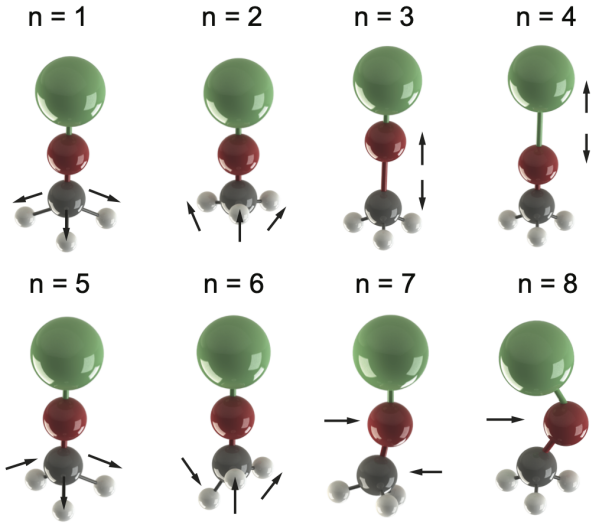

Figure 10.1: Illustration of the vibrational modes of $CaOCH_3$. Arrows represent the relative motion of specific atoms. Reproduced from Ref. [47].

10.1.2 Rotational structure

To describe the angular momentum structure of $CaOCH_3$, we will once again use Hund's case (b) for nondegenerate states ($\widetilde{X}^2A_1$ and $\widetilde{B}^2A_1$) and Hund's case (a) for the degenerate $\widetilde{A}^2E$ state. These angular momentum coupling schemes are illustrated in Fig. 10.2.

The $\widetilde{X}^2A_1$ state

Symmetric top molecules have two distinct moments of inertia. In $CaOCH_3$, which is a prolate symmetric top, $I_A < I_B = I_C$ so that the rotational constants are $A > B = C$. As described in chapter 2, in a nondegenerate electronic state (e.g. $\widetilde{X}^2A_1$, $\widetilde{B}^2A_1$) the rotational energies are

$$E_{\text{rot}} = BN(N+1) + (A-B)K^2 \tag{10.1}$$

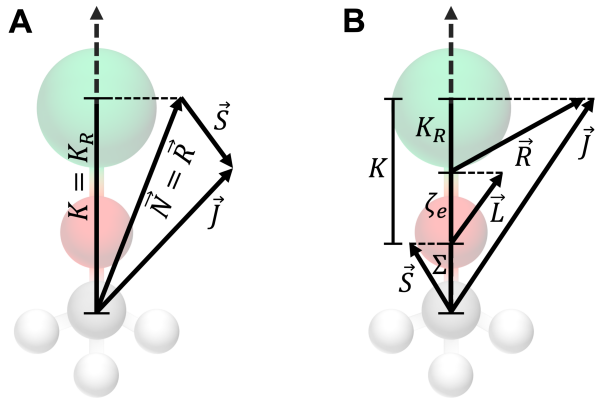

Figure 10.2: Quantum numbers for the electronic states of $CaOCH_3$ used in this work. The vertical axis is the (molecule-fixed) symmetry axis. **(A)** The $\tilde{X}\,^2A_1$ and $\tilde{B}\,^2A_1$ states are well described by Hund's case (b), with no electronic angular momentum. $\vec{R}$ is the total rigid-body rotation and K_R is its projection onto the symmetry axis. $\vec{N} = \vec{R} + \vec{L}$ also includes the electronic orbital angular momentum, and K is its projection. $\vec{S}$ and $\vec{J}$ are the electron spin and total (excluding nuclear spin) angular momenta, respectively. **(B)** The $\tilde{A}\,^2E$ state is well described by Hund's case (a). This state has an electronic orbital angular momentum projection $\zeta_e \approx 1$, so that $K \approx K_R \pm 1$. Reproduced from Ref. [47].

where N is the rotational quantum number and K is its projection onto the molecular symmetry axis. In the $\widetilde{X}^2A_1$ state of $CaOCH_3$, $A = 163.34$ GHz and $B = 3.49$ GHz [385, 386]. Therefore, the structure is split into widely spaced K stacks, each of which contains a ladder of rotational levels N (Fig. 10.3).

$CaOCH_3$ also has an electron spin $S = 1/2$, which causes spin-rotation interactions within each N manifold. In general, polyatomic molecules have a tensor with components $\epsilon_{\alpha\beta}$ describing spin-rotation interaction [252]. In the ground state of $CaOCH_3$, the only nonzero spin-rotation parameter is ϵ_{bc}, which is equivalent to γ in CaOH. Therefore, the spin rotation splittings have a similar formula to the bending mode of CaOH:

$$E_{\text{sr}}(J = N + 1/2) = \frac{\epsilon_{bc}}{2}\left[1 - \frac{K^2}{N(N+1)}\right]N \tag{10.2a}$$

$$E_{\text{sr}}(J = N - 1/2) = -\frac{\epsilon_{bc}}{2}\left[1 - \frac{K^2}{N(N+1)}\right](N+1) \tag{10.2b}$$

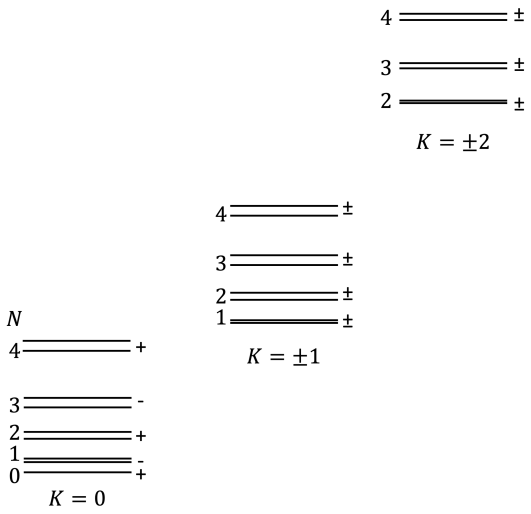

Figure 10.3: Rotational structure of the $\widetilde{X}^2A_1$ state of $CaOCH_3$. J is not labeled, with the two spin-rotation components in each state taking values $J = N - 1/2$ (lower state) and $J = N + 1/2$ (upper state). Not to scale.

In the $\widetilde{X}^2A_1$ state, $\epsilon_{bc} = 12.5$ MHz [385, 386]. This means that in the $N = 1$ level of the $K = 0$ stack, the spin-rotation splitting between $J = 1/2$ and $J = 3/2$ is approximately 19 MHz. In the $N = 1$ level of the $K = 1$ stack, the spin-rotation splitting is approximately 9 MHz. Both of these are on the edge of being optically resolved, and we do not need sidebands to address these states during laser cooling.

Finally, states with $K \neq 0$ have both parities (like CaOH bending modes with $\ell \neq 0$) due to the fact that K can be positive or negative. In $CaOCH_3$, the degeneracy of these opposite parity "K-doublets" is lifted by a hyperfine interaction arising from the three $I = 1/2$ hydrogen nuclear spins [95]. The parity doubling is less than 100 kHz in the $N = 1, K = 1$ state. Hyperfine interactions are also small, on the order of hundreds of kHz [95].

Fig. 10.3 shows the structure of low-lying states in $\widetilde{X}^2A_1$, including rotational and spin-rotation structure. Quantitative energy calculations can be carried out using the Hamiltonian and parameters from Refs. [95, 385,

386], with matrix elements from Ref. [252]. The matrix elements for this state are very similar to those discussed in Appendix A for the CaOH $\widetilde{X}(010)$ bending mode.

The $\widetilde{A}^2E$ state

Because the $\widetilde{A}^2E$ electronic state is degenerate, it has a somewhat different structure (in the same way that the degenerate $\widetilde{A}^2\Pi$ state in CaOH has different structure than the ground state).[2] Like in CaOH, the biggest effect is a spin-orbit interaction, which splits the state into two manifolds, $^2E_{1/2}$ and $^2E_{3/2}$ that are split by approximately 2 THz [386]. We will just focus on the lower, $\widetilde{A}^2E_{1/2}$ manifold, which is used for laser cooling. See Ref. [252] for a more detailed description of the Hamiltonian for symmetric top molecules in a ^2E state.

The dominant contributions are from molecular rotation and a first-order Coriolis interaction [252, 386]:

$$E_A = BJ(J+1) + (A-B)K^2 - 2A\zeta_t K \tag{10.3}$$

where we used K as a stand-in for the case(a) quantum numbers $P-\Sigma$. The first two terms describe the standard molecular rotation effects from earlier, while the third term is typically called a first-order Coriolis interaction, in the sense that it comes from a term $\sim AL_zN_z$, i.e. a coupling between the molecular rotation and electronic angular momentum. ζ_t is a parameter that describes quenching of the electronic angular momentum. In $CaOCH_3$, $\zeta_t \approx 0.999$ [386], so that the electronic angular momentum is essentially fully unquenched. In this limit, the projection of $\boldsymbol{R}$ onto the internuclear axis, $K_R = K - \zeta_e \approx K \pm 1$ is an approximately good quantum

[2] The effective Hamiltonian can be derived in a similar manner to what we did for the $\widetilde{A}$ state of CaOH in chapter 2, i.e. by starting with the rotational Hamiltonian written in terms of the rigid body rotation $\boldsymbol{R}$ and its projection K_R, then rewriting in terms of $\boldsymbol{J}$ and expanding. However, here we jump straight to the results.

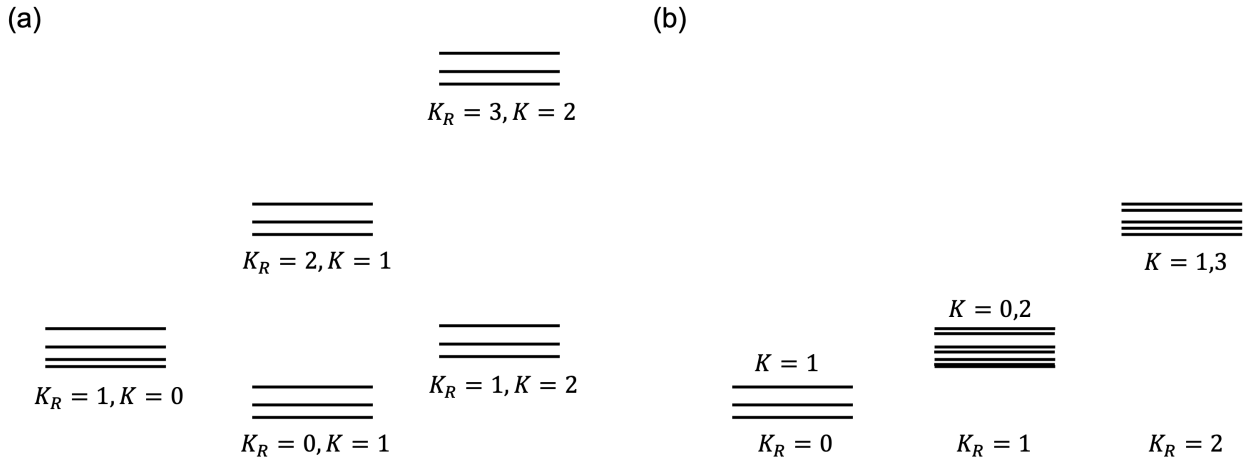

Figure 10.4: Rotational structure of the $\widetilde{A}^2E_{1/2}$ state of $CaOCH_3$. (a) Grouped by K. (b) Grouped into "K_R stacks." Not to scale.

number.[3]

The structure of $CaOCH_3$ in the $\widetilde{A}^2E_{1/2}$ state is shown in Fig. 10.4. As shown in the figure, the structure can be grouped into "K_R stacks" analogous to the K stacks in the ground state. Moreover, in the ground state $K = K_R$ and there is a $\Delta K_R = 0$ selection rule for electronic transitions, so this relabeling is very helpful for designing rotationally closed optical cycling schemes, as described below.

Note that there is an analogue of Λ-type doubling in the $\widetilde{A}^2E_{1/2}$ state of $CaOCH_3$, but it leads to significant splittings only in the $K = 1, K_R = 0$ state [252, 386].[4] Quantitative calculations of the structure of the $\widetilde{A}^2E$ state can be carried out using the Hamiltonian and parameters from Ref. [386], using matrix elements from Refs. [252, 387].

[3] ζ_e and ζ_t are different in states with vibrational angular momentum, but in our case they are effectively the same quantity [252].

[4] This is because the term that causes Λ doubling (proportional to the parameter h_1) only has diagonal matrix elements within $K = 1$.

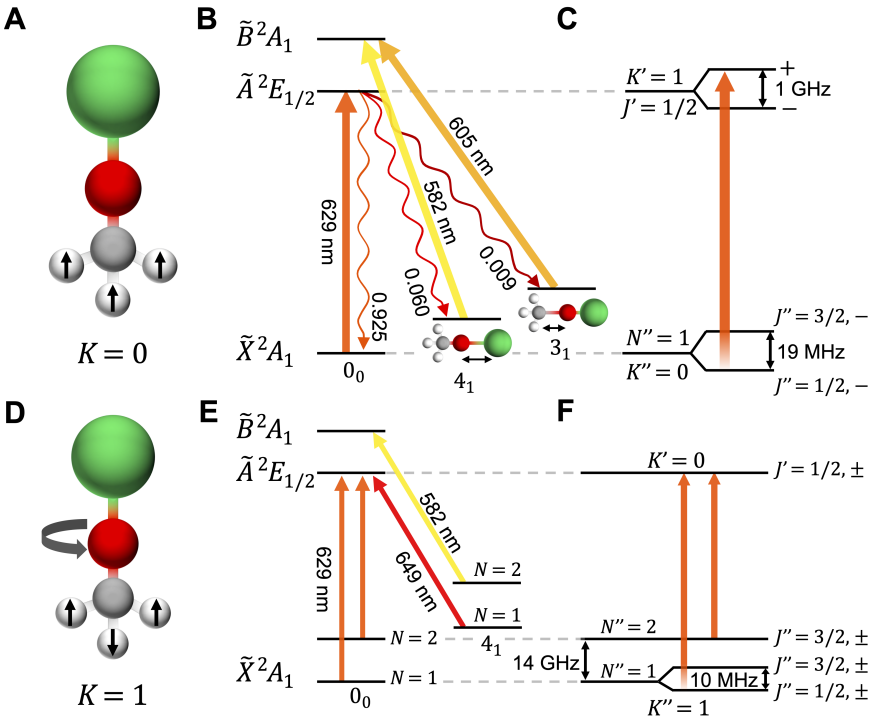

Figure 10.5: $CaOCH_3$ laser cooling schemes. (A),(D) We use two optical cycling schemes, which target molecules differing in their angular momentum quantum number K and their nuclear spin statistics (represented by arrows on the hydrogen nuclei). (B),(C) For ortho-$CaOCH_3$, we address the 0_0, 4_1, and 3_1 vibrational levels of the $\tilde{X}^2A_1(K'' = 0)$ ground state. Vibrational branching ratios are illustrated by downward arrows. Rotational closure is achieved by addressing $N'' = 1$, $J'' = 1/2, 3/2$ ground-state manifolds. The total parity of each state is indicated by $+$ and $-$ signs. (E),(F) For para-$CaOCH_3$, we address the 0_0 and 4_1 vibrational levels of the $\tilde{X}^2A_1(K'' = 1)$ electronic ground state, driving transitions from $N'' = 1$ and $N'' = 2$ to achieve rotational closure. Each J state contains an unresolved parity doublet denoted by $\pm$. Reproduced from Ref. [47].

10.2 Closed cycling transitions for symmetric tops

The optical cycling transitions used for laser cooling $CaOCH_3$ are shown in Fig. 10.5. We laser cool molecules in $K = 0$ and $K = 1$ states, which correspond to different nuclear spin configurations and also have different rotational closure requirements.

We optically cycle photons on the $\tilde{X}\,^2A_1 - \tilde{A}\,^2E_{1/2}0_0^0$ transition in $CaOCH_3$.[5] To prevent rotational branching we exploit angular momentum selection rules involving K_R, the projection of the total rigid body rotation $\vec{R}$ onto the molecular symmetry axis, and K, the projection of the total angular momentum excluding spin, $\vec{N}$. Note that the quantum number K also includes the electronic angular momentum ζ_e about the symmetry axis. The relevant quantum numbers are illustrated in Fig. 10.2. In the non-degenerate states $\tilde{X}\,^2A_1$ and $\tilde{B}\,^2A_1$ we have $K \approx K_R$ while for the doubly-degenerate $\tilde{A}\,^2E$ state $|K| \approx |K_R| \pm 1$. These two rotational levels are split by a large Coriolis interaction. Because almost all of the change in angular momentum comes from the electron's orbital angular momentum, K_R is approximately conserved during excitation on the $\tilde{A} - \tilde{X}$ band. We therefore group states by K_R and look for closed rotational transitions within these "K_R stacks" [388, 389].

Within the $K_R = 0$ stack, we drive transitions from $\tilde{X}\,^2A_1(K'' = 0)$ to $\tilde{A}\,^2E_{1/2}(K' = 1)$. The ground state is well described by Hund's case (b), with individual rotational levels N'' split into two components $J'' = N'' \pm 1/2$ by the spin-rotation interaction, while the $\tilde{A}\,^2E$ state is well described by Hund's case (a). Rotational closure is attained by addressing ${}^rP_{11}$ and ${}^rQ_{12}$ transitions from $N'' = 1$, i.e. $\tilde{X}\,^2A_1(K'' = 0, N'' = 1, J'' = 1/2, 3/2, -) \rightarrow \tilde{A}\,^2E_{1/2}(K' = 1, J' = 1/2, +)$, where signs indicate the parity of each state (see Fig. 10.5).[6] The $\tilde{B}\,^2A_1$ state is described by Hund's case (b), and repumping lasers through this state address the $(K' = 0, N' = 0, J' = 1/2, +)$ rotational level. The spin-rotation splitting in the ground state is 19 MHz [386]. All repumping lasers are tuned halfway between these two components and are sufficiently power-broadened to address both levels. The main cooling laser also consists of a single frequency component and can be scanned in

[5] The vibrational notation is $i_{v''}^{v'}$, where i labels the mode, and v' and v'' are the vibrational quantum numbers in mode i for the upper and lower states, respectively.

[6] We adopt the notation used in Ref. [390] and label transitions ${}^{\Delta K}\Delta J_{F_1F_2}$, where $\Delta K = K' - K''$, $\Delta J = J' - J''$, and F_1 and F_2 denote the component character of the excited and ground state, respectively. $F_1 = 1$ applies to the $\Omega = 1/2$ spin-orbit component of the excited state, while $F_2 = 1, 2$ correspond to the upper and lower spin-rotation component of the ground state, respectively.

the vicinity of one or both states. Hyperfine structure due to the nuclear spin of the hydrogen atoms is below the natural linewidth of the optical transitions and is therefore neglected [95].

We also laser cool molecules in the $|K_R| = 1$ stack. Because states with $K_R = \pm 1$ come in unresolved opposite parity doublets, it is necessary to address more states to achieve rotational closure. Here we drive ${}^pP_{11}$, ${}^pQ_{12}$, and ${}^pP_{12}$ transitions from $K'' = 1$ to $K' = 0$, addressing $N'' = 1$ and $N'' = 2$ in the ground state, as previously proposed in Ref. [34] (see Fig. 10.5). The spin-rotation splitting between $(N'' = 1, J'' = 1/2, 3/2)$ in the ground state is 10 MHz and is bridged by a single power-broadened laser. The combined rotational line strength of the ${}^pP_{11}$ and ${}^pQ_{12}$ transitions from $N'' = 1$ is approximately 3x stronger than the ${}^pP_{12}$ transition from $N'' = 2$ [390]. In this work, we laser cool para-$CaOCH_3$ molecules using three lasers addressing the $0_0(N'' = 1, 2)$ and $4_1(N'' = 1)$ levels of the $\tilde{X}\,{}^2A_1$ electronic state. This optically pumps population into the $4_1(N'' = 2)$ state, which is recovered in the cleanup region prior to detection (described later).

All three of these lasers are directed through $\widetilde{A}^2E_{1/2}$. Optical cycling via the $\tilde{B}\,{}^2A_1$ state for $|K_R| = 1$ is limited in $CaOCH_3$ by the fact that the $N'' = 1 \rightarrow N' = 1$ laser will also drive the nearby $N'' = 2 \rightarrow N' = 2$ transition, tending to pump molecules out of the cooling cycle (Fig. 10.6).

The final repumping laser addresses the $\tilde{X}\,{}^2A_1(K'' = 1, N'' = 2, J'' = 3/2, \pm) \rightarrow \tilde{B}\,{}^2A_1(K' = 1, N' = 1, J' = 1/2, \pm)$ transition through the $\tilde{B}\,{}^2A_1$ state. However, because the spin-rotation splitting between $(K' = 1, N' = 1, J' = 1/2, 3/2)$ is only 70 MHz (Fig. 10.6), excessive power broadening could lead to rotational loss via $J' = 3/2$. Therefore, we keep the intensity of this laser low.

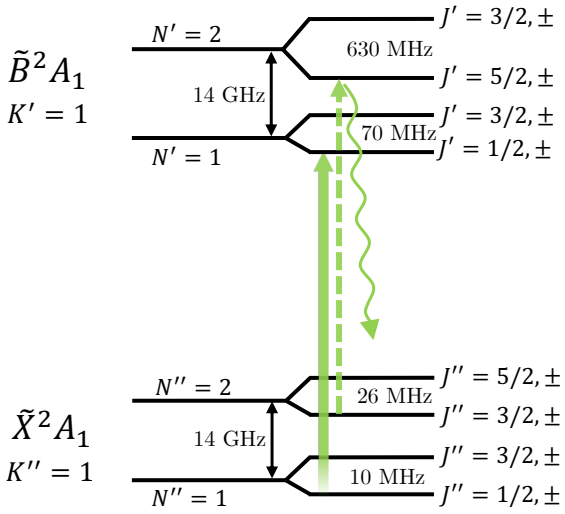

Figure 10.6: Limitations of $|K_R| = 1$ optical cycling through the $\tilde{B}$ state. Due to a structural coincidence in $CaOCH_3$, the laser required to address $N'' = 1$ population (solid arrow) is near-resonant with another transition that pumps molecules from $N'' = 2$ to $J' = 5/2$ and out of the cooling cycle (dashed arrow). This prevents laser cooling and many repumping pathways via the $\tilde{B}\,^2A_1$ state in the para-$CaOCH_3$ scheme used in this work.

10.2.1 Relationship between K_R stacks and nuclear spin isomers

Cooling molecules in the $K_R = 0$ and $|K_R| = 1$ stacks can also be interpreted in light of the nuclear spin statistics of the molecule, briefly described here.

Symmetry arguments within the C_{3v} molecular symmetry group relate the nuclear spin state to the magnitude of K_R. Because rovibronic states with $K_R = 0$ transform like A_1 or A_2, and the total internal state, including nuclear spin, must also transform like A_1 or A_2 due to Fermi-Dirac statistics, the nuclear spin state corresponding to $K'' = K_R = 0$ is $I = 3/2$, which is called the ortho-$CaOCH_3$ nuclear spin isomer (NSI), which has A_1 character. Similarly, rovibronic states with $|K_R| = 1$ transform like E, meaning that the nuclear spin state must also have E character. This corresponds to the para-$CaOCH_3$ NSI and total nuclear spin $I = 1/2$ [101, 252, 391]. Note that, because ortho $\leftrightarrow$ para transitions are highly suppressed, nuclear spin statistics help to enforce the

$\Delta K_R = 0$ selection rule. See Ref. [244] for more details on molecular symmetry.

10.3 Optical cycling in $CaOCH_3$

Before proceeding to laser cool $CaOCH_3$, we first had to demonstrate that the expected optical cycling transitions were rotationally closed. We also had to search for vibrational repumping transitions, which were not known at high resolution prior to this work.

10.3.1 Apparatus

We performed spectroscopy, optical cycling checks, and laser cooling of $CaOCH_3$ using the CaOH apparatus, in a configuration very similar to what is described in Refs. [220, 251]. We produced $CaOCH_3$ molecules by reacting Ca with methanol in the buffer gas cell, then produced a CBGB. The beam passed through a 3x3 mm aperture, which reduced the initial transverse temperature for laser cooling demonstrations, and also allowed us to ensure that the full beam was addressed by optical cycling laser. For initial optical cycling tests, we collected fluorescence using a PMT, in a detection region approximately 65 cm downstream from the buffer gas cell. We applied a small magnetic field in the detection region to remix dark states.

10.3.2 Rotational closure

Our first task was to find the rotationally closed optical cycling lines on the $\widetilde{X}^2A_1 \rightarrow \widetilde{A}^2E_{1/2}0_0^0$ transition. These transitions were previously measured at high resolution in the literature [386], so they were straightforward to find. We then confirmed that they provided the expected increase in fluorescence compared to rotationally open transitions.

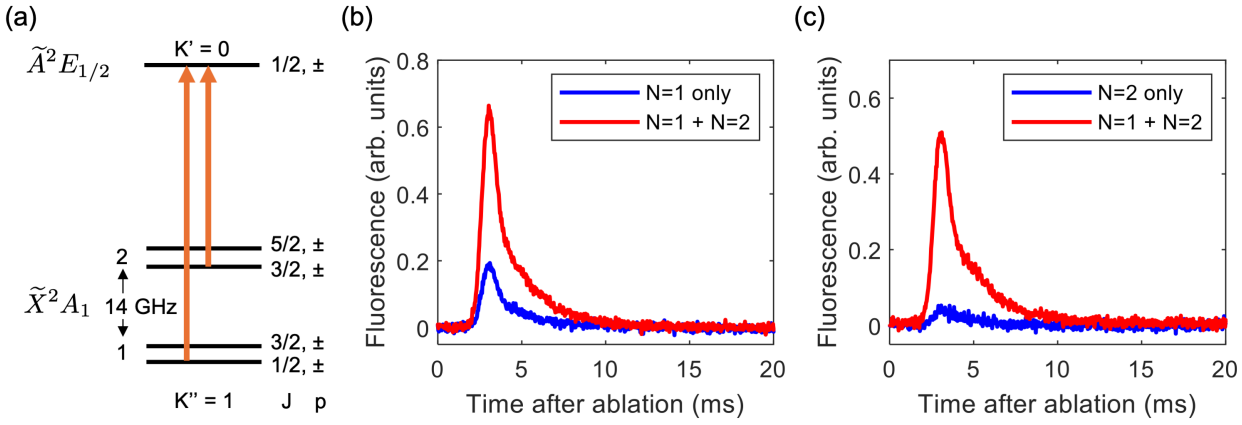

Figure 10.7: Tests of rotational closure for $K = 1$ optical cycling. (a) Rotationally closed optical cycling transition, with an $N = 1$ and $N = 2$ laser. (b) Fluorescence with and without the $N = 2$ laser. (c) Fluorescence with and without the $N = 1$ laser.

Fig. 10.7 shows tests of rotational closure for optical cycling in the $K_R = 1$ stack. Because this transition requires two lasers addressing $N'' = 1$ and $N'' = 2$, it is simple to check optical cycling by removing one of the repumping lasers. With both lasers, we see an increase in molecular fluorescence as measured on the PMT, due to the larger number of photons that can be scattered. By comparing to expected rotational branching ratios[7], we can determine whether the optical cycling transition is performing as expected. In this case, we see a 3.5x increase in fluorescence with both lasers compared to just $N = 1$, and a 9x increase with both lasers compared to just $N = 2$. Both of these agree well with the expected enhancement based on calculated branching ratios (3.6x and 11x, respectively).

For $K_R = 0$ optical cycling, the spin-rotation ground states are close enough together (19 MHz apart) that it is challenging to "turn off" optical cycling by addressing a single level, as done in Ref. [216]. Instead, we compare

[7] These can be looked up from tables in Ref. [390], or determined by calculating electric dipole matrix elements using the Hamiltonian for the $\widetilde{X}$ and $\widetilde{A}$ states [252, 386]. The expected increase in fluorescence also assumes a diagonal VBR of 0.931, as measured in Ref. [213].

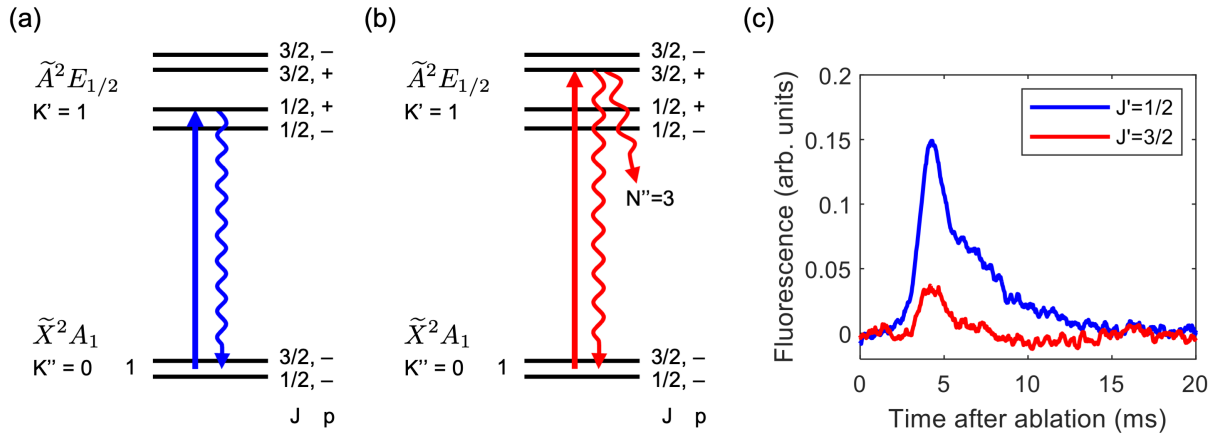

Figure 10.8: Tests of rotational closure for $K = 0$ optical cycling. (a) Rotationally closed transition. The laser is power broadened over both ground spin-rotation states, which are split by 19 MHz. (b) Rotationally open transition. The $J' = 3/2^+$ excited state can decay to $N'' = 3, J'' = 5/2^-$ in the ground state. (c) Comparison of molecule fluorescence with the two excited states.

the signal from this transition to a rotationally open transition, by exciting to $J' = 3/2^+$ (Fig. 10.8). We observe a ∼3.5x enhancement when using the optical cycling transition compared to the rotationally lossy transition, which is in decent agreement with the calculated ratio of 4.5x, given experimental uncertainty.

Based on the calculated rotational branching ratios, these results are consistent with being able to scatter approximately 10-15 photons from $CaOCH_3$.

10.3.3 Spectroscopy of repumping transitions

Having demonstrated that rotational branching appears to behave as expected, the next task was to begin repumping vibrational leakage channels. Based on calculations [213], we expected that we would need to repump the 4_1 (Ca–O stretch) and 3_1 (O–C stretch) vibrational states to scatter >100 photons. Neither of these states had been observed at high resolution, so we relied on previous low-resolution spectroscopy [295, 392] to provide an initial guess, and expected to have to scan over several wavenumbers to find the repumping transitions.

Spectroscopy of the $\widetilde{X}^2A_1 \rightarrow \widetilde{B}^2A_1 4_1^0$ repumping transition

Similar to CaOH, we decided to decouple the repumpers and repump 4_1 through the $\widetilde{B}^2A_1$ state. To search for this repumping laser, we depleted molecules into 4_1 by optically cycling on the 629 nm $\widetilde{X}^2A_1 \rightarrow \widetilde{A}^2E_{1/2}0_0^0$ transition in the $K_R = 0$ stack (to avoid needing extra rotational repumpers). This depletion was done upstream, before the molecules reached the detection region. We then scanned the 582 nm repumping laser in the detection region, while looked for $\widetilde{B}^2A_1 \rightarrow \widetilde{X}^2A_1 0_0^0$ diagonal fluorescence at 565 nm. This detection scheme is background free, and we knew from our work with CaOH that it is favorable for PMT detection with high signal-to-noise ratios. These scans were done in a "switch-2" configuration, where the signal was compared with and without the optical cycling depletion laser. This helps confirm that the detected signal is in the correct rotational state needed for optical cycling (compared to natural population in other rotational states).

Fig. 10.9 shows the results of the spectroscopy. After 10s of GHz of scanning, we observed a large peak that was amplified in the data with depletion compared to the natural beam, indicating that it originated from $N'' = 1$. Further checks confirmed that this was the $N'' = 1 \rightarrow N' = 0$ transition required for repumping. Once this feature was found, we quickly also found the corresponding repumping transitions for the $K_R = 1$ laser cooling scheme.

Spectroscopy of the $\widetilde{X}^2A_1 \rightarrow \widetilde{B}^2A_1 3_1^0$ repumping transition

To search for the next repumper, we depleted with the first two lasers ($\widetilde{X}^2A_1 \rightarrow \widetilde{A}^2E_{1/2}0_0^0$ and $\widetilde{X}^2A_1 \rightarrow \widetilde{B}^2A_1 4_0^1$, at 629 nm and 582 nm, respectively), then scanned a 605 nm laser in the detection region while looking for 565 nm $\widetilde{B} \rightarrow \widetilde{X}$ fluorescence. Similar to before, we used a "switch-2" configuration, where we switched the

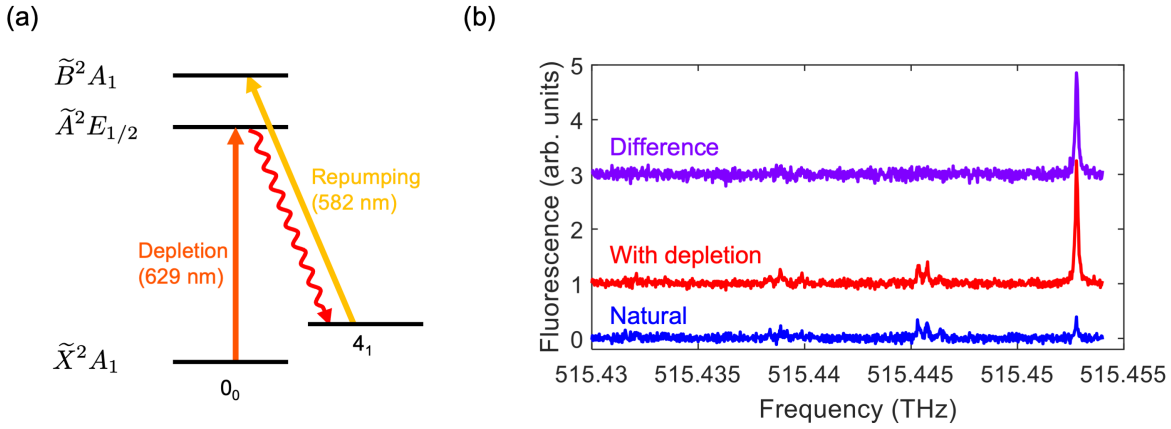

Figure 10.9: Spectroscopic search for the $\widetilde{X}^2A_1 \rightarrow \widetilde{B}^2A_1 4_1^0$ repumping laser at 582 nm. (a) Spectroscopy setup. The depletion laser is alternately switched on and off to pump population into 4_1. The 582 nm repumping laser is scanned to recover population, which is then detected. (b) Spectroscopy data. The repumping transition shows up very clearly when subtracting the data with and without depletion, which subtracts out the effect of natural population in the beam.

first two lasers on and of to distinguish between natural population and population accumulating in $N'' = 1$ after optical cycling. Again, here we used the $K_R = 0$ cycling scheme to avoid needing rotational repumping lasers.

The results of this scan are shown in Fig. 10.10. Here, our initial guess happened to be near the R branch, and we almost immediately saw signal in the naturally populated beam that did not increase with depletion. However, once we scanned far enough to observe a few of these features, it became clear that we were in the R branch. We could then jump down using known rotational constants and find the expected laser cooling line, which is in the P branch. In this way, with a bit of luck and an ability to interpret the rotational spectrum, it did not take long to find the correct repumping transition.

Frequencies of the cooling and repumping transitions we observed can be found in appendix E.

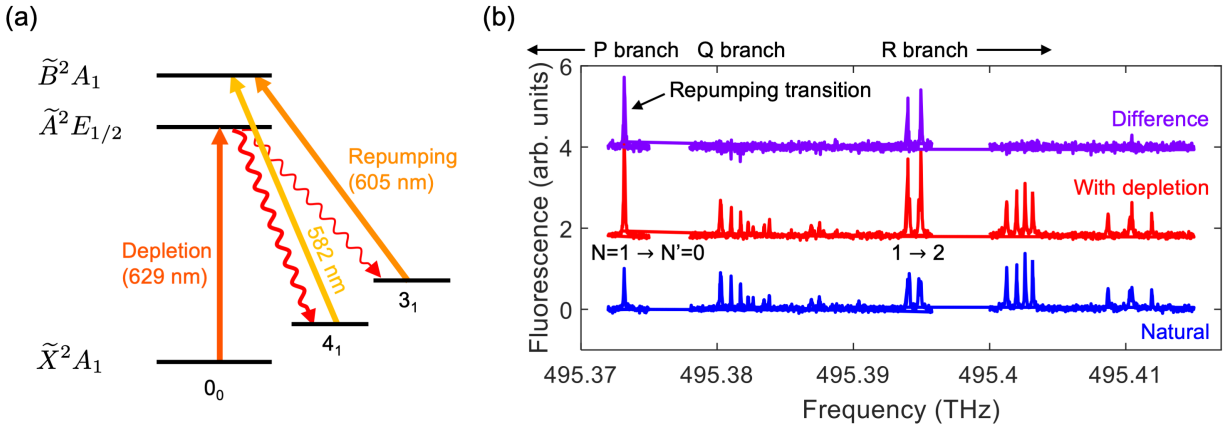

Figure 10.10: Spectroscopic search for the $\widetilde{X}^2A_1 \rightarrow \widetilde{B}^2A_1 3_1^0$ repumping laser at 605 nm. (a) Spectroscopy setup. The depletion laser and first repumping laser are alternately switched on and off to pump population into 3_1. The 605 nm repumping laser is scanned to recover population, which is then detected. (b) Spectroscopy data. The data with depletion identifies which transitions originate from $N'' = 1$. The leftmost $N'' = 1$ peak corresponds to the P branch, which is used for repumping.

10.3.4 VIBRATIONAL CLOSURE AND DEPLETION-REVIVAL MEASUREMENTS

Fig. 10.11 shows depletion-revival tests of the $\widetilde{X}^2A_1 \rightarrow \widetilde{B}^2A_1\, 4_1^0$ vibrational repumping. In an upstream depletion region, we optically cycle with the $\widetilde{X}^2A_1 \rightarrow \widetilde{A}^2E_{1/2}\, 0_0^0$ main line laser, which pumps molecules into dark vibrational states, including 4_1. If we also include the repumping laser in detection, it will recover all population lost to 4_1. We observe approximately 80% revival, indicating that 4_1 is the dominant vibrational loss channel, as we expected. These measurements were performed using the $K_R = 0$ rotational closure scheme, but they are expected to be unchanged for $K_R = 1$ optical cycling.

After we found the $\widetilde{X}^2A_1 \rightarrow \widetilde{B}^2A_1\, 3_1^0$ repumping laser, we performed similar tests, this time by depleting with both the main line laser and the first repumper. We observed approximately 50% revival in this case.

Taken together, these depletion-revival measurements allow us to estimate the vibrational branching ratios

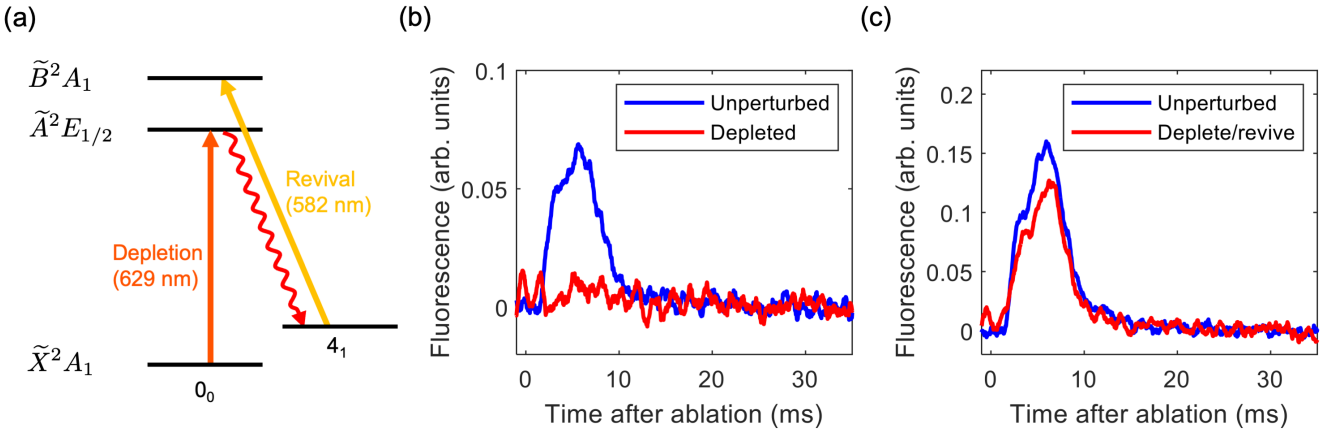

Figure 10.11: Depletion-revival tests of the 4_1 vibrational repumper. (a) Level structure. These tests were done for the $K_R = 0$ rotational closure scheme (rotational states not shown). (b) Beam signal with and without depletion laser, detecting only $\widetilde{X}^2A_1\,0_0$. $\lesssim 10\%$ of the beam survives after depletion. (c) Same data but with the $\widetilde{X}^2A_1 \rightarrow \widetilde{B}^2A_1\,4_1^0$ repumper also in detection. This revives the depleted population, recovering approximately 80% of the molecules.

for $CaOCH_3$ (similar to the depletion-revival measurements described for CaOH in chapter 4). VBRs were previously measured for $CaOCH_3$ in Ref. [213], but these DLIF measurements provide no information about loss channels below the noise floor. In order to estimate the effect of these small decay channels, we assume there is an additional branching ratio r_{other} characterizing loss to all such states. We then vary this parameter subject to two conditions: (1) the remaining VBRs, when rescaled to ignore the effect of r_{other}, agree within error with Ref. [213], and (2) the results agree with the depletion-revival measurements. For purposes of this estimation, we assume a 10% error on the depletion-revival measurements. Using this procedure, we infer VBRs for decay from the $\tilde{A}\,^2E_{1/2}$ state, given in Table 10.1. We cannot independently determine the VBRs from the $\tilde{B}\,^2A_1$ state and fix these at the values from Ref. [213] while conservatively including an additional loss $r^B_{\text{other}} = 0.005$, though this only weakly affects the final result.

We use these results to estimate the number of photons scattered in the laser cooling experiment (described be-

Decay	Branching Ratio
$0_0^0\tilde{A}^2E_{1/2} \rightarrow \tilde{X}^2A_1$	$0.925(7)$
$4_1^0\tilde{A}^2E_{1/2} \rightarrow \tilde{X}^2A_1$	$0.060(2)$
$3_1^0\tilde{A}^2E_{1/2} \rightarrow \tilde{X}^2A_1$	$8.6^{+0.7}_{-3.2} \times 10^{-3}$
Other	$6.4^{+5.3}_{-5.0} \times 10^{-3}$

Table 10.1: Approximate branching ratios determined for $CaOCH_3$ laser cooling transitions as described in the text. These rely on existing dispersed fluorescence measurements [213] and on the depletion-revival measurements described in the text.

low). This is done using the survival fraction, defined as the ratio of the integrated area of the Sisyphus cooled/heated images to that of the unperturbed beam. This provides a measure of the number of molecules remaining in the optical cycling transition, or equivalently, the fraction of molecules lost to vibrational dark states. The survival fraction is directly related to the number of scattered photons via the VBRs, and its variation with detuning and intensity is shown in Fig. 10.12. For optimized Sisyphus cooling parameters of 600 mW/cm^2, $\Delta = +25$ MHz, and $|B| = 1$ G, we measure a survival fraction of 49(3)%, while the survival fraction reaches a minimum value of 38(1)% on resonance where the scattering rate is maximized. These depletion fractions correspond to approximately 80 photons scattered during optimal Sisyphus cooling, and 110 photons scattered during resonant depletion.

10.4 Sisyphus laser cooling of $CaOCH_3$

Having established rotational and vibrational closure of $CaOCH_3$, with the ability to scatter more than 100 photons, the next step was to demonstrate transverse laser cooling of the molecular beam. We studied laser cooling of both nuclear-spin isomers (NSIs) of $CaOCH_3$, each of which corresponds to a specific set of K states.

To cool the symmetric (ortho) NSI, we laser excited molecules in ground states with $K'' = 0$ (Fig. 10.5A-

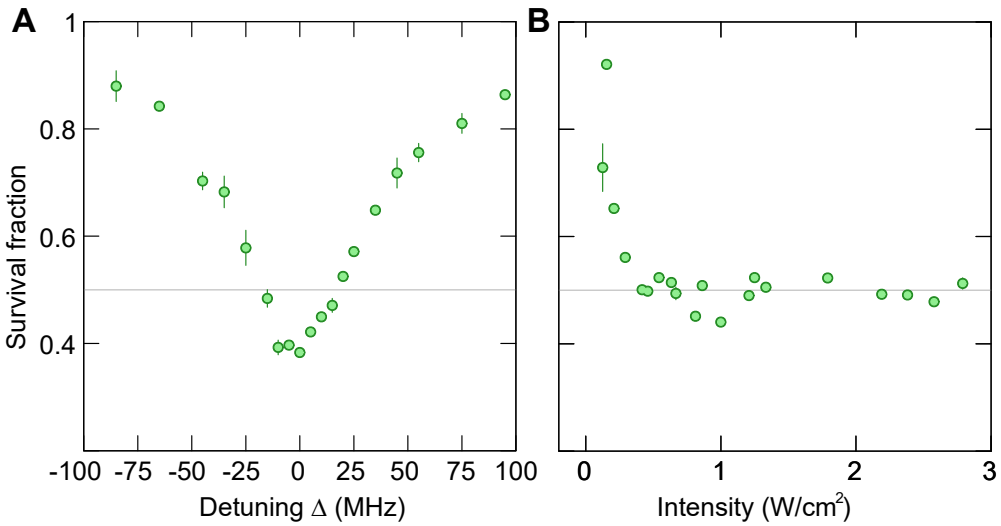

Figure 10.12: Variation of survival fraction for ortho-$CaOCH_3$. **(A)** Variation of the survival fraction with detuning Δ at an intensity of 400 mW/cm^2 and a remixing field of $|B| = 1$ G. On resonance, the survival fraction reaches a minimum of 38(1)%. It increases away from resonance as the scattering rate decreases. **(B)** Variation with cooling laser intensity at $\Delta = +25$ MHz and $|B| = 1$ G. The survival fraction saturates to 49(3)% for intensities greater than $\sim$ 600 mW/cm^2. In both panels, the grey line indicates a survival fraction of 50%. Reproduced from Ref. [47].

C). To high order, $K'' = 0$ states effectively "freeze out" the particular additional complexity of symmetric top molecules compared to their linear counterparts, and this cooling approach looks similar to that used for diatomic and linear triatomic molecules. Due to the favorable FCFs of $CaOCH_3$, we used only three lasers to address the 0_0 (no excitation), 4_1 (Ca–O stretch), and 3_1 (O–C stretch) vibrational manifolds of the $\tilde{X}\,^2A_1$ electronic ground state, enabling each molecule to scatter an average of 120 photons before being lost to other vibrational levels [213]. To laser cool the asymmetric (para) isomer, we instead excited ground states that have $K'' = 1$ (Fig. 10.5D-F). In this case, the existence of unresolved (opposite) parity doublets means that full optical closure required addressing additional rotational components of the $\tilde{X}\,^2A_1$ ground state. Using three cooling and repumping lasers enabled scattering an average of 30 photons before molecules were optically pumped into a fourth rovibronic state. Including three additional lasers would allow scattering 120 photons on average, just as in the ortho-$CaOCH_3$ scheme. Because both cooling schemes are limited only by vibrational decay pathways, scattering >1000 photons could be achieved by adding approximately 4 additional repumping lasers [213].

10.4.1 Apparatus

A schematic of the experimental apparatus used for laser cooling is shown in Fig. 10.13. Compared to our optical cycling measurements, we added another detection chamber (based on a KF50 six-way cross) further downstream, which allowed the molecules to expand further after laser cooling so changes in temperature would be easier to discern. The KF cross was blackened with MH2200 paint, and the detection laser was sent through long blackened nipples, with baffles, to reduce scattered light. This blackening was important for achieving good signal-

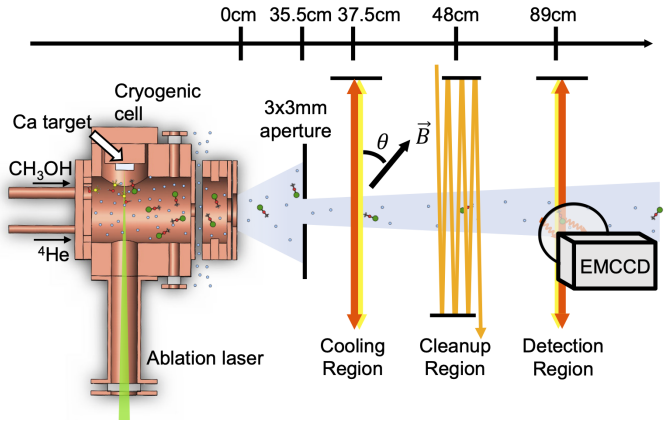

Figure 10.13: Schematic of the experimental apparatus, illustrating the beam source, laser cooling, cleanup, and detection regions (not to scale). The cooling region contains a near-resonant standing wave generated by retroreflecting a single, linearly polarized, 6 mm $1/e^2$ diameter Gaussian laser beam. In the cleanup region, molecules are repumped out of the $\tilde{X}\,^2A_1 3_1$ (ortho-$CaOCH_3$) and $\tilde{X}\,^2A_1(N''=2)4_1$ (para-$CaOCH_3$) states before being imaged onto an EMCCD camera via laser-induced fluorescence (LIF) detection. Modified from Ref. [47].

to-noise, which ended up making the laser cooling experiments relatively quick in the end.[8] The apparatus is described in more detail in the following paragraphs. It is relatively similar to the apparatus used in Refs. [220, 251].

$CaOCH_3$ molecules were produced in a cryogenic buffer gas environment by ablation of a calcium metal target in the presence of methanol vapor. The resulting beam had a mean forward velocity of 150±30 m/s and was collimated to a transverse temperature of ∼22 mK by a 3×3 mm square aperture immediately preceding the cooling region, after which $\sim 10^4$ molecules (in a single pulse) remained with a density of $\sim 10^3$ cm^{-3}.

Molecules enter the cooling region 2 cm further downstream. Here, molecules experience a variable magnetic field produced by a circular coil with 15 cm diameter, mounted 10 cm from the cooling region and used to remix magnetic dark states. The standing wave used for Sisyphus cooling is composed of several frequencies needed for optical cycling (described above). For ortho-$CaOCH_3$ cooling, the main cooling laser intensity is variable,

[8] The final data for this experiment was taken the week of March 9-March 15, 2020, racing against the clock before Harvard (and the world) shut down for COVID.

while the intensity of each repumping laser is $\sim$ 400 mW/cm^2. For para-$CaOCH_3$ each repumping laser has an intensity of $\sim$ 100 mW/cm^2. The main cooling laser light is generated by the second harmonic of a 1258 nm Raman fiber amplifier (RFA) seeded by an external cavity diode laser (ECDL), while all repumping and imaging light is produced by continuous-wave (cw) dye lasers.[9]

After cooling, the molecules propagate ∼10 cm before passing through a cleanup region containing multiple retroreflected passes of repumping light, spanning $\sim$ 25 mm in the longitudinal direction and with sufficient transverse width to address the full molecular beam. No magnetic field is applied, as the Earth's magnetic field is sufficient to remix dark states. The molecules are detected 41 cm further downstream by a circular, $\sim$ 11 mm diameter beam with ∼ 20 mW of resonant light addressing the main cooling transition, $\tilde{X}\,^2A_1 - \tilde{A}\,^2E_{1/2}0_0^0$, but produced using an independent laser. For para-$CaOCH_3$, this light contains $N'' = 1$ and $N'' = 2$ components, each with $\sim$ 8 mW of power. To address all magnetic sublevels, the polarization of the light is switched between orthogonal linear polarizations at a rate of 1 MHz using a Pockels cell. In addition, we add ∼ 50-100 mW of 4_1^0 repumping light to increase the number of scattered photons in the detection region (for para-$CaOCH_3$ this only contains the $N'' = 1$ component). Laser-induced fluorescence (LIF) photons are collected on an EMCCD camera (Andor iXon Ultra 897) for a duration of 15 ms starting 1 ms after the initial ablation pulse. The experiment is run at a repetition rate of $\sim$ 2 s^{-1}, with shots alternating between Sisyphus cooled/heated and unperturbed configurations. To account for fluctuations in molecule numbers, beam images and traces depicted in Figs. 10.15 and 10.16 are the average of 150 successive shots, and each data point taken for parameter scans (Fig. 10.17) is the average of 50 shots.

[9] The RFA was the same 629 nm RFA used for $\widetilde{X}(02^00) \rightarrow \widetilde{A}(100)$ repumping in CaOH (chapters 4-5). The dye lasers were mostly Coherent 899s, with one Coherent 699 also used [214].

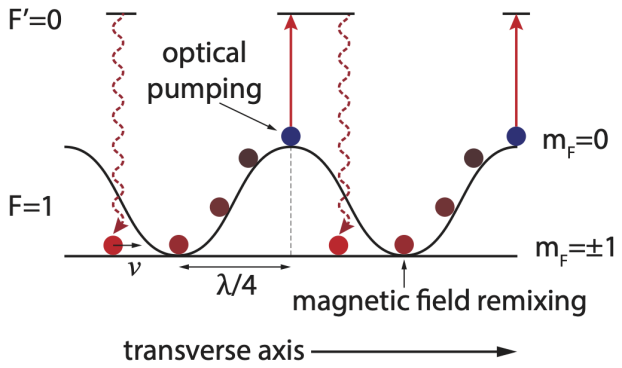

Figure 10.14: Sisyphus cooling scheme for the case of $\Delta > 0$ for a $F = 1 \rightarrow F' = 0$ transition, as described in the text. Reproduced from Ref. [47].

10.4.2 Magnetically assisted Sisyphus cooling

Laser cooling of $CaOCH_3$ was accomplished using the magnetically-assisted Sisyphus effect, a highly efficient and robust cooling method first demonstrated with atoms, and also frequently used for efficient transverse cooling of molecular beams [191, 217, 219, 307, 311, 393]. In this method, molecules pass through a standing wave of near-resonant, linearly-polarized light containing all of the optical frequencies necessary to establish optical cycling. For blue-detuned light ($\Delta > 0$), as a molecule approaches a peak in the periodic, AC Stark-shifted potential landscape formed by the standing wave, it returns non-adiabatically to a potential minimum by a combination of optical pumping and magnetic state remixing (by an external magnetic field $|B| \approx 1$ G aligned at an angle $\theta \sim 45°$ to the laser polarization axis). Repeated iterations of this process lead to cooling. Red-detuned light ($\Delta < 0$) results in heating via a similar, but inverted, mechanism. Fig. 10.14 provides a schematic overview of this process.

This Sisyphus cooling process is optimized if the time between photon scattering events γ^{-1}, where γ is the scattering rate, corresponds to the travel time of the molecule from a node to an antinode of the potential, $\lambda/4v$,

where λ is the laser wavelength and v is the molecule's velocity. For ortho-$CaOCH_3$, this gives an estimated capture velocity $v_c = \lambda\gamma/4 \approx 2$ m/s, using our measured scattering rate of $\gamma/(2\pi) \approx 2 \times 10^6$ s^{-1}. This estimate is consistent with values determined from the cooling data described below.

Molecules undergo Larmor precession near nodes of the standing wave due to the external magnetic field, allowing remixing of the m_F sublevels. This effect is optimized when the precession time, $(g_{\text{eff}}\mu_B B/\hbar)^{-1}$, is equal to the travel time of the molecule from antinode to node of the standing wave. Here μ_B is the Bohr magneton, B is the applied magnetic field, $\hbar$ is the Planck constant, and $g_{\text{eff}} = 1/3$ is the degeneracy-weighted Landé g-factor of the ground state hyperfine components of $CaOCH_3$. This gives an estimate for the optimal B field $B_0 = 4\hbar v/(g_{\text{eff}}\mu_B\lambda) \approx 1.6$ G for ortho-$CaOCH_3$, assuming the average velocity is $v_c/2$ [311].

10.4.3 Laser cooling results

We implement Sisyphus cooling by varying the detuning (Δ) of the main line $\widetilde{X}^2A_1 \rightarrow \widetilde{A}^2E_{1/2}\,0_0^0$ laser, which is aligned to form a standing wave of linearly polarized light. Figures 10.15B-D show representative beam images of the ortho NSI ($K'' = 0$) for unperturbed, Sisyphus heated ($\Delta < 0$), and Sisyphus cooled ($\Delta > 0$) configurations, and clearly indicate strong optical forces manipulating the molecular velocity distribution.

By integrating along the direction of molecular beam propagation we obtained one-dimensional (1D) beam profiles, shown in Fig. 10.16 for both the ortho (A) and para (B) NSI cooling schemes. The cooled and heated profiles fit well to a sum of Gaussian distributions with two distinct widths, corresponding to two classes of molecules, those that were Sisyphus laser cooled and those that were not. The cooled molecules were those with transverse velocities less than the capture velocity, $v < v_c$. Molecules with $v > v_c$ were instead subject predominantly to Doppler cooling and heating, depending on laser detuning. For blue detuning ($\Delta > 0$), a large

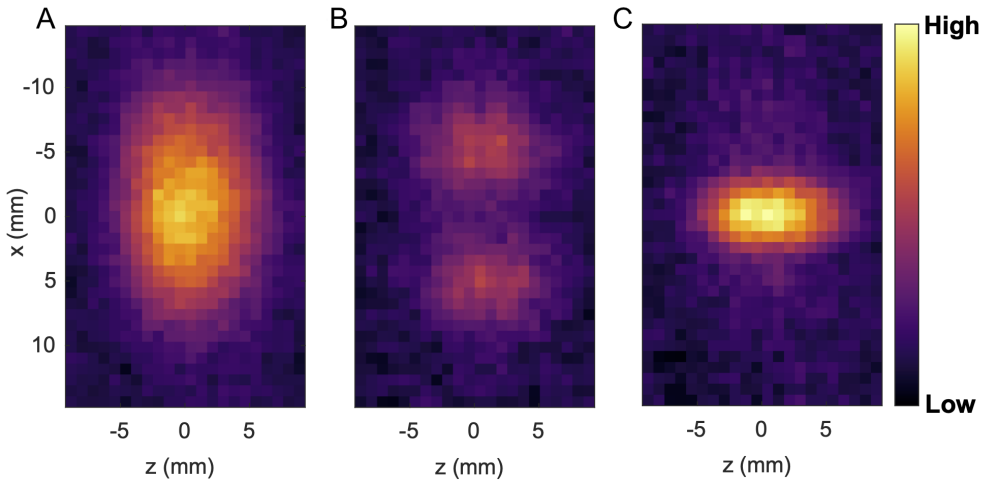

Figure 10.15: Beam images for ortho-$CaOCH_3$ ($K'' = 0$) laser cooling. (A) Unperturbed beam. (B) Sisyphus heated beam ($\Delta = -15$ MHz). (C) Sisyphus cooled beam ($\Delta = +25$ MHz). Modified from Ref. [47].

fraction of molecules fell within v_c and were cooled into a central, narrow peak on top of a broad Doppler heated background. For red detuning ($\Delta < 0$), molecules slower than v_c were heated while faster ones were Doppler cooled. This competition led to a concentration of molecules at velocities where the Doppler and Sisyphus forces balanced, corresponding to approximately v_c. From the positions of these two peaks we estimated a capture velocity $v_c \approx 1.5$ m/s for $K'' = 0$ cooling of the ortho NSI, in good agreement with the model described below. Unperturbed and resonantly depleted profiles fit well to single Gaussian distributions.

The integrated area of each of the three ortho-$CaOCH_3$ profiles with 1.1 W/cm^2 of cooling light applied was approximately 50% that of the unperturbed profile (Fig. 10.16A). This effect is understood to be due to losses to vibrational states that were not repumped, most notably $\tilde{X}\,^2A_1 4_2$ and $\tilde{X}\,^2A_1 3_1 4_1 8_1$. Combining the observed depletion with branching ratios previously measured for $CaOCH_3$ [213], we determined that 80^{+100}_{-30} photons were scattered in the cooling process and 110^{+150}_{-40} photons were scattered in resonant depletion (see above). From this observation we inferred an average scattering rate of $\sim 2 \times 10^6$ s^{-1} across the cooling region, which is

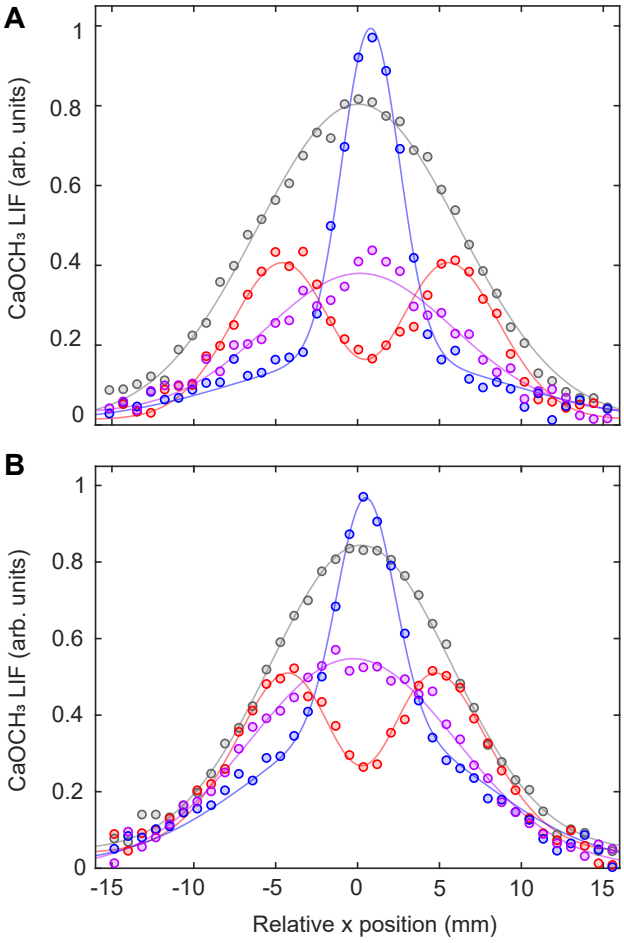

Figure 10.16: Sisyphus cooled and heated beam profiles. Integrated laser induced fluorescence (LIF) vs. position for **(A)** ortho-$CaOCH_3$ ($K'' = 0$) and **(B)** para-$CaOCH_3$ ($K'' = 1$) cooling schemes. Sisyphus cooling at a positive detuning $\Delta = +25$ MHz ($\Delta = +20$ MHz) for the ortho (para) isomer manifests itself as a narrowing of the detected distribution (blue), while Sisyphus heating appears as a bimodal distribution ($\Delta = -15$ MHz for both; red). Unperturbed (cooling lasers off; gray) and resonantly depleted ($\Delta = 0$; purple) profiles have the same width but different integrated area due to optical pumping into dark vibrational states. Solid curves are fits to single or double Gaussians as described in the supplemental material of Ref. [47]. Reproduced from Ref. [47].

similar to scattering rates observed for laser cooling of diatomic and linear triatomic molecules [192–195, 217, 219]. We determined the temperature of the molecules by fitting a Monte Carlo simulation of the molecular beam propagation to our data. This calculation gave an initial transverse temperature $T_\perp = 22 \pm 1$ mK, which was reduced by Sisyphus laser cooling to $T_\perp = 1.8 \pm 0.7$ mK. Combined with the enhancement in on-axis molecule density seen in Fig. 10.16A, this 10x temperature reduction corresponded to a 4x increase in the on-axis phase-space density of the molecular cloud.[10] Finally, we varied the laser detuning, intensity, and magnetic field for ortho-$CaOCH_3$ Sisyphus cooling and compared with the results of a model obtained by solving optical Bloch equations for molecules subject to the cooling light. We found good agreement between experimental results and the model, further strengthening our understanding of the cooling mechanism involved (see below).

Figure 10.16B shows beam profiles for para-$CaOCH_3$ ($K'' = 1$) laser cooling, taken at a laser intensity of 250 mW/cm^2. We observed significant Sisyphus cooling and heating, though the effect was weaker than for ortho-$CaOCH_3$ ($K'' = 0$), as expected, because there were more ground states coupled to the same excited electronic state, leading to a lower scattering rate by a factor of $\sim$2. Additionally, the reduced laser intensity used, set by technical limitations, resulted in a smaller capture velocity and cooled fraction. Using the same analysis as above, we found that the cooled molecules here scattered an average of 25 ± 10 photons, corresponding to an estimated scattering rate of $\sim 0.75 \times 10^6$ s^{-1}. Cooling of the para NSI would be improved with higher laser intensity and/or interaction length.

[10] We defined the phase-space density as $\rho = n\lambda_x^{dB}\lambda_y^{dB}\lambda_z^{dB}$, where n is the number density and $\lambda_i^{dB} \sim 1/\sqrt{T_i}$ is the de Broglie wavelength defined in terms of the temperature along the ith spatial direction. Because we cooled in 1D only, ρ scales as $1/\sqrt{T}$.

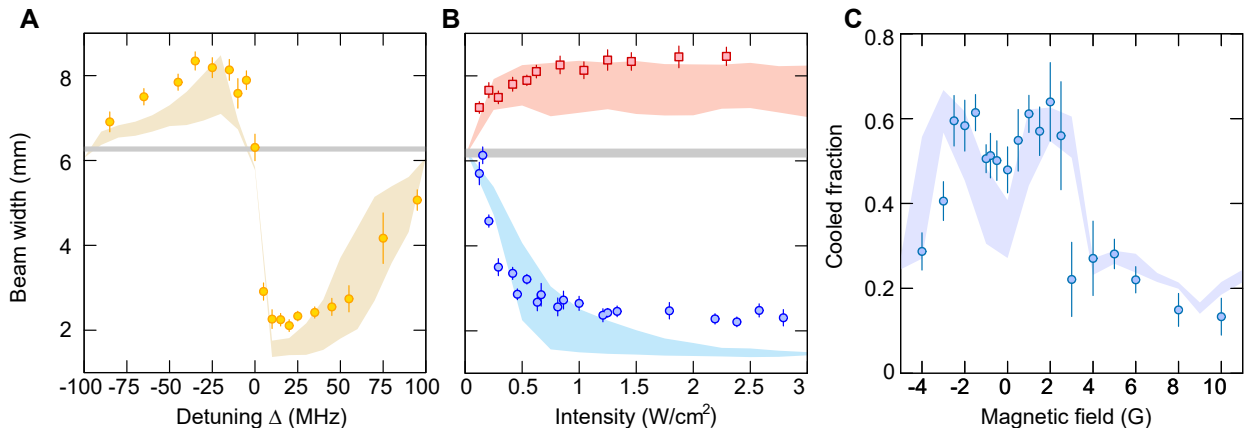

Figure 10.17: Experimental parameter scans and theory comparison. **(A)** Variation of beam width as a function of detuning Δ at a cooling laser intensity of 400 mW/cm^2 and a magnetic field of $|B| = 1$ G. The grey band depicts the unperturbed molecular beam width. **(B)** Variation of beam width as a function of laser intensity for $\Delta = +25$ MHz (blue circles) and $\Delta = -15$ MHz (red squares). **(C)** Variation of the fraction of cooled molcules as a function of magnetic field, taken at a laser intensity of 400 mW/cm^2 and a detuning of $\Delta = +20$ MHz. Shaded regions represent the results of the model described in the text, with error bands set by experimental uncertainty in the number of scattered photons. All error bars and bands for experimental data are standard error of the mean.

10.4.4 Cooling parameter scans

Varying the laser detuning, intensity, and magnetic field allows us to characterize the Sisyphus laser cooling for ortho-$CaOCH_3$ and compare it to optical Bloch equation-based simulations, as shown in Fig. 10.17. The dependence of the $1/\sqrt{e}$ molecular beam width[11] on detuning (Δ) is shown in Fig. 10.17A. The sign of this dependence is opposite that of Doppler cooling and is a clear signature of the magnetically-assisted Sisyphus effect. Both Sisyphus heating and cooling are optimized at detunings of $\Delta \approx \pm 20$ MHz, and we observe a $\sim$ 3x decrease in molecular beam width for optimal cooling, corresponding to a significant increase in on-axis beam brightness. The magnetic field was set to 1 G and aligned at an angle $\theta = 45°$ to the laser polarization axis.

The dependence of the molecular beam width on cooling laser intensity is shown in Fig. 10.17B. For both Sisy-

[11] This is determined by fitting to a sum of Gaussian functions, as described in the supplemental material of Ref. [47].

phus cooling ($\Delta > 0$; circles) and Sisyphus heating ($\Delta < 0$; squares), the beam width changes monotonically from its unperturbed value until saturating around an intensity of 600 mW/cm^2. This occurs at a maximum cooled fraction (defined as the portion of molecules captured by the Sisyphus effect and cooled into the narrow central peak) of 72(7)%. This saturated value indicates that we are able to cool all molecules in our cryogenic beam with velocity $v_{\text{trans}} < v_c$, given the initial Gaussian velocity spread $\sigma_v \approx 1.6$ m/s $\approx v_c$. For the case of heating, the magnetic field had a magnitude $|B| = 1$ G and was aligned at an angle $\theta = 45°$ to the laser polarization axis. In the case of cooling, the magnetic field was $|B| = 2$ G aligned at an angle $\theta = 90°$. We note that the beam width was observed to be only weakly dependent on this angle.

Finally, we plot the cooled fraction as a function of applied magnetic field for $\Delta > 0$ (Fig. 10.17C). As expected, Sisyphus cooling is suppressed at $|B| = 0$, though incomplete cancellation of Earth's magnetic field nonetheless allows residual remixing of dark states. The cooling efficiency improves up to fields of $|B| \approx 1 - 2$ G, which is consistent with the optimal field $B_0 \approx 1.6$ G predicted by equating the Larmor precession time due to the remixing field with the time for a molecule to travel from an antinode to a node of the standing wave (see above). At large fields $|B| > 3$ G we see a significantly weaker Sisyphus effect due to undesirable remixing of bright and dark states away from nodes of the standing wave. The magnetic field was aligned at an angle $\theta = 90°$ to the laser polarization axis for this scan.

Shaded regions in Fig 10.17 show results of an optical Bloch equation simulation, which is described in the supplemental material of Ref. [47]. The model exhibits good overall agreement with the experimental data, helping to validate our understanding of the cooling mechanism.

10.5 Conclusion and outlook

In this chapter, we have demonstrated two methods for achieving rotationally closed optical cycling in $CaOCH_3$ and shown that we can scatter >100 photons from $CaOCH_3$ by repumping two vibrational states. We then demonstrated efficient transverse laser cooling, via the magnetically assisted Sisyphus effect, of a beam of $CaOCH_3$, reducing the transverse temperature by an order of magnitude to temperatures near 1 mK.

Our results demonstrate the feasibility of directly laser cooling complex, nonlinear polyatomic molecules into the millikelvin temperature regime [394, 395]. This work opens the door to a number of future experiments that span a range of modern physical and chemical research frontiers. Because Sisyphus cooling is effective down to the recoil limit [396] (corresponding to $\sim$ 500 nK for molecules with similar mass to $CaOCH_3$), these techniques could be used to achieve bright, highly-collimated, few-μK molecular beams useful for precision measurements and studies of ultracold chemistry [397]. Efficient and state-selective laser cooling of both nuclear spin isomers also offers a method to separate them using radiation pressure beam deflection of specific spin species, a topic of interest in physical chemistry [398–401]. By adding a small number of other laser frequencies to the laser cooling of $CaOCH_3$ [213], optical tweezer arrays of symmetric top molecules should be possible, as recently accomplished with diatomic species [202]. These arrays would offer an ideal starting point for realizing new polyatomic quantum simulation and computation platforms [101, 110]. Laser cooling could also be extended to asymmetric tops, including biochemically relevant chiral molecules [34, 37, 147, 148]. Finally, laser cooling and trapping of the heavier symmetric top molecule $YbOCH_3$ would allow precise searches for time-reversal violating interactions at a previously inaccessible energy scale, and ultracold chiral molecules such as YbOCHDT could enable precision probes of fundamental parity violation [140, 219].

After the work described in this chapter was completed, vibrational branching ratios were measured with higher sensitivity for $CaOCH_3$ and $SrOCH_3$ [214, 215]. Those measurements indicate that scattering the $\gtrsim$ 10000 photons needed to load a magneto-optical trap (MOT) would require repumping approximately 10-12 vibrational states. This appears to be feasible given our experience with CaOH, especially if the $K_R = 0$ optical cycle is used so that rotational repumping can be avoided.

11

Outlook

In this thesis, we have described our efforts to optically cycle and laser cool CaOH molecules, load them into optical traps and tweezer arrays, and coherently control their internal quantum states. We have also described our first efforts to use the rich structure of CaOH molecules for science applications. These included demonstrating a scheme for electron electric dipole moment (eEDM) measurements with linear polyatomic molecules;

demonstrating the ability to control single molecules in optical tweezers for quantum science applications; and controlling the internal states of CaOH to tune their collisional properties.

In this chapter, we discuss prospects for future experiments with optically trapped CaOH, and also describe some outstanding challenges that will need to be addressed in future work. We also discuss prospects for extending our work to larger, nonlinear polyatomic molecules. These molecules have parity-doublet states with much longer intrinsic lifetimes than CaOH, among other favorable properties.

ii.i Quantum science with CaOH

One of the long-term goals of our work is to demonstrate the potential of ultracold polyatomic molecules for quantum science applications, i.e. for quantum information processing and for quantum simulation. The key advantages of polyatomic molecules for such applications are their large number of internal states, long-range dipolar interactions, long coherence times, and parity-doublet structure. While we have driven Rabi oscillations on parity-doublet states in optical tweezers, none of these other advantages have yet been studied in detail.

ii.i.i Choice of qubit states

Fig. ii.i shows potential qubit schemes enabled by the CaOH bending mode. Here we describe prospects for quantum information science with both of these architectures in polyatomic molecules

Parity-doublet qubits

At zero electric field, the bending mode is split into opposite-parity states (parity-doublet states), which in CaOH are split by 43 MHz by the ℓ-type parity-doubling interaction. If we pick two states with identical quantum num-

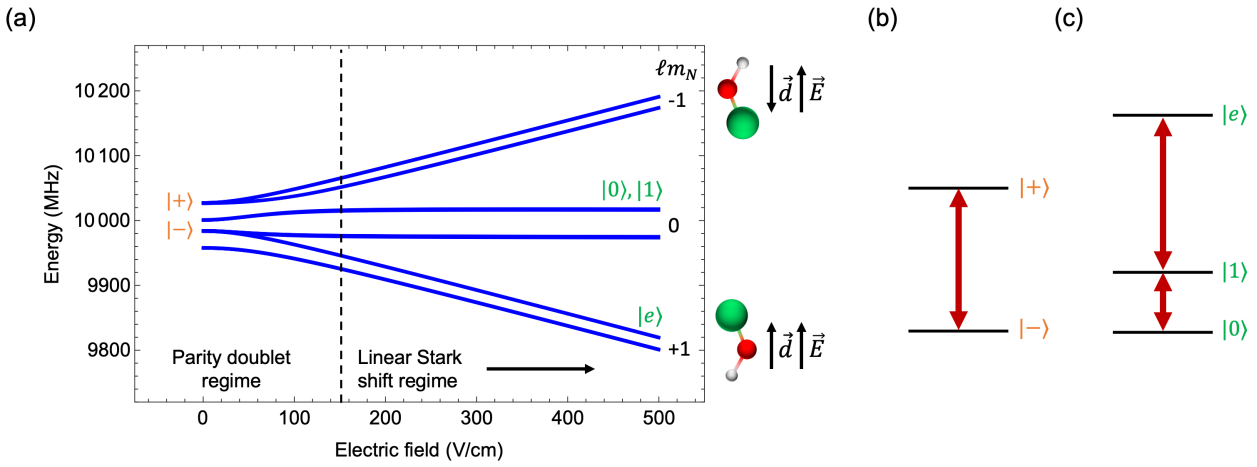

Figure 11.1: (a) Structure of the CaOH $\widetilde{X}(010)(N = 1)$ bending mode, with "parity-doublet" and "high-field" qubit states indicated. (b) Parity-doublet qubit scheme. (c) High-field qubit scheme.

bers besides parity (e.g. $|+\rangle = |F = 2, m_F = 2, +\rangle, |-\rangle = |F = 2, m_F = 2, -\rangle$), these states should have effectively zero differential sensitivity to magnetic fields,[1] and quadratic sensitivity to electric fields (since they couple the opposite parity states and push them apart). Additionally, while there are differential AC Stark shifts between these states (see chapter 6 and appendix A.6), these "parity-dependent" shifts are approximately 1-2% as large as "normal" tensor Stark shifts (i.e. the shift between states that differ by more than just the parity quantum number). This provides an excellent starting point for suppressing AC Stark shifts further, e.g. by using a magic angle [205]. For these reasons, it is likely that parity-doublet qubit states will have excellent bare coherence times, due to their lack of sensitivity to external fields.

The choice of specific hyperfine states determines the electric dipole matrix element between the states. For example, the $|F = 2, m_F = 2, \pm\rangle$ stretched states have the maximum possible dipole moment in the bending mode ($d\ell^2/N(N+1) = d/2 = 0.73$ D for CaOH in the $\widetilde{X}(010)(N = 1)$ manifold), while the $|F =$

[1] There are likely parity-dependent Zeeman splittings, somewhat reminiscent of those in the $\widetilde{A}^2\Pi$ state. However, these are expected to be extremely small, probably around or below 1 Hz/G.

$0, m_F = 0, \pm\rangle$ states have zero transition dipole moment. Molecules in parity-doublet states can interact via dipolar exchange interactions (the same interactions used for rotational gates in diatomic molecules [31, 32, 63]), with the strength of the interaction being proportional to the transition dipole moment squared, $|\langle +|d|-\rangle|^2$. Therefore, parity-doublet states with a large transition dipole moment could be good for two-molecule interactions and entangling gates, while states with no dipole moment would be good for storage due to their lack of electric field sensitivity.

High field/polarized qubits

An alternative choice is to use "high-field" qubits (Fig. 11.1(c)), which exist at electric fields above ∼150 V/cm, once the parity doublets are mixed and the molecule is aligned in the laboratory frame. In this approach, the qubit states (labeled $|0\rangle$ and $|1\rangle$) are chosen to be non-interacting, by encoding them in hyperfine states in the zero-dipole moment manifold. Interactions are turned on by using a third state, $|e\rangle$, which is in one of the polarized manifolds and interacts with other molecules in $|e\rangle$ via resonant, $S_Z S_Z$-type dipolar interactions. The interaction strength is proportional to the lab-frame dipole moment squared, d^2. In the $\widetilde{X}(010)(N = 1)$ state of CaOH, $d = 0.73$ D (which is suppressed by 2x compared to the molecule-frame dipole moment by the $\ell^2/N(N+1)$ factor mentioned above (and in chapter 1).

This approach is similar in concept to what is used for Rydberg atom quantum computing, where the qubits are stored in non-interacting hyperfine states and a third state is used to turn on interactions. The ability to implement switchable interactions in this way is important for quantum information processing, where it is desirable for the qubits not to interact with each other unless they are participating in an entangling gate. It was previously proposed to use "dipolar blockade" interactions (analogous to what is used for Rydberg atoms [360, 361]

but with resonant dipole-dipole interactions) to implement entangling gates between molecules in the high-field qubit scheme [101]. However, because of the low interaction strengths between molecules, this would require extremely long gate times.[2] An alternative approach would be to implement a resonant phase gate, where molecules in the state $|e\rangle|e\rangle$ accumulate a phase $\phi = \omega_{\mathrm{DDI}} t$ due to dipolar interactions, where ω_{DDI} is the dipolar interaction energy. In this approach, molecules in state $|1\rangle$ are transferred to the $|e\rangle$ state with a π pulse, held there for a time t, and then brought back to $|1\rangle$. Using a hold time chosen so that $\phi = \pi$ would implement the CZ gate $|00\rangle \rightarrow |00\rangle; |01\rangle \rightarrow |01\rangle; |10\rangle \rightarrow |10\rangle; |11\rangle \rightarrow -|11\rangle$.

Switchable interactions could also be implemented using parity-doublet qubits, by using three or more states (possibly at the expense of long coherence times). A similar technique has also been proposed and demonstrated for rotational states in diatomic molecules using dipolar spin-exchange interactions [63, 98]. However, the high-field qubit architecture could possibly have some advantages. For instance, the resonant dipolar interactions in the high-field qubit scheme are qualitatively distinct from the dipolar spin-exchange interactions used for parity-doublet states, which could possibly be beneficial for entangling gates, e.g. by not requiring two transitions to be tuned into resonance with each other. It is also possible that having access to these polarized states will enable new approaches to mediating molecular entangling gates with Rydberg atoms (as proposed in Refs. [106, 107] for diatomic molecules), e.g. by not requiring two Rydberg states to be tuned close in energy to a molecular transition. High-field states could also be useful for qudit architectures, because there are a large number of hyperfine states in each polarized manifold that have identical dipole moments and correspondingly identical interaction strengths. For example, two pairs of qubit states ($|0\rangle$ and $|1\rangle$; $|2\rangle$ and $|3\rangle$; together comprising a $d = 4$ qudit)

[2] For a blockade scheme to work, the Rabi frequency for the $|1\rangle \leftrightarrow |e\rangle$ transitions should be $\sim$10x lower than the interaction strength between molecules in the $|e\rangle$ state.

could be encoded in four zero-dipole moment hyperfine states, with each pair having a corresponding hyperfine state in the polarized manifold ($|e_{12}\rangle$; $|e_{34}\rangle$) that is used to implement two-qudit gates. Having the same dipole moment for both interacting states may be important so that the gate sequence is independent of the specific encoded qudit state.

One disadvantage of the high-field qubit approach is that coherence times are likely to be worse than in parity-doublet qubit states. The qubit storage states $|0\rangle$ and $|1\rangle$ can be chosen to have very small differential magnetic field and electric field sensitivity, but in general they will be susceptible to larger tensor AC Stark shifts than the parity-doublet qubits. Nonetheless, these AC Stark shifts are comparable to those seen in diatomic molecules like CaF and could be suppressed with magic angle trapping and dynamical decoupling to the point that two-qubit gates are practical [31, 32, 205]. More critically, there is a large differential electric field sensitivity between the $|e\rangle$ state and the qubit storage states. However, this could also be mitigated with dynamical decoupling techniques and electric field stabilization.[3]

Even more states (!)

In addition to the qubit schemes described above for parity doublet states, there are many more structures that could be harnessed for quantum information processing. For instance, there are proposals for encoding error-corrected qubits in polyatomic molecules, by creating large superpositions of rotational states [104]. These schemes require that the superposition include states not only of different rotational quantum number N, but also with different angular momentum projection quantum number K. In CaOH, $K = \ell$, which necessarily

[3] It is worth noting that Rydberg atoms suffer from even higher electric field sensitivity (with correspondingly higher interaction strengths), but they have nonetheless been used for high-fidelity entangling gates.

means that different vibrational states would need to participate. Creating these states remains a significant challenge, and is probably more practical in symmetric or asymmetric top molecules, where different values of K are available in the ground vibrational state.

11.1.2 Dipolar interactions

Another important milestone will be to demonstrate controlled dipolar interactions and entangling gates between CaOH molecules. The dipolar interaction strength between two molecules with dipole moments aligned along Z is

$$E_{\mathrm{DDI}} = \frac{d^2}{4\pi\epsilon_0}(1 - 3\cos^2\theta) \tag{11.1}$$

where θ is the angle between Z and the vector pointing between the two molecules ($\theta = 0$ is the "head-to-tail" configuration and $\theta = \pi/2$ is the "side-by-side" configuration). For parity doublet manifolds in CaOH, the dipole moment of maximally aligned states is $d = \mu\ell^2/N(N+1)$, where $\mu = 1.465$ D is the molecule frame dipole moment [256], ℓ is the vibrational angular momentum projection quantum number, and N is the rotational quantum number. In the $\widetilde{X}(010)(N = 1)$ state, this means that the maximum dipole moment is $d = 0.73$ D, which occurs for the polarized states and is also the transition dipole moment between the stretched $F = 2, m_F = 2$ parity doublet states (relevant for dipolar spin-exchange interactions between parity-doublet qubits). The dipolar interaction energy for these states is shown as a function of distance in Fig. 11.2.

From Fig. 11.2, we see that the interaction strength for molecules separated by 1 μm is 160 Hz for head-to-tail alignment and 80 Hz for side-to-side alignment. For a realistic tweezer spacing of 2 μm, the interaction energies decrease to 20 Hz and 10 Hz, respectively. By comparison, the CaOH bending mode lifetime of $\sim$350 ms

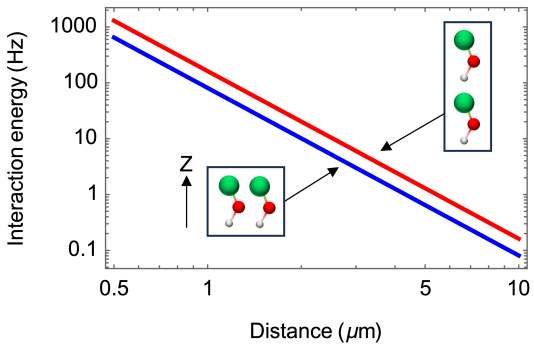

Figure 11.2: Dipolar interaction energy for maximally aligned states in the CaOH $\widetilde{X}(010)(N=1)$ bending mode. The red (top) curve is for a head-to-tail geometry, and the blue (bottom) curve is for a side-by-side geometry.

means that an interaction strength of $\sim$3 Hz is necessary just to achieve just a single dipolar interaction cycle in the lifetime of the state. Getting >10 dipolar interaction cycles in the bending mode lifetime requires spacings $\lesssim 1.5\ \mu$m.

Achieving these goals will likely require significant upgrades to our tweezer setup. For state-of-the-art molecule tweezer experiments, spacings around 1.5 μm are achievable [31]. However, at this separation, axial motion in the traps can cause rapid dephasing of the dipolar interactions, and so we would likely need axial confinement and/or Raman sideband cooling [30, 206, 322] to make such an approach feasible.

An alternative approach for achieving high interaction energies would be load the molecules into a lattice. At our temperatures and phase-space densities, lattice filling would be extremely low, but it may be possible to deterministically prepare lattices by loading from movable optical tweezers, e.g. similar to the setup described in Ref. [402].

For experiments with optical tweezers, especially those that require rearrangement, we will also need to significantly improve our imaging fidelity compared to what was achieved in chapter 8. One limitation of our current

tweezer setup is that the 780 nm tweezer light limits the number of photons that can be scattered, so switching to 1064 nm tweezers may be necessary. Even then, our full photon budget of ∼14000 photons is a limitation. Imaging with <1% molecule loss requires scattering only $\lesssim 140$ photons, and so the collection efficiency of our imaging system would need to be very high to do so while also maintaining high fidelity. This seems feasible, but may require careful engineering of the imaging system.

11.1.3 Quantum simulation

One direction that we have not yet explored is to use the linear Stark shifts in CaOH for quantum simulation, specifically of quantum magnetism models, as proposed in Refs. [109, 110]. Once we are able to demonstrate dipolar interactions between molecules, the technical requirements of some of these schemes could be relatively straightforward. For instance, one scheme for implementing anisotropic quantum magnetism Hamiltonians [110] would require microwave dressing of the $\widetilde{X}(010)(N=1)$ state via off-resonant 40 GHz coupling to $N=2$. We have already demonstrated the ability to couple these states with microwaves (though dressing would likely have much stricter requirements on phase stability than what we have needed so far).

For quantum simulation of the physics of spin-1 dipoles, the ability to drive transitions between $m_N = -1, 0, +1$ states in the linear Stark shift regime would be necessary. This should also be relatively straightforward given the techniques we have already developed, namely the ability to prepare single quantum states, polarize the molecules, and drive RF transitions within the $\widetilde{X}(010)(N=1)$ bending mode.

11.2 Ultracold collisions with CaOH

In the work described in chapter 9, we demonstrated that there are certain states in the $\widetilde{X}(010)(N=1)$ bending mode with shielding factors (i.e. the ratio of elastic to inelastic collision rates) that could be sufficient for evaporative cooling. In these experiments, we were limited by molecules trapped in vibrational dark states, so realizing these favorable shielding factors in practice will requirement improvements to state preparation (described below). With improvements to state preparation and also loading more molecules into an ODT with high density, demonstrating evaporative cooling may be possible. The combination of numbers and densities required for initial evaporative cooling work could be achieved in the near term by transferring molecules from the conveyor belt MOT to a large ODT, and then into a small ODT. Using a crossed ODT geometry would also likely provide large gains in this direction.

Another interesting direction to pursue would be to attempt to study collisions in parity doublet states at lower temperatures. It has been predicted [126, 131] that parity doublet states have long-range interaction potentials that support "field-linked" bound states, which would enable the observation of collision resonances, and even the formation of weakly bound dimers, at temperatures around 1 μK. This could present an avenue to the formation and study of cold $(CaOH)_2$ hexatomic molecules, in a similar manner to recent work creating weakly-bound tetratomic molecules with field-linked resonances [133].

11.3 Improved cooling and state purity

Two significant limitations to the experiments described in this thesis have been (1) relatively high temperatures ($\sim$30-100 μK in optical traps, depending on trap depth) and (2) molecules in vibrational dark states, primarily

from blackbody radiation (BBR) and optical cycling losses.

High temperatures led to increased decoherence in the context of single-molecule control experiments, and also limited the density and the collision rates in our collision experiments. When implementing interactions between molecules in tweezers, high temperatures will significantly increase motional dephasing.

One route to lower temperatures is Raman sideband cooling in optical tweezers, as demonstrated for CaF [30, 206]. However, it is possible that there will be room to gain with standard sub-Doppler cooling techniques. The temperatures we have achieved with sub-Doppler cooling, including both Λ cooling and single-frequency (SF) cooling, are higher than what was seen for CaF molecules [231, 232]. We do not currently understand this difference, and do not know whether it is a fundamental consequence of the molecular structure, or whether it is due to technical imperfections in the experiment. Better modeling of sub-Doppler cooling in molecules will be required to understand these effects in more detail. Either way, with a reliable model it should be possible to both debug technical sources of noise and also to potentially design more efficient sub-Doppler cooling schemes tailored to specific molecular structure.

Another limitation of the experiments described in this thesis has been molecular population in dark vibrational states. For the collision experiments in chapter 9, background collisions with these molecules limited the lowest detectable inelastic loss rates. For single-molecule experiments, this background population typically leads to offsets in our data, due to molecules that were shelved in a dark state during state preparation but then reappear in a bright state (due to blackbody dynamics) prior to imaging.

We believe that there are two sources of these background molecules. The first is optical cycling losses, whereby molecules decay with a probability around 5-10 $\times$ 10^{-5} to a vibrational dark state after scattering a photon. These states are relatively high in the vibrational potential (e.g. $\widetilde{X}(220)$, $\widetilde{X}(040)$, etc.), and so they radiatively de-

cay over ∼100 ms timescales to lower-lying states, some of which may be bright. A second source of background molecules are those that were originally prepared in the correct state, but then are driven by BBR or spontaneous decay to dark states. This effect could be improved by cooling the environment to cryogenic temperatures, using similar techniques to what is now being done with, e.g. trapped ion and Rydberg atom experiments. However, going to cryogenic temperatures will not help reduce the number of molecules shelving in dark states by optical cycling losses. Mitigating these losses will require an improved photon budget, careful efforts to minimize the number of photons scattered from the molecules once they are loaded into an optical trap, and/or the development of techniques to remove these molecules from the trap once they are shelved in dark states.

11.4 Towards laser cooling of more complex molecules

Even after cooling the environment to cryogenic temperatures, experiments with parity doublet states in CaOH will be fundamentally limited by the ∼700 ms lifetime of the $\widetilde{X}(010)$ bending mode (with higher vibrational levels having even shorter lifetimes). Therefore, in future work it will be important to move to a nonlinear molecule, which has parity doublet structure in the vibrational ground state.

With this challenge comes the opportunity to apply what we have learned to choosing a molecule that is well optimized for laser cooling and for specific applications available with parity doublet states. Table 11.1 summarizes the properties of a few Ca-containing polyatomic molecules that have been proposed (or demonstrated) as viable candidates for laser cooling and trapping [34, 37, 42, 213–215]. We have listed the molecule-frame dipole moment, the parity-doublet splitting in the lowest-lying parity-doubled state in the molecule (i.e. $N = 1, K = 1$), and the wavelengths and measured vibrational branching ratios for low-lying electronic transitions. Note that

Molecule (Symmetry)	Dipole Moment	K=1 Parity doubling	Transition	Wavelength	Diagonal VBR	Refs.
CaOH	1.465 D	43 MHz	$X \to A$	626 nm	0.945	[237, 269]
($C_{\infty v}$)	[256]	[94**?**]	$X \to B$	555 nm	0.968	[238]
$CaOCH_3$	1.58 D	<50 kHz	$X \to A$	629 nm	0.929	[214, 386]
(C_{3v})	[95]	[95]	$X \to B$	565 nm	0.91	[213, 385]
$CaNH_2$	1.74 D	~230 MHz	$X \to A$	647 nm	0.936	[214, 403]
(C_{2v})	[403]	[403–406]	$X \to B$	630 nm	0.957	[214, 404]
			$X \to C$	576 nm	<0.9	[214, 405]
CaSH	5.36 D	~70 MHz	$X \to A$	650 nm	–[a]	[407]
(C_s)	[408]	[409]	$X \to B$	631 nm	0.96	[214, 408]
			$X \to C$	622 nm	0.628	[214, 409]

[a] Calculated to be 0.83 based on measured geometries and vibrational frequencies [37, 409].

Table 11.1: Summary of Ca-containing polyatomic laser cooling candidates of various symmetries.

the Sr-containing analog any of these molecules (e.g. $SrNH_2$) could also be laser cooled. The advantage of the Sr-containing molecules is that their higher mass would make them better suited to certain precision measurements [140], but at the expense of being more challenging to trap in a magneto-optical trap [221]. Here we briefly describe some of the advantages and disadvantages of each species.

11.4.1 Symmetric top molecules: $CaOCH_3$

Symmetric top molecules (STMs) are a natural next choice for laser cooling. Their structure is very similar to that of CaOH in the vibrational bending mode, except with much smaller parity doubling (which is caused by, e.g. hyperfine interactions, and is <100 kHz in a molecule like $CaOCH_3$ [95]). Among symmetric top molecules, $CaOCH_3$ and $SrOCH_3$ are probably the most natural choices. One alternative option, $CaCH_3$ (or $SrCH_3$), is smaller and therefore will have fewer vibrational states to worry about, but unfortunately these molecules are weakly bound and suffer from predissociation in the $\widetilde{A}^2E$ state [410].

We have demonstrated laser cooling of $CaOCH_3$ in this thesis by scattering approximately 100 photons, so it appears that there are no major issues with optical cycling. Moreover, it is possible to optically cycle using $K = 0$ states, which do not suffer from rotational branching losses. A challenge with this approach is that after laser cooling, the molecules need to be transferred into the $K = 1$ manifold. This could probably be done with 160 GHz microwave radiation, though it is likely that the transition matrix element between these states is extremely small, making it difficult to drive.[4] For laser cooling directly in the $K = 1$ manifold, two lasers addressing $N = 1$ and $N = 2$ will be necessary for nearly every vibrational state.

Vibrational branching ratios of $CaOCH_3$ have previously been measured in Refs. [47, 213, 214, 295], though none have the 10^{-5} sensitivity necessary to determine the feasibility of cycling 10,000 photons for laser cooling. However, measurements and calculations have been performed with high sensitivity for $SrOCH_3$ in Ref. [215], suggesting that approximately 11 vibrational repumping lasers will be required to achieve a photon budget of $\gtrsim$ 15000 photons. There appear to be no substantial differences between these measurements and the lower-sensitivity $CaOCH_3$ results, suggesting that $CaOCH_3$ will require a similar number of vibrational repumping lasers. The primary reason for the large number of decay channels is the large number of vibrational modes in these molecules. Nonetheless, this appears to be a feasible number of repumping lasers, especially if the $K = 0$ optical cycling scheme is used so as to avoid rotational repumping.[5] However, the challenge in that case will be finding a way to populate the $K = 1$ parity doublet state after laser cooling.

$CaOCH_3$ will be best suited to applications where having very small parity doublet spacing is desired. This

[4] Transferring from $K = 0$ to $K = 1$ involves changing the total nuclear spin from $I = 3/2$ to $I = 1/2$, making it very suppressed. It is possible that small hyperfine mixings induced by the Hamiltonian described in Ref. [95] could turn on a small matrix element, but this requires further investigation.

[5] There are still open questions about the $K = 0$ scheme at the >1000 photon level, e.g. at what level Jahn-Teller mixing will mix K_R stacks and interrupt rotational closure.

would be useful for any applications that rely only on linear Stark shifts, e.g. for certain quantum simulation applications [109, 110], or quantum computing and/or error correction using the "high-field" qubit encoding [101, 104]. On the other hand, having a larger parity doublet spacing appears to be desirable for collisional shielding (chapter **??**) and for the use of parity-doublet qubits, which will be less sensitive to electric field noise at larger parity doublet splittings.

The electric dipole moment of $CaOCH_3$ is very similar to that of CaOH, so there is no clear advantage for implementing dipolar interactions.

11.4.2 Asymmetric top molecules

Moving from symmetric to asymmetric top molecules (ATMs) has a number of advantages, including the ability to cool smaller nonlinear molecules, which would likely help with vibrational branching. Moreover, in asymmetric species, electronic angular momentum is quenched, which may help reduce the number of perturbations in excited states. Finally, the asymmetric structure leads to larger parity doublet splittings, which could be useful for certain applications, particularly parity-doublet qubit states and, potentially, collisional shielding.

A number of asymmetric molecules have been proposed for laser cooling, including large organic molecules and chiral molecules [34, 37, 38]. Here we focus just on two of the smallest ATMs, which have fewer vibrational modes and therefore may be more practical for full 3D laser cooling and trapping in the near term.

Unlike STMs, no ATM has been laser cooled to date, though efforts have been made in this direction [51]. Accordingly, there are more fundamental unanswered questions about laser cooling ATMs than STMs. While we do not anticipate fundamental challenges with the small ATMs discussed here (aside from the significant rotational branching expected in CaSH; discussed below), there is always the possibility of unexpected problems.

$CaNH_2$

$CaNH_2$ has C_{2v} symmetry, which provides significant symmetry protection for rotational branching, as discussed in Ref. [215]. Vibrational branching ratios have only been measured with 10^{-3} level sensitivity for $CaNH_2$ [51, 214], though measurements and calculations for $SrNH_2$ suggest that approximately nine repumping lasers will be required to cycle $\gtrsim 15000$ photons [215]. We anticipate $CaNH_2$ to require a similar number of lasers.

Though there are rotationally closed transitions in $CaNH_2$ and $SrNH_2$ that do not require $N = 2$ rotational repumping, it appears that this is only possible if all repumping lasers are sent through the same electronic state ($\widetilde{A}^2B_2$). If we "decouple" the repumpers to increase the scattering rate (as is done with CaOH), $N = 2$ vibrational repumping will be necessary. It remains to be seen what the optimal approach to this tradeoff will be.

$CaNH_2$ has a large parity doubling in the $K = 1$ state of approximately 230 MHz.[6] This will likely make it a favorable choice for implementing parity-doublet qubit states with long coherence times, and potentially for collisional shielding, since the large parity doubling suppresses inelastic losses (chapter 9). One open question for parity doublet qubit states in ATMs is whether there are parity-dependent AC Stark shifts like we see in the CaOH vibrational bending mode.

The electric dipole moment of $CaNH_2$ is slightly larger than that of CaOH, but not by enough that it can be considered a large advantage.

One final benefit of $CaNH_2$ compared to lower-symmetry molecules is that the nuclear spin state is different for $K = 1$ and $K = 0$ (similar to $CaOCH_3$). Because of the difficulty of changing the nuclear spin isomer, this means that $K = 1$ is metastable despite its relatively high energy. This will be helpful for molecule production

[6] The parity doubling in ATMs is due to the molecular asymmetry, specifically the fact that the moment of inertia is different along the b and c axes.

and also potentially for the lifetime of the state during quantum science experiments.

CaSH

CaSH has C_s symmetry, which means there is a lack of symmetry protection for both rotational and vibrational branching, as discussed in Ref. [215]. The primary concern is that mixing of K states is allowed in the electronic excited state, which in turn means that there is significant rotational branching to $K = 0$, $K = 1$, and $K = 2$ in the ground state during optical cycling. This branching was observed to be of order unity in SrSH [215]. For CaSH, the perturbation that causes this mixing is probably a bit weaker [409],[7] but not to a sufficient degree to eliminate the problem. Moreover, the measured vibrational branching ratios for both CaSH [214] and SrSH [215] appear to be unfavorable. It thus seems like laser cooling CaSH would require a significant amount of work, and a large number of repumping lasers.

If these difficulties can be overcome, the advantage of CaSH is that it has a very large molecule frame dipole moment of 5.36 D [408], leading to an order-of-magnitude higher dipole-dipole interaction strength than CaOH. Moreover, the parity doubling is relatively large, which could be useful for parity-doublet qubits. Though these advantages are tantalizing, laser cooling would nonetheless likely present too high a degree of difficulty for experiments in the near term.

ii.4.3 Blackbody lifetimes

While nonlinear polyatomic molecules are appealing because of the long lifetime of their parity doublet states, these long lifetimes can only be achieved if the environment is cooled to cryogenic temperatures. At room tem-

[7] At least some component of this perturbation arises from a spin-orbit interaction.

Molecule	Lifetime (s)	N_{vib}	$N(\tau_i < 20\text{ s})$
CaF	4.0	1	1
CaOH	1.1	4	3
SrOH	1.3	4	3
YbOH	1.2	4	3
CaSH	3.7	3	2
$CaNH_2$	1.7	6	2
$CaOCH_3$	2.5	12	2
CaOPh	1.2	33	6

Table 11.2: Calculated blackbody lifetimes at 300K for laser-coolable molecules. Also shown are the total number of vibrational modes, N_{vib}, and the number of modes with blackbody excitation times less than 20 s (see text). Reproduced from Ref. [44].

perature, blackbody radiation (BBR) can excite molecules from the ground vibrational state to excited vibrational levels, decreasing the lifetime to ∼1 s, as was observed for CaOH. As part of our work modeling BBR lifetimes of CaOH (described in chapter 6), we also worked with the group of Lan Cheng to calculate BBR lifetimes of some larger polyatomic molecules proposed for laser cooling, as described in Ref. [44]. The results are reproduced in Tab 11.2.

The room temperature BBR lifetime of the vibrational ground state in each molecule is listed, along with the total number of vibrational modes and the total number of "BBR-active" vibrational modes, i.e. those that are excited by room temperature BBR on a timescale of under 20 s. We see that even for large polyatomic molecules, only a few vibrational modes are significantly excited by BBR. The remaining states are generally high-frequency vibrations present in the ligand and far away from the Ca optical cycling center atom. Thus, the "BBR-inactive" modes are generally the same states that have very small Franck-Condon factors. In this way, the fact that BBR lifetimes are relatively similar for these molecules is a consequence of the same structure that makes them laser coolable in the first place.

In the end, all of these molecules have BBR lifetimes of around 1-2 s at room temperature. Therefore, it will be important to install blackbody shielding to extract the most out of trapped polyatomic molecules in future experiments.

A

Matrix Elements

This appendix contains matrix elements used to calculate energies, eigenstates, and other properties (e.g. transition dipole moments) for CaOH. The majority of these results can be found elsewhere (e.g. in Refs. [252, 253]), and are included here as a (mostly) complete reference for calculations related to this linear triatomic molecule. Note that many of the matrix elements presented for the $\widetilde{X}(010)$ bending mode can also be used to describe the $\widetilde{X}^2A_1$ ground state of $CaOCH_3$.

A.1 Computational procedure

To calculate energies and eigenvalues for a state described by the effective Hamiltonian H_{eff}, one picks a basis in which to evaluate matrix elements, then builds the Hamiltonian before computationally diagonalizing it. The procedure is as follows:

1. Pick a basis (either Hund's case (a) or case (b) for CaOH), typically chosen to make the Hamiltonian as close to diagonal as possible, though this is not essential. Because the rotational ladder is nominally infinite, we need to pick a maximum angular momentum at which to truncate the basis. Unless large electric fields are applied to mix many rotational states, $N_{\text{max}} = 3$ (or $J_{\text{max}} = 5/2$ for case (a)) is sufficient for most calculations of laser cooling states in CaOH. Define some ordering of basis states that will be used when writing the Hamiltonian in matrix form. For example, for a case (b) basis (excluding hyperfine and vibrational angular momentum) $|N, S, J, M\rangle$ with $N_{\text{max}} = 3$, we might define the basis states as $\{|1\rangle = |0, 1/2, 1/2, -1/2\rangle; |2\rangle = |0, 1/2, 1/2, +1/2\rangle; \ldots; |i_{\text{max}}\rangle = |3, 1/2, 7/2, +7/2\rangle\}$.
2. Compute matrix elements and build the Hamiltonian. This is done by building a two-dimensional, square table or array with elements $\langle i|H_{\text{eff}}|j\rangle$, where $|i\rangle$ and $|j\rangle$ are the basis states. i and j both run from 1 to i_{max}, where i_{max} is the size of the basis defined in step 1. The matrix elements $\langle i|H_{\text{eff}}|j\rangle$ are computed using expressions described in the remainder of this appendix.
3. Numerically compute eigenvalues and eigenvectors of the assembled array. These are the energies and eigenvectors of the molecular eigenstates.
4. The eigenvectors define a transformation from the computational basis (i.e. the bare case (a) or case (b) basis) to the basis of molecular eigenstates. If desired, this can be used to calculate other properties of the molecular eigenstates, e.g. transition dipole moments or expectation values, as long as matrix elements for the desired operator are known in the computational basis.

A.2 Useful spherical tensor algebra results

We will use spherical tensor algebra to write down and calculate matrix elements of the Hamiltonian. This is described in detail in many places, including Refs. [253, 411]. Here we provide a brief overview of useful identities used when calculating matrix elements in the following sections.

A.2.1 Relationship between spherical and cartesian coordinates

An operator $\boldsymbol{A}$ is written in spherical tensor notation as the spherical tensor operator $T^k(\boldsymbol{A})$, whose components are $T^k_p(\boldsymbol{A})$. k is the rank of the tensor, and it has $2k+1$ components $p = -k, -k+1, \ldots, k-1, k$. A rank-0 tensor is a scalar, a rank-1 tensor is a vector, and so on. To get our bearings, the relationship between the components of a rank-1 spherical tensor (vector) and its Cartesian equivalent is

$$T^1_1(\boldsymbol{J}) = -\frac{1}{\sqrt{2}}(J_X + iJ_Y) = -\frac{1}{\sqrt{2}}J_+ \tag{A.1a}$$

$$T^1_0(\boldsymbol{J}) = J_Z \tag{A.1b}$$

$$T^1_{-1}(\boldsymbol{J}) = \frac{1}{\sqrt{2}}(J_X - iJ_Y) = \frac{1}{\sqrt{2}}J_- \tag{A.1c}$$

A.2.2 Scalar product

The scalar product $\boldsymbol{A} \cdot \boldsymbol{B}$ between two rank-k operators can be written in spherical tensor notation as

$$T^k(\boldsymbol{A}) \cdot T^k(\boldsymbol{B}) = \sum_p (-1)^p T^k_p(\boldsymbol{A}) T^k_{-p}(\boldsymbol{B}) \tag{A.2}$$

It can be verified using the relationship between spherical and Cartesian coordinates (eqn A.1 above), that for two vectors this yields $A_X B_X + A_Y B_Y + A_Z B_Z$ in Cartesian coordinates.

Matrix elements. Sometimes we will need to calculate matrix elements of a scalar product $T^k(\boldsymbol{A}_1) \cdot T^k(\boldsymbol{A}_2)$ in a coupled angular momentum basis $|j_1 j_2 J M\rangle$, where $T^k(\boldsymbol{A}_1)$ acts on the $|j_1\rangle$ subspace and $T^k(\boldsymbol{A}_2)$ acts on the $|j_2\rangle$ subspace. The angular momenta are coupled so that $\boldsymbol{j}_1 + \boldsymbol{j}_2 = \boldsymbol{J}$. The matrix elements are [252][1]

$$\begin{aligned}\langle j_1, j_2, J, M | T^k(\boldsymbol{A}_1) \cdot T^k(\boldsymbol{A}_2) | j_1', j_2', J', M' \rangle = \delta_{JJ'} \delta_{MM'} (-1)^{j_1' + j_2 + J} \begin{Bmatrix} j_2 & j_1 & J \\ j_1' & j_2' & k \end{Bmatrix} \\ \times \langle j_1 || T^k(\boldsymbol{A}_1) || j_1' \rangle \langle j_2 || T^k(\boldsymbol{A}_2) || j_2' \rangle\end{aligned} \tag{A.3}$$

where the term in curly brackets is a Wigner $6j$ symbol. This identity will be useful, for instance, when calculating matrix elements of the Fermi contact hyperfine interaction $\sim \boldsymbol{J} \cdot \boldsymbol{I}$ in the coupled basis $|J, I, F, M\rangle$.

[1] Note that there is no M dependence (i.e. no $3j$ symbol in front) since the operator is a scalar.

A.2.3 Tensor product

Two spherical tensors can be coupled together using Clebsch-Gordan coefficients to form a new tensor [253]

$$\begin{aligned} T_P^K(\boldsymbol{R}^{k_1}, \boldsymbol{S}^{k_2}) &= \sum_{p_1,p_2} \langle k_1, k_2, p_1, p_2 | K, P\rangle T_{p_1}^{k_1}(\boldsymbol{R}) T_{p_2}^{k_2}(\boldsymbol{S}) \\ &= \sum_{p_1,p_2} (-1)^{-k_1+k_2-P} \sqrt{2K+1} \begin{pmatrix} k_1 & k_2 & K \\ p_1 & p_2 & -P \end{pmatrix} T_{p_1}^{k_1}(\boldsymbol{R}) T_{p_2}^{k_2}(\boldsymbol{S}) \end{aligned} \tag{A.4}$$

where $\boldsymbol{R}$ is a tensor of rank k_1, $\boldsymbol{S}$ is a tensor of rank k_2, and these can be combined to form a tensor $T_P^K(\boldsymbol{R}^{k_1}, \boldsymbol{S}^{k_2})$ of any rank K between $|k_1 - k_2|$ and $k_1 + k_2$. The symbol $\langle k_1, k_2, p_1, p_2 | K, P\rangle$ in the first line is a Clebsch-Gordan coefficient, and in the second line it was rewritten as a Wigner $3j$ symbol.

Note that two operators of the same rank, $T^k(\boldsymbol{R})$ and $T^k(\boldsymbol{S})$, can be combined in this way to form a scalar operator $T_0^0(\boldsymbol{R}^k, \boldsymbol{S}^k)$. However, this operator differs by a constant prefactor compared to the scalar product defined above.

A.2.4 Wigner-Eckart Theorem

The Wigner-Eckart theorem relates matrix elements of the form $\langle \eta, JM | T_p^k(\boldsymbol{A}) | \eta', J'M'\rangle$ for fixed values of J, J', and k but different angular momentum projections M, M', and q. Here η describes all quantum numbers in the basis besides J and M. The Wigner-Eckart theorem says

$$\langle \eta, JM | T_p^k(\boldsymbol{A}) | \eta', J'M'\rangle = (-1)^{J-M} \begin{pmatrix} J & k & J' \\ -M & p & M' \end{pmatrix} \langle \eta, J || T^k(\boldsymbol{A}) || \eta', J'\rangle \tag{A.5}$$

where $\langle \eta, J||T^k(\boldsymbol{A})||\eta', J'\rangle$ is the "reduced matrix element."

One reduced matrix element we will commonly encounter is that of an angular momentum vector operator $\boldsymbol{J}$ acting on angular momentum states $|J\rangle$ [252, 253]:

$$\langle J||T^1(\boldsymbol{J})||J\rangle = [J(J+1)(2J+1)]^{1/2} \tag{A.6}$$

This can be derived by noting that $\langle J, M|T^1_0(\boldsymbol{J})|J, M\rangle = M$, then dividing out the appropriate $3j$ symbol (with $k = 1, p = 0$) to convert to a reduced matrix element [252, 253].

A.2.5 Matrix elements in coupled angular momentum schemes

We will often need to calculate matrix elements of an operator that acts on only one component of a coupled angular momentum scheme. For instance, we may need to evaluate matrix elements of $\boldsymbol{N}$ in the coupled basis $|NSJM\rangle$, where $\boldsymbol{J} = \boldsymbol{N} + \boldsymbol{S}$.

Say we have an operator $T^k(\boldsymbol{A}_1)$ that acts on the j_1 component of the coupled basis $|j_1 j_2 JM\rangle$, where $\boldsymbol{J} = \boldsymbol{j}_1 + \boldsymbol{j}_2$. Its reduced matrix elements are [252, 253]

$$\begin{aligned}\langle j_1, j_2, J||T^k(\boldsymbol{A}_1)||j_1', j_2', J'\rangle =& \delta_{j_2,j_2'}(-1)^{j_1+j_2+J'+k}\begin{Bmatrix} j_1 & J & j_2 \\ J' & j_1' & k\end{Bmatrix} \\ &\times \left[(2J+1)(2J'+1)\right]^{1/2}\langle j_1||T^k(\boldsymbol{A}_1)||j_1'\rangle\end{aligned} \tag{A.7}$$

Similarly, if an operator $T^k(\boldsymbol{A}_1)$ acts only on the *second* part j_2 of the coupled scheme, its matrix elements

are [252, 253]

$$\langle j_1, j_2, J||T^k(\boldsymbol{A}_2)||j_1', j_2', J'\rangle = \delta_{j_1,j_1'}(-1)^{j_1+j_2'+J+k}\begin{Bmatrix} j_2 & J & j_1 \\ J' & j_2' & k \end{Bmatrix} \times \left[(2J+1)(2J'+1)\right]^{1/2}\langle j_2||T^k(\boldsymbol{A}_2)||j_2'\rangle \tag{A.8}$$

A.2.6 Rotating between the lab and molecule frame

It will sometimes be necessary to rotate operators between the molecule and laboratory frame. For instance, the molecule's electric dipole moment is referenced to the molecule frame (aligned along z in the molecule-fixed coordinate system), but we need to access it in the lab frame when applying external fields (for instance, an electric field aligned along the lab Z axis). We use lowercase letters to refer to molecule-frame Cartesian coordinates, and uppercase letters for lab frame Cartesian coordinates. For spherical tensors, p is a lab-frame index and q is a molecule-frame index.

Rotations between the two frames are done using elements of the Wigner rotation matrix $\mathcal{D}^{(j)}$, which are the expansion coefficients when rotating an angular momentum state $|j, m\rangle$ through Euler angles $\omega = (\phi, \theta, \chi)$ [253]:

$$R(\phi, \theta, \chi)|j, m\rangle = \sum_{m'} |j, m'\rangle \mathcal{D}^{(j)}_{m',m}(\omega) \tag{A.9}$$

Components of the rotation matrix can also be used to rotate spherical tensor operators between the lab frame

and the molecule frame, using the relationship [253]

$$T_p^k(\boldsymbol{A}) = \sum_q \mathcal{D}_{pq}^k(\omega)^* T_q^k(\boldsymbol{A}) \tag{A.10}$$

and its inverse,

$$T_q^k(\boldsymbol{A}) = \sum_p \mathcal{D}_{pq}^k(\omega) T_p^k(\boldsymbol{A}) = \sum_p (-1)^{p-q} \mathcal{D}_{-p,-q}^k(\omega)^* T_p^k(\boldsymbol{A}) \tag{A.11}$$

Practically speaking, we will need to evaluate matrix elements of $\mathcal{D}_{pq}^k(\omega)^*$. These are conveniently evaluated in a symmetric top basis $|NKM\rangle$, where K is the projection of N onto the molecule-frame z axis and M is its projection onto the lab Z axis. The matrix elements are [253]

$$\begin{aligned}\langle NKM|\mathcal{D}_{pq}^k(\omega)^*|N'K'M'\rangle = (-1)^{M-K}\sqrt{(2N+1)(2N'+1)} \\ \times \begin{pmatrix} N & k & N' \\ -K & q & K' \end{pmatrix} \begin{pmatrix} N & k & N' \\ -M & p & M' \end{pmatrix}\end{aligned} \tag{A.12}$$

Sometimes it is preferable to instead evaluate *reduced* matrix elements, which can be read off from the Wigner-Eckart theorem as [253]

$$\langle NK||\mathcal{D}_{\cdot q}^k(\omega)^*||N'K'\rangle = (-1)^{N-K}\sqrt{(2N+1)(2N'+1)} \begin{pmatrix} N & k & N' \\ -K & q & K' \end{pmatrix} \tag{A.13}$$

where the dot in place of p means that the matrix element is reduced with respect to the p coordinate.

Anomalous commutation relations in the molecule frame. One tricky and annoying aspect of working

in the molecule frame is that angular momenta tied to three-dimensional rotations of a rigid body (e.g. $\boldsymbol{N}$ and $\boldsymbol{J}$, but not $\boldsymbol{S}$ or $\boldsymbol{L}$) obey *anomalous* commutation relations, $[J_x, J_y] = -iJ_z$, in the molecule frame (meanwhile, in the lab frame they behave like normal angular momenta, $[J_X, J_Y] = iJ_Z$). Therefore, when working in the molecule frame $T^1(\boldsymbol{N})$ and $T^1(\boldsymbol{J})$ do not behave like true spherical tensor operators. This topic is discussed in detail in section 5.5.6 of Ref. [253], with the key point being that one should rotate these operators back into the lab frame before using the spherical tensor identities from above.

This process is worked through for the case of a vector operator ($k = 1$) in Ref. [253]. Specifically, they define an operator $T^1_q(\boldsymbol{J})$ acting in the molecule frame as

$$T^1_q(\boldsymbol{J}) \equiv \sum_p (-1)^p T^1_p(\boldsymbol{J}) \mathcal{D}^1_{-pq}(\omega)^* \tag{A.14}$$

which is defined such that the scalar product with a "normal" (not anomalous) angular momentum (e.g. $\boldsymbol{S}$) looks like

$$\boldsymbol{J} \cdot \boldsymbol{S} = \sum_p (-1)^p T^1_p(\boldsymbol{J}) T^1_{-p}(\boldsymbol{S}) \equiv \sum_q T^1_q(\boldsymbol{J}) T^1_q(\boldsymbol{S}) \tag{A.15}$$

Using the matrix elements of $\mathcal{D}^k_{pq}(\omega)^*$ from above, it is found that matrix elements of $T^1_q(\boldsymbol{J})$ are [253]

$$\langle J, P, M | T^1_q(\boldsymbol{J}) | J, P', M \rangle = (-1)^{J-P} \begin{pmatrix} J & 1 & J \\ -P & q & P' \end{pmatrix} \sqrt{J(J+1)(2J+1)} \tag{A.16}$$

where P is the projection of $\boldsymbol{J}$ onto the molecule frame z axis. Though this looks awfully similar to the Wigner-Eckart theorem for a $k = 1$ spherical tensor operator, one should keep in mind that $T^1_q(\boldsymbol{J})$ is technically not

a spherical tensor operator. The most notable difference is that one should use eqn. A.15 when evaluating scalar products of these anomalous operators in the molecule frame.

A.3 The $\widetilde{X}^2\Sigma^+$ state of CaOH

We evaluate matrix elements of the effective Hamiltonian in the electronic ground state using a Hund's case (b) basis $|N, \ell, S, J, I, F, M\rangle$, where we have not explicitly included $\Lambda = 0$ in the basis. Here we specifically consider states with $\ell = 0$ [e.g. $\widetilde{X}(000)$, $\widetilde{X}(100)$, $\widetilde{X}(02^00)$] and $\ell = 1$ [e.g. $\widetilde{X}(010)$]. For $\widetilde{X}(02^20)$, we refer the reader to the Hamiltonian in Ref. [250].

The matrix elements discussed in this section should also apply to other Σ electronic states, e.g. $\widetilde{B}^2\Sigma^+$.

A.3.1 Nondegenerate vibrational states, e.g. $\widetilde{X}^2\Sigma^+(000)$

The effective Hamiltonian for these states is

$$H_{\text{eff}} = H_{\text{rot}} + H_{\text{sr}} + H_{\text{hf}} + H_{\text{Z}} + H_{\text{S}} + H_{\text{AC}} \tag{A.17}$$

Matrix elements of the Zeeman (H_{Z}), Stark (H_{S}), and AC Stark (H_{AC}) Hamiltonians are described later.

Rotational Hamiltonian

The rotational Hamiltonian is

$$H_{\text{rot}} = B\boldsymbol{N}^2 - D\boldsymbol{N}^4 \tag{A.18}$$

It is diagonal in the case (b) basis, with matrix elements

$$\langle N, S, J, I, F, M | H_{\text{rot}} | N, S, J, I, F, M \rangle = BN(N+1) - DN^2(N+1)^2 \tag{A.19}$$

Note that here and for all results below, when a quantum number is unprimed in both the bra and the ket it is implied that the matrix is diagonal with respect to that quantum number. For example, the above could be rewritten as

$$\begin{aligned} &\langle N,S, J, I, F, M | H_{\text{rot}} | N', S', J', I', F', M' \rangle \\ &\quad = \left[BN(N+1) - DN^2(N+1)^2 \right] \delta_{N,N'} \delta_{\ell,\ell'} \delta_{S,S'} \delta_{J,J'} \delta_{I,I'} \delta_{F,F'} \delta_{M,M'} \end{aligned}$$

For notational compactness, we will usually omit the Kronecker Deltas for matrix elements in this appendix, and instead just use primes to indicate which quantum numbers can be changed by the Hamiltonian term.

Spin-rotation interaction

For any polyatomic molecule, the spin-rotation interaction can be written as [252]

$$H_{\text{sr}} = \frac{1}{2} \sum_{\alpha,\beta} \epsilon_{\alpha\beta} (N_\alpha S_\beta + N_\beta S_\alpha) \tag{A.20}$$

where $\alpha, \beta = x, y, z$ label the principal axes in the molecule frame, and $\epsilon_{\alpha\beta}$ is a component of the spin-rotation coupling tensor. For linear and symmetric top molecules, only the diagonal elements of this tensor are nonzero, while for molecules of lower symmetry, off-diagonal elements can occur [252]. In the ground state of a linear

molecule like CaOH, $\epsilon_{xx} = \epsilon_{yy} \equiv \gamma$, where γ is the spin-rotation parameter. All other components are zero.[2] Therefore, in CaOH, the spin-rotation Hamiltonian reduces to

$$H_{\text{sr}} = \gamma(N_x S_x + N_y S_y) = \frac{\gamma}{2}(N_+ S_- + N_- S_+) \tag{A.21}$$

For nondegenerate vibrational states specifically, $N_z = 0$ so it is safe to use the standard form seen in diatomic molecules

$$H_{\text{sr}} = \gamma \boldsymbol{N} \cdot \boldsymbol{S} \qquad [\ell = 0 \text{ only}] \tag{A.22}$$

Matrix elements of eqn.A.22 are

$$\begin{aligned}
&\langle N, S, J, I, F, M | \gamma T^1(\boldsymbol{N}) \cdot T^1(\boldsymbol{S}) | N, S, J, I, F, M \rangle \\
&\qquad = \gamma (-1)^{N+S+J} \begin{Bmatrix} S & N & J \\ N & S & 1 \end{Bmatrix} \langle N || T^1(\boldsymbol{N}) || N \rangle \langle S || T^1(\boldsymbol{S}) || S \rangle \\
&\qquad = \gamma (-1)^{N+S+J} \begin{Bmatrix} S & N & J \\ N & S & 1 \end{Bmatrix} \{ N(N+1)(2N+1) S(S+1)(2S+1) \}^{1/2}
\end{aligned} \tag{A.23}$$

where in the first line we used eqn. A.3 and in the second line we used eqn. A.6. Again, note that this only applies to nondegenerate vibrational states, with $\ell = 0$. For nondegenerate vibrational states, we will evaluate matrix elements of the more general spin-rotation Hamiltonian (see below).

[2] It is possible to have ϵ_{zz} be nonzero in a vibrational bending mode with $\ell \neq 0$ (it is called γ' [259]). However, we have not seen evidence of this term in our spectroscopy of the CaOH $\widetilde{X}(010)$ bending mode and keep $\epsilon_{zz} = \gamma' = 0$ in our Hamiltonian.

Hyperfine interaction

The hyperfine Hamiltonian is

$$H_{\text{hf}} = b_F \boldsymbol{I} \cdot \boldsymbol{S} + \frac{c}{3}(3I_z S_z - \boldsymbol{I} \cdot \boldsymbol{S}) \tag{A.24}$$

where the first term is the Fermi contact interaction and the second term is the dipolar hyperfine interaction. This is occasionally seen in the literature as

$$H_{\text{hf}} = b\boldsymbol{I} \cdot \boldsymbol{S} + cI_z S_z \tag{A.25}$$

where $b = b_F - c/3$ (this is the "Frosch and Foley" convention [412]).

Fermi contact term. Matrix elements of the Fermi contact interaction $b_F \boldsymbol{I} \cdot \boldsymbol{S}$ are evaluated as

$$\begin{aligned}
&\langle N, \ell, S, J, I, F, M_F | b_F T^1(\boldsymbol{S}) \cdot T^1(\boldsymbol{I}) | N, \ell, S, J', I, F, M_F \rangle \\
&\qquad = b_F (-1)^{J'+I+F} \begin{Bmatrix} I & J & F \\ J' & I & 1 \end{Bmatrix} \langle I || T^1(\boldsymbol{I}) || I \rangle \langle N, S, J || T^1(\boldsymbol{S}) || N, S, J' \rangle \\
&\qquad = b_F (-1)^{J'+I+F} \begin{Bmatrix} I & J & F \\ J' & I & 1 \end{Bmatrix} (-1)^{J+N+S+1} \begin{Bmatrix} S & J & N \\ J' & S & 1 \end{Bmatrix} \\
&\qquad \times \left\{ I(I+1)(2I+1) S(S+1)(2S+1)(2J+1)(2J'+1) \right\}^{1/2}
\end{aligned} \tag{A.26}$$

where in the first line we used matrix elements of the scalar product eqn. A.3 and in the second line we calculated reduced matrix elements of $\boldsymbol{S}$ in the coupled basis $|N, S, J\rangle$ using equation A.8. Reduced matrix elements of $\boldsymbol{S}$ and $\boldsymbol{I}$ were calculated using eqn. A.6.

Dipolar hyperfine term. The dipolar part of the hyperfine interaction can be written for a general (not necessarily linear) molecule as

$$H_{\text{dd}} = \boldsymbol{S} \cdot \boldsymbol{T} \cdot \boldsymbol{I} \tag{A.27}$$

where $\boldsymbol{T}$ is a second-rank traceless tensor that accounts for the various possible hyperfine couplings:

$$\boldsymbol{T} = \begin{pmatrix} T_{xx} & T_{xy} & T_{xz} \\ T_{xy} & T_{yy} & T_{yz} \\ T_{xz} & T_{yz} & T_{zz} \end{pmatrix}$$

Note that, because the trace is zero, $T_{zz} = -T_{xx} - T_{yy}$, and by cylindrical symmetry $T_{xx} = T_{yy}$. Additionally, for a linear molecule, all the off-diagonal components should vanish (for nonlinear molecules like $CaOCH_3$ we find that the off-diagonal components do contribute). Comparison with equation A.24 allows us to relate c to the components of $\boldsymbol{T}$:

$$\begin{aligned} \boldsymbol{S} \cdot \boldsymbol{T} \cdot \boldsymbol{I} &= T_{xx} I_x S_x + T_{yy} I_y S_y + T_{zz} I_z S_z = \frac{T_{zz}}{2}(2 I_z S_z - I_x S_x - I_y S_y) \\ &\equiv \frac{c}{3}(3 I_z S_z - \boldsymbol{I} \cdot \boldsymbol{S}) = \frac{c}{3}(2 I_z S_z - I_x S_x - I_y S_y) \end{aligned}$$

which implies that $c/3 = T_{zz}/2$.

In spherical tensor notation, we can combine $\boldsymbol{S}$ and $\boldsymbol{T}$ into a vector, and then take the scalar product with $\boldsymbol{I}$ [252, 253]:

$$H_{\text{dd}} = -\sqrt{10} T^1(\boldsymbol{I}) \cdot T^1(T^1(\boldsymbol{S}), T^2(\boldsymbol{T})) \tag{A.28}$$

where the scalar product and the tensor product are defined as described in section A.2. The components of the dipolar hyperfine tensor $T^2(\boldsymbol{T})$ are

$$T^2_0(\boldsymbol{T}) = \frac{T_{zz}}{2} = -\frac{1}{2}(T_{xx} + T_{yy}) \tag{A.29a}$$

$$T^2_{\pm1}(\boldsymbol{T}) = \mp\frac{1}{\sqrt{6}}(T_{xz} \pm iT_{yz}) \tag{A.29b}$$

$$T^2_{\pm2}(\boldsymbol{T}) = \frac{1}{\sqrt{24}}(T_{xx} - T_{yy} \pm 2iT_{xy}) \tag{A.29c}$$

where, again, for CaOH $T^2_0(\boldsymbol{T}) = T_{zz}/2 = c/3$ and all other terms are zero. The $\boldsymbol{T}$ tensor is related to physical quantities in the molecule by [252, 253]

$$T^2_q(\boldsymbol{T}) = g_S g_N \mu_B \mu_N \left(\frac{\mu_0}{4\pi}\right) T^2_q(C)$$

where

$$T^2_q(C) \equiv \langle \eta\Lambda | C^2_q(\theta,\phi) r^{-3} | \eta\Lambda \rangle$$

is a matrix element with respect to the electronic wavefunction $|\eta, \Lambda\rangle$, and $C^2_q(\theta,\phi)$ is related to the spherical harmonics by

$$C^k_q(\theta,\phi) = \left(\frac{4\pi}{2k+1}\right)^{1/2} Y^k_q(\theta,\phi)$$

Matrix elements of eqn. A.28 are evaluated using spherical tensor algebra following Refs. [95, 252, 413]. In the

general case including all allowed components of $\boldsymbol{T}$, the result is[3]

$$\begin{aligned}
&\langle N, K, S, J, I, F, M_F | H_{\rm dd} | N', K', S, J', I, F, M_F \rangle \\
&\quad = -\sqrt{30}(-1)^{J'+I+F} \left\{ (2J+1)(2J'+1)(2N+1)(2N'+1) \right\}^{1/2} \\
&\quad \times \begin{Bmatrix} I & J & F \\ J' & I & 1 \end{Bmatrix} \begin{Bmatrix} N & N' & 2 \\ S & S & 1 \\ J & J' & 1 \end{Bmatrix} \left\{ S(S+1)(2S+1) I(I+1)(2I+1) \right\}^{1/2} \\
&\quad \times \sum_q (-1)^{N-K} \begin{pmatrix} N & 2 & N' \\ -K & q & K' \end{pmatrix} T^2_q(\boldsymbol{T})
\end{aligned} \tag{A.30}$$

where the two symbols in curly brackets are a $6j$ symbol and a $9j$ symbol.

Specifying to a linear molecule like CaOH, for which $T^2_0(\boldsymbol{T}) = c/3$ and all other components are zero, we

[3] Here we specifically use the result from Ref. [413], which we believe is correct. This is slightly different from the expressions in Refs. [95, 252].

have

$$\begin{aligned}
&\langle N, \ell, S, J, I, F, M_F | H_{\rm dd} | N', \ell, S, J', I, F, M_F \rangle \\
&\quad = -c\frac{\sqrt{30}}{3}(-1)^{J'+I+F}\left\{(2J+1)(2J'+1)(2N+1)(2N'+1)\right\}^{1/2} \\
&\quad \times \begin{Bmatrix} I & J & F \\ J' & I & 1 \end{Bmatrix} \begin{Bmatrix} N & N' & 2 \\ S & S & 1 \\ J & J' & 1 \end{Bmatrix} \{S(S+1)(2S+1)I(I+1)(2I+1)\}^{1/2} \\
&\quad \times (-1)^{N-\ell} \begin{pmatrix} N & 2 & N' \\ -\ell & 0 & \ell \end{pmatrix}
\end{aligned} \tag{A.31}$$

This also applies to states with $\ell \neq 0$.

A.3.2 The $\widetilde{X}^2\Sigma^+(010)$ Bending Mode of CaOH

As discussed in chapter 2, the effective Hamiltonian for an $\ell = 1$ bending mode is

$$H_{\rm eff} = H_{\rm rot} + H_{\ell \rm d} + H_{\rm sr} + H_{\rm hf} + H_{\rm Z} + H_{\rm S} + H_{\rm AC} \tag{A.32}$$

Below, we provide matrix elements in the case (b) basis $|N, \ell, S, J, I, F, M\rangle$ for the rotation ($H_{\rm rot}$), ℓ-type doubling ($H_{\ell \rm d}$), and spin-rotation ($H_{\rm sr}$) interactions. Matrix elements of the hyperfine Hamiltonian ($H_{\rm hf}$) are the same as for $\ell = 0$ states in sec. A.3.1. Matrix elements of the Zeeman ($H_{\rm Z}$), Stark ($H_{\rm S}$), and AC Stark ($H_{\rm AC}$) Hamiltonians are described later and are also the same for states with any ℓ.

Rotational Hamiltonian

The rotational Hamiltonian for a bending mode with $\ell \neq 0$ is

$$H_{\text{rot}} = B(\boldsymbol{N}^2 - \ell^2) - D(\boldsymbol{N}^2 - \ell^2)^2$$

It is diagonal in the case (b) basis, with matrix elements

$$\langle N, \ell, S, J, I, F, M | H_{\text{rot}} | N, \ell, S, J, I, F, M \rangle = B[N(N+1) - \ell^2] - D[N(N+1) - \ell^2]^2 \tag{A.33}$$

ℓ-type doubling

As discussed in chapter 2, the effective Hamiltonian for ℓ-type doubling is

$$H_{\ell\text{d,eff}} = \frac{1}{2} q_v (N_+^2 + N_-^2)$$

This mixes states with $\Delta\ell = \pm 2$.

The matrix elements of this Hamiltonian are derived very similarly to Λ-doubling matrix elements, which are discussed below and in the literature [253]. In spherical tensor notation, the ℓ-doubling Hamiltonian is

$$H_{\ell\text{d, eff}} = q_v \sum_{q=\pm 1} T^2_{2q}(\boldsymbol{N}, \boldsymbol{N})$$

where the tensor product is $T^2_{\pm 2}(\boldsymbol{N}, \boldsymbol{N}) = T^1_{\pm 1}(\boldsymbol{N}) T^1_{\pm 1}(\boldsymbol{N})$ (since the Clebsch-Gordan coefficients in eqn. A.4

are just 1). Applying the Wigner-Eckart theorem gives[4]

$$\begin{aligned}
&\langle N, \ell, S, J, I, F, M_F | H_{\ell\mathrm{d,\,eff}} | N, \ell', S, J, I, F, M_F \rangle \\
&= q_v \sum_{q=\pm 1} (-1)^{N-\ell} \begin{pmatrix} N & 2 & N \\ -\ell & 2q & \ell' \end{pmatrix} \langle N || T^2(\boldsymbol{N}, \boldsymbol{N}) || N \rangle \\
&= q_v \sum_{q=\pm 1} (-1)^{N-\ell} \begin{pmatrix} N & 2 & N \\ -\ell & 2q & \ell' \end{pmatrix} \frac{1}{2\sqrt{6}} \{(2N+3)(2N+2)(2N+1)(2N)(2N-1)\}^{1/2}
\end{aligned} \tag{A.34}$$

where in the second line we used equation 8.402 (or 5.133) of Ref. [253] to evaluate the reduced matrix element.

Spin-rotation interaction

As discussed in section A.3.1 and in Ref. [259], in an $\ell \neq 0$ bending mode we can no longer use the "linear-molecule" spin-rotation Hamiltonian $\gamma \boldsymbol{N} \cdot \boldsymbol{S}$ (though this ends up being a decent approximation for high N). Instead, we will evaluate matrix elements of the general spin-rotation Hamiltonian discussed above (eqn. A.20).

In spherical tensor notation, the spin-rotation Hamiltonian (eqn. A.20) is written as [252]

$$H_{\mathrm{sr}} = \frac{1}{2} \sum_{k=0}^{2} [T^k(\boldsymbol{\epsilon}) \cdot T^k(\boldsymbol{N}, \boldsymbol{S}) + T^k(\boldsymbol{N}, \boldsymbol{S}) \cdot T^k(\boldsymbol{\epsilon})] \tag{A.35}$$

[4] Technically, one should rotate into the laboratory frame, since the components of $\boldsymbol{N}$ obey anomalous commutation relations in the molecule frame, as discussed in sec. 5.5 of Ref. [253]. However, it is found that going through this rotation procedure nonetheless results in an expression that looks very similar to the Wigner-Eckart theorem in the molecule frame.

where

$$T_p^k(\boldsymbol{N},\boldsymbol{S}) = (-1)^p(2k+1)^{1/2}\sum_{p_1,p_2} T_{p_1}^1(\boldsymbol{N})T_{p_2}^1(\boldsymbol{S})\begin{pmatrix} 1 & 1 & k \\ p_1 & p_2 & -p \end{pmatrix}$$

is the product of the spherical tensor operators $T^1(\boldsymbol{N})$ and $T^1(\boldsymbol{S})$ (i.e. the rotational angular momentum and the electron spin angular momentum). $T(\boldsymbol{\epsilon})$ is the rank-2 spin-rotation tensor. In Cartesian coordinates, the nonzero elements are $\epsilon_{xx} = \epsilon_{yy} = \gamma$ for CaOH. The nonzero elements in spherical tensor notation are therefore

$$T_0^0(\boldsymbol{\epsilon}) = -\frac{1}{\sqrt{3}}(\epsilon_{xx}+\epsilon_{yy}+\epsilon_{zz}) = -\frac{2}{\sqrt{3}}\gamma$$
$$T_0^2(\boldsymbol{\epsilon}) = \frac{1}{\sqrt{6}}(2\epsilon_{zz}-\epsilon_{xx}-\epsilon_{yy}) = -\frac{2}{\sqrt{6}}\gamma$$

Other components are listed in Ref. [252], and may be necessary for molecules of lower symmetry.[5]

Matrix elements of eqn. A.35 can be worked out using spherical tensor identities (e.g. from section A.2 and

[5] As discussed above, $\epsilon_{zz} = \gamma'$ is not necessarily zero for CaOH [259], but we have not seen evidence for this term in our spectroscopy.

Ref. [252]). The result is [252]

$$
\begin{aligned}
&\langle N, \ell, S, J, I, F, M_F | H_{\mathrm{sr}} | N', \ell', S, J, I, F, M_F \rangle \\
&= \sum_{k=0}^{2} (2k+1)^{1/2} \left\{ S(S+1)(2S+1)(2N+1)(2N'+1) \right\}^{1/2} (-1)^{J+S+N} \begin{Bmatrix} N' & S & J \\ S & N & 1 \end{Bmatrix} \\
&\times \frac{1}{2} \left[\{N(N+1)(2N+1)\}^{1/2} \begin{Bmatrix} 1 & 1 & k \\ N' & N & N \end{Bmatrix} + (-1)^k \{N'(N'+1)(2N'+1)\}^{1/2} \begin{Bmatrix} 1 & 1 & k \\ N & N' & N' \end{Bmatrix} \right] \\
&\times \sum_q (-1)^{N-\ell} \begin{pmatrix} N & k & N' \\ -\ell & q & \ell' \end{pmatrix} T^k_q(\boldsymbol{\epsilon})
\end{aligned} \tag{A.36}
$$

This expression is general, and can be applied to nonlinear molecules by replacing ℓ with the more general quantum number K, which is the projection of $\boldsymbol{N}$ onto the molecule-frame z axis. In the specific case of CaOH, these matrix elements conserve ℓ because the only nonzero components of $T^k_q(\boldsymbol{\epsilon})$ have $q = 0$. Note that unlike the $\ell = 0$ case, where N is conserved by the spin-rotation interaction, for $\ell \neq 0$ H_{sr} can also mix states with $\Delta N = \pm 1$.

A.3.3 Stark and Zeeman shifts

Zeeman shifts (DC magnetic fields)

In a $^2\Sigma^+$ state, for which $\Lambda = 0$, the dominant term in the effective Zeeman Hamiltonian is

$$H_{\text{Zeeman}} = g_S \mu_B \boldsymbol{S} \cdot \boldsymbol{B} = g_S \mu_B \sum_p (-1)^p T^1_p(\boldsymbol{S}) T^1_{-p}(\boldsymbol{B}) \tag{A.37}$$

where $g_S \approx 2.0023$.[6]

The Hund's case (b) matrix elements can be evaluated using the Wigner-Eckart theorem along with eqns. A.6, A.7, and A.8) [252]:

$$\begin{aligned}
&\langle N, \ell, S, J, I, F, M_F | H_{\text{Zeeman}} | N, \ell, S, J', I, F', M'_F \rangle \\
&\quad = g_S \mu_B \sum_p (-1)^p T^1_{-p}(\boldsymbol{B}) (-1)^{F - M_F} \begin{pmatrix} F & 1 & F' \\ -M_F & p & M'_F \end{pmatrix} \langle N, \ell, S, J, I, F || T^1(\boldsymbol{S}) || N, \ell, S, J', I, F' \rangle \\
&\quad = g_S \mu_B \sum_p (-1)^p T^1_{-p}(\boldsymbol{B}) (-1)^{F - M_F} \begin{pmatrix} F & 1 & F' \\ -M_F & p & M'_F \end{pmatrix} (-1)^{J+I+F'+1} \begin{Bmatrix} J & F & I \\ F' & J' & 1 \end{Bmatrix} \\
&\quad \times (-1)^{N+S+J+1} \begin{Bmatrix} S & J & N \\ J' & S & 1 \end{Bmatrix} \left\{ S(S+1)(2S+1)(2F+1)(2F'+1)(2J+1)(2J'+1) \right\}^{1/2}
\end{aligned} \tag{A.38}$$

[6] This may not be exact due to the effective Hamiltonian formulation, whereby mixing between electronic states could change the effective value of the Hamiltonian parameters.

For the typical case where $\boldsymbol{B} = B_Z \hat{Z}$, only the $p = 0$ term survives, with $T^1_0(\boldsymbol{B}) = B_Z$.

Stark shifts (DC electric fields)

The Stark Hamiltonian for interactions with an external electric field $\boldsymbol{E}$ is

$$H_{\text{Stark}} = -\boldsymbol{\mu} \cdot \boldsymbol{E} \tag{A.39}$$

where $\boldsymbol{\mu}$ is the molecule-frame electric dipole moment. In spherical tensor notation, we take the scalar product and then rotate the dipole moment from the lab to the molecule frame (as discussed above):

$$H_{\text{Stark}} = -\sum_p (-1)^p T^1_p(\boldsymbol{E}) T^1_{-p}(\boldsymbol{\mu}) = -\sum_p (-1)^p T^1_p(\boldsymbol{E}) \sum_q \mathcal{D}^1_{-p,q}(\omega)^* T^1_q(\boldsymbol{\mu}) \tag{A.40}$$

Applying the Wigner-Eckart theorem (along with eqn. A.7 for matrix elements in the full coupled angular momentum scheme and eqn. A.13 for matrix elements of the rotation matrix) gives [252]:

$$\begin{aligned}
&\langle N, K, S, J, I, F, M_F | H_{\text{Stark}} | N', K', S, J', I, F', M_F' \rangle \\
&\quad = -\sum_p (-1)^p T^1_p(\boldsymbol{E}) (-1)^{F-M_F} \begin{pmatrix} F & 1 & F' \\ -M_F & -p & M_F' \end{pmatrix} (-1)^{J+I+F'+1} \begin{Bmatrix} J & F & I \\ F' & J' & 1 \end{Bmatrix} \\
&\quad \times (-1)^{N+S+J'+1} \begin{Bmatrix} N & J & S \\ J' & N' & 1 \end{Bmatrix} \left\{ (2J+1)(2J'+1)(2F+1)(2F'+1) \right\}^{1/2} \\
&\quad \times \sum_q T^1_q(\boldsymbol{\mu}) (-1)^{N-K} \left[(2N+1)(2N'+1) \right]^{1/2} \begin{pmatrix} N & 1 & N' \\ -K & q & K' \end{pmatrix}
\end{aligned} \tag{A.41}$$

In CaOH, the dipole moment is along the molecule-frame z axis, so $T^1_{q=0}(\boldsymbol{\mu}) = \mu = 1.465$ D, with the other components of $T^1_q(\boldsymbol{\mu})$ being zero. Typically we will apply an electric field along the laboratory Z axis, so $T^1_{p=0}(\boldsymbol{E}) = E_Z$ and the other components are zero. As before, in CaOH the projection of N onto the molecular axis is $K = \ell$.

A.4 The $\widetilde{A}^2\Pi$ state of CaOH

In this section we will provide matrix elements relevant to $\ell = 0$ states in the $\widetilde{A}^2\Pi$ electronic manifold. While similar matrix elements could be derived for $\ell \neq 0$ states, in practice during this work we have simply used the Hamiltonian provided in Ref. [**?**] for $\widetilde{A}(010)$ and in Ref. [250] for $\widetilde{A}(020)$.

Because of its electronic angular momentum, the $\widetilde{A}^2\Pi$ state is well described by a Hund's case (a) basis, $|\Lambda S \Sigma J I F M\rangle$,

where $\Lambda = \pm 1$ is the projection of the electronic angular moment onto the molecule-frame z axis and $\Sigma = \pm 1/2$ is the projection of the electron spin onto the molecule z axis. We will evaluate matrix elements in the bare case (a) basis, though note that the parity eigenstates of the molecule will be linear combinations $|\pm\rangle = 2^{-1/2}\left[|\Lambda, S, \Sigma, J, I, F, M\rangle \pm (-1)^{J-S}|-\Lambda, S, -\Sigma, J, I, F, M\rangle\right]$. Hyperfine structure in the $\widetilde{A}^2\Pi$ is unresolved (and the hyperfine constants are not known). However, we include hyperfine quantum numbers in the basis for generality and to aid when calculating transition strengths to the $\widetilde{X}$ state.

As discussed in chapter 2, the effective Hamiltonian for the $\widetilde{A}^2\Pi$ state can be derived by beginning with just spin-orbit and rotational terms, $H = A\boldsymbol{L}\cdot\boldsymbol{S} + B\boldsymbol{R}^2$, then making the replacement $\boldsymbol{R} = \boldsymbol{J} - \boldsymbol{S} - \boldsymbol{L}$ and expanding. The resulting effective Hamiltonian (ignoring external fields and hyperfine structure) is

$$H_{\text{eff},A} = H_{\text{diag}} + H_{\text{SU}} + H_{\Lambda\text{d}} \tag{A.42}$$

where H_{diag} includes the diagonal spin-orbit interaction and the rotational ladder, H_{SU} is the "spin uncoupling" interaction, and $H_{\Lambda\text{d}}$ is the Λ-doubling interaction.

The diagonal part of the Hamiltonian is

$$H_{\text{diag}} = (A+2B)L_zS_z + B\boldsymbol{J}^2 + B\left[\boldsymbol{S}^2 + L_z^2 - 2J_z(S_z+L_z)\right] \tag{A.43}$$

and its matrix elements are just

$$\begin{aligned}&\langle \Lambda S\Sigma JIFM|H_{\text{diag}}|\Lambda S\Sigma JIFM\rangle \\ &\qquad = A\Lambda\Sigma + BJ(J+1) + B\left[S(S+1) + \Lambda^2 - 2P^2 + 2\Lambda\Sigma\right]\end{aligned} \tag{A.44}$$

where $P = \Lambda + \Sigma$ is the projection of J onto the molecule-frame z axis, and (as above) the lack of primed quantum numbers implies that there are Kronecker Deltas enforcing that none of the quantum numbers can change. The first term is the spin-orbit interaction, the 2nd term describes the rotational ladder, and the third term is an offset (which is different for the $\Pi_{1/2}$ and $\Pi_{3/2}$ manifolds).

The spin uncoupling Hamiltonian is

$$H_{\text{SU}} = -B(J_+S_- + J_-S_+) = -2B\sum_{q=\pm1} T^1_q(J)T^1_q(S) \tag{A.45}$$

which mixes the $\Pi_{1/2}$ and $\Pi_{3/2}$ manifolds, causing them to have different "effective" rotational constants.[7] It is also responsible for a transition from case (a) to case (b) structure at high J. The matrix elements are [253]

$$\begin{aligned}\langle \Lambda S\Sigma JIFM|H_{\text{SU}}|\Lambda S\Sigma' JIFM\rangle &= -2B\sqrt{J(J+1)(2J+1)S(S+1)(2S+1)} \\ &\times \sum_{q=\pm1}(-1)^{J-P+S-\Sigma}\begin{pmatrix} J & 1 & J \\ -P & q & P'\end{pmatrix}\begin{pmatrix} S & 1 & S \\ -\Sigma & q & \Sigma'\end{pmatrix}\end{aligned} \tag{A.46}$$

where we used the Wigner-Eckart theorem to evaluate matrix elements of $T^1_q(S)$, and eqn. A.16 for matrix ele-

[7] The form of this term in spherical tensor notation is due to the anomalous commutation relations for $\boldsymbol{J}$ in the molecule frame, and specifically comes from the modified form of the scalar product for $T^1_q(\boldsymbol{J})$ (eqn. A.15).

ments of $T^1_q(J)$. (Note that the latter looks just like the Wigner-Eckart theorem, but is technically derived using rotation matrices, as described in section A.2.6, since J has anomalous commutation relations in the molecule frame.) Here, again, $P = \Sigma + \Lambda$.

Lambda doubling. The Λ-doubling Hamiltonian in spherical tensor notation is [253]

$$H_{\Lambda\mathrm{d}} = \sum_{q=\pm 1} \left\{ q_v T^2_{2q}(\boldsymbol{J}, \boldsymbol{J}) - (p_v + 2q_v) T^2_{2q}(\boldsymbol{J}, \boldsymbol{S}) + (o_v + p_v + q_v) T^2_{2q}(\boldsymbol{S}, \boldsymbol{S}) \right\} \tag{A.47}$$

which is the analogue of eqn. 2.42 in chapter 2. Note that implicit in this Hamiltonian is the selection rule $\Delta\Lambda = \pm 2$, since it was derived by applying the raising and lowering operators $L^2_\pm$ for the electronic angular momentum.

The first term is analogous to the ℓ-doubling Hamiltonian discussed above in the context of the $\widetilde{X}(010)$ state. Its matrix elements are

$$\begin{aligned} \langle \Lambda S \Sigma J I F M | \sum_{q=\pm 1} q_v T^2_{2q}(\boldsymbol{J}, \boldsymbol{J}) | \Lambda' S \Sigma J I F M \rangle &= q_v \sum_{q=\pm 1} \delta_{\Lambda, \Lambda' \pm 2} (-1)^{J-P} \\ &\times \begin{pmatrix} J & 2 & J \\ -P & 2q & P' \end{pmatrix} \frac{1}{2\sqrt{6}} \left\{ (2J+3)(2J+2)(2J+1)(2J)(2J-1) \right\}^{1/2} \end{aligned} \tag{A.48}$$

This couples states according to the selection rules $\Delta\Lambda = \pm 2$, $\Delta\Sigma = 0$. Therefore, it connects the $\Pi_{1/2}$ and $\Pi_{3/2}$ spin-orbit manifolds.

The second term can be evaluated by expanding the tensor product (according to eqn. A.4), which yields $T^2_{2q}(\boldsymbol{J}, \boldsymbol{S}) = (-1)^q T^1_{-q}(\boldsymbol{J}) T^1_q(\boldsymbol{S})$ after accounting for the anomalous commutation relations (section A.2.6

and Ref. [253]). Using the Wigner-Eckart theorem and eqn. A.16 then gives

$$\langle \Lambda S\Sigma JIFM|(p_v+2q_v)\sum_{q=\pm1} T^1_{-q}(\boldsymbol{J})T^1_q(\boldsymbol{S})|\Lambda' S\Sigma' JIFM\rangle = (p_v+2q_v)\sum_{q=\pm1}\delta_{\Lambda,\Lambda'\pm2}(-1)^{J-P+S-\Sigma} \times \begin{pmatrix} J & 1 & J \\ -P & -q & P' \end{pmatrix}\begin{pmatrix} S & 1 & S \\ -\Sigma & q & \Sigma' \end{pmatrix}\sqrt{J(J+1)(2J+1)S(S+1)(2S+1)} \tag{A.49}$$

This term has selection rules $\Delta\Lambda = \mp 2$, $\Delta\Sigma = \pm 1$, which means that it has diagonal matrix elements within the $\Pi_{1/2}$ manifold ($|\Lambda = 1, \Sigma = -1/2\rangle \leftrightarrow |\Lambda = -1, \Sigma = 1/2\rangle$). This is the dominant term contributing to Λ-doubling in the $^2\Pi_{1/2}$ state, which has a correspondingly much larger Λ-doublet splitting than the $^2\Pi_{3/2}$ component.

The third term in the Λ-doubling Hamiltonian is zero, since $S = 1/2$.

Hyperfine structure. Because hyperfine structure is unresolved in the CaOH $\widetilde{A}^2\Pi$ state, we do not include it in the Hamiltonian (and even if we were to, the constants are unknown). As discussed in Ref. [261], hyperfine structure is already weak in the $\widetilde{A}^2\Pi$ state of CaF, and is likely even weaker for CaOH.[8] Matrix elements of the hyperfine interaction in a $^2\Pi$ state can be found in section 8.5.2 of Ref. [253].

A.4.1 Zeeman Hamiltonian

As discussed in chapter 2, the Zeeman Hamiltonian for CaOH in the $\widetilde{A}^2\Pi$ state is [257, 414]

$$H_Z = g_S\mu_B\boldsymbol{S}\cdot\boldsymbol{B} + g'_L\mu_B\boldsymbol{L}\cdot\boldsymbol{B} + g_l\mu_B\left(S_xB_x + S_yB_y\right) + g'_l\mu_B\left(e^{-2i\phi}S_+B_+ + e^{+2i\phi}S_-B_-\right) \tag{A.50}$$

[8] For comparison, the hyperfine constants are 1-2 orders of magnitude smaller in CaOH than in CaF for the $\widetilde{X}^2\Sigma^+$ ground state.

As we saw there, the dominant term in $\widetilde{A}^2\Pi_{1/2}$ is the final term, proportional to the parity-dependent anisotropic g factor, $g_l' \approx p/2B \approx -0.065(4)$ [166]. The g_l term is suppressed because it requires coupling $^2\Pi_{1/2}$ and $^2\Pi_{3/2}$, while the first two terms roughly cancel in the $^2\Pi_{1/2}$ state since $g_S\Sigma + g_L'\Lambda \approx 0$. In the final term, ϕ is the electronic azimuthal angle, with $e^{\pm i\phi}$ acting like a raising/lowering operator on the electronic angular momentum projection Λ [264].

Matrix elements of the first term (electron spin Zeeman) are evaluated by taking the scalar product and then rotating $T^1_p(\boldsymbol{S})$ into the molecule frame [253]:

$$
\begin{aligned}
&\langle \Lambda S\Sigma JIFM_F | g_S\mu_B \boldsymbol{S}\cdot\boldsymbol{B} | \Lambda S\Sigma' J'IF'M_F'\rangle \\
&= g_S\mu_B \sum_p (-1)^p T^1_{-p}(\boldsymbol{B})(-1)^{F-M_F}
\begin{pmatrix} F & 1 & F' \\ -M_F & p & M_F' \end{pmatrix}
\sum_q \langle \Lambda S\Sigma JIF || \mathcal{D}^1_{\cdot q}(\omega)^* T^1_q(\boldsymbol{S}) || \Lambda S\Sigma' J'IF'\rangle \\
&= g_S\mu_B \sum_p (-1)^p T^1_{-p}(\boldsymbol{B})(-1)^{F-M_F}
\begin{pmatrix} F & 1 & F' \\ -M_F & p & M_F' \end{pmatrix}
\sum_q (-1)^{J+I+F'+1}
\begin{Bmatrix} J & F & I \\ F' & J' & 1 \end{Bmatrix} \\
&\times (-1)^{J-P+S-\Sigma}
\begin{pmatrix} J & 1 & J' \\ -P & q & P' \end{pmatrix}
\begin{pmatrix} S & 1 & S \\ -\Sigma & q & \Sigma' \end{pmatrix}
\sqrt{S(S+1)(2S+1)(2J+1)(2J'+1)(2F+1)(2F'+1)}
\end{aligned}
\tag{A.51}
$$

Here $g_S \approx 2.0023$, $P = \Lambda + \Sigma$, and for the typical case where the magnetic field is aligned along the laboratory Z axis, $T^1_0(\boldsymbol{B}) = B_Z$.

The second term (electronic orbital Zeeman) has matrix elements which can be evaluated similarly [253]:

$$\begin{aligned}
&\langle \Lambda S\Sigma J I F M_F | g_L' \mu_B \boldsymbol{L}\cdot\boldsymbol{B} | \Lambda S\Sigma J' I F' M_F' \rangle \\
&= g_L' \mu_B \Lambda \sum_p (-1)^p T^1_{-p}(\boldsymbol{B}) (-1)^{F-M_F} \begin{pmatrix} F & 1 & F' \\ -M_F & p & M_F' \end{pmatrix} (-1)^{J+I+F'+1} \begin{Bmatrix} J & F & I \\ F' & J' & 1 \end{Bmatrix} \\
&\times (-1)^{J-P} \begin{pmatrix} J & 1 & J' \\ -P & 0 & P \end{pmatrix} \sqrt{(2J+1)(2J'+1)(2F+1)(2F'+1)}
\end{aligned} \tag{A.52}$$

where we used only the $q = 0$ component of $\langle \Lambda || T^1_q(\boldsymbol{L}) || \Lambda \rangle$ after rotating into the molecule frame (this is just Λ for $q = 0$), since the other terms couple different electronic states. Since g_L' is an effective Hamiltonian parameter is does not have to be 1; however, it was found that $g_L' = 1$ fit the spectrum of CaF well [257], so it is likely that the same is true for CaOH.

The third term (g_l anisotropic Zeeman) is written in spherical tensor notation as (noting that S_x and B_x are referenced to molecule frame coordinates):

$$\begin{aligned}
g_l \mu_B (S_x B_x + S_y B_y) &= g_l \mu_B \sum_{q=\pm 1} (-1)^q T^1_q(\boldsymbol{S}) T^1_{-q}(\boldsymbol{B}) \\
&= g_l \mu_B \sum_{q=\pm 1} (-1)^q T^1_q(\boldsymbol{S}) \sum_p (-1)^{p+q} \mathcal{D}^1_{pq}(\omega)^* T^1_{-p}(\boldsymbol{B})
\end{aligned} \tag{A.53}$$

where in the second line we used eqn. A.11 to rotate $T^1_{-q}(\boldsymbol{B})$ back into the lab frame, where it is most useful. Matrix elements of this expression can be evaluated using the Wigner-Eckart theorem and matrix elements of

$\mathcal{D}^1_{pq}(\omega)^*$, with the result being [414]:[9]

$$\begin{aligned}
&\langle \Lambda S\Sigma J I F M_F | g_l \mu_B \sum_p \sum_{q=\pm 1} T^1_q(\boldsymbol{S})(-1)^p \mathcal{D}^1_{pq}(\omega)^* T^1_{-p}(\boldsymbol{B}) | \Lambda S\Sigma' J' I F' M'_F \rangle \\
&= g_l \mu_B \sum_p (-1)^p T^1_{-p}(\boldsymbol{B})(-1)^{F-M_F} \begin{pmatrix} F & 1 & F' \\ -M_F & p & M'_F \end{pmatrix} \sum_{q=\pm 1} (-1)^{J+I+F'+1} \begin{Bmatrix} J & F & I \\ F' & J' & 1 \end{Bmatrix} \\
&\times (-1)^{J-P+S-\Sigma} \begin{pmatrix} J & 1 & J' \\ -P & q & P' \end{pmatrix} \begin{pmatrix} S & 1 & S \\ -\Sigma & q & \Sigma' \end{pmatrix} \sqrt{S(S+1)(2S+1)(2J+1)(2J'+1)(2F+1)(2F'+1)}
\end{aligned} \tag{A.54}$$

Note that there is a Curl relationship, $g_l \approx -\gamma/2B$, that can be used to estimate g_l. However, this term ends up being negligible in the $\widetilde{A}^2\Pi$ state, as seen in Ref. [257] for CaF.

The final term (g'_l parity-dependent anisotropic Zeeman), is evaluated somewhat similarly, using[10]

$$\begin{aligned}
g'_l \mu_B (e^{-2i\phi} S_+ B_+ + e^{i2\phi} S_- B_-) &= g'_l \mu_B \sum_{q=\pm 1} e^{-i2q\phi} T^1_q(\boldsymbol{S}) T^1_q(\boldsymbol{B}) \\
&= g'_l \mu_B \sum_{q=\pm 1} e^{-i2q\phi} T^1_q(\boldsymbol{S}) \sum_p (-1)^{-p-q} \mathcal{D}^1_{p,-q}(\omega)^* T^1_{-p}(\boldsymbol{B})
\end{aligned} \tag{A.55}$$

[9] Note that we have fixed what appears to be a typo in the equation from Ref. [414].

[10] The convention for the raising and lowering operators for this particular equation appears to be $S_\pm = T^1_{\pm 1}(\boldsymbol{S})$, forgoing the usual factor of $1/\sqrt{2}$. This can be deduced by comparing the g'_l term in Refs. [257, 414] with the spherical tensor notation in eqn. (9.70) of Ref. [253].

Matrix elements of this expression are [214, 253]:

$$\langle \Lambda S\Sigma J I F M_F| - g_l'\mu_B \sum_p \sum_{q=\pm 1} e^{-i2q\phi} T^1_q(\boldsymbol{S})(-1)^p \mathcal{D}^1_{p,-q}(\omega)^* T^1_{-p}(\boldsymbol{B})|\Lambda' S\Sigma' J' I F' M_F'\rangle$$

$$= -g_l'\mu_B \sum_p (-1)^p T^1_{-p}(\boldsymbol{B})(-1)^{F-M_F} \begin{pmatrix} F & 1 & F' \\ -M_F & p & M_F' \end{pmatrix} \sum_{q=\pm 1} \delta_{\Lambda,\Lambda'\mp 2}(-1)^{J+I+F'+1} \begin{Bmatrix} J & F & I \\ F' & J' & 1 \end{Bmatrix}$$

$$\times (-1)^{J-P+S-\Sigma} \begin{pmatrix} J & 1 & J' \\ -P & -q & P' \end{pmatrix} \begin{pmatrix} S & 1 & S \\ -\Sigma & q & \Sigma' \end{pmatrix} \sqrt{S(S+1)(2S+1)(2J+1)(2J'+1)(2F+1)(2F'+1)} \tag{A.56}$$

where we used $\langle \Lambda | e^{-i2q\phi} | \Lambda' \rangle = \delta_{\Lambda,\Lambda'-2q}$ (since $e^{i\phi}$ acts like a raising operator on the angular momentum projection Λ [264]). g_l' can be estimated from the Curl-like relationship $g_l' \approx p/2B \approx -0.063$ [214, 257]. This estimate agrees very well with the measured value of $g_l' = -0.065(4)$ [166, 214].

For the $\widetilde{A}^2\Pi_{1/2}(J = 1/2^+)$ state used for CaOH laser cooling, eqn. A.56 gives $\Delta E = \pm\frac{1}{3} g_l'\mu_B B_Z$ for the Zeeman shift of the $(F = 1, M_F = \pm 1)$ stretched states when the field is along the Z axis.

A.4.2 DC Stark Hamiltonian

The DC Stark effect is treated very similarly in the $\widetilde{A}^2\Pi$ state as the $\widetilde{X}^2\Sigma^+$ state. The Hamiltonian is

$$\begin{aligned} H_{\text{Stark}} = -\boldsymbol{\mu}\cdot\boldsymbol{E} &= -\sum_p (-1)^p T^1_{-p}(\boldsymbol{E}) T^1_p(\boldsymbol{\mu}) \\ &= -\sum_p (-1)^p T^1_{-p}(\boldsymbol{E}) \sum_q \mathcal{D}^1_{pq}(\omega)^* T^1_q(\boldsymbol{\mu}) \end{aligned} \tag{A.57}$$

The matrix elements of this Hamiltonian are evaluated using the Wigner-Eckart theorm, eqn. A.7, and matrix elements of $\mathcal{D}^1_{pq}(\omega)^*$ as

$$\begin{aligned}
&\langle \Lambda S\Sigma JIFM_F|H_{\text{Stark}}|\Lambda' S\Sigma' J'IF'M'_F\rangle \\
&\quad = -\sum_p (-1)^p T^1_{-p}(\boldsymbol{E})(-1)^{F-M_F}\begin{pmatrix} F & 1 & F' \\ -M_F & p & M'_F\end{pmatrix}(-1)^{J+I+F'+1}\begin{Bmatrix} J & F & I \\ F' & J' & 1\end{Bmatrix} \\
&\quad \times \sum_q T^1_q(\boldsymbol{\mu})(-1)^{J-P}\begin{pmatrix} J & 1 & J' \\ -P & q & P'\end{pmatrix}\left\{(2J+1)(2J'+1)(2F+1)(2F'+1)\right\}^{1/2} \qquad \text{(A.58)}
\end{aligned}$$

In CaOH, the dipole moment is aligned along the molecule-frame z axis by cylindrical symmetry, so $T^1_{q=0}(\boldsymbol{\mu}) = \mu$, with values for the dipole moment in the $\widetilde{A}^2\Pi$ state given in chapter 2. Typically, the electric field is aligned along the lab Z axis, with $T^1_{p=0} = E_Z$. In this case, only the $p = 0$ and $q = 0$ terms in the sums contribute.

A.5 Electric dipole transitions

As discussed in chapter 2, calculating relative line strengths of electric dipole allowed transitions requires evaluating matrix elements of the electric dipole operator in a basis of rotational states. For rotational transitions, the line strength is proportional to $\langle N, K, M|\hat{\epsilon}\cdot\boldsymbol{\mu}|N', K', M'\rangle \equiv \mu\langle N, K, M|\hat{\epsilon}\cdot\hat{\mu}|N', K', M'\rangle$, where μ is the magnitude of the molecule's electric dipole moment, $\hat{\mu}$ is its orientation (referenced to the molecule frame coordinates), and $\hat{\epsilon}$ is the polarization of the driving electric field in the lab frame. For vibrational and electronic transitions the line strength is proportional to $\langle N, K, M|\hat{\epsilon}\cdot\hat{\mu}|N', K', M'\rangle$, where $\hat{\mu}$ is the the orientation of the transition dipole moment (reference to the molecule frame).

Matrix elements of $\langle N, K, M|\hat{\epsilon}\cdot\hat{\mu}|N', K', M'\rangle$ are evaluated the same way as the DC Stark matrix elements described earlier. In a Hund's case (b) basis $|\Lambda, N, \ell, S, J, I, F, M_F\rangle$, we have

$$\begin{aligned}
&\langle \Lambda, N, \ell, S, J, I, F, M_F|\hat{\epsilon}\cdot\hat{\mu}|\Lambda', N', \ell', S, J', I, F', M_F'\rangle \\
&\quad= \sum_p (-1)^p T_p^1(\hat{\epsilon})(-1)^{F-M_F}\begin{pmatrix} F & 1 & F' \\ -M_F & -p & M_F' \end{pmatrix}(-1)^{J+I+F'+1}\begin{Bmatrix} J & F & I \\ F' & J' & 1 \end{Bmatrix} \\
&\quad\times(-1)^{N+S+J'+1}\begin{Bmatrix} N & J & S \\ J' & N' & 1 \end{Bmatrix}\left\{(2J+1)(2J'+1)(2F+1)(2F'+1)\right\}^{1/2} \\
&\quad\times\sum_q T_q^1(\hat{\mu})(-1)^{N-K}\left[(2N+1)(2N'+1)\right]^{1/2}\begin{pmatrix} N & 1 & N' \\ -K & q & K' \end{pmatrix}
\end{aligned} \tag{A.59}$$

where $K = \ell + \Lambda$. $T_p^1(\hat{\epsilon})$ is a spherical tensor describing the electric field polarization, and $T_q^1(\hat{\mu})$ is a spherical tensor describing the orientation of the transition dipole moment in the molecule frame.

The transition dipole moment and corresponding molecule-frame selection rules depend on the type of transition. For rotational transitions, $\hat{\mu} = \hat{z}$ since these transitions couple to the permanent molecule-frame dipole moment. Therefore, $q = 0$ only, and $\Delta\Lambda = \Delta\ell = \Delta K = 0$ (since these transitions couple to neither the electronic or vibrational degrees of freedom). For vibrational transitions, $\Delta\Lambda = 0$ but $\Delta\ell = 0, \pm 1$ depending on the transition. Therefore, $\hat{\mu}$ can be aligned along the molecular symmetry axis ("parallel transition", $\Delta K = \Delta\ell = 0$) or perpendicular to the molecular symmetry axis ("perpendicular transition", $\Delta K = \Delta\ell = \pm 1$). For electronic transitions, the opposite is true: $\Delta\ell = 0$ always, and $\Delta K = \Delta\Lambda = 0, \pm 1$ for parallel and perpendicular transitions.

A.5.1 Converting from case (a) to case (b)

When calculating transition dipole moments between the $\widetilde{X}^2\Sigma^+$ and $\widetilde{A}^2\Pi$ states, we encounter a problem, which is that the $\widetilde{X}$ state was described in a Hund's case (b) basis but the $\widetilde{A}$ state was described in a case (a) basis. To rectify this problem, we need to first rotate the $\widetilde{A}$ state Hamiltonian and/or eigenstates into the case (b) basis, at which point we can evaluate transition dipole moments using eqn. A.59. This can be done using [252]

$$|NKSJM\rangle = \sum_{\Sigma,P}(-1)^{-J+P+2S}(2N+1)^{1/2}\begin{pmatrix} J & N & S \\ P & -K & -\Sigma \end{pmatrix}|JPM\rangle|S\Sigma\rangle \tag{A.60}$$

A.6 AC Stark shifts

In this section, we work through matrix elements of the AC Stark Hamiltonian using spherical tensor algebra. This is closely based on prior work by Luke Caldwell [322, 323]. However, we have expanded that treatment slightly in an effort to account for parity-dependent AC Stark shifts in the CaOH $\widetilde{X}(010)$ bending mode.

A.6.1 Hamiltonian

As discussed in chapter 6, the AC Stark Hamiltonian is $H_{\text{AC}} = -\vec{\mu}\cdot\vec{E}$, where $\vec{E}(t) = \mathcal{E}_0(\hat{\epsilon}e^{-i\omega t} + \hat{\epsilon}^* e^{i\omega t})$ is the electric field of the laser. In 2nd-order perturbation theory, the Hamiltonian ultimately becomes a sum over excited states [322]:

$$H_{\text{AC}} = -|\mathcal{E}_0|^2\sum_j\left(\frac{(\hat{\epsilon}^*\cdot\vec{\mu})|j\rangle\langle j|(\hat{\epsilon}\cdot\vec{\mu})}{\hbar(\omega_j-\omega)} + \frac{(\hat{\epsilon}\cdot\vec{\mu})|j\rangle\langle j|(\hat{\epsilon}^*\cdot\vec{\mu})}{\hbar(\omega_j+\omega)}\right) \tag{A.61}$$

where ω_j is the resonance frequency of the electronic transition to state j, ω is the laser frequency, $\hat{\epsilon}$ is the laser polarization unit vector, $\vec{\mu}$ is the electric dipole operator, and $|\mathcal{E}_0|^2 = I/(2\epsilon_0 c)$ is the electric field amplitude (squared) of the laser, where I is the laser intensity. Matrix elements of H_{AC} can be obtained, in principle, by directly calculating and summing over matrix elements of the dipole operator. This approach is conceptually simple, and should give accurate results, provided the energies and transition strengths are known for a sufficient number of excited electronic states. However, a more elegant approach is to use spherical tensor algebra and parametrize the molecular excited-state structure in terms of polarizabilities, as discussed in this section. Along with making matrix elements simpler to calculate, the entire sum over excited states is condensed into a polarizability tensor, whose components can be spectroscopically measured. Note that this section closely follows a derivation previously worked out for $^1\Sigma$ and $^2\Sigma$ molecules by Luke Caldwell [322, 323].

We begin by expressing eqn. A.61 in spherical coordinates as[11]

$$\begin{aligned} H_{\mathrm{AC}} &= -|\mathcal{E}_0|^2 \sum_{j,p,q} (-1)^{p+q} \left(\frac{\mu_p |j\rangle\langle j| \mu_q \epsilon^*_{-p} \epsilon_{-q}}{\hbar(\omega_j - \omega)} + \frac{\mu_q |j\rangle\langle j| \mu_p \epsilon_{-q} \epsilon^*_{-p}}{\hbar(\omega_j + \omega)} \right) \\ &\equiv -|\mathcal{E}_0|^2 \sum_{p,q} (-1)^{p+q} \left[(\mu_p \mathcal{R}^- \mu_q)(\epsilon^*_{-p}\epsilon_{-q}) + (\mu_q \mathcal{R}^+ \mu_p)(\epsilon_{-q}\epsilon^*_{-p}) \right] \end{aligned} \tag{A.62}$$

where p and q are summed from -1 to 1, since $\vec{\mu}$ and $\hat{e}$ are rank-1 tensors (note that we've dropped the hat on e for notational convenience). In the 2nd line, we defined the operator

$$\mathcal{R}^{\pm} = \sum_j \frac{|j\rangle\langle j|}{\hbar(\omega_j \pm \omega)} \tag{A.63}$$

[11] This follows from the definition of the scalar product, $T^k(\vec{A}) \cdot T^k(\vec{B}) = \sum_p (-1)^p T^k_p(\vec{A}) T^k_{-p}(\vec{B})$.

which encodes the sum over excited states.

We now notice that each term in eqn. A.62 contains the product of two rank-1 dipole operators and two (rank-1) polarization vectors. The dipole operators (with $\mathcal{R}^{\pm}$ sandwiched between) can be combined to form a rank-2 tensor operator, and the polarization vectors can be combined to form a rank-2 tensor. To do this, we make use of the formula for the product of two spherical tensors (see, e.g., Brown and Carrington eqn. 5.109 [253]):

$$\begin{aligned} T^K_P(\boldsymbol{A}^{k_1}, \boldsymbol{B}^{k_2}) &= \sum_{p_1,p_2} \langle k_1, k_2, p_1, p_2 | K, P \rangle T^{k_1}_{p_1}(\boldsymbol{A}) T^{k_2}_{p_2}(\boldsymbol{B}) \\ &= \sum_{p_1,p_2} (-1)^{-k_1+k_2-P} \sqrt{2K+1} \begin{pmatrix} k_1 & k_2 & K \\ p_1 & p_2 & -P \end{pmatrix} T^{k_1}_{p_1}(\boldsymbol{A}) T^{k_2}_{p_2}(\boldsymbol{B}) \end{aligned} \tag{A.64}$$

and its inverse,

$$\begin{aligned} T^{k_1}_{p_1}(\boldsymbol{A}) T^{k_2}_{p_2}(\boldsymbol{B}) &= \sum_{K,P} \langle k_1, k_2, p_1, p_2 | K, P \rangle T^K_P(\boldsymbol{A}^{k_1}, \boldsymbol{B}^{k_2}) \\ &= \sum_{K,P} (-1)^{-k_1+k_2-P} \sqrt{2K+1} \begin{pmatrix} k_1 & k_2 & K \\ p_1 & p_2 & -P \end{pmatrix} T^K_P(\boldsymbol{A}^{k_1}, \boldsymbol{B}^{k_2}) \end{aligned} \tag{A.65}$$

We will now use these identities to rewrite the expressions $\mu_p(\mathcal{R}^{\pm}\mu_q)$ and $\epsilon^*_{-p}\epsilon_{-q}$ from eqn. A.62 as rank-2

spherical tensors. Note that $\mathcal{R}^{\pm}\mu_q$ is a vector operator. Plugging into the sum in eqn A.62, we find

$$
\begin{aligned}
H_{\text{AC}} &= -|\mathcal{E}_0|^2 \sum_{p,q} (-1)^{p+q} \left[T^1_p(\mu) T^1_q(\mathcal{R}^- \mu) T^1_{-q}(\epsilon) T^1_{-p}(\epsilon^*) + T^1_q(\mu) T^1_p(\mathcal{R}^+ \mu) T^1_{-q}(\epsilon) T^1_{-p}(\epsilon^*) \right] \\
&= -|\mathcal{E}_0|^2 \sum_{K=0}^{2} \sum_{P=-K}^{K} \\
&\quad \times \left(\sum_p (-1)^P (2K+1) \begin{pmatrix} 1 & 1 & K \\ p & (P-p) & -P \end{pmatrix} \begin{pmatrix} 1 & 1 & K \\ -(P-p) & -p & P \end{pmatrix} T^K_P(\mu, \mathcal{R}^- \mu) T^K_{-P}(\epsilon, \epsilon^*) \right. \\
&\quad \left. + \sum_p (-1)^P (2K+1) \begin{pmatrix} 1 & 1 & K \\ (P-p) & p & -P \end{pmatrix} \begin{pmatrix} 1 & 1 & K \\ -(P-p) & -p & P \end{pmatrix} T^K_P(\mu, \mathcal{R}^+ \mu) T^K_{-P}(\epsilon, \epsilon^*) \right) \\
&= -|\mathcal{E}_0|^2 \sum_{K=0}^{2} \sum_{P=-K}^{K} (-1)^P \left[T^K_P(\mu, \mathcal{R}^- \mu) T^K_{-P}(\epsilon, \epsilon^*) + (-1)^K T^K_P(\mu, \mathcal{R}^+ \mu) T^K_{-P}(\epsilon, \epsilon^*) \right]
\end{aligned} \tag{A.66}
$$

where in the 2nd line we enforced the condition $P = p + q$, and in the third line we used spherical tensor identities to simplify the sum over $3j$ symbols.[12]

Finally (again following Caldwell [322, 323]), we simplify the Hamiltonian to read

$$
H_{\text{AC}} = -|\mathcal{E}_0|^2 \sum_{K=0}^{2} \sum_{P=-K}^{K} (-1)^P \mathcal{A}^K_P \mathcal{P}^K_{-P} \tag{A.67}
$$

where $\mathcal{A}^K_P$ is the rank-2 polarizability tensor operator, and $\mathcal{P}^K_P$ is the rank-2 laser polarization tensor. They are

[12] The specific identities used were $\sum_p \begin{pmatrix} 1 & 1 & K \\ p & (P-p) & -P \end{pmatrix} \begin{pmatrix} 1 & 1 & K \\ -(P-p) & -p & P \end{pmatrix} = 1/(2K+1)$ and $\sum_p \begin{pmatrix} 1 & 1 & K \\ (P-p) & p & -P \end{pmatrix} \begin{pmatrix} 1 & 1 & K \\ -(P-p) & -p & P \end{pmatrix} = (-1)^K/(2K+1)$, both of which were numerically verified in Mathematica.

Polarization	$\mathcal{P}_0^0$	$\mathcal{P}_0^1$	$\mathcal{P}_{\pm1}^1$	$\mathcal{P}_0^2$	$\mathcal{P}_{\pm1}^2$	$\mathcal{P}_{\pm2}^2$
Z	1	0	0	1	0	0
X	1	0	0	$-\frac{1}{2}$	0	$\frac{1}{2}\sqrt{\frac{3}{2}}$
Y	1	0	0	$-\frac{1}{2}$	0	$-\frac{1}{2}\sqrt{\frac{3}{2}}$
Angle θ in X-Z plane	1	0	0	$\frac{1}{4}[1+3\cos(2\theta)]$	$\mp\sqrt{\frac{3}{2}}\cos\theta\sin\theta$	$\frac{1}{2}\sqrt{\frac{3}{2}}\sin^2\theta$
$\sigma^{\pm}$	1	∓1	0	$-\frac{1}{2}$	0	0

Table A.1: Polarization tensor components for various polarization configurations.

defined as

$$\mathcal{A}_P^K = \frac{1}{z_K} T_P^K(\mu, \mathcal{R}^-\mu) + \frac{1}{z_K}(-1)^K T_P^K(\mu, \mathcal{R}^+\mu) \tag{A.68}$$

$$\mathcal{P}_P^K = z_K T_P^K(\epsilon, \epsilon^*) \tag{A.69}$$

where $\mathcal{R}^{\pm}$ is defined in eqn. A.63 and the tensor products $T_P^K(A, B)$ can be evaluated using eqn. A.64. The z_K are numerical prefactors, chosen to be $z_0 = -\sqrt{3}$, $z_1 = -\sqrt{2}$, $z_2 = \sqrt{3/2}$. While these may seem annoying and unnecessary, they ensure consistency with the conventional definition of the scalar polarizability used in chapter 6.

Components of the polarization tensor (eqn. A.69) can be calculated by writing the polarization as a spherical vector $T_p^1(\epsilon)$ and using eqn. A.64 to compute the tensor product. Some examples are given in Tab. A.1.

The remaining task is to calculate matrix elements of the polarizability operator $\mathcal{A}_P^K$. This is the topic of the remainder of this section. We will do this at various levels of precision. First, we will ignore substructure in excited electronic states, which does a reasonable job of getting the scalar and tensor polarizabilities (sec. A.6.2). Then, we will include spin-orbit and vibronic structure in the $\widetilde{A}^2\Pi_{1/2}$ state, which also turns on a small vector polariz-

ability in all ground states, and a small parity-dependent polarizability in the $\widetilde{X}(010)$ bending mode (sec. A.6.3). For most purposes, the first approximation is fine, but the latter corrections may be useful for certain applications where an understanding of kHz-level AC Stark shifts is important.

A.6.2 Matrix elements and polarizabilities, neglecting excited-state structure

Before calculating matrix elements of H_{AC} (eqn. A.67), we need to decide at what level of precision to consider the molecular structure. For large laser detunings, all substructure within each electronic state can be approximated as degenerate, which simplifies both the matrix elements and the sums over excited states used to calculate polarizabilities. This approach gives accurate results for the scalar and tensor polarizabilities, which are the dominant contributions to AC Stark shifts in CaOH.[13] However, it turns out that this approximation causes some components of the polarizability tensor to strictly vanish. While these components are small, a treatment including excited state structure – in particular, spin-orbit and vibronic structure in degenerate electronic states – allows these components to become nonzero. Specifically, we will see that spin-orbit structure leads to nonzero vector polarizability, while vibronic interactions can cause parity-dependent polarizabilities in CaOH bending modes. We treat consider the former case in this section, and the latter case in sec. A.6.3.

Matrix elements

Because the polarizability operator is the only part of H_{AC} in eqn. A.67 that acts on the molecular states (the polarization tensor components $\mathcal{P}_K^P$ are just scalars), calculating matrix elements of H_{AC} reduces to taking matrix elements of $\mathcal{A}_P^K$. We will calculate these in the case (b) basis $|\Lambda, \ell, N, S, J, I, F, M\rangle$.

[13] As discussed in chapter 6, this approximation is helped by having a nearly diagonal Franck-Condon matrix, so that only one vibrational level of each electronic manifold contributes significantly.

In this case, the only quantum number that the polarizability operator acts on directly is the electronic angular momentum projection Λ. Therefore, we begin calculating matrix elements by applying the Wigner-Eckart theorem and decoupling both the nuclear and electron spins. Note that here and below, we will use lowercase indices k and p for the spherical tensors (e.g. $\mathcal{A}^k_p$) to avoid confusion with the projections of N and J onto the molecular axis ($K = \Lambda + \ell$ and $P = \Lambda + \ell + \Sigma$, respectively).

$$\begin{aligned}
&\langle \Lambda, \ell, N, S, J, I, F, M | \mathcal{A}^k_p | \Lambda', \ell', N', S, J', I, F', M' \rangle = \\
&\quad = (-1)^{F-M} \begin{pmatrix} F & k & F' \\ -M & p & M' \end{pmatrix} (-1)^{J+I+F'+k} \sqrt{(2F+1)(2F'+1)} \begin{Bmatrix} J & F & I \\ F' & J' & k \end{Bmatrix} \\
&\quad \times (-1)^{N+S+J'+k} \sqrt{(2J+1)(2J'+1)} \begin{Bmatrix} N & J & S \\ J' & N' & k \end{Bmatrix} \langle \Lambda, \ell, N || \mathcal{A}^k || \Lambda', \ell', N' \rangle
\end{aligned} \tag{A.70}$$

Next, to evaluate the reduced matrix elements $\langle \Lambda, \ell, N || \mathcal{A}^k || \Lambda', \ell', N' \rangle$, we note that the polarizability operator acts in the *molecule*-fixed coordinate system, and therefore we need to rotate from the lab frame into the molecule frame. This is done by applying a rotation matrix $\mathcal{D}^k$, such that (Brown & Carrington eqn. 5.143 [253])

$$\mathcal{A}^k_p = \sum_q (\mathcal{D}^k_{pq})^* \mathcal{A}^k_q \tag{A.71}$$

or, when reduced with respect to p,

$$\mathcal{A}^k = \sum_q (\mathcal{D}^k_{.q})^* \mathcal{A}^k_q \tag{A.72}$$

where the dot replacing p in the subscript indicates that it is reduced with respect to p (note that p denotes lab-

frame coordinates and q denotes molecule-frame coordinates). The matrix elements of this reduced rotation matrix are (Brown & Carrington eqn. 5.148 [253])

$$\langle NK||(\mathcal{D}^k_{.q})^*||N'K'\rangle = (-1)^{N-K}\sqrt{(2N+1)(2N'+1)}\begin{pmatrix} N & k & N' \\ -K & q & K' \end{pmatrix} \tag{A.73}$$

Putting eqns. A.72 and A.73 together, we find for the reduced matrix elements

$$\langle \Lambda,\ell,N||\mathcal{A}^k||\Lambda',\ell',N'\rangle = \sum_q (-1)^{N-K}\sqrt{(2N+1)(2N'+1)}\begin{pmatrix} N & k & N' \\ -K & q & K' \end{pmatrix}\langle \Lambda,\ell|\mathcal{A}^k_q|\Lambda',\ell'\rangle \tag{A.74}$$

where we have used $K = \Lambda+\ell$ to compactify the notation. Substituting into eqn. A.70, and then into eqn. A.67,

gives for the matrix elements of H_{AC}:

$$\begin{aligned}
&\langle \Lambda, \ell, N, S, J, I, F, M | H_{\mathrm{AC}} | \Lambda, \ell, N', S, J', I, F', M' \rangle = \\
&\quad = -\frac{I}{2\epsilon_0 c} \sum_{k=0}^{2} \sum_{p=-k}^{k} (-1)^p \mathcal{P}^k_{-p} \\
&\qquad \times (-1)^{F-M} \begin{pmatrix} F & k & F' \\ -M & p & M' \end{pmatrix} (-1)^{J+I+F'+k} \sqrt{(2F+1)(2F'+1)} \begin{Bmatrix} J & F & I \\ F' & J' & k \end{Bmatrix} \\
&\qquad \times (-1)^{N+S+J'+k} \sqrt{(2J+1)(2J'+1)} \begin{Bmatrix} N & J & S \\ J' & N' & k \end{Bmatrix} \\
&\qquad \times (-1)^{N-K} \sqrt{(2N+1)(2N'+1)} \begin{pmatrix} N & k & N' \\ -K & 0 & K' \end{pmatrix} \alpha_k
\end{aligned} \tag{A.75}$$

where we have defined $\alpha_k \equiv \langle \Lambda, \ell | \mathcal{A}^k_{q=0} | \Lambda, \ell \rangle$, noting that only $q = 0$ components are allowed since $\mathcal{A}^k$ cannot change Λ or ℓ in the absence of excited state structure (elaborated upon below). Again, note that $K = \Lambda + \ell$, and that the conditions $\Delta\Lambda = 0$ and $\Delta\ell = 0$ should be enforced when calculating matrix elements. The polarizabilities α_k are discussed below (with the final result being eqn. A.78), and the polarization tensor components $\mathcal{P}^k_p$ were discussed above.

Polarizabilities

The polarizabilities themselves are numerical factors that encode the sum of electric dipole transitions over excited states that ultimately causes AC Stark shifts. The spherical tensor algebra above was meant to strip away

the dependence on most of the angular momentum quantum numbers, leaving just electronic transition dipole moments to be calculated, specifically, the matrix elements $\langle\Lambda|\mathcal{A}_q^k|\Lambda\rangle$.

To do this, it is helpful to explicitly write out the components of $\mathcal{A}_q^k$, using eqns. A.64 and A.68:

$$\mathcal{A}_0^0 = \frac{1}{3}\left[-\mu_1(\mathcal{R}^- + \mathcal{R}^+)\mu_{-1} + \mu_0(\mathcal{R}^- + \mathcal{R}^+)\mu_0 - \mu_{-1}(\mathcal{R}^- + \mathcal{R}^+)\mu_1\right] \tag{A.76a}$$

$$\mathcal{A}_0^1 = \frac{1}{2}\left[\mu_{-1}(\mathcal{R}^- - \mathcal{R}^+)\mu_1 - \mu_1(\mathcal{R}^- - \mathcal{R}^+)\mu_{-1}\right] \tag{A.76b}$$

$$\mathcal{A}_0^2 = \frac{1}{3}\left[\mu_1(\mathcal{R}^- + \mathcal{R}^+)\mu_{-1} + 2\mu_0(\mathcal{R}^- + \mathcal{R}^+)\mu_0 + \mu_{-1}(\mathcal{R}^- + \mathcal{R}^+)\mu_1\right] \tag{A.76c}$$

$$\mathcal{A}_{\pm 2}^2 = \sqrt{\frac{2}{3}}\mu_{\pm 1}(\mathcal{R}^- + \mathcal{R}^+)\mu_{\pm 1} \tag{A.76d}$$

where we have omitted the $q = \pm 1$ components, which will turn out not to be relevant. The dipole operators μ_{q_i} act in the molecule frame by raising and lowering the electronic angular momentum, $\mu_{q_i}|\Lambda\rangle \propto |\Lambda + q_i\rangle$. Therefore, the terms with $\mu_{\pm 1}$ drive perpendicular transitions, and terms with μ_0 drive parallel transitions. Note that each term of the form $\mathcal{A}_q^k \sim \mu_{q_1}\mathcal{R}\mu_{q_2}$ conserves the angular momentum projection $q = q_1 + q_2$, and the selection rule for a matrix element $\langle\Lambda|\mathcal{A}_q^k|\Lambda'\rangle$ is $\Lambda = \Lambda' + q$.

We see that for all but Π ($\Lambda = \pm 1$) ground states, only the $q = 0$ terms are important, since $q \neq 0$ couples different electronic states, which are split by very large energies. On the other hand, for Π states the $|\Lambda = \pm 1\rangle$ ground states are degenerate, and the $\mathcal{A}_{\pm 2}^2$ term can couple these states via the two-photon pathway $|\Lambda = \mp 1\rangle \to |\Lambda' = 0\rangle \to |\Lambda = \pm 1\rangle$. For the rest of this section, we will specialize to $\Lambda = 0$ ground states, like in CaOH, and ignore the $\mathcal{A}_{\pm 2}^2$ components. Note, however, that these $q = \pm 2$ components will reappear in the next section, where we show that vibronic coupling in the excited states allows them to couple degenerate ground states with $\ell = \pm 1$ in CaOH.

The $q = 0$ matrix elements contain terms of the form $\mu_{\pm1}\mathcal{R}\mu_{\mp1}$ (perpendicular transitions), and $\mu_0\mathcal{R}\mu_0$ (parallel transitions). Therefore, it is natural to define the parallel and perpendicular polarizabilities;

$$\alpha_\parallel = \langle\Lambda|\mu_0(\mathcal{R}^- + \mathcal{R}^+)\mu_0|\Lambda\rangle = \sum_j \left(\frac{1}{\hbar(\omega_j - \omega)} + \frac{1}{\hbar(\omega_j + \omega)}\right)|\langle\Lambda|\mu_0|j,\Lambda\rangle|^2 \tag{A.77a}$$

$$= \sum_j \left(\frac{1}{\hbar(\omega_j - \omega)} + \frac{1}{\hbar(\omega_j + \omega)}\right)|\langle\Sigma|\mu_0|j,\Sigma\rangle|^2$$

$$\alpha_\perp = -\langle\Lambda|\mu_{\mp1}(\mathcal{R}^- + \mathcal{R}^+)\mu_{\pm1}|\Lambda\rangle = \sum_j \left(\frac{1}{\hbar(\omega_j - \omega)} + \frac{1}{\hbar(\omega_j + \omega)}\right)|\langle\Lambda|\mu_{\mp1}|j,\Lambda\pm1\rangle|^2 \tag{A.77b}$$

$$= \sum_j \left(\frac{1}{\hbar(\omega_j - \omega)} + \frac{1}{\hbar(\omega_j + \omega)}\right)|\langle\Sigma|\mu_{\mp1}|j,\Pi\rangle|^2$$

where the sum is over all excited states $|j,\Lambda'\rangle$ with electronic angular momentum Λ', and in the second line we specialized to Σ states ($\Lambda = 0$). The minus sign in the definition of $\alpha_\perp$ is because $\langle\Lambda|\mu_{-q}\mathcal{R}^\pm\mu_q|\Lambda\rangle = (-1)^q\langle\Lambda+q|\mathcal{R}^\pm|\Lambda+q\rangle$, since $(\mu_q)^\dagger = (-1)^q\mu_{-q}$. Expressions in terms of the natural linewidth Γ for each electronic state can be found in chaper 6.

With these definitions, we find for the polarizabilities α_k:

$$\alpha_0 \equiv \langle\Sigma|\mathcal{A}_0^0|\Sigma\rangle = \frac{1}{3}(\alpha_\parallel + 2\alpha_\perp) \tag{A.78a}$$

$$\alpha_1 \equiv \langle\Sigma|\mathcal{A}_0^1|\Sigma\rangle = 0 \tag{A.78b}$$

$$\alpha_2 \equiv \langle\Sigma|\mathcal{A}_0^2|\Sigma\rangle = \frac{2}{3}(\alpha_\parallel - \alpha_\perp) \tag{A.78c}$$

From this, it is clear that the scalar polarizability α_0 is the average across all excited states (since perpendicular transitions have double weight), while the tensor polarizability α_2 is proportional to the polarizability anisotropy.

A.6.3 Including spin-orbit and vibronic structure

Here we include the largest energy splittings in degenerate excited states, namely the spin-orbit and vibronic structure in $^2\Pi$ states, which leads to different manifolds split by THz energy scales (e.g. the $^2\Pi_{1/2}$ and $^2\Pi_{3/2}$ manifolds in $\widetilde{A}(000)$, and the $\mu^2\Sigma$ and $\kappa^2\Sigma$ vibronic states in $\widetilde{A}(010)$). This will change the perpendicular, but not the parallel, polarizability. To do this, we will include the electron spin degree of freedom when calculating matrix elements of $\mathcal{A}_q^k$ in the molecule frame.

Matrix elements

We begin as usual by applying the Wigner-Eckart theorem and decoupling the hyperfine degree of freedom, but this time *not* decoupling the electron spin degree of freedom, since it is resolved by the spin-orbit interaction.

$$\begin{aligned}\langle \Lambda, \ell, N, S, J, I, F, M|\mathcal{A}_p^k|\Lambda', \ell', N', S, J', I, F', M'\rangle = \\ =(-1)^{F-M}\begin{pmatrix} F & k & F' \\ -M & p & M'\end{pmatrix}(-1)^{J+I+F'+k}\sqrt{(2F+1)(2F'+1)}\begin{Bmatrix} J & F & I \\ F' & J' & k\end{Bmatrix} \\ \times \langle \Lambda, \ell, N, S, J||\mathcal{A}^k||\Lambda, \ell', N', S, J'\rangle \end{aligned} \tag{A.79}$$

Next, we convert to the a Hund's case (a) basis, which will make treating the vibronic and spin-orbit structure of the $^2\Pi$ excited states much simpler (we will ignore the substructure of the $^2\Sigma$ excited states, so this basis transformation does not present any added difficulty for those states). Specifically, the spin-orbit Hamiltonian is diagonal in the case (a) basis $|\Lambda, \ell, S, \Sigma, J\rangle$, and the energy splittings between spin-orbit components are large

enough to generate significant contributions to the polarizability for sufficiently close detuning. We use Hirota eqn. (2.3.3) [252] to change from case (b) to case (a):

$$|\Lambda, \ell, N, S, J\rangle = \sum_{\Sigma=-1/2}^{1/2} (-1)^{-J+P+2S}\sqrt{2N+1} \begin{pmatrix} J & N & S \\ P & -K & -\Sigma \end{pmatrix} |\Lambda, \ell, S, \Sigma, J\rangle \tag{A.80}$$

where $K = \Lambda + \ell$ is the projection of N onto the molecular axis, and $P = \Lambda + \ell + \Sigma$ is the projection of J.

Applying this to the reduced matrix elements of $\mathcal{A}^k$ gives

$$\begin{aligned}\langle \Lambda, \ell, N, S, J||\mathcal{A}^k||\Lambda, \ell', N', S, J'\rangle = \sum_{\Sigma}\sum_{\Sigma'}(-1)^{-J-J'+P+P'+4S}\sqrt{(2N+1)(2N'+1)} \\ \times \begin{pmatrix} J & N & S \\ P & -K & -\Sigma \end{pmatrix} \begin{pmatrix} J' & N' & S \\ P' & -K' & -\Sigma' \end{pmatrix} \langle \Lambda, \ell, S, \Sigma, J||\mathcal{A}^k||\Lambda, \ell' S, \Sigma', J'\rangle\end{aligned} \tag{A.81}$$

Next, as before, we rotate the reduced matrix elements $\langle \Lambda, \ell, S, \Sigma, J||\mathcal{A}^k||\Lambda, \ell' S, \Sigma', J'\rangle$ into the molecule frame, using eqn. A.74, but this time using J and P as the total angular momentum and angular momentum

projection. Combining everything gives:

$$\begin{aligned}
&\langle \Lambda, \ell, N, S, J, I, F, M | \mathcal{A}_p^k | \Lambda', \ell', N', S, J', I, F', M' \rangle = \\
&\quad = (-1)^{F-M} \begin{pmatrix} F & k & F' \\ -M & p & M' \end{pmatrix} (-1)^{J+I+F'+k} \sqrt{(2F+1)(2F'+1)} \begin{Bmatrix} J & F & I \\ F' & J' & k \end{Bmatrix} \\
&\qquad \times \sum_{\Sigma} \sum_{\Sigma'} (-1)^{-J-J'+P+P'+4S} \sqrt{(2N+1)(2N'+1)} \begin{pmatrix} J & N & S \\ P & -K & -\Sigma \end{pmatrix} \begin{pmatrix} J' & N' & S \\ P' & -K' & -\Sigma' \end{pmatrix} \\
&\qquad \times \sum_{q} (-1)^{J-P} \sqrt{(2J+1)(2J'+1)} \begin{pmatrix} J & k & J' \\ -P & q & P' \end{pmatrix} \alpha_q^k
\end{aligned} \tag{A.82}$$

where we defined $\alpha_q^k \equiv \langle \Lambda, \ell, \Sigma | \mathcal{A}_q^k | \Lambda', \ell', \Sigma' \rangle$ to allow the possibility of $q \neq 0$ components of the polarizability tensor.

As discussed below, in most cases $\Sigma = \Sigma'$, so we can collapse one of the sums. It is also possible to further simplify the matrix elements in this case, as described in Refs. [322, 323].

Polarizabilities

We now calculate each component of the polarizability tensor, $\alpha_q^k \equiv \langle \Lambda, \ell, \Sigma | \mathcal{A}_q^k | \Lambda', \ell', \Sigma' \rangle$, referring to eqns. A.76. As before, we are looking for matrix elements that connect states within the same electronic manifold, $\Lambda = \Lambda'$. (Note that $\Lambda = -\Lambda' = \pm 1$ is allowed the special case of Π states, though we will not consider this case here.) Below, we will specifically consider the CaOH $\widetilde{X}^2\Sigma^+(000)$ and $\widetilde{X}^2\Sigma^+(010)$ states, though these results apply generally to $\ell = 0$ and $\ell = 1$ levels in a $^2\Sigma$ state. The $q = 0$ components are treated similarly to

above, and all components can now exist, including the vector polarizability α_0^1. These will be written out below.

For $q \neq 0$ components, the rigorous selection rule for the polarizability matrix elements is that $\Delta P = q$, where $P = \Lambda + \ell + \Sigma$. The electric dipole transitions that contribute to the polarizability only change Λ, not ℓ or Σ, but internal molecular interactions that couple these angular momenta in the excited state can allow any of them to change in a two-photon process via that excited state. In the presence of this coupling, we can write each excited state $|j\rangle$ as a linear combination of basis states, $|j\rangle = \sum_k c_k |\Lambda_k, \ell_k, \Sigma_k\rangle$. Applying the dipole selection rules for operator μ_{q_i} ($\Delta\Lambda = q_i, \Delta\ell = 0, \Delta\Sigma = 0$) we see that each term in eqn. A.76 of the form $\mu_{q_2}\mathcal{R}^{\pm}\mu_{q_1}$ can potentially couple states with $\Lambda = \Lambda'$ according to:

$$\begin{aligned}\langle \Lambda, \ell', \Sigma' | \mu_{q_2}\mathcal{R}^{\pm}\mu_{q_1} | \Lambda, \ell, \Sigma\rangle &= \sum_j \frac{1}{\hbar(\omega_j \pm \omega)} \langle \Lambda, \ell', \Sigma' | \mu_{q_2} | j\rangle \langle j | \mu_{q_1} | \Lambda, \ell, \Sigma\rangle \\ &= \sum_j \frac{c_1^j c_2^j}{\hbar(\omega_j \pm \omega)} \langle \Lambda, \ell', \Sigma' | \mu_{q_2} | \Lambda - q_2, \ell', \Sigma'\rangle \langle \Lambda + q_1, \ell, \Sigma | \mu_{q_1} | \Lambda, \ell, \Sigma\rangle\end{aligned}$$

where c_1^j and c_2^j are the coefficients on the relevant basis states in the expansion of excited state j: $|j\rangle \equiv c_1^j|\Lambda + q_1, \ell, \Sigma\rangle + c_2^j|\Lambda - q_2, \ell', \Sigma'\rangle + \ldots$, and we have only written out the non-vanishing cross term above. We therefore require nonzero c_1^j and c_2^j, such that excited state $|j\rangle$ has a finite mixing between the basis states $|\Lambda + q_1, \ell, \Sigma\rangle$ and $|\Lambda - q_2, \ell', \Sigma'\rangle$. The corresponding selection rules for the excited state interaction coupling these basis states are $\Delta(\ell + \Sigma) = q$ and $\Delta\Lambda = -q$, where $q = q_1 + q_2$.[14]

For $q = \pm 1$, the required excited-state interaction must mix basis states with $\Delta\Lambda = \mp 1$. However, this always means that different electronic states are being mixed, leading to very weak interactions that can be ignored for

[14] The first of these follows from the selection rule $\Delta P = q$ for the polarizability matrix elements and the fact that we have enforced $\Delta\Lambda = 0$ between the two ground states. The second arises since $(\Lambda - q_2) - (\Lambda + q_1) = -q$.

purposes of the polarizability.

For $q = \pm 2$, the $\Delta\Lambda = \mp 2, \Delta(\ell + \Sigma) = \pm 2$ selection rules can mix basis states within a $^2\Pi$ electronic manifold, leading to potentially large interactions. The three lowest-order interaction terms obeying these selection rules are proportional to $(L_-^2 G_+^2)$, $(L_-^2 S_+^2)$, and $(L_-^2 S_+ G_+)$, where L_- is the lowering operator for Λ, G_+ is the raising operator for ℓ, and S_+ is the raising operator for Σ. The first term is a vibronic interaction that occurs in states with $\Lambda = \pm 1, \ell = \mp 1$, e.g. $\widetilde{A}^2\Pi(010)$. The 2nd term contributes to Λ-doubling in molecules with $S > 1/2$, but is zero for the doublet molecules considered here (since Σ can't be increased by two). The third term raises ℓ by 1 and therefore mixes different vibrational states, so it will be suppressed by a large energy denominator. Therefore, only the first interaction will contribute to $q = 2$ polarizabilities, and thus only states with $\ell = \pm 1$ have a $q = 2$ term in the polarizability tensor.

$\widetilde{X}^2\Sigma^+(000)$ ($\ell = 0$) polarizabilities

In this section, for notational simplicity we will drop ℓ in the state vectors. The relevant excited states we couple to are the $\widetilde{A}^2\Pi_{1/2}$ and $\widetilde{A}^2\Pi_{3/2}$ components (and $^2\Pi_{1/2}$, $^2\Pi_{3/2}$ components of higher-lying electronic states). In the $|\Lambda, \Sigma\rangle$ basis, these states are approximately written as:

$$|^2\Pi_{1/2}, \pm\rangle = \frac{1}{\sqrt{2}}(|1, -1/2\rangle \pm (-1)^{J-S}|-1, 1/2\rangle)$$
$$|^2\Pi_{3/2}, \pm\rangle = \frac{1}{\sqrt{2}}(|1, 1/2\rangle \pm (-1)^{J-S}|-1, -1/2\rangle)$$

The matrix elements of $d_1\mathcal{R}^{\pm}d_{-1}$ are evaluated as, for example [note that in this section we have changed the notation for the dipole operator from μ_q to d_q]:

$$\begin{aligned}
&\langle \Lambda = 0, \Sigma = 1/2 || d_1\mathcal{R}^{\pm}d_{-1} || \Lambda = 0, \Sigma = 1/2\rangle \\
&= -\langle \Lambda = -1, \Sigma = 1/2 || \frac{|^2\Pi_{1/2}\rangle\langle ^2\Pi_{1/2}|}{\hbar(\omega_{1/2} \pm \omega_L)} + \frac{|^2\Pi_{3/2}\rangle\langle ^2\Pi_{3/2}|}{\hbar(\omega_{3/2} \pm \omega_L)} || \Lambda = -1, \Sigma = 1/2\rangle \\
&= -\frac{1}{2}\sum_i \frac{1}{\hbar(\omega_{1/2,i} \pm \omega_L)} |\langle \widetilde{X}^2\Sigma^+ | d_{\pm 1} | i, ^2\Pi_{1/2}\rangle|^2
\end{aligned}$$

where in the second line we used that $(d_q)^\dagger = (-1)^q d_{-q}$ and in the last line we added a sum over all excited $^2\Pi_{1/2}$ states. Similarly, we have

$$\begin{aligned}
\langle 0, -1/2 || d_1\mathcal{R}^{\pm}d_{-1} || 0, -1/2\rangle &= -\frac{1}{2}\sum_i \frac{1}{\hbar(\omega_{3/2,i} \pm \omega_L)} |\langle \widetilde{X}^2\Sigma^+ | d_{\pm 1} | i, ^2\Pi_{3/2}\rangle|^2 \\
\langle 0, 1/2 || d_{-1}\mathcal{R}^{\pm}d_{1} || 0, 1/2\rangle &= -\frac{1}{2}\sum_i \frac{1}{\hbar(\omega_{3/2,i} \pm \omega_L)} |\langle \widetilde{X}^2\Sigma^+ | d_{\pm 1} | i, ^2\Pi_{3/2}\rangle|^2 \\
\langle 0, -1/2 || d_{-1}\mathcal{R}^{\pm}d_{1} || 0, -1/2\rangle &= -\frac{1}{2}\sum_i \frac{1}{\hbar(\omega_{1/2,i} \pm \omega_L)} |\langle \widetilde{X}^2\Sigma^+ | d_{\pm 1} | i, ^2\Pi_{1/2}\rangle|^2
\end{aligned}$$

This motivates the definitions:

$$\begin{aligned}
\alpha_{\perp,1/2} &= \sum_i \left(\frac{1}{\hbar(\omega_{1/2,i} - \omega_L)} + \frac{1}{\hbar(\omega_{1/2,i} + \omega_L)}\right) |\langle \widetilde{X}^2\Sigma^+ | d_{\pm 1} | i, ^2\Pi_{1/2}\rangle|^2 \\
\alpha_{\perp,3/2} &= \sum_i \left(\frac{1}{\hbar(\omega_{3/2,i} - \omega_L)} + \frac{1}{\hbar(\omega_{3/2,i} + \omega_L)}\right) |\langle \widetilde{X}^2\Sigma^+ | d_{\pm 1} | i, ^2\Pi_{3/2}\rangle|^2 \\
\alpha_{\perp} &= \frac{1}{2}\left(\alpha_{\perp,1/2} + \alpha_{\perp,3/2}\right)
\end{aligned} \tag{A.83}$$

These will be used for the scalar polarizability $\alpha_0^0 \equiv \alpha_0 = \langle \Lambda = 0, \Sigma || \mathcal{A}_0^0 || \Lambda = 0, \Sigma \rangle$ and the tensor polarizability $\alpha_0^2 \equiv \alpha_2 = \langle \Lambda = 0, \Sigma || \mathcal{A}_0^2 || \Lambda = 0, \Sigma \rangle$. Meanwhile, the vector polarizability $\alpha_0^1 \equiv \alpha_1 = \langle \Lambda = 0, \Sigma || \mathcal{A}_0^1 || \Lambda = 0, \Sigma \rangle$ will depend on Σ. Let's define the following:

$$\begin{aligned}
\beta_{\perp,1/2} &= \sum_i \left(\frac{1}{\hbar(\omega_{1/2,i} + \omega_L)} - \frac{1}{\hbar(\omega_{1/2,i} - \omega_L)} \right) |\langle \widetilde{X}^2\Sigma^+ | d_{\pm 1} | i, ^2\Pi_{1/2} \rangle|^2 \\
\beta_{\perp,3/2} &= \sum_i \left(\frac{1}{\hbar(\omega_{3/2,i} + \omega_L)} - \frac{1}{\hbar(\omega_{3/2,i} - \omega_L)} \right) |\langle \widetilde{X}^2\Sigma^+ | d_{\pm 1} | i, ^2\Pi_{3/2} \rangle|^2
\end{aligned} \tag{A.84}$$

Combining everything, we arrive at

$$\begin{aligned}
\alpha_0 &= \frac{1}{3} \left(\alpha_\parallel + 2\alpha_\perp \right) \\
\alpha_1(\Sigma) &= \frac{1}{2} (-1)^{\Sigma - 1/2} \left(\beta_{\perp,1/2} - \beta_{\perp,3/2} \right) \\
\alpha_2 &= \frac{2}{3} \left(\alpha_\parallel - \alpha_\perp \right)
\end{aligned} \tag{A.85}$$

where we used $\alpha_k \equiv \alpha_q^k$. Here we have made $\alpha_1(\Sigma)$ depend explicitly on Σ to achieve the correct sign. Alternatively, we could have added an extra phase factor in the matrix elements (which is what Caldwell does [322, 323]). It is left as an exercise to the reader to confirm that there is no sign error in the vector polarizability defined here.

$\widetilde{X}^2\Sigma^+(010)$ ($\ell = 1$) polarizabilities

For this state, we consider coupling to the $\widetilde{A}^2\Pi(010)$ manifold, which was discussed in chapter 2. We refer to the vibronic eigenstates in in the $|\Lambda, \ell, \Sigma\rangle$ basis.

As before, we evaluate individual matrix elements as follows (for example):

$$\begin{aligned}
&\langle \Lambda = 0, \ell = 1, \Sigma = 1/2 || d_1 \mathcal{R}^{\pm} d_{-1} || \Lambda = 0, \ell = 1, \Sigma = 1/2 \rangle \\
&= -\langle -1, 1, 1/2 || \frac{|\mu^2\Sigma^{(+)}\rangle\langle\mu^2\Sigma^{(+)}|}{\hbar(\omega_\mu \pm \omega_L)} + \frac{|\kappa^2\Sigma^{(-)}\rangle\langle\kappa^2\Sigma^{(-)}|}{\hbar(\omega_\kappa \pm \omega_L)} + \frac{|^2\Delta_{3/2}\rangle\langle^2\Delta_{3/2}|}{\hbar(\omega_{3/2} \pm \omega_L)} + \frac{|^2\Delta_{5/2}\rangle\langle^2\Delta_{5/2}|}{\hbar(\omega_{5/2} \pm \omega_L)} || -1, 1, 1/2 \rangle \\
&= -\frac{1}{2} \sum_i \left(\frac{\cos^2\beta}{\hbar(\omega_{\mu,i} \pm \omega_L)} + \frac{\sin^2\beta}{\hbar(\omega_{\kappa,i} \pm \omega_L)} \right) |\langle \widetilde{X}^2\Sigma^+ | d_{\pm 1} | i, ^2\Pi \rangle|^2
\end{aligned}$$

where we have factored out the electronic transition matrix element, assuming it changes negligibly for the different vibronic components.

The other matrix elements are evaluated similarly:

$$\langle 0, 1, 1/2 || d_{-1} \mathcal{R}^{\pm} d_1 || 0, 1, 1/2 \rangle = -\frac{1}{2} \sum_i \frac{1}{\hbar(\omega_{5/2,i} \pm \omega_L)} |\langle \widetilde{X}^2\Sigma^+ | d_{\pm 1} | i, ^2\Pi \rangle|^2$$

$$\langle 0, 1, -1/2 || d_1 \mathcal{R}^{\pm} d_{-1} || 0, 1, -1/2 \rangle = -\frac{1}{2} \sum_i \left(\frac{\sin^2\beta}{\hbar(\omega_{\mu,i} \pm \omega_L)} + \frac{\cos^2\beta}{\hbar(\omega_{\kappa,i} \pm \omega_L)} \right) |\langle \widetilde{X}^2\Sigma^+ | d_{\pm 1} | i, ^2\Pi \rangle|^2$$

$$\langle 0, 1, -1/2 || d_{-1} \mathcal{R}^{\pm} d_1 || 0, 1, -1/2 \rangle = -\frac{1}{2} \sum_i \frac{1}{\hbar(\omega_{3/2,i} \pm \omega_L)} |\langle \widetilde{X}^2\Sigma^+ | d_{\pm 1} | i, ^2\Pi \rangle|^2$$

$$\langle 0, -1, 1/2 || d_1 \mathcal{R}^{\pm} d_{-1} || 0, -1, 1/2 \rangle = -\frac{1}{2} \sum_i \frac{1}{\hbar(\omega_{3/2,i} \pm \omega_L)} |\langle \widetilde{X}^2\Sigma^+ | d_{\pm 1} | i, ^2\Pi \rangle|^2$$

$$\langle 0, -1, 1/2 || d_{-1} \mathcal{R}^{\pm} d_1 || 0, -1, 1/2 \rangle = -\frac{1}{2} \sum_i \left(\frac{\sin^2\beta}{\hbar(\omega_{\mu,i} \pm \omega_L)} + \frac{\cos^2\beta}{\hbar(\omega_{\kappa,i} \pm \omega_L)} \right) |\langle \widetilde{X}^2\Sigma^+ | d_{\pm 1} | i, ^2\Pi \rangle|^2$$

$$\langle 0, -1, -1/2 || d_1 \mathcal{R}^{\pm} d_{-1} || 0, -1, -1/2 \rangle = -\frac{1}{2} \sum_i \frac{1}{\hbar(\omega_{5/2,i} \pm \omega_L)} |\langle \widetilde{X}^2\Sigma^+ | d_{\pm 1} | i, ^2\Pi \rangle|^2$$

$$\langle 0, -1, -1/2 || d_{-1} \mathcal{R}^{\pm} d_1 || 0, -1, -1/2 \rangle = -\frac{1}{2} \sum_i \left(\frac{\cos^2\beta}{\hbar(\omega_{\mu,i} \pm \omega_L)} + \frac{\sin^2\beta}{\hbar(\omega_{\kappa,i} \pm \omega_L)} \right) |\langle \widetilde{X}^2\Sigma^+ | d_{\pm 1} | i, ^2\Pi \rangle|^2$$

The trend is that when ℓ and Σ have the same sign, the $d_{\pm1}\mathcal{R}^{\pm}d_{\mp1}$ terms connect to the $\Delta_{5/2}$ and μ-dominant vibronic states (since $\cos^2\beta > \sin^2\beta$ for CaOH). When ℓ and Σ have the opposite sign, they instead connect to the $\Delta_{3/2}$ and the κ-dominant states.

To write out the scalar, vector, and tensor polarizabilities, we define the following quantities, in analogy with the $\widetilde{X}^2\Sigma^+(000)$ case above:

$$
\begin{aligned}
\alpha_{\perp,\mu} &= \sum_i \left(\frac{\cos^2\beta}{\hbar(\omega_{\mu,i}-\omega_L)} + \frac{\cos^2\beta}{\hbar(\omega_{\mu,i}+\omega_L)} + \frac{\sin^2\beta}{\hbar(\omega_{\kappa,i}-\omega_L)} + \frac{\sin^2\beta}{\hbar(\omega_{\kappa,i}+\omega_L)} \right) |\langle \widetilde{X}^2\Sigma^+ | d_{\pm1} | i, {}^2\Pi \rangle|^2 \\
\alpha_{\perp,\kappa} &= \sum_i \left(\frac{\sin^2\beta}{\hbar(\omega_{\mu,i}-\omega_L)} + \frac{\sin^2\beta}{\hbar(\omega_{\mu,i}+\omega_L)} + \frac{\cos^2\beta}{\hbar(\omega_{\kappa,i}-\omega_L)} + \frac{\cos^2\beta}{\hbar(\omega_{\kappa,i}+\omega_L)} \right) |\langle \widetilde{X}^2\Sigma^+ | d_{\pm1} | i, {}^2\Pi \rangle|^2 \\
\alpha_{\perp,3/2} &= \sum_i \left(\frac{1}{\hbar(\omega_{3/2,i}-\omega_L)} + \frac{1}{\hbar(\omega_{3/2,i}+\omega_L)} \right) |\langle \widetilde{X}^2\Sigma^+ | d_{\pm1} | i, {}^2\Pi \rangle|^2 \\
\alpha_{\perp,5/2} &= \sum_i \left(\frac{1}{\hbar(\omega_{5/2,i}-\omega_L)} + \frac{1}{\hbar(\omega_{5/2,i}+\omega_L)} \right) |\langle \widetilde{X}^2\Sigma^+ | d_{\pm1} | i, {}^2\Pi \rangle|^2 \\
\alpha_{\perp}(\ell,\Sigma) &= \begin{cases} \frac{1}{2}\left(\alpha_{\perp,\mu} + \alpha_{\perp,5/2}\right), & \mathrm{sgn}(\ell\Sigma) > 0 \\ \frac{1}{2}\left(\alpha_{\perp,\kappa} + \alpha_{\perp,3/2}\right), & \mathrm{sgn}(\ell\Sigma) < 0 \end{cases}
\end{aligned}
\tag{A.86}
$$

$$\beta_{\perp,\mu} = \sum_i \left(\frac{\cos^2\beta}{\hbar(\omega_{\mu,i}+\omega_L)} - \frac{\cos^2\beta}{\hbar(\omega_{\mu,i}-\omega_L)} + \frac{\sin^2\beta}{\hbar(\omega_{\kappa,i}+\omega_L)} - \frac{\sin^2\beta}{\hbar(\omega_{\kappa,i}-\omega_L)} \right) |\langle \widetilde{X}^2\Sigma^+ | d_{\pm 1} | i, ^2\,\Pi\rangle|^2$$

$$\beta_{\perp,\kappa} = \sum_i \left(\frac{\sin^2\beta}{\hbar(\omega_{\mu,i}+\omega_L)} - \frac{\sin^2\beta}{\hbar(\omega_{\mu,i}-\omega_L)} + \frac{\cos^2\beta}{\hbar(\omega_{\kappa,i}+\omega_L)} - \frac{\cos^2\beta}{\hbar(\omega_{\kappa,i}-\omega_L)} \right) |\langle \widetilde{X}^2\Sigma^+ | d_{\pm 1} | i, ^2\,\Pi\rangle|^2$$

$$\beta_{\perp,3/2} = \sum_i \left(\frac{1}{\hbar(\omega_{3/2,i}+\omega_L)} - \frac{1}{\hbar(\omega_{3/2,i}-\omega_L)} \right) |\langle \widetilde{X}^2\Sigma^+ | d_{\pm 1} | i, ^2\,\Pi\rangle|^2$$

$$\beta_{\perp,5/2} = \sum_i \left(\frac{1}{\hbar(\omega_{5/2,i}+\omega_L)} - \frac{1}{\hbar(\omega_{5/2,i}-\omega_L)} \right) |\langle \widetilde{X}^2\Sigma^+ | d_{\pm 1} | i, ^2\,\Pi\rangle|^2$$

$$\beta_\perp(\ell,\Sigma) = \begin{cases} \frac{1}{2}\left(\beta_{\perp,\mu} - \beta_{\perp,5/2}\right), & \mathrm{sgn}(\ell\Sigma) > 0 \\ \frac{1}{2}\left(\beta_{\perp,\kappa} - \beta_{\perp,3/2}\right), & \mathrm{sgn}(\ell\Sigma) < 0 \end{cases} \tag{A.87}$$

Using these definitions, we ultimately end up with the following polarizabilities:

$$\begin{aligned} \alpha_0^0(\ell,\Sigma) &= \frac{1}{3}\left[\alpha_\parallel + 2\alpha_\perp(\ell,\Sigma)\right] \approx \frac{1}{3}\left(\alpha_\parallel + 2\alpha_\perp\right) \\ \alpha_0^1(\ell,\Sigma) &= \frac{1}{2}(-1)^{(1-\ell)/2}\beta_\perp(\ell,\Sigma) \\ \alpha_0^2(\ell,\Sigma) &= \frac{2}{3}\left[\alpha_\parallel - \alpha_\perp(\ell,\Sigma)\right] \approx \frac{2}{3}\left(\alpha_\parallel - \alpha_\perp\right) \end{aligned} \tag{A.88}$$

where the approximation neglects the dependence on $\mathrm{sgn}(\ell\Sigma)$, which is a small correction. Realistically, it is sufficient to just use the "standard" values of $\alpha_\parallel$ and $\alpha_\perp$ for these expressions. While the above should be interpreted as a sketch of the process, I make no guarantees that there aren't sign errors in these expressions.

Where things get interesting is in the $q = \pm 2$ terms. Once again, we write out the matrix elements, relating the vibronic eigenstates to the $|\Lambda, \ell, \Sigma\rangle$ basis. We will find that the only nonzero matrix elements occur for $\Delta\ell =$

± 2:

$$\begin{aligned}
&\langle \Lambda = 0, \ell = 1, \Sigma = 1/2 || d_1 \mathcal{R}^{\pm} d_1 || \Lambda = 0, \ell = -1, \Sigma = 1/2 \rangle \\
&= -\langle -1, 1, 1/2 || \frac{|\mu^2\Sigma^{(+)}\rangle\langle\mu^2\Sigma^{(+)}|}{\hbar(\omega_\mu \pm \omega_L)} + \frac{|\kappa^2\Sigma^{(-)}\rangle\langle\kappa^2\Sigma^{(-)}|}{\hbar(\omega_\kappa \pm \omega_L)} + \frac{|^2\Delta_{3/2}\rangle\langle^2\Delta_{3/2}|}{\hbar(\omega_{3/2} \pm \omega_L)} + \frac{|^2\Delta_{5/2}\rangle\langle^2\Delta_{5/2}|}{\hbar(\omega_{5/2} \pm \omega_L)} || 1, -1, 1/2 \rangle \\
&= +\frac{\sin\beta\cos\beta}{2} \sum_i \left(\frac{1}{\hbar(\omega_{\mu,i} \pm \omega_L)} - \frac{1}{\hbar(\omega_{\kappa,i} \pm \omega_L)} \right) |\langle \widetilde{X}^2\Sigma^+ | d_{\pm 1} | i, ^2\Pi \rangle|^2 \\
&= \langle 0, 1, -1/2 || d_1 \mathcal{R}^{\pm} d_1 || 0, -1, -1/2 \rangle \\
&= \langle 0, -1, 1/2 || d_{-1} \mathcal{R}^{\pm} d_{-1} || 0, 1, 1/2 \rangle \\
&= \langle 0, -1, -1/2 || d_{-1} \mathcal{R}^{\pm} d_{-1} || 0, 1, -1/2 \rangle
\end{aligned}$$

Notice that these matrix elements are nonzero because (1) the RT interaction leads to cross terms in the μ and κ excited states that look like $\pm(\sin\beta\cos\beta)/2|-1,1,1/2\rangle\langle 1,-1,1/2|$ and (2) the μ and κ states are nondegenerate.

Based on this, let's define the $q = \pm 2$ polarizabilities as follows:

$$\begin{aligned}
\alpha_2^2 = \alpha_{-2}^2 = \sqrt{\frac{2}{3}} \frac{\sin\beta\cos\beta}{2} \sum_i &\left(\frac{1}{\hbar(\omega_{\mu,i} - \omega_L)} + \frac{1}{\hbar(\omega_{\mu,i} + \omega_L)} - \frac{1}{\hbar(\omega_{\kappa,i} - \omega_L)} - \frac{1}{\hbar(\omega_{\kappa,i} + \omega_L)} \right) \\
&\times |\langle \widetilde{X}^2\Sigma^+ | d_{\pm 1} | i, ^2\Pi \rangle|^2
\end{aligned} \tag{A.89}$$

Note that we don't need to enforce that the $q = +2$ implements $\Delta\ell = -2$ and vice versa, since there is a $3j$ symbol in the matrix elements that will do this for us.

Using spectroscopic parameters for the $\widetilde{A}(010)$ state (chapter 2) gives us an estimate of $\alpha_2^2 \approx -0.3$ a.u. at

1064 nm. Preliminary measurements on the experiment suggest that $\alpha_2^2 \approx 1$ a.u. Therefore, this gets roughly the right size of the interaction. However, there appears to be a sign error that will need to be tracked down at a later date. One possibility is that this is due to a disagreement in the parity phase conventions for the ground and excited states used in this derivation.

Combining everything, the matrix elements of the AC Stark shift Hamiltonian, H_S, for the $\widetilde{X}(010)$ state, are:

$$\begin{aligned}
&\langle \Lambda, \ell; N, S, J, I, F, M | H_S | \Lambda', \ell'; N', S, J', I, F', M' \rangle \\
&\quad = -\frac{\mathcal{E}_0^2}{4} \sum_{k=0}^{2} \sum_{p=-k}^{k} (-1)^p \mathcal{P}_{-p}^k \\
&\qquad \times (-1)^{F-M} \begin{pmatrix} F & k & F' \\ -M & p & M' \end{pmatrix} (-1)^{J+I+F'+k} \sqrt{(2F+1)(2F'+1)} \begin{Bmatrix} J & F & I \\ F' & J' & k \end{Bmatrix} \\
&\qquad \times \sum_{\Sigma=-1/2}^{1/2} (-1)^{-J-J'+P+P'+4S} \sqrt{(2N+1)(2N'+1)} \begin{pmatrix} J & N & S \\ P & -K & -\Sigma \end{pmatrix} \begin{pmatrix} J' & N' & S \\ P' & -K' & -\Sigma \end{pmatrix} \\
&\qquad \times \sum_{q=-k}^{k} (-1)^{J-P} \sqrt{(2J+1)(2J'+1)} \begin{pmatrix} J & k & J' \\ -P & q & P' \end{pmatrix} \alpha_q^k(\ell, \Sigma)
\end{aligned} \tag{A.90}$$

with the polarizabilities $\alpha_q^k(\ell, \Sigma)$ defined above.

B

Branching Ratio Calculations

In this appendix, we describe semi-empirical calculations of vibrational branching ratios in CaOH. These use previously measured spectroscopic parameters to estimate rovibronic branching ratios that account for Franck-Condon factors, vibronic coupling, and Fermi resonance perturbations. This appendix is reproduced, with small modifications, from Ref. [251].

The strength of generic, dipole-allowed rovibronic decays is governed by the Einstein A coefficient [236]

$$A_{J'\to J''} = \frac{16\pi^3\nu^3|\langle\mu\rangle|^2}{3\epsilon_0 hc^3(2J'+1)}, \tag{B.1}$$

where $|\langle\mu\rangle|^2 = \sum_{M'M''}|\langle\eta', v', J'M'|\mu|\eta'', v'', J''M''\rangle|^2$ is the degeneracy-weighted line strength of the electric dipole transition and ν is the transition frequency. The rovibronic states are $|\eta, v, JM\rangle$ and consist of electronic, $|\eta\rangle$, vibrational, $|v\rangle$, and rotational, $|JM\rangle$, components. The line strength may be approximately separated as follows:

$$|\langle\mu\rangle|^2 \approx q_{v'-v''}|\mathbf{R}_e|^2 S^{J'}_{J''}(\zeta', \zeta''), \tag{B.2}$$

where $|\mathbf{R}_e|^2$ is the electronic transition dipole moment and

$$q_{v'-v''} = |\langle v''|v'\rangle|^2 \tag{B.3}$$

is the Franck-Condon factor (FCF). $S^{J'}_{J''}(\zeta', \zeta'')$ is the Hönl-London (HL) factor, which characterizes the rotational line strength but depends in general on the vibronic states involved, labeled $|\zeta\rangle \equiv |\eta, v\rangle$ for notational convenience. Some relevant HL factors are given in Table B.1.

Both the FCFs and the HL factors may be calculated for CaOH using empirical methods. The transition dipole moment $|\mathbf{R}_e|^2$, meanwhile, is treated as constant for all rovibronic transitions in an electronic band, and may be factored out. This approximation is justified by the good agreement of calculated VBRs with experimental results (section B.4), and by the practical value of calculations grounded solely in empirical parameters (determination of $|\mathbf{R}_e|^2$ would necessarily require some reference to *ab initio* methods). Under this approximation,

Excited State		Ground State	$N''=1$ $J''=1/2$	$N''=1$ $J''=3/2$	$N''=2$ $J''=3/2$
$\widetilde{A}(000)^2\Pi_{1/2}$	$\rightarrow$	$\widetilde{X}(000)^2\Sigma^+$	$2/3$	$1/3$	–
$\widetilde{B}(000)^2\Sigma^+$	$\rightarrow$	$\widetilde{X}(000)^2\Sigma^+$	$1/3$	$2/3$	–
$\widetilde{A}(010)\mu^2\Sigma^{(+)}$	$\rightarrow$	$\widetilde{X}(01^10)^2\Pi$	0.108	0.826	0.066
$\widetilde{A}(010)\kappa^2\Sigma^{(+)}$	$\rightarrow$	$\widetilde{X}(01^10)^2\Pi$	0.559	0.007	0.434
$\widetilde{B}(01^10)^2\Pi$	$\rightarrow$	$\widetilde{X}(01^10)^2\Pi$	$1/3$	$1/6$	$1/2$
$\widetilde{A}(02^20)^2\Pi_{1/2}$	$\rightarrow$	$\widetilde{X}(02^20)^2\Delta$	–	–	1

Table B.1: Degeneracy-weighted rotational line strengths, $S^{J'}_{J''}(\zeta', \zeta'')$, calculated for transitions from $J' = 1/2, (+)$ parity excited states. The same factors hold for other vibrational levels of the $\widetilde{X}^2\Sigma^+$ ground state with similar vibronic symmetry. All ground states listed have $(-)$ parity. Calculations make use of dipole matrix elements found, e.g., in Ref. [252] and Appendix A.

the branching ratio from an excited state $|\zeta', J'\rangle$ to a ground state $|\zeta'', J''\rangle$ is

$$P_{|\zeta',J'\rangle\rightarrow|\zeta'',J''\rangle} \equiv \frac{\nu^3 q_{v'-v''} S^{J'}_{J''}(\zeta', \zeta'')}{\mathcal{N}}, \tag{B.4}$$

where

$$\mathcal{N} = \sum_i \nu_i^3 q_{v'-v''_i} S^{J'}_{J''_i}(\zeta', \zeta''_i) \tag{B.5}$$

is a normalization factor. The sum is over all ground states $|\zeta''_i, J''_i\rangle$ to which the initial state may decay.

In section B.1 below, we determine FCFs for CaOH by evaluating Eq. B.3 in the harmonic approximation. In sections B.2 and B.3 we consider vibronic mixing due to Renner-Teller perturbations and Fermi resonance that significantly alters the results obtained from harmonic FCFs alone. In section B.4 we combine these effects to estimate VBRs for CaOH.

B.1 FCF calculations in the harmonic approximation

Within the harmonic approximation, Eq. B.3 may be evaluated analytically using empirically measured force constants, bond lengths, and vibrational frequencies for CaOH. We evaluate these integrals by first performing a classical Wilson GF-matrix analysis of the normal modes [415], then evaluating the overlap integrals (including Duschinsky rotations) using the formalism of Sharp and Rosenstock [416, 417]. This method is the same as the one used in Ref. [213].

Briefly, we begin by constructing the Wilson force and kinetic energy-related matrices $\mathbf{F}$ and $\mathbf{G}$, which are related to the vibrational potential energy V and kinetic energy K by

$$2V = \left(\vec{S}\right)^T \mathbf{F}\vec{S}, \quad 2K = \left(\dot{\vec{S}}\right)^T \mathbf{G}^{-1}\dot{\vec{S}} \tag{B.6}$$

where $\vec{S}$ is a vector of $3N-5$ internal molecular coordinates and $[\ldots]^T$ denotes the vector transpose. For CaOH, we define the internal coordinates so that $S_1 = \Delta r_{31}$, $S_2 = \Delta r_{32}$ and $S_3 = (r_{31}r_{32})^{1/2}\,\Delta\phi$, where r_{31} and r_{32} are the equilibrium Ca–O and O–H bond lengths, respectively, Δr_{31} and Δr_{32} give the change in bond length, and $\Delta\phi$ is the change in the bending angle. From geometrical arguments the $\mathbf{G}$ matrix can be expressed as [415]

$$\mathbf{G} = \begin{pmatrix} \mu_1+\mu_3 & -\mu_3 & 0 \\ -\mu_3 & \mu_2+\mu_3 & 0 \\ 0 & 0 & G_{33} \end{pmatrix},$$
$$G_{33} = \mu_1\frac{r_{32}}{r_{31}} + \mu_2\frac{r_{31}}{r_{32}} + \mu_3\frac{(r_{31}+r_{32})^2}{r_{31}r_{32}} \tag{B.7}$$

where $\mu_1 = 1/m_{\mathrm{Ca}}$, $\mu_2 = 1/m_{\mathrm{H}}$, $\mu_3 = 1/m_{\mathrm{O}}$.

The $\mathbf{F}$ matrix consists of second derivatives of the potential energy surface with respect to the internal coordinates. Because there is at most only very weak coupling between the stretching and bending vibrations, we write $\mathbf{F}$ as

$$\mathbf{F} = \begin{pmatrix} F_{11} & F_{12} & 0 \\ F_{21} & F_{22} & 0 \\ 0 & 0 & F_{33} \end{pmatrix} \tag{B.8}$$

Diagonalizing the matrix product $\mathbf{GF}$ is equivalent to solving the secular equation, and its eigenvalues and eigenvectors are the frequencies and coordinates of the normal modes of vibration. In particular, properly-normalized eigenvectors of $\mathbf{GF}$ form the columns of the $\mathbf{L}$ matrix, which transforms normal coordinates $\vec{Q}$ into internal coordinates $\vec{S} = \mathbf{L}\vec{Q}$.

For the $\widetilde{\mathrm{A}} \rightarrow \widetilde{\mathrm{X}}$ transition, we use measured vibrational frequencies and bond lengths from Ref. [250] to solve for the force constants F_{ij}. This calculation makes use of equations given in Refs. [93, 250]. For the $\widetilde{\mathrm{B}} \rightarrow \widetilde{\mathrm{X}}$ transition we use the measured bond lengths from Ref. [242], in conjunction with vibrational frequency calculations from Ref. [325]. There is insufficient data on the $\widetilde{\mathrm{B}}$ state to extract the off-diagonal force constants (these require data from CaOD as well), so we make the approximation that $F_{21} = F_{12} = 0$ for the $\widetilde{\mathrm{B}}$ state. We find that this has little impact on the final result.

After solving for the normal modes using the $\mathbf{GF}$ matrix approach, harmonic overlap integrals may be factored as

$$\langle \overline{v''|v'} \rangle = \prod_i \int \psi^*_{v''_i} \psi_{v'_i} dQ_i \,, \tag{B.9}$$

where ψ_{v_i} is a harmonic oscillator eigenfunction and Q_i is a normal coordinate. Eq. B.9 may be evaluated by transforming the normal coordinates $\vec{Q}''$ of the final state to those of the initial state $\vec{Q}'$ via a Duschinsky rotation,

$$\vec{Q}' = \mathbf{J}\vec{Q}'' + \vec{K}. \tag{B.10}$$

The method employed here, due to Sharp and Rosenstock, relates $\mathbf{J}$ and $\vec{K}$ to the transformation matrices $\mathbf{L}''$, $\mathbf{L}'$ of the ground and excited states, as well as their equilibrium geometries. The solution makes use of generating functions, and the results may be calculated using standard computational tools [416, 417].

In the case where the vibrational eigenstates are mixed by perturbations to the potential energy surface (as in the Renner-Teller and Fermi resonance interactions discussed below), FCFs may still be computed using the harmonic calculations described here. For example, if the ground and excited state vibrational wavefunctions are given by

$$|v'\rangle = a|\overline{v'_a}\rangle + b|\overline{v'_b}\rangle, \quad |v''\rangle = c|\overline{v''_a}\rangle + d|\overline{v''_b}\rangle,$$

where the horizontal bar denotes a harmonic oscillator eigenstate, the FCF is

$$\begin{aligned} q_{v'-v''} &= \left|\langle v''|v'\rangle\right|^2 \\ &= \left|ac^*\langle\overline{v''_a|v'_a}\rangle + ad^*\langle\overline{v''_a|v'_b}\rangle + \dots\right|^2 \end{aligned}$$

where each term on the right-hand side is a harmonic overlap integral (Eq. B.9) and can be computed by the means described above.

The resulting VBRs, accounting for the frequency and Hönl-London scaling factors (Eq. B.4), are shown in

Table B.2: Comparison of calculated and observed rovibronic branching ratios from the combined $\widetilde{\mathrm{A}}\,^2\Pi_{1/2}(000) \leftarrow \widetilde{\mathrm{X}}\,^2\Sigma^+(000) + \widetilde{\mathrm{B}}\,^2\Sigma^+(000) \leftarrow \widetilde{\mathrm{X}}\,^2\Sigma^+(100)$ photon cycling scheme. The measurements ("observed") use the depletion-revival technique described in chapter 4. Branching ratio calculations based on unperturbed harmonic wavefunction overlap ("harmonic") fail to adequately capture decay to the $\widetilde{\mathrm{X}}\,^2\Sigma^+(02^00)$, (02^20), and (01^10) bending modes. These discrepancies are resolved by including Fermi resonance and Renner-Teller interactions. All measured and calculated branching ratios are rotationally resolved, with listed decays from $J' = 1/2$, $(+)$ parity excited states to $\widetilde{\mathrm{X}}\,^2\Sigma^+\left(v_1v_2^\ell v_3\right)$, $N'' = 1$, $(-)$ parity ground states. Reproduced from Ref. [251].

Decay	Harmonic	Corrected[a]	Observed
(000)	0.957	0.955	$0.9492(27)$
(100)	0.042	0.038	$0.0426(19)$
(200)	0.6×10^{-3}	0.4×10^{-3}	$2.5(3) \times 10^{-3}$
(02^00)	1.6×10^{-4}	4.6×10^{-3}	$3.3(4) \times 10^{-3}$
(02^20)	o	1.0×10^{-3}	$8.2(1.3) \times 10^{-4}$
$(01^10), N'' = 1$	o	4.3×10^{-4}	$6.4(1.1) \times 10^{-4}$
Other	1.0×10^{-4}	6.3×10^{-4}	$1.1(1) \times 10^{-3}$

[a] Corrections due to Renner-Teller and Fermi resonance couplings, as described in the text.

the first column of Table B.2. While this calculation accurately reproduces observed decays to the Ca–O stretching modes, it underestimates the observed (02^00) bending mode decay by an order of magnitude and also fails to explain $\Delta\ell \neq 0$ transition strength. A more accurate description of these discrepancies requires consideration of additional perturbations.

B.2 Renner-Teller perturbation

Vibrational branching to the $\widetilde{\mathrm{X}}\left(01^10\right)$ and $\widetilde{\mathrm{X}}\left(02^20\right)$ states is suppressed due to the nominal selection rule $\Delta\ell = 0$ due to the Born-Oppenheimer (BO) approximation. However, BO approximation breakdown at the level of a few parts per thousand is not unexpected. Transitions with $|\Delta\ell| = 1$ have been previously observed in

SrOH [267, 418], BaOH [419], and CaOH [93, 420]. In this work, we consider two decays in which $|\Delta\ell| \neq 0$: $\widetilde{\mathrm{A}}^2\Pi_{1/2}\,(000) \rightarrow \widetilde{\mathrm{X}}^2\Sigma^+\,(01^10)$ and $\widetilde{\mathrm{A}}^2\Pi_{1/2}\,(000) \rightarrow \widetilde{\mathrm{X}}^2\Sigma^+\,(02^20)$. These decays are due to Renner-Teller (RT) induced vibronic coupling.

The Renner-Teller Hamiltonian has been covered in depth elsewhere [252, 264, 421–425]. It may be written as [252, 264–268]

$$H_{\mathrm{RT}} = \frac{V_{11}}{2}(q_+L_- + q_-L_+) + \frac{V_{22}}{2}(q_+^2L_-^2 + q_-^2L_+^2) + \ldots \tag{B.11}$$

where $L_\pm$ and $q_\pm$ are ladder operators in the electronic angular momentum Λ and the vibrational angular momentum ℓ, respectively. The matrix elements of $q_\pm$ are [266, 268, 422]

$$\begin{aligned}\langle v_2+1, \ell \pm 1|q_\pm|v_2,\ell\rangle &= \frac{1}{\sqrt{2}}(v_2+2\pm\ell)^{1/2}\\ \langle v_2-1, \ell \pm 1|q_\pm|v_2,\ell\rangle &= \frac{1}{\sqrt{2}}(v_2\mp\ell)^{1/2}\end{aligned} \tag{B.12}$$

while $L_\pm$ connects states satisfying $L_\pm|\Lambda\rangle \propto |\Lambda \pm 1\rangle$. The first, dipolar, term of H_{RT} therefore has matrix elements only between different electronic states, while the second, quadrupolar, term supports matrix elements within a single Π state.

There are three RT-induced vibronic coupling pathways relevant to this work: (1) direct RT mixing between $\widetilde{A}(000)$ and $\widetilde{B}(01^10)$; (2) second-order coupling between $\widetilde{A}(000)$ and $\widetilde{A}(01^10)$; and (3) direct RT mixing between $\widetilde{A}(000)$ and $\widetilde{A}(02^20)$. Each of these contributions is discussed in more detail below.

B.2.1 $\widetilde{A}^2\Pi_{1/2}\,(000) \rightarrow \widetilde{X}^2\Sigma^+\,(01^10)$ decay

The $|\Delta\ell| = 1$ transition has been previously observed in several alkaline-earth monohydroxides [93, 267, 418–420]. This transition could gain strength due to direct vibronic coupling between $\widetilde{B}^2\Sigma^+\,(01^10)$ and $\widetilde{A}^2\Pi_{1/2}\,(000)$, or through a second-order spin-orbit vibronic coupling [268]. Previous authors have favored the latter explanation based on the observation that the intensity grows with atomic spin-orbit constant [267, 418, 420]. In this work we find that both contributions are necessary to satisfactorily explain the observed $|\Delta\ell| = 1$ branching in CaOH.[1]

Direct vibronic coupling

The direct vibronic mixing between $\widetilde{A}(000)$ and $\widetilde{B}(01^10)$ may be evaluated in perturbation theory as

$$\begin{aligned} |\langle \widetilde{B}(\overline{01^10})^2\Pi|\widetilde{A}(000)^2\Pi_{1/2}\rangle|^2 &\approx \frac{|\langle \widetilde{B}|H_{\mathrm{RT}}|\widetilde{A}\rangle|^2}{(\Delta E_{AB}-\omega_2)^2} \\ &\approx \frac{g_K}{\omega_2\left(1-\frac{\omega_2}{\Delta E_{AB}}\right)^2} \\ &\approx 1.2\times 10^{-3} \end{aligned} \tag{B.13}$$

where $\Delta E_{AB} = E(\widetilde{A}) - E(\widetilde{B})$ is the splitting between the $\widetilde{A}$ and $\widetilde{B}$ state energy origins, ω_2 is the bending vibrational frequency, and the strength of the relevant RT interaction is contained in the spectroscopic parameter

[1] Note, however, that it was later pointed out in Ref. [269] that the direct vibronic coupling is generally stronger. This is because the spin-orbit vibronic coupling effect is suppressed by an energy denominator proportional to the spin-orbit constant.

Parameter	Value (cm^{-1})	Ref.
A_{SO}	66.8181	[93]
g_K	0.5937	[93]
ω_2	366.435	[250]
$\epsilon\omega_2$	-36.5641	[250]
ΔE_{AB}	-2024.14	[93, 238]
$\Delta E_{(020)}$	-702.051	[93, 250]
g_{22}	7.5314	[250]

Table B.3: Compiled spectroscopic parameters, as defined in the text, used in the branching ratio calculations in this work.

g_K [264, 266]:

$$g_K \approx \frac{\omega_2 |\langle \widetilde{B}|V_{11}L_+|\widetilde{A}\rangle|^2}{4\Delta E_{AB}^2} \tag{B.14}$$

This parameter appears as an energy offset $g_K(\Lambda + \ell)$ in the effective Hamiltonian for vibronically perturbed levels of a Π electronic state, and was previously fit for CaOH [93, 250]. In eqn. B.13, a bar is used to specify unperturbed basis states, which are eigenstates of the molecular Hamiltonian absent the perturbations considered here. All spectroscopic quantities were measured in Refs. [93, 238, 250] and are compiled in Table B.3.

Spin-orbit vibronic coupling

Vibronic mixing between $\widetilde{A}(000)$ and $\widetilde{A}(01^10)$ is induced by the $H_{\rm RT} \times H_{\rm SO}$ interaction, where $H_{\rm SO}$ is the spin-orbit Hamiltonian. This second-order interaction proceeds via both the $\widetilde{B}(000)^2\Sigma^+$ and the $\widetilde{B}(01^10)^2\Pi$ states, as described here. The spin-orbit Hamiltonian is

$$H_{\rm SO} = A_{\rm SO}L_zS_z + \frac{1}{2}A_{\rm SO}(L_+S_- + L_-S_+) \tag{B.15}$$

where S_z, $S_\pm$ are angular momentum operators acting on the electronic spin state $|S,\Sigma\rangle$. Their matrix elements are defined as usual,

$$\langle S,\Sigma\pm1|S_\pm|S,\Sigma\rangle = [S(S+1)-\Sigma(\Sigma\pm1)]^2 \tag{B.16}$$

The $\widetilde{A}^2\Pi(010)$ state is split into several vibronic components due to Renner-Teller and spin-orbit interactions, as shown in Fig. 2.10 of chapter 2 [93, 263]. Both the $\widetilde{A}(010)\mu^2\Sigma^{(+)}$ and $\widetilde{A}(010)\kappa^2\Sigma^{(-)}$ components are mixed with $\widetilde{A}(000)^2\Pi_{1/2}$ and contribute to vibronic decay. The second-order mixing amplitudes of these states due to the $H_{\mathrm{RT}}\times H_{\mathrm{SO}}$ perturbation are [268]

$$\begin{aligned}&\langle\widetilde{A}(010)\mu^2\Sigma^{(+)}|\widetilde{A}(000)^2\Pi_{1/2}\rangle\\ &\qquad\approx 2\frac{\langle\widetilde{A}|A_{\mathrm{SO}}L_-|\widetilde{B}\rangle\langle\widetilde{B}|V_{11}L_+|\widetilde{A}\rangle}{4\omega_2\Delta E_{AB}}\times(\cos\beta-\sin\beta)\end{aligned} \tag{B.17}$$

$$\begin{aligned}&\langle\widetilde{A}(010)\kappa^2\Sigma^{(+)}|\widetilde{A}(000)^2\Pi_{1/2}\rangle\\ &\qquad\approx 2\frac{\langle\widetilde{A}|A_{\mathrm{SO}}L_-|\widetilde{B}\rangle\langle\widetilde{B}|V_{11}L_+|\widetilde{A}\rangle}{4\omega_2\Delta E_{AB}}\times(\cos\beta+\sin\beta)\end{aligned} \tag{B.18}$$

where the prefactor of 2 comes from the two contributions via $\widetilde{B}(000)$ and $\widetilde{B}(01^10)$, respectively. The mixing angle β defines the vibronic character of the μ and κ states [252, 263],

$$\beta=\frac{1}{2}\arcsin\left(\frac{2\epsilon\omega_2}{\sqrt{(2\epsilon\omega_2)^2+A_{\mathrm{SO}}^2}}\right) \tag{B.19}$$

where ϵ is the Renner parameter.

The common factor in eqns. B.17-B.18 may be evaluated using the pure precession approximation, $\langle\widetilde{A}|\frac{1}{2}A_{\mathrm{SO}}L_-|\widetilde{B}\rangle\approx$

$A_{SO}/\sqrt{2}$, which holds well in CaOH [237, 238]. The result is

$$\left|\frac{\langle\widetilde{A}|A_{SO}L_-|\widetilde{B}\rangle\langle\widetilde{B}|V_{11}L_+|\widetilde{A}\rangle}{2\omega_2\Delta E_{AB}}\right|^2 \approx \frac{2g_K A_{SO}^2}{\omega_2^3} \tag{B.20}$$

which may be used to find the mixing probabilities,

$$\begin{aligned}|\langle\widetilde{A}(010)\mu^2\Sigma^{(+)}|\widetilde{A}(000)^2\Pi_{1/2}\rangle|^2 &\approx 1.9\times10^{-4}\\ |\langle\widetilde{A}(010)\kappa^2\Sigma^{(+)}|\widetilde{A}(000)^2\Pi_{1/2}\rangle|^2 &\approx 3\times10^{-5}\end{aligned} \tag{B.21}$$

The sum of these contributions is double the mixing fraction that would be calculated if the vibronic structure of the $\widetilde{A}^2\Pi(01^10)$ manifold were ignored.

Combining these two contributions, we get an effective expression for the total mixing between $\widetilde{A}(000)$ and $\widetilde{A}(010)$:

$$\begin{aligned}|\langle\widetilde{A}(\overline{010})^2\Sigma|\widetilde{A}(000)^2\Pi_{1/2}\rangle|^2 &\approx 2\left|\frac{2\langle\widetilde{A}|H_{SO}|\widetilde{B}\rangle\langle\widetilde{B}|H_{RT}|\widetilde{A}\rangle}{\omega_2\Delta E_{AB}}\right|^2\\ &\approx \frac{4g_K A_{SO}^2}{\omega_2^3} \approx 2.2\times10^{-4}\end{aligned} \tag{B.22}$$

where A_{SO} is the spin-orbit constant in the $\widetilde{A}^2\Pi$ state. The factor of 2 in the numerator of the first line accounts for contributions via the $\widetilde{B}(000)$ and $\widetilde{B}(01^10)$ states, which constructively interfere. An additional, overall factor of 2 arises due to the presence of two distinct vibronic components of the $\widetilde{A}^2\Pi(010)$ vibrational manifold, which approximately doubles the total admixture, as described above.

Total estimated branching to $\widetilde{X}(010)$

Applying the scaling factors of Eq. B.4, for the $N'' = 1$ rotational component of $\widetilde{X}^2\Sigma^+(01^10)$ we arrive at a branching ratio of

$$P_{(000)-(01^10)} \approx \frac{\nu^3}{\mathcal{N}} \times \sum_{\substack{N''=1 \\ J''=1/2,3/2}} \left| \sum_{\zeta'} \langle \widetilde{A}(000)^2\Pi_{1/2}|\zeta'\rangle \langle \zeta'|\widetilde{X}(010)\rangle \langle \mu \rangle^{\zeta'}_{N'',J''} \right|^2 \approx 3.4 \times 10^{-4} \tag{B.23}$$

where the second sum is over the excited vibronic states $\zeta' = \widetilde{A}(\overline{010})\mu$, $\widetilde{A}(\overline{010})\kappa$, and $\widetilde{B}(\overline{010})$ (other states with $\ell \neq 1$ are symmetry-forbidden). Each term is the product of a vibronic mixing amplitude $\langle \widetilde{A}(000)^2\Pi_{1/2}|\zeta'\rangle$, a harmonic FCF $\langle \zeta'|\widetilde{X}(\overline{010})\rangle$, and a rotational factor $\langle \mu \rangle^{\zeta'}_{N'',J''}$. The relative rotational transition intensities are given by the Hönl-London factors, $S^{J'}_{J''}(\zeta', \zeta'') \equiv |\langle \mu \rangle^{\zeta'}_{N'',J''}|^2$, shown in Table B.1. The VBR is less than the sum of the mixing probabilities in Eqs. B.13 and B.22 because only decay to $N'' = 1$ is considered ($N'' = 2$ contributes another $\sim 3 \times 10^{-4}$), and because interference between terms in the summation of Eq. B.23 reduces the total.

Performing similar calculations for the $\widetilde{B}^2\Sigma^+(000)$ state of CaOH, we determine VBRs (dominated by direct RT mixing with the $\widetilde{A}(010)^2\Sigma$ states) of 2.5×10^{-3} to $N'' = 1$ and 3.6×10^{-4} to $N'' = 2$. This agrees very well with the measured (rotationally-unresolved) VBR of 3×10^{-3} from previous dispersed-fluorescence experiments [213]. Because $\sim$4.3% of the total photons scattered in the experimental cycling scheme (chapter 4)

are from $\widetilde{B}(000)$, we therefore calculate an "effective" VBR for $\widetilde{X}(01^10), N'' = 1$ decay of $0.957 \times (3.4 \times 10^{-4}) + 0.043 \times (2.5 \times 10^{-3}) \approx 4.3 \times 10^{-4}$.

B.2.2 $\widetilde{A}^2\Pi_{1/2}\,(000) \rightarrow \widetilde{X}^2\Sigma^+\,(02^20)$ decay

The $|\Delta\ell| = 2$ transition gains transition strength due to mixing of the $\widetilde{\mathrm{A}}^2\Pi_{1/2}\,(000)$ state with the $\widetilde{\mathrm{A}}^2\Pi_{1/2}\,(02^20)$ state by the Renner-Teller Hamiltonian. The quadrupolar term in H_{RT} can couple states according to the selection rules $\Delta\Lambda = \pm 2$, $\Delta\ell = \mp 2$, $\Delta\Sigma = 0$. This term therefore mixes certain components of the $\widetilde{\mathrm{A}}\,^2\Pi(000)$ and $\widetilde{\mathrm{A}}\,^2\Pi(020)$ states at first order. (The dipolar term of H_{RT} also contributes at second order to this mixing [264].) A very similar interaction has previously been observed between $\widetilde{\mathrm{A}}\,^2\Pi(01^10)$ and $\widetilde{\mathrm{A}}\,^2\Pi(03^30)$ in CaOH [93].

The relevant interactions are parametrized by the quantity $\epsilon\omega_2$, where ϵ is the Renner parameter. The Renner parameter is $\epsilon \approx \epsilon^{(1)} + \epsilon^{(2)}$, where the first-order contribution,

$$\epsilon^{(1)} \approx \langle \tilde{A}|V_{22}L_-^2|\tilde{A}\rangle/\omega_2 \tag{B.24}$$

quantifies direct quadrupolar mixing within the $\widetilde{A}$ state. The second-order contribution is

$$\epsilon^{(2)} \approx -\frac{|\langle \widetilde{A}|V_{11}L_-|\widetilde{B}\rangle|^2}{2\omega_2\Delta E_{AB}} \approx -\frac{2g_K\Delta E_{AB}}{\omega_2^2}, \tag{B.25}$$

and arises due to dipolar mixing via the $\widetilde{B}$ state [252, 264].

The matrix element connecting the $\widetilde{A}(000)$ and $\widetilde{A}(02^20)$ states is $\epsilon\omega_2/\sqrt{2}$ [93], and the resulting admixture

is

$$|\langle \widetilde{\mathrm{A}}(\overline{02^20})^2\Pi_{1/2}|\widetilde{\mathrm{A}}(000)^2\Pi_{1/2}\rangle|^2 \approx \frac{(\epsilon\omega_2/\sqrt{2})^2}{(\Delta E_{(020)} - 4g_{22})^2} \approx 1.2\times10^{-3} \tag{B.26}$$

where $\Delta E_{(020)} = E_{(000)} - E_{(020)}$ is the difference between the $\widetilde{A}(000)$ and $\widetilde{A}(02^00)$ origin energies, and $g_{22}\ell^2$ is the energy shift of a state with vibrational angular momentum $\ell \neq 0$.

Applying Eq. B.4, the VBR for decay from $\widetilde{A}(000)^2\Pi_{1/2} \rightarrow \widetilde{X}(02^20)^2\Delta$ is therefore

$$\begin{aligned} P_{(000)-(02^20)} \approx& \frac{\nu^3}{\mathcal{N}}|\langle \widetilde{\mathrm{A}}(\overline{02^20})^2\Pi_{1/2}|\widetilde{\mathrm{A}}(000)^2\Pi_{1/2}\rangle|^2 \\ &\times S^{1/2}_{3/2}(\widetilde{A}(02^20), \widetilde{X}(02^20))q_{(02^20)-(02^20)} \\ \approx& 1.0\times10^{-3} \end{aligned} \tag{B.27}$$

where $q_{(02^20)-(02^20)} \approx 0.95$ is the harmonic FCF defined in Eq. B.3, and all decay is to the $(N'' = 2, J'' = 3/2, -)$ rotational level.

B.3 Fermi resonance

Because the Ca–O stretching frequency is approximately double that of the Ca–O–H bending frequency in CaOH [250], vibrational states differing by $\Delta v_1 = \pm1, \Delta v_2 = \mp2$ come in closely spaced groups, e.g., $(100) \sim (020)$ and $(200) \sim (120) \sim (040)$ (see Fig. 2.2 in chapter 2). States of the same vibronic symmetry within these polyads are mixed by a cubic term in the potential energy surface of the form $V_F = k_{122}Q_1Q_2^2$

[247, 248], where Q_1 and Q_2 are normal coordinates associated with Ca–O stretching and Ca–O–H bending, respectively. This leads to intensity borrowing which can significantly affect the magnitude of vibronic decay channels including $\widetilde{\mathrm{X}}\,^2\Sigma^+(02^00)$ and $\widetilde{\mathrm{X}}\,^2\Sigma^+(12^00)$. This effect is well understood, and is known as the Fermi resonance interaction [247, 248]. This is described in more detail in chapter 2.

The Fermi resonance interaction is quantified by a parameter W, which is proportional to k_{122} and parametrizes the strength of the cubic mixing. It is estimated that $W \approx -10.7\ \mathrm{cm}^{-1}$ in the $\widetilde{\mathrm{X}}\,^2\Sigma^+$ state based on prior measurements in CaOH (see chapter 2 and Ref. [251]). Including this off-diagonal coupling within the $\widetilde{\mathrm{X}}(100) \sim (02^00)$ Fermi dyad leads to the following mixing amplitudes:

$$\begin{aligned} |\widetilde{\mathrm{X}}(100)\rangle &= 0.96|\widetilde{\mathrm{X}}(\overline{100})\rangle + 0.28|\widetilde{\mathrm{X}}(\overline{02^00})\rangle \\ |\widetilde{\mathrm{X}}(02^00)\rangle &= -0.28|\widetilde{\mathrm{X}}(\overline{100})\rangle + 0.96|\widetilde{\mathrm{X}}(\overline{02^00})\rangle. \end{aligned} \tag{B.28}$$

where a bar is used to denote the unperturbed harmonic oscillator basis states. The VBR from $\widetilde{\mathrm{A}}^2\Pi_{1/2}(000) \rightarrow \widetilde{\mathrm{X}}^2\Sigma^+(02^00)$ is then given by

$$\begin{aligned} &P_{(000)-(02^00)} \\ &\quad\approx \left|0.96\langle\widetilde{\mathrm{X}}(\overline{02^00})|\widetilde{\mathrm{A}}(\overline{000})\rangle - 0.28\langle\widetilde{\mathrm{X}}(\overline{100})|\widetilde{\mathrm{A}}(\overline{000})\rangle\right|^2 \\ &\qquad\times \frac{\nu^3(S^{1/2}_{3/2} + S^{1/2}_{1/2})}{\mathcal{N}} \approx 4.6\times 10^{-3}, \end{aligned} \tag{B.29}$$

where each inner product on the right-hand side is a harmonic overlap integral that can be evaluated using the methods of section B.1, and the Hönl-London factors are those for $\ell = 0$ states in Table B.1. A similar expression

applies to the $\widetilde{X}^2\Sigma^+(100)$ branching ratio. The Fermi resonance mixing therefore increases the branching ratio to $\widetilde{X}(02^00)$ by an order of magnitude compared to the purely harmonic result.

Fermi mixing between $\widetilde{X}(200)$ and $\widetilde{X}(12^00)$ also causes significant branching to the $\widetilde{X}\,^2\Sigma^+(12^00)$ state, which we repump for CaOH laser cooling.

B.4 Calculation results

B.4.1 Comparison with depletion-revival results

Table B.2 compares calculated branching ratios with the depletion-revival measurements of chapter 4 and Ref. [251]. The calculations generally exhibit good agreement with measured branching ratios. While branching to the Ca–O stretching modes (000), (100), and (200) is dominated by harmonic wavefunction overlap, decay to the bending modes arises predominantly from other mechanisms. Branching to $\widetilde{X}\,^2\Sigma^+(02^00)$ occurs primarily due to Fermi resonance mixing with the $\widetilde{X}\,^2\Sigma^+(100)$ state, while decay to the $\ell \neq 0$ bending modes (02^20) and (01^10) arises from vibronic perturbations in the $\widetilde{A}$ and $\widetilde{B}$ states, as described in section B.2. The largest remaining disagreement is in decay to the (200) stretching mode, which is likely enhanced due to anharmonic terms in the potential energy surface not included in these calculations [426]. All other values agree within a factor of 2 with their experimental counterparts and may be regarded as useful predictors of the relative significance of vibrational branching pathways.

For most states the $\widetilde{A} \rightarrow \widetilde{X}$ VBR is a good approximation to the observed branching out of the experimental cycling scheme, which employs both $\widetilde{X}\,^2\Sigma^+(000) \rightarrow \widetilde{A}\,^2\Pi_{1/2}(000)$ and $\widetilde{X}\,^2\Sigma^+(100) \rightarrow \widetilde{B}\,^2\Sigma^+(000)$ transitions. One notable exception, however, is the $\widetilde{X}(01^10)$ state, which experiences significant decay from $\widetilde{B}(000)$

with a VBR of $3(1) \times 10^{-3}$ [213]. To account for this, we scale the separately-calculated $\widetilde{\mathrm{A}} \rightarrow \widetilde{\mathrm{X}}$ and $\widetilde{\mathrm{B}} \rightarrow \widetilde{\mathrm{X}}$ VBRs by the relative number of photon scattering events through each excited state [213]. The effective branching ratio out of the experimental cycling scheme is therefore approximately

$$P_{\text{eff}} \approx 0.957 P_{\widetilde{\mathrm{A}} \rightarrow \widetilde{\mathrm{X}}} + 0.043 P_{\widetilde{\mathrm{B}} \rightarrow \widetilde{\mathrm{X}}} \tag{B.30}$$

since on average ∼95.7% (∼4.3%) of the surviving molecular population is excited from $\widetilde{\mathrm{X}}(000)$ ($\widetilde{\mathrm{X}}(100)$) based on the measured branching ratios. This correction is significant only for the $\widetilde{\mathrm{X}}(01^{1}0)$ state, though makes small contributions to the other VBRs included in Table B.2.

B.4.2 VBRs for weaker transitions

The same techniques described above can be used, in principle, to calculate branching ratios down to the 10^{-5} level. Table B.4 shows the result of these calculations (which use formulas very similar to those described above) alongside the dispersed fluorescence measurement results described in chapter 4.

Overall, the agreement of the semiempirical calculations with measured branching ratios is quite good, even up to decay channels at the $\sim 10^{-5}$ level. The primary disagreement between the semi-empirical calculations and the DLIF measurements is in the higher-lying Ca–O stretching modes, (200) and (300). This is because the harmonic approximation used for FCF calculations breaks down for these higher states, with anharmonic contributions significantly increase the branching to these states.

State	DLIF	Calc.
(000)	0.9471	0.955
(100)	0.0463	0.038
(02^00)	2.57×10^{-3}	4.6×10^{-3}
(200)	1.70×10^{-3}	0.4×10^{-3}
$(010)(N=1)$	8.4×10^{-4}	4.0×10^{-4}
(02^20)	6.3×10^{-4}	1.2×10^{-3}
$(010)(N=2)$	3.6×10^{-4}	3.0×10^{-4}
(12^00)	1.9×10^{-4}	1.4×10^{-4}
(300)	6.4×10^{-5}	2×10^{-6}
(110)	8.7×10^{-5}	7×10^{-5}
(12^20)	4.8×10^{-5}	4×10^{-5}

Table B.4: Comparison of measured "effective" branching ratios for the CaOH optical cycling transition with semi-empirical calculations ("calc."). The measured values come from the DLIF results in chapter 4, specifically Table 4.8.

C

Experimental Details

In this section, we describe miscellaneous details of the experimental apparatus that were omitted from the main text of the thesis.

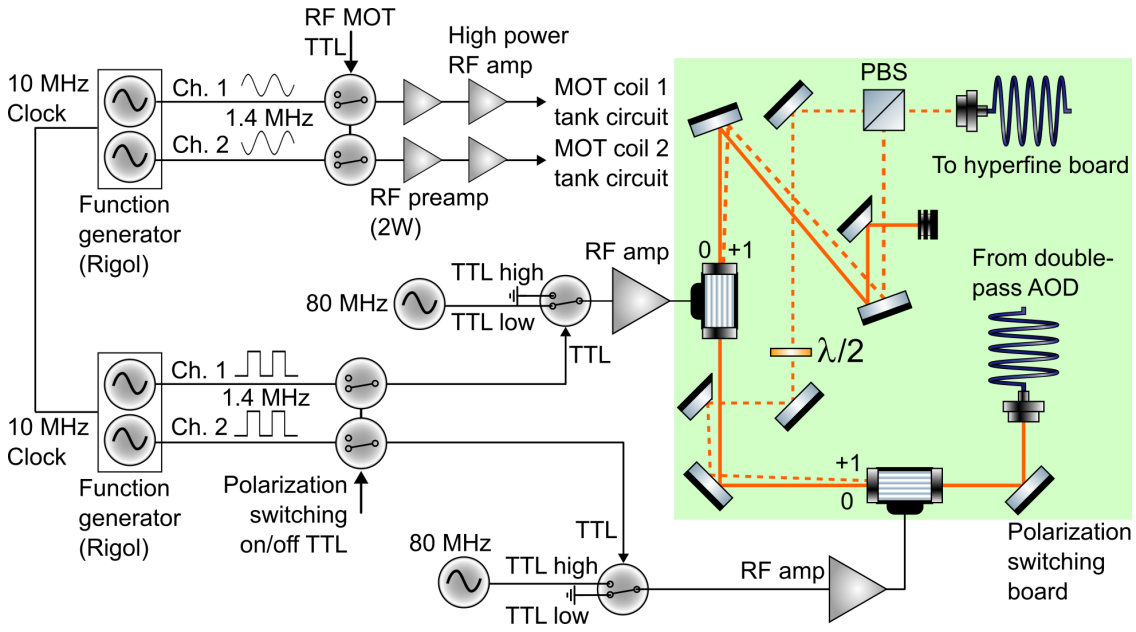

Figure C.1: Setup used for polarization switching of the MOT light, and synchronization with the RF MOT coils.

C.1 Preparation of MOT and cooling light

In this section, we describe (in more detail) the setup used to prepare the MOT light. A schematic overview of the setup is provided in Fig. 5.18 of chapter 5.

As shown in Fig. 5.18, the 626 nm MOT SFG laser is locked to the wavemeter, then frequency shifted by a double-pass AOM, then by switching AOMs on the polarization switching board, and then by AOMs on the sideband board (or "hyperfine board").

C.1.1 Polarization switching

Fig. C.1 shows the setup of the polarization switching board and associated RF electronics. The MOT laser light is fiber coupled from the double-pass AOD to the polarization switching board (green region in the figure), which uses two AOMs that can be switched on and off to choose which of two orthogonal polarizations is fiber coupled out from the board. The two AOMs are switched on and off using TTL signals consisting of 1.4 MHz square waves generated by two channels of a signal generator (Rigol). Alternatively, the square wave signal can be turned off, in which case one of the AOMs will be continuously on and the other continuously off (this configuration is used for sub-Doppler cooling, the conveyor belt MOT, and other configurations where polarization switching is not needed). The signal generator that drives the polarization switching square wave is clocked by another signal generator, which generates the 1.4 MHz RF signal used to drive the RF MOT coils. In this way, the polarization switching and RF MOT magnetic field gradient remain phase locked.

C.1.2 Sideband board

After the polarization switching board, the MOT light is fiber coupled to the sideband board, or hyperfine board, which adds sidebands needed for different cooling configurations (e.g. RF MOT, sub-Doppler cooling, conveyor MOT, imaging, etc.). The sideband board is shown in Fig. C.2.

The sideband board contains three AOMs, which generate multiple frequency components and multiple corresponding beam paths. The polarization of each of these components is set with a $\lambda/2$ waveplate before being coupled into a 4x4 polarization-maintaining fiber splitter (Evanescent Optics), where they are combined before being sent to the MOT chamber. The AOMs are driven with Siglent function generators, and switched on, off,

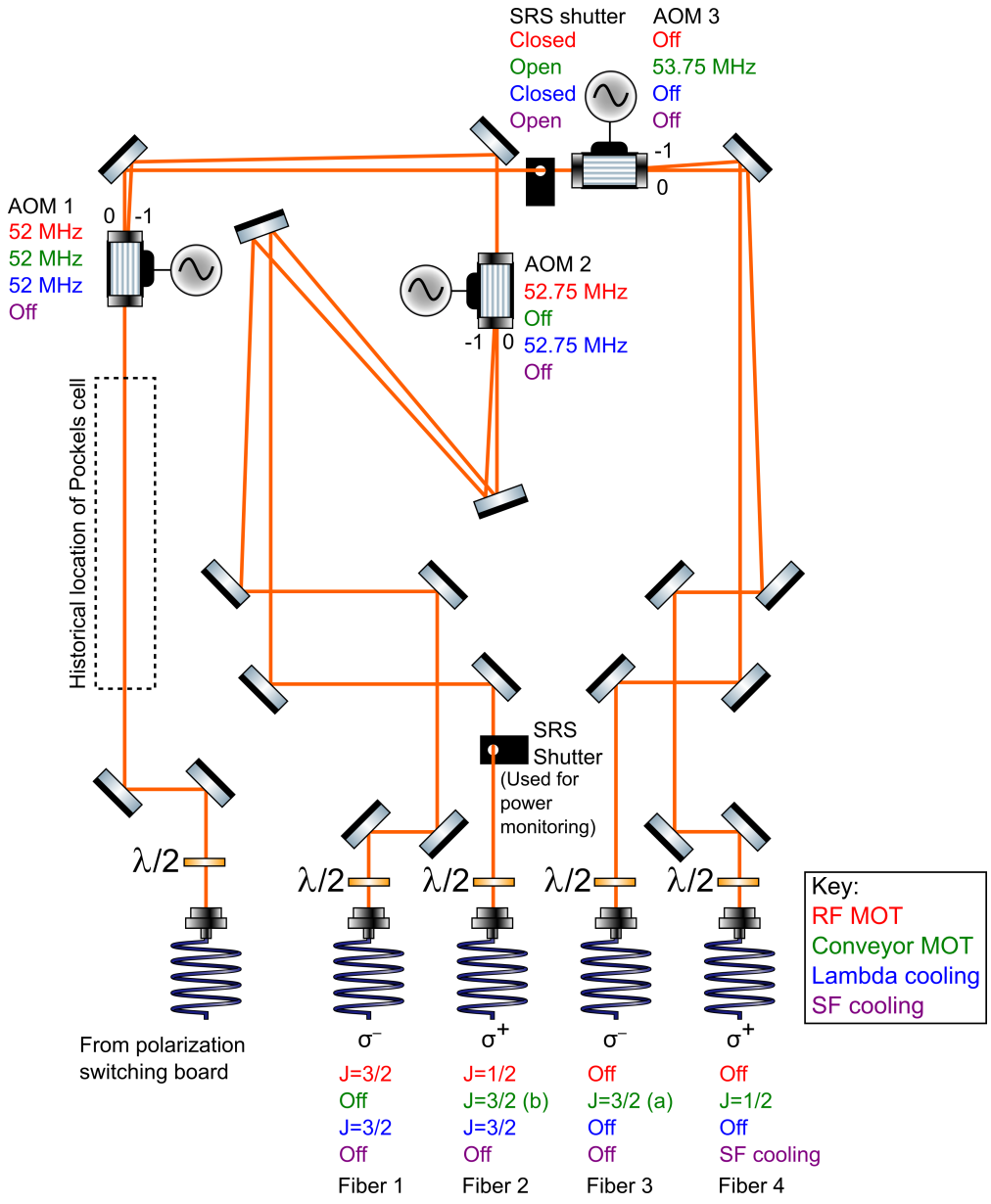

Figure C.2: Diagram of the sideband board, or "hyperfine board." Light enters through a fiber from the polarization switching board, and then is divided into several paths by AOMs, which generate multiple frequency components. These frequencies are coupled into the four input fibers of a 4x4 PM fiber splitter, which combines the frequencies before delivering them to the MOT chamber.

and between different frequencies and RF powers using RF switches controlled by the experimental control software.

There are four primary hyperfine board configurations used for the CaOH experiment (as of this writing), corresponding to RF MOT, blue-detuned conveyor belt MOT, Λ cooling, and single-frequency (SF) cooling. The AOM frequencies (and shutter state) used for each of these configurations are shown in Fig. C.2. The frequency (relative to the incident light) and fractional power in each of the four fibers is:

Configuration	Fiber 1	Fiber 2	Fiber 3	Fiber 4
RF MOT	$J = 3/2$	$J = 1/2$	Off	Off
	-104.75 MHz	-52 MHz	–	–
	$\sim 67\%$	$\sim 33\%$	–	–
Conveyor belt MOT	Off	$J = 3/2$ (b)	$J = 3/2$ (a)	$J = 1/2$
	–	-52 MHz	-53.75 MHz	0 MHz
	–	35%	28%	37%
Λ cooling	$J = 3/2$	$J = 1/2$	Off	Off
	-104.75 MHz	-52 MHz	–	–
	$\sim 33\%$	$\sim 67\%$	–	–
SF Cooling	Off	Off	Off	SF cooling
	–	–	–	0 MHz
	–	–	–	100%

where the fibers are labeled 1-4 from left to right in Fig. C.2.

C.1.3 Cooling laser frequencies

The total frequency shift of the cooling light compared to the SFG lockpoint is the sum of the double-pass AOD frequency shift, the shift from the 80 MHz polarization switching AOMs, and the AOM frequencies added on the sideband board.

The double-pass AOD frequency is set using a voltage controlled oscillator (VCO; ZX95-100-S+). We found that the frequency response is approximately linear between 2-17V control voltage, roughly following the equation $\nu(V) = 45.2 + 3.70 \times V$ MHz. The double-pass AOD imparts twice the frequency shift, so the cooling light frequency scales as roughly 7.4 MHz times the control voltage. However, the experimental control software only outputs -10 to 10 V, so we can't access the full VCO range. Therefore, we add 5.1 V to the Cicero output voltage (this specific value was chosen for historical reasons), and control the VCO with a voltage $V_{\text{VCO}} = V_{\text{Cicero}} + 5.1$ V.

Combining everything, we can work out the detuning of the cooling light from resonance. For example, the RF MOT hold occurs at an AOD control voltage of 4.6 V, implying a VCO frequency of 80.6 MHz.[1] The SFG laser is locked to a frequency of 478.599869 MHz, which is shifted up to 478.600030 MHz after the AOD and to 478.600110 MHz after the polarization switching board. Finally, the two frequency components of the MOT are red-shifted by 52 MHz and 104.75 MHz (see the table above), yielding final frequencies of 478.600058 MHz for the $J = 3/2$ component and 478.600005 MHz for the $J = 1/2$ component. These are detuned by approximately $\Delta \approx -10$ MHz from resonance (per our wavemeter).[2]

C.1.4 Cooling light intensity stabilization

As shown in Fig. 5.18 of chapter 5, the cooling light is intensity stabilized using a photodiode and a PID controller (SRS SIM960), which sets the intensity by controlling the RF power driving the double-pass AOD.[3] One problem with this setup is that we have a separate RF switch that can be used to fully cut the RF power to the AOD, for when we want to shut off the cooling light entirely. When this happens, the PID integrator can saturate, since

[1] This value is taken by interpolating over measured frequencies, and is approximately 0.5 MHz away from the value gotten via the linear fit above.

[2] Note that our wavemeter reads frequencies ~ 500 MHz below their absolute, literature-referenced value.

[3] This is done with a voltage variable attenuator (VVA).

in this condition the output voltage from the PID no longer has any effect on the error signal. Then, when the RF switch is turned back on, there will be a large intensity spike as the PID integrator resets.

To fix this issue, we added a multiplexer (ADG508) acting as a DC switch in the setup. When the MOT AOM is on, the voltages are connected as usual, with a Cicero DAQ channel determining the PID setpoint, the PID measuring the photodiode voltage, and the output signal going to the AOD VVA. However, when the AOD is switched off, the DC switch is used to directly route the PID output voltage back to its measurement input. This way, the PID voltage just stabilizes to the whatever the setpoint is, and the integrator no longer saturates.

C.1.5 Power monitoring

Because of the large number of lasers on the experiment, is important to be able to monitor the powers of every laser on the experiment table in an automated way. (Manually measuring the power of each slowing laser daily would be a prohibitively tedious task.) To do this, we run a monitoring sequence at the start of every experimental run. The experimental control software turns on each slowing laser in succession for 2 ms, with the powers being monitored using a pickoff and photodiode in the slowing laser path, after the white-light EOMs. The photodiode voltage is read into Labview, with a simple script extracting the power of each slowing laser based on the photodiode voltage at the time when it was turned on. The Cicero sequence is shown in Fig. C.3, along with an example photodiode signal.

During the slowing power monitor sequence, we use an analogous procedure to monitor the MOT/cooling light powers. While the total power of the MOT light is intensity stabilized and always monitored on an oscilloscope near the experiment, the relative powers in each frequency component are not stabilized. Therefore, in the monitoring sequence at the start of each experimental repetition, we run a sequence that checks the relative pow-

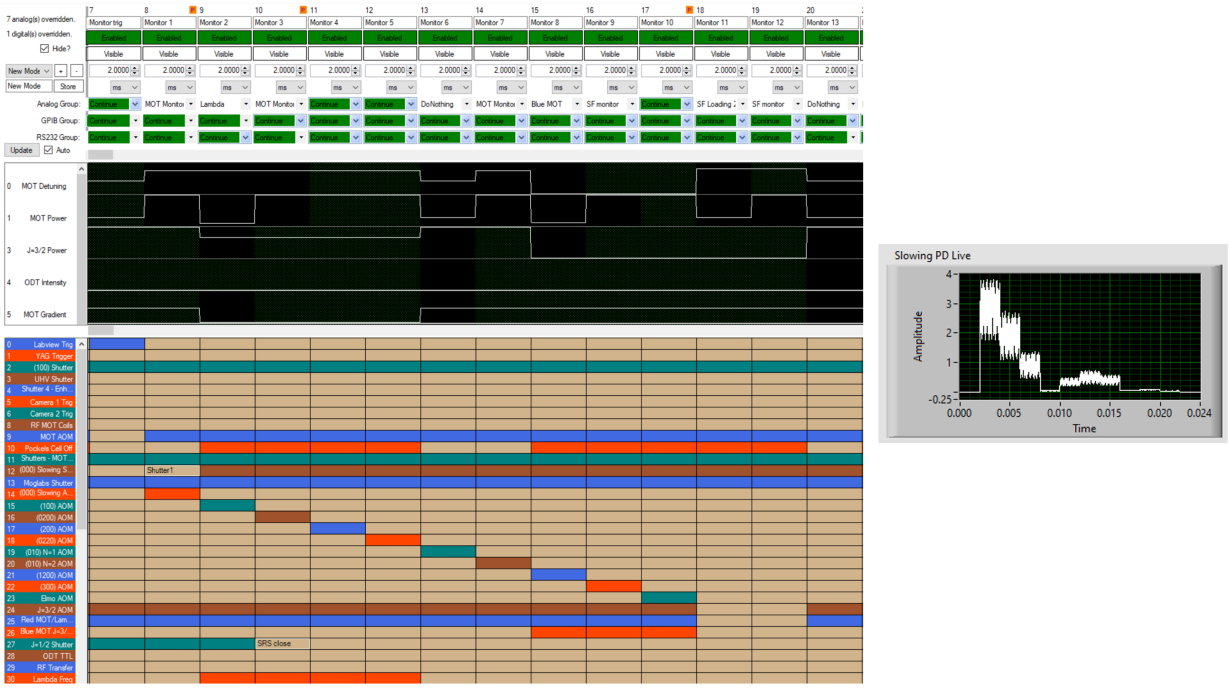

Figure C.3: Left: Cicero sequence used for slowing and cooling power monitoring. Right: sample photodiode trace for the slowing laser monitoring.

ers of the $J = 3/2$ and $J = 1/2$ components for the MOT and Λ cooling configurations, and also checks the power during SF cooling. Another word overrides the PID and checks the maximum power, which gives a sense of how much power overhead we have before the PID will fail to stabilize the intensity. Part of this sequence can also be seen in Fig. C.3. It happens at the same time as the slowing power monitor sequence, and is carried out using both digital and analog channels.

Note that while the SRS shutter before Fiber 2 on the hyperfine board (Fig. C.2) is not needed for any of the cooling configurations, it *is* important for the power monitoring, since it can be used to block the $J = 1/2$ component so as to check the $J = 3/2 : J = 1/2$ power ratio for RF MOT and Λ cooling.

Note that many other powers are also monitored on oscilloscopes near the control desk. This includes the ODT power, tweezer power, RF MOT coil current and MOT light polarization, microwave pulse powers, RF drive power applied to the MOT coils, applied DC magnetic field, applied DC electric field, etc. The goal is to have as few unmonitored experimental parameters as possible so as to maximize reliability and/or minimize the debugging time required if something does go wrong.

C.2 Experimental control

Experimental control is done using Cicero Word Generator, which has a (relatively) intuitive sequence-based GUI and was developed at MIT for cold atom experiments. We use a modified version of Cicero that reduces buffer generation time [278]. This is important since the software was originally designed for BEC experiments with long $>$ 10 s cycle times, but here we run at a $\sim$ 0.5 $-$ 1 Hz repetition rate, at which point $\sim$1 second buffer generation times become a limitation. Cicero directly controls a number of National Instruments DAQ cards

to generate digital and analog signals (as of this writing we have enough cards for up to 96 digital channels and 48 analog channels). We also use it to communicate with USB and RS232 devices, and with the camera image acquisition software, using virtual COM ports as described in Ref. [274].

The analog and digital cards are clocked at 500 kHz, meaning that we have 2 μs time resolution. For microwave and RF π pulses that cannot be an integer multiple of 2 μs, we use Cicero to trigger a function generator that outputs an arbitrary-length pulse. We also use external function generators for certain critical tasks. For instance, to avoid accidentally switching the DC and RF MOT power supplies onto the MOT coils simultaneously, when switching to the DC MOT we use Cicero to trigger a function generator, which switches to the DC MOT supply and then back to the RF MOT tank circuit a fixed amount of time later. This prevents user error in sequence programming from potentially damaging the experiment.

The experiment is triggered by an external source that runs at a constant repetition rate (this can be varied depending on the sequence) and is synchronized to the mains for 60 Hz phase stability. A flip-flop chip is used to delay the trigger (as seen by the National Instruments hardware), so that it is aligned with a rising edge of the clock signal. This prevents shot-to-shot timing jitter between the analog and digital cards.

Data acquisition is done using Python software (with a PyQT GUI) written by Yicheng Bao [274]. This reads out images from the Andor EMCCDs on the experiment and saves them along with scan variables output from Cicero. The readout speed is significantly faster than from previous software written in MATLAB, which is important for experiments where we wish to take two images in relatively quick succession (10s of ms apart).

C.3 Stability of the 1K system

At the lowest temperatures and for normal running conditions (with heat loads from ablation, the hot fill line, slowing lasers, etc.), the closed-loop helium system is susceptible to a thermal runaway effect that can impede continuous running. As the heat load on the buffer gas cell and helium pot increases, helium boils off at a faster rate, thereby increasing the rate at which the helium must be recooled on the 40 K stage before returning to the pot. This causes the temperature of the 40 K stage to increase. If the system does not equilibrate below a certain critical temperature, a runaway effect occurs at which point both the 40 K temperature and the output pressure at the scroll pump increase without ever stabilizing. At this point, the experiment must be paused and the helium flow rate dramatically reduced to return the system to a stable condition. This problem has become worse over time, which is likely from increased heat loads on the cell during later experiments, or possibly from aging of the scroll pump or the pulse tube.

This effect can be mitigated to a degree by adjusting the needle valve (which trades off between the helium flow rate into the chamber and the amount of expansion cooling achieved at the pot). However, we typically find that the most reliable way to stabilize the system is to partially close a valve in the pumping line between the helium pot and the low-pressure side of the scroll pump, thereby reducing the conductance of the line. This trades off base temperature for cooling power, increasing the temperature of the pot and cell but reducing the helium boiloff rate and therefore stabilizing the system. We find that increasing the cell temperature to $\sim$2.5 K (compared to a lowest possible temperature around 2 K) stabilizes the system without significantly reducing the number of CaOH molecules trapped in the MOT.

We also find that this behavior depends on whether or not the liquid nitrogen cold trap is installed in the sys-

tem. Some circumstantial evidence indicates that the higher impedance of the cold trap between the high pressure side of the pump and the input to the cold head is actually beneficial for stability, at least under certain conditions.

D

Rate Equation Modeling of CaOH Internal State Dynamics

In this appendix, we describe a modified version of the vibrational state lifetime rate equation model from chapter 6 that applies to the CaOH experiment. We also describe the procedure we used to determine the lifetime of low-lying vibrational states in CaOH. Finally, we describe modified rate equations used for modeling trapped

molecular population in dark states during CaOH collision measurements. The majority of this appendix is reproduced, with modifications, from Refs. [44] and [342].

D.1 Rate equation model of the vibrational lifetime measurement sequence

To apply the rate equations of sec. 6.4.2 to our measurement of the CaOH lifetime, we need to make a few modifications and additions to more closely model the specific experimental protocol used for the vibrational lifetime measurement (sec. 6.4.3). First, we modify the rate equations to account not just for the rotational state N but also the total angular momentum state J. This is because our detection method is sensitive to specific J states in certain manifolds, so we cannot treat it as an unresolved degree of freedom. We also add a vacuum lifetime τ_{vac} to the model.

Another important modification is to account for the initial state of the molecules when propagating the rate equations. While we would like to prepare all molecules in, say $\widetilde{X}(010)(N = 1)$ and measure their lifetime, in reality we need to first load the ODT and hold the molecules there for a finite time before and during state preparation. During this time, BBR dynamics are already occurring, and so we model these effects, taking into account the full experimental sequence as well as possible.

D.1.1 Rate equations

The internal state dynamics of CaOH molecules in the experiment are described by the rate equations in eqn. 6.33, plus a term accounting for vacuum loss:

$$\frac{dn_i}{dt} = -\sum_j R_{ij} n_i - \sum_{j<i} A_{ij} n_i + \sum_j R_{ji} n_j + \sum_{j>i} A_{ji} n_j - \frac{n_i}{\tau_{\text{vac}}}, \tag{D.1}$$

where τ_{vac} is the (state-independent) vacuum lifetime. In the experiment, the in-vacuum coils used to form the MOT are cooled to $\sim$0°C to minimize outgassing and improve the vacuum pressure. The solid angle of the coils is $0.57 \times 4\pi$ sr, so the blackbody rates R_{ij} (eqn. 6.27) include two terms such that 57% of the blackbody radiation seen by the molecules is at 273 K while the remaining 43% is at room temperature (295 K). To preserve normalization of the population vector when integrating the rate equations, a "lost" population is also included according to

$$\frac{dn_{\text{loss}}}{dt} = \sum_i \frac{n_i}{\tau_{\text{vac}}}. \tag{D.2}$$

Other sources of loss discussed in Sec. 6.4.2 are expected to be negligible in this system.

While hyperfine structure is spectroscopically unresolved in the experiment and can therefore be omitted from the model, the photon-cycling detection does distinguish between the spin-rotation (J) sublevels in certain rotational manifolds. We therefore use a basis of rovibronic states described by the quantum numbers $|v_1, v_2, \ell, N, J, p\rangle$, where v_1 and v_2 are the vibrational quantum numbers of the Ca–O stretch and Ca–O–H bending modes, ℓ is the magnitude of the vibrational angular momentum projected onto the molecular axis, N is the rotational quantum number, J is the total electronic angular momentum, and p is the parity. We neglect the O–H stretching

mode because its frequency is far from the peak of the blackbody spectrum at room temperature. All states with $\ell = 0$ have Σ^+ symmetry and their parity is $p = (-1)^N$. For states with $\ell \neq 0$, each rotational manifold has two opposite parity levels, $|\ell, N, \pm\rangle = 2^{-1/2}\left\{|\ell, N\rangle \pm (-1)^{N-\ell}|-\ell, N\rangle\right\}$. Because J is included in the basis, the Hönl-London factors in eqn. 6.29 are modified to read:

$$\begin{aligned} S_{ij}^{\text{rot}} &= \delta_{p_i,-p_j}(1 + \delta_{\ell_i 0} + \delta_{\ell_j 0} - 2\delta_{\ell_i 0}\delta_{\ell_j 0}) \\ &\times (2N_i + 1)(2N_j + 1) \begin{pmatrix} N_i & 1 & N_j \\ -\ell_i & \ell_i - \ell_j & \ell_j \end{pmatrix}^2 \\ &\times (2J_i + 1)(2J_j + 1) \begin{Bmatrix} N_j & J_j & S \\ J_i & N_i & 1 \end{Bmatrix}^2 , \end{aligned} \tag{D.3}$$

The rate equations are solved by numerically integrating eqns. D.1-D.2 (sometimes with additional terms described below) applied to a population vector including all states with $v_1 \leq 2$, $v_2 \leq 2$, $N \leq 5$. The populations of the highest states included in each rotational and vibrational ladder are typically <5% over the experimental timescale ($t \lesssim 5$ s), implying that inclusion of higher-energy states is unnecessary.

Note that for the CaOH modeling we employ the double-harmonic approximation described in sec. 6.4.2, and omit anharmonic terms in the potential. This limits the number of required fit parameters and makes the fitting process tractable. Because the majority of the dynamics considered in this work occur in vibrational levels near the bottom of the molecular potential, the harmonic approximation is expected to be reasonably appropriate. Nonetheless, the fitted values of $|d\vec{\mu}_e/dQ_i|$ should be interpreted as "effective" parameters that include the contribution of anharmonic effects on the measured (000), (010), and (100) lifetimes. These contributions are

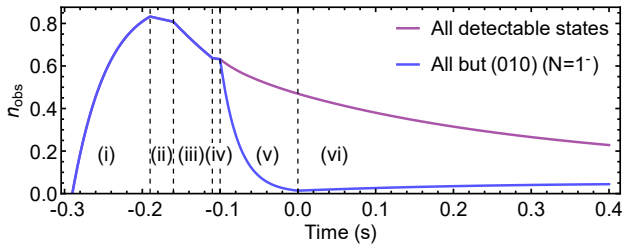

Figure D.1: Population in detectable states (purple curve) and detectable states except $\widetilde{X}(010)(N = 1^-)$ (blue curve) calculated from the best-fit rate equation for the $\widetilde{X}(010)$ lifetime sequence. The steps in the sequence are (i) ODT loading (ii) hold (iii) first image (iv) hold (v) optical pumping into $\widetilde{X}(010)$ and (vi) lifetime hold. $t = 0$ here is the same as in Fig. 6.11. Reproduced from Ref. [44].

expected to be relatively small: *ab initio* calculations indicate that anharmonicity in the molecular potential is expected to have a ∼10-20% effect on the vibrational lifetimes [44].

D.1.2 Modeling the experimental sequence

To accurately determine the lifetimes of the $\widetilde{X}(000)$, (01^10), and (100) states of CaOH, we use rate equations to model the full experimental sequence used to perform the lifetime measurements. This approach accounts for blackbody dynamics that occur prior to the lifetime measurement hold time, ensuring accurate initial conditions. It is found that significant population accumulates in dark vibrational levels during the ODT loading, imaging, and optical pumping steps, justifying their inclusion in the model.

The sequence is modeled as follows, and is chosen to exactly match the experimental protocol unless otherwise specified. As an example, Fig. D.1 shows the detectable population throughout the $\widetilde{X}(01^10)$ lifetime measurement sequence, illustrating the key steps in the experimental protocol and the corresponding rate equation model. The simulation is initialized with all molecules in the untrapped state, $n_{\text{loss}}(t = 0) = 1$. This population is pumped into the trapped state $\widetilde{X}^2\Sigma^+(000)(N = 1, J = 3/2)$ with a characteristic rate of

$R_{\text{load}} = 1/(48.5\text{ ms})$, fit from the experimental data (Fig. 2 of Ref. [43]). This optical pumping step, as well as the trap imaging described later, is performed with optical cycling light in a single-frequency (SF) cooling configuration, which simultaneously cools the molecules inside the optical trap [43]. It is assumed that population accumulates entirely in the $\widetilde{X}^2\Sigma^+(000)(N = 1, J = 3/2)$ level during SF cooling since this is the furthest-detuned ground-state level. Additionally, coherent dark states are formed within the $J = 3/2$ manifold during SF cooling [232]. Therefore, whenever SF cooling light is on, an additional term is added to the rate equations which pumps population from $\widetilde{X}^2\Sigma^+(000)(N = 1, J = 1/2)$ to $\widetilde{X}^2\Sigma^+(000)(N = 1, J = 3/2)$ at a rate corresponding to the SF scattering rate of $R_{\text{sc}} = 45 \times 10^3\text{ s}^{-1}$ [43, 262].

As soon as the molecules are trapped, their internal states begin evolving according to eqns. D.1-D.2. Prior to ODT loading, these dynamics are suppressed because any molecule which is blackbody-excited out of the cycling scheme will not be cooled/loaded into the ODT (this is enforced in the rate equations because the population n_{loss} is not subject to blackbody terms). After the ODT loading time of 100 ms, the loading is turned off and the remaining molecules evolve through each step in the experimental sequence. First, the molecules are held in the ODT and propagate according to eqns. D.1-D.2 for 30 ms. Next, the molecules undergo 50 ms of "normalization" SF imaging, used to determine the number of molecules loaded into the trap. In addition to the dynamics in eqns. D.1-D.2, during this time molecules in detectable states are pumped into dark vibrational levels n_{loss} (which are high-lying and therefore neglected for the remainder of the simulation) at a rate corresponding to a branching ratio of $v_{\text{dark}} = 8.5 \times 10^{-5}$ and a scattering rate of $R_{\text{sc}} = 45 \times 10^3\text{ s}^{-1}$ [42, 43]. Additionally, molecules in repumped vibrational levels are pumped back into $\widetilde{X}^2\Sigma^+(000)(N = 1)$ during the imaging at a rate of 10^3 s^{-1}, and molecules in $\widetilde{X}^2\Sigma^+(000)(N = 1, J = 1/2)$ are pumped into $\widetilde{X}^2\Sigma^+(000)(N = 1, J = 3/2)$ as described above.

After the normalization image, the rate equation propagation proceeds differently for the $\widetilde{X}(000)$, $\widetilde{X}(010)$, and $\widetilde{X}(100)$ states. For the $\widetilde{X}(000)$ data, the populations propagate according to eqns. D.1-D.2 for a variable time. For comparison to the experimental data in Fig. 6.11, $t = 0$ occurs immediately after the imaging light is turned off. The detectable population, $n_{\text{obs}}(t) = \sum_{i\in\{\text{det}\}} n_i(t)$, for the best fit parameters (see below) is plotted as a solid curve in Fig. 6.11(a). Note that here we make the approximation that the molecules are detected instantaneously, whereas in the experiment the final image is collected over 50 ms. We have run the model including finite imaging time and confirmed that this approximation does not change the results.

For the $\widetilde{X}(010)$ and $\widetilde{X}(100)$ lifetimes the molecules propagate according to eqns. D.1-D.2 for a short time (10 ms for (010) and 90 ms for (100)) following the normalization image. This is followed by optical pumping into the desired vibrational state, which is modeled by adding a term that pumps population in detectable states into the excited vibrational level at a rate $R_{\text{pump},i} = R_{\text{sc}} v_i S_i$, where $R_{\text{sc}} = 45 \times 10^3\ \text{s}^{-1}$ is the SF scattering rate, $v_{(010)} = 8.2 \times 10^{-4}$ is the vibrational branching ratio (VBR) to $\widetilde{X}(010)(N = 1^-)$, and $v_{(100)} = 4.75 \times 10^{-2}$ is the VBR to $\widetilde{X}(100)(N = 1)$ [43]. The rotational branching factors for $\widetilde{X}(010)$ are $S_{1/2} = 0.73$ and $S_{3/2} = 0.27$ to $J = 1/2$ and $J = 3/2$, respectively, and for $\widetilde{X}(100)$ they are $S_{1/2} = 2/3$ and $S_{3/2} = 1/3$ [251]. Loss to dark vibrational states at a rate $R_{\text{dark}} = R_{\text{scatt}} v_{\text{dark}}$, where $v_{\text{dark}} = 8.5 \times 10^{-5}$, is also included. The $\widetilde{X}(010)$ pumping is turned on for 100 ms, and the $\widetilde{X}(100)$ pumping for 2 ms.

After optical pumping, the populations propagate according to eqns. D.1-D.2 for a variable time. In Fig. 6.11, $t = 0$ is defined as immediately after the optical pumping/state transfer light is turned off. The observable population, as well as the detectable population in all states besides $\widetilde{X}(010)(N = 1^-)$, is plotted in Fig. D.1 for the full $\widetilde{X}(010)$ lifetime sequence.

D.2 Vibrational lifetime fitting and results

We fit the model results to the experimental data as follows. The rate equations for the $\widetilde{X}(000)$, $\widetilde{X}(010)$, and $\widetilde{X}(100)$ measurement sequences are first propagated for given values of the vacuum lifetime, τ_{vac}, and the dipole derivatives $|d\vec{\mu}_e/dQ_1|$ (symmetric stretch) and $|d\vec{\mu}_e/dQ_2|$ (bend). We then calculate the observable population, $n_{\text{obs}}(t) = \sum_{i\in\{\text{det}\}} n_i(t)$, where $\{\text{det}\}$ is the subset of states which are detectable, i.e., the $(N = 1, J = 1/2^-)$, $(N = 1, J = 3/2^-)$, and $(N = 2, J = 3/2^-)$ levels of repumped vibrational states (Tab. D.1). Finally, the results are scaled by constant prefactors $a_{\{v\}_i}$, and a constant offset $a_{\text{off},\{v\}_i}$ (present due to imperfections in the imaging background subtraction, or imperfect state preparation) is added to each of the three traces. The resulting fit functions depend on a total of 9 fit parameters:

$$f_{(000)}(t) = a_{(000)} n_{\text{obs},(000)} \left(t, \left|\frac{d\vec{\mu}_e}{dQ_1}\right|, \left|\frac{d\vec{\mu}_e}{dQ_2}\right|, \tau_{\text{vac}}\right) + a_{\text{off},(000)}, \tag{D.4}$$

$$f_{(010)}(t) = a_{(010)} n_{\text{obs},(010)} \left(t, \left|\frac{d\vec{\mu}_e}{dQ_1}\right|, \left|\frac{d\vec{\mu}_e}{dQ_2}\right|, \tau_{\text{vac}}\right) + a_{\text{off},(010)}, \tag{D.5}$$

$$f_{(100)}(t) = a_{(100)} n_{\text{obs},(100)} \left(t, \left|\frac{d\vec{\mu}_e}{dQ_1}\right|, \left|\frac{d\vec{\mu}_e}{dQ_2}\right|, \tau_{\text{vac}}\right) + a_{\text{off},(100)}. \tag{D.6}$$

These functions are plotted as solid curves in Fig. 6.11 for the best fit parameters determined below.

To perform the fit, the fit parameters are scanned on a discrete 9-dimensional grid and the fit functions are calculated at each point. Step sizes of 0.025 D for the dipole derivatives, 0.5 s for the vacuum lifetime, 0.05 for the

$(v_1 v_2^\ell v_3)$	N	J		$(v_1 v_2^\ell v_3)$	N	J
(000)	1	$1/2, 3/2$		$(02^0 0)$	1	$1/2, 3/2$
(100)	1	$1/2, 3/2$		$(02^2 0)$	2	$3/2$
(200)	1	$1/2, 3/2$		$(11^1 0)$	1	$1/2, 3/2$
(300)	1	$1/2, 3/2$		$(11^1 0)$	2	$3/2$
$(01^1 0)$	1	$1/2, 3/2$		$(12^0 0)$	1	$1/2, 3/2$
$(01^1 0)$	2	$3/2$		$(12^2 0)$	2	$3/2$

Table D.1: Rovibrational states detected while imaging the trap after the lifetime measurements. In all cases only negative parity ($p = -1$) states are detected. Reproduced from Ref. [44].

amplitudes, and 0.02 for the offset are used. The sum of squared errors,

$$S = \sum_i \left[f^{\text{exp}}_{(000)}(t_i) - f_{(000)}(t_i) \right]^2 + \sum_i \left[f^{\text{exp}}_{(010)}(t_i) - f_{(010)}(t_i) \right]^2 + \sum_i \left[f^{\text{exp}}_{(100)}(t_i) - f_{(100)}(t_i) \right]^2, \tag{D.7}$$

where $f^{\text{exp}}_{\{v\}}(t_i)$ is the experimentally measured survival at time t_i and i sums over the experimental data points, is then calculated for each point on the 9-dimensional grid. The optimal fit parameters are determined by fitting the 10,000 lowest S values (approximately 1% of the full grid) to a second-order polynomial. The fit is constrained to this subset of points in order to minimize the effect of higher-order curvature of the error surface. The parameter errors determined from this fit are negligible compared to error sources described below.

The primary source of uncertainty in the fitted lifetimes is due to correlations between parameters, for example between the bending mode lifetime and fit amplitude, $|d\vec{\mu}_e/dQ_2|$ and $a_{(010)}$. These correlations have the potential to make the fit results overly sensitive to the precise values of the individual data points. Additionally, the $\widetilde{X}(010)$ radiative decay occurs on a similar timescale to blackbody excitation and vacuum loss, making it difficult to isolate. To account for these factors and adequately estimate the parameter errors, we repeat the fitting

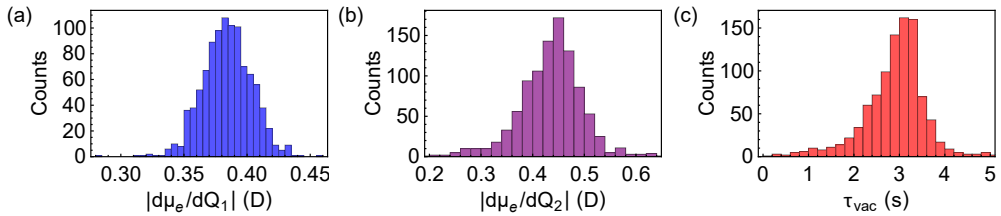

Figure D.2: Histograms of the parameters (a) $|d\vec{\mu}_e/dQ_1|$, (b) $|d\vec{\mu}_e/dQ_2|$, and (c) τ_{vac} generated by fitting the rate equation model to ∼1000 synthetic data sets accounting for experimental error bars, as described in the text. Reproduced from Ref. [44].

Parameter	Median	68% Conf. Int.
$\lvert d\vec{\mu}_e/dQ_1\rvert$	0.384 D	(0.365, 0.404) D
$\lvert d\vec{\mu}_e/dQ_2\rvert$	0.440 D	(0.380, 0.486) D
τ_{vac}	2.99 s	(2.33, 3.43) s
$a_{(000)}$	1.36	(1.29, 1.43)
$a_{(010)}$	1.31	(1.18, 1.40)
$a_{(100)}$	1.18	(1.11, 1.24)
$a_{\text{off},(000)}$	-0.015	(-0.044, 0.018)
$a_{\text{off},(010)}$	0.045	(0.032, 0.061)
$a_{\text{off},(100)}$	0.063	(0.049, 0.076)

Table D.2: Fit parameters and 68% confidence intervals for the rate equation fit. Reproduced from Ref. [44].

procedure ∼1000 times, each time fitting to a "synthetic" data set produced by sampling the value of each point, $f^{\text{exp}}_{\{v\}}(t_i)$, from a normal distribution corresponding to the mean and standard deviation of the measured data point (i.e., of the data plotted in Fig. 6.11). This is meant to approximate the variation in the fit parameters expected if the experiment were to be repeated 1000 times. Histograms of the resulting fit parameters are shown in Fig. D.2. The parameters and error bars are determined by taking the median of the histogram as the center value and the middle 68% of the distribution as the 1σ confidence interval. Results for each of the fit parameters are shown in Tab. D.2.

The state lifetimes are calculated from the fitted parameters and eqns. 6.26-6.27 by summing over all allowed

State	τ_{spont}	τ_{bbr}	τ_{tot}
$\widetilde{X}(000)$	–	$1.3^{+0.3}_{-0.2}$	$0.90^{+0.20}_{-0.16}$
$\widetilde{X}(010)$	$0.72^{+0.25}_{-0.13}$	$0.95^{+0.26}_{-0.16}$	$0.36^{+0.11}_{-0.07}$
$\widetilde{X}(100)$	$0.19^{+0.03}_{-0.03}$	$0.81^{+0.09}_{-0.08}$	$0.14^{+0.02}_{-0.02}$

Table D.3: State lifetimes and 68% confidence intervals determined from the rate equation fit. The vacuum lifetime is constant for all states and fits to $\tau_{\text{vac}} = 3.0^{+0.4}_{-0.7}$ s.

transitions, i.e.,

$$\tau_{\text{spont},i} = \left(\sum_{j<i} A_{ij} \right)^{-1}, \tag{D.8}$$

$$\tau_{\text{bbr},i} = \left(\sum_{j} R_{ij} \right)^{-1}, \tag{D.9}$$

$$\tau_{\text{tot},i} = \left(\frac{1}{\tau_{\text{spont},i}} + \frac{1}{\tau_{\text{bbr},i}} + \frac{1}{\tau_{\text{vac}}} \right)^{-1}. \tag{D.10}$$

The results for CaOH are given in Tab. D.3 and agree well with *ab initio* calculations described in Sec. 6.4.3 and Ref. [44].

The amplitudes $a_{(000)}$, $a_{(010)}$, and $a_{(100)}$ can be understood as scale factors between the calculated populations, which are normalized to 1, and the measured populations, which are normalized to the number of molecules detected in the first image. From the fitted model, the detectable population at the start of the first image is $n_{\text{obs}}(t = t_{\text{img}}) = 0.81$, so the model results need to be scaled by $1/0.81 = 1.24$ to match the experimental data. The fitted amplitudes in Tab. D.2 are in good agreement with this expectation.

D.3 Rate equations including collisions

For the CaOH collision experiment described in chapter 9, we used rate equation modeling to estimate the number of trapped molecules in dark vibrational states during the collision lifetime measurements. We used the model described above with a few additions: (1) loss of molecules to vibrational dark states during optical cycling, and (2) lossy two-body collisions between trapped molecules.[1]

To model optical cycling losses, molecules are transferred to the $\widetilde{X}(22^{0}0)(N = 1, J = 3/2)$ state with a probability $P_{\text{loss}} \approx 7 \times 10^{-5}$ per scattered photon during ODT loading and imaging.[2] Light-assisted collisions during loading and imaging are also included, with a measured rate constant $k_{\text{SF}} \approx 2 \times 10^{-10}$ cm^3 s^{-1} for SF cooling of molecules in bright states.

To model two-body collisions, we need to account for collisions between molecules in all pairs of states, as described in the following sections.

[1] Also note that we don't cool the MOT coils like we did for the lifetime measurements, so the environment temperature is ∼300 K everywhere.

[2] Optical cycling losses in CaOH are likely dominated by decay to the (220), (040), and $(030)(N = 2)$ states [42, 269]. However, here we approximate all losses as ending up in $\widetilde{X}(220)$ since it is the only one of these states included in the model. The key point is that the losses are to a relatively high-lying state in the vibrational potential, which can quickly (over ∼100 ms) decay down to a number of lower-lying states (some of which may even be detectable).

D.3.1 Rate equations for two-body collisions

Molecules in a single state

The rate equation describing the time evolution of the molecule density, $n(t)$, in the presence of two-body collisions with a collisional loss rate constant k is

$$\dot{n}(t) = -kn(t)^2 \tag{D.11}$$

We now wish to express this instead in terms of the molecule number, $N(t)$.

In the ODT, the density as a function of position is $n(t, x, y, z) = n_0(t) \exp[-U(x, y, z)/k_B T(t)]$, where $U(x, y, z)$ is the trap potential energy, $n_0(t)$ is the peak density, and $T(t)$ is the molecule temperature (which may depend on time). For a harmonic trap, this becomes

$$n(t, x, y, z) = N(t) \frac{\omega_x \omega_y \omega_z}{[2\pi k_B T(t)]^{3/2}} \exp\left(\frac{-m(\omega_x^2 x^2 + \omega_y^2 y^2 + \omega_z^2 z^2)}{2k_B T(t)}\right) \tag{D.12}$$

where ω_i is the trap frequency along axis i and m is the mass.

To rewrite eqn. D.11 in terms of the molecule number, we plug in eqn. D.12 and integrate over all space. The result is

$$\dot{N}(t) = -\frac{k}{V_{\text{eff}}(T)} N(t)^2 \tag{D.13}$$

where $V_{\text{eff}}(T) = (4\pi k_B T/m)^{3/2} (\omega_x \omega_y \omega_z)^{-1}$ is the effective trap volume.

Now, the temperature will also change over time, since molecules will be preferentially lost from the bottom

of the trap where they have the least energy (since the density is highest there), leading to heating. This can be derived by calculating the rate of the change of the total molecule energy, $\dot{E}(t) = \int E(x,y,z)\dot{n}(t,x,y,z)dxdydz$, where $E(x,y,z) = U(x,y,z) + \frac{3}{2}k_B T$. This can then be converted to a rate of change in the temperature using $T = E/3k_B N$. The result is

$$\dot{T}(t) = \frac{k}{4}\frac{1}{V_{\text{eff}}(T)}N(t)T(t) \tag{D.14}$$

Note that this assumes the molecules' energy distribution remains thermal, i.e. that there are a sufficiently high elastic rate constant that the remaining molecules rethermalize after a lossy collision occurs.

Eqns. D.13 and D.14 form a set of coupled rate equations that can be used to solve for $N(t)$.

Multiple internal states

These equations are generalized to the case of many internal states i as follows. The equation for the molecule density $n_i(t)$ is

$$\dot{n}_i(t) = -\sum_j k_{ij} n_j(t) n_i(t) \tag{D.15}$$

where k_{ij} is the collisional loss rate constant for collisions between a molecule in state i and one in state j. The sum is over all states, including the initial state i.

Converting to an equation for the molecule number gives

$$\dot{N}_(t) = -\sum_j \frac{k_{ij}}{V_{\text{eff}}(T)} N_j(t) N_i(t) \tag{D.16}$$

For the temperature, we assume that all molecules maintain the same temperature (via elastic collisions), with

the change in energy due to a lossy collision being absorbed by all molecules. It turns out that this ends up meaning that we average over collisions between all pairs of molecules:

$$\dot{T}(t) = \frac{1}{4}\sum_{ij}\frac{k_{ij}N_i(t)N_j(t)}{N(t)V_{\text{eff}}(T)}T(t) \tag{D.17}$$

These equations can be used in combination with the single-body rate equations (eqn. D.1) to model the full system in the presence of collisions. However, we need to know the value of the loss rates k_{ij}.

D.3.2 Estimating two-body collision rate constants

To model two-body collisions, we use a matrix of loss rate constants k_{ij} that describes collisions between all pairs of rovibrational states i and j included in the model. The loss rate constants k_{ij} are important for determining the background loss rate, k_{bg}, but are unknown for most combinations of states i and j. We estimate these rates using calculated universal/Langevin rate constants along with measurements taken during this work. The state pairs fall into two categories. The first consists of states i and j coupled by an electric dipole-allowed transition, which could be a vibrational transition (selection rules $\Delta v_i = \pm 1, \Delta v_{j\neq i} = 0, \Delta N = 0, \pm 1, p = +1 \leftrightarrow -1$) [44] or a rotational transition. These rate constants are estimated using the Langevin capture model for a $-C_3/r^3$ potential [377], with $C_3 = |\langle i|d|j\rangle|^2/(4\pi\epsilon_0)$, where d is the electric dipole operator. They typically fall in the range $k_{ij} \sim 1 - 10 \times 10^{-10}$ cm^3 s^{-1}. The second category consists of pairs of states which are not directly coupled by an electric dipole transition. These states typically interact via attractive $-C_6/r^6$ (van der Waals, vdW) interactions, whereby the electric dipole interaction acts at second order (see chapter 9). For two molecules in any $\ell = 0$ state, we use the measured rate constant $k = 0.7 \times 10^{-10}$ cm^3 s^{-1} for molecules in $\widetilde{X}(000)$, since

in all cases the dominant vdW interaction comes from mixing of rotational states. For one molecule in an $\ell = 0$ state and one molecule in an $\ell = 1$ state, C_6 is typically higher since the second-order dipolar coupling mixes rotational states in the $\ell = 0$ molecule but only needs to mix parity-doublet states in the $\ell = 1$ molecule. Thus, the energy denominator in the second-order perturbation theory sum (chapter 9) is generally smaller than in the $\ell = 0 + \ell = 0$ case. We estimate these collision rates using the Langevin capture model described in sec. 9.4.3 and find rates ranging from $k_{ij}(\ell_i = 0, \ell_j = 1) \sim 1 - 5 \times 10^{-10}$ cm^3 s^{-1} depending on the combination of rotational states (an "effective" rate for $\ell = 0 + \ell = 1$ collisions is fit as described below). Finally, for two molecules in $\ell \neq 0$ states, vdW interactions arise from mixing of closely-spaced parity doublet states, and we use $k_{ij}(\ell_i \neq 0, \ell_j \neq 0) \approx 5 \times 10^{-10}$ cm^3 s^{-1}, which is similar to the universal rate for two molecules in $\widetilde{X}(010)(N = 1^-)$. Note that in all cases these rate constants are at best semi-quantitative estimates, and in reality there will be significant dependence on the specific rotational state. However, they do provide a starting point for the rate equation model and can be expected to give reasonable results when averaged over the large number of states in the model.

D.3.3 Rate equation implementation

We implement the rate equations slightly differently for the collision situation than for the vibrational lifetime measurements. Specifically, we no longer enforce normalization of the state vector, and instead have the entries correspond to the total number of molecules in that state, rather than the fractional number. We no longer include n_{loss}, but we do keep track of the temperature as an entry in the state vector. We assume that the molecules instantaneously thermalize via elastic collisions and that a single temperature can therefore be used to describe all the molecules.

E

Optical Transitions in CaOH and $CaOCH_3$

In this appendix, we list optical transition frequencies in CaOH and $CaOCH_3$ that have been observed on our experiment. Many of these transitions were already known at high resolution, but others represent the first known high-resolution measurements. We also describe the spectroscopy procedures used to find these new lines at high resolution.

E.1 Wavemeter offset

The HighFinesse WS7 wavemeter used on our experiment has good frequency precision (sufficient for sub-MHz laser locking and good passive stability using the techniques from Ref. [278]), but we find that its absolute frequency readings are several hundred MHz below the corresponding literature values.[1] A coarse comparison with other wavemeters in the lab and with literature values for known Ca atomic transitions indicates that our frequencies read $\sim$450 MHz below absolute in the 550-650 nm range where most CaOH transitions lie.[2] All frequencies listed in this appendix are *uncorrected*, however, so the offset should be added back to get close to the absolute frequency.

E.2 Observed optical transitions in CaOH

In tables E.1, E.2, and E.3, we list the observed frequencies for various optical transitions in CaOH. Many of these were previously given in Louis Baum's thesis [273]. Compared to that work, we have now also found the $\widetilde{X}(110)$ and $\widetilde{X}(03^10)$ states at high resolution. Most other states were previously observed at high resolution in Refs. [237, 238, 242, 249, 250, 270, 420, 427**?** , 428].

E.3 Spectroscopy of CaOH repumping transitions

Out spectroscopy of most of the transitions observed in CaOH is described in Ref. [273]. Here we describe the search for the $\widetilde{X}(110)$ and $\widetilde{X}(03^10)$ states, which had not previously been observed at high resolution. In both

[1] This appears to be an anomaly of our specific wavemeter, which is specified to have a much better frequency accuracy than this. Other WS7 wavemeters in the lab do meet spec and have good accuracy.

[2] This offset appears to depend on the wavelength, with the offset roughly fitting to $\Delta(\lambda) \approx 53 - 302000/\lambda$ MHz over the range 423-671 nm, where λ is the wavelength in nm.

Table E.1: Transitions used for optical cycling of CaOH. For optical cycling transitions addressing multiple spin-rotation components, the listed frequency corresponds approximately to the lowest-frequency component (e.g. $N = 1, J = 3/2$ in the ground state for $\ell = 0$ vibrational states).

Ground state	Excited state	Frequency (THz)	Wavelength
$\widetilde{X}^2\Sigma^+(000)$	$\widetilde{A}^2\Pi_{1/2}(000)$	478.600015	626.4 nm
$\widetilde{X}^2\Sigma^+(100)$	$\widetilde{B}^2\Sigma^+(000)$	522.015345	574.3 nm
$\widetilde{X}^2\Sigma^+(02^00)$	$\widetilde{A}^2\Pi_{1/2}(100)$	476.582353	629.0 nm
$\widetilde{X}^2\Sigma^+(200)$	$\widetilde{A}^2\Pi_{1/2}(100)$	460.948200	650.4 nm
$\widetilde{X}^2\Sigma^+(010)(N = 1)$	$\widetilde{B}^2\Sigma^+(000)$	529.702860	566.0 nm
$\widetilde{X}^2\Sigma^+(02^20)$	$\widetilde{A}^2\Pi_{1/2}(100)$	475.852270	630.0 nm
$\widetilde{X}^2\Sigma^+(010)(N = 2)$	$\widetilde{A}(010)\kappa^2\Sigma^{(-)}$	481.310198	622.9 nm
$\widetilde{X}^2\Sigma^+(12^00)$	$\widetilde{A}(020)\mu^2\Pi_{1/2}$	460.678719	650.8 nm
$\widetilde{X}^2\Sigma^+(300)$	$\widetilde{B}^2\Sigma^+(100)$	504.431104	594.3 nm
$\widetilde{X}^2\Sigma^+(110)(N = 1)$	$\widetilde{A}(010)\mu^2\Sigma^{(+)}$	460.456027	651.1 nm
$\widetilde{X}^2\Sigma^+(12^20)$	$\widetilde{A}(020)\kappa^2\Pi_{1/2}$	464.124968	645.9 nm
$\widetilde{X}^2\Sigma^+(03^10)(N = 1)$	$\widetilde{A}(010)\mu^2\Sigma^{(+)}$	458.004800	654.6 nm
$\widetilde{X}^2\Sigma^+(110)(N = 2)$	$\widetilde{A}(010)\kappa^2\Sigma^{(-)}$	$\sim$463.3894[a]	647.0 nm
$\widetilde{X}^2\Sigma^+(03^10)(N = 2)$	$\widetilde{A}(010)\kappa^2\Sigma^{(-)}$	460.9379[b]	650.4 nm

[a] Only observed with frequency broadened slowing light; uncertainty is several hundred MHz

[b] Has not been used for repumping in experiments to date, but could be added

Table E.2: Other observed transitions between the $\widetilde{X}$ and $\widetilde{A}$ states. All transitions listed are the rotationally closed optical cycling line (to the $J = 1/2^+$ excited state) unless otherwise specified.

Ground state	Excited state	Frequency (THz)	Wavelength
$\widetilde{X}^2\Sigma^+(000)$	$\widetilde{A}(010)\mu^2\Sigma^{(+)}$	488.947546	613.1 nm
$\widetilde{X}^2\Sigma^+(000)$	$\widetilde{A}(010)\kappa^2\Sigma^{(-)}$	491.920690	609.4 nm[a]
$\widetilde{X}^2\Sigma^+(000)$	$\widetilde{A}^2\Pi_{1/2}(100)$	497.227900	602.9 nm
$\widetilde{X}^2\Sigma^+(000)$	$\widetilde{A}(020)\mu^2\Pi_{1/2}$	499.117130	600.6 nm
$\widetilde{X}^2\Sigma^+(000)$	$\widetilde{A}(020)\kappa^2\Pi_{1/2}$	503.172718	595.8 nm
$\widetilde{X}^2\Sigma^+(010)(N=1)$	$\widetilde{A}^2\Pi_{1/2}(000)$	468.029550	640.5 nm
$\widetilde{X}^2\Sigma^+(010)(N=1)$	$\widetilde{A}(010)\mu^2\Sigma^{(+)}$	478.377094	626.7 nm
$\widetilde{X}^2\Sigma^+(010)(N=2)$	$\widetilde{A}^2\Pi_{1/2}(000)$	467.989536	640.6 nm
$\widetilde{X}^2\Sigma^+(010)(N=2)$	$\widetilde{A}(010)\mu^2\Sigma^{(+)}$	478.337041	626.7 nm
$\widetilde{X}^2\Sigma^+(100)$	$\widetilde{A}^2\Pi_{1/2}(000)$	460.342042	651.2 nm
$\widetilde{X}^2\Sigma^+(02^00)$	$\widetilde{A}^2\Pi_{1/2}(000)$	457.954463	654.6 nm
$\widetilde{X}^2\Sigma^+(02^00)$	$\widetilde{A}(020)\kappa^2\Pi_{1/2}$	482.527179	621.3 nm
$\widetilde{X}^2\Sigma^+(02^20)$	$\widetilde{A}(020)\kappa^2\Pi_{1/2}$	481.797102	622.2 nm
$\widetilde{X}^2\Sigma^+(12^00)$	$\widetilde{A}^2\Pi_{1/2}(100)$	458.789511	653.4 nm
$\widetilde{X}^2\Sigma^+(12^20)$	$\widetilde{A}^2\Pi_{1/2}(100)$	458.180145	654.3 nm
$\widetilde{X}^2\Sigma^+(12^20)$	$\widetilde{A}(020)\mu^2\Pi_{1/2}$	460.069392	651.6 nm

[a] Used to populate the bending mode for the optical tweezer and collision experiments in this thesis

Table E.3: Other observed transitions between the $\widetilde{X}$ and $\widetilde{B}$ states. All transitions listed are the rotationally closed optical cycling line (to the $J = 1/2^+$ excited state) unless otherwise specified.

Ground state	Excited state	Frequency (THz)	Wavelength
$\widetilde{X}^2\Sigma^+(000)$	$\widetilde{B}^2\Sigma^+(000)$	540.273320	554.9 nm
$\widetilde{X}^2\Sigma^+(02^00)$	$\widetilde{B}^2\Sigma^+(100)$	519.627790	576.9 nm
$\widetilde{X}^2\Sigma^+(200)$	$\widetilde{B}^2\Sigma^+(000)$	503.993613	594.8 nm
$\widetilde{X}^2\Sigma^+(200)$	$\widetilde{B}^2\Sigma^+(100)$	522.203949	574.1 nm
$\widetilde{X}^2\Sigma^+(12^00)$	$\widetilde{B}^2\Sigma^+(100)$	520.045270	576.5 nm
$\widetilde{X}^2\Sigma^+(110)(N=1)$	$\widetilde{B}^2\Sigma^+(100)$	529.992127	565.7 nm

cases, we knew the vibrational state energy to within $\sim\pm 5$ cm^{-1}, based on previous dispersed fluorescence measurements [240, 269].

E.3.1 Spectroscopic search for the $\widetilde{X}(110)$ state

To search for the $\widetilde{X}(110)$ state, we used molecular beam spectroscopy with a depletion region followed by a repumping and detection region.

In the depletion region, we optically cycled on the $\widetilde{X}(010) \rightarrow \widetilde{A}(010)$ transition, which would eventually decay with a reasonably high probability to $\widetilde{X}(110)$. Specifically, this region included a $\widetilde{X}(000) \rightarrow \widetilde{A}(010)\mu^2\Sigma^{(+)}$ laser to pump ground state population into $\widetilde{X}(010)$, along with lasers addressing $\widetilde{X}(000)(N=1) \rightarrow \widetilde{A}(010)\mu^2\Sigma^{(+)}$ and $\widetilde{X}(000)(N=2) \rightarrow \widetilde{A}(010)\kappa^2\Sigma^{(-)}$. In the repumping and detction region, we scanned a dye laser to find the $\widetilde{X}(110)(N=1) \rightarrow \widetilde{B}^2(100)$ transition, which would decay to $\widetilde{X}(100)$. We then detected background-free 555 nm fluorescence using a PMT, with the fluorescence produced from $\widetilde{B}(000) \rightarrow \widetilde{X}(000)$ decay when optically cycling with the $\widetilde{X}(000) \rightarrow \widetilde{A}(000)$ and $\widetilde{X}(100) \rightarrow \widetilde{B}(000)$ lasers. When taking data, we alternate shots with and without the spectroscopy laser, so that the signal we are searching for is a difference in brightness with and without repumping the desired state.

Importantly, we also run calibration scans in a switch-4 configuration (similar to what is used for the depletion-revival VBR measurements in chapter 4), wherein we scan the spectroscopy laser over the known $\widetilde{X}(010) \rightarrow \widetilde{B}(000)$ transition. This is used to confirm that the depletion is actually removing molecules from the ground state (and presumably putting them into $\widetilde{X}(110)$), and it also gives a sense of the expected broadening of the target signal (since the calibration $\widetilde{X}(010) \rightarrow \widetilde{B}(000)$ transition should have a very similar line strength to the $\widetilde{X}(110) \rightarrow \widetilde{B}(100)$ transition).

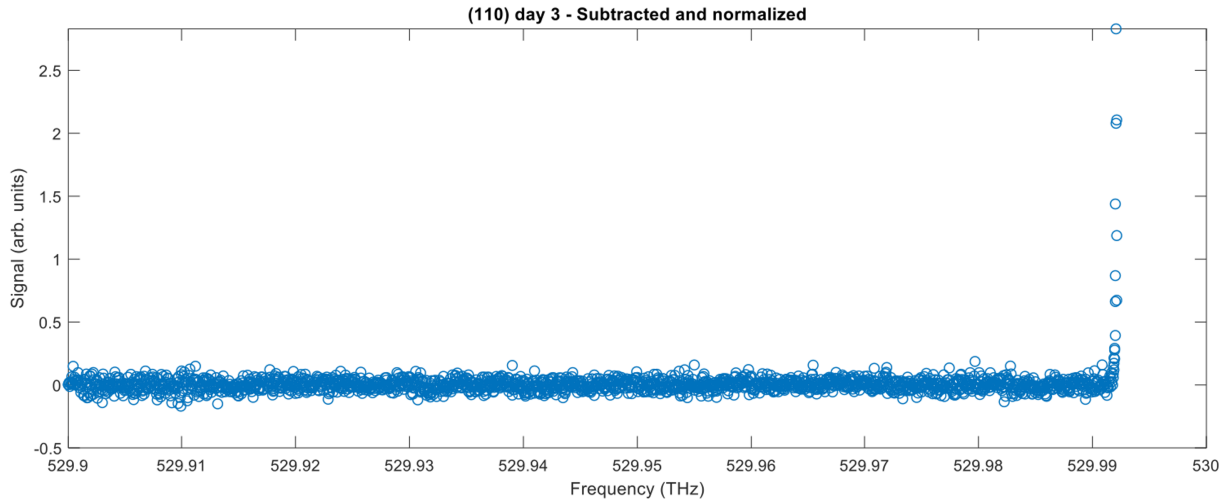

Figure E.1: Portion of the scan searching for the $\widetilde{X}(110) \rightarrow \widetilde{B}(100)$ transition. The line appears as a very clear feature at the far right hand side.

We scanned over approximately 150 GHz, in 50 MHz steps, before finding the transition. This took around 10 hours of scanning (spread over 2 days) once everything was set up. A portion of the spectrum is shown in Fig. E.1, showing a very clear feature in the background-subtracted data. After finding the line, we confirmed that this was the $N = 1$ ground state, then found the repumping transition through $\widetilde{A}(010)$ using the known energy difference between the different excited states.

We also searched for transitions out of $\widetilde{X}(110)(N = 2)$ but found nothing, likely due to technical issues. Once we had a MOT, we added the $\widetilde{X}(110)(N = 2)$ repumper and observed signal very close to the predicted frequency.

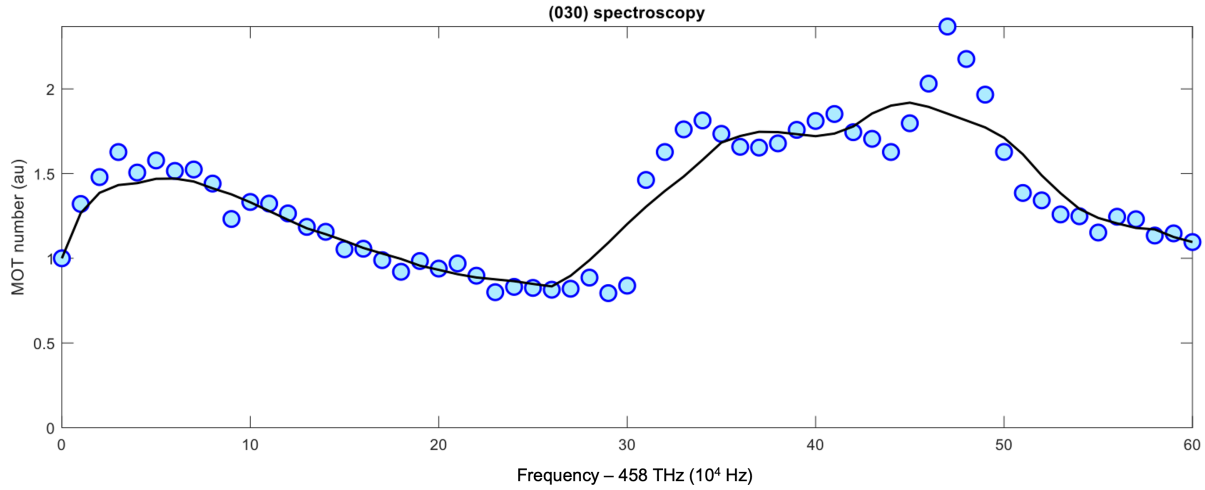

Figure E.2: Portion of the scan searching for the $\widetilde{X}(03^10)(N=1) \rightarrow \widetilde{A}(010)\mu^2\Sigma^{(+)}$ repumping transition. The black curve is an interpolation over the slow drift of the MOT number vs. time. The feature manifests itself as a relatively sharp increase in fluorescence near 458.005 THz.

E.3.2 Spectroscopic search for the $\widetilde{X}(03^10)$ state

We looked for this state once we already had a MOT, with the goal being to improve our MOT signal and lifetime by adding another repumping laser. We simply added a laser that could be scanned over the predicted $\widetilde{X}(03^10) \rightarrow \widetilde{A}(010)\mu^2\Sigma^{(+)}$ frequency. Since adding this repumper would be expected to increase the MOT lifetime, we imaged the MOT for 50 ms (longer than the $1/e$ lifetime with the previous repumpers), which should make the total integrated signal sensitive to the lifetime. We did not switch the repumper on and off, and instead just relied on the drift in the MOT signal due to ablation fluctuations having a slower timescale than the time it would take to scan over resonance. This worked well enough, with the repumping transition appearing as a sharp feature on top of a broadly drifting background after approximately 70 GHz of scanning. A portion of the scan including the observed feature is shown in Fig. E.2. This technique could certainly be improved, but it

was sufficient to find the line in this case.

After finding $\widetilde{X}(03^10)$, we spent several days searching for the $\widetilde{X}(22^00) \rightarrow \widetilde{A}(12^00)$ transition in the MOT, using a similar technique. This was a new challenge because neither state had previously been observed at high resolution. We used *ab initio* calculations of vibrational energies from Lan Cheng and Chaoqun Zhang as a starting point (the estimated frequency was $\sim$ 461.422 THz). We scanned over the range 461.150 THz to 461.617 THz and observed no clear signature of the repumping transition. It is possible that this was because of technical problems (i.e. the spectroscopy technique not being sufficiently sensitive), or because the transition is not found in this frequency range.

We observed a loss feature around 461.565 THz during this scan, which likely corresponds to population being depleted out of one of the ground states used for optical cycling. We did not attempt to assign the line, but possibilities include $\widetilde{X}(12^00) \rightarrow \widetilde{A}(02^20)$, $\widetilde{X}(12^20) \rightarrow \widetilde{A}(02^20)$, or $\widetilde{X}(300) \rightarrow \widetilde{A}(200)$.

E.4 Laser cooling transitions in $CaOCH_3$

The transition frequencies used for $CaOCH_3$ laser cooling are found in tables E.4 and E.5. Transitions on the origin $\widetilde{X}^2A_1 \rightarrow \widetilde{A}^2E0_0^0$ band relied on previous high-resolution spectroscopy [386]. The repumping transitions were not previously known at high resolution. Spectroscopic searches for those transitions are described in chapter 10.

Table E.4: Transitions used for $K_R = 0$ laser cooling in $CaOCH_3$.

Ground state	Excited state	Frequency (THz)	Wavelength (nm)
$\widetilde{X}^2A_1 0_0$	$\widetilde{A}^2E_{1/2} 0_0$	476.252450	629.5
$\widetilde{X}^2A_1 4_1$	$\widetilde{B}^2A_1 0_0$	515.452780	581.6
$\widetilde{X}^2A_1 3_1$	$\widetilde{B}^2A_1 0_0$	495.373190	605.2

Table E.5: Transitions used for $|K_R| = 1$ laser cooling in $CaOCH_3$.

Ground state	Excited state	Frequency (THz)	Wavelength (nm)
$\widetilde{X}^2A_1 0_0 (N'' = 1)$	$\widetilde{A}^2E_{1/2} 0_0$	476.255328	629.5
$\widetilde{X}^2A_1 0_0 (N'' = 2)$	$\widetilde{A}^2E_{1/2} 0_0$	476.241400	629.5
$\widetilde{X}^2A_1 4_1 (N'' = 1)$	$\widetilde{B}^2A_1 0_0$	515.459220	581.6[a]
$\widetilde{X}^2A_1 4_1 (N'' = 2)$	$\widetilde{B}^2A_1 0_0$	515.445382	581.6
$\widetilde{X}^2A_1 4_1 (N'' = 1)$	$\widetilde{A}^2E_{1/2} 0_0$	461.609552	649.5

[a] Not used due to accidental overlap with a rotationally lossy transition (described in chapter 10).

References

[1] W. D. Phillips, "Nobel lecture: Laser cooling and trapping of neutral atoms," Rev. Mod. Phys. **70**, 721 (1998).

[2] S. Chu, "Nobel lecture: The manipulation of neutral particles," Rev. Mod. Phys. **70**, 685 (1998).

[3] L. Henriet, L. Beguin, A. Signoles, T. Lahaye, A. Browaeys, G.-O. Reymond, and C. Jurczak, "Quantum computing with neutral atoms," Quantum **4**, 327 (2020).

[4] C. D. Bruzewicz, J. Chiaverini, R. McConnell, and J. M. Sage, "Trapped-ion quantum computing: Progress and challenges," Applied Physics Reviews **6**, 021314 (2019).

[5] I. Bloch, J. Dalibard, and S. Nascimbene, "Quantum simulations with ultracold quantum gases," Nature Physics **8**, 267–276 (2012).

[6] E. Altman, K. R. Brown, G. Carleo, L. D. Carr, E. Demler, C. Chin, B. DeMarco, S. E. Economou, M. A. Eriksson, K.-M. C. Fu, M. Greiner, K. R. Hazzard, R. G. Hulet, A. J. Kollár, B. L. Lev, M. D. Lukin, R. Ma, X. Mi, S. Misra, C. Monroe, K. Murch, Z. Nazario, K.-K. Ni, A. C. Potter, P. Roushan, M. Saffman, M. Schleier-Smith, I. Siddiqi, R. Simmonds, M. Singh, I. Spielman, K. Temme, D. S. Weiss, J. Vučković, V. Vuletić, J. Ye, and M. Zwierlein, "Quantum simulators: Architectures and opportunities," PRX Quantum **2**, 017003 (2021).

[7] I. Bloch, J. Dalibard, and W. Zwerger, "Many-body physics with ultracold gases," Rev. Mod. Phys **80**, 885 (2008).

[8] I. Bloch, "Quantum gases," Science **319**, 1202–1203 (2008).

[9] A. D. Ludlow, M. M. Boyd, J. Ye, E. Peik, and P. O. Schmidt, "Optical atomic clocks," Rev. Mod. Phys. **87**, 637 (2015).

[10] C. L. Degen, F. Reinhard, and P. Cappellaro, "Quantum sensing," Rev. Mod. Phys. **89**, 035002 (2017).

[11] M. S. Safronova, D. Budker, D. DeMille, D. F. J. Kimball, A. Derevianko, and C. W. Clark, "Search for new physics with atoms and molecules," Rev. Mod. Phys. **90**, 025008 (2018).

[12] M. Tarbutt, "Laser cooling of molecules," Contemp. Phys. **59**, 356–376 (2018).

[13] D. McCarron, "Laser cooling and trapping molecules," J. Phys. B **51**, 212001 (2018).

[14] N. Fitch and M. Tarbutt, "Chapter three - laser-cooled molecules," in *Advances In Atomic, Molecular, and Optical Physics*, Advances In Atomic, Molecular, and Optical Physics, Vol. 70, edited by L. F. Dimauro, H. Perrin, and S. F. Yelin (Academic Press, 2021) pp. 157–262.

[15] B. Gadway and B. Yan, "Strongly interacting ultracold polar molecules," Journal of Physics B: Atomic, Molecular and Optical Physics **49**, 152002 (2016).

[16] S. A. Moses, J. P. Covey, M. T. Miecnikowski, D. S. Jin, and J. Ye, "New frontiers for quantum gases of polar molecules," Nature Physics **13**, 13–20 (2017).

[17] T. Langen, G. Valtolina, D. Wang, and J. Ye, "Quantum state manipulation and cooling of ultracold molecules," Nature Physics **20**, 702–712 (2024).

[18] Y. Takasu, K. Maki, K. Komori, T. Takano, K. Honda, M. Kumakura, T. Yabuzaki, and Y. Takahashi, "Spin-singlet Bose-Einstein condensation of two-electron atoms," Phys. Rev. Lett. **91**, 040404 (2003).

[19] S. Stellmer, M. K. Tey, B. Huang, R. Grimm, and F. Schreck, "Bose-Einstein condensation of strontium," Phys. Rev. Lett. **103**, 200401 (2009).

[20] A. Griesmaier, J. Werner, S. Hensler, J. Stuhler, and T. Pfau, "Bose-Einstein condensation of chromium," Phys. Rev. Lett. **94**, 160401 (2005).

[21] M. Lu, N. Q. Burdick, S. H. Youn, and B. L. Lev, "Strongly dipolar Bose-Einstein condensate of dysprosium," Phys. Rev. Lett. **107**, 190401 (2011).

[22] G. Uhlenberg, J. Dirscherl, and H. Walther, "Magneto-optical trapping of silver atoms," Phys. Rev. A **62**, 063404 (2000).

[23] S. Eustice, J. Schrott, A. Stöltzel, J. Wolf, D. Novoa, K. Cassella, and D. M. Stamper-Kurn, "Magneto-optical trap of titanium atoms," Phys. Rev. Res. **7**, 023025 (2025).

[24] I. S. Madjarov, J. P. Covey, A. L. Shaw, J. Choi, A. Kale, A. Cooper, H. Pichler, V. Schkolnik, J. R. Williams, and M. Endres, "High-fidelity entanglement and detection of alkaline-earth rydberg atoms," Nature Physics **16**, 857–861 (2020).

[25] A. Jenkins, J. W. Lis, A. Senoo, W. F. McGrew, and A. M. Kaufman, "Ytterbium nuclear-spin qubits in an optical tweezer array," Phys. Rev. X **12**, 021027 (2022).

[26] S. Ma, A. P. Burgers, G. Liu, J. Wilson, B. Zhang, and J. D. Thompson, "Universal gate operations on nuclear spin qubits in an optical tweezer array of ^{171}Yb atoms," Phys. Rev. X **12**, 021028 (2022).

[27] S. Baier, M. J. Mark, D. Petter, K. Aikawa, L. Chomaz, Z. Cai, M. Baranov, P. Zoller, and F. Ferlaino, "Extended Bose-Hubbard models with ultracold magnetic atoms," Science **352**, 201–205 (2016).

[28] L. Su, A. Douglas, M. Szurek, R. Groth, S. F. Ozturk, A. Krahn, A. H. Hébert, G. A. Phelps, S. Ebadi, S. Dickerson, F. Ferlaino, O. Marković, and M. Greiner, "Dipolar quantum solids emerging in a Hubbard quantum simulator," Nature **622**, 724–729 (2023).

[29] N. Bigagli, W. Yuan, S. Zhang, B. Bulatovic, T. Karman, I. Stevenson, and S. Will, "Observation of Bose-Einstein condensation of dipolar molecules," Nature **631**, 289–293 (2024).

[30] Y. Bao, S. S. Yu, J. You, L. Anderegg, E. Chae, W. Ketterle, K.-K. Ni, and J. M. Doyle, "Raman sideband cooling of molecules in an optical tweezer array to the 3d motional ground state," Phys. Rev. X **14**, 031002 (2024).

[31] Y. Bao, S. S. Yu, L. Anderegg, E. Chae, W. Ketterle, K.-K. Ni, and J. M. Doyle, "Dipolar spin-exchange and entanglement between molecules in an optical tweezer array," Science **382**, 1138–1143 (2023).

[32] C. M. Holland, Y. Lu, and L. W. Cheuk, "On-demand entanglement of molecules in a reconfigurable optical tweezer array," Science **382**, 1143–1147 (2023).

[33] T. A. Isaev and R. Berger, "Polyatomic candidates for cooling of molecules with lasers from simple theoretical concepts," Phys. Rev. Lett. **116**, 063006 (2016).

[34] I. Kozyryev, L. Baum, K. Matsuda, and J. M. Doyle, "Proposal for laser cooling of complex polyatomic molecules," ChemPhysChem **17**, 3641–3648 (2016).

[35] T. A. Isaev, A. V. Zaitsevskii, and E. Eliav, "Laser-coolable polyatomic molecules with heavy nuclei," J. Phys. B **50**, 225101 (2017).

[36] M. J. O'Rourke and N. R. Hutzler, "Hypermetallic polar molecules for precision measurements," Phys. Rev. A **100**, 022502 (2019).

[37] B. L. Augenbraun, J. M. Doyle, T. Zelevinsky, and I. Kozyryev, "Molecular asymmetry and optical cycling: Laser cooling asymmetric top molecules," Phys. Rev. X **10**, 031022 (2020).

[38] C. E. Dickerson, H. Guo, A. J. Shin, B. L. Augenbraun, J. R. Caram, W. C. Campbell, and A. N. Alexandrova, "Franck-Condon tuning of optical cycling centers by organic functionalization," Phys. Rev. Lett. **126**, 123002 (2021).

[39] C. E. Dickerson, H. Guo, G.-Z. Zhu, E. R. Hudson, J. R. Caram, W. C. Campbell, and A. N. Alexandrova, "Optical cycling functionalization of arenes," The Journal of Physical Chemistry Letters **12**, 3989–3995 (2021).

[40] H. Guo, C. E. Dickerson, A. J. Shin, C. Zhao, T. L. Atallah, J. R. Caram, W. C. Campbell, and A. N. Alexandrova, "Surface chemical trapping of optical cycling centers," Phys. Chem. Chem. Phys. **23**, 211–218 (2021).

[41] P. Yu, A. Lopez, W. A. Goddard, and N. R. Hutzler, "Multivalent optical cycling centers: towards control of polyatomics with multi-electron degrees of freedom," Phys. Chem. Chem. Phys. **25**, 154–170 (2023).

[42] N. B. Vilas, C. Hallas, L. Anderegg, P. Robichaud, A. Winnicki, D. Mitra, and J. M. Doyle, "Magneto-optical trapping and sub-doppler cooling of a polyatomic molecule," Nature **606**, 70–74 (2022).

[43] C. Hallas, N. B. Vilas, L. Anderegg, P. Robichaud, A. Winnicki, C. Zhang, L. Cheng, and J. M. Doyle, "Optical trapping of a polyatomic molecule in an ℓ-type parity doublet state," Phys. Rev. Lett. **130**, 153202 (2023).

[44] N. B. Vilas, C. Hallas, L. Anderegg, P. Robichaud, C. Zhang, S. Dawley, L. Cheng, and J. M. Doyle, "Blackbody thermalization and vibrational lifetimes of trapped polyatomic molecules," Phys. Rev. A **107**, 062802 (2023).

[45] L. Anderegg, N. B. Vilas, C. Hallas, P. Robichaud, A. Jadbabaie, J. M. Doyle, and N. R. Hutzler, "Quantum control of trapped polyatomic molecules for eEDM searches," Science **382**, 665–668 (2023).

[46] N. B. Vilas, P. Robichaud, C. Hallas, G. K. Li, L. Anderegg, and J. M. Doyle, "An optical tweezer array of ultracold polyatomic molecules," Nature **628**, 282–286 (2024).

[47] D. Mitra, N. B. Vilas, C. Hallas, L. Anderegg, B. L. Augenbraun, L. Baum, C. Miller, S. Raval, and J. M. Doyle, "Direct laser cooling of a symmetric top molecule," Science **369**, 1366–1369 (2020).

[48] G.-Z. Zhu, D. Mitra, B. L. Augenbraun, C. E. Dickerson, M. J. Frim, G. Lao, Z. D. Lasner, A. N. Alexandrova, W. C. Campbell, J. R. Caram, J. M. Doyle, and E. R. Hudson, "Functionalizing aromatic compounds with optical cycling centres," Nature Chemistry **14**, 995–999 (2022).

[49] D. Mitra, Z. D. Lasner, G.-Z. Zhu, C. E. Dickerson, B. L. Augenbraun, A. D. Bailey, A. N. Alexandrova, W. C. Campbell, J. R. Caram, E. R. Hudson, and J. M. Doyle, "Pathway toward optical cycling and laser cooling of functionalized arenes," The Journal of Physical Chemistry Letters **13**, 7029–7035 (2022).

[50] B. L. Augenbraun, S. Burchesky, A. Winnicki, and J. M. Doyle, "High-resolution laser spectroscopy of a functionalized aromatic molecule," The Journal of Physical Chemistry Letters **13**, 10771–10777 (2022).

[51] S. Burchesky, *Engineered Collisions, Molecular Qubits, and Laser Cooling of Asymmetric Top Molecules*, Ph.D. thesis, Harvard University (2023).

[52] B. L. Augenbraun, L. Anderegg, C. Hallas, Z. D. Lasner, N. B. Vilas, and J. M. Doyle, "Chapter two - direct laser cooling of polyatomic molecules," in *Advances in Atomic, Molecular, and Optical Physics*, Advances In Atomic, Molecular, and Optical Physics, Vol. 72, edited by L. F. DiMauro, H. Perrin, and S. F. Yelin (Academic Press, 2023) pp. 89–182.

[53] D. DeMille, "Quantum computation with trapped polar molecules," Phys. Rev. Lett. **88**, 067901 (2002).

[54] A. Micheli, G. Brennen, and P. Zoller, "A toolbox for lattice-spin models with polar molecules," Nature Physics **2**, 341–347 (2006).

[55] S. L. Cornish, M. R. Tarbutt, and K. R. A. Hazzard, "Quantum computation and quantum simulation with ultracold molecules," Nature Physics **20**, 730–740 (2024).

[56] N. Balakrishnan, "Perspective: Ultracold molecules and the dawn of cold controlled chemistry," J. Chem. Phys. **145**, 150901 (2016).

[57] J. L. Bohn, A. M. Rey, and J. Ye, "Cold molecules: Progress in quantum engineering of chemistry and quantum matter," Science **357**, 1002–1010 (2017).

[58] B. R. Heazlewood and T. P. Softley, "Towards chemistry at absolute zero," Nat. Rev. Chem. **5**, 125–140 (2021).

[59] L. D. Carr, D. DeMille, R. V. Krems, and J. Ye, "Cold and ultracold molecules: science, technology and applications," New J. Phys. **11**, 055049 (2009).

[60] B. Yan, S. A. Moses, B. Gadway, J. P. Covey, K. R. A. Hazzard, A. M. Rey, D. S. Jin, and J. Ye, "Observation of dipolar spin-exchange interactions with lattice-confined polar molecules," Nature **501**, 521–525 (2013).

[61] L. Christakis, J. S. Rosenberg, R. Raj, S. Chi, A. Morningstar, D. A. Huse, Z. Z. Yan, and W. S. Bakr, "Probing site-resolved correlations in a spin system of ultracold molecules," Nature **614**, 64–69 (2023).

[62] A. N. Carroll, H. Hirzler, C. Miller, D. Wellnitz, S. R. Muleady, J. Lin, K. P. Zamarski, R. R. W. Wang, J. L. Bohn, A. M. Rey, and J. Ye, "Observation of generalized *t-J* spin dynamics with tunable dipolar interactions," Science **388**, 381–386 (2025).

[63] L. R. B. Picard, A. J. Park, G. E. Patenotte, S. Gebretsadkan, D. Wellnitz, A. M. Rey, and K.-K. Ni, "Entanglement and iSWAP gate between molecular qubits," Nature **637**, 821–826 (2025).

[64] D. K. Ruttley, T. R. Hepworth, A. Guttridge, and S. L. Cornish, "Long-lived entanglement of molecules in magic-wavelength optical tweezers," Nature **637**, 827–832 (2025).

[65] K.-K. Ni, S. Ospelkaus, D. Wang, G. Quéméner, B. Neyenhuis, M. H. G. de Miranda, J. L. Bohn, J. Ye, and D. S. Jin, "Dipolar collisions of polar molecules in the quantum regime," Nature **464**, 1324–1328 (2010).

[66] M. Guo, X. Ye, J. He, M. L. González-Martínez, R. Vexiau, G. Quéméner, and D. Wang, "Dipolar collisions of ultracold ground-state bosonic molecules," Phys. Rev. X **8**, 041044 (2018).

[67] X. Ye, M. Guo, M. L. González-Martínez, G. Quéméner, and D. Wang, "Collisions of ultracold ^{23}Na^{87}Rb molecules with controlled chemical reactivities," Science Advances **4** (2018).

[68] P. D. Gregory, M. D. Frye, J. A. Blackmore, E. M. Bridge, R. Sawant, J. M. Hutson, and S. L. Cornish, "Sticky collisions of ultracold RbCs molecules," Nature Communications **10**, 3104 (2019).

[69] L. W. Cheuk, L. Anderegg, Y. Bao, S. Burchesky, S. S. Yu, W. Ketterle, K.-K. Ni, and J. M. Doyle, "Observation of collisions between two ultracold ground-state CaF molecules," Phys. Rev. Lett. **125**, 043401 (2020).

[70] Z. Z. Yan, J. W. Park, Y. Ni, H. Loh, S. Will, T. Karman, and M. Zwierlein, "Resonant dipolar collisions of ultracold molecules induced by microwave dressing," Phys. Rev. Lett. **125**, 063401 (2020).

[71] P. D. Gregory, J. A. Blackmore, S. L. Bromley, and S. L. Cornish, "Loss of ultracold ^{87}Rb^{133}Cs molecules via optical excitation of long-lived two-body collision complexes," Phys. Rev. Lett. **124**, 163402 (2020).

[72] Y. Liu, M.-G. Hu, M. A. Nichols, D. D. Grimes, T. Karman, H. Guo, and K.-K. Ni, "Photo-excitation of long-lived transient intermediates in ultracold reactions," Nature Physics **16**, 1132–1136 (2020).

[73] J. J. Park, Y.-K. Lu, A. O. Jamison, T. V. Tscherbul, and W. Ketterle, "A Feshbach resonance in collisions between triplet ground-state molecules," Nature **614**, 54–58 (2023).

[74] J. J. Burau, K. Mehling, M. D. Frye, M. Chen, P. Aggarwal, J. M. Hutson, and J. Ye, "Collisions of spin-polarized YO molecules for single partial waves," Phys. Rev. A **110**, L041306 (2024).

[75] G. Valtolina, K. Matsuda, W. G. Tobias, J.-R. Li, L. De Marco, and J. Ye, "Dipolar evaporation of reactive molecules to below the fermi temperature," Nature **588**, 239–243 (2020).

[76] K. Matsuda, L. D. Marco, J.-R. Li, W. G. Tobias, G. Valtolina, G. Quéméner, and J. Ye, "Resonant collisional shielding of reactive molecules using electric fields," Science **370**, 1324–1327 (2020).

[77] L. Anderegg, S. Burchesky, Y. Bao, S. S. Yu, T. Karman, E. Chae, K.-K. Ni, W. Ketterle, and J. M. Doyle, "Observation of microwave shielding of ultracold molecules," Science **373**, 779–782 (2021).

[78] J.-R. Li, W. G. Tobias, K. Matsuda, C. Miller, G. Valtolina, L. De Marco, R. R. W. Wang, L. Lassablière, G. Quéméner, J. L. Bohn, and J. Ye, "Tuning of dipolar interactions and evaporative cooling in a three-dimensional molecular quantum gas," Nature Physics **17**, 1144–1148 (2021).

[79] A. Schindewolf, R. Bause, X.-Y. Chen, M. Duda, T. Karman, I. Bloch, and X.-Y. Luo, "Evaporation of microwave-shielded polar molecules to quantum degeneracy," Nature **607**, 677–681 (2022).

[80] S. Ospelkaus, K.-K. Ni, D. Wang, M. De Miranda, B. Neyenhuis, G. Quéméner, P. Julienne, J. Bohn, D. Jin, and J. Ye, "Quantum-state controlled chemical reactions of ultracold potassium-rubidium molecules," Science **327**, 853–857 (2010).

[81] M.-G. Hu, Y. Liu, D. Grimes, Y.-W. Lin, A. Gheorghe, R. Vexiau, N. Bouloufa-Maafa, O. Dulieu, T. Rosenband, and K.-K. Ni, "Direct observation of bimolecular reactions of ultracold krb molecules," Science **366**, 1111–1115 (2019).

[82] Y. Liu, M.-G. Hu, M. A. Nichols, D. Yang, D. Xie, H. Guo, and K.-K. Ni, "Precision test of statistical dynamics with state-to-state ultracold chemistry," Nature **593**, 379–384 (2021).

[83] J. J. Hudson, D. M. Kara, I. J. Smallman, B. E. Sauer, M. R. Tarbutt, and E. A. Hinds, "Improved measurement of the shape of the electron," Nature **473**, 493–496 (2011).

[84] J. Baron, W. C. Campbell, D. DeMille, J. M. Doyle, G. Gabrielse, Y. V. Gurevich, P. W. Hess, N. R. Hutzler, E. Kirilov, I. Kozyryev, *et al.*, "Order of magnitude smaller limit on the electric dipole moment of the electron," Science **343**, 269–272 (2014).

[85] W. B. Cairncross, D. N. Gresh, M. Grau, K. C. Cossel, T. S. Roussy, Y. Ni, Y. Zhou, J. Ye, and E. A. Cornell, "Precision measurement of the electron's electric dipole moment using trapped molecular ions," Phys. Rev. Lett. **119**, 153001 (2017).

[86] A. Collaboration, "Improved limit on the electric dipole moment of the electron," Nature **562**, 355 (2018).

[87] T. S. Roussy, L. Caldwell, T. Wright, W. B. Cairncross, Y. Shagam, K. B. Ng, N. Schlossberger, S. Y. Park, A. Wang, J. Ye, and E. A. Cornell, "An improved bound on the electron's electric dipole moment," Science **381**, 46–50 (2023).

[88] C. M. Tesch and R. de Vivie-Riedle, "Quantum computation with vibrationally excited molecules," Phys. Rev. Lett. **89**, 157901 (2002).

[89] I. Kozyryev, Z. Lasner, and J. M. Doyle, "Enhanced sensitivity to ultralight bosonic dark matter in the spectra of the linear radical SrOH," Phys. Rev. A **103**, 043313 (2021).

[90] E. B. Norrgard, S. P. Eckel, C. L. Holloway, and E. L. Shirley, "Quantum blackbody thermometry," New Journal of Physics **23**, 033037 (2021).

[91] L. M. K. Vandersypen, M. Steffen, G. Breyta, C. S. Yannoni, M. H. Sherwood, and I. L. Chuang, "Experimental realization of shor's quantum factoring algorithm using nuclear magnetic resonance," Nature **414**, 883–887 (2001).

[92] W. Klemperer, K. K. Lehmann, J. K. G. Watson, and S. C. Wofsy, "Can molecules have permanent electric dipole moments?" The Journal of Physical Chemistry **97**, 2413–2416 (1993).

[93] M. Li and J. A. Coxon, "High-resolution analysis of the fundamental bending vibrations in the $\tilde{A}^2\Pi$ and $\tilde{X}^2\Sigma^+$ states of CaOH and CaOD: Deperturbation of Renner-Teller, spin-orbit and K-type resonance interactions," J. Chem. Phys. **102**, 2663–2674 (1995).

[94] D. A. Fletcher, M. A. Anderson, J. Barclay, W. L., and L. M. Ziurys, "Millimeter-wave spectroscopy of vibrationally excited ground state alkaline-earth hydroxide radicals ($X^2\Sigma^+$)," J. Chem. Phys. **102**, 4334–4339 (1995).

[95] K.-i. C. Namiki, J. S. Robinson, and T. C. Steimle, "A spectroscopic study of $CaOCH_3$ using the pump/probe microwave and the molecular beam/optical stark techniques," The Journal of Chemical Physics **109**, 5283–5289 (1998).

[96] N. R. Hutzler, "Polyatomic molecules as quantum sensors for fundamental physics," Quantum Science and Technology **5**, 044011 (2020).

[97] S. Yelin, K. Kirby, and R. Côté, "Schemes for robust quantum computation with polar molecules," Physical Review A **74**, 050301 (2006).

[98] K.-K. Ni, T. Rosenband, and D. D. Grimes, "Dipolar exchange quantum logic gate with polar molecules," Chemical science **9**, 6830–6838 (2018).

[99] R. Sawant, J. A. Blackmore, P. D. Gregory, J. Mur-Petit, D. Jaksch, J. Aldegunde, J. M. Hutson, M. R. Tarbutt, and S. L. Cornish, "Ultracold polar molecules as qudits," New J. Phys. **22**, 013027 (2020).

[100] Q. Wei, S. Kais, B. Friedrich, and D. Herschbach, "Entanglement of polar symmetric top molecules as candidate qubits," J. Chem Phys **135**, 154102 (2011).

[101] P. Yu, L. W. Cheuk, I. Kozyryev, and J. M. Doyle, "A scalable quantum computing platform using symmetric-top molecules," New J. Phys. **21**, 093049 (2019).

[102] Z.-Y. Zhang and J.-M. Liu, "Quantum correlations and coherence of polar symmetric top molecules in pendular states," Scientific Reports **7** (2017).

[103] D. Cory, R. Laflamme, E. Knill, L. Viola, T. Havel, N. Boulant, G. Boutis, E. Fortunato, S. Lloyd, R. Martinez, C. Negrevergne, M. Pravia, Y. Sharf, G. Teklemariam, Y. Weinstein, and W. Zurek, "NMR based quantum information processing: Achievements and prospects," Fortschritte der Physik **48**, 875–907 (2000).

[104] V. V. Albert, J. P. Covey, and J. Preskill, "Robust encoding of a qubit in a molecule," Phys. Rev. X **10**, 031050 (2020).

[105] D. Bluvstein, S. J. Evered, A. A. Geim, S. H. Li, H. Zhou, T. Manovitz, S. Ebadi, M. Cain, M. Kalinowski, D. Hangleiter, J. P. Bonilla Ataides, N. Maskara, I. Cong, X. Gao, P. Sales Rodriguez, T. Karolyshyn, G. Semeghini, M. J. Gullans, M. Greiner, V. Vuletić, and M. D. Lukin, "Logical quantum processor based on reconfigurable atom arrays," Nature **626**, 58–65 (2024).

[106] C. Zhang and M. Tarbutt, "Quantum computation in a hybrid array of molecules and rydberg atoms," PRX Quantum **3**, 030340 (2022).

[107] K. Wang, C. P. Williams, L. R. Picard, N. Y. Yao, and K.-K. Ni, "Enriching the quantum toolbox of ultracold molecules with rydberg atoms," PRX Quantum **3**, 030339 (2022).

[108] M. Wall, K. Hazzard, and A. M. Rey, "Quantum magnetism with ultracold molecules," in *From Atomic To Mesoscale: The Role of Quantum Coherence in Systems of Various Complexities* (World Scientific, 2015) pp. 3–37.

[109] M. L. Wall, K. Maeda, and L. D. Carr, "Simulating quantum magnets with symmetric top molecules," Ann. Phys. (Berlin) **525**, 845–865 (2013).

[110] M. Wall, K. Maeda, and L. D. Carr, "Realizing unconventional quantum magnetism with symmetric top molecules," New J. Phys. **17**, 025001 (2015).

[111] C. Miller, A. N. Carroll, J. Lin, H. Hirzler, H. Gao, H. Zhou, M. D. Lukin, and J. Ye, "Two-axis twisting using Floquet-engineered XYZ spin models with polar molecules," Nature **633**, 332–337 (2024).

[112] T. Lahaye, C. Menotti, L. Santos, M. Lewenstein, and T. Pfau, "The physics of dipolar bosonic quantum gases," Reports on Progress in Physics **72**, 126401 (2009).

[113] C. Chin, R. Grimm, P. Julienne, and E. Tiesinga, "Feshbach resonances in ultracold gases," Rev. Mod. Phys. **82**, 1225–1286 (2010).

[114] Z. Idziaszek and P. S. Julienne, "Universal rate constants for reactive collisions of ultracold molecules," Phys. Rev. Lett. **104**, 113202 (2010).

[115] M. D. Frye, P. S. Julienne, and J. M. Hutson, "Cold atomic and molecular collisions: approaching the universal loss regime," New Journal of Physics **17**, 045019 (2015).

[116] M. Mayle, G. Quéméner, B. P. Ruzic, and J. L. Bohn, "Scattering of ultracold molecules in the highly resonant regime," Phys. Rev. A **87**, 012709 (2013).

[117] A. Christianen, M. W. Zwierlein, G. C. Groenenboom, and T. Karman, "Photoinduced two-body loss of ultracold molecules," Phys. Rev. Lett. **123**, 123402 (2019).

[118] R. Bause, A. Christianen, A. Schindewolf, I. Bloch, and X.-Y. Luo, "Ultracold sticky collisions: Theoretical and experimental status," The Journal of Physical Chemistry A **127**, 729–741 (2023).

[119] A. V. Avdeenkov, M. Kajita, and J. L. Bohn, "Suppression of inelastic collisions of polar $^1\Sigma$ state molecules in an electrostatic field," Phys. Rev. A **73**, 022707 (2006).

[120] T. Karman and J. M. Hutson, "Microwave shielding of ultracold polar molecules," Phys. Rev. Lett. **121**, 163401 (2018).

[121] J. Toscano, H. J. Lewandowski, and B. R. Heazlewood, "Cold and controlled chemical reaction dynamics," Phys. Chem. Chem. Phys. **22**, 9180–9194 (2020).

[122] B. C. Sawyer, B. K. Stuhl, M. Yeo, T. V. Tscherbul, M. T. Hummon, Y. Xia, J. Kłos, D. Patterson, J. M. Doyle, and J. Ye, "Cold heteromolecular dipolar collisions," Phys. Chem. Chem. Phys. **13**, 19059–19066 (2011).

[123] X. Wu, T. Gantner, M. Koller, M. Zeppenfeld, S. Chervenkov, and G. Rempe, "A cryofuge for cold-collision experiments with slow polar molecules," Science **358**, 645–648 (2017).

[124] M. Koller, F. Jung, J. Phrompao, M. Zeppenfeld, I. M. Rabey, and G. Rempe, "Electric-field-controlled cold dipolar collisions between trapped CH_3F molecules," Phys. Rev. Lett. **128**, 203401 (2022).

[125] A. V. Avdeenkov and J. L. Bohn, "Collisional dynamics of ultracold OH molecules in an electrostatic field," Phys. Rev. A **66**, 052718 (2002).

[126] A. V. Avdeenkov and J. L. Bohn, "Linking ultracold polar molecules," Phys. Rev. Lett. **90**, 043006 (2003).

[127] A. V. Avdeenkov and J. L. Bohn, "Ultracold collisions of fermionic OD radicals," Phys. Rev. A **71**, 022706 (2005).

[128] B. K. Stuhl, M. T. Hummon, M. Yeo, G. Quéméner, J. L. Bohn, and J. Ye, "Evaporative cooling of the dipolar hydroxyl radical," Nature **492**, 396–400 (2012).

[129] L. D. Augustovičová and J. L. Bohn, "No evaporative cooling of nitric oxide in its ground state," Phys. Rev. A **96**, 042712 (2017).

[130] L. D. Augustovičová and J. L. Bohn, "NO evaporative cooling in the $^2\Pi_{3/2}$ state," Phys. Rev. A **97**, 062703 (2018).

[131] L. D. Augustovičová and J. L. Bohn, "Ultracold collisions of polyatomic molecules: CaOH," New J. Phys. **21**, 103022 (2019).

[132] X.-Y. Chen, A. Schindewolf, S. Eppelt, R. Bause, M. Duda, S. Biswas, T. Karman, T. Hilker, I. Bloch, and X.-Y. Luo, "Field-linked resonances of polar molecules," Nature **614**, 59–63 (2023).

[133] X.-Y. Chen, S. Biswas, S. Eppelt, A. Schindewolf, F. Deng, T. Shi, S. Yi, T. A. Hilker, I. Bloch, and X.-Y. Luo, "Ultracold field-linked tetratomic molecules," Nature **626**, 283–287 (2024).

[134] M. Morita, J. Kłos, A. A. Buchachenko, and T. V. Tscherbul, "Cold collisions of heavy $^2\Sigma$ molecules with alkali-metal atoms in a magnetic field: Ab initio analysis and prospects for sympathetic cooling of SrOH ($^2\Sigma^+$) by Li (^2S)," Physical Review A **95**, 063421 (2017).

[135] P. Wójcik, T. Korona, and M. Tomza, "Interactions of benzene, naphthalene, and azulene with alkali-metal and alkaline-earth-metal atoms for ultracold studies," The Journal of Chemical Physics **150**, 234106 (2019).

[136] C. Zhang, S. T. Rittenhouse, T. V. Tscherbul, H. R. Sadeghpour, and N. R. Hutzler, "Sympathetic cooling and slowing of molecules with rydberg atoms," Phys. Rev. Lett. **132**, 033001 (2024).

[137] W. C. Campbell and J. M. Doyle, "Cooling, trap loading, and beam production using a cryogenic helium buffer gas," in *Cold Molecules: Theory, Experiment, Applications* (CRC Press: Boca Raton, FL, 2009) pp. 473–508.

[138] N. R. Hutzler, H.-I. Lu, and J. M. Doyle, "The buffer gas beam: an intense, cold, and slow source for atoms and molecules," Chem. Rev. **112**, 4803–4827 (2012).

[139] Y.-X. Liu, L. Zhu, J. Luke, J. J. A. Houwman, M. C. Babin, M.-G. Hu, and K.-K. Ni, "Quantum interference in atom-exchange reactions," Science **384**, 1117–1121 (2024).

[140] I. Kozyryev and N. R. Hutzler, "Precision measurement of time-reversal symmetry violation with laser-cooled polyatomic molecules," Phys. Rev. Lett. **119**, 133002 (2017).

[141] D. E. Maison, L. V. Skripnikov, and V. V. Flambaum, "Theoretical study of ^{173}YbOH to search for the nuclear magnetic quadrupole moment," Phys. Rev. A **100**, 032514 (2019).

[142] P. Yu and N. R. Hutzler, "Probing fundamental symmetries of deformed nuclei in symmetric top molecules," Phys. Rev. Lett. **126**, 023003 (2021).

[143] A. Zakharova and A. Petrov, "$\mathcal{P}$, $\mathcal{T}$-odd effects for the RaOH molecule in the excited vibrational state," Phys. Rev. A **103**, 032819 (2021).

[144] C. Zhang, P. Yu, A. Jadbabaie, and N. R. Hutzler, "Quantum-enhanced metrology for molecular symmetry violation using decoherence-free subspaces," Phys. Rev. Lett. **131**, 193602 (2023).

[145] Y. Takahashi, C. Zhang, A. Jadbabaie, and N. R. Hutzler, "Engineering field-insensitive molecular clock transitions for symmetry violation searches," Phys. Rev. Lett. **131**, 183003 (2023).

[146] E. B. Norrgard, D. S. Barker, S. Eckel, J. A. Fedchak, N. N. Klimov, and J. Scherschligt, "Nuclear-spin dependent parity violation in optically trapped polyatomic molecules," Communications Physics **2**, 1–6 (2019).

[147] M. Quack, "How important is parity violation for molecular and biomolecular chirality?" Angew. Chem. **41**, 4618–4630 (2002).

[148] D. G. Blackmond, "The origin of biological homochirality," Philos. Trans. R. Soc. B **366**, 2878–2884 (2011).

[149] A. Cournol, M. Manceau, M. Pierens, L. Lecordier, D. Tran, R. Santagata, B. Argence, A. Goncharov, O. Lopez, M. Abgrall, Y. Le Coq, R. Le Targat, H. Álvarez Martinez, W. Lee, D. Xu, P.-E. Pottie, R. Hendricks, T. Wall, J. Bieniewska, B. Sauer, M. Tarbutt, A. Amy-Klein, S. Tokunaga, and B. Darquié, "A new experiment to test parity symmetry in cold chiral molecules using vibrational spectroscopy," Quantum Electronics **49**, 288 (2019).

[150] K. Gaul, M. G. Kozlov, T. A. Isaev, and R. Berger, "Chiral molecules as sensitive probes for direct detection of $\mathcal{P}$-odd cosmic fields," Phys. Rev. Lett. **125**, 123004 (2020).

[151] C. N. Cohen-Tannoudji, "Nobel lecture: Manipulating atoms with photons," Rev. Mod. Phys. **70**, 707–719 (1998).

[152] S. Y. Van De Meerakker, H. L. Bethlem, and G. Meijer, "Taming molecular beams," Nature Physics **4**, 595–602 (2008).

[153] D. Comparat, "Molecular cooling via Sisyphus processes," Phys. Rev. A **89**, 043410 (2014).

[154] A. Prehn, M. Ibrügger, R. Glöckner, G. Rempe, and M. Zeppenfeld, "Optoelectrical cooling of polar molecules to submillikelvin temperatures," Phys. Rev. Lett. **116**, 063005 (2016).

[155] L. De Marco, G. Valtolina, K. Matsuda, W. G. Tobias, J. P. Covey, and J. Ye, "A degenerate Fermi gas of polar molecules," Science **363**, 853–856 (2019).

[156] F. Wolf, Y. Wan, J. C. Heip, F. Gebert, C. Shi, and P. O. Schmidt, "Non-destructive state detection for quantum logic spectroscopy of molecular ions," Nature **530**, 457–460 (2016).

[157] C.-w. Chou, C. Kurz, D. B. Hume, P. N. Plessow, D. R. Leibrandt, and D. Leibfried, "Preparation and coherent manipulation of pure quantum states of a single molecular ion," Nature **545**, 203–207 (2017).

[158] J. D. Weinstein, R. DeCarvalho, T. Guillet, B. Friedrich, and J. M. Doyle, "Magnetic trapping of calcium monohydride molecules at millikelvin temperatures," Nature **395**, 148–150 (1998).

[159] W. C. Campbell, E. Tsikata, H.-I. Lu, L. D. van Buuren, and J. M. Doyle, "Magnetic trapping and zeeman relaxation of NH ($X\,^3\Sigma^-$)," Phys. Rev. Lett. **98**, 213001 (2007).

[160] H.-I. Lu, I. Kozyryev, B. Hemmerling, J. Piskorski, and J. M. Doyle, "Magnetic trapping of molecules via optical loading and magnetic slowing," Physical review letters **112**, 113006 (2014).

[161] A. Singh, L. Maisenbacher, Z. Lin, J. J. Axelrod, C. D. Panda, and H. Müller, "Dynamics of a buffer-gas-loaded, deep optical trap for molecules," Phys. Rev. Res. **5**, 033008 (2023).

[162] H. L. Bethlem, G. Berden, and G. Meijer, "Decelerating neutral dipolar molecules," Phys. Rev. Lett. **83**, 1558–1561 (1999).

[163] N. Akerman, M. Karpov, L. David, E. Lavert-Ofir, J. Narevicius, and E. Narevicius, "Simultaneous deceleration of atoms and molecules in a supersonic beam," New Journal of Physics **17**, 065015 (2015).

[164] R. Fulton, A. I. Bishop, and P. F. Barker, "Optical stark decelerator for molecules," Phys. Rev. Lett. **93**, 243004 (2004).

[165] N. Fitch and M. Tarbutt, "Principles and design of a Zeeman–Sisyphus decelerator for molecular beams," ChemPhysChem **17**, 3609–3623 (2016).

[166] B. L. Augenbraun, A. Frenett, H. Sawaoka, C. Hallas, N. B. Vilas, A. Nasir, Z. D. Lasner, and J. M. Doyle, "Zeeman-Sisyphus deceleration of molecular beams," Phys. Rev. Lett. **127**, 263002 (2021).

[167] S. Chervenkov, X. Wu, J. Bayerl, A. Rohlfes, T. Gantner, M. Zeppenfeld, and G. Rempe, "Continuous centrifuge decelerator for polar molecules," Phys. Rev. Lett. **112**, 013001 (2014).

[168] H. L. Bethlem, G. Berden, F. M. Crompvoets, R. T. Jongma, A. J. Van Roij, and G. Meijer, "Electrostatic trapping of ammonia molecules," Nature **406**, 491–494 (2000).

[169] S. Y. van de Meerakker, P. H. Smeets, N. Vanhaecke, R. T. Jongma, and G. Meijer, "Deceleration and electrostatic trapping of OH radicals," Phys. Rev. Lett. **94**, 023004 (2005).

[170] B. C. Sawyer, B. L. Lev, E. R. Hudson, B. K. Stuhl, M. Lara, J. L. Bohn, and J. Ye, "Magnetoelectrostatic trapping of ground state OH molecules," Phys. Rev. Lett. **98**, 253002 (2007).

[171] S. Hoekstra, J. J. Gilijamse, B. Sartakov, N. Vanhaecke, L. Scharfenberg, S. Y. T. van de Meerakker, and G. Meijer, "Optical pumping of trapped neutral molecules by blackbody radiation," Phys. Rev. Lett. **98**, 133001 (2007).

[172] N. Akerman, M. Karpov, Y. Segev, N. Bibelnik, J. Narevicius, and E. Narevicius, "Trapping of molecular oxygen together with lithium atoms," Phys. Rev. Lett. **119**, 073204 (2017).

[173] Y. Segev, M. Pitzer, M. Karpov, N. Akerman, J. Narevicius, and E. Narevicius, "Collisions between cold molecules in a superconducting magnetic trap," Nature **572**, 189–193 (2019).

[174] Y. Liu, M. Vashishta, P. Djuricanin, S. Zhou, W. Zhong, T. Mittertreiner, D. Carty, and T. Momose, "Magnetic trapping of cold methyl radicals," Phys. Rev. Lett. **118**, 093201 (2017).

[175] M. Zeppenfeld, M. Motsch, P. W. Pinkse, and G. Rempe, "Optoelectrical cooling of polar molecules," Physical Review A **80**, 041401 (2009).

[176] M. Zeppenfeld, B. G. Englert, R. Glöckner, A. Prehn, M. Mielenz, C. Sommer, L. D. van Buuren, M. Motsch, and G. Rempe, "Sisyphus cooling of electrically trapped polyatomic molecules," Nature **491**, 570 (2012).

[177] A. Prehn, M. Ibrügger, G. Rempe, and M. Zeppenfeld, "High-resolution "magic"-field spectroscopy on trapped polyatomic molecules," Phys. Rev. Lett. **127**, 173602 (2021).

[178] M. Löw, M. Ibrügger, G. Rempe, and M. Zeppenfeld, "Coherence of symmetry-protected rotational qubits in cold polyatomic molecules," Phys. Rev. Lett. **134**, 113402 (2025).

[179] K.-K. Ni, S. Ospelkaus, M. De Miranda, A. Pe'Er, B. Neyenhuis, J. Zirbel, S. Kotochigova, P. Julienne, D. Jin, and J. Ye, "A high phase-space-density gas of polar molecules," Science **322**, 231–235 (2008).

[180] J. T. Zhang, L. R. B. Picard, W. B. Cairncross, K. Wang, Y. Yu, F. Fang, and K.-K. Ni, "An optical tweezer array of ground-state polar molecules," Quantum Science and Technology **7**, 035006 (2022).

[181] D. K. Ruttley, A. Guttridge, T. R. Hepworth, and S. L. Cornish, "Enhanced quantum control of individual ultracold molecules using optical tweezer arrays," PRX Quantum **5**, 020333 (2024).

[182] H. Yang, D.-C. Zhang, L. Liu, Y.-X. Liu, J. Nan, B. Zhao, and J.-W. Pan, "Observation of magnetically tunable feshbach resonances in ultracold $^{23}Na^{40}K + ^{40}K$ collisions," Science **363**, 261–264 (2019).

[183] H. Yang, X.-Y. Wang, Z. Su, J. Cao, D.-C. Zhang, J. Rui, B. Zhao, C.-L. Bai, and J.-W. Pan, "Evidence for the association of triatomic molecules in ultracold $^{23}Na^{40}K + ^{40}K$ mixtures," Nature **602**, 229–233 (2022).

[184] H. Yang, J. Cao, Z. Su, J. Rui, B. Zhao, and J.-W. Pan, "Creation of an ultracold gas of triatomic molecules from an atom–diatomic molecule mixture," Science **378**, 1009–1013 (2022).

[185] J. Cao, B.-Y. Wang, H. Yang, Z.-J. Fan, Z. Su, J. Rui, B. Zhao, and J.-W. Pan, "Observation of photoassociation resonances in ultracold atom-molecule collisions," Phys. Rev. Lett. **132**, 093403 (2024).

[186] A. Younes and W. C. Campbell, "Laser-type cooling with unfiltered sunlight," Phys. Rev. E **109**, 034109 (2024).

[187] A. Younes, R. Putnam, P. Hamilton, and W. C. Campbell, "Internal state cooling of an atom with thermal light," Entropy **27** (2025), 10.3390/e27030222.

[188] W. Campbell and B. Augenbraun, "Photon spin molasses for laser cooling molecular rotation," Journal of Molecular Spectroscopy **385**, 111596 (2022).

[189] M. Di Rosa, "Laser-cooling molecules," Eur. Phys. J. D **31**, 395–402 (2004).

[190] B. K. Stuhl, B. C. Sawyer, D. Wang, and J. Ye, "Magneto-optical trap for polar molecules," Phys. Rev. Lett. **101**, 243002 (2008).

[191] E. S. Shuman, J. F. Barry, and D. DeMille, "Laser cooling of a diatomic molecule," Nature **467**, 820 (2010).

[192] J. F. Barry, D. McCarron, E. Norrgard, M. Steinecker, and D. DeMille, "Magneto-optical trapping of a diatomic molecule," Nature **512**, 286 (2014).

[193] S. Truppe, H. Williams, M. Hambach, L. Caldwell, N. Fitch, E. Hinds, B. Sauer, and M. Tarbutt, "Molecules cooled below the Doppler limit," Nat. Phys. **13**, 1173 (2017).

[194] L. Anderegg, B. L. Augenbraun, E. Chae, B. Hemmerling, N. R. Hutzler, A. Ravi, A. Collopy, J. Ye, W. Ketterle, and J. M. Doyle, "Radio frequency magneto-optical trapping of CaF with high density," Phys. Rev. Lett. **119**, 103201 (2017).

[195] A. L. Collopy, S. Ding, Y. Wu, I. A. Finneran, L. Anderegg, B. L. Augenbraun, J. M. Doyle, and J. Ye, "3D magneto-optical trap of yttrium monoxide," Phys. Rev. Lett. **121**, 213201 (2018).

[196] Z. Zeng, S. Deng, S. Yang, and B. Yan, "Three-dimensional magneto-optical trapping of barium monofluoride," Phys. Rev. Lett. **133**, 143404 (2024).

[197] H. Williams, L. Caldwell, N. Fitch, S. Truppe, J. Rodewald, E. Hinds, B. Sauer, and M. Tarbutt, "Magnetic trapping and coherent control of laser-cooled molecules," Phys. Rev. Lett. **120**, 163201 (2018).

[198] D. McCarron, M. Steinecker, Y. Zhu, and D. DeMille, "Magnetic trapping of an ultracold gas of polar molecules," Phys. Rev. Lett. **121**, 013202 (2018).

[199] L. Anderegg, B. L. Augenbraun, Y. Bao, S. Burchesky, L. W. Cheuk, W. Ketterle, and J. M. Doyle, "Laser cooling of optically trapped molecules," Nat. Phys. **14**, 890 (2018).

[200] T. K. Langin, V. Jorapur, Y. Zhu, Q. Wang, and D. DeMille, "Polarization enhanced deep optical dipole trapping of Λ-cooled polar molecules," Phys. Rev. Lett. **127**, 163201 (2021).

[201] Y. Wu, J. J. Burau, K. Mehling, J. Ye, and S. Ding, "High phase-space density of laser-cooled molecules in an optical lattice," Phys. Rev. Lett. **127**, 263201 (2021).

[202] L. Anderegg, L. W. Cheuk, Y. Bao, S. Burchesky, W. Ketterle, K.-K. Ni, and J. M. Doyle, "An optical tweezer array of ultracold molecules," Science **365**, 1156–1158 (2019).

[203] C. M. Holland, Y. Lu, and L. W. Cheuk, "Bichromatic imaging of single molecules in an optical tweezer array," Phys. Rev. Lett. **131**, 053202 (2023).

[204] V. Jorapur, T. K. Langin, Q. Wang, G. Zheng, and D. DeMille, "High density loading and collisional loss of laser-cooled molecules in an optical trap," Phys. Rev. Lett. **132**, 163403 (2024).

[205] S. Burchesky, L. Anderegg, Y. Bao, S. S. Yu, E. Chae, W. Ketterle, K.-K. Ni, and J. M. Doyle, "Rotational coherence times of polar molecules in optical tweezers," Phys. Rev. Lett. **127**, 123202 (2021).

[206] Y. Lu, S. J. Li, C. M. Holland, and L. W. Cheuk, "Raman sideband cooling of molecules in an optical tweezer array," Nature Physics **20**, 389–394 (2024).

[207] E. B. Norrgard, Y. Chamorro, C. C. Cooksey, S. P. Eckel, N. H. Pilgram, K. J. Rodriguez, H. W. Yoon, L. c. v. F. Pašteka, and A. Borschevsky, "Radiative decay rate and branching fractions of MgF," Phys. Rev. A **108**, 032809 (2023).

[208] Q. Sun, C. E. Dickerson, J. Dai, I. M. Pope, L. Cheng, D. Neuhauser, A. N. Alexandrova, D. Mitra, and T. Zelevinsky, "Probing the limits of optical cycling in a predissociative diatomic molecule," Phys. Rev. Res. **5**, 043070 (2023).

[209] S. Hofsäss, M. Doppelbauer, S. C. Wright, S. Kray, B. G. Sartakov, J. Pérez-Ríos, G. Meijer, and S. Truppe, "Optical cycling of AlF molecules," New Journal of Physics **23**, 075001 (2021).

[210] J. R. Daniel, J. C. Shaw, C. Wang, L.-R. Liu, B. K. Kendrick, B. Hemmerling, and D. J. McCarron, "Hyperfine structure of the $A^1\Pi$ state of AlCl and its relevance to laser cooling and trapping," Phys. Rev. A **108**, 062821 (2023).

[211] J. C. Schnaubelt, J. C. Shaw, and D. J. McCarron, "Cold CH radicals for laser cooling and trapping," arXiv:2109.03953 (2021).

[212] A. M. Ellis, "Main group metal-ligand interactions in small molecules: New insights from laser spectroscopy," International Reviews in Physical Chemistry **20**, 551–590 (2001).

[213] I. Kozyryev, T. C. Steimle, P. Yu, D.-T. Nguyen, and J. M. Doyle, "Determination of CaOH and $CaOCH_3$ vibrational branching ratios for direct laser cooling and trapping," New J. Phys. **21**, 052002 (2019).

[214] B. L. Augenbraun, *Methods for Direct Laser Cooling of Polyatomic Molecules*, Ph.D. thesis, Harvard University (2021).

[215] A. Frenett, Z. Lasner, L. Cheng, and J. M. Doyle, "Vibrational branching fractions for laser cooling of nonlinear strontium-containing molecules," Phys. Rev. A **110**, 022811 (2024).

[216] I. Kozyryev, L. Baum, K. Matsuda, B. Hemmerling, and J. M. Doyle, "Radiation pressure force from optical cycling on a polyatomic molecule," Journal of Physics B: Atomic, Molecular and Optical Physics **49**, 134002 (2016).

[217] I. Kozyryev, L. Baum, K. Matsuda, B. L. Augenbraun, L. Anderegg, A. P. Sedlack, and J. M. Doyle, "Sisyphus laser cooling of a polyatomic molecule," Phys. Rev. Lett. **118**, 173201 (2017).

[218] I. Kozyryev, L. Baum, L. Aldridge, P. Yu, E. E. Eyler, and J. M. Doyle, "Coherent bichromatic force deflection of molecules," Phys. Rev. Lett. **120**, 063205 (2018).

[219] B. L. Augenbraun, Z. D. Lasner, A. Frenett, H. Sawaoka, C. Miller, T. C. Steimle, and J. M. Doyle, "Laser-cooled polyatomic molecules for improved electron electric dipole moment searches," New J. Phys. **22**, 022003 (2020).

[220] L. Baum, N. B. Vilas, C. Hallas, B. L. Augenbraun, S. Raval, D. Mitra, and J. M. Doyle, "1D magneto-optical trap of polyatomic molecules," Phys. Rev. Lett. **124**, 133201 (2020).

[221] Z. D. Lasner, A. Frenett, H. Sawaoka, L. Anderegg, B. Augenbraun, H. Lampson, M. Li, A. Lunstad, J. Mango, A. Nasir, T. Ono, T. Sakamoto, and J. M. Doyle, "Magneto-optical trapping of a heavy polyatomic molecule for precision measurement," Phys. Rev. Lett. **134**, 083401 (2025).

[222] J. F. Barry, E. Shuman, E. Norrgard, and D. DeMille, "Laser radiation pressure slowing of a molecular beam," Phys. Rev. Lett. **108**, 103002 (2012).

[223] B. Hemmerling, E. Chae, A. Ravi, L. Anderegg, G. K. Drayna, N. R. Hutzler, A. L. Collopy, J. Ye, W. Ketterle, and J. M. Doyle, "Laser slowing of CaF molecules to near the capture velocity of a molecular MOT," J. Phys. B **49**, 174001 (2016).

[224] S. Truppe, H. Williams, N. Fitch, M. Hambach, T. Wall, E. Hinds, B. Sauer, and M. Tarbutt, "An intense, cold, velocity-controlled molecular beam by frequency-chirped laser slowing," New J. Phys. **19**, 022001 (2017).

[225] K. N. Jarvis, J. A. Devlin, T. E. Wall, B. E. Sauer, and M. R. Tarbutt, "Blue-detuned magneto-optical trap," Phys. Rev. Lett. **120**, 083201 (2018).

[226] J. J. Burau, P. Aggarwal, K. Mehling, and J. Ye, "Blue-detuned magneto-optical trap of molecules," Phys. Rev. Lett. **130**, 193401 (2023).

[227] S. J. Li, C. M. Holland, Y. Lu, and L. W. Cheuk, "Blue-detuned magneto-optical trap of CaF molecules," Phys. Rev. Lett. **132**, 233402 (2024).

[228] C. Hallas, G. K. Li, N. B. Vilas, P. Robichaud, L. Anderegg, and J. M. Doyle, "High compression blue-detuned magneto-optical trap of polyatomic molecules," arXiv:2404.03636 (2024).

[229] S. S. Yu, J. You, Y. Bao, L. Anderegg, C. Hallas, G. K. Li, D. Lim, E. Chae, W. Ketterle, K.-K. Ni, and J. M. Doyle, "A conveyor-belt magneto-optical trap of CaF," arXiv:2409.15262 (2024).

[230] G. K. Li, C. Hallas, and J. M. Doyle, "Conveyor-belt magneto-optical trapping of molecules," New Journal of Physics **27**, 043002 (2025).

[231] L. W. Cheuk, L. Anderegg, B. L. Augenbraun, Y. Bao, S. Burchesky, W. Ketterle, and J. M. Doyle, "Λ-enhanced imaging of molecules in an optical trap," Phys. Rev. Lett. **121**, 083201 (2018).

[232] L. Caldwell, J. Devlin, H. Williams, N. Fitch, E. Hinds, B. Sauer, and M. Tarbutt, "Deep laser cooling and efficient magnetic compression of molecules," Phys. Rev. Lett. **123**, 033202 (2019).

[233] S. Ding, Y. Wu, I. A. Finneran, J. J. Burau, and J. Ye, "Sub-Doppler cooling and compressed trapping of YO molecules at μK temperatures," Phys. Rev. X **10**, 021049 (2020).

[234] W. Demtröder, *Molecular Physics: Theoretical Principles and Experimental Methods* (WILEY-VCH Verlag GmbH & Co. KGaA, 2005).

[235] S. F. Rice, H. Martin, and R. W. Field, "The electronic structure of the calcium monohalides. a ligand field approach," J. Chem. Phys. **82**, 5023–5034 (1985).

[236] P. F. Bernath, *Spectra of Atoms and Molecules* (New York: Oxford University Press, 2005).

[237] R. C. Hilborn, Z. Qingshi, and D. O. Harris, "Laser spectroscopy of the AX transitions of CaOH and CaOD," J. Mol. Spectrosc. **97**, 73–91 (1983).

[238] P. Bernath and S. Kinsey-Nielsen, "Dye laser spectroscopy of the $B^2\Sigma^+$-$X^2\Sigma^+$ transition of CaOH," Chem. Phys. Lett. **105**, 663–666 (1984).

[239] C. Jarman and P. Bernath, "High resolution laser spectroscopy of the $\widetilde{C}^2\delta$–$\widetilde{X}^2\sigma^+$ transition of CaOH and CaOD: Vibronic coupling and the Renner–Teller effect," J. Chem. Phys. **97**, 1711–1718 (1992).

[240] R. Pereira and D. H. Levy, "Observation and spectroscopy of high-lying states of the CaOH radical: Evidence for a bent, covalent state," J. Chem. Phys. **105**, 9733–9739 (1996).

[241] R. A. Hailey, C. Jarman, and P. F. Bernath, "Optical–optical double resonance spectroscopy: The $\widetilde{G}^2\pi$ state of CaOH and CaOD," The Journal of Chemical Physics **107**, 669–670 (1997).

[242] M. Dick, P. Sheridan, J.-G. Wang, S. Yu, and P. Bernath, "Optical-optical double resonance spectroscopy of the $\widetilde{D}^2\Sigma^+ - \widetilde{A}^2\Pi_{1/2}$ transition of CaOH," J. Mol. Spectrosc. **240**, 238 – 243 (2006).

[243] J. V. Ortiz, "Ground and excited states of $CaCH_3$, $CaNH_2$, CaOH, and CaF through electron propagator calculations," The Journal of Chemical Physics **92**, 6728–6731 (1990).

[244] P. R. Bunker and P. Jensen, *Molecular Symmetry and Spectroscopy* (NRC Research Press, 2006).

[245] G. Herzberg, *Molecular spectra and molecular structure. Vol. 3: Electronic spectra and electronic structure of polyatomic molecules* (New York: Van Nostrand, 1966).

[246] G. Herzberg, *Molecular spectra and molecular structure. Vol. 2: Infrared and Raman spectra of polyatomic molecules* (New York: Van Nostrand, 1945).

[247] E. Fermi, "Über den ramaneffekt des kohlendioxyds," Z. Phys. **71**, 250–259 (1931).

[248] J. T. Hougen, "Fermi resonance in linear triatomic molecules in Π electronic states," J. Chem. Phys. **37**, 403–408 (1962).

[249] J. A. Coxon, M. Li, and P. I. Presunka, "Investigation of excited vibrational levels in the $\widetilde{X}^2\sigma^+$ state of CaOH and CaOD by resolved fluorescence spectroscopy," Mol. Phys. **76**, 1463–1476 (1992).

[250] M. Li and J. A. Coxon, "Dye laser excitation studies of the $\widetilde{A}^2\pi$ (100)/(020)–$\widetilde{X}^2\sigma$+(020)/(000) bands of CaOD: Analysis of the $\widetilde{A}^2\pi$ (100) (020) Fermi resonance," J. Chem. Phys. **104**, 4961–4977 (1996).

[251] L. Baum, N. B. Vilas, C. Hallas, B. L. Augenbraun, S. Raval, D. Mitra, and J. M. Doyle, "Establishing a nearly closed cycling transition in a polyatomic molecule," Phys. Rev. A **103**, 043111 (2021).

[252] E. Hirota, *High-Resolution Spectroscopy of Transient Molecules*, Springer Series in Chemical Physics, Vol. 40 (Springer Berlin Heidelberg, Berlin, Heidelberg, 1985).

[253] J. M. Brown and A. Carrington, *Rotational Spectroscopy of Diatomic Molecules* (Cambridge University Press, 2003).

[254] C. Scurlock, D. Fletcher, and T. Steimle, "Hyperfine structure in the (0,0,0) $\tilde{X}^2\Sigma^+$ state of CaOH observed by pump/probe microwave-optical double resonance," J. Mol. Spectrosc. **159**, 350–356 (1993).

[255] D. Trung, Private Communication (2019).

[256] T. Steimle, D. Fletcher, K. Jung, and C. Scurlock, "A supersonic molecular beam optical stark study of CaOH and SrOH," Journal Chem. Phys. **96**, 2556–2564 (1992).

[257] J. Devlin, M. Tarbutt, D. Kokkin, and T. Steimle, "Measurements of the Zeeman effect in the $a^2\pi$ and $b^2\sigma^+$ states of calcium fluoride," Journal of Molecular Spectroscopy **317**, 1–9 (2015).

[258] W. Quapp and B. P. Winnewisser, "What you thought you already knew about the bending motion of triatomic molecules," Journal of Mathematical Chemistry **14**, 259–285 (1993).

[259] A. Merer and J. Allegretti, "Rotational energies of linear polyatomic molecules in vibrationally degenerate levels of electronic $^2\Sigma$ and $^3\Sigma$ states," Canadian Journal of Physics **49**, 2859–2869 (1971).

[260] W. T. Raynes, "Spin splittings and rotational structure of nonlinear molecules in doublet and triplet electronic states," The Journal of Chemical Physics **41**, 3020–3032 (1964).

[261] M. Tarbutt and T. Steimle, "Modeling magneto-optical trapping of CaF molecules," Physical Review A **92**, 053401 (2015).

[262] M. Tarbutt, "Magneto-optical trapping forces for atoms and molecules with complex level structures," New J. Phys. **17**, 015007 (2015).

[263] J. T. Hougen, "Rotational energy levels of a linear triatomic molecule in a $^2\Pi$ electronic state," J. Chem. Phys. **36**, 519 (1962).

[264] J. M. Brown, "The effective Hamiltonian for the Renner-Teller effect," J. Mol. Spectrosc. **68**, 412–422 (1977).

[265] P. Bolman and J. Brown, "The Renner-Teller effect and vibronically induced bands in the electronic spectrum of NCO," Chem. Phys. Lett. **21**, 213 – 216 (1973).

[266] F. Northrup and T. J. Sears, "Renner-Teller, spin-orbit and Fermi-resonance interactions in $X^2\Pi$ NCS investigated by LIF spectroscopy," Mol. Phys. **71**, 45–64 (1990).

[267] P. I. Presunka and J. A. Coxon, "Laser spectroscopy of the $\widetilde{A}^2\pi$–$\widetilde{X}^2\sigma^+$ transition of SrOH: Deperturbation analysis of K-resonance in the $v_2 = 1$ level of the $\widetilde{A}^2\pi$ state," J. Chem. Phys. **101**, 201–222 (1994).

[268] M. Li and J. A. Coxon, "The CaCCH $\tilde{A}\,^2\Pi - \tilde{X}\,^2\Sigma^+$ 5_2^2 and 5_2^0 bands studies by high resolution spectroscopy: The Ca–C–C bending vibration and vibronic interaction," J. Mol. Spectrosc. **183**, 250–262 (1997).

[269] C. Zhang, B. L. Augenbraun, Z. D. Lasner, N. B. Vilas, J. M. Doyle, and L. Cheng, "Accurate prediction and measurement of vibronic branching ratios for laser cooling linear polyatomic molecules," J. Chem. Phys. **155**, 091101 (2021).

[270] M. Li and J. A. Coxon, "Laser spectroscopy of the CaOH $\widetilde{A}^2\pi$–$\widetilde{X}^2\sigma^+$(020)–(000) band: Deperturbation of the Fermi resonance, Renner–Teller, and spin–orbit interactions," J. Chem. Phys. **97**, 8961–8969 (1992).

[271] E. E. Whiting, A. Schadee, J. B. Tatum, J. T. Hougen, and R. W. Nicholls, "Recommended conventions for defining transition moments and intensity factors in diatomic molecular spectra," J. Mol. Spectrosc. **80**, 249–256 (1980).

[272] A. Hansson and J. K. Watson, "A comment on Hönl-London factors," J. Mol. Spectrosc. **233**, 169–173 (2005).

[273] L. W. Baum, *Laser cooling and 1D magneto-optical trapping of calcium monohydroxide*, Ph.D. thesis, Harvard University (2020).

[274] Y. Bao, *Ultracold molecules in an optical tweezer array: From dipolar interaction to ground state cooling*, Ph.D. thesis, Harvard University (2024).

[275] W. C. Campbell, *Magnetic Trapping of Imidogen Molecules*, Ph.D. thesis, Harvard University (2008).

[276] H.-I. Lu, J. Rasmussen, M. J. Wright, D. Patterson, and J. M. Doyle, "A cold and slow molecular beam," Physical Chemistry Chemical Physics **13**, 18986–18990 (2011).

[277] H. Lu, *Magnetic trapping of molecules via optical loading and magnetic slowing*, Ph.D. thesis, Harvard University (2013).

[278] L. Anderegg, *Ultracold molecules in optical arrays: from laser cooling to molecular collisions*, Ph.D. thesis, Harvard University (2019).

[279] M. D. Oberlander and J. M. Parson, "Laser excited fluorescence study of reactions of excited ca and sr with water and alcohols: Product selectivity and energy disposal," The Journal of Chemical Physics **105**, 5806–5816 (1996).

[280] A. Jadbabaie, N. H. Pilgram, J. Klos, S. Kotochigova, and N. R. Hutzler, "Enhanced molecular yield from a cryogenic buffer gas beam source via excited state chemistry," New J. Phys. (2020).

[281] J. K. os and S. Kotochigova, Private Communication (2020).

[282] D. Patterson and J. M. Doyle, "Bright, guided molecular beam with hydrodynamic enhancement," J. Chem. Phys. **126**, 154307 (2007).

[283] A. Roth, *Vacuum technology* (Amsterdam: Elsevier, 1990).

[284] J. F. Barry, *Laser cooling and slowing of a diatomic molecule*, Ph.D. thesis, Yale University (2013).

[285] S. Popa, S. Schaller, A. Fielicke, J. Lim, B. G. Sartakov, M. R. Tarbutt, and G. Meijer, "Understanding inner-shell excitations in molecules through spectroscopy of the $4f$ hole states of YbF," Phys. Rev. X **14**, 021035 (2024).

[286] I. Kozyryev, *Laser Cooling and Inelastic Collisions of the Polyatomic Radical SrOH*, Ph.D. thesis, Harvard University (2017).

[287] E. Murad, "Thermochemical properties of the gaseous alkaline earth monohydroxides," The Journal of Chemical Physics **75**, 4080–4085 (1981).

[288] L. T. Earls, "Intensities in $^2\Pi - {}^2\Sigma$ transitions in diatomic molecules," Phys. Rev. **48**, 423 (1935).

[289] D. J. Berkeland and M. G. Boshier, "Destabilization of dark states and optical spectroscopy in Zeeman-degenerate atomic systems," Phys. Rev. A **65**, 033413 (2002).

[290] M. J. Dick, *Spectroscopy of selected calcium and strontium containing polyatomic molecules*, Ph.D. thesis, University of Waterloo (2007).

[291] N. H. Pilgram, A. Jadbabaie, Y. Zeng, N. R. Hutzler, and T. C. Steimle, "Fine and hyperfine interactions in ^{171}YbOH and ^{173}YbOH," J. Chem. Phys. **154**, 244309 (2021).

[292] C. Zhang, N. R. Hutzler, and L. Cheng, "Intensity-borrowing mechanisms pertinent to laser cooling of linear polyatomic molecules," Journal of Chemical Theory and Computation **19**, 4136–4148 (2023).

[293] Z. Lasner, A. Lunstad, C. Zhang, L. Cheng, and J. M. Doyle, "Vibronic branching ratios for nearly closed rapid photon cycling of sroh," Phys. Rev. A **106**, L020801 (2022).

[294] D.-T. Nguyen, T. C. Steimle, I. Kozyryev, M. Huang, and A. B. McCoy, "Fluorescence branching ratios and magnetic tuning of the visible spectrum of SrOH," J. Mol. Spectrosc. **347**, 7–18 (2018).

[295] A. C. Paul, K. Sharma, M. A. Reza, H. Telfah, T. A. Miller, and J. Liu, "Laser-induced fluorescence and dispersed-fluorescence spectroscopy of the $\widetilde{A}^2E - \widetilde{X}^2A_1$ transition of jet-cooled calcium methoxide ($CaOCH_3$) radicals," The Journal of Chemical Physics **151**, 134303 (2019).

[296] E. T. Mengesha, A. T. Le, T. C. Steimle, L. Cheng, C. Zhang, B. L. Augenbraun, Z. Lasner, and J. Doyle, "Branching ratios, radiative lifetimes, and transition dipole moments for YbOH," J. Phys. Chem. A **124**, 3135–3148 (2020).

[297] H. Williams, S. Truppe, M. Hambach, L. Caldwell, N. Fitch, E. Hinds, B. Sauer, and M. Tarbutt, "Characteristics of a magneto-optical trap of molecules," New J. Phys. **19**, 113035 (2017).

[298] M. Tarbutt, B. Sauer, J. Hudson, and E. Hinds, "Design for a fountain of YbF molecules to measure the electron's electric dipole moment," New J. Phys. **15**, 053034 (2013).

[299] E. Norrgard, D. McCarron, M. Steinecker, M. Tarbutt, and D. DeMille, "Submillikelvin dipolar molecules in a radio-frequency magneto-optical trap," Phys. Rev. Lett. **116**, 063004 (2016).

[300] C. J. Foot *et al.*, *Atomic physics*, Vol. 7 (Oxford University Press, 2005).

[301] M. Petzold, P. Kaebert, P. Gersema, M. Siercke, and S. Ospelkaus, "A Zeeman slower for diatomic molecules," New J. Phys. **20**, 042001 (2018).

[302] M. Petzold, P. Kaebert, P. Gersema, T. Poll, N. Reinhardt, M. Siercke, and S. Ospelkaus, "Type-II Zeeman slowing: Characterization and comparison to conventional radiative beam-slowing schemes," Phys. Rev. A **98**, 063408 (2018).

[303] E. Chae, *Laser Slowing of CaF Molecules and Progress towards a Dual-MOT for Li and CaF*, Ph.D. thesis, Harvard University (2015).

[304] E. Raab, M. Prentiss, A. Cable, S. Chu, and D. E. Pritchard, "Trapping of neutral sodium atoms with radiation pressure," Physical Review Letters **59**, 2631 (1987).

[305] M. T. Hummon, M. Yeo, B. K. Stuhl, A. L. Collopy, Y. Xia, and J. Ye, "2D magneto-optical trapping of diatomic molecules," Phys. Rev. Lett. **110**, 143001 (2013).

[306] J. A. Devlin and M. R. Tarbutt, "Three-dimensional doppler, polarization-gradient, and magneto-optical forces for atoms and molecules with dark states," New J. Phys. **18** (2016).

[307] O. Emile, R. Kaiser, C. Gerz, H. Wallis, A. Aspect, and C. Cohen-Tannoudji, "Magnetically assisted Sisyphus effect," J. Phys. II France **3**, 1709–1733 (1993).

[308] A. Aspect, E. Arimondo, R. Kaiser, N. Vansteenkiste, and C. Cohen-Tannoudji, "Laser cooling below the one-photon recoil energy by velocity-selective coherent population trapping," Phys. Rev. Lett. **61**, 826–829 (1988).

[309] J. Lawall, S. Kulin, B. Saubamea, N. Bigelow, M. Leduc, and C. Cohen-Tannoudji, "Three-dimensional laser cooling of helium beyond the single-photon recoil limit," Phys. Rev. Lett. **75**, 4194–4197 (1995).

[310] A. T. Grier, I. Ferrier-Barbut, B. S. Rem, M. Delehaye, L. Khaykovich, F. Chevy, and C. Salomon, "Λ-enhanced sub-Doppler cooling of lithium atoms in D_1 gray molasses," Phys. Rev. A **87**, 063411 (2013).

[311] J. Lim, J. Almond, M. Trigatzis, J. Devlin, N. Fitch, B. Sauer, M. Tarbutt, and E. Hinds, "Laser cooled YbF molecules for measuring the electron's electric dipole moment," Phys. Rev. Lett. **120**, 123201 (2018).

[312] J. A. Devlin and M. R. Tarbutt, "Laser cooling and magneto-optical trapping of molecules analyzed using optical Bloch equations and the Fokker-Planck-Kramers equation," Phys. Rev. A **98**, 063415 (2018).

[313] T. Rieger, T. Junglen, S. A. Rangwala, P. W. Pinkse, and G. Rempe, "Continuous loading of an electrostatic trap for polar molecules," Phys. Rev. Lett. **95**, 173002 (2005).

[314] J. Kleinert, C. Haimberger, P. J. Zabawa, and N. P. Bigelow, "Trapping of ultracold polar molecules with a thin-wire electrostatic trap," Phys. Rev. Lett. **99**, 143002 (2007).

[315] B. G. U. Englert, M. Mielenz, C. Sommer, J. Bayerl, M. Motsch, P. W. H. Pinkse, G. Rempe, and M. Zeppenfeld, "Storage and adiabatic cooling of polar molecules in a microstructured trap," Phys. Rev. Lett. **107**, 263003 (2011).

[316] T. Takekoshi, B. M. Patterson, and R. J. Knize, "Observation of optically trapped cold cesium molecules," Phys. Rev. Lett. **81**, 5105–5108 (1998).

[317] L. R. Liu, J. D. Hood, Y. Yu, J. T. Zhang, N. R. Hutzler, T. Rosenband, and K.-K. Ni, "Building one molecule from a reservoir of two atoms," Science **360**, 900–903 (2018).

[318] Y. Lu, C. M. Holland, and L. W. Cheuk, "Molecular laser cooling in a dynamically tunable repulsive optical trap," Phys. Rev. Lett. **128**, 213201 (2022).

[319] L. Caldwell, H. J. Williams, N. J. Fitch, J. Aldegunde, J. M. Hutson, B. E. Sauer, and M. R. Tarbutt, "Long rotational coherence times of molecules in a magnetic trap," Phys. Rev. Lett. **124**, 063001 (2020).

[320] R. Grimm, M. Weidemüller, and Y. B. Ovchinnikov, "Optical dipole traps for neutral atoms," in *Adv. At. Mol. Opt. Phys., Vol. 42*, edited by B. Bederson and H. Walther (Academic Press, 2000) Chap. 4, pp. 95–170.

[321] D. A. Steck, "Quantum and atom optics," Available online at `http://steck.us/teaching`.

[322] L. Caldwell and M. R. Tarbutt, "Sideband cooling of molecules in optical traps," Phys. Rev. Res. **2**, 013251 (2020).

[323] L. Caldwell, *Deep laser cooling and coherent control of molecules*, Ph.D. thesis, Imperial College London (2020).

[324] L. Cheng, Private Communication (2023).

[325] C. M. Taylor, R. K. Chaudhuri, and K. F. Freed, "Electronic structure of the calcium monohydroxide radical," J. Chem. Phys. **122**, 044317 (2005).

[326] P. D. Gregory, L. M. Fernley, A. L. Tao, S. L. Bromley, J. Stepp, Z. Zhang, S. Kotochigova, K. R. A. Hazzard, and S. L. Cornish, "Second-scale rotational coherence and dipolar interactions in a gas of ultracold polar molecules," Nature Physics **20**, 415–421 (2024).

[327] T. Rosenband, D. D. Grimes, and K.-K. Ni, "Elliptical polarization for molecular Stark shift compensation in deep optical traps," Opt. Express **26**, 19821–19825 (2018).

[328] A. J. Park, L. R. B. Picard, G. E. Patenotte, J. T. Zhang, T. Rosenband, and K.-K. Ni, "Extended rotational coherence of polar molecules in an elliptically polarized trap," Phys. Rev. Lett. **131**, 183401 (2023).

[329] R. A. Cline, J. D. Miller, M. R. Matthews, and D. J. Heinzen, "Spin relaxation of optically trapped atoms by light scattering," Opt. Lett. **19**, 207–209 (1994).

[330] C. Tuchendler, A. M. Lance, A. Browaeys, Y. R. P. Sortais, and P. Grangier, "Energy distribution and cooling of a single atom in an optical tweezer," Phys. Rev. A **78**, 033425 (2008).

[331] N. Vanhaecke and O. Dulieu, "Precision measurements with polar molecules: the role of the black body radiation," Mol. Phys. **105**, 1723–1731 (2007).

[332] S. Y. Buhmann, M. R. Tarbutt, S. Scheel, and E. A. Hinds, "Surface-induced heating of cold polar molecules," Phys. Rev. A **78**, 052901 (2008).

[333] C. W. Chou, A. L. Collopy, C. Kurz, Y. Lin, M. E. Harding, P. N. Plessow, T. Fortier, S. Diddams, D. Leibfried, and D. R. Leibrandt, "Frequency-comb spectroscopy on pure quantum states of a single molecular ion," Science **367**, 1458–1461 (2020).

[334] K. B. Ng, Y. Zhou, L. Cheng, N. Schlossberger, S. Y. Park, T. S. Roussy, L. Caldwell, Y. Shagam, A. J. Vigil, E. A. Cornell, and J. Ye, "Spectroscopy on the electron-electric-dipole-moment–sensitive states of ThF^+," Phys. Rev. A **105**, 022823 (2022).

[335] R. Glöckner, A. Prehn, B. G. U. Englert, G. Rempe, and M. Zeppenfeld, "Rotational cooling of trapped polyatomic molecules," Phys. Rev. Lett. **115**, 233001 (2015).

[336] M. Zeppenfeld, *Electric trapping and cooling of polyatomic molecules*, Ph.D. thesis, Technical University of Munich (2013).

[337] W. C. Campbell, G. C. Groenenboom, H.-I. Lu, E. Tsikata, and J. M. Doyle, "Time-domain measurement of spontaneous vibrational decay of magnetically trapped NH," Phys. Rev. Lett. **100**, 083003 (2008).

[338] O. O. Versolato, M. Schwarz, A. K. Hansen, A. D. Gingell, A. Windberger, L. Kłosowski, J. Ullrich, F. Jensen, J. R. Crespo López-Urrutia, and M. Drewsen, "Decay rate measurement of the first vibrationally excited state of MgH^+ in a cryogenic paul trap," Phys. Rev. Lett. **111**, 053002 (2013).

[339] V. V. Kozlov, Y. Rostovtsev, and M. O. Scully, "Inducing quantum coherence via decays and incoherent pumping with application to population trapping, lasing without inversion, and quenching of spontaneous emission," Phys. Rev. A **74**, 063829 (2006).

[340] T. V. Tscherbul and P. Brumer, "Long-lived quasistationary coherences in a v-type system driven by incoherent light," Phys. Rev. Lett. **113**, 113601 (2014).

[341] A. Dodin, T. Tscherbul, R. Alicki, A. Vutha, and P. Brumer, "Secular versus nonsecular Redfield dynamics and Fano coherences in incoherent excitation: An experimental proposal," Phys. Rev. A **97**, 013421 (2018).

[342] N. B. Vilas, P. Robichaud, C. Hallas, J. Tao, L. Anderegg, G. K. Li, H. Lampson, L. D. Augustovičová, J. L. Bohn, and J. M. Doyle, "Quantum-state-controlled collisions of ultracold polyatomic molecules," arXiv:2505.09592 (2025).

[343] G. Herzberg, *Spectra of diatomic molecules, molecular spectra and molecular structure* (Van Nostrand, New York, 1950).

[344] D. DeMille, J. M. Doyle, and A. O. Sushkov, "Probing the frontiers of particle physics with tabletop-scale experiments," Science **357**, 990–994 (2017).

[345] T. E. Chupp, P. Fierlinger, M. J. Ramsey-Musolf, and J. T. Singh, "Electric dipole moments of atoms, molecules, nuclei, and particles," Rev. Mod. Phys. **91**, 015001 (2019).

[346] C. Cesarotti, Q. Lu, Y. Nakai, A. Parikh, and M. Reece, "Interpreting the electron EDM constraint," Journal of High Energy Physics **2019** (2019).

[347] M. Pospelov and A. Ritz, "Electric dipole moments as probes of new physics," Annals of Physics **318**, 119–169 (2005).

[348] R. Alarcon, J. Alexander, V. Anastassopoulos, T. Aoki, R. Baartman, S. Baeßler, L. Bartoszek, D. H. Beck, F. Bedeschi, R. Berger, M. Berz, H. L. Bethlem, T. Bhattacharya, M. Blaskiewicz, T. Blum, T. Bowcock, A. Borschevsky, K. Brown, D. Budker, S. Burdin, B. C. Casey, G. Casse, G. Cantatore, L. Cheng, T. Chupp, V. Cianciolo, V. Cirigliano, S. M. Clayton, C. Crawford, B. P. Das, H. Davoudiasl, J. de Vries, D. DeMille, D. Denisov, M. V. Diwan, J. M. Doyle, J. Engel, G. Fanourakis, R. Fatemi, B. W. Filippone, V. V. Flambaum, T. Fleig, N. Fomin, W. Fischer, G. Gabrielse, R. F. G. Ruiz, A. Gardikiotis, C. Gatti, A. Geraci, J. Gooding, B. Golub, P. Graham, F. Gray, W. C. Griffith, S. Haciomeroglu, G. Gwinner, S. Hoekstra, G. H. Hoffstaetter, H. Huang, N. R. Hutzler, M. Incagli, T. M. Ito, T. Izubuchi, A. M. Jayich, H. Jeong, D. Kaplan, M. Karuza, D. Kawall, O. Kim, I. Koop, W. Korsch, E. Korobkina, V. Lebedev, J. Lee, S. Lee, R. Lehnert, K. K. H. Leung, C.-Y. Liu, J. Long, A. Lusiani, W. J. Marciano, M. Maroudas, A. Matlashov, N. Matsumoto, R. Mawhorter, F. Meot, E. Mereghetti, J. P. Miller, W. M. Morse, J. Mott, Z. Omarov, L. A. Orozco, C. M. O'Shaughnessy, C. Ozben, S. Park, R. W. Pattie, A. N. Petrov, G. M. Piacentino, B. R. Plaster, B. Podobedov, M. Poelker, D. Pocanic, V. S. Prasannaa, J. Price, M. J. Ramsey-Musolf, D. Raparia, S. Rajendran, M. Reece, A. Reid, S. Rescia, A. Ritz, B. L. Roberts, M. S. Safronova, Y. Sakemi, P. Schmidt-Wellenburg, A. Shindler, Y. K. Semertzidis, A. Silenko, J. T. Singh, L. V. Skripnikov, A. Soni, E. Stephenson, R. Suleiman, A. Sunaga, M. Syphers, S. Syritsyn, M. R. Tarbutt, P. Thoerngren, R. G. E. Timmermans, V. Tishchenko, A. V. Titov, N. Tsoupas, S. Tzamarias, A. Variola, G. Venanzoni, E. Vilella, J. Vossebeld, P. Winter, E. Won, A. Zelenski, T. Zelevinsky, Y. Zhou, and K. Zioutas, "Electric dipole moments and the search for new physics," arXiv:2203.08103 (2022).

[349] Y. Zhou, Y. Shagam, W. B. Cairncross, K. B. Ng, T. S. Roussy, T. Grogan, K. Boyce, A. Vigil, M. Pettine, T. Zelevinsky, J. Ye, and E. A. Cornell, "Second-Scale Coherence Measured at the Quantum Projection Noise Limit with Hundreds of Molecular Ions," Phys. Rev. Lett. **124**, 053201 (2020).

[350] K. Gaul and R. Berger, "Ab initio study of parity and time-reversal violation in laser-coolable triatomic molecules," Phys. Rev. A **101**, 012508 (2020).

[351] B. L. Augenbraun, Z. D. Lasner, A. Frenett, H. Sawaoka, A. T. Le, J. M. Doyle, and T. C. Steimle, "Observation and laser spectroscopy of ytterbium monomethoxide, $YbOCH_3$," Phys. Rev. A **103**, 022814 (2021).

[352] A. Jadbabaie, Y. Takahashi, N. H. Pilgram, C. J. Conn, Y. Zeng, C. Zhang, and N. R. Hutzler, "Characterizing the fundamental bending vibration of a linear polyatomic molecule for symmetry violation searches," New Journal of Physics **25**, 073014 (2023).

[353] N. Schlosser, G. Reymond, I. Protsenko, and P. Grangier, "Sub-poissonian loading of single atoms in a microscopic dipole trap," Nature **411**, 1024–1027 (2001).

[354] N. Schlosser, G. Reymond, and P. Grangier, "Collisional blockade in microscopic optical dipole traps," Phys. Rev. Lett. **89**, 023005 (2002).

[355] M. Endres, H. Bernien, A. Keesling, H. Levine, E. R. Anschuetz, A. Krajenbrink, C. Senko, V. Vuletic, M. Greiner, and M. D. Lukin, "Atom-by-atom assembly of defect-free one-dimensional cold atom arrays," Science **354**, 1024–1027 (2016).

[356] D. Barredo, V. Lienhard, S. de Léséleuc, T. Lahaye, and A. Browaeys, "Synthetic three-dimensional atomic structures assembled atom by atom," Nature **561**, 79–82 (2018).

[357] D. Bluvstein, H. Levine, G. Semeghini, T. T. Wang, S. Ebadi, M. Kalinowski, A. Keesling, N. Maskara, H. Pichler, M. Greiner, V. Vuletić, and M. D. Lukin, "A quantum processor based on coherent transport of entangled atom arrays," Nature **604**, 451–456 (2022).

[358] A. M. Kaufman and K.-K. Ni, "Quantum science with optical tweezer arrays of ultracold atoms and molecules," Nature Physics **17**, 1324–1333 (2021).

[359] A. Browaeys and T. Lahaye, "Many-body physics with individually controlled Rydberg atoms," Nature Physics **16**, 132–142 (2020).

[360] H. Levine, A. Keesling, G. Semeghini, A. Omran, T. T. Wang, S. Ebadi, H. Bernien, M. Greiner, V. Vuletić, H. Pichler, and M. D. Lukin, "Parallel implementation of high-fidelity multiqubit gates with neutral atoms," Phys. Rev. Lett. **123**, 170503 (2019).

[361] S. J. Evered, D. Bluvstein, M. Kalinowski, S. Ebadi, T. Manovitz, H. Zhou, S. H. Li, A. A. Geim, T. T. Wang, N. Maskara, H. Levine, G. Semeghini, M. Greiner, V. Vuletić, and M. D. Lukin, "High-fidelity parallel entangling gates on a neutral-atom quantum computer," Nature **622**, 268–272 (2023).

[362] H. Bernien, S. Schwartz, A. Keesling, H. Levine, A. Omran, H. Pichler, S. Choi, A. S. Zibrov, M. Endres, M. Greiner, *et al.*, "Probing many-body dynamics on a 51-atom quantum simulator," Nature **551**, 579–584 (2017).

[363] S. Ebadi, T. T. Wang, H. Levine, A. Keesling, G. Semeghini, A. Omran, D. Bluvstein, R. Samajdar, H. Pichler, W. W. Ho, S. Choi, S. Sachdev, M. Greiner, V. Vuletić, and M. D. Lukin, "Quantum phases of matter on a 256-atom programmable quantum simulator," Nature **595**, 227–232 (2021).

[364] P. Scholl, M. Schuler, H. J. Williams, A. A. Eberharter, D. Barredo, K.-N. Schymik, V. Lienhard, L.-P. Henry, T. C. Lang, T. Lahaye, A. M. Läuchli, and A. Browaeys, "Quantum simulation of 2D antiferromagnets with hundreds of Rydberg atoms," Nature **595**, 233–238 (2021).

[365] G. Semeghini, H. Levine, A. Keesling, S. Ebadi, T. T. Wang, D. Bluvstein, R. Verresen, H. Pichler, M. Kalinowski, R. Samajdar, A. Omran, S. Sachdev, A. Vishwanath, M. Greiner, V. Vuletić, and M. D. Lukin, "Probing topological spin liquids on a programmable quantum simulator," Science **374**, 1242–1247 (2021).

[366] M. A. Norcia, A. W. Young, W. J. Eckner, E. Oelker, J. Ye, and A. M. Kaufman, "Seconds-scale coherence on an optical clock transition in a tweezer array," Science **366**, 93–97 (2019).

[367] I. S. Madjarov, A. Cooper, A. L. Shaw, J. P. Covey, V. Schkolnik, T. H. Yoon, J. R. Williams, and M. Endres, "An atomic-array optical clock with single-atom readout," Phys. Rev. X **9**, 041052 (2019).

[368] A. W. Young, W. J. Eckner, W. R. Milner, D. Kedar, M. A. Norcia, E. Oelker, N. Schine, J. Ye, and A. M. Kaufman, "Half-minute-scale atomic coherence and high relative stability in a tweezer clock," Nature **588**, 408–413 (2020).

[369] L. A. Reynolds, E. Schwartz, U. Ebling, M. Weyland, J. Brand, and M. F. Andersen, "Direct measurements of collisional dynamics in cold atom triads," Phys. Rev. Lett. **124**, 073401 (2020).

[370] D. K. Ruttley, A. Guttridge, S. Spence, R. C. Bird, C. R. Le Sueur, J. M. Hutson, and S. L. Cornish, "Formation of ultracold molecules by merging optical tweezers," Phys. Rev. Lett. **130**, 223401 (2023).

[371] M. Hirsch, R. J. Wareham, M. L. Martin-Fernandez, M. P. Hobson, and D. J. Rolfe, "A stochastic model for electron multiplication charge-coupled devices – from theory to practice," PLOS ONE **8**, 1–13 (2013).

[372] S. Raouafi, G.-H. Jeung, and C. Jungen, "Permanent and transition dipole moments in CaF and CaCl," The Journal of Chemical Physics **115**, 7450–7459 (2001).

[373] Y. Yu, K. Wang, J. D. Hood, L. R. B. Picard, J. T. Zhang, W. B. Cairncross, J. M. Hutson, R. Gonzalez-Ferez, T. Rosenband, and K.-K. Ni, "Coherent optical creation of a single molecule," Phys. Rev. X **11**, 031061 (2021).

[374] A. B. Henson, S. Gersten, Y. Shagam, J. Narevicius, and E. Narevicius, "Observation of resonances in penning ionization reactions at sub-Kelvin temperatures in merged beams," Science **338**, 234–238 (2012).

[375] J. L. Bohn, "Inelastic collisions of ultracold polar molecules," Phys. Rev. A **63**, 052714 (2001).

[376] S. Jurgilas, A. Chakraborty, C. J. H. Rich, L. Caldwell, H. J. Williams, N. J. Fitch, B. E. Sauer, M. D. Frye, J. M. Hutson, and M. R. Tarbutt, "Collisions between ultracold molecules and atoms in a magnetic trap," Phys. Rev. Lett. **126**, 153401 (2021).

[377] M. T. Bell and T. P. Softley, "Ultracold molecules and ultracold chemistry," Molecular Physics **107**, 99–132 (2009).

[378] J. L. Bohn, M. Cavagnero, and C. Ticknor, "Quasi-universal dipolar scattering in cold and ultracold gases," New Journal of Physics **11**, 055039 (2009).

[379] M. Cavagnero and C. Newell, "Inelastic semiclassical collisions in cold dipolar gases," New Journal of Physics **11**, 055040 (2009).

[380] H. Levine, D. Bluvstein, A. Keesling, T. T. Wang, S. Ebadi, G. Semeghini, A. Omran, M. Greiner, V. Vuletić, and M. D. Lukin, "Dispersive optical systems for scalable Raman driving of hyperfine qubits," Phys. Rev. A **105**, 032618 (2022).

[381] H. J. Levine, *Quantum Information Processing and Quantum Simulation with Programmable Rydberg Atom Arrays*, Ph.D. thesis, Harvard University (2021).

[382] P. Horowitz and W. Hill, *The Art of Electronics: The X Chapters* (Cambridge University Press, 2020).

[383] H. R. Sadeghpour, J. L. Bohn, M. J. Cavagnero, B. D. Esry, I. I. Fabrikant, J. H. Macek, and A. R. P. Rau, "Collisions near threshold in atomic and molecular physics," Journal of Physics B: Atomic, Molecular and Optical Physics **33**, R93 (2000).

[384] M. Lemeshko, R. V. Krems, J. M. Doyle, and S. Kais, "Manipulation of molecules with electromagnetic fields," Mol. Phys. **111**, 1648–1682 (2013).

[385] C. Whitham, S. Beaton, Y. Ito, and J. Brown, "Laser excitation spectroscopy of the $\widetilde{B}^2A_1 - \widetilde{X}^2A_1$ transition of the $CaOCH_3$ radical," Journal of Molecular Spectroscopy **191**, 286–294 (1998).

[386] P. Crozet, F. Martin, A. Ross, C. Linton, M. Dick, and A. Adam, "The $\widetilde{A}^2E - \widetilde{X}^2A_1$ System of $CaOCH_3$," J. Mol. Spectrosc. **213**, 28 – 34 (2002).

[387] Y. Endo, S. Saito, and E. Hirota, "The microwave spectrum of the methoxy radical ch30," The Journal of Chemical Physics **81**, 122–135 (1984), https://pubs.aip.org/aip/jcp/article-pdf/81/1/122/18948867/122_1_online.pdf .

[388] C. R. Brazier and P. F. Bernath, "The $\widetilde{A}^2E - \widetilde{X}^2A_1$ transition of monomethyl calcium: A rotational analysis," J. Chem. Phys. **91**, 4548–4554 (1989).

[389] A. J. Marr, F. Grieman, and T. C. Steimle, "A molecular beam optical/stark study of calcium monomethyl," J. Chem. Phys. **105**, 3930–3937 (1996).

[390] J. M. Brown, "Rotational energy levels of symmetric top molecules in ^2e states," Mol. Phys. **20**, 817–834 (1971).

[391] J. T. Hougen, "Double group considerations, Jahn-Teller induced rovibronic effects, and the nuclear spin-electron spin hyperfine Hamiltonian for a molecule of symmetry C_{3v} in an electronic ^2E state," J. Mol. Spectrosc. **81**, 73 – 92 (1980).

[392] R. Wormsbecher and R. Suenram, "Laser spectroscopy and chemiluminescence from the monomethoxides of Ca, Sr, and Ba," Journal of Molecular Spectroscopy **95**, 391–404 (1982).

[393] B. Sheehy, S.-Q. Shang, P. van der Straten, S. Hatamian, and H. Metcalf, "Magnetic-field-induced laser cooling below the Doppler limit," Phys. Rev. Lett. **64**, 858–861 (1990).

[394] M. V. Ivanov, S. Gulania, and A. I. Krylov, "Two cycling centers in one molecule: Communication by through-bond interactions and entanglement of the unpaired electrons," J. Phys. Chem. Lett. **11**, 1297–1304 (2020).

[395] J. Kłos and S. Kotochigova, "Prospects for laser cooling of polyatomic molecules with increasing complexity," Phys. Rev. Research **2**, 013384 (2020).

[396] M. D. Hoogerland, H. C. W. Beijerinck, K. A. H. van Leeuwen, P. van der Straten, and H. J. Metcalf, "Magnetically induced laser cooling for Ne*: Approaching the recoil limit," Europhys. Lett. **19**, 669–674 (1992).

[397] E. Lavert-Ofir, Y. Shagam, A. B. Henson, S. Gersten, J. Klos, P. S. Zuchowski, J. Narevicius, and E. Narevicius, "Observation of the isotope effect in sub-Kelvin reactions," Nature Chemistry **6**, 332–335 (2014).

[398] J. Küpper, F. Filsinger, and G. Meijer, "Manipulating the motion of large neutral molecules," Faraday Discuss. **142**, 155–173 (2009).

[399] Z.-D. Sun, "Separation and conversion dynamics of four nuclear spin isomers of ethylene," Science **310**, 1938–1941 (2005).

[400] T. Kravchuk, M. Reznikov, P. Tichonov, N. Avidor, Y. Meir, A. Bekkerman, and G. Alexandrowicz, "A magnetically focused molecular beam of ortho-water," Science **331**, 319–321 (2011).

[401] Z.-D. Sun, M. Ge, and Y. Zheng, "Separation and conversion dynamics of nuclear-spin isomers of gaseous methanol," Nat. Commun. **6**, 6877 (2015).

[402] A. W. Young, W. J. Eckner, N. Schine, A. M. Childs, and A. M. Kaufman, "Tweezer-programmable 2D quantum walks in a Hubbard-regime lattice," Science **377**, 885–889 (2022).

[403] A. J. Marr, M. Tanimoto, D. Goodridge, and T. C. Steimle, "A study of the $\widetilde{A}^2B_2 - \widetilde{X}^2A_1$ band system of $CaNH_2$ employing molecular beam optical Stark spectroscopy," The Journal of Chemical Physics **103**, 4466–4475 (1995).

[404] Z. Morbi, C. Zhao, J. W. Hepburn, and P. F. Bernath, "High-resolution visible laser spectroscopy of the $\widetilde{B}^2B_1 - \widetilde{X}^2A_1$ transition of $CaNH_2$," The Journal of Chemical Physics **108**, 8891–8898 (1998).

[405] Z. Morbi, C. Zhao, and P. F. Bernath, "A high-resolution analysis of the $\widetilde{C}^2A_1 - \widetilde{X}^2A_1$ transition of $CaNH_2$: Pure precession in polyatomic molecules," The Journal of Chemical Physics **106**, 4860–4868 (1997).

[406] M. A. Brewster and L. M. Ziurys, "The pure rotational spectrum of $CaNH_2$ and $CaND_2$ ($\widetilde{X}^2A_1$): Additional proof of planarity," The Journal of Chemical Physics **113**, 3141–3149 (2000).

[407] C. N. Jarman and P. F. Bernath, "A high-resolution analysis of the $\widetilde{A}^2A' - \widetilde{X}^2A'$ transition of CaSH by laser excitation spectroscopy," The Journal of Chemical Physics **98**, 6697–6703 (1993).

[408] C. T. Scurlock, T. Henderson, S. Bosely, K. Y. Jung, and T. C. Steimle, "Molecular beam optical stark spectroscopy of CaSH," The Journal of Chemical Physics **100**, 5481–5490 (1994).

[409] P. M. Sheridan, M. J. Dick, J.-G. Wang, and P. F. B. and, "High-resolution investigation of the excited electronic states of CaSH and SrSH by laser excitation spectroscopy," Molecular Physics **105**, 569–583 (2007).

[410] C. R. Brazier and P. F. Bernath, "Observation of gas phase organometallic free radicals: Monomethyl derivatives of calcium and strontium," The Journal of Chemical Physics **86**, 5918–5922 (1987).

[411] R. N. Zare, *Angular Momentum: Understanding spatial aspects in chemistry and physics* (John Wiley & Sons, 1988).

[412] R. A. Frosch and H. M. Foley, "Magnetic hyperfine structure in diatomic molecules," Phys. Rev. **88**, 1337–1349 (1952).

[413] Y. Endo, C. Yamada, S. Saito, and E. Hirota, "The microwave spectrum of the trifluoromethyl radical," The Journal of Chemical Physics **77**, 3376–3382 (1982).

[414] J. Chen, J. Gengler, T. C. Steimle, and J. M. Brown, "Optical Zeeman spectroscopy of calcium monohydride," Phys. Rev. A **73**, 012502 (2006).

[415] E. B. Wilson, J. C. Decius, and P. C. Cross, *Molecular Vibrations: The Theory of Infrared and Raman Vibrational Spectra* (New York: Dover Publications, 1955).

[416] T. Sharp and H. Rosenstock, "Franck-Condon factors for polyatomic molecules," J. Chem. Phys. **41**, 3453–3463 (1964).

[417] J. Weber and G. Hohlneicher, "Franck-Condon factors for polyatomic molecules," Mol. Phys. **101**, 2125–2144 (2003).

[418] C. Brazier and P. Bernath, "Laser and Fourier transform spectroscopy of the $\tilde{A}^2\Pi$-$\tilde{X}^2\Sigma^+$ transition of SrOH," J. Mol. Spectrosc. **114**, 163–173 (1985).

[419] S. Kinsey-Nielsen, C. R. Brazier, and P. F. Bernath, "Rotational analysis of the $\tilde{B}\,^2\Sigma^+ - \tilde{X}^2\Sigma^+$ transition of BaOH and BaOD," J. Chem. Phys. **84**, 698–708 (1986).

[420] J. A. Coxon, M. Li, and P. I. Presunka, "Laser spectroscopy of the (010)$^2\Sigma^{(+)}$, $^2\Sigma^{(-)}$ -(000) $^2\Sigma^+$ parallel bands in the $\widetilde{A}^2\Pi - \widetilde{X}^2\Sigma^+$system of CaOH," J. Mol. Spectrosc. **164**, 118–128 (1994).

[421] J. Aarts, "The Renner effect in $^2\Pi$ electronic states of linear triatomic molecules," Mol. Phys. **35**, 1785–1803 (1978).

[422] J. M. Brown and F. Jorgensen, "Vibronic energy levels of a linear triatomic molecule in a degenerate electronic state: a unified treatment of the Renner-Teller effect," in *Advances in Chemical Physics, Volume LII*, edited by I. Prigogine and S. A. Rice (Wiley & Sons Ltd., 1983) pp. 117–180.

[423] P. Jensen, G. Osmann, and P. R. Bunker, "The Renner effect," in *Computational Molecular Spectroscopy*, edited by P. Jensen and P. R. Bunker (Wiley & Sons Ltd., 2000) Chap. 15, pp. 485–515.

[424] J. M. Brown, "The Renner-Teller effect: The effective Hamiltonian approach," in *Computational Molecular Spectroscopy*, edited by P. Jensen and P. R. Bunker (Wiley & Sons Ltd., 2000) Chap. 16, pp. 517–537.

[425] J. M. Brown, "The rotational dependence of the Renner-Teller interaction: a new term in the effective Hamiltonian for linear triatomic molecules in Π electronic states," Mol. Phys. **101**, 3419–3426 (2003).

[426] J. Koput and K. A. Peterson, "Ab initio potential energy surface and vibrational-rotational energy levels of $X^2\Sigma^+$ CaOH," J. Phys. Chem. A **106**, 9595–9599 (2002).

[427] P. Bernath and C. Brazier, "Spectroscopy of CaOH," The Astrophysical Journal **288**, 373–376 (1985).

[428] J. A. Coxon, M. Li, and P. I. Presunka, "Laser fluorescence excitation spectroscopy of CaOH and CaOD: The $\widetilde{A}^2\Pi$-$\widetilde{X}^2\Sigma^+$(100)-(000) band system and the (100)-(020) Fermi resonance," Journal of Molecular Spectroscopy **150**, 33–45 (1991)

ProQuest Number: 32042685

INFORMATION TO ALL USERS
The quality and completeness of this reproduction is dependent on the quality
and completeness of the copy made available to ProQuest.

Distributed by
ProQuest LLC a part of Clarivate (2025).
Copyright of the Dissertation is held by the Author unless otherwise noted.

This work is protected against unauthorized copying under Title 17,
United States Code and other applicable copyright laws.

This work may be used in accordance with the terms of the Creative Commons license
or other rights statement, as indicated in the copyright statement or in the metadata
associated with this work. Unless otherwise specified in the copyright statement
or the metadata, all rights are reserved by the copyright holder.

ProQuest LLC
789 East Eisenhower Parkway
Ann Arbor, MI 48108 USA